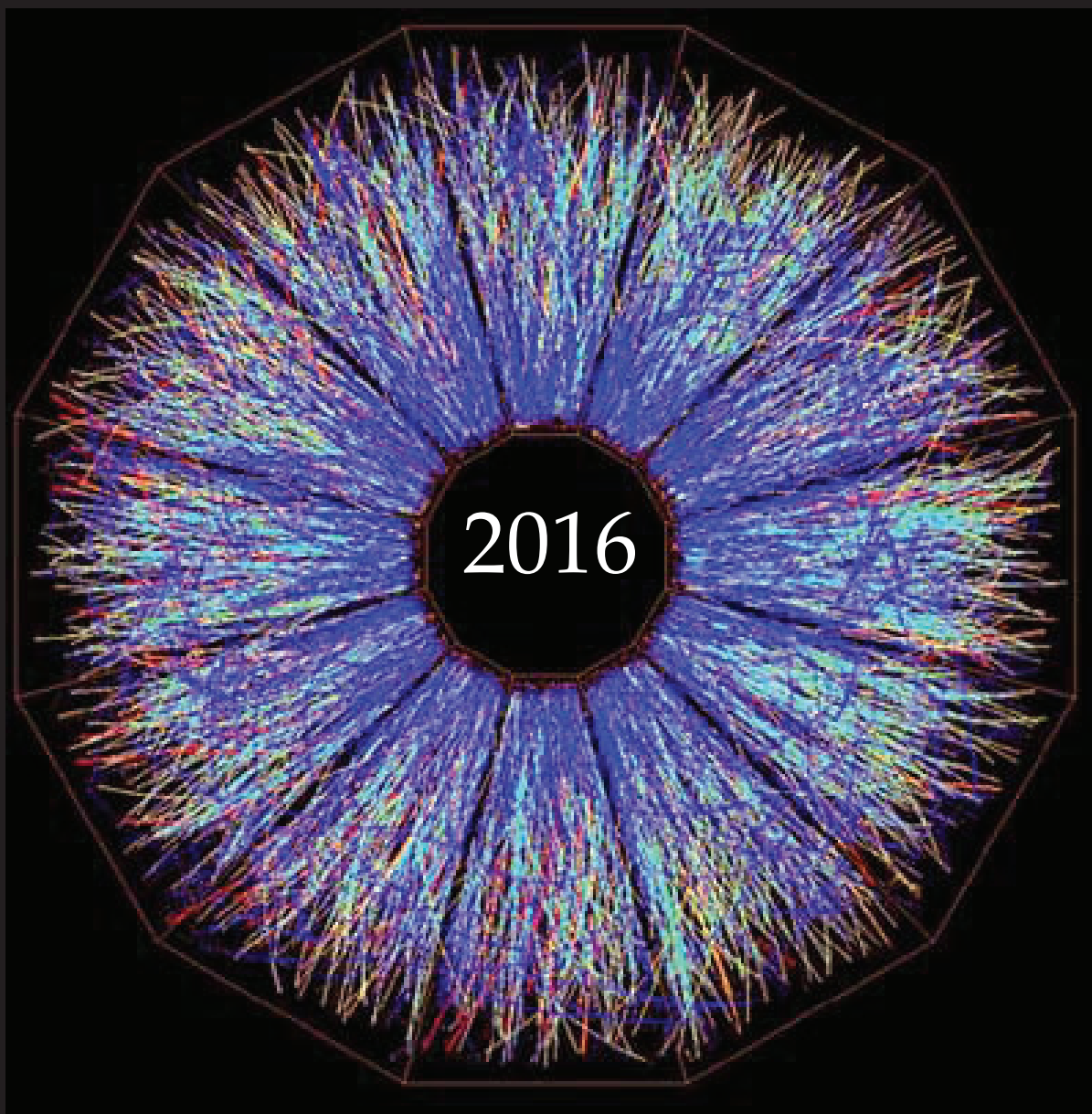


A Compilation of Internship Reports



Prepared for The Office of Educational Programs
Brookhaven National Laboratory
Office of Educational Programs

DISCLAIMER

This work was prepared as an account of work sponsored by an agency of the United States Government. Neither the United States Government nor any agency thereof, nor any of their employees, nor any of their contractors, subcontractors or their employees, makes any warranty, express or implied, or assumes any legal liability or responsibility for the accuracy, completeness, or any third party's use or the results of such use of any information, apparatus, product, or process disclosed, or represents that its use would not infringe privately owned rights. Reference herein to any specific commercial product, process, or service by trade name, trademark, manufacturer, or otherwise, does not necessarily constitute or imply its endorsement, recommendation, or favoring by the United States Government or any agency thereof or its contractors or subcontractors. The views and opinions of authors expressed herein do not necessarily state or reflect those of the United States Government or any agency thereof.



BROOKHAVEN
NATIONAL LABORATORY

Table of Contents

Creating a protection system using strain gages and level probes for the LARP (LHC accelerator research program) magnet	7
<i>Rajith Radhakrishnan and Rishi Anand</i>	
The interaction of ionizing radiation with soft tissue	10
<i>Jessica Abbruzzese and Mamoudou Ba</i>	
Testing compression algorithms for macromolecular diffraction images.	13
<i>Kaden Badalian and Herbert J. Bernstein</i>	
Biochemical and genetic analysis of lipid mutants of Arabidopsis	17
<i>Christopher Baglivi</i>	
Maximizing computing efficiency through cycle-scavenging in a high performance computing environment	19
<i>Joshua Barnett</i>	
Wildland/Urban fire interface: prevention and the development of new innovative fire suppression tactics for wildfire	23
<i>Jonathan Bernal</i>	
Synthesis and characterization of weakly coordinating anions and cations as electrolytes in low polarity solvents.	29
<i>Rebecca Boucard, Paige Reagan, and Ghislain Mandouma</i>	
High precision gamma-ray spectroscopy for enhancing applications of the medical isotopes Bromine-77 and Manganese-52.	33
<i>B.A. Broder</i>	
Effects of electron delocalization on infrared vibrations and redox potentials	38
<i>Chase Bryant, Danielle Caro, and Juchao Yan</i>	
Design and analyses of fixtures and tools for the sPHENIX calorimeters	43
<i>Brenna Buckley</i>	
Analyzing time-dependent noise in the MicroBooNE experiment and parallel track reconstruction in liquid argon time-projection chambers	47
<i>Brendon Bullard</i>	
Design and analysis of the cradle support structure: Transportation components and alignment mechanisms for the sPHENIX Project at RHIC	57
<i>Daniel Cacace</i>	
Coil assembly for direct current solenoid gun corrector magnets	63
<i>Taylor Campbell</i>	
Measuring inorganic aerosol composition with the Particle Into Liquid Sampler (PILS) . . .	66
<i>Mark Chan</i>	
Developing an Arduino controlled datalogger for pyranometers	71
<i>Daniel Christiansen</i>	
Reviving a demo synchrotron	77
<i>Melissa De Jesus</i>	
Development of an electronic testing framework and procedures for protoDUNE	81
<i>Amanda Depoian</i>	

Optimization of the LBNF/DUNE beamline for tau neutrinos.	85
<i>Michael Dolce</i>	
Development of real time data visualization and analysis software for the National Synchrotron Light Source II X-ray Powder Diffraction Beam Line.	90
<i>Caleb Duff</i>	
Cumulus congestus cloud growth during the Green Ocean Amazon 2014/5 campaign.	93
<i>Jordan Eissner</i>	
Comparing vegetative fuel loading and developing custom fuel models for Brookhaven National Laboratory.	98
<i>Sean Foote and Julia Riley</i>	
Mass calibration for the PROSPECT shortbaseline reactor neutrino experiment	105
<i>Nicholas Gabriel</i>	
A fundamental study and characterization of the surface structure of a Cs/TiO ₂ (110) model catalyst	109
<i>Isamar Garrido Rodriguez</i>	
Nuclear structure studies of ²⁰² Hg and ²⁰³ Tl using deep-inelastic collisions	112
<i>E. J. Gass</i>	
Structural study of polycyclic aromatic ligands and salen-type metal complexes	115
<i>Stephanie N. Ortiz Castillo Gellyz, N. Gonzalez Diaz, and Dalice M. Piñero Cruz</i>	
Design and implementation of temporary beam pipes and their stands for sPHENIX	119
<i>Howard Graham Giese</i>	
Measuring techniques for detecting axions through photon splitting	123
<i>Mal'Lica Gordon</i>	
Trending analysis of internal assessments within the radiological waste management division	126
<i>Matthew Harris</i>	
Catalytic aromatization of methane: ex and in situ structural determination of metal exchanged zeolite catalysts	130
<i>Tate Harvey and Sheima J. Khatib</i>	
Optimization of conductive carbon additive in Lithium-Sulfur (Li-S) battery.	138
<i>Jian Huang</i>	
Developing the dipole corrector power supply beam permit system	143
<i>Nida Imtiaz</i>	
Developing growth procedure and measuring spectral response of NaKSb photocathodes.	147
<i>Riley Joinnides</i>	
Testing and troubleshooting of High Temperature Superconductor Dipole Magnet Coils	151
<i>Shresht Joshi</i>	
Developing data process management routines in MATLAB for Thermo Gravimetric Analyzer experiments	154
<i>Javier Joya</i>	
Analysis of the electron-ion timing resolution in a proportional gas chamber.	163
<i>Ian D. Kotler, John Blakley, and Robert Neblett II</i>	

Simulating cosmic events in the protoDUNE detector	165
<i>Jacob Larkin</i>	
Evaluation of ^{86}Kr cross sections for use in fusion diagnostics	168
<i>Amanda Lewis</i>	
Designing and prototyping the electromagnetic calorimeter for sPHENIX	177
<i>Spencer Laddy-Locks</i>	
Designing new magnets for future circular colliders	180
<i>Nicholas Maineri</i>	
eRHIC 18 GeV electron storage ring: Magnet design with water cooling system, support facilities, and power supply analysis	184
<i>Lisa Marone</i>	
Thermal characterization of organic and inorganic compounds used in homemade explosives	188
<i>Morgan Matthews</i>	
Mechanism for CO oxidation over a CuO_x catalyst: An in situ XRD and DRIFTS study . . .	191
<i>Nataniel Medina Berríos</i>	
Tools for the characterization and improvement of the electron beam orbit stability for the National Synchrotron Light Source – II storage ring	197
<i>Jessica Mele</i>	
Pulsed reactant in-situ studies of copper doped ceria redox catalysis for CO oxidation using DRIFTS, XRD, and PSD	202
<i>Shane Michtavy</i>	
Determining the fluorescence quantum yield of a water-based liquid scintillator	203
Imaging ultrafast single photon events using the Timepix camera.	208
<i>Jayke Nguyen</i>	
Analyzing photographs of solar flare on a fish-eye camera lens	213
<i>John Pavacic</i>	
Visualizing cesium on hydrated titanium dioxide at the nanoscale	215
<i>Allison Pereira</i>	
An in situ examination of copper/ceria catalysts' properties and effects on the water-gas shift reaction mechanism	220
<i>David Salazar</i>	
Radiological surveying and monitoring of laboratories at Brookhaven National Laboratory	223
<i>Rachel Sanders and John Shlonsky</i>	
Radiation damage studies in silicon photomultiplier with gamma rays and neutrons.	225
<i>Taylor Shimek</i>	
Oxidation of ethanol under the surface of CeO_2 supported on Platinum using an electrochemical chamber setup.	236
<i>Joesene Soto, Angel Ortiz, and Carlos Cabrera</i>	
Integrated Facility Management: Keeping the laboratories alive	239
<i>Derek Squires</i>	
Relationship analysis between Order Chiroptera and burned forest areas	241
<i>Emma Squires</i>	

Analysis and design of thermal management concepts for sPHENIX calorimeters.	245
<i>Emily Tacopina</i>	
Development of automated batch workflow and real-time data processing for x-ray fluorescence tomography.	249
<i>Derek Tropf</i>	
Development of computer vision and image processing libraries at the National Synchrotron Light Source - II	252
<i>William Watson</i>	
A numerical model of the transverse feedback system for the National Synchrotron Light Source II storage ring	258
<i>Zechun Yang</i>	
Charge transfer efficiency of charge-coupled devices for the Large Synoptic Survey Telescope	263
<i>Daniel Yates</i>	

Creating a protection system using strain gages and level probes for the LARP (LHC accelerator research program) magnet

Rajith Radhakrishnan and Rishi Anand

Electrical Engineering, Stony Brook University, Stony Brook, NY, 11794

Piyush Joshi

Magnet Division, Brookhaven National Laboratory, Upton, NY, 11973

Abstract

Highly precise superconducting magnets are used to steer and collide two particles such as protons and heavy ions at speeds close to those of light. When accelerating these high energy particles, the magnet will be under heavy stress. In order to monitor the forces acting on the magnet, strain gages are used. A strain gage is a type of gage that will provide information on the amount of deformation that the magnet will undergo. These gages are placed on the outer/inner shell of the magnet and will provide the user with information on axial, torsion al, bending, and shear strain. The software that interfaces with hardware will acquire raw data from 64 strain gages placed along the magnet and will provide the user with interpretable information. The software, created using the LabVIEW programming environment, will use Data Acquisition technology from National Instruments to obtain the data. In addition to strain gages, the magnets will have liquid helium level probes to monitor the helium levels. The software had to be designed to obtain levels, and automatically control the valves to allow addition of liquid helium when the level decreases. These testing processes are crucial in order to design the next generation of superconducting magnets for the Relativistic Heavy Ion Collider (RHIC) and the Large Hadron Collider (LHC). In the process, we have learned about the physics behind strain gages, level probes and power electronics components like thyristors, silicon controlled rectifier (SCRs), and insulated-gate bipolar transistor (IGBTs) which

are used to control high current and voltage equipment. As an outcome, we expect to have design and fully implemented this protection system. We also had the opportunity to explore the field of cryogenics, and how it plays a major role in the workings of a superconducting magnet. Through this internship, we have gained experiences on how to design and test a superconducting magnet and are now familiar with the widely used LabVIEW program. This internship has also provided us with insight into modern day power electronics as our school mainly focuses on digital electronics.

I. Background

In order to accelerate high energy particles through a magnet at speeds closer to the speed of light, the magnet must be operating under a very high magnetic field (around 8 tesla). To achieve this, the magnet must be cooled down to 1.9K to reach its superconducting state of almost zero resistance, which allows for large currents to be conducted leading to a larger magnetic field. The process of bringing a magnet to its superconducting state requires a large amount of liquid helium in order to bring the temperature down. The changes in liquid helium level inside the magnets have to be precisely monitored and the valves supplying the liquid helium have to be opened and closed in response to these level changes. The levels are monitored with specially designed level probes that will monitor at temperatures of 4K and 1.9K liquid helium levels. The information from these probes will be used to control the valves using PID loops. When the liquid helium is

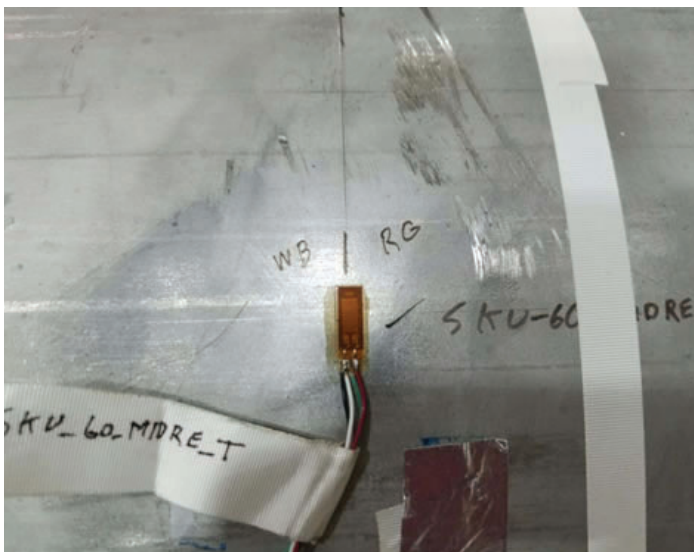


Figure 1 & 2: Figure 1 shows one of the 64 strain gages on the outer shell of the LARP test magnet. Figure 2 shows the chassis setup for the level probes. A cryostat filled with 60L of liquid helium is shown as it was used in for sensor calibration.

pumped to bring the magnet to a superconducting state, enormous strain builds up in the form of contraction. When turned off, the magnet will reach room temperature causing strain in the form of expansion on the outer and inner shell of the magnet. To monitor the stress, strain gages are placed in various locations that will allow one to see the amount of stress induced in that specific location. If any strain gage detects a change in resistance while the magnet is in its superconducting state, which could be attributed to any flux jumps or mechanical fault in the magnet construction, the program built around the strain gages should provide the user with sufficient information that could allow for measures in order to prevent damage to the magnet. If not attended to, the magnet will quench, drop from its superconducting state. In a superconducting magnet, if such an instance is not found quick enough, the magnet can burn from the growing resistance and high current.

II. Methods

A. Strain Gages

In implementing the strain gages, a chassis was built that would support up to 64 channels of data that would read voltages across the gauges, as well as, account for the corrected strain coefficients which is done in the LabView program built around it. The chassis consists of 8 relay cards connected to a Cytec scanner. Each relay card would read 8 channels, so 8 cards would result in the necessary 64 channels. The scanner would read the corresponding voltages for each strain gage from the terminal blocks above the scanner. The terminal blocks were used in order to terminate the corresponding ends of the hypertronics connector into the chassis. From there, the LabView implemented program will cycle through all 8 cards providing voltage read outs for all 64 channels. The resulting data obtained will then be compared to the corresponding data sheets provided for the strain gages for verification.

The program written for the strain gage readings was intended to provide the user with an easy interface for a quick analysis. The program includes a feature that will allow the user to either constantly monitor a single strain gage or do a scan of all strain gages. An option was included to allow a timed scan and an in-

stant scan. The timed scan will allow for data capture every couple of minutes as specified. This feature will be helpful in monitoring how the stress changes in the magnet throughout couple of hours or days or weeks. It will also be helpful in finding out in any particular area is undergoing a lot of strain when the magnet is hoisted up and down. Since each sensor does not function as per the theoretical prediction, a minor offset has to be made in order to obtain exact measurements. The program will allow user to easily monitor and change these offset values. The data obtained from the sensors will be automatically logged into a file. A file saving feature was implemented with an ability to save data on the same file or use different files based on different run. The names of the sensor will be automatically integrated into the file for easier analysis, along with date, time and the current that was entering in.

B. Level Probes

The level probe sensors are used to obtain the information regarding the liquid helium levels inside the dewar. The level probes are specially designed to operate at temperature of 4K and 2K liquid helium's. There are 14 liquid helium level probes that will be placed at specific spot in the dewar as shown in the figure below. These level probes are interfaced with the computer using transmitter boxes and Model 1800 instruments from the American magnetics. The transmitter will supply the current turn on a small heater built inside the probes. Since a wire will be having zero resistance when dipped, i.e reaching superconducting state, the heater will make the un-submerged part conducting, thus producing a voltage reading equivalent to the non exposed part of the probe. This voltage reading from these probes will be used to control the valves using PID loops. The model 1800 itself functions as a separate system by heating up the level probes at a constant interval and storing the data. A LabView program was designed to acquire the information from the sensors which are stored in the model 1800. The PID loop in the program will constantly monitor the levels, and open and close the valves automatically in order to adjust the liquid helium levels. The model 1800 instrument, transmitter, and the computer are connected in the same network switch, where the data will communicate over the network. There

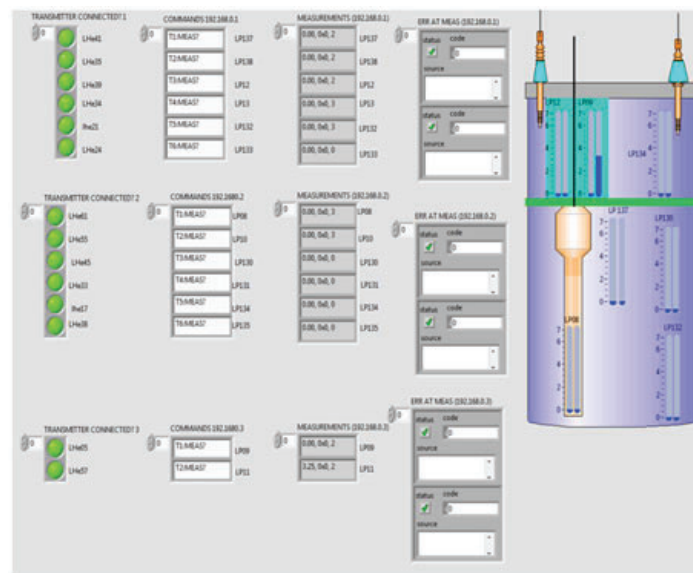
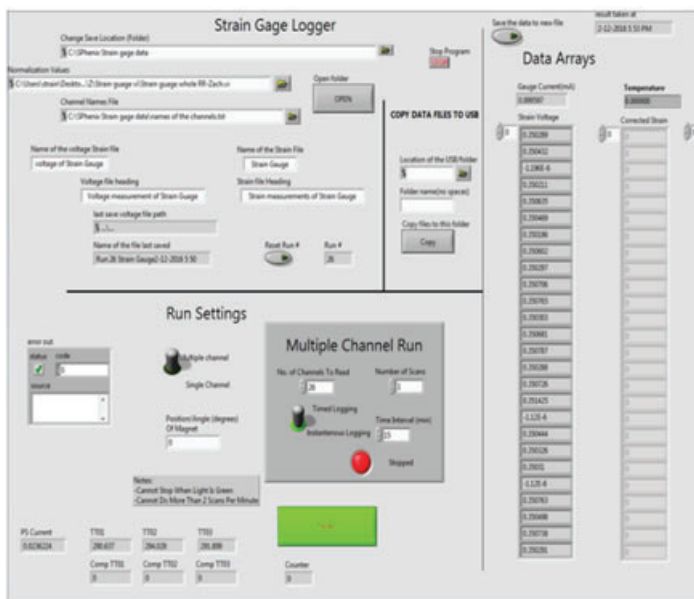


Figure 3 & 4: Figure 3 shows the program that will run through all 64 strain gauges. Figure 4 shows the structure of the dewar as well as the locations of the liquid helium sensors and their respective levels.

are transmitters calibrated specifically for 2k and 4k temperature level probes. The process of monitoring liquid helium level is critical since the superconducting magnet will quench or lose its superconducting state when the temperature rises above 4 Kelvin.

The instruments used to acquire the level measurement are newly released, and implemented for the first time in this lab. In addition to the strain gages, we were assigned with a task of setting up and programming the new instruments. Since the product was not well documented, the network port through which the communication occurred had to be figured out. Although the product was marketed to obtain reading from 8 different level probe sensor, by testing it was found that the instruments can only handle 6 sensors each. This information was supplied to the manufacturer and steps were taken to correcting the mistake in the firmware and the instrument.

III. Data and Results

Although the magnet has not been fully available for testing, the strain gage measurement program that was designed during the internship has helped to identify the sensors that were faulty. The error in the connections and wiring has also been fixed, and the whole chassis is ready to be deployed for extensive testing of the LARP magnet that will be used for the particle accelerator upgrade at CERN.

For the level probe testing, 60 liters of liquid helium was purchased in order to test the quality of the sensors, transmitter, instruments and the program controlling them. By comparing the data reading with a working level probe with a analog measurement device, the validity of the setup was confirmed. The program precisely outputted the reading and showed any changed the level probe movements. After extensively testing the setup is now connected the all the sensors that will be placed inside the dewars, and the program will be deployed once the superconducting magnet testing begins.

IV. References

¹LabVIEW. Program documentation. National Instruments. Vers. 2014. Public, n.d. Web. 28 July 2015. Continuous data acquisition and digital trigger. Piyush Joshi. 28 July 2016.

²“Measuring Strain with Strain Gages.” - National Instruments. N.p., 25 May 2016. Web. 01 Aug. 2016.

V. Acknowledgments

This project was supported in part by the U.S. Department of Energy, Office of Science, Office of Workforce Development for Teachers and Scientists (WDTS) under the Science Undergraduate Laboratory Internships Program (SULI). We would like to thank our mentor Piyush Joshi for his guidance in our projects as well as Sonny Dimaiuta , Rick Felter, Joe D’Ambra , Joe Muratore, Michael Hartsough, Drew Carleton ,and the rest of the employees who were kind enough to bring us under their supervision.

The interaction of ionizing radiation with soft tissue

Jessica Abbruzzese

Department of Cell Biology/Biochemistry, Bucknell University, Lewisburg, PA 17837

Mamoudou Ba

Department of Physics and Astronomy, State University of New York at New Paltz, New Paltz, NY 12561

Nicholaos Tsoupas

Collider Accelerator Department, Brookhaven National Laboratory, Upton, NY 11973

Stephen Kahn

Collider Accelerator Department, Brookhaven National Laboratory, Upton, NY 11973

Abstract

One of the techniques used to treat cancer patients is radiotherapy, which means irradiating tumor cells using ionizing radiation. Electrons and protons have been used extensively to treat shallow and deep cancer tumors, respectively, but Carbon-12 (^{12}C) may be a better alternative. Gamma radiation has also been used to treat brain tumors. In this project, we investigated the interaction between these ionizing radiations with soft tissue using simulation programs G4beamline. We obtain a Bragg curve by studying the energy loss by each particle as a function of the material depth. This Bragg curve reaches a Bragg peak at a depth called radiation length where most of the energy is deposited. The goal is to maximize the dose at the tumor location while minimizing the exposure of the surrounding body tissue. We compare the radiation lengths for protons at 250 MeV per nucleon, ^{12}C at 450 MeV per nucleon, electrons at 80 MeV per particle, and gamma rays at 500 keV. Minimizing beam scattering also minimizes the exposure of surrounding tissues, so by comparing the scattering for different sources, we can determine which might be better for targeting localized tumors. In addition to the radiation length, we also compare multiple scattering for these ionizing radiations at the peaks of their respective Bragg curves.

I. Introduction

Ionizing radiation can be either a particle or electromagnetic wave that has enough energy to remove an electron from an atom. The electromagnetic ionizing radiation can be in the form of gamma rays or x-rays. The high energy particles that are emitted are the electrons, protons, and other ions. Ionizing radiation can be used as a cancer treatment because it can kill tumor cells, however it can also damage normal cells that are nearby. Radiation therapy is based on the exposure of malignant tumor to significant doses of ionizing radiation to destroy the tumor cells. To observe the biological effects of the ionizing radiation we must know how much energy is deposited per particle for one radiation length which can be determined by the Bragg curve. The transverse beam spread must also be calculated for the ionizing radiation. These factors would show where the most energy is deposited in the body, hopefully directly at the site of the tumor. The radiation therapy most commonly used for tumors is gamma rays and electrons. There has been an increase in the use of proton radiation for tumors that are found deeper in the body. Research on carbon ion beams

has been on the rise as it seems to be another viable option for deep-seated tumors. It is currently only available at a few treatment centers around in Asia and Europe, but being considered in the United States to be used as a treatment along with other types of ionizing radiation. Gamma rays, electrons, protons and carbon ions were compared for a comprehensive overview of current ionizing radiation therapy.

II. Method

G4beamline is a simulation program that does particle tracking and calculations such as its kinetic energy, and its interactions with other particles. This program is used for designing particle accelerators and detectors. It has a variety of complex uses in high energy physics. In this project, we use G4beamline to simulate and study the interactions of various ionizing radiations with soft tissue. G4beamline uses the NIST Material Database, which is available on the web. Soft tissue used in this study has density of 1 g/cm³. And the chemical compositions of the material are listed in the table below.

The resulting system is shown in Figure 1, where protons at kinetic energy 250 MeV are interacting with soft tissue. That is followed by Figure 2, which shows gamma radiation interacting with the same material.

To calculate the total energy deposited in each material, we divided the soft tissue into layers. Each layer is 1 cm deep. Then we use the command “totalenergy” to get the energy deposited in that layer. The total energies obtained from this command are stored in a text file. We also needed to know how many particles were registered in each layer; so we placed a “zntuple” in front of each layer. This “zntuple” acts as a virtual detector. This does two things for us: one the number of particles in each layer is printed out on the screen, two a root file is generated that has the positions and momentums of each particle.

The following formula is called Bethe stopping power formula, which describes the mean energy loss of charged particles as they traverse into matter. Protons, and ^{12}C obey this equation when interacting with matter, but electrons and photons do not.

$$\left\langle -\frac{dE}{dx} \right\rangle = Kz^2 \frac{Z}{A} \frac{1}{\beta^2} \left[\frac{1}{2} \ln \frac{2m_e c^2 \beta^2 \gamma^2 W_{\max}}{I^2} - \beta^2 - \frac{\delta(\beta\gamma)}{2} \right]$$

element	H	C	N	O	Na	Mg	P	S	Cl	K	Ca	Fe	Zn
density	0.104472	0.23219	0.02488	0.630238	0.00113	0.00013	0.00133	0.00199	0.00134	0.00199	0.00023	5e-5	3e-5

Table 1. The chemical compositions of the soft tissue and their densities in g/cm³.

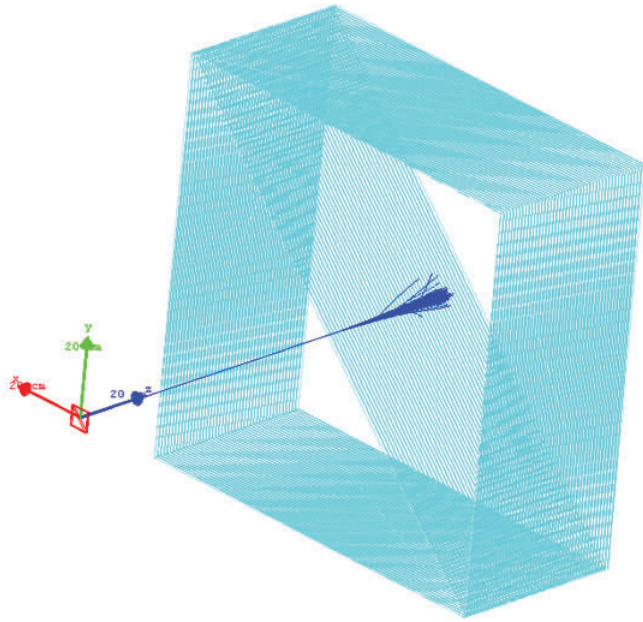


Figure 1. The interaction of protons at kinetic energy 250 MeV with soft tissue. The blue beam are positively charged particles (protons) emanating from a protons source in the z-direction towards the soft tissue.

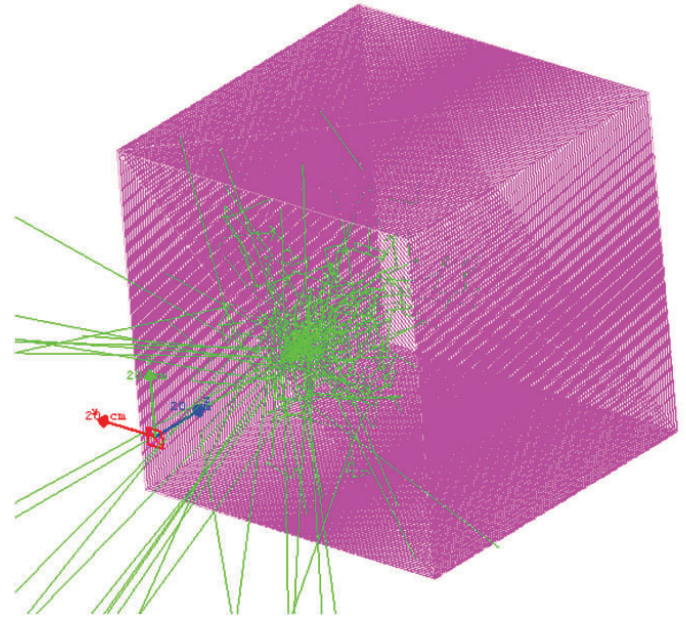


Figure 2. The interaction of neutrally charged particles (photons) at 500 keV with soft tissue. This is backscattering that originated from the photoelectric and compton interactions.

III. Analysis and Results

After the simulation is done and we have the text and root files, we proceed to analysis. To calculate the energy deposited per particle, per cm, we have to divide the total energy deposited

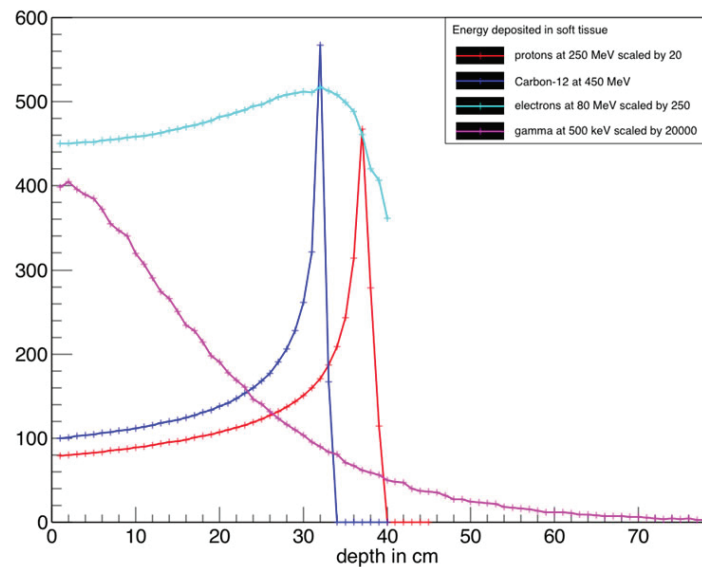


Figure 3. The interaction of ionizing radiation with soft tissue. Bragg curve for electrons at 80 MeV, gamma rays at 500 keV, protons at 250 MeV/n, and 12C at 450 MeV/n. For visualization, the curves were scaled by 20 for protons, 250 for electrons, and 20000 for gamma rays all in the vertical axes. The table below lists the radiation lengths for electrons, protons and 12C. The energy of the gamma rays is well below pair production range (which is greater than 1.1 MeV), so the observed interaction is due to photoelectric and compton effects.

Soft tissue	Electrons at 80 MeV	Protons at 250 MeV	12C at 450 MeV/n
Radiation length (cm)	32	37	32

Table 2. The radiation length for electrons, protons and 12C. The radiation length for gamma rays is not shown because they do not exhibit a Bragg peak. As Figure 3 shows, the energy of the gamma rays decreases exponentially.

in each layer of cm by the number of entries in that layer. This is $-dE/dx$ in the Bethe stopping power formula. If we plot that result as a function of the depth in cm, we obtain the curves in Figure 3. These are the well established Bragg curves that describe the interaction of ionizing radiation with matter.

The graph in Figure 3 shows the energy deposited by ionizing radiation with soft tissue. Bragg curve for electrons at 80 MeV, gamma radiation at 500 keV, protons at 250 MeV/n, and 12C at 450 MeV/n. For visualization, the curves were scaled by 20 for protons, 250 for electrons, and 20000 for gamma rays all in the vertical axes. The table below lists the radiation lengths for electrons, protons and 12C. The energy of the gamma rays is well below pair production range (which is greater than 1.1 MeV), so the observed interaction is due to photoelectric and compton effects.

Thus far, we have compared the radiations length for electrons, protons, 12C, and gamma radiation. Next we analyze the beam scattering. Ionizing radiation has various ways to interact with matter. Whether it is an electronic or nuclear interaction, the ionizing radiation is bound to completely lose its energy or change direction. Changing direction results in beam scattering; so at the radiation lengths listed in Table 2, we study how much the each beam scatters using the root file generated in the simulation. To achieve this, we need to draw a histogram of where the particles land in the x-axis. Then we perform a gaussian fit to the histogram assuming that this histogram is very well described by a gaussian distribution. The transverse beam scattering for protons, 12C, and electrons, the scattering was taken at the radiation length. For gamma rays, there is no obvious peak, so the scattering was taken at 1 cm. Scaling was applied for visualization:

Protons at 250 MeV kinetic energy is not scaled, while 12C at 450 MeV/n was scaled by $\frac{1}{2}$, electrons at 80 MeV was scaled by 3, and photons at 500 keV was not scaled but shifted to the left by 15 units. It is worth noting that for gamma rays, the gaussian distribution does not represent the simulation results. Comparing the RMS value we obtain from the histogram and the sigma from the fit, we can tell how well the gaussian distribution describes the simulation results.

IV. Conclusion

12C has the smallest transverse spread making it less likely to reach the surrounding normal tissue. The Bragg curve also showed a steeper peak for 12C, indicating that the highest dose of radiation will be deposited at the target tumor. In addition, 12C produces nuclear reactions involving the breaking of the 12C nucleus and the productions of other particles, but these events are not nearly enough to repulse the benefits of 12C therapy. So with all things considered, 12C is the more viable object for the patient. Although 12C seems like the best option for deep-seated tumors, it is not used in the United States because of its excessive cost and it's not covered by health insurance. Gamma rays still continue to be the most widely used form of radiation.

V. References

Cember, Herman and Thomas E. Johnson. Introduction to Health Physics. 4th ed. The McGraw-Hill Companies. USA. 2009.

Roberts, Tom. G4beamline User's Manual. Muons, Inc. 2016.

K.A. Olive et al. (Particle Data Group), Chinese Physics C38, 090001 (2014).

National Institute of Standards and Technology. Geant4 Material Database. June - August 2016.

National Cancer Institute at the National Institute of Health. July - August 2016. www.cancer.gov

World Health Organization. July-August 2016. www.WHO.int

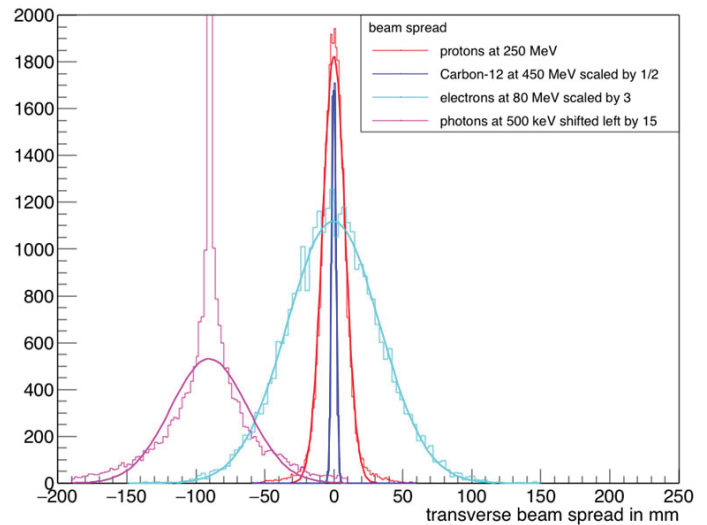


Figure 4. Transverse beam scattering. For protons, 12C, and electrons, the scattering was taken at the radiation length. For gamma rays, there is no obvious peak, so the scattering was taken at 1 cm. Scaling was applied for visualization: Protons at 250 MeV kinetic energy is not scaled, while 12C at 450 MeV/n was scaled by $\frac{1}{2}$, electrons at 80 MeV was scaled by 3, and photons at 500 keV was not scaled but shifted to the left by 15 units. It is worth noting that for gamma rays, the gaussian distribution does not represent the simulation results. Refer to the below table for quantitative comparison.

Beam spread	Electrons	Gamma rays	Protons	12C
RMS (cm)	3.41	5.18	0.999	0.156
Sigma (cm)	3.36	8.36	0.81	0.154

Table 3. Beam scattering at the radiation lengths. For electrons, protons, and 12C, gaussian distribution is a good representation of the simulation while for gamma radiation it does not.

Testing compression algorithms for macromolecular diffraction images

Kaden Badalian

Watson School of Engineering and Applied Sciences, Binghamton University, Binghamton, NY 13902

Herbert J. Bernstein

School of Chemistry and Materials Science, Rochester Institute of Technology, Rochester, NY 14623

Robert M. Sweet

NSLS II, Brookhaven National Laboratory, Upton, NY 11973

Abstract

Macromolecular Crystallography is the most effective method to determine the three-dimensional structures of large biological molecules. Collecting diffraction-image data rapidly and accurately is imperative to this technique, but the new generation of x-ray pixel-array-detectors, such as the DECTRIS Eiger, makes this task challenging because these new detectors produce very high volumes of data that can't be transferred or stored efficiently. In order to conserve resources, these images need to be compressed quickly and at a high compression ratio with little to no data loss. In order to test and compare different compression algorithms, I wrote programs that timed the compressions, compared the output file size, and compared the original image to the decompressed image both as a whole and focusing on the peaks. I tested lossless compressions, which lose no data and have lower compression ratios, and "lossy" compressions, which sacrifice some data but have higher compression ratios. One type of compression that maintains peaks of an image, features that are vital even when it is "lossy," is called wavelet compression. For this reason, I focused my "lossy" compression testing on the open-source wavelet compression software called Epsilon, which became the basis for the preferred "lossy" compression software. For the lossless compression, I tested a JPEG2000 compression which uses wavelet encoding, and an open-source compression called FLIF which uses arithmetic encoding, a type of entropy encoding. FLIF seems to outperform JPEG2000 as it compresses the images into smaller files and takes less than a third of the time to encode. For these reasons, FLIF would make a reasonable choice to investigate for the lossless compression of diffraction images. Testing these programs has demonstrated the importance of investigating all possibilities in computer science and has developed my ability to do so.

I. Background

A. Synchrotrons and Macromolecular Crystallography

Macromolecular Crystallography (MX) is the most effective method to determine the three dimensional structures of large biological molecules. Such molecules include proteins, viruses, and nucleic acids. These large molecules can be crystallized under regulated conditions, but they tend to form small, imperfect, and weakly diffracting crystals that make collecting accurate data difficult. In order to overcome this, synchrotrons are used because of their extreme brightness.

A synchrotron light source is a facility with a small synchrotron, used to get the electron to a speed close to the speed of light,

and a large synchrotron called the storage ring. Once the electron is released from the small synchrotron into the storage ring, the energy (electromagnetic radiation) released by the electron is captured by tangential beamlines where experiments take place. For MX, the most heavily used electromagnetic radiation is x-ray. An MX beamline will have the macromolecule crystal of interest in the sample position followed by a pixel-array-detector to capture the diffraction pattern of the crystal.

The crystal is rotated and a diffraction image is captured at all angles. These diffraction patterns are then used by software to produce a three-dimensional model of the macromolecule. This information can then be used to advance knowledge of the relationship between structure and function, protein folding, and evolutionary relationships. One major application of this information is rational drug design.

B. New Detectors

Collecting data fast and accurately is imperative for MX. This necessity encourages companies to make new detectors that better capture MX experiments. In NSLS-II at Brookhaven National Laboratory, the detector used since its release in 2007 was the DECTRIS Pilatus. This detector has about six million pixels, each being 172 x 172 micrometers, and for the uses at Brookhav-

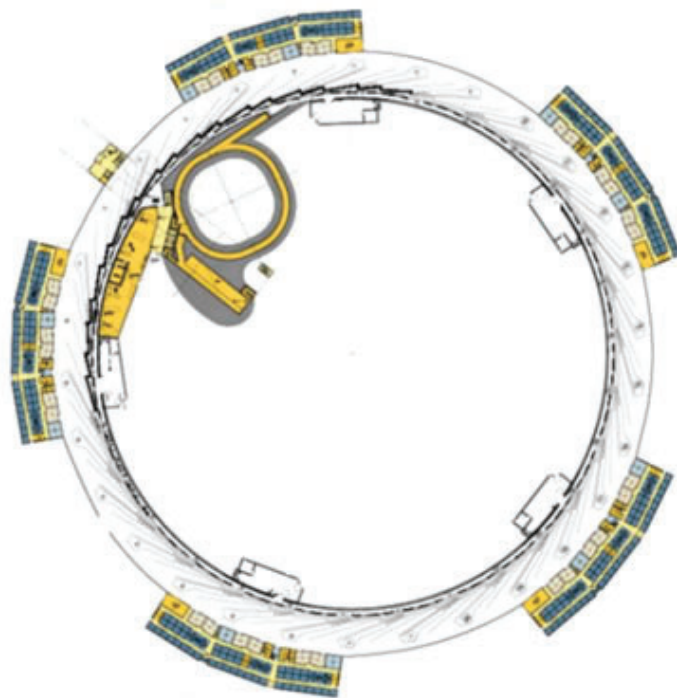


Figure 1. NSLS-II

en National Lab, a frequency of 25 Hz. Along with this detector came the need to compress diffraction images because the computers and networks could not keep up with this influx of raw data. Diffraction images are compressed for two main reasons: to minimize transfer time and to conserve storage. Storing this much raw data can become very costly. This expense is reduced if the data is compressed. Trying to move too much data through a network or onto a hard drive disk can not only result in data loss, but can delay other flows of data on the same networks or storage systems. Using compressions on the data reduces these risks.

The Pilatus detector is currently being replaced by the DECTRIS Eiger which has about eighteen million pixels, each being 75 x 75 micrometers, and a possible frequency of 133 Hz. This increase of data creates the need for a more powerful compression. This is the basis for the first part of my project: to find a compression that compresses diffraction images with high compression ratios and little to no difference between the raw and compressed image.

C. Compressions

There are two very broad types of compressions: lossless and “lossy.” A lossless compression doesn’t lose any information, but the compression ratio isn’t as high as in a “lossy” compression. A “lossy” compression sacrifices data to achieve this higher compression ratio. It is disputed whether “lossy” compression should be used on MX data. Some will argue that no data should be altered in the diffraction images. Others will claim that some “lossy” compression algorithms maintain the integrity of the important parts of the diffraction image, the peaks/spots. Compression algorithms that use the wavelet transform seemed like they would be effective on diffraction images because the signals in diffraction images are the peaks which are brief, making the localized wavelet used in the wavelet transform seem appropriate.

The wavelet transform starts out by choosing a mother wavelet. One example of a mother wavelet is the Haar wavelet. Two forms of the mother wavelet, the high and low pass filter, are convoluted with the data to be compressed. The low-pass filter smoothes the data so it can be stored easier. According to the Nyquist sampling theorem, about half of this data is required to faithfully reconstruct all of it. The high-pass filter essentially takes the difference between the original data and the new smoother data, so the original data can be reconstructed. The high-pass data is typically very small numbers and can be stored in few bits. This process is repeated recursively. The Wavelet Transform becomes “lossy” by throwing away the high-pass data after a few passes because it will eventually become negligible. This information that is thrown away pertains to the features in the background, so the “lossy” transformation sacrifices the background detail and adds noise, but the spots in the diffraction image are maintained.

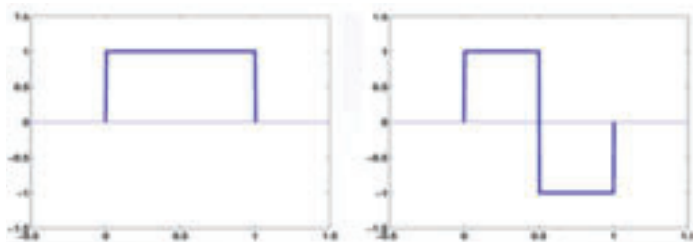
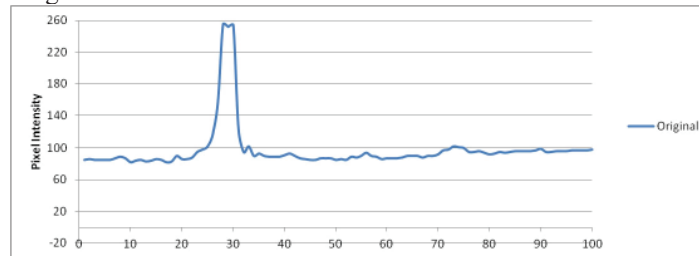


Figure 2. Haar Wavelet. Low-pass filter on left and high-pass filter on right.

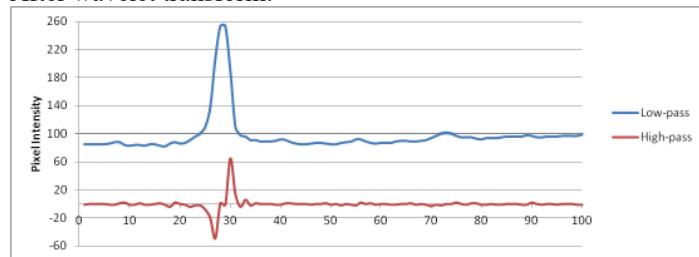
Here is an example of a wavelet transform using the Haar wavelet:

Original:



This is a selection of 100 consecutive pixel intensities from Figure 3.

After wavelet transform:



The blue line is generated by putting the original data into equation 1 (low-pass filter) to get a smooth line that requires storing about half the data points.

The red line is produced by using the original data in equation 2 (high-pass filter) to get small numbers that require fewer bits to store.

Other compression algorithms use entropy encoding. Entropy encoding is effective on any type of image because it essentially takes the most used pixel intensities and stores them with the fewest bits possible, and stores the least common pixel intensities with the most bits necessary. Here is an example of entropy encoding:

150	150	150	150	150	150	150	0	0	0	0	0	0	0	0	0	0
150	150	160	160	160	160	150	150	0	0	1	1	1	1	0	0	0
150	160	190	190	190	160	150	0	1	3	3	3	3	1	0	0	0
150	170	210	220	210	170	150	0	2	5	4	5	2	2	0	0	0
150	170	220	240	220	170	150	0	2	4	4	8	4	2	0	0	0
150	180	230	255	230	180	150	0	6	7	9	7	6	0	0	0	0
150	170	220	240	220	170	150	0	2	4	4	8	4	2	0	0	0
150	170	210	220	210	170	150	0	2	5	4	4	5	2	0	0	0
150	160	190	190	190	160	150	0	1	3	3	3	3	1	0	0	0
150	150	160	160	160	150	150	0	0	1	1	1	1	0	0	0	0
150	150	150	150	150	150	150	0	0	0	0	0	0	0	0	0	0

The compression software that I tested was focused around the wavelet transform and entropy encoding.

II. Methods

A. Testing Compressions

After researching open-source compression options, this became the list of compression software that I would test:

- ImageMagick (JPEG, High Quality JPEG, PNG)
- Epsilon
- FLIF
- OpenJPEG (JPEG2000)

JPEG and High Quality JPEG is a “lossy” compression that uses the discrete cosine transform which is similar to the wavelet transform but uses cosine functions instead of wavelets. Epsilon and JPEG2000 are wavelet compressions, but Epsilon is “lossy” and JPEG2000 is lossless. FLIF and PNG are lossless compressions that incorporate types of entropy encoding.

To test the effectiveness of these compressions I wrote a Py-

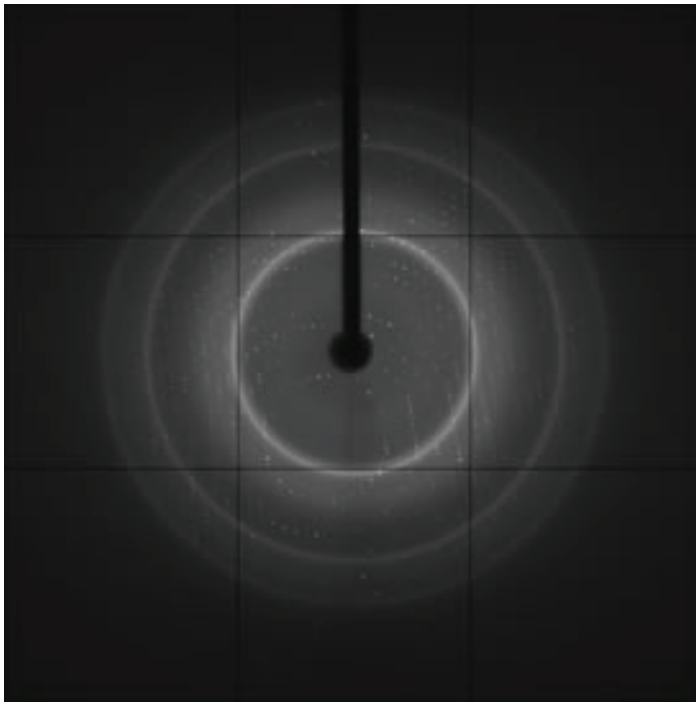


Figure 3. Diffraction Image

thon script that compared each pixel of the raw image to the corresponding pixel in the compressed image and then output the average difference of any given pixel and the greatest difference between corresponding pixels. This script was soon revised to focus on the peaks of Figure 1. The peaks were defined as any pixel with an intensity over 25 for this 8-bit image. This definition of a peak is broad and inaccurate, which became the segue to the next part of my project: a spot finder.

Other important factors of a compression algorithm are the time it takes to encode, and the output file size. To time the compression, I used the command “time” in front of the command used for encoding in Terminal.

B. Spot Finder

The spot-finding-algorithm that I used was to get the average and standard deviation of the pixel intensities in a given box around the pixel of interest, making sure to exclude outliers. To exclude the outliers, the top and bottom 10% of pixel intensities in the box were excluded from the average and standard deviation. After finding these values, the pixel of interest is defined as a spot if it is some number of standard deviations above this local average. For a proof of concept test, I coded this algorithm in Python and, for simplicity, entirely recalculated the average and

standard deviation of the box around the pixel of interest every time. This program took a very long time to run because all of the pixels in each box had to be fetched even though most of the pixels between adjacent boxes overlapped. The complexity of this algorithm was about $O(n^2)$. To avoid this, I implemented a sliding box algorithm to keep as much of the sum of the middle 80% of data as possible to calculate the average. I knew that using the traditional standard deviation equation, none of the calculations could be kept, but using the alternate standard deviation equation below, all I would have to do is add a variable that keeps the sum of the squares since I already have the sum for the average. With these changes, each pixel only has to be fetched when being added to or subtracted from a box, making the complexity $O(2n)$.

$$\sigma = \sqrt{\frac{n * \sum x_i^2 - (\sum x_i)^2}{n * (n-1)}}$$

III. Results and Conclusions

A. Testing Compressions

Figure 3 is the image I tested the compressions on. It was originally 9.4 MB and 8-bit, so numbers are in the range of 0-255. Below is a table of the results. (See table 1 below.)

Out of the lossless compressions (PNG, FLIF, and JPEG2000), FLIF performed the best. Not only did it compress the image the best, but it compressed the fastest as well. From the “lossy” compressions, I will be focusing on Epsilon because the desired compression ratio can be chosen and I won’t run into copyright issues using it. For these reasons, FLIF and Epsilon will be further investigated for their use in MX.

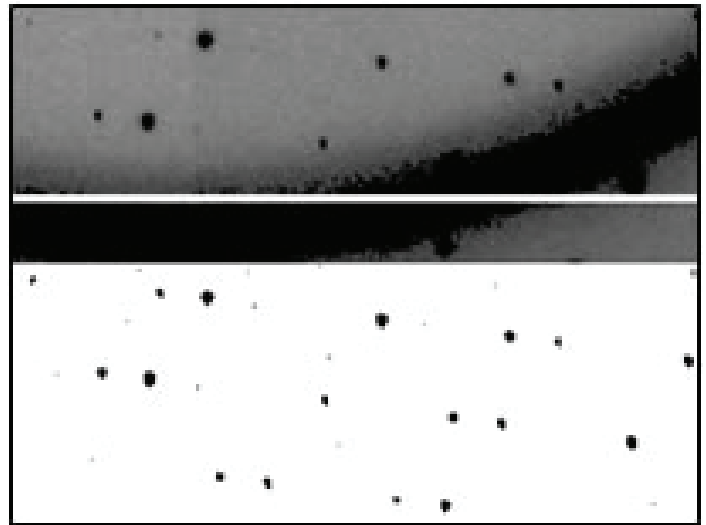


Figure 4. Part of Fig. 2 on top and output of spot finder below it

Compression	Greatest Spot Difference	Average Spot Difference	Output File Size (MB)	Time (s)
JPEG	4	0.0018	0.88	0.16
High Quality JPEG	1	0.046	1.8	0.2
PNG	0	0	3.8	1.0
Epsilon	7	0.6	1.3	1.3
FLIF	0	0	2.4	1.0
JPEG2000	0	0	2.5	3.5

Table 1.

B. Spot Finder

After testing the spot finder with different box sizes and spot definitions, I settled on a box size of 21 and defined the spots as 5 standard deviations above the average for my test image. Some variables in this algorithm are subject to change depending on the size of the spots in an image. Images with larger peaks will need either larger boxes or a larger barrier because all of the outliers won't be absorbed by the 10% barrier of a smaller box. As seen in the image to the left, the algorithm accurately finds the spots, even across difficult features of images such as the ice ring seen in this sample image. Since the algorithm seems to work pretty well, it will continue to be developed and hopefully used to identify useful images.

IV. References

Figure 1: Young, Leonardo. "1 BROOKHAVEN SCIENCE ASSOCIATES EFAC Review Conventional Facilities Update Marty Fallier Director for Conventional Facilities May 10, 2007." <http://slideplayer.com/slide/8995828/>

Figure 2: Cheng, Kileen. "Example Wavelets." <https://cnx.org/contents/K5j4YUB6@4/Example-Wavelets>

Figure 3: Myoglobin image courtesy of Christopher Nielsen of Area Detector Systems Corporation

V. Acknowledgements

This project was supported in part by the U.S. Department of Energy, Office of Science, Office of Workforce Development for Teachers and Scientists (WDTS) under the Science Undergraduate Laboratory Internships Program (SULI).

Biochemical and genetic analysis of lipid mutants of Arabidopsis

Christopher Baglivi

Biology Department, Emmanuel College, Boston, Ma 02115

Changcheng Xu

Biology Department, Brookhaven National Laboratory, Upton NY 11973

Abstract

Traditionally plant oils have been researched due to their capability as potential feedstocks for the production of biodiesel and industrial chemicals. As a result, the main focus of the research is analyzing the mutations of the plant Arabidopsis on the biochemical and genetic levels. A better understanding of these mutations will enable the manipulation and characterization of the genetic makeup of the plant. The broad overview of what is a truly extensive process consists of several general steps. The first step consists of planting M2 seeds of mutants (mutations caused by seed exposure to the chemical EMS) and then extracting lipids from the leaf from the M2 plants and performing Thin Layer Chromatography (TLC) in order to find the mapping population. The mutant plants showing different lipids from the wild type plant will be used for the mapping population. Once the mapping population is solidified containing plants with a favorable phenotype, we will extract the DNA from the plants and use genetic markers for each chromosome and perform a Polymerase Chain Reaction (PCR). This allows us to locate the position of the mutation and its association or linkage with the marker. Bettering our knowledge of the genetic makeup of the plant Arabidopsis and how the different mutations affect the plants genotype and phenotype will, in turn, further our understanding of biofuels and improve our chances of producing a potentially more viable alternative fuel source such as biodiesel.

I. Introduction

The goal of this research is to characterize the putative mutants at biochemical and genetic levels. This is done by taking a seed-specific oleosin-green fluorescent protein (GFP) that was overproduced in vegetative tissues of the model plant Arabidopsis to allow the visualization of oil droplets in leaves. A chemical mutagen is used to mutagenize the seeds of the homozygous transgenic plants carrying the oleosin-GFP transgene. These seeds are then sowed on soil allowing the plants to self-pollinate to produce the M2 generation, which is screened. The seeds that are selected via fluorescence microscopy in order to identify favorable characteristics such as plants with abnormal size and number of oil droplets are transferred to soil. The plants leaves from the M2 generation are analyzed further through fluorescence microscopy. In order to characterize the putative mutants, leaf oil content and lipid composition are analyzed through thin-layer chromatography to facilitate the subsequent identification of mutations responsible for accumulating oil, which will then be crossed with each other and the wild-type plants. Lastly, genetic analyses (PCR) are used to identify whether the mutations are dominant or recessive and whether the mutations are responsible for the oil accumulating phenotypes. This process of determining the linkages between the mutations and the plants phenotypes or things such as oil accumu-

lation in the leaves, also known as positional cloning, allows us to pinpoint the general location of the mutation on the genome in relation to the genetic marker, thus enabling the characterization and manipulation of the mutations and how they affect the plant.

II. Background

A. Positional Cloning / Gene Mapping

Positional cloning is a method of gene identification (gene of specific phenotype identification). During positional cloning when the DNA clone is at or close to the mutant allele the recombination frequency should be close to zero. If the chromosome walk proceeds through the mutant allele, the new polymorphisms will start to show an increase in recombination frequency compared to the mutant phenotype. Depending on the size of the mapping population the mutant allele can be narrowed down to a small region. Sequence comparison between wild type and mutant DNA in that region is then required to locate the DNA mutation that causes the different phenotypes in Arabidopsis. Each new clone (a polymorphism) is identified and tested in the mapping population for its recombination frequency compared to the mutant phenotype.¹

Gene mapping consists of placing a collection of molecular markers onto their respective positions on the genome. Genes can be viewed as a special type of genetic marker in the construction of the genome maps. In other words, gene mapping is the process that identifies the locus of a gene and the distances between the gene. The purpose of mapped-based cloning is to narrow the genetic intervals containing mutations by successfully excluding other parts of the genome. The most common ecotypes used in combination for mapping purposes is Landsberg erecta (Ler) X Columbia (Col). These two accessions have been estimated to differ in four to eleven positions every 1,000 base pairs; there is also a large library that has accumulated that facilitates the Ler X Col populations. The molecular marker SSLP is used because it has two important properties which consists of codominance and being PCR based. Codominance allows both chromosomes of a plant to be genotyped, allowing maximum amount of information from mapping populations. These two characteristics of the markers enable a high success rate for locating the linkages between the mutation and the genetic markers.¹

B. Mutagenesis of Arabidopsis

The chemical that the seeds are exposed to is ethyl methane-sulfonate (EMS) that induces chemical modification of nucleotides, which results in mispairing and base changes. EMS in Arabidopsis generates randomly distributed mutations throughout the genome. As a result, chemical mutagenesis can be used not only to search for loss or gain of function but can also provide useful information for understanding the functions of essential genes by creating weak and non-lethal alleles. All in all, mutagenesis creates a generation of diverse mutant alleles in the same gene and

provides critical tools to understand the role of these genes in the function of the plant.²

III. Materials and Methods

Using materials such as pipettes, vortex machines, Ependorf tubes, electronic scales, centrifuges, petri dishes, soil pots and trays, soil, fertilizer, tweezers, and spray bottles, as well as performing procedures such as sowing seeds in agar, transplanting plants from agar to soil, PCR, TLC, and gel electrophoresis, we were able to successfully make advancements on locating the position of the marker with the linkage to the mutation.

IV. Discussion / Conclusion

Since my results are still left to be determined, I will have to conclude that all the results obtained throughout the summer have contributed to narrowing down the position of the mutation linkage to the marker on the genome of Arabidopsis. The “narrowing down” process consists of numerous TLC and PCR procedures of the different mutated M2 generation plants and as a result conclusive results will not be obtained until further research is performed.

V. Acknowledgments

This project was supported in part by the U.S. Department of Energy, Office of Science, Office of Workforce Development for Teachers and Scientists (WDTS) under the Science Undergraduate Laboratory Internships Program (SULI). I would like to thank the following people for their patience guidance and leadership Chengchang Xu (Mentor), Jillian Fan, and Mel Morris as well as the United States Department of Energy, the SULI Program, and Brookhaven National Laboratory.

VI. References

¹American Society of Plant Biologists. “Positional Cloning in Arabidopsis. Why it Feels Good to Have a Genome Initiative Working for You.” July 2000

²Methods in Molecular Biology vol. 323: Arabidopsis Protocols, Second Edition. “EMS Mutagenesis of Arabidopsis.”

Maximizing computing efficiency through cycle-scavenging in a high performance computing environment

Joshua Barnett

Physics, Georgia Institute of Technology, Atlanta, GA 30332
William Strecker-Kellogg, Costin Caramarcu, and Tony Wong
Physics Brookhaven National Laboratory, Upton, NY 11973

Abstract

In traditional High Performance Computing (HPC) environments, resources are fairly allocated to enable a single job to operate with a large number of resources. Recently, the field of High Throughput Computing (HTC) has evolved to accommodate tasks that do not necessarily benefit from HPC environments because there are an abundance of jobs which require relatively few resources; such tasks allow for the maximum use of resources over a long period of time. On the other hand, HPC computing is not necessarily concerned with the efficiency of the allocation of resources over large time scales (months and years). Furthermore, in an HPC environment it is inevitable that computing resources will become idle either due to the indivisibility of remaining cores for large parallelized tasks or simply because there is a lack of demand for HPC resources. Incorporating HTC software in an HPC environment alleviates these inefficiencies by allocating idle resources that cannot be utilized by tasks that require multiple threads (i.e. a single idle core on a node that is otherwise fully occupied). By scavenging spare cycles, the utility of each available core can be maximized throughout its lifetime by eliminating wasted CPU-hours.

I. Problem Description

The Institutional Cluster (IC) at Brookhaven National Lab (BNL) is an HPC cluster that is currently under construction and is scheduled to come online in late 2016. As with any HPC cluster, it faces issues with the indivisibility of certain resources either due to network topology, core-usage in individual nodes, or limitations on available memory in certain machines. The IC will attempt to alleviate some of these issues with a variety of measures that include a fat-tree topology that allows for effective inter-node communication and whole node scheduling that prevents wasted CPU-hours within a running node. Despite all this, the fundamental problem of packing jobs efficiently will remain an issue.

As illustrated by figure 1, even optimizing scheduling to utilize the maximum amount of available resources at any given time still results in lost node-hours. As it turns out, HTC jobs are more 'narrow' allowing them to more easily fit the gaps in usage as they typically only require a single core and can only vary their footprint in a single parameter (time). HPC jobs can vary their footprint by both number of utilized CPU's and time, rendering them generally more difficult to schedule.

The goal is to limit these inefficiencies by routing excess HTC jobs from another batch system on a different pool. In the context of cycle-scavenging of the IC at BNL, jobs originating from the Relativistic Heavy Ion Collider (RHIC) experiments (STAR and PHENIX) fit this requirement. In fact, both experiments utilize

HTCondor—a popular HTC batch scheduling system—to manage their existing computing clusters.² In contrast, the IC will utilize HPC scheduling software known as Slurm.³

II. HTCondor and Slurm

HTCondor and Slurm are both open source batch management systems utilized by the RACF and the IC respectively. These software packages were constructed with profoundly different philosophies and purposes in mind and therefore have specific use cases. HTCondor—as the name might imply—is designed to allocate HTC jobs to ensure maximum utilization of available resources over a long period of time. Slurm, on the other hand, allocates HPC jobs to ensure fairness of use of available resources superseding the need for full utilization.

To ensure maximum usage, HTCondor utilizes a greedy algorithm when allocating jobs. Namely, jobs in the queue will be matched if any open slots exist regardless of how many other jobs that user is running concurrently. In fact, users will often have many jobs running at once due to the embarrassingly parallel nature of HTC jobs. HTCondor uses a fair-share algorithm to ensure the eventual fair distribution of resources. It has an internal attribute called Priority that grows linearly proportional to the number of CPU-hours used. When another user submits a job and the pool is under a full load, the user who has built up sufficient Priority can have his or her job Preempted. Preemption causes a running job to be sent back to the queue in a non-running state. While a user has no jobs in the queue running, Priority decreases exponentially with time eventually allowing the user to have jobs either find empty slots or preempt other users. Because Priority decreases much more quickly than it increases, it ensures that users can have jobs running much more often than not.

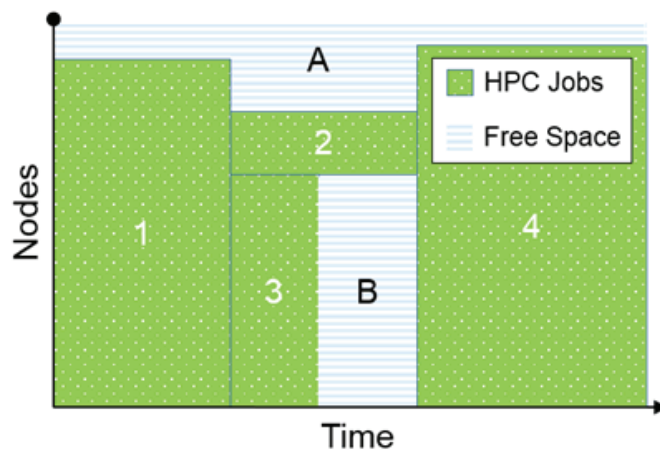


Figure 1: Node-time diagram showing packing inefficiency.³

Slurm is designed for fair allocation of resources for HPC jobs. This is partly because it is much harder to try to fill all resources in HPC as a single job—taking up multiple CPU’s over a potentially long period of time—is much harder to schedule. The current setup for the IC is configured to use a back-filling algorithm that stages jobs in such a way that tasks with smaller footprints are attempted to fit into open spaces when possible apart from user priority.

In regards to network configuration, HTCondor is far more flexible than Slurm purely due to the differences between HTC and HPC. HPC requires low latency interconnects in the network such that nodes are able to efficiently relay data. HTC, on the other hand, requires only basic networking between nodes.

III. Job Routing

When jobs are submitted to an HTCondor pool, the Schedd—a daemon responsible for the scheduling of jobs—connects idle jobs with open slots. Once all slots are full, jobs will wait in an idle state until either a running job becomes a candidate for preemption or a slot becomes free. This scheduling process is demonstrated in figure 2 by lines being fed from the Schedd to available slots in the pool. The figure also shows another option for the placement of jobs, which is the Job Router—a daemon responsible for transforming HTCondor jobs.

When and if a job is routed depends both upon the local configuration and the Job Description File—a simple text file that

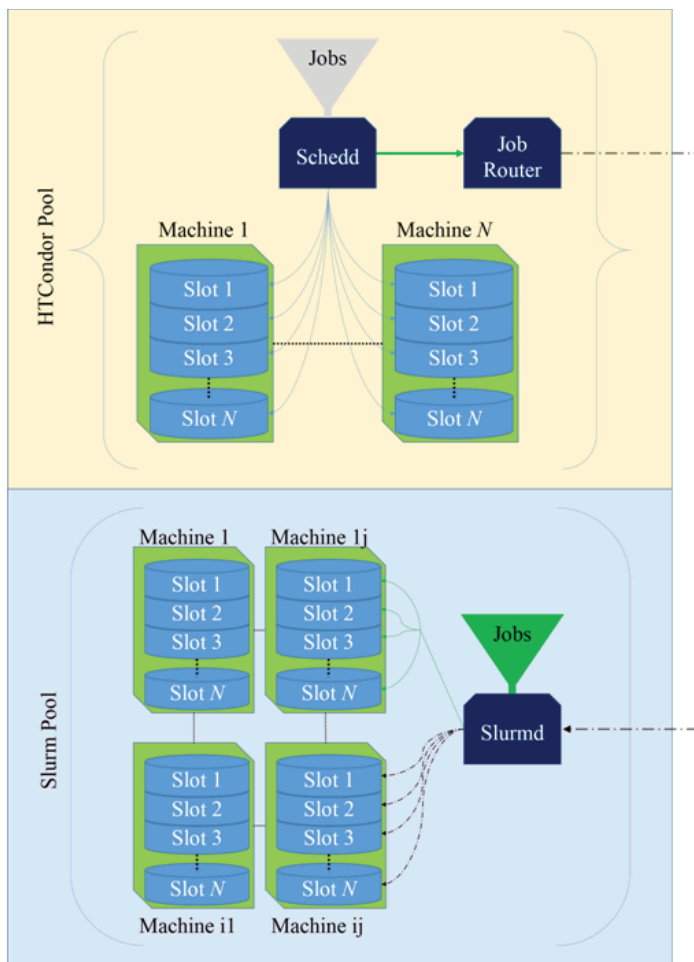


Figure 2: Diagram of scheduling daemons (dark blue) and job routing between computing pools

describes the environment and location of the executable. The example configuration used in this report requires that jobs must be idle for a certain number of minutes prior to being a candidate. Assuming all conditions are met and the job hasn’t already been claimed locally, the routing process begins with creating a copy. The remote job is actually a duplicate of the job called the routed copy, while the original copy remains on the local submission host and passively reflects the state of this copy.

A routed job is transferred to a specified HTCondor pool and Schedd, which can either be the same as the local pool or those of a remote site. The case of the choosing a remote site—an obvious choice at first glance—leads to many accounting and managing issues. The configuration chosen here is to specify the local pool and daemon.

After the Job Router gives the job back to its own pool, it is transformed according to the JOB ROUTER DEFAULTS and the specific site it was routed to in JOB ROUTER ENTRIES. For instance, in the example configuration shown below, there can be no more than twenty idle jobs in the routing queue at once and no more than one-hundred jobs in any state at any given time.

```

DAEMON LIST = $(DAEMON LIST) JOB ROUTER

JOB ROUTER SCHEDD2 NAME = condtest 02 . rcf . bnl . gov
JOB ROUTER SCHEDD2 POOL = condtest 01 . rcf . bnl . gov

# All routes take on the values set in this ClassAd attribute
JOB ROUTER DEFAULTS = \
[ \
  requirements=target . WantJobRouter is True ; \
  MaxIdle Jobs = 20 ; \
  MaxJobs = 100 ; \
]

JOB ROUTER ENTRIES = \
[ Grid Resource = "condor acas 1681 . usatlas . bnl . gov acas 1681 . usatlas . bnl . gov " ; \
  name = "Slurm Pool" ; \
  set remote Job Universe = 9 ; \
  set remote Grid Resource = "batch slurm" ; \
]

```

The remote destination is given by a GridResource, which points to the Slurm testbed head node in this example. Upon arrival, set remote attributes are evaluated, which requires HTCondor to also be installed on the remote host. The attribute set remote JobUniverse = 9 will change the Universe of the job to the Grid Universe (note: jobs that pass through the router are automatically transformed to Grid Universe but was included here for the sake of clarity). Setting this along with GridResource = “batch slurm” will trigger a new cascade of events.

IV. Gridmanager and GAHP

When the routed copy lands on the remote pool and transforms into a Grid Universe job, it triggers the spawning of the Gridmanager daemon on both the local and remote pools. Both Gridmanagers start a Grid Ascii Helper Protocol (GAHP) server that is responsible for accepting job descriptions from HTCondor and converting them to render them comprehensible to other batch management systems, or even another Condor Schedd. For instance, the local GAHP will manage the original copy while

the remote GAHP translates the job description to a simple Bash script that is submitted directly to Slurm.

V. Condor-Slurm Interfacing

By running `srn` with the necessary parameters that are specified by the GAHP, including the generated Bash script wrapper, Slurm then takes control of the job placing it inside of its queue. Submitting between HTCondor and Slurm inserts an additional layer of complexity: Slurm has an internal database of allowed users which will not necessarily have one-to-one correspondence with users on the original pool. For convenience, any user who chooses to have a job routed should automatically have his or her username added to Slurm's database.

HTCondor seemingly has a variety of routes that makes this possible. The clearest option would be to find way to execute a script (a hook in HTCondor language) upon the receipt of a job description. Unfortunately the trigger that does exist to implement this hook only functions for local HTCondor jobs because it is purely associated with the Stard –where jobs will never arrive in the configuration we are describing. There do exist specific Job Router Hooks that trigger at the appropriate time, but implementing one would make it necessary to re-implement the functionality of the Job Router which would be a cumbersome and needlessly complex task. Further, funneling a script through such a trigger would run for every instance of a submitted job, a potentially massive number in the context of HTC. A different kind of solutions was needed.

After much deliberation, the most elegant solution was implementing a simple script as a Cron job. This would allow a single instance of a task to manage every incoming job simultaneously, making it much less resource intensive. This task would run every minute to add users to the Slurm database who have jobs running in the Job Router. A naive implementation would be simply to add every user that appears to have routed jobs regardless of whether or not that user already exists, but on a large scale this method is wasteful and could lead to unnecessarily large CPU usage over time. The implementation of a rudimentary cache system goes a long way to reduce the number of system calls made as simply reading and writing to text file is much less expensive over time than calling `sacctmgr`–Slurm's interface for account management–several times in less than a second. The logic follows the pseudo code below:

```
read sys.std in for list of users with routed jobs

if (number of users is 0) : exit
else:
    conduser set = convert to set(users in sys.std in)
    cache user set = convert to set(users in cache file)

user to add = difference between conduser set and cache
user set

if (length of user to add is 0) : exit

while (length of users to add is not 0) : user = users
to add . remove ()
    add user to Slurm
    if (user already exists) : write user to cache
    elif (user was added successfully) : write user to
cache
    else:
        warn that problem occurred
        exit
```

Implementing the code in such a way allows for script to add users only when necessary, and perform gracefully even when the cache file is deleted. The shrewd reader may wonder what happens if a job is routed and attempted to run on Slurm prior to that user being added. There is very little problem with such an edge case. This will occur very infrequently during production as upon landing in the router locally, there is a latency period of approximately six minutes before a job will actually appear on the remote pool. If it does still appear prior to script running and the user hasn't been added, the job will simply be rejected while the original copy will become idle in the local queue either to run locally or become routed once again. This bouncing process would occur on the order of a few minutes, and considering that most HTC jobs run for as short as an hour to as long as a few days, this loss in time is largely negligible.

VI. Job Monitoring and State Propagation

The local pool where jobs are submitted must have accurate accounting information for the state of remote processes. Because a routed job is ultimately not running on HTCondor, real time monitoring is not currently available. In fact, there are two layers through which a job's status propagates in order to be visible to the local pool. On the remote side, condor periodically gathers the status of each job from Slurm then reflects it in its own queue. A pre-existing script is responsible for relaying this information by calling Slurm commands and feeding information about the state to the GAHP. Additionally, the local submit pool queries the remote Schedd for job status. This leads to a few more minutes of latency. Combined, these typically result in a propagation time of roughly three to five minutes. Considering that most jobs run for an order of magnitude longer than this, the delay is negligible.

If necessary, local job status changes can be pushed to the remote pool as well. The primary example of this is removing the original copy from the local pool. Canceling across all pools is made possible by the addition of simple scripts that sends the cancel request to the appropriate Slurm process.

VII. Testing the Setup

In order to test the setup, a general use case was considered. The local HTCondor pool will have an abundance of jobs while there are free cores on the remote machine. To emulate this, 250 jobs were submitted that last roughly from 20 minutes to an hour that include all typical inputs and outputs of files. Figure 3 is the result of this testing. In the first roughly twenty minutes, jobs only appear to run locally, after which the Job Router begins to pick up idle jobs (in keeping with our configuration). These remote jobs begin to run remotely, represented by the green area above the red area (representing local running jobs).

The figure clearly demonstrates a dramatic increase in available resources, although this is by construction. The dashed blue line represents the cap in the number of jobs that are possible to run at a given time due to native Slurm jobs in the IC, but this threshold is never reached in our test due to most remote cores being free.

VIII. Limitations and Future Work

As mentioned in previous sections, there are a few issues that exist with the current implementation. Although the latency is-

sues associated with state propagation are negligible due to the typical length of an HTC job, sometimes the local submission pool can report inaccurate data for total running time. This is by no more than a few minutes, and it is mitigated by the fact that, when finished, the job adopts the running time of the routed copy which has more accurate timing information. If user accounting was desirable, it would be necessary to ensure that run-time data syncs more accurately.

Another issue is the reliance on a shared file system. Although the IC will indeed have a Network File System (NFS) enabled, it would be more flexible and more widely applicable if this configuration was not necessary. The problem lies with the way that the GAHP transfers files. When a job is converted to the Grid Universe, files are automatically transferred to the remote host which is the desired result. The issue arises when Slurm tries to access the spool directory where HTCondor placed these files. Only the node running the HTCondor daemons that receives the files is able to execute them; the other nodes do not have access to that spool directory. The easy solution was to simply make this spool directory a part of the NFS. Future work would include augmenting the GAHP such that file transfers to all necessary nodes is possible, removing the need for a shared spool directory.

IX. References

- ¹”Documentation.” Simple Linux Utility for Resource Management. Accessed August 08, 2016. <http://slurm.schedmd.com/>.
- ²”Computing with HTCondorTM.” HTCondor. Accessed August 08, 2016. <https://research.cs.wisc.edu/htcondor/>.
- ³Iqbal, Saeed, Rinku Gupta, and Yung-Chin Fang. ”Planning Considerations for Job Scheduling in HPC Clusters.” Power Solutions, November 2005, 133-36.

X. Acknowledgments

This project was supported in part by the U.S. Department of Energy, Office of Science, Office of Workforce Development for Teachers and Scientists (WDTS) under the Science Undergraduate Laboratory Internships Program (SULI). I would like to especially thank William Strecker-Kellogg, Costin Caramarcu, and Tony Wong for their support, wisdom, and patience throughout this project.

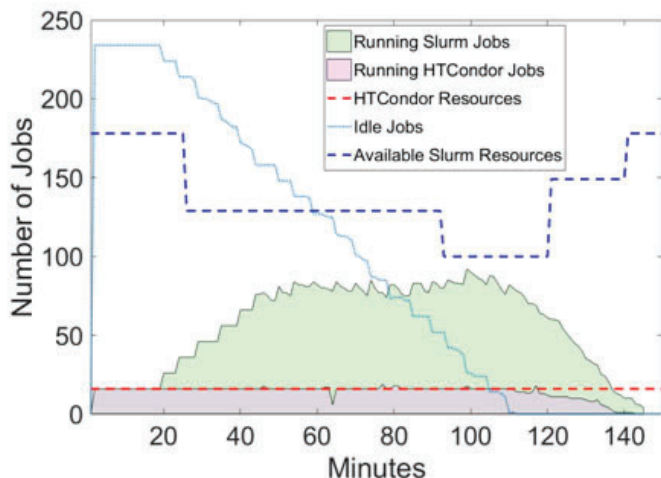


Figure 3: Plot of scheduled jobs and general status over time including resources available to routed jobs

Wildland/Urban fire interface: prevention and the development of new innovative fire suppression tactics for wildfire

Jonathan Bernal

Engineering Sciences, Queensborough Community College, NY 11358

Joseph Terranova

Fire Protection Engineering, Brookhaven National Laboratory, Upton, NY 11973

Abstract

The Wildland-Urban Interface (WUI) is the zone where Brookhaven National Laboratory's (BNL) buildings meet the forest. The overgrowth within BNL's 3,450 acres of woodland raises a concern of wildfires spreading and involving the structures on-site. Assessments of the fire access roads were performed, and evaluated against forest encroachment, tree canopy height, signage, and road conditions. Additionally a new innovative portable water delivery system was developed and tested in order to expand the WUI firefighting capabilities at BNL. Performance calculations and analysis of this system known as the Action Ready Multi-Use Sprinkler Suppression System (ARMSSS) were done using the Hazen-Williams equations. The extents of the conditions were documented for fire department access to map-out the delivery of fire suppression water to a site.

I. Introduction

Most homes in America have at least one smoke detector, but the woods and wildlife that surrounds us do not. There is no early-stage detection installed in the woods for fire fighters to get an early start as they would in a commercial facility or residential home. This is why wildfires are one of the most challenging battles to fight for fire fighters, and pose economical burdens on those who live around them. An area as such is called a wildland-urban interface. This term is used to define an area where forested lands border with homes and businesses.¹ It is very important for those in Wildland-Urban Interface (WUI) areas to have a proactive approach to wildfire prevention. This is essential when heavy defoliation occur in dense tree stands from pests and animals. Defoliation is the destruction and widespread loss of leaves from trees. Maintaining a two-way interface of prevention with protecting structures from wildfires and, protecting the woodland from structure fires is of concern. The regulation of animal populations, implementations of mechanical thinning, building construction, and prescribed burns at BNL has lowered the risk of fire. Fires are self-sustaining chemical reactions that perpetuate themselves as long as all three elements of the fire triangle—fuel, heat, and oxygen—remain available.² Following is a simplified equation illustrating the combustion process:¹⁴

Heat of Ignition + Oxygen + Fuel(s) \Rightarrow ΔH (heat) + Products of Combustion

In order for a fire to start in the wildland there must be available fuels plus a competent ignition source. Fuels can include everything from trees, underbrush, to litter. Since fuels attain their heat by absorbing the surrounding solar radiation the temperature of a fuel influences its susceptibility to ignition.³ Part of my research is to conduct a survey of all current road conditions along-

side with the Environmental Protection Division (EPD). By the end of the survey we will have covered the fire breaks, and trails along BNL to help fire-rescue understand the current conditions of the roads. These conditions will outline the width of the road, the tree canopy over the roads, and road conditions. If a wildfire happens to start water is still today's most effective, and lowest cost extinguishing agent against fires. For most of the country having water available in the woodland is a great challenge. That is why the FPE department is in the process of developing solutions to combat that issue.

II. Background

A. WUI fuel

Dry Biomass is fuel which contributes to fire under dry conditions. Vegetation (fuel) if left unmanaged increase fuel loading over time with catastrophic consequences which may be exacerbated by climate change.⁵ With BNL's high value properties and the FPE's mission to help prevent loss of life and property it is critical to have a dedicated approach in WUI prevention. There are three ways to categorize wildfire; it is possible that an individual fire can contain characteristics of all three. A surface fire also known as a ground fire--- is one of the three different types of wildfires--- burns needles, leaves, grass, and other small biomass within a foot or so of the ground and rapidly move on.⁵ Fire must constantly continue to look for fuel, so while a ground fire is burning it is looking for ladder fuels. Ladder fuels are shrubs and (dead) branches created by the white tailed deer at BNL & pests that defoliated trees. Without the implantation of a mechanical thinning process fires can easily move from ladder fuels into the canopy. The other type of fire is called a "crown fire" which burns biomasses at all levels, from the canopy to the surface.

B. WUI pests

The orange-striped oakworm feeds off the leaves of oak trees in the late summer into early autumn.⁶ During a female oakworms's life span as a moth, usually a month long, it may lay up to 500 eggs. These eggs hatch after a week. Since BNL is home to many oak trees it is not uncommon for outbreaks of orange-striped oakworms to occur. An outbreak is defined by the US Department of Agriculture (USDA) as one or more, multiple-tree infestations per 100 acres of the same tree.⁷ According to BNL's EPD Kathy Schwager the current status of the Oakworm it not of a concern. During outbreaks these insects can cause severe defoliation of the trees. In ordinary environments outside of BNL, this outbreak rarely affects the tree's health. But since BNL is also home to many other parasites, such as the gypsy moth and, the southern pine beetle, the tree's health undergoes too much stress for it to recover.

The outbreak of southern pine beetles, *Dendroctonus frontalis*, is one of the largest contributors to fire fuel load at BNL. The female southern pine beetle typically initiates the attack on pine trees.⁷ After the female locates a host, she releases a pheromone called frontalin.⁷ This pheromone helps attract the males, who then in turn release their own pheromones. Verbenone is a pheromone produced essentially by males, and at high concentrations it can inhibit landing and cause beetles to switch to adjacent pines.⁷ Frontalin usually replenishes almost 3-5 days after the initial attack.⁸ If sufficient numbers of beetles are attracted, host resistance is overcome and the tree is successfully colonized. Usually on healthy pine trees, the tree is able to produce enough resin to “pitch out” the beetles.⁷ The male and female may work together to clear away the resin and successfully enter the bark of the tree.

Once the pine tree is successfully colonized by the southern pine beetle both brood adults and reemerging parents can fly and attack new trees, restarting the process.⁷ Large infestations may spread at a rate over 120 ft/day.⁷ These beetles can also inoculate pines with blue stain fungi which penetrate the sapwood. The performance of the fungi will cause the tree to create blockage of the water conducting tissue, leading the tree to rapid tree death and adding more fuel to the load.⁷

Clerids, *Thanasimus dubius*, is a major predator of both adult and larval southern pine beetles.⁹ Clerids usually lay their eggs at the entrances of the southern pine beetle’s gallery.⁹ Once the eggs have hatched the larvae attack beneath the bark, feasting upon bark beetle eggs and larvae.⁹ There they eat until they are fully grown, at which point they carve out a chamber for pupation in the outer bark.⁹

Natural enemies, such as the Clerids, diseases, and temperature can help reduce the southern pine beetle population level. Climate temperature in particular has strong effects on the southern pine beetle. Extreme temperatures can induce mortality of southern pine beetle that increases the probability of spot death prior to producing dispersing adults the following spring and reduces the number of dispersing adults that are produced by surviving spots. When the lowest winter temperature drops below about -14 °C, populations tend to decline. Development rates, re-emergence rates, and probably the location of host trees by flying adults generally increase from approximately zero at 5°-10 °C, to a maximum at 27°-32 °C, and decline at higher temperatures. Thinning also reduces the likelihood that expanding infestations will become established by increasing tree vigor and by changing the stand’s microenvironment. Increased tree vigor increases the likelihood that beetles will be “pitched-out” due to higher resin flows.

C. WUI wildlife

The white-tailed deer, *Odocoileus virginianus*, over population along with the other pests and diseases destroy the health of the trees here at BNL leaving much debris. Numerous studies have shown that over browsing by deer decreases plant growth, survivorship, and reproduction and can affect understory vegetation cover, plant density, or plant diversity. This debris adds for more fire fuel being added. Deer in forests can cause economic and ecological losses by reducing tree survival and growth, and altering species and age composition. The continued overabundances of deer were directly threatening the future of sustainable forestry. Limiting the size and growth of white-tailed deer populations near a WUI environment will help prevent, maintain viable

native plant, and healthy tree populations. According to New York State’s Department of Environmental Conservation deer population management report for 2015, Long Island was deemed to have experienced a decrease in population. This decrease was caused by culling deer and, by the harsh winters of 2014/2015 which produced deep snow and sub-zero temperatures. Culling is the selective removal of presumably inferior deer in order to improve the quality of the remaining population.¹⁵ Numerous studies have shown that over browsing by deer decreases plant growth, survivorship, and reproduction and can affect understory vegetation cover, plant density, or plant diversity. Forest and savannah sites with over abundant white-tailed deer populations may have lower species diversity of forbs due to preferential feeding. BNL regularly monitors over browsing by deer through the use of fence enclosures.

III. Combating the Problem

A. ARMSSS (Action Ready Multi-Use Sprinkler and Suppression System)

Why is water so important as an extinguishing agent?¹⁴ Water is an efficient agent because it works in two ways: First, by cooling, water helps to eliminate the ignition source. In changing water from a liquid to steam, 1,190 Btu per pound of water is absorbed. Second, in this transition to steam, water undergoes a volume expansion by a factor of 1,700.¹⁴ Therefore, one cubic foot of water can create 1,700 cubic feet of steam.¹⁴ The dilution of the air by the steam results in displacement of some of the oxygen molecules by water vapor molecules.¹⁴ This effectively reduces the amount of oxygen available to support the combustion process and tends to smother the fire.¹⁴

It is obviously how well water works against fire that’s why the FPE department at BNL recently finished constructing its newest addition to the WUI fire suppression program. A vehicle trailer with two electric motor pumps, a portable generator, 10 sprinkler heads, and 1,200ft of forestry fire hose. Each sprinkler head requires a minimum supply of 7.2 GPM at 50 psi. This trailer is capable of supplying water suppression from a hydrant or from one of the many environmental test wells on the BNL site, and/or provides a supply as a portable water source for BNL fire department to attack the fire. One of the hardest tasks for fighting fires in the woodlands is the lack of hydrants and readily available water. Fortunately the Environmental and Waste Management Services Division at BNL uses wells to monitor contamination, with the primary mission to remediate soil and groundwater contamination, in order to prevent additional contamination from migrating off the BNL site.⁴ With the approval from the Department of Energy, the use of these wells will now be used for firefighting



purposes and distinguished by bright red painted caps.

This summer I was able to compute and establish the design parameters of the ARMSSS trailer with multiple variables using researched data and the empirical equation of Hazen-Williams (Eq.1). In the absence of solid scientific data, engineers in the past have experimented with and used empirical equations for determination of friction losses in pipe flow.¹² The Hazen-Williams friction coefficient “C” is not a function of velocity or pipe diameter.¹² Its validity depends on the successful selection of the constant friction loss coefficient “C”, which is a function of pipe material, pipe linings and pipe age to indicate the roughness of a pipe interior.¹² The higher the C-factor, the smoother the pipe will be and more water can flow thru. Most of the time there will be a C-factor table which will provide a fixed C-factor. During my research I was able to find a 143 C-factor for the 4 foot ¾ in schedule 40 steel pipes. I used equation 1 to calculate the c factors for type II forestry fire hoses.

$$\frac{P}{\text{perfootofpipe}} = \frac{4.52(Q^{1.85})}{(C^{1.85})(d^{4.87})} \quad \text{Eq. 1}$$

Where P is the pressure lost to friction in psi per foot, Q is flow rate in gallons per minute, d is the internal pipe diameter in inches, and C is the Hazen-Williams coefficient of roughness.¹⁴ One of the variables that I had to account for was the additional pressure needed due to the depth of the electric pump in the environmental test wells.

$$K = \frac{Q}{\sqrt{P}} \quad \text{Eq.2}$$

Where P is the required pressure in psi, Q is the required flow at the first sprinkler in GPM, and K is the nominal discharge coefficient of the sprinklers being used.¹⁴

The interesting result that was found when calculating the c factor for Keyhose¹³ Type II forestry firehose was how the C-factor rose with additional flow suggesting that the inner hose diameter is fluctuating.

B. Fire Access Roads Survey

According to the National Fire Protection Association (NFPA) code book 1141, Standard for Fire Protection Infrastructure for Land Development in Wildland Rural and Suburban Areas, and the International WUI Code (IWUIC) there are some baseline minimums required for roadways, dead ends, and signage that BNL must adhere to. Some of these conditions are listed as such:

- At least 13ft 6 in. (4.2 m) nominal vertical clearance shall be provided and maintained over the full width of the roadway
- Turns in roadways shall be constructed with a minimum radius of 60ft (18.2 m) to the outside of the turn
- Fire apparatus access roads shall be all-weather roads with minimum width of 20ft
- Every dead-end roadway more than 300ft (91 m) in length shall be provided at the closed end with a turnaround having no less than a 120ft (36.6 m) outside diameter of the traveled way
- The beginning of every dead-end roadway and developments with only single access shall have signage indicating that there is not a second outlet
- Sign assemblies with the name of each road shall be constructed of noncombustible material and installed at each intersection. These signs shall be installed a minimum of 7ft (2.1 m) above the traveled way

Using this information the FPE department created a system to survey the roads and fire breaks that encompass the developed area of BNL. Together with the EPD intern, Caitlin Gormley, we traveled around while using a handheld device which could geo-tag the locations on a digital map. Once a point in the map was selected we determined the following: road conditions, vertical clearance, horizontal clearance, and signage. Each condition was distinguished by a number and color code (see table 1) on a map.

Suppression treatments include cut-and-remove, cut-and-leave, cut-and-hand spray, and pile-and-burn. Cut-and-leave is the most effective when used on smaller infestations (<100 trees) and limited access. On other situations cut-and-remove has proven to be the most effective, with an efficacy rate of 97%. The idea behind leaving the tree there is to cut the tree during the winter to expose the beetles to the harsh temperatures, reducing the population. Stand density is thought to be one of the most critical factors in determining the chances of spot initiation and the rate of spot expansion within a stand. Thinning is the preferred forest management tool used to attain desired stand densities, and it is widely recommended that stands with a basal area greater than 120 ft² per acre should be thinned below 80 ft² per acre.⁷

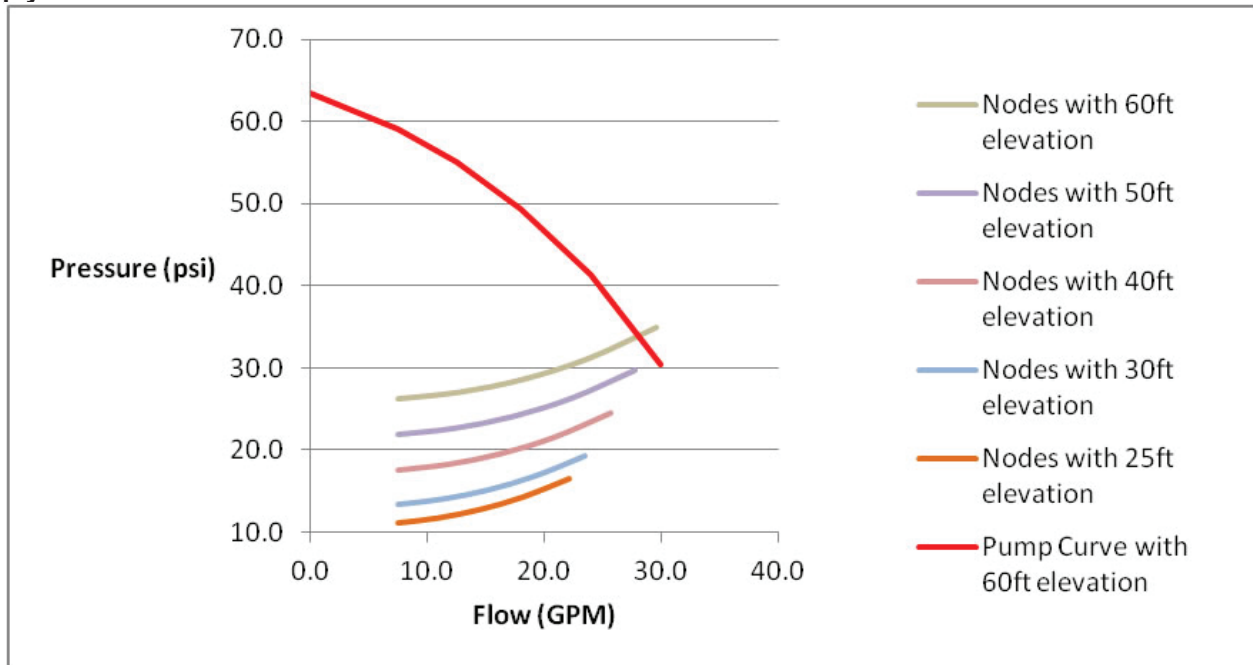
Table #1: Fire access road survey parameters

Horizontal clearance (ft)			Vertical clearance (ft)			Surface conditions			Signage	
< 20	2	Red	<13	2	Red	Obstructed	2	Red	Yes	No
20-25	1	Yellow	>13	1	Yellow	Eroded, Rutted, Partially Obstructed	1	Yellow		
>25	0	Green	Open Sky	0	Green	Level/graded	0	Green		

IV. Data Collection
A. Hydraulic Calculations

Node	elevation (ft)	Diameter (in)	Total Length (ft)	psi loss	psi loss by length	psi loss by elevation	C-factor	K-factor	q (flow supply)	Q (flow demand)	P (psi demand)
1	60	1.5	100	0.003	0.31	25.98	128	1.038	7.5	5.3	26.3
1	50	1.5	100	0.003	0.31	21.65	128	1.038	7.5	4.9	22.0
1	40	1.5	100	0.003	0.31	17.32	128	1.038	7.5	4.4	17.6
1	30	1.5	100	0.003	0.31	12.99	128	1.038	7.5	3.8	13.3
1	25	1.5	100	0.003	0.31	10.83	128	1.038	7.5	3.5	11.1
2		1.5	100	0.008	0.82	0	128	1.038	12.8	5.4	27.1
2		1.5	100	0.008	0.77	0	128	1.038	12.4	4.9	22.7
2		1.5	100	0.007	0.71	0	128	1.038	11.9	4.4	18.3
2		1.5	100	0.007	0.65	0	128	1.038	11.3	3.9	14.0
2		1.5	100	0.006	0.62	0	128	1.038	11.0	3.6	11.8
3		1.5	100	0.016	1.56	0	128	1.038	18.2	5.6	28.7
3		1.5	100	0.014	1.42	0	128	1.038	17.3	5.1	24.2
3		1.5	100	0.013	1.28	0	128	1.038	16.3	4.6	19.6
3		1.5	100	0.011	1.12	0	128	1.038	15.2	4.0	15.1
3		1.5	100	0.010	1.03	0	128	1.038	14.5	3.7	12.8
4		1.5	100	0.025	2.54	0	128	1.038	23.8	5.8	31.2
4		1.5	100	0.023	2.28	0	128	1.038	22.4	5.3	26.4
4		1.5	100	0.020	2.00	0	128	1.038	20.9	4.8	21.6
4		1.5	100	0.017	1.72	0	128	1.038	19.2	4.3	16.8
4		1.5	100	0.016	1.56	0	128	1.038	18.2	3.9	14.4
5		1.5	100	0.038	3.77	0	128	1.038	29.6	6.1	35.0
5		1.5	100	0.034	3.36	0	128	1.038	27.8	5.7	29.8
5		1.5	100	0.029	2.93	0	128	1.038	25.7	5.1	24.6
5		1.5	100	0.025	2.47	0	128	1.038	23.4	4.6	19.3
5		1.5	100	0.022	2.23	0	128	1.038	22.2	4.2	16.6

B. Supply/Demand Curve



C. Test Results of ARMSSS trailer with 60ft depth of Environmental Test Well

Test Results of ARMSSS trailer with 60ft depth of ETW e-pump #1			Test Results of ARMSSS trailer with 60ft depth of ETW e-pump #2		
Static: 56 psi	Test 1	Test 2	Static: 57.	Test 1	Test 2
Node 1 Psi	52	57	Node 1 Ps	53.6	54.7
Node 2 Psi	46	53.2	Node 2 Ps	47.9	49.7
Node 3 Psi	40	48.8	Node 3 Ps	40.9	42.9
Node 4 Psi	34	42	Node 4 Ps	35.6	36.8
Node 5 Psi	29	36	Node 5 Ps	29.8	30.7

V. Data Analysis

There were four tests completed with the ARMSSS trailer. The first test had two objectives. The first aim was to analyze and understand the functionality of the system against a hydrant and secondly determine the optimal distance per node for fire suppression. During the first test of the sprinkler system eight lengths of hose were directly connected to a class AA hydrant. According to NFPA 291 standard class AA hydrants are marked by light blue paint around the tops and nozzle caps and must be able to produce no less than 1,500 GPM. In order to apply appropriate fire suppression an observation of any dry areas, and between nodes in the system, the sprinkler heads were rotated to only face the asphalt. It was observed that the system had approximately 30ft of dry asphalt between each 100ft length of hose. In order to accommodate for some slack and to shorten the distance between each node it is recommended for future use to establish the system's nodes <60ft apart from each other.

The second & third tests objectives were to evaluate the system at different depths of the environmental test wells. These tests were conducted along the fire breaks where there are no hydrants. The second test along the East Fire Break went to a depth of 30ft. The third test was located at the corner of the North/East Fire-break. At this location both electric water pumps were used and placed at a depth of 40ft with two simultaneous charged lines the hoses. Both test showed adequate water pressure. With the design capabilities of each pump to max flow at 40 GPM it may be used for fire-rescue to fill their 500 gallon bladder. The use of a bladder in wildfires is a quick assembly relay storage tank which provides temporary storage of liquids in remote areas. This will be useful since the BNL FD brush truck tank only holds 350 gallons. This bladder can help refill the tank without having to take 20+ mins to travel to a hydrant.

The intent of the fourth test was to obtain data that correlated with the system's hydraulic calculations. Primarily an increase in elevation requires more pressure to overcome gravity's friction. This being said it is important to understand the functionality of the system at its lowest depth (60ft). For the purpose of this test the environmental test wells located at the North gate were chosen. The results are shown in section V.(a).

In order for BNL fire-rescue to apply successful firefighting tactics they must understand the current road conditions amongst the woodland trails and firebreaks. After conducting a detailed survey it can be concluded that forest encroachment has become a major underlying issue along the west side of BNL. These issues if not treated immediately can continue to spread to become a fire hazard for the buildings. Some roads were found to be fully obstructed and entail not able to be passed by a fire truck. A fully obstructed road was classified by any large objects, mainly tree branches, blocking passage. Some examples of fully obstructed roads would be tall grass, or sandy roads. Some of the sandy roads were so bad the kubota vehicle had trouble passing thru.

VI. Conclusion

The ARMSSS trailer provides an effective tool for the BNL fire department against wildfires. By finding the boundaries of the trailer against the different depths of environmental test wells together with the research that has been conducted of the fire access roads, the fire department will be able to implement the trailer in an optimal location. It has always been clear that the more sprinkler heads available the better suppression of fires. As shown

there is a current limitation placed on the amount of action-ready sprinkler heads that can be used from the environmental test wells. These constraints can be overcome by using the hydraulic centrifugal pump on the trailer, which will raise the amount of sprinkler heads that can be used.

VII. Acknowledgements

I would like to give a special thanks to my mentor Joseph Terranova and the manager of the Fire Protection Fire Protection engineering department, Michael Kretschmann, for all of their knowledge and guidance on these projects. Additionally Caitlin Gormley from the Environmental Protection Division who has helped me with the fire access roads map project. Additionally thanks to Sean Toole who named the ARMSSS trailer and Kathy L. Schwager who helped during the operation of the ARMSSS trailer. This project was supported in part by the U.S. Department of Energy, Office of Science, and Office of Workforce Development for Teachers and Scientists (WDTS) under the Community College Internships Program (CCI).

VIII. References

- ¹Bianchard, B and Ryan, RL North Atlantic Fire Service Exchange "Wildland-Urban Interface in the Northeast: Preceptions of Fire Risk and Hazard Reduction Startgies" 2007
- ²NFPA, "Wildland/Urban Interface: Fire Department Wildfire Preparedness and Readiness Capabilities" Nov 2015
- ³U.S. Department of the Interior, National Park Service "Fire Behavior"
- ⁴W.R. Dorsch, Environmental and Waste Management Services Division "Groundwater remediation program at Brookhaven National Laboratory" April 2007
- ⁵Congressional Research Service, "Wildfire Protection in the Wildland-Urban Interface" Jan 2014
- ⁶Siegert, NW and McCullogh, DG, Michigan State University "Identification and Management of Orange-striped Oakworm" (May 1998)
- ⁷Clarke, SR and Nowak, JT U.S. Department of Agriculture "Forest Insect & Disease Leaflet 49" April 2009
- ⁸Dupuis, G and Berland, N "Frontalin:orgin and synthesis" (2000)
- ⁹Felt, EP "Insects Affecting Park and Woodland Trees" (1906)
- ¹⁰Ayres, M , Martinson, S, and Friedenber, NA, Dartmouth College "Southern Pine Beetle Ecology: Populations within Stands"
- ¹¹Hurst, J N.Y.S. Department of Environmental of Conservation "Deer Hunting Season Forecast" (2015)
- ¹²American Society of Plumping Engineers (ASPE) Handbook
- ¹³Keyhose, a KFH Industries Company, Keyhose.com
- ¹⁴Brock, P , Fire Protection Hydraulics and Water Supply Analysis (March 2012)
- ¹⁵Ozoga, J, The Facts and Truth About Culling Bucks Deeranddeerhunting.com (April 2016)

IX. Appendix

Participants	Institutions	Roles
Joseph Terranova	Fire Protection Engineering	Mentor
Michael Kretschmann	Fire Protection Engineering	Mentor
Jim Vaz	Fire Protection Engineering	Mentor
Kathy L. Schwager	Environmental Protection Division	Mentor
Jennifer Higbie	Environmental Protection Division	Mentor
Sean Toole	Environmental Protection Division	Intern
Caitlin Gormley	Environmental Protection Division	Intern

Synthesis and characterization of weakly coordinating anions and cations as electrolytes in low polarity solvents

Rebecca Boucard, Paige Reagan and Ghislain Mandouma
Chemistry, Albany State University, Albany, Ga, 31721

Tomo Mani, Matt Bird and John Miller
Chemistry, Brookhaven National Laboratory, Upton, NY, 11973

Abstract

Weakly coordinating cation (WCCs) have been synthesized in order to determine the perfect electrolyte for electrochemistry in non-polar media. These WCCs and WCAs constitute a new class of molecular ions which can promote charge dissociation even in low polarity solvents because of their large size and bulkiness. The result being an increased conductivity in those media that can be useful for electrochemistry, advances in catalysis, battery technology, petroleum handling and other uses. The WCCs were accessed via a Palladium-catalyzed approach followed by simple filtration and isolation of the

product. We are proposing that these tetraarylphosphonium/tetrakis (pentafluorophenyl) borate (TAP) salts, will probe and fine tune ion association and dissociation in electrolytes due to their unique solubility in low polarity solvents. Over the past few weeks we have grown to understand how the push-pulling by different substituents of the tetraarylphosphonium ions affect the ion's dissociation in electrolytes and the relevance electrochemistry has for the next generation of batteries. Throughout this internship, we have gained valuable research experience that has helped us to become proficient and useful contributors to the scientific community.

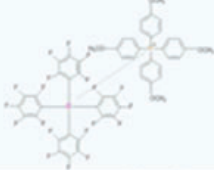

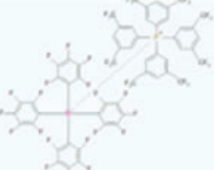
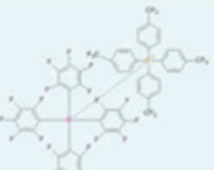
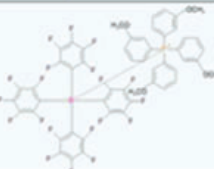
Aryl Halide/ Triflate	Tetraarylphosphonium Tetrakis Pentafluorophenyl Borate Salts	Conditions		Reaction Time	
		Synthesis of "PAr4"	Metathesis w/ Li[B(C6F5)4].nEt2O	Synthesis of "PAr4"	Metathesis w/ Li[B(C6F5)4].nEt2O
R = OCH ₃ (para)		<ul style="list-style-type: none"> • 25 mL O-Xylene • 10% Palladium(II) acetate-catalyst • Heat • Magnetic stirrer • Condenser 	<ul style="list-style-type: none"> • 25 mL methanol • Magnetic stirrer • Water bath • Condenser 	• 3-4 Hours	• 12 Hours
R = CH ₃ (meta)		<ul style="list-style-type: none"> • 25 mL O-Xylene • 10% Palladium(II) acetate-catalyst • Heat • Magnetic Stirrer • Condenser 	<ul style="list-style-type: none"> • 25 mL Dichloromethane • Magnetic stirrer • Water bath • Condenser 	• 5 Hours	<ul style="list-style-type: none"> • 46 Hours without heat • 2 hours in water bath
R = CF ₃ (meta)		<ul style="list-style-type: none"> • 25 mL O-Xylene • 10% Palladium(II) acetate-catalyst • Heat • Magnetic stirrer • Condenser 	<ul style="list-style-type: none"> • 25 mL Dichloromethane • Magnetic stirrer • Water bath • Condenser 	• 5 Hours	<ul style="list-style-type: none"> • 46 Hours without heat • 2 hours in water bath
R=CF ₃ (para)		<ul style="list-style-type: none"> • 25 mL O-Xylene • 10% Palladium(II) acetate-catalyst • Heat • Magnetic stirrer • Condenser 	<ul style="list-style-type: none"> • 25 mL methanol • Magnetic stirrer • Heating mantle • Condenser 	• 3-4 hours	• 2-3 hours
R=OCH ₃ (meta)		<ul style="list-style-type: none"> • 25 mL O-Xylene • 10% palladium(II) acetate-catalyst • Heat • Magnetic Stirrer • Condenser 	<ul style="list-style-type: none"> • 25 mL Dichloromethane • Magnetic Stirrer 	• 4-5 hours	• 48 Hours

Table 1. Conditions and reaction time for both synthesis and metathesis reactions.

I. Background

Ion pairing is a fundamental concept in chemistry and biology that can contribute to the improvement of anything from catalysis to battery technology. Electrochemistry is typically performed in a conductive polar solution because nonpolar solutions have a low dielectric permittivity and therefore lack the ability to produce a current flow. Electrolytes are often used to increase conductivity and dissipate ion pairs. The addition of electrolytes

can affect the redox potential which can give a false reading on the measurements. It is necessary to synthesize electrolytes that will not affect the redox potential in non-polar solvents. Equilibrium electrochemistry deals with interaction of ions in the solutions while non-equilibrium electrochemistry considers effects that occur when the system undergoes distress by an electric current passing through the system. The Bjerrum theory predicts that ions might exist separately only if their size ion exceeds a certain

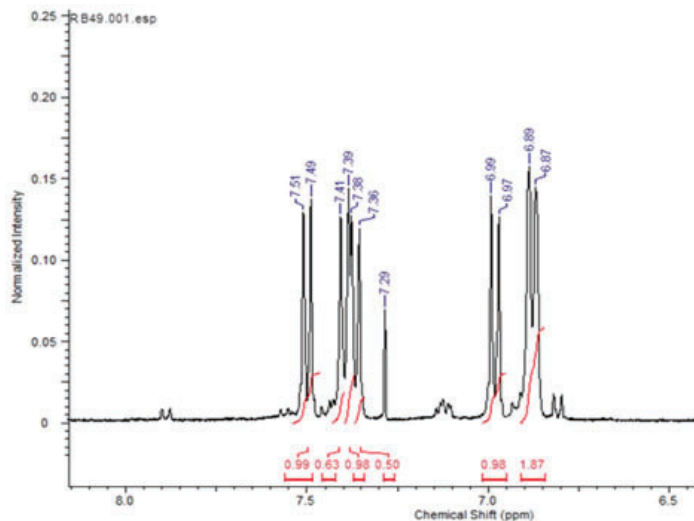
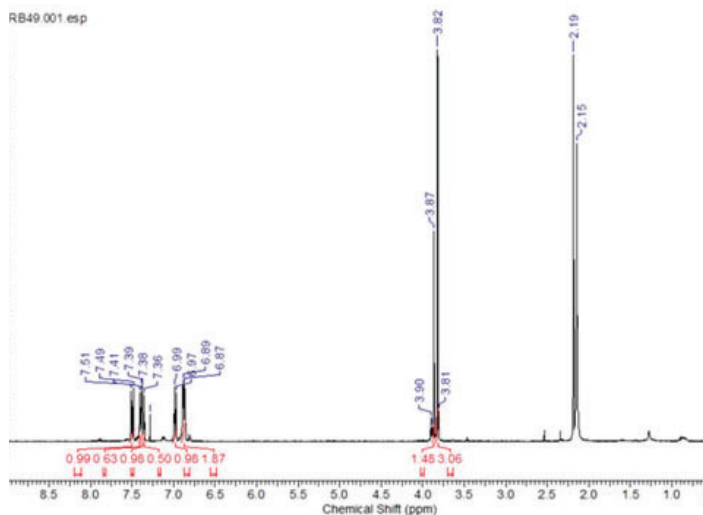


Figure 1. Proton NMR of full spectrum and zoomed in spectrum of final salt 1 (R= para OCH₃).

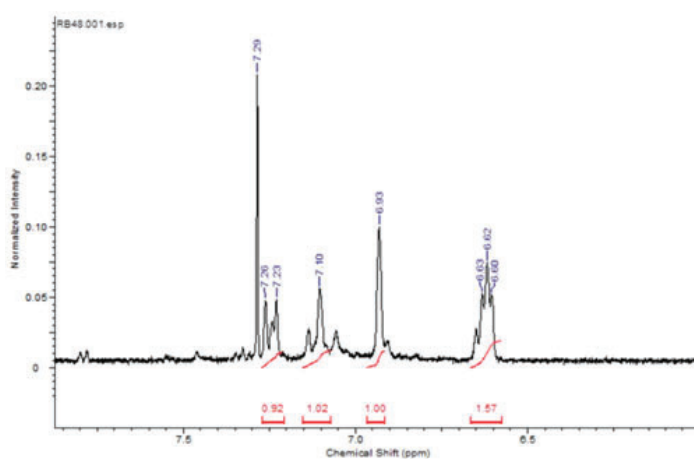
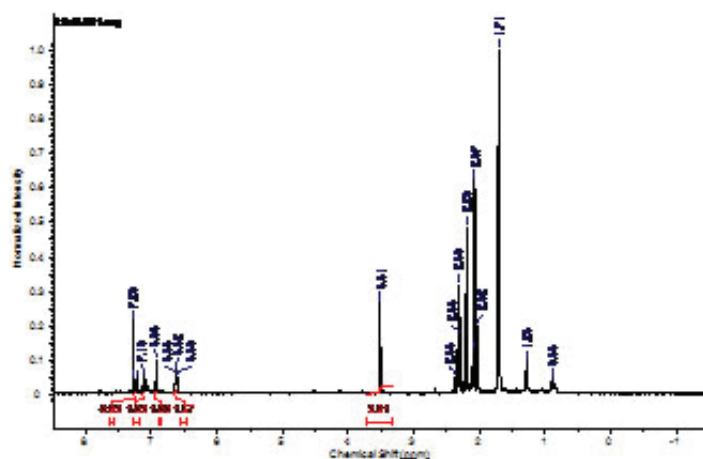


Figure 2. Proton NMR of full spectrum and zoomed in spectrum of final salt 2 (R= meta CH₃).

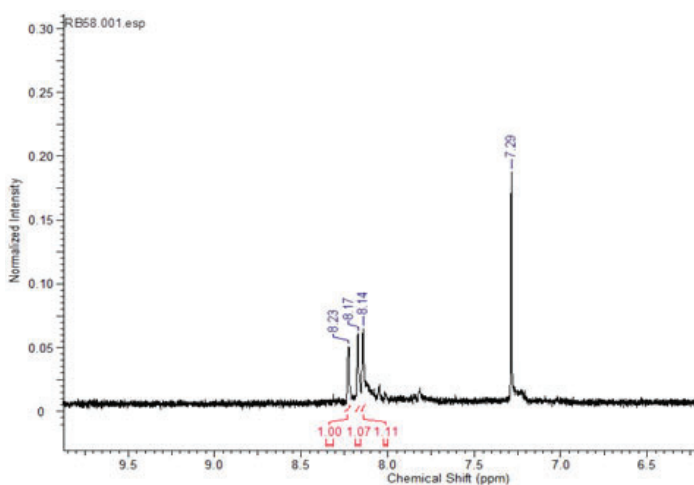
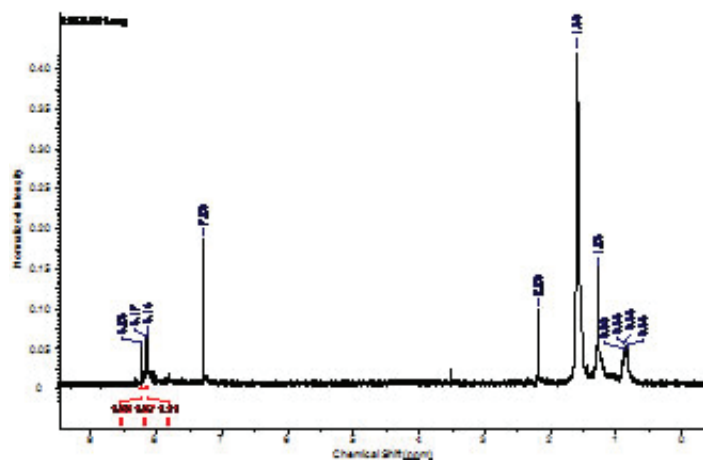


Figure 3. Proton NMR of full spectrum and zoomed in spectrum of final salt 3 (R= meta CF₃).

value, the Bjerrum radius (sB), otherwise the ions would build cation-anion pairs and the thermal motion would not be able to prevent their aggregation at small distances. This can be satisfied by using soluble molecules that can dissociate into large ions or that can further solubilize ions into larger micelles. We began by preparing salts or “ion pairs” that, due to the bulkier sizes of their constitutive ions, will dissociate into large cation and anions or prevent the ions from reuniting into pairs. Electrostatic attraction, declared by Coulomb’s Law, pulls these cations and anions together creating these ion pairs. They exist in dynamic balance between electrostatic attraction and destructive thermal motion. The conductivity measurements can confirm ionization but does not yield sufficient information on the size of the resulting ions or their dissociation constant.

II. Methods

Three functionalized aryl halides underwent a palladium-catalyzed coupling reaction with corresponding triarylphosphines in boiling o-xylene in order to produce new tetraarylphosphonium salts. The insoluble phosphonium was isolated from the reaction media by simple filtration. The metathesis reaction allowed an ex-

change of ions between the phosphonium that was synthesized and the lithium tetrakis boron pentafluorobenzene salt, which resulted in the formation of lithium bromide and the desired tetraarylphosphonium salt.

III. Data and Results

Below are the NMRs from each salt which proves that they were each completely synthesized. The conductivity could not be measured unless each salt was fully formed into their proposed tetraarylphosphonium salt.

Conductivity of our salts 1-4 were measured as displayed in the following figures. We disregarded any readings with the conductivity below 10^{-7} , since we cannot trust the probe readings, but this still shows that the salts with the CF₃ substituents have the lowest conductivity measurements and the lowest dissociation constant. Our preliminary results confirm the hypothesis that WCCs are excellent electrolytes in non-polar solvents. Compounds 1, 3, and 4 have shown strong conductivity in acetonitrile or any other solvents used. For the case of compound five with

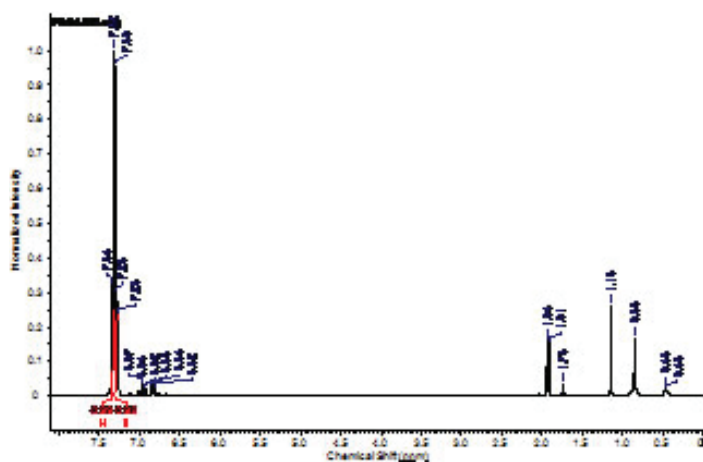


Figure 4. Proton NMR of full spectrum and zoomed in spectrum of final salt 4 (R= para CF₃).

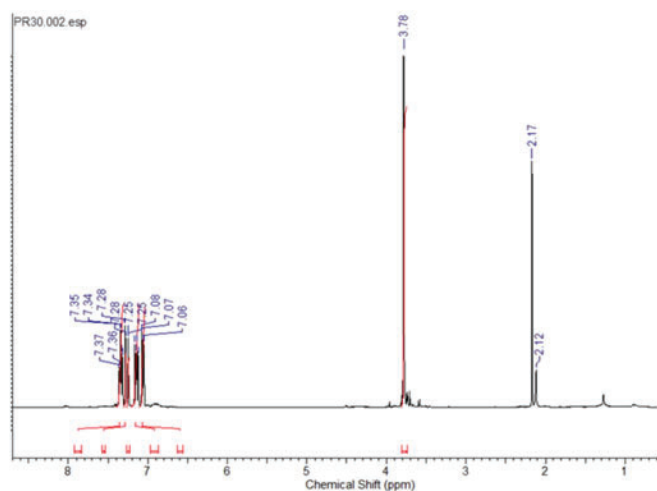


Figure 5. Proton NMR of full spectrum and zoomed in spectrum of final salt 5 (R= meta OCH₃).

intermediate results, we propose to conduct measure of conductivity in THF which has characteristics that may be more favorable for hydrophobic WCCs.

Substituents	Disassociation constant (Kd)	Limiting conductivity (Λ_0)
R=CF ₃ (para)	5.6 E-8 M	68.2 S/m
R=OCH ₃ (meta)	2.29E-4 M	90.1 S/m
R=CH ₃ (meta)	4.75 E-5 M	66.0 S/m
R=CF ₃ (meta)	1.3 E-8 M	61.3 S/m
TBA/TFAB	3.5 E-4 M	86.2 S/m
TBA/PF6	2.77 E -6 M	122.4 S/m

Table 2. Measurements taken from Figure 7.

IV. Future Studies

The larger WCCs have a smaller association constant and ionize readily from TFAB to allow a greater conductivity as corroborated in the conductivity graph. We expected that since the OCH₃ substituent to have the highest conductivity readings compared to both the para and meta CF₃, which is the smallest substituent. When we ran our conductivity measurements, we found that our hypothesis was correct. The para and meta OCH₃ substituents, did in fact have the highest conductivity measurements and therefore has the highest dissociation constant.

Since our results yielded two pairs of salts with completely different conductivity measurements, we propose to run the conductivity portion be measured again in THF in order to confirm these preliminary results in future studies. We would also propose that the conductivity measurements be carried out in another low polarity solvent just to make sure that the THF is not playing a factor in the conductivity and that the measurements hold relatively true throughout different low polarity solvents.

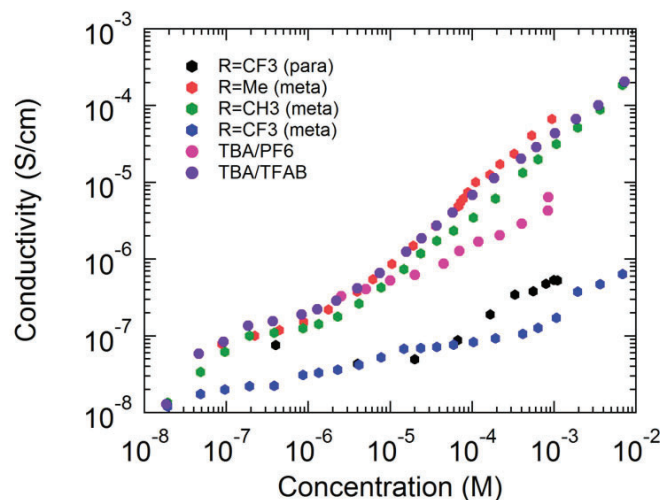


Figure 6. Raw data of concentration versus conductivity of TFAB salts

V. References

- LeSuer, R. J.; Geiger, W. E., Improved electrochemistry in low-polarity media using tetrakis(pentafluorophenyl)-borate salts as supporting electrolytes. *Angew Chem Int Edit* 2000, 39, 248-250.
- Marcoux, D.; Charette, A. B., Palladium-catalyzed synthesis of functionalized tetraarylphosphonium salts. *J Org Chem* 2008, 73, 590-593.
- Moritz, R.; Wagner, M.; Schollmeyer, D.; Baumgarten, M.; Mullen, K., Hydrophobic Encapsulated Phosphonium Salts-Synthesis of Weakly Coordinating Cations and their Application in Wittig Reactions. *Chem-Eur J* 2015, 21, 9119-9125.
- Moritz, R.; Zardalidis, G.; Butt, H. J.; Wagner, M.; Mullen, K.; Floudas, G., Ion Size Approaching the Bjerrum Length in Solvents of Low Polarity by Dendritic Encapsulation. *Macromolecules* 2014, 47, 191-196.
- Mpoukouvalas, K.; Turp, D.; Wagner, M.; Mullen, K.; Butt, H. J.; Floudas, G., Dissociation and Charge Transport in Salts of Dendronized Ions in Solvents of Low Polarity. *J Phys Chem B* 2011, 115, 5801-5806.

VI. Acknowledgements

This project was supported in part by the National Science Foundation, Louis Stokes Alliance(s) for Minority Participation (LSAMP) at Albany State University under the LSAMP Internship Program at Brookhaven National Laboratory.

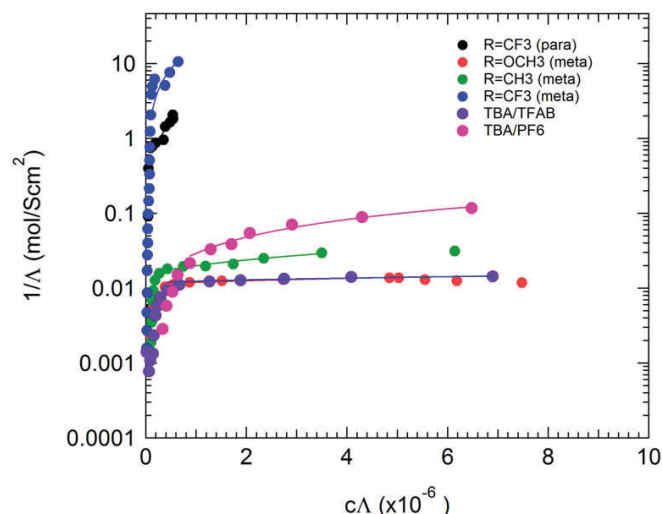


Figure 7. Graph charting the dissociation constant of each salt.

High precision gamma-ray spectroscopy for enhancing applications of the medical isotopes Bromine-77 and Manganese-52

B.A. Broder

Department of Physics and Astronomy, Western Kentucky University, Bowling Green, Kentucky 42101

E.A. McCutchan

National Nuclear Data Center, Brookhaven National Laboratory, Upton, New York 11973

S.V. Smith

Brookhaven Linear Isotope Producer, Brookhaven National Laboratory, Upton, New York 11973

J.P. Greene, M.P. Carpenter, and S. Zhu

Physics Division, Argonne National Laboratory, Argonne, Illinois 60439

C.J. Lister

Department of Physics and Applied Physics, University of Massachusetts Lowell, Lowell, Massachusetts 01854

L. Muench

Brookhaven Linear Isotope Producer,

Brookhaven National Laboratory, Upton, New York 11973

A.A. Sonzogni

National Nuclear Data Center, Brookhaven National Laboratory, Upton, New York 11973

P.A. Ellision and R.J. Nickles

Department of Medical Physics, University of Wisconsin--Madison, Madison, Wisconsin 53706

Abstract

Radioactive isotopes are used in countless imaging scans and medical procedures annually. However, many were last studied decades ago using low-sensitivity detection systems. The purpose of this project is to more accurately characterize the decay of Bromine-77 (used for radiotherapy) and Manganese-52 (used for Proton Emission Tomography imaging) by precisely quantifying the emitted gamma and beta radiation. Establishing isotope properties enables the identification of their optimal use in industry. As a result of data analysis, newly discovered gamma energies were added to the current list of energy levels. Additionally, several gamma energies and energy levels from both isotopes were not found and subsequently eliminated from the decay scheme. Finally, the total radiation emitted by each isotope was quantified and the resulting dose to the patient determined. These results can be applied to better understand radiation doses received during medical procedures as well as aid in more cost-effective and efficient production of the isotopes at facilities like the Brookhaven Linac Isotope Producer (BLIP).

I. INTRODUCTION

Mn-52 and Br-77 were last studied several decades ago: Br-77 was analyzed in 1974 and Mn-52 in 1977 [1] [2]. Both isotopes are being investigated for uses in medical imaging or radiotherapy.

Manganese-enhanced Magnetic Resonance Imaging (MEMRI) has previously been investigated due to its enhanced contrast in viewing anatomical detail and its ability to trace neuronal connections in vivo; Mn is transported by neurons in an activity-dependent manner, allowing the activity of the brain to be viewed with MEMRI [3]. However, MEMRI requires great concentrations of MnCl₂ to be effective, which could provide adverse ef-

fects in imaging subjects [4]. Subsequently, manganese is being further investigated as an isotope for use in Positron Emission Tomography (PET) imaging. Substantially less manganese would be required for this process, limiting the potential adverse effects of the Manganese. Additionally, PET scans can detect accumulation of the isotope in bone, whereas MRI cannot.

Br-77 is being investigated for several uses in medical imaging, as well as for internal radiotherapy in cancer treatment. Although radiobromides have been previously used in medicine, Br-77 has a longer half-life than Br-76 or Br-75, allowing for change to be viewed over a longer period of time [5]. Br-77 was shown to have high accumulation in tumor through sigma receptors, which are highly expressive in many human cancers and are thought to be an early prognostic tool for the success of therapeutic drugs [6]. The isotope was also favorable because its long half-life allowed accumulation in tumor over time, making it an ideal PET tracer for sigma receptor imaging. De Spiegeleer et al. has also investigated Br-77 as a SPECT isotope to be paired with a drug for HIV treatment [7].

In general, most current PET isotopes have extremely short half-lives: of the commonly used PET isotopes, the shortest half-life is Oxygen-15 at 2.04 minutes, and the longest is Fluorine-18 at 109.77 minutes [8][9]. In contrast, Mn-52 has a half-life of 5.591 days, more than seventy-three times longer than F-18, while Br-77 has a half-life of 57.036 hours, thirty one times that of F-18. Longer half-lives allow for images to be taken over several days and the progression of the image to be observed.

Despite their recent prevalence in emerging medical techniques, the decay radiation of the isotopes has not been assessed for decades and was done using detection systems of much lower sensitivity and accuracy. Yaffe and Meyer released the findings of their assessment in 1977; to measure the gamma rays, a low-energy photon spectrometer and several large volume Ge(Li)

spectrometers were used to determine the relative intensity. In contrast, this study utilized over 70 high-purity germanium detectors, allowing for a more precise analysis of data. Since Mn-52 and Br-77 are highly relevant and applicable in emerging modern medicine, the study of their decay schemes is necessary to ensure the isotopes are properly characterized in order to optimize its use and potential for future applications.

II. EXPERIMENT

The Br-77 sample was produced at the University of Wisconsin by irradiating a Nickel Selenium pellet with a 10 MeV proton beam. The Mn-52 sample was created at BLIP by projecting a 107 MeV proton beam on a natural Nickel foil of 0.0075 mm thickness. The samples were transported to Argonne National Laboratory and placed in Gammasphere, a spectrometer comprised of 110 spherically arranged high purity Compton-suppressed germanium detectors, at a source to detector distance of 23 cm. For the Br-77 experiment, 76 detectors were active; for the Mn-52, 83 detectors. Data was taken with a singles trigger, which was used to create a singles histogram of counts versus gamma-ray energy.

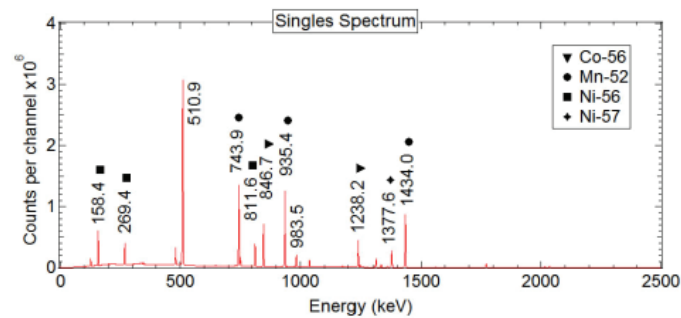


FIG. 1. Singles spectrum for Mn-52

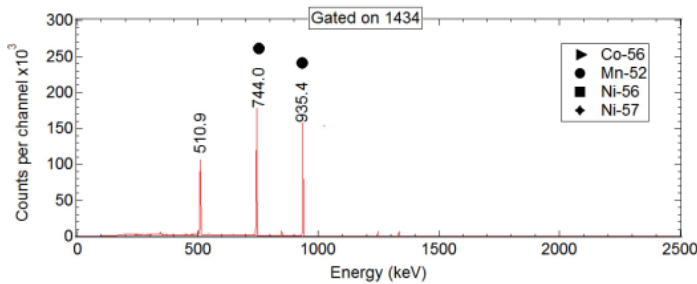


FIG. 3. Gated spectrum for Mn-52

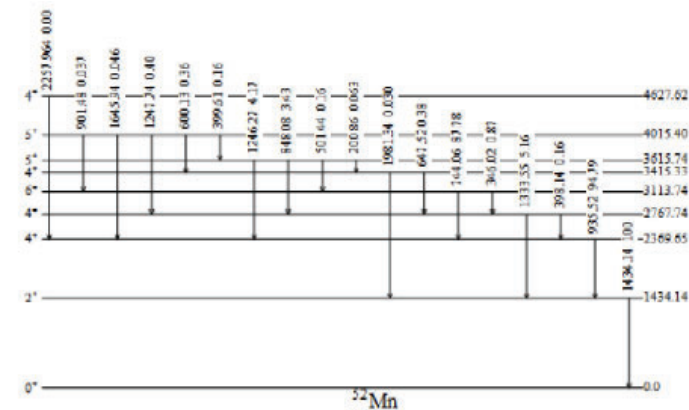


FIG. 5. Level scheme for Mn-52 obtained in the present work.

A matrix was constructed by selecting only gamma-ray transition which came within a short (20 ns) time window.

In total, 2.99×10^8 gamma events were observed in the spectrum and 6.82×10^7 events were observed in the gamma-gamma coincidence matrix for Mn-52; 1.60×10^{10} events were observed in the Br-77 spectrum and 4.90×10^9 events were observed in the gamma-gamma coincidence matrix. The gamma ray energies for Mn-52 vary from 200.58 to 2257.42, while the Br-77 energies vary from 13.4 keV to 1230.5 keV [1][2]. The efficiency calibration was done with an array of isotopes covering that energy range including Tantalum-182, Europium-152, and Cobalt-56 for Mn-52, and those isotopes plus Americium-243 for Br-77. Altogether, the calibration of Br-77 provided 55 data points, which were fitted into a 4th order polynomial equation; the calibration of Mn-52 provided 51 data points that were fitted to a 6th order polynomial equation. The log of each gamma energy associated with the isotope was found and inserted into their respective equations; the value was taken to the tenth power to find the efficiency.

The spectra of each were written in Root and analyzed in RadWare [10][11]. The energy levels were calibrated by finding

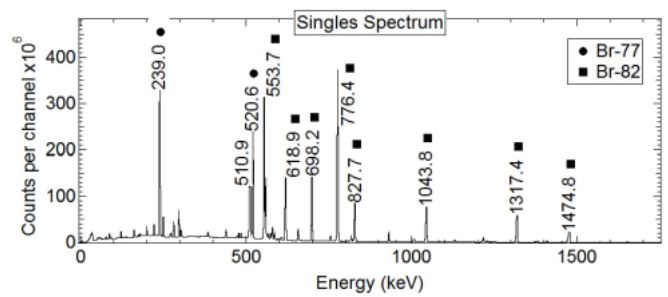


FIG. 2. Singles spectrum for Br-77

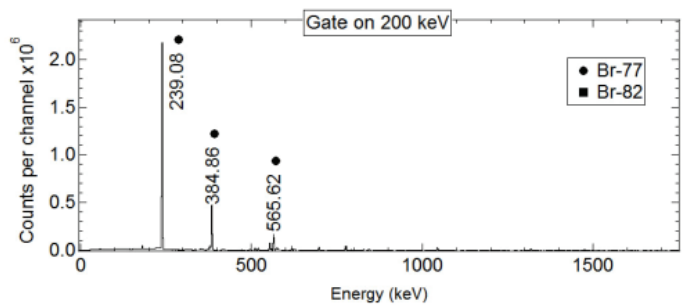


FIG. 4. Gated spectrum for Br-77

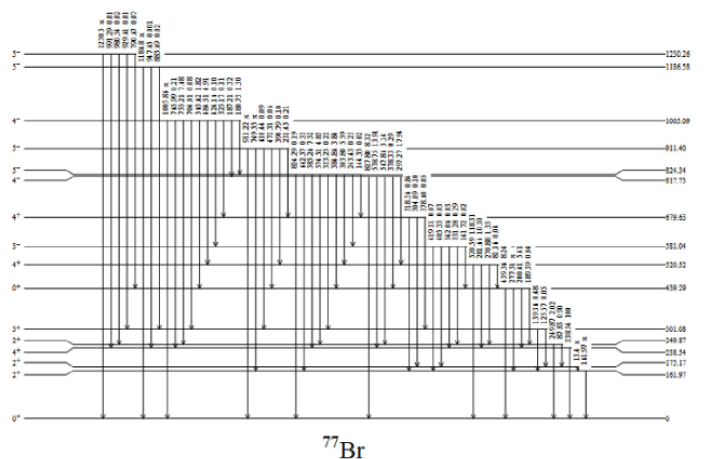


FIG. 6. Level scheme for Br-77 obtained in the present work.

the centroids of the energies given by Yaffe and Meyer and Braga and Sarantites in the spectrum and finding a linear fit of the given values and those determined in the data set. A sample singles spectrum for Mn-52 is given in Figure 1 and for Br-77 in Figure 2.

In addition to peaks from each isotope, peaks from Nickel-56, Nickel-57, and Cobalt-56 were seen in the Mn-52 spectrum, and can be seen in Figure 1. Figure 2 shows that Br-82 was the primary contaminant for Br-77; however, Br-76, Br-80m, and 56-Co are other contaminants in the spectrum. The matrix decreases the amount of contaminant peaks seen in the spectra because it requires a coincident gamma ray. Figure 3 shows a spectrum obtained by requiring a gate on the 1434-keV transition in 52Mn; whereas six contaminant peaks are visible in its spectrum (denoted in the legend by markers of other isotopes), no contaminant peaks are visible in the spectrum obtained from the matrix. The decrease in contamination increases the accuracy of the true peaks by decreasing the background that could be included in their gates. Figure 4 displays a gated spectrum for Br-77. Similar to the Mn-52, the spectrum resulting from a gate on the 200 keV transition of Br-77 brings the spectrum down from eight contaminant peaks to no contaminant peaks.

Aside from diminishing the prevalence of contaminants, the gamma-gamma coincident data allows improvement over previous measurements taken only as a spectrum, particularly for weak-intensity transitions and double peaks. The use of a matrix in this experiment would preclude a higher degree of accuracy. The peak area of cascading gamma rays was used to calculate intensity; Equation 1 is used for the singles data and Equation 2 is used for the doubles data.

$$I_1 = \frac{A_1}{\varepsilon_1 N} \quad (1)$$

$$I_2 = \frac{A_2}{\varepsilon_1 \varepsilon_2 B} \quad (2)$$

where I is the intensity for each peak, A is the area associated with each peak, ε_1 is the efficiency for the gamma being measured, ε_2 is the efficiency for the gamma being isolated, B is the branching ratio of the gamma, and N is an arbitrary constant. I_1 was the intensity in the spectrum, while I_2 was the intensity in a gated spectrum. Each gamma ray value was assessed by finding the centroid of its associated peak; the gamma rays in a cascade were summed together to find the energy level for the corresponding cascade. The energy level and intensity values were then used to calculate the beta radiation and overall dose according to an ENSDF calculation file. The values for each gamma, the energy level, and intensity were compiled into decay schemes in Figure 5 and Figure 6 using SciDraw in Mathematica [12][13].

To determine level spins and transition multipolarities, an angular correlation analysis was also performed. The 776 keV gamma and 1434 keV gammas were gated on to observe the $4^+ \rightarrow 2^+ \rightarrow 0^+$ spin transition and the area of the 1044 and 1650 keV gammas, and 952 and 1081 keV gammas, respectively, was taken for 18 matrices representing the range of angles from 0° to 180° . The corresponding intensities for each were calculated using the above equation. For comparison, each value of intensity was compared to a theoretical value given by Equation 3.

$$\omega(\theta) = A_{2,4}^2 A_{2,0}^2 P_2 \cos(\theta) + A_{2,4}^4 A_{2,0}^4 P_4 \cos(\theta) \quad (3)$$

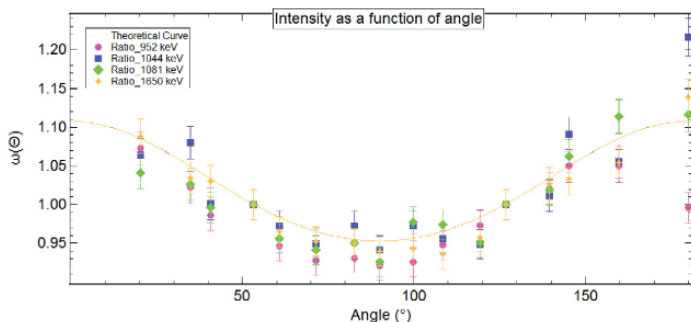


FIG. 7. Angular correlations for Br-77. The area was measured of each gamma in a lower gamma gate for a matrix representing 18 angles bins

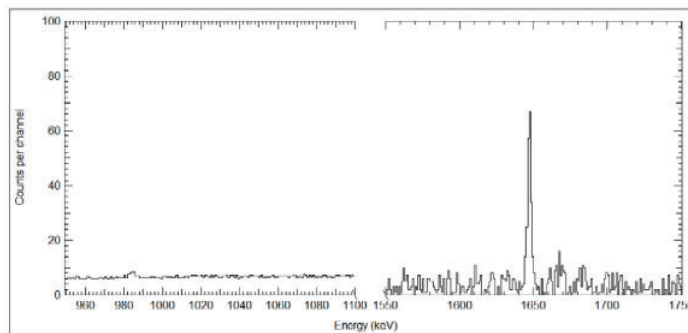


FIG. 8. Missing peak at 1045 keV in the Mn-52 isotope

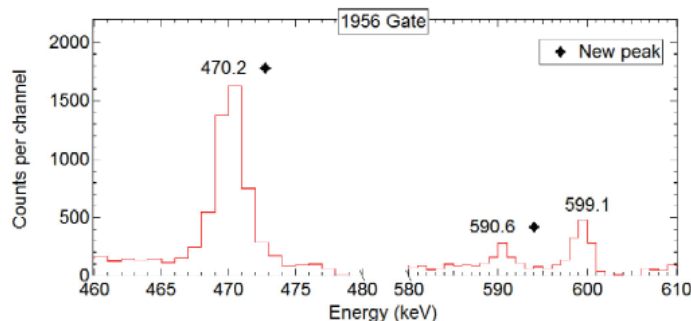


FIG. 9. Peaks are seen at 470.2 keV and 590.6 keV comparable to the 599 keV.

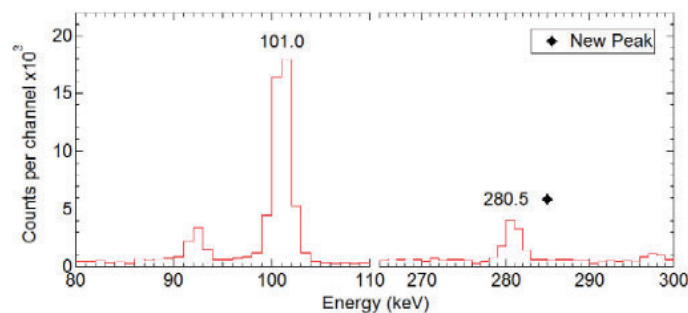


FIG. 10. A peak is seen at 280.5 keV. While not as large as the peak at 101.0 keV, its area is proportional when considering the relative intensities of both.

Where $\omega(\theta)$ is a function of intensity, A is a constant based on the spin associated with a given energy level, and the P functions are Legendre polynomials. The theoretical values of intensity according to Equation 3 are graphed in Figure 7 and are represented by the solid line. The experimental values found in each of the 18 matrices are denoted by solid markers in Figure 7; each type of marker represents one of the aforementioned $4^+ \rightarrow 2^+ \rightarrow 0^+$ spin transitions. The error bars show a 2% error in the $w(0)$ direction.

III. RESULTS

Precise values for gamma and beta radiation were quantified as a result of this project and compiled in the level schemes in Figure 5 and Figure 6. In particular, new values of gamma energies, energy levels, intensity, and beta intensity were found. While new transitions were not found in either isotope, some previous transitions were eliminated. For Mn-52, the 1045 keV gamma energy was eliminated from the decay scheme. Figure 8 shows a spectrum without a significant peak; if the 1045 keV gamma did exist, it would be visible therein.

In Br-77 several peaks were unidentified, but could not be definitively eliminated because they decay to the ground state; they are included in Figure 6, but their intensities are noted with an x. The intensity for all gammas was calculated and included a 2% baseline systematic error, although the intensities of some gamma rays had much larger error. Ten values for Mn-52 had an uncertainty below 10% of the intensity value and all except for the 2257 keV were less than 30%. More than half of the Mn-52 intensities had percent differences less than 10% and most were less than 25% with the exception of the 398 keV channel, with a percent difference of 60%. Br-77 had much smaller uncertainties: all were below 5% and most were below 2%. The percent differences varied widely depending on the gamma from 0.7% for the 424 keV gamma to 110% for the 189 keV gamma.

TABLE I. Overall radiation dose values for Mn-52

Mn-52: Energy Balance (keV)	Old	New	Percent Difference
Gammas	$3.46E+3 \pm 5$	$3.46E+3 \pm 5$	0%
X-Rays	0.94 ± 3	0.92 ± 3	1%
β^+	72.5 ± 24	84 ± 14	7%
Auger Electrons	2.67 ± 7	2.62 ± 5	0.9%
Sum	$4.71E+3 \pm 6$	4711.2 ± 19	0.1%

TABLE II. Overall radiation dose values for Br-77

Br-77: Energy Balance (keV)	Old	New	Percent Difference
Gammas	315 ± 3	317 ± 4	0.6%
X-Rays	5.96 ± 15	5.95 ± 15	0.2%
β^+	1.11 ± 5	1.11 ± 6	0%
Auger Electrons	4.92 ± 6	4.92 ± 7	0%
Sum	1365 ± 17	1364 ± 18	0.04%

IV. DISCUSSION

The energy values and intensities were used to calculate the overall radiation dose; although the individual values are relevant, the overall dose provides the sum of the radiation to the patient. In particular, the β^+ radiation is important for Mn-52 because PET scans detect positrons and the Auger electrons are im-

portant for Br-77 because they comprise Auger Therapy, in which cancer cells are damaged via short-range radiation. While neither isotope saw substantial changes in terms of the values, there were slight changes in both. The new and old values are displayed in Tables 1 and 2.

The total gamma energy was found according to Equation 4:

$$Q_\gamma = \sum E_\gamma I_\gamma \quad (4)$$

Where E_γ is the energy value for each gamma ray and I_γ is the corresponding intensity of that gamma ray. Although most of the changes are marginal, the largest increase can be attributed to the β^+ energy in the Mn-52 with a 18% difference. Since β^+ energy emits a positron, the increase in β^+ energy seen in Mn-52 could make it a more viable candidate for PET imaging. In contrast, the Auger electron value for Br-77 did not see any change in value. The stability in the Auger electron energy indicates that currently known radiation values for that treatment are consistent. While Br-77 and Mn-52 were the primary isotopes analyzed, it was also necessary to examine their contaminants to separate potential new energy levels from contaminant energy levels. The primary contaminant of Br-77 was Br-82; therefore, the energy levels were also analyzed for that isotope. Five new gamma energies were found in Br-82: a 2051 keV gamma; a 472 keV gamma; a 591 keV gamma; a 281 keV gamma; and a 272 keV gamma. Though these peaks are relatively small in intensity, they are comparable to other peaks seen within their gates and comparable or more intense to other, previously established peaks. Figure 9 and Figure 10 show gates in which the peaks are seen, as well as a peak of comparable intensity within the same gate for comparison.

V. CONCLUSION

In this project, potential PET isotope Mn-52 and radiotherapy isotope Br-77 were analyzed using GammSphere to more accurately detail their individual gamma energies and overall radiation dose. While both isotopes are of interest in emerging medicine, neither had been studied for decades, warranting their analysis and necessitating better characterization as they are considered in research and industry. The analysis revealed new values for intensity and individual gamma ray energies. When compiled into an overall value, the total radiation dose did not change significantly. However, the value for β^+ radiation did increase for Mn-52, indicating that it would be an even more promising PET isotope than previously though because it would provide more positrons than anticipated. Conversely, the analysis of Br-77 did not reveal a changed value of Auger electrons, used in radiotherapy. This does not mean that Br-77 would not make a good radiotherapy isotope but rather, that the previously known statistics are consistent. Analyzing Br-77 also revealed new gamma energies in its contaminant, Br-82.

VI. ACKNOWLEDGEMENTS

I'd like to thank my mentor, Libby McCutchan, for exposing me to this field of research and providing guidance and insight over the course of this project. Her mentorship will undoubtedly prove invaluable in my future research career. DOE Isotope Program is acknowledged for funding ST5001030. Work supported by the U.S. DOE under Grant No. DE-FG02-94ER40848 and Contract Nos. DE-AC02-98CH10946 and DE-AC02-06CH11357 and by the DOE Office of Science, Office of Workforce De-

velopment for Teachers and Scientists (WDTS) under the Science Undergraduate Laboratory Internships Program (SULI). The figures for this article have been created using the SciDraw scientific figure preparation system.

VII. REFERENCES

- [1] Braga, R. A. & Sarantites, D. G., 1974. Multipole mixing ratios in ^{77}Se from Gamma-Gamma directional correlations following 56-h ^{77}Br decay. *Physical Review C*, 9(4), pp. 1493-1505.
- [2] Yaffe, R. & Meyer, R., 1977. Levels of ^{52}Cr populated in the decay of ^{52}V , $^{52}\text{Mn}(g)$ and in the Sequence $^{52}\text{Fe}^-$ -, $^{52}\text{Mn}(m)$ -, ^{52}Cr . *Physical Review C*, 16(4), pp. 1581-1589.
- [3] Massaad, C. & Pautler, R., 2011. Manganese-enhanced magnetic resonance imaging (MEMRI). *Methods in Molecular Biology*, Volume 711, pp. 145-174.
- [4] Topping, G. et al., 2013. Manganese-52 positron emission tomography tracer characterization and initial results in phantoms and in vivo. *Medical Physics*, pp. 50-62.
- [5] Spahn, I. et al., 2011. Investigation of production possibilities of radiobromines for diagnostic and therapeutic applications. *Journal of the Korean Physical Society*, 59(1), pp. 1983-1986.
- [6] Ogawa, K. et al., 2013. Development and evaluation of a radiobromine-labeled sigma ligand for tumor imaging. *Nuclear Medicine and Biology*, Volume 40, pp. 445-450.
- [7] De Spiegeleer, B. et al., 2006. Synthesis and HPLC-purification of [^{77}Br]TMC125-R165335 (etravirine), a new anti-HIV drug of the DAPY-NNRTI class. *Journal of Labelled Compounds and Radiopharmaceuticals*, Volume 49, pp. 683-686.
- [8] Brookhaven National Laboratory, n.d. NuDat 2.
- [9] Mayfield Clinic, n.d. Positron Emission Tomography (PET). Available at: <http://www.mayfieldclinic.com/PDF/PE-PET.pdf>
- [10] Radford, D., 2000. RadWare.
- [11] CERN, 2016. Root.
- [12] Caprio, M., 2005. *Comput. Phys. Commun.* 171 (107).
- [13] Wolfram Research, Inc., 2016. *Mathematica*, Volume Version 9.
- [14] Schmitz, R. E., Alessio, A. M. & Kinahan, P. E., n.d. The physics of PET/CT scanners. Available at: <http://depts.washington.edu/imreslab/education/Physics%20of%20PET.pdf>

Effects of electron delocalization on infrared vibrations and redox potentials

Chase Bryant

Chemistry, Eastern New Mexico University, Portales, NM 88130

Danielle Caro

Chemistry, Eastern New Mexico University, Portales, NM 88130

Juchao Yan

Chemistry, Eastern New Mexico University, Portales, NM 88130

Tomo Mani and John Miller

Chemistry, Brookhaven National Laboratory, Upton, NY 11973

Abstract

While many think of silica based solar panels as the main medium used for solar energy, conjugated organic polymers can also be used in these applications. Conjugated polymers can be used for solar energy because of electron delocalization in the pi orbitals that allows for electron transfer along their structures. While electron delocalization opens many possibilities because it allows for the production of flexible, durable, and low cost printing of organic solar cells which leads to renewable and sustainable energy for our society, the efficiency of such cells still needs improvement. To complete this research we must first synthesize rigid, planar oligomers and then use Fourier Transform Infrared analysis (FTIR), cyclic voltammetry, and pulse radiolysis to provide possible conclusions on the structure-property relationship of electron delocalization. Nitrile groups have shown to be effective probes for electron delocalization in terms of infrared vibrations. We plan to establish the structure-property relationships, focusing on the effect of dihedral or torsional angles on electron delocalization by utilizing nitrile IR vibrations to probe the degree of electron delocalization. We are also interested in determining the redox potentials of newly synthesized molecules in an electrolyte-free environment of very low dielectric constant. Suzuki-cross coupling, cyclization, bromination, alkylation, and nitrilization were used for synthesis. In addition, extraction, rotoevaporation, thin-layer chromatography (TLC), and column chromatography (CC) were utilized to isolate each product in the multi-step synthesis. The first step of the synthesis of our first organic molecule (denoted as "L3") was confirmed with Nuclear Magnetic Resonance (NMR) analysis. The bromination, cyclization, and alkylation of the second organic molecule (denoted "L4") were also confirmed by NMR. This research can provide data to assist in the optimization of organic solar cell efficiency by providing information about what structural properties aid in maximizing electron delocalization. We have gained knowledge concerning organic synthesis along with the lab techniques that are involved. We have learned new techniques for setting up, work up, and purification of newly synthesized organic molecules.

I. Introduction

Determining the efficiency of electron transport through organic conjugated molecules is based on the localization and delocalization of electrons. To apply this science to real world applications, such as solar panels, we must be able to understand the electronic energy and dynamics that control electron trans-

port capabilities in one dimensional conjugated chains. It has been shown through time-resolved infrared and pulse radiolysis that nitrile $\nu(\text{C}\equiv\text{N})$ vibrations respond to the degree of electron localization in nitrile-substituted oligomers (Mani et al. 2015). Measuring aryl nitrile anions allows us to conclude that the more electron localization in the nitrile anion, the larger the IR shifts (Mani et al. 2015). We expect to see smaller IR shifts with our rigid, planar oligomers as a sign of increasing the degree of electron delocalization, and thus providing possible structure-property relationships that could possibly allow for applications to increase organic solar cell efficiency. By experimenting with the shift of the nitrile $\nu(\text{C}\equiv\text{N})$ IR vibrational bands, we can determine how the electron is localized in anions of nitrile-functionalized oligofluorenes, which we plan to synthesize. Also, determining redox potentials of our synthesized oligomers allows insight into the energy of electron transfer.

II. Methods/Materials

A. L3PCN

In the process of synthesizing L3PCN we were able to make it as far as the first step, synthesizing an uncyclized three ring benzene through the use of suzuki-coupling. We completed this process twice with two different reactions, each with their own starting material, but both resulting in the same product. In reaction 1, we used 1,4 dichloro-2,5-dibromobenzene and o-toylboronic acid as our reactants (see Fig. 2), while in reaction 2 we

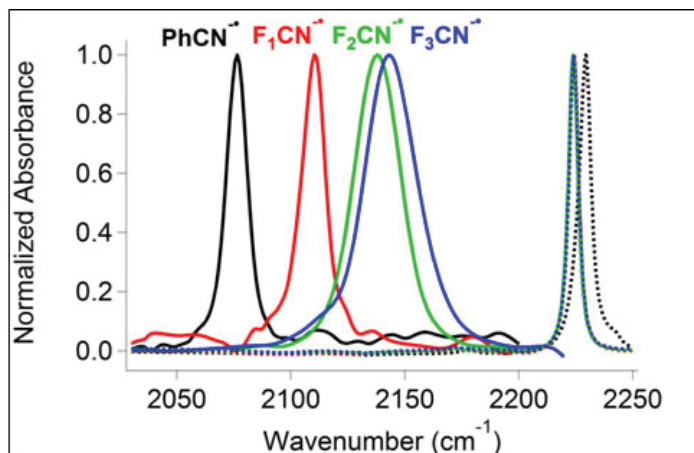


Figure 1. IR spectra showing narrowing of IR peaks in the absence of torsional angles due to degree of electron delocalization in cyanated oligofluorene anions containing varied phenyl groups as well as cyanated benzene (Mani et al. 2015).

used 1,4-dibromo-2,5-dimethylbenzene and 2-chlorophenylboronic acid (see Fig. 3). Both were tested using ^1H - and ^{13}C -NMR spectroscopy to determine the purity and confirm the structure of the idealized compound. In order to run this reaction for both sets of reactants, we started using the same materials: Potassium Carbonate (K_2CO_3), Palladium (II) Acetate ($\text{Pd}(\text{OAc})_2$), Tricyclohexylphosphine ($\text{P}(\text{Cy})_3$), Pivalic Acid ($t\text{-BuCOOH}$), and Dimethylacetamide (DMA). We had to calculate the molar ratios of all of the reactants to determine the amounts to be used. In the first reaction of 1,4-dichloro-2,5-dibromobenzene and *o*-toylboronic acid we used the 1,4-dichloro-2,5-dibromobenzene compound as the molar standard and based everything else off of it. The other main reactant, *o*-toylboronic acid, was applied at 200% of the molar value of 1,4-dichloro-2,5-dibromobenzene, although we decided to make a modification and add an excess of 20%, making a total of 220% in order to ensure the reactions' completion. As for the ligands, $\text{P}(\text{Cy})_3$ and $t\text{-BuCOOH}$, they were added as 6% and 100% of the molar standard. The catalyst $\text{Pd}(\text{OAc})_2$ was added initially as 3% of the molar standard, but throughout the reaction we would sometimes add more to increase the concentration in order drive the reaction forward. Finally, the base K_2CO_3 was added at 600% of the molar standard. For the second reaction, we used the same ratios for the ligands, base, and catalyst, but used 1,4-dibromo-2,5-dimethylbenzene as the molar standard, and added 2-chlorophenylboronic acid at 200%.

We conducted both of the experiments in a 500 mL three neck round bottom flask, one opening for the condenser, one for a SEPTA rubber to allow the reaction to bubble under Argon gas, and the last for a glass stopper to allow for easy and frequent monitoring. Before beginning the reaction we degassed the DMA under Argon for thirty minutes prior to the addition of the reactants. Once adding the reactants we left the round bottom on a hotplate at 140°C with constant stirring and a running condenser, until TLC monitoring showed the absence of the starting material (typically the reaction was left over night).

Once the reaction was completed we washed the solution in a separatory funnel with both dichloromethane (DCM) and then brine (water saturated with NaCl) in order to separate out the targeted organic layer. Then, we dried the solution in MgSO_4 overnight to ensure that all of the water was removed. Next, we used vacuum filtration to remove the solid MgSO_4 particles before running the rotoevaporator to remove the DCM from the solution. Once all of this was completed we used column chromatography

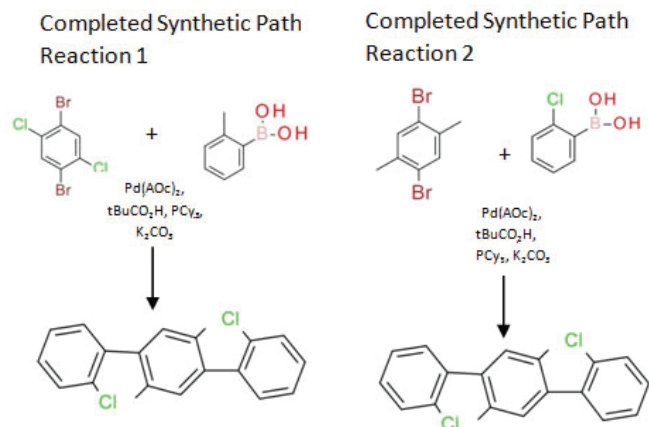


Figure 2 (left). Rxn 1 Synthetic Path.
Figure 3 (right). Rxn 2 Synthetic Path.

to separate out our target compounds from the last bit of impurities. This process was monitored by TLC plates during the column and finalized by NMR after drying and rotavaping out the solvent used in the column, hexane.

After completing the steps shown above we would have to additionally complete the following path to reach the complete L3PCN compound. Future pathways (see Fig. 4).

B. L4PCN

In the process of synthesizing L4CPN we were able to complete the coupling, cyclization, bromination, alkylation, and second coupling of our product. The reaction setups was similar to that of L3PCN using 3-neck roundbottoms and a condenser for heated reactions. All solvents used in each reaction were degassed for 1 hour using an Argon gas needle and rubber septa. After completion of each reaction, the resulting mixtures were quenched with distilled water. Then the resulting reaction mixtures were extracted using DCM except in the alkylation step, in which ethyl acetate was used for extraction. A brine wash was used in each extraction to increase transfer of products to the organic phase. Sodium thiosulfate solution was also used for the bromination step. After extraction the target compounds were isolated utilizing column chromatography and thin-layer chromatography with hexane solvent. Rotoevaporation was used to remove all solvents after extraction and isolation. The fluorene, dibrominated fluorene, alkylated-dibrominated fluorene, and coupled four-phenyl ring compounds were assessed for purity and confirmed using ^1H - and ^{13}C -NMR spectroscopy.

Reaction 1 was completed through using Suzuki-cross coupling in a single reaction vessel containing 3-bromo-4-chloro toluene and 2,5-dimethylphenyl boronic acid in which the product is then cyclized utilizing the same mechanism. For reaction 1, the reactants 3-bromo-4-chloro toluene and 2,5-dimethylphenyl boronic acid are used in a 1:1 ratio and are used as the molar standard. The reagents Potassium Carbonate (K_2CO_3), Palladium (II) Acetate ($\text{Pd}(\text{OAc})_2$), Tricyclohexylphosphine ($\text{P}(\text{Cy})_3$) and Pivalic Acid ($t\text{-BuCOOH}$) were used in molar percentages of 600%,

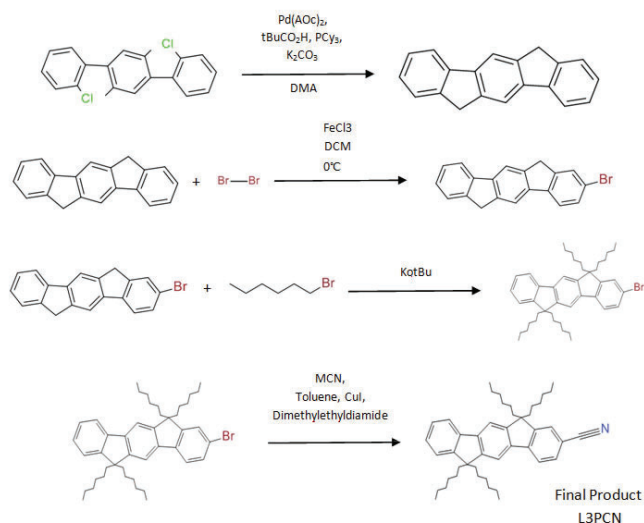


Figure 4. Future Synthetic Pathways for L3PCN (Mani et al. 2015; Kobin et al. 2012; Zanon et al. 2003; and Liu et al. 2010).

3%, 6%, and 100% in DMA solvent at 140°C with stirring for 24 hours (see Fig. 5).

In reaction 2, the cyclized diphenyl compound, known as fluorene, is brominated at 0°C for 2 hours using a 1:2 ratio of fluorene to dibromine in DCM solvent. The reagent iron (III) chloride was first added at a 1% molar percentage to fluorene after cooling in ice bath with stirring and then dibromine was added dropwise (see Fig. 6).

In reaction 3, the dibrominated fluorene is alkylated at 40°C for 3 hours using a 1:2 ratio of dibrominated fluorene to 1-bromo-

hexane in tetrahydrofuran (THF) solvent. The reagent Potassium t- butoxide (KotBu) is used at 300% molar percentage to the dibrominated fluorene and 1-bromohexane is added dropwise (see Fig. 7).

In reaction 4, the diphenyl compound is then coupled again by using 2-chlorophenyl boronic acid in a 1:2 ratio using Suzuki-coupling to create a four- phenyl ring structure. The resulting compound is then cyclized utilizing the same mechanism. This reaction was completed using the same procedure and molar percentages as reaction 1 (see Fig. 8).

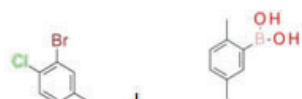


Figure 5. Reaction 1. (left)
Figure 6. Reaction 2. (right)

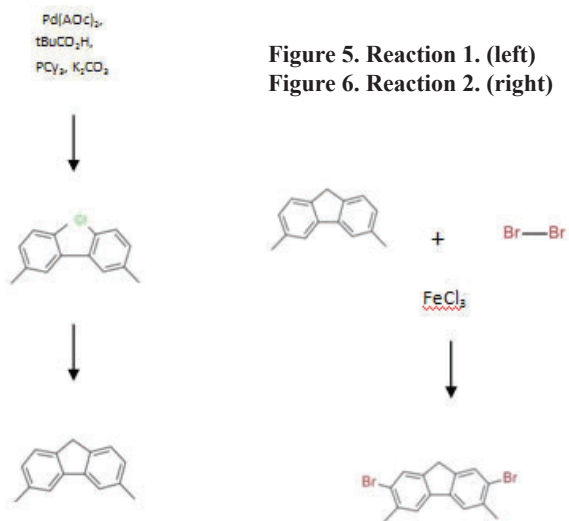


Figure 9. Future synthetic path for L4CPN (Mani et al. 2015; Kobin et al. 2012; Zanon et al. 2003; and Liu et al. 2010).

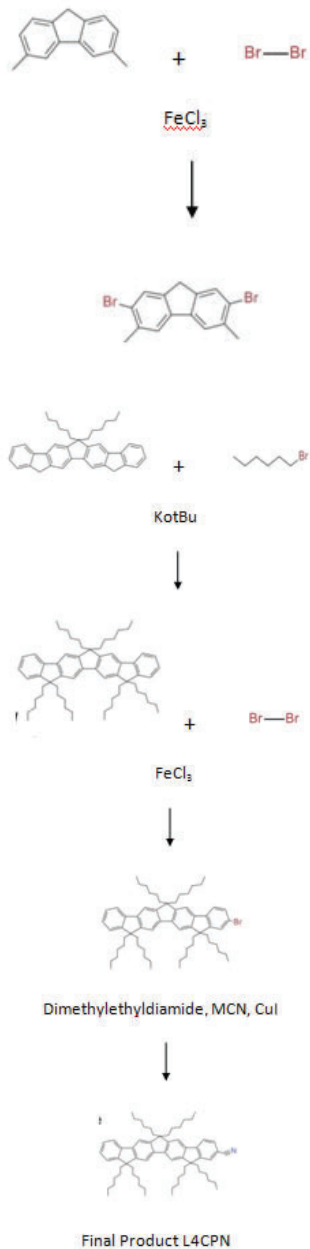


Figure 7. Reaction 3. (left)
Figure 8. Reaction 4. (right)

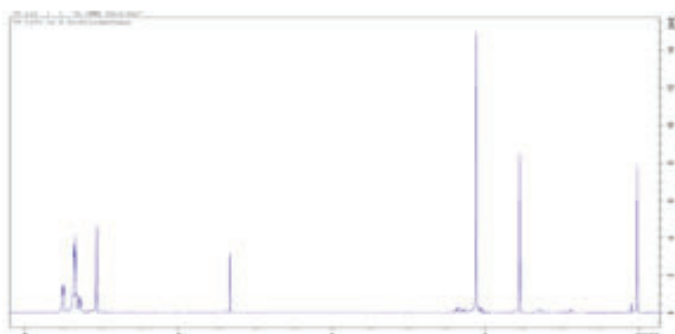
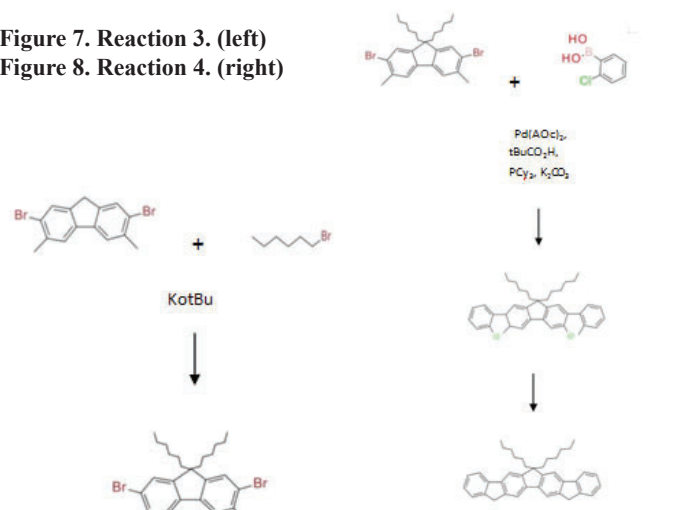


Figure 10. 1H-NMR for reaction 1.



Figure 11. 1H-NMR for reaction 2.

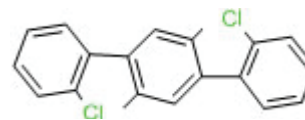


Figure 12. Uncyclized 3-phenyl compound.

The future pathways that would have been taken would be alkylation and bromination completed as before with a 1:1 ratio used for bromination instead. Nitrilization would then be completed (see Fig. 9).

III. Results

A. L3PCN

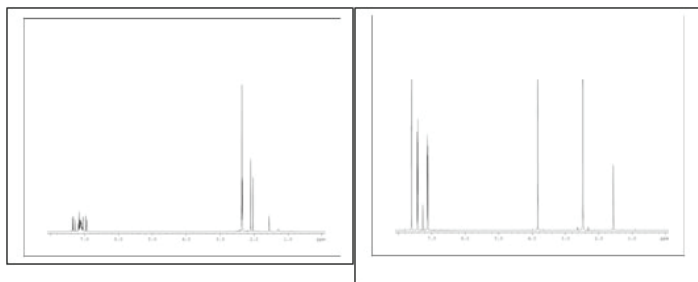
After running the first step of the synthesis for both reactions of L3PCN we ran NMR in a dichloromethane-d solvent and came up with the results shown below (see Fig. 10-11). Both of the NMR proton spectra show a pure substance for both reactions due to conformation of ratios and peaks. Splitting the symmetrical compound in half you should find one peak for the three hydrogens on the methyl group of the center benzene ring, one hydrogen from the center benzene ring, and four others on the outer ring, one of which will be shifted downfield due to its location next to the chlorine group.

Although the compounds were very pure, the yield came out being extremely low (see Table 1). This could have been for a variety of reasons, such as the lack of solubility in DMA, deactivation of Pd Catalyst, and possible fluctuations in the heat applied to the reaction. This synthesis requires many complicated steps. To reach even one intermediate, you must complete all of the steps that were listed in the methods and materials sections. The organic compound that we were able to successfully synthesize is shown here (see Fig. 12).

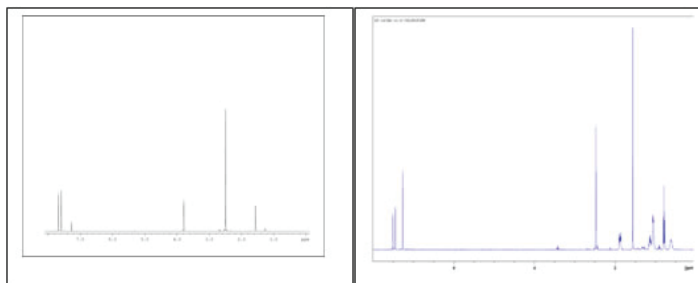
Reaction	% Yield
1	15.0%
2	12.4%

Table 1. Percent yields for L3PCN.

B. L4CPN



(Left) Figure 13. ¹H-NMR for un-cyclized fluorene, aromatic and halogen protons shifted downfield. (right) Figure 14. ¹H-NMR for fluorene, aromatic and halogen protons shifted downfield.



(Left) Figure 15. ¹H-NMR for brominated fluorene, aromatic and halogen protons shifted downfield. (right) Figure 16. ¹H-NMR for alkylated-brominated fluorene, aromatic and halogen protons shifted downfield.

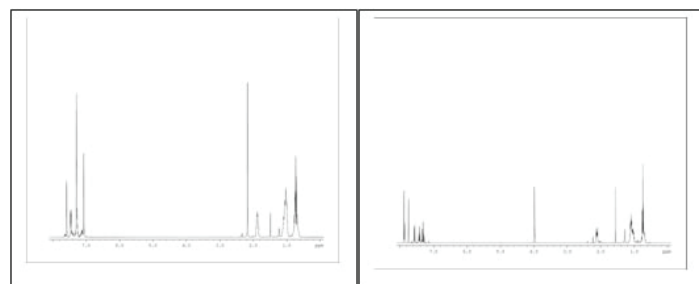
We obtained NMR spectra for the completed reactions for the target compound L4PCN, along with percent yields, for each reaction step in both chloroform-d and dichloromethane-d solvents. The un-cyclized fluorene precursor has a 6:4:3:1:1 ratio of protons in which 6 would be the two equivalent methyl groups, 4 would be the 4 equivalent aromatic protons, 3 would be the single methyl group to be cyclized, 1 being the proton close to the single methyl group, and 1 being the proton close to the chlorine atom (see Fig. 13). The fluorene compound has a 6:2:2:2:2 ratio in which 6 would be the two equivalent methyl groups, 2 would be on the newly formed carbon bond where the cyclization occurs, and 2:2:2 being the aromatic protons attached to different phenyl carbons (see Fig. 14). The brominated fluorene would have a 6:2:2:2 ratio in which 6 would be the two equivalent methyl groups and 2:2:2 would be the aromatic protons attached to different phenyl carbons (see Fig. 15). The alkylated-brominated fluorene would have a 12:6:6:4:4:2:2 ratio in which 12 would be in the middle of the hexyl chains, 6 would be the end of the hexyl chains, 6 for the methyl groups, 4 would be the start of the hexyl chains from the cyclization site, 4 would be attached to the second carbons in the hexyl chains, and 2:2 would be for the aromatic protons (see Fig. 16). The un-cyclized and cyclized coupled products would have similar ratios to the un-cyclized and cyclized fluorenes in which would be doubled due to addition of the phenyl groups (see Fig. 17- 18). NMR analysis confirms decent purities due to correspondence with chemical structures and percent yields were fairly decent with all being greater than 50% (see Table 2).

Reaction	% Yield
1	67.3%
2	68.4%
3	91.3%
4	75.7%

Table 2. Percent yields for L4CPN.

IV. Discussion/Conclusion

Due to the time-taking, multi-step synthesis required to obtain compounds for our analysis, we cannot yet establish conclusions on the degree of electron delocalization or redox behavior of the target compounds. However, it is expected that the rigid, planar nature of our target compounds will give narrower IR peaks because of the minimization of torsional angles (Mani and Miller, 2014). For our L3 compound future steps would be to continue on with the cyclization, bromination, alkylation, and nitrilization to



(Left) Figure 17. ¹H-NMR for un-cyclized coupled product, aromatic and halogen protons shifted downfield. (right) Figure 18. ¹H-NMR for cyclized coupled product, aromatic and halogen protons shifted downfield.

achieve our final synthesized product (mechanisms shown to the above). Upon completion of the synthesis of L3PCN we would move on to cyclic voltammetry of the synthesized compounds in the presence of TBA⁺PF₆ in THF, TRIR following pulse radiolysis to measure the electron delocalization on the basis of vibrational stark shift, and the determination the redox potentials of our compounds using conductivity and spectrophotometric measurements in order to complete our study in the hopes of increasing the efficiency of solar panels (Mani et al. 2015). For our L4 compound we plan to alkylate, mono-brominate, and add a nitrile group the coupled four-phenyl ring structure. We will then also run TRIR, pulse radiolysis, and cyclic voltammetry on this compound.

V. References

- ¹Kobin, B., Grubert, L., Blumstengel, S., Henneberger, F., Hecht, S., *J. Mater. Chem.* 2012, 22, 4383-4390.
- ²Liu, T.P., Xing, C.H., Hu, Q.S., *Angew. Chem. Int. Ed.* 2010, 49, 2909-2912.
- ³Mani, T., Miller, J.R., *J. Phys. Chem. A* 2014, 118, 9451-9459.
- ⁴Mani, T., Grills, D.C., Miller, J.R., *J. Am. Chem. Soc.* 2015, 137, 1136-1140.
- ⁵Mani, T., Grills, D.C., Newton, M.D., and Miller, J.R. *J. Am. Chem. Soc.* 2015, 137, 10979–1099155.
- ⁶Zanon, J., Klapars, A., Buchwald, S.L. *J. Am. Chem. Soc.* 2003, 125, 2890-2891.

VI. Acknowledgments

This project was supported in part by the U.S. Department of Energy, Office of Science, Office of Workforce Development for Teachers and Scientists (WDTS) under the Visiting Faculty Program (VFP).

Design and analyses of fixtures and tools for the sPHENIX calorimeters

Brenna Buckley

MANE Department, Rensselaer Polytechnic Institute, Troy, NY 12180

Donald Lynch and Richard Ruggiero

Physics Department, Brookhaven National Laboratory, Upton, NY 11973

Abstract

To expand experimentation at the Relativistic Heavy Ion Collider (RHIC), one of the major facilities at Brookhaven National Laboratory (BNL), a new detector known as the super Pioneering High Energy Nuclear Interaction eXperiment (sPHENIX) is being developed. This detector is composed of five main subsystems, the largest being the outer hadronic calorimeter (HCal). The outer HCal collectively weighs nearly 480 tons, with each of its thirty-two sectors having a length of over twenty one feet and weighing just under fifteen tons. In order to assemble and install the detector, there must be fixtures to store, lift, and rotate sections of the outer HCal. Designing these fixtures required conceptualization, modeling, analysis and modification of ideas. Directly attached to each sector are two trunions, one on either side, which are the main components of the lifting assembly. To support the sectors on the ground, there will be adjustable stands on either side that attach to the trunions. To lift the sectors, there will be a hook that pins into the trunion and attaches to a spreader bar above to lift the sectors. Each fixture was analyzed for stresses to insure that the applied load could be supported. Alterations were then made to make the fixtures more efficient. As a result of my assignment at BNL I have become familiar with Autodesk Inventor and gained experience with the practical implementation of engineering design.

I. Background

The current PHENIX detector at RHIC has allowed scientists to study quark-gluon plasma through energy mapping of ion collisions. sPHENIX is a proposed upgrade to the current project which will allow for more detailed analyzation of this plasma, hopefully leading to a further understanding of its nature. This upgrade involves a redesign of the entire PHENIX detector and major renovations to its current infrastructure. The new detector, as currently proposed, will consist of six major components.

These include the endcaps, electromagnetic calorimeter (EMCal), support rings, cryostat, inner hadronic calorimeter, and outer hadronic calorimeter (HCal). A diagram of the components can be seen in Figure 1. As part of this upgrade, there need to be fixtures to prepare and transport the various components so they can be installed in the detector.

Each of the three calorimeters are composed of 32 sectors which, when assembled, form a cylindrical shell. In the hollow area of each calorimeter other components will be installed. The pedestal, the main structural support for the detector, will be assembled first. Once in place, the lower 180° of outer HCal sectors need to be positioned on the pedestal. Then the other systems can be installed, namely the two remaining calorimeters and the cryostat. The remaining sectors of the outer HCal are to be installed last, after the internal portions of the detector are secured. Every component of the detector will be centered on the interaction point of the RHIC beam pipe. Figure 2 shows an assembled view of sPHENIX. Due to the abnormal size and shape of each component the installation fixture and procedure is complex but needs to be precise. The sectors of the outer HCal must be installed individually, each in a different orientation, and set within a 2 millimeter tolerance of one another.

II. Methods

Designing fixtures for lifting and holding the outer HCal requires consideration of available tools. In the assembly hall for sPHENIX, there is a 40 ton crane which will be used to lift all components. There are also chain falls, slings and shackles available at BNL that can be used for this project. In addition, set tolerances must be met. This includes the 2 millimeter gap between installed sectors and maintaining the 0.75 millimeters between plates and tiles within each sector.

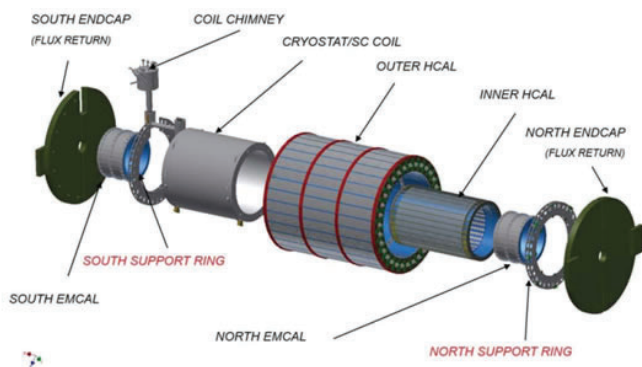


Figure 1: sPHENIX detector components

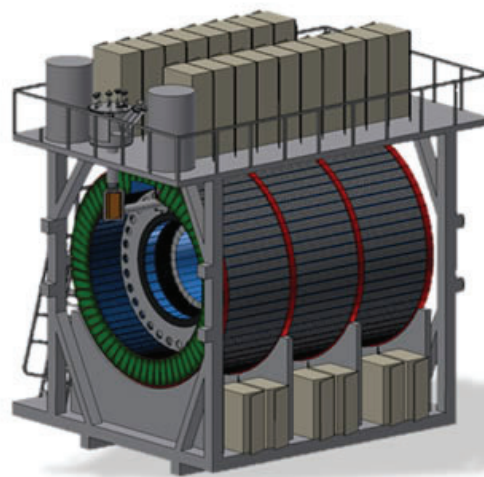


Figure 2: Assembled sPHENIX detector

A. Lifting Fixtures

There is a single 40 ton crane hook in the assembly hall, around which the lifting procedures for the outer HCal sectors must be developed. Since the sectors are each 21.22 feet long, a spreader beam would be necessary to transport the sectors with minimal lifting stresses. Optimizing the angle of the sling between the beam and sector will help reduce the stresses, and Table 1 determines the ideal length assuming a custom spreader beam is not available (which would create a 90° angle). These beams are typically adjustable in one foot increments, so calculations were done accordingly and it was determined that a 21 foot length would be ideal, but since those are typically not available a 22 foot length would be preferable.

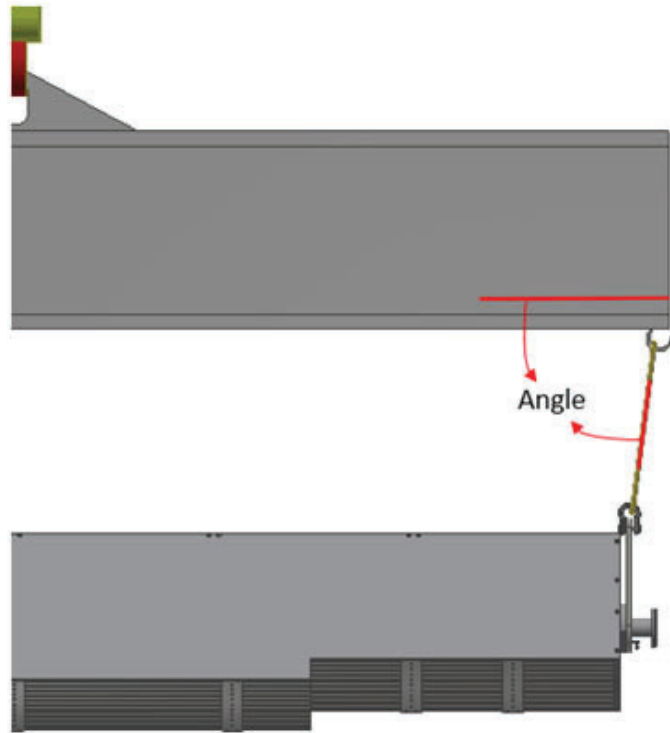
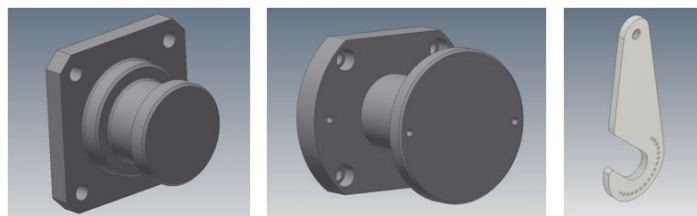


Figure 3: Angle measurement reference



From left to right: Figure 4: Original trunion. Figure 5: Updated trunion. Figure 6: Hook.

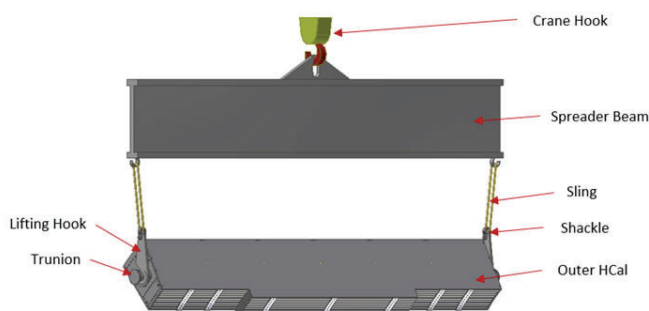


Figure 7: Labeled lifting assembly.

Table 1: Sling angle measurements

Spread	20'	21'	22'	23'
Angle	101.76°	92.13°	82.56°	72.78°

Attached to the outer HCal sectors must be fixtures that allow connection and support by means of the spreader beam. Due to the individuality of the sectors, custom hooks and attachments were the most appropriate design solution. Directly connected to the sectors will be a trunion on either end. The trunion design that was already proposed, shown in Figure 4, was modified to accommodate hooks and other fixtures. This updated design can be seen in Figure 5. Hooks, in Figure 6, were designed to accompany and attach to the trunions. A significant feature of this design is the inclusion of indexing holes, which will allow the sector to be rotated and held in the appropriate position for installation. There are two holes on the trunion and seventeen on the hook, to facilitate alignment for each of the 32 sectors. With these hole patterns the sectors can be fixed to any installation angle and pinned in place, so only fine adjustments are needed during installation. The recommended pin is listed in Appendix A.

Other tools needed for lifting the sectors include slings and shackles. The slings and shackles must be able to support the 15 ton load of the sectors. In order to place the final sector, the sling must be 3 feet at most so there is enough head room to clear the detector. Listed in Appendices B and C are samples of an appropriate chain and shackle for this procedure. An assembled view of the lifting fixtures can be seen in Figure 7.

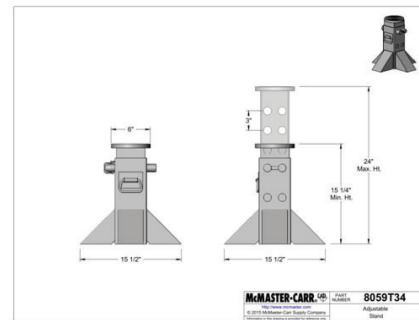


Figure 8: McMaster-Carr Stand

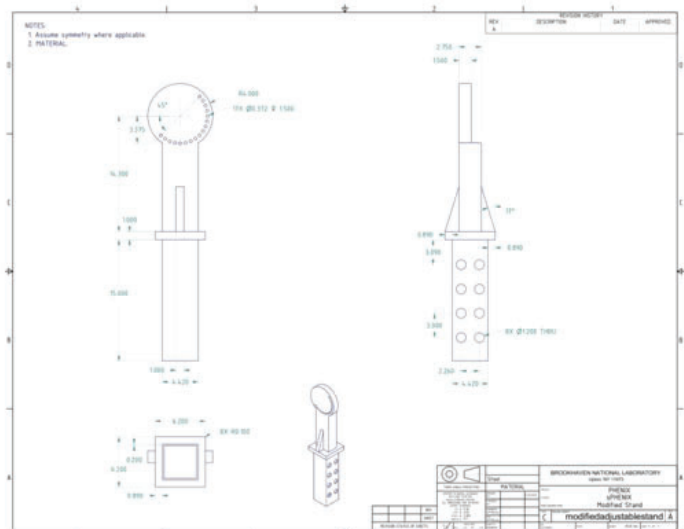


Figure 9: Stand Modification

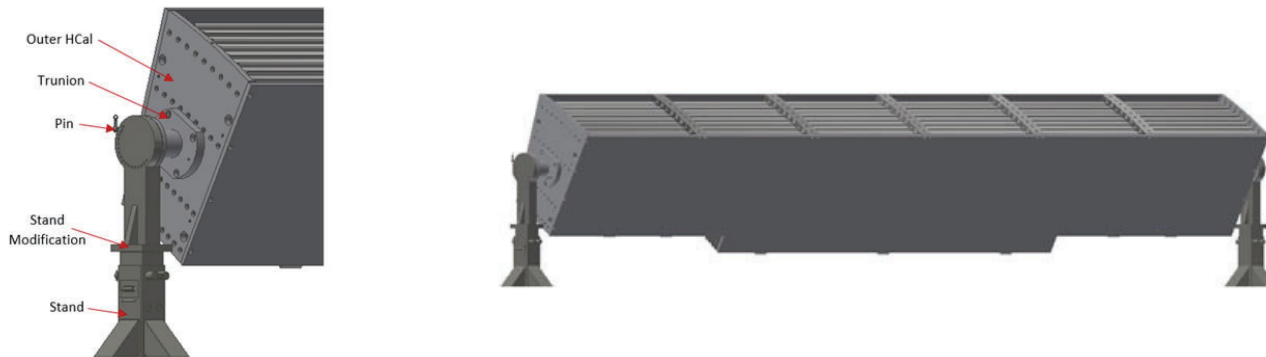


Figure 10: Labeled Holding Fixtures

B. Holding Fixtures

To prepare and store the outer HCal sectors prior to installation, it is necessary to have holding stands that allow for accessibility to the sectors. Requirements for the stand include supporting a 15 ton load and the ability to hold from any point along a 21 foot span. Different options were researched and the stand shown in Figure 8 was the most suitable option. It has a capacity of 20 tons and consists of two independent stands, allowing for support at any spread.

Since the tolerances within the sector are less than 1mm, the best way to support the sectors is from each endplate. In order to hold the HCal from its endplates, additional fixtures were designed. The trunions in figure 4 had already been proposed and were modified to accommodate the stand. The outer cylinder of the trunion was enlarged and holes were added for indexing. The indexing holes are an important design feature, as they allow for the sector to be adjusted to the proper angle prior to lifting. For indexing to work, there must also be holes on the stand to lock the sector in place. A stand modification was designed that would fit within the stand base and also contain additional support for the sector to rest on. The modified fixture can be seen in figure 9. To hold the sector at the desired angle, the same pins from the lifting design can be used (Appendix A).

III. Results and Discussion

To ensure each of the designed fixtures can support the appropriate load, finite element analysis was performed on each one in Autodesk Inventor. This helped determine any failures in the structure and led to the modification of some parts. The sector stresses had been previously analyzed and were not the focus of this analysis.

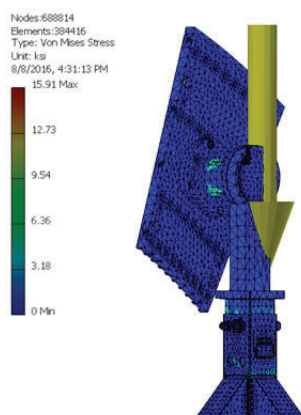


Figure 11: Holding Stresses

A. Lifting Fixtures

For the lifting assembly, stress concentrations on the trunions and hooks are important to consider. Analysis shows the maximum stress concentrations at screw locations on the sector, which have been formerly accounted for and are not relevant in this review. Figure 8 displays the stresses from lifting the sector. Apart from this maximum stress, a locale with a maximum stress of 20 ksi occurs at the 1.25" shackle hole on the hooks. This means the factor of safety in the hooks will be just under 3, enough to bear the load of the sector. The trunions have no notable stress concentrations to be evaluated.

B. Holding Fixtures

The main fixtures to be considered when analyzing the holding system are the trunions, stand modifications, and the stand bases. The largest stress is concentrated at the bases, it occurs at the weldment between the legs and central tube. These stands are rated to support 20 tons and the maximum stress they experience is 15.91 ksi, according to analysis, which leaves a safety factor of over 3.5. Each stand modification experiences a small loading stress around the connection with the base. These stresses are under 10 ksi, so they will not cause any failures for the assembly. Similarly, there is a stress concentration of less than 10 ksi on the trunions. Using steel, there is still a large enough factor of safety that this stress is not problematic. A model of this analysis can be seen in Figure 11.

IV. Recommendations and Future Work

Use of the aforementioned fixtures will satisfy the requirements for lifting and holding the outer HCal sectors of sPHENIX. Further research has to be done into which of these parts are available at BNL and which would need to be purchased. There should also be more discussion about rotating fixtures. Chainfalls seem to be a viable option, although there are other solutions such as an automated sling system. More complex systems could significantly increase cost, at which point their benefit may not be worthwhile. In addition, guides that attach to each sector to assist with installation should be considered.

V. Acknowledgements

This project was supported in part by the U.S. Department of Energy, Office of Science, Office of Workforce Development for Teachers and Scientists (WDTS) under the Science Undergraduate Laboratory Internships Program (SULI). I would also like to thank my mentor, Don Lynch (sPHENIX Chief Engineer), as well as Rich Ruggiero (sPHENIX Chief Designer) and the entire sPHENIX team for their guidance throughout my appointment.

Analyzing time-dependent noise in the MicroBooNE experiment and parallel track reconstruction in liquid argon time-projection chambers

Brendon Bullard

Physics, Brandeis University, Waltham, MA 02454

Mary Bishai

Physics, Brookhaven National Laboratory, Upton, NY 11973

Abstract

MicroBooNE and the Deep Underground Neutrino Experiment (DUNE) are two large-scale neutrino beam experiments that utilize liquid argon time-projection chambers (LArTPC) to detect and reconstruct neutrino interactions. The electronic detector group at Brookhaven National Laboratory has put much energy into characterizing detector performance in MicroBooNE, an effort that includes studies of various sources of noise; however, the time dependence of the noise has not yet been studied. To this end, we calculate various metrics for root-mean-squared noise and frequency content of the 8256 channels across the three wire planes of the TPC per event as they vary over data taken between February and July of 2016. This work is crucial in understanding the performance of a general large-scale LArTPC, technology which will be used for the next generation of neutrino detectors including DUNE. We observe effects due to mis-configured channels in the U plane and hypothesize causes for other characteristics of the plotted metrics. Another point of interest for event reconstruction in LArTPC is measurement of tracks that are parallel to the wire readout planes. Such tracks are difficult to reconstruct and could have a large enough effect on primary signals and backgrounds to warrant a design change in the DUNE TPCs. We study the simulated expected charged current signal and neutral pion decay backgrounds in order to understand the impact to signal efficiency and background rejection in DUNE using a readout plane parallel and perpendicular to the beam. We see that using a perpendicular wire plane significantly reduces problematic cases using both lepton and hadron angle cuts.

I. INTRODUCTION

A. The Liquid Argon Time Projection Chamber

The liquid argon time projection chamber (LArTPC) is a type of particle detector that measures ionizing particles produced by a neutrino beam. An illustration of how a LArTPC functions is shown in Figure 1. A detector is filled with a medium (in this case, liquid argon) and a constant electric field is applied between a cathode plane and an anode plane. In the anode plane, three planes of wire readout channels are strung to measure incoming electrons. From innermost to outermost, the wire planes are labeled U, V, and Y. The U plane is biased with a negative voltage, the V plane is grounded, and the Y plane biased with a positive voltage such that electric field lines do not terminate on the U and V plane wires i.e. electrons will only induce a current in these wires. For this reason, these two planes are called the induction planes. Electric field lines will then terminate on the Y plane, and so electrons collect on its wires. Hence, it is called the collection

plane. Light detection devices are situated on the outside of the active volume (volume of medium bound by the cathode/anode planes) to detect scintillation light, which is comprised of photons that are emitted when argon atoms de-excite after gaining energy from passing particles. As a charged particle passes through the medium, it ionizes and excites argon atoms. Ionization electrons are pulled to the anode planes by the electric field and the signal is read off from the readout wires. Scintillation light is used as a trigger, since photons travel much faster than the drift electrons. In MicroBooNE, photomultiplier tubes (PMT) are used for scintillation light detection.

Using the 3 wire planes, one can reconstruct the y and z coordinates of the origin of a measured ionization electron. Electrons move at a constant speed in the electric field and since the time of the creation of the ionizing particles is known due to the beam specifications, the x coordinate can also be reconstructed. This yields a high resolution, 3D reconstruction for charged particle tracks within the active volume.

Liquid argon is a good choice for detector medium for several reasons. Liquid argon is inert, and so it does not absorb passing ionization electrons. Argon scintillates more strongly than other noble gases, which is useful for triggering and energy reconstruction. Argon is also much more abundant on Earth than other noble gases like Xenon, and so it is relatively inexpensive. Finally, and most importantly for neutrino interactions, liquid argon is

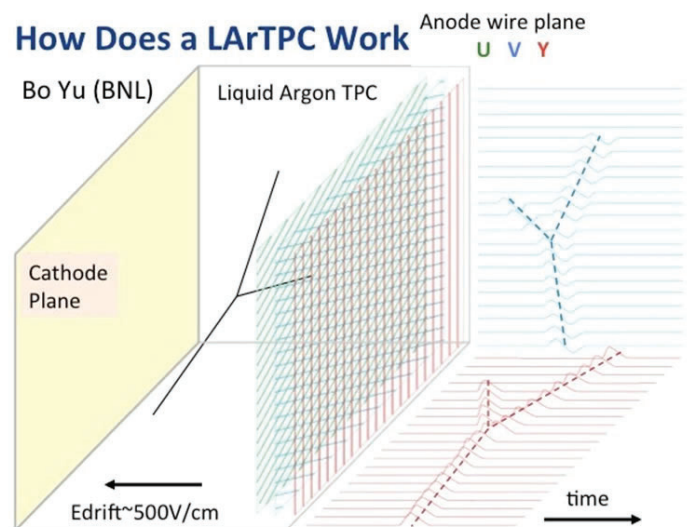


FIG. 1. An illustration of the working process of a LArTPC. The coordinate system typically used orients the positive x direction pointing opposite of the electric field, the y direction pointing upwards, and the z direction pointing forward, which is the neutrino beam direction.

very dense. Since neutrinos only interact weakly with matter, one needs to use a lot of matter in order to measure interactions with enough frequency to conclude statistically significant results.

B. The MicroBooNE Experiment

The MicroBooNE experiment is a booster neutrino experiment that utilizes a LArTPC with an active mass of 89 ton to detect neutrino interactions. Its goal is to measure neutrino-argon cross sections, which is very important for the future of LArTPC physics, and to explore the low energy electron excess measured by its predecessor experiment, MiniBooNE, which could lead to the discovery of new physics beyond the standard model. A to-scale rendering of MicroBooNE is shown in Figure 2. Various sources of noise were detected soon after MicroBooNE's commissioning. Sophisticated methods were developed in order to remove these sources of noise from measurements. Members of the MicroBooNE collaboration working at Brookhaven National Laboratory have spent a great deal of time attempting to describe this noise and understand fully the source of it. Doing so is crucial for research and development efforts of future large LArTPCs. The current understanding of MicroBooNE noise is summarized in a public note².

Each readout channel measures a signal as a function of time. Due to various hardware specifications, the time resolution is finite and each division of time that can be measured is called a time tick. For any particular readout channel (of which there are 8256, 2400 in the U and V planes, 3456 in the Y plane) one can use a Fast Fourier Transform (FFT) algorithm to study the frequency content of measured signal waveform. This has been done across all the readout channels and various sources of noise identified and described. Between 10 and 30 kHz there is a coherent noise, so named because the appearance of the noise is correlated amongst multiple channels. Next is a sharp peak at 36 kHz and its third harmonic at 108 kHz. There are also peaks at higher odd harmonics but they have much lower magnitudes.

These are caused by the high voltage supply. There is also a

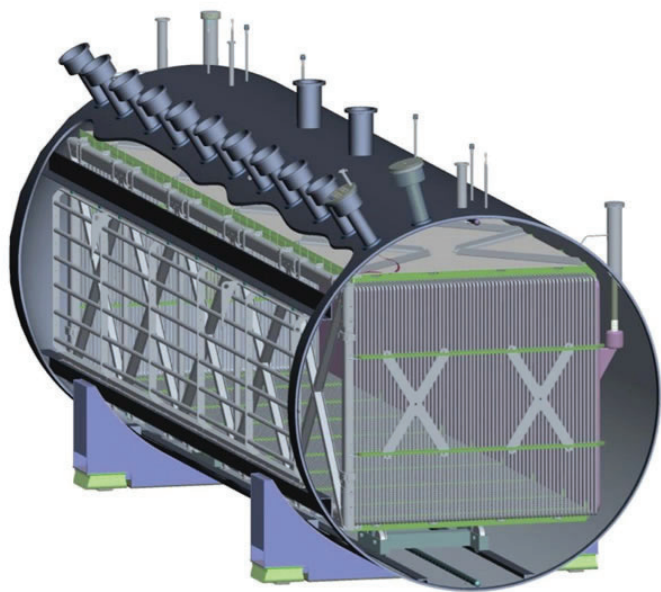


FIG. 2. A rendering of the MicroBooNE TPC³. The high voltage source for the cathode plane enters the detector on the right. The anode plane can be seen through the cut-away on the left.

wide-band noise, called a burst noise, centered at 900 kHz. The source of this noise is not fully understood. There is also an effect referred to as chirping by which a channel may yield zero signal for some amount of time and then become active again. This is due to ASIC saturation. Over saturation is due to microphonics caused by the wires' motion in the liquid argon.

The noise in MicroBooNE has been studied for individual events, but a thorough study of the noise as it varies in time has not yet been done. Doing so is important in order to understand how the noise changes and, if it does, help identify the source of the noise. It is also important to observe that the proportion of dead channels is not progressively growing, which would indicate that the detector longevity is poor.

C. Parallel Track Reconstruction

Due to the finite time resolution of a LArTPC, ionization can only be resolved to time slices. Particles that travel near parallel to the wire plane will fire multiple wires at the same time (within the time resolution to the detector). This will reduce the spatial resolution of the track depending on the track's angle. This effect can be seen in Figure 3 for cosmic muons traveling near parallel to the wire plane generated by a Monte Carlo (MC) simulation. The cosmic muon track in the lateral center has several blue squares encompassing the track, each of which correspond to sets of wires fired within the same time slice.

The effect of parallel track degeneracy is problematic for two reasons. First, parallel signal events cannot be adequately resolved in the y-z plane. This will negatively impact how well these events can be measured. Secondly, due to the reduced information one can obtain from the detector, background events that can normally be discerned from signal events might be mistaken for true signal events. This would be problematic for multi-billion dollar experiments like the Deep Underground Neutrino Experiment (DUNE), which is still in its developmental phase. The effect of parallel track degeneracy can be mitigated if the wire plane is oriented to be perpendicular to the beam instead of parallel (the MicroBooNE TPC uses a parallel wire plane). In order to decide on which plane orientation configuration to use for DUNE, the effect of parallel track degeneracy must be studied in detail to obtain event rates for good and bad signal and background events.

II. ANALYSIS

A. MicroBooNE Noise Time Dependence

We use MicroBooNE physics data taken between February 10th and July 7th 2016. We select one subrun from each available run within this time frame. For each subrun, we create a celltree file, run the wire-cell reconstruction algorithm⁴, and run an analysis module on each contained event, of which there are typically 6-10, in batch mode. The online analysis module is responsible

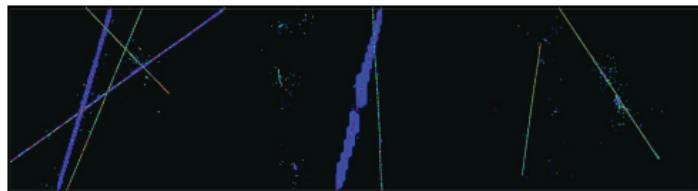


FIG. 3. Bee display⁴ for a MC ν_n neutral current event with parallel cosmic muon tracks showing degeneracy. The colored lines correspond to the MC truth i.e. what is generated by the simulation and the blue corresponds to the tracks after reconstruction.

for extracting the ADC pedestal (noise), computing a set of metrics on the pedestal, and saving average frequency content for different sets of channels. We also compute a set of metrics for the average FFT magnitude plots offline.

To extract the ADC pedestal for each event, we fill a histogram with ADC measurements from a particular channel (each ADC measurement is from a different time tick). We assume that this forms a Gaussian distribution and compute the 16th, 50th, and 84th percentile. If we represent these values as p_{16} , p_{50} , and p_{84} , respectively, then the RMS is taken to be

$$\text{RMS} = \sqrt{\frac{(p_{50} - p_{16})^2 + (p_{84} - p_{50})^2}{2}}$$

Since a real signal would be measured at above the 84th percentile, this method for calculating the RMS is not sensitive to signal. Hence, it is the RMS in the ADC pedestal. If the RMS for a channel is less than a threshold of 0.1, then it is set to zero and taken to be unusable. This calculation is done for each channel and a plot similar to Figure 4 is obtained. Recall that channels 1-2400, 2401-4800, and 4801-8256 correspond to the U, V, and Y plane. The ADC pedestal for the Y plane is flat because its readout wires are vertical, and so the length of these wires is constant along the length of the detector. However, since the U and V plane wires are oriented at $\pm 60^\circ$ to the Y plane wires, the wires at the upstream and downstream ends of the detector become shorter. One should then expect that the noise measured in progressively shorter wires to be progressively lower. The wire lengths for each set of channels is given in Table I. Note that although the lengths of the wires may approach zero, the ADC pedestal does not go to zero.

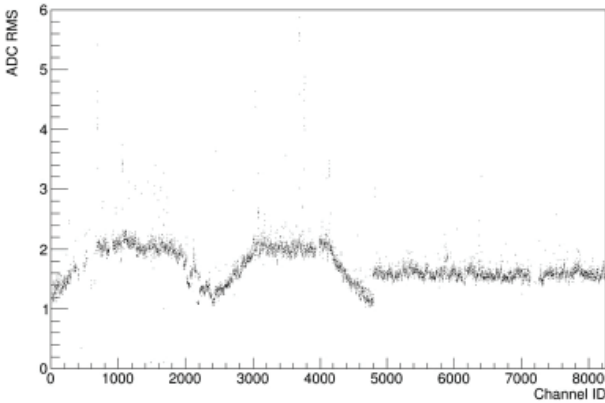


FIG. 4. ADC pedestal for run 5545, subrun 0, event 10.

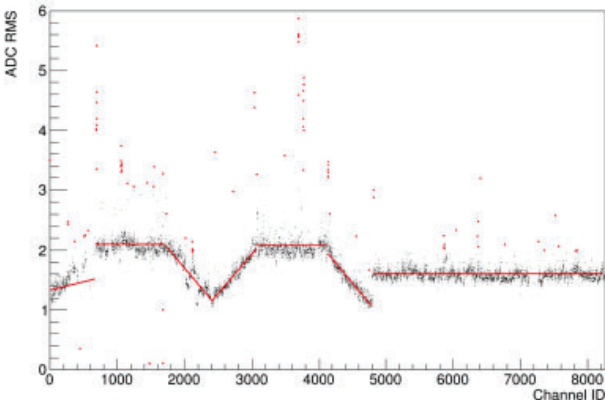


FIG. 5. ADC pedestal for run 5545, subrun 0, event 10 with linear fits and outlier metrics applied. Outliers are marked in red.

Next, we compute a set of metrics for the ADC pedestal. For the Y, long wire U, and long wire V channels we compute the mean RMS, standard deviation, and the number of outlier channels. Here, we define an outlier channel to be one where the RMS is outside of the mean plus or minus three times the standard deviation. We do a similar analysis for the upstream and downstream sections of the U and V plane. We do a linear fit to RMS as a function of Channel ID, where the fit parameters take the place of the mean as a metric. We then compute the root mean squared of the fit residuals as well as the number of outliers, where an outlier is taken to be a channel having RMS outside of the fit plus or minus three times the residual root mean squared. We also count the number of dead channels for each of the three wire planes. Finally, we compute the mean and standard deviation for the RMS for three sets of mis-configured channels: 2016-2095, 2192-2302, and 2352-2383. These channels correspond to ASICs which are set with a different shaping time and gain than the rest of the ASICs2. Figure 5 shows the ADC pedestal for run 5545, subrun 0, event 10 with a visualization of the applied metrics. The fit of the upstream U plane RMS is biased by the large number of dead channels.

In order to study the frequency content of the noise, we create an average FFT magnitude plot for the U, V, and Y planes, as well as for the long wires of the U and V plane and the mis-configured channels. The plots are generated and saved online. We do not save FFT plots for individual channels because it would be computationally intense and would require a large amount of disk space. It is also useful to do average FFT plots to suppress random noise. An example of the average FFT plots is given in Figure 6. Note that the 36 kHz and burst noise are not present in the Y plane due to shielding from the other two planes.

We developed offline code to compute a set of metrics of the FFT magnitude plots. We compute the average magnitude for the following frequency ranges: 10-30 kHz, 36 ± 0.83 kHz, 108 ± 0.83 kHz, 900 ± 42 kHz, 42-104 kHz, 108-208 kHz, and 667-833 kHz. Here, the first four ranges correspond to noise sources and the last three are wider ranges of frequency considered to capture the overall structure of the frequency distribution. In particular, 667-833 kHz has the lowest magnitude and is relatively flat, as can be seen in Figure 6.

B. Parallel Track Event Selection

In order to understand how parallel track degeneracy will affect data statistics for DUNE, we must consider simulated data. We use generator level Fast MC of a ν_μ beam using the optimized LBNE beam with oscillation and protons on target (POT) weights

Subset Name	Channel ID	Length Range (cm)
Upstream U	1-672	0.6-465.5
Long Wire U	673-1728	465.9
Downstream U	1729-2400	465.5-0.6
Upstream V	2401-3072	0.6-465.5
Long Wire V	3073-4128	465.9
Downstream V	4129-4800	465.5-0.6
Y	4801-8256	233

TABLE I. Wire lengths of subsets of channels in the MicroBooNE TPC.

to simulate interactions with liquid argon. The simulated event rates are normalized using a detector having a mass of 34 kton, exposure time of 3 years, and 1.1×10^{21} POT/year. We consider tracks to be parallel to the wire plane if the angle of the track with respect to the wire plane is greater than a specified angle. The chosen angle is dependent on the time resolution of the TPC and since the hardware specifications for DUNE are not yet finalized, we consider three different angles that define parallel events: 7.5, 5.0, and 2.5 degrees. We study the impact of changing the wire plane configuration from parallel to the neutrino beam, as it is in MicroBooNE, to perpendicular to the beam.

Figure 7 shows the number of charged current (CC) νe signal events as a function of electron angle and energy separated into three channels: quasi-elastic scattering (QE), hadronic resonance (Res), and deep inelastic scattering (Dis). We observe that events having electron energy over 6 GeV are highly parallel, but most events are in fact below this energy. Therefore, we only consider CC signal events where the electron energy is less than 6 GeV.

It is possible for final state hadrons produced in νe CC interactions to shadow the electron if there is hadronic showering parallel to the wire plane. Therefore, we consider signal events to be “bad” for three different cases: when the electron angle is less than the specified cut, when the minimum final state hadron angle is less than the specified cut, and when both angles are less than the cut. However, in the third case we require that the selected hadron be traveling in the same direction as the electron relative to the wire plane (toward or away) since we naively expect to be able to differentiate tracks traveling in different directions. Additionally, hadrons that do not travel more than 1.5 cm should not shadow the electron and hence will not be problematic for reconstruction. Therefore, we set energy thresholds for charged pions, kaons, and protons at 17.5, 30, and 39 MeV, respectively, according to the particle range shown in Figure 8. We do not consider neutrons or neutral pions.

Since background events cannot be distinguished from sig-

nal events when there is degeneracy, we consider background events having characteristics that would lead to misidentification as signal. The first background is π^0 decays in νe CC events. The main decay mode for these is to a diphoton final state, having a branching ratio of about 99%. The second largest decay mode is to $e^+e^-\gamma$, having a branching ratio of about 1%. It is possible for one of these final state particles to be misidentified as a signal event electron. For each CC event, we compute the minimum angle of these final states with respect to the wire plane. We require that the energy of the selected final state particle be less than 6 GeV and that a selected photon convert to an e^+e^- pair within 3 cm of the interaction vertex. We simulate this conversion process manually using an exponential probability distribution, with an average conversion length of 18 cm.

There are also background events from $\nu\mu$ NC events that produce π^0 that decay to EM final states as are produced in νe CC events. However, these are expected to be much more problematic than in the previous case. We establish a different selection criteria for these events when computing the minimum angle of final state EM tracks. Again, we keep only final state EM particles having an energy less than 6 GeV. A selected electron should have a final state hadron within the specified angle and on the same side of the wire plane as the electron. The hadron must also satisfy the energy threshold and particle ID criteria that is used for CC signal event hadrons. A selected photon should have a conversion length between 1 and 5 cm. There should also be a final state π^\pm within

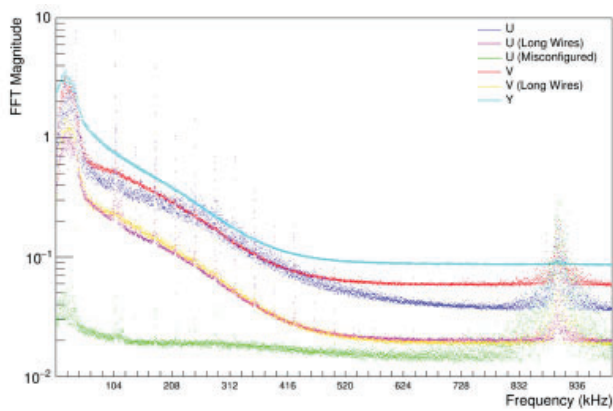


FIG. 6. Frequency content for run 5545, subrun 0, event 10.

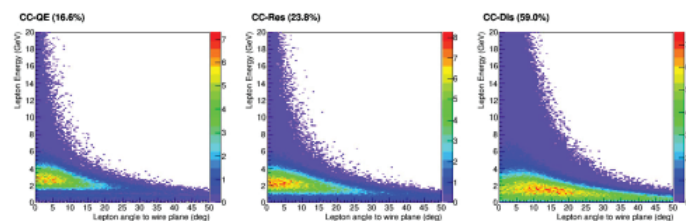


FIG. 7. Number of CC events as a function of electron angle and energy.

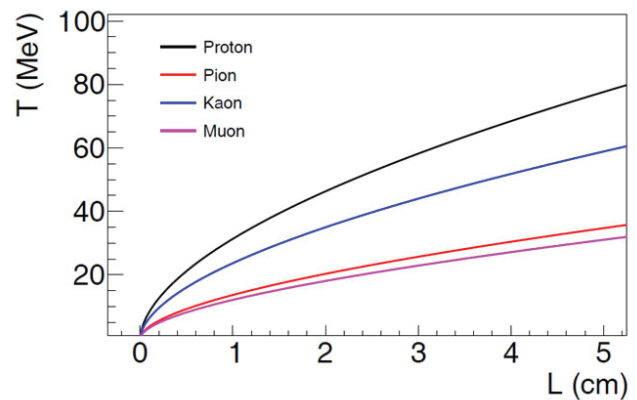


FIG. 8. Stopping distance for hadrons in liquid argon as a function of energy.

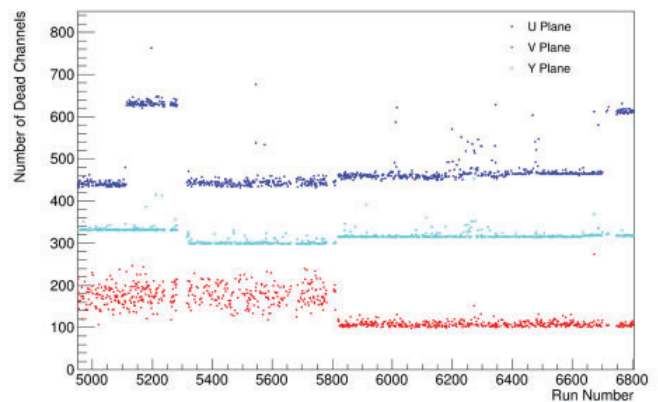


FIG. 9. Average number of dead or noisy channels as a function of run number. The average for each run is taken over each event that is contained in the run’s chosen subrun.

the specified angle and on the same side of the wire plane as the photon.

III. RESULTS MicroBooNE Noise

A plot of bad channels (noisy or dead) is shown in Figure 9. There are two ranges of runs where the average number of bad channels increases significantly in the U plane. There are also a large number of runs where the average number of bad channels is significantly higher than the runs immediately before and after it. This is mainly due to the correction that is applied on the mis-configured channels; it seems that for these two periods of time, misconfigured channels are behaving normally. We are still in the process of understanding the cause of it. In the V plane, we observe a large range in bad channels up until around run 5800, where it drops to a more consistent value for the remainder of the runs. After considering detector operations, we found out that there were some replacement of the cryogenics pump during that run range and after changing the pump, we observed significant decrease in noisy channels. We observe relative stability in the number of dead channels in the Y plane, with a dip starting around run 5300 and ending around run 5800.

The average and standard deviation of the mis-configured channels pedestal are given in Figures 10-12. Here, each data point corresponds to one event, so there are multiple points for each run number. The structure of these plots indicates that there is some correlation between the mis-configured channels and the number of noisy channels in the U plane. Plots for the remaining metrics as a function of run number are given in Appendix A. These plots reinforce the suspicion that the mis-configured chan-

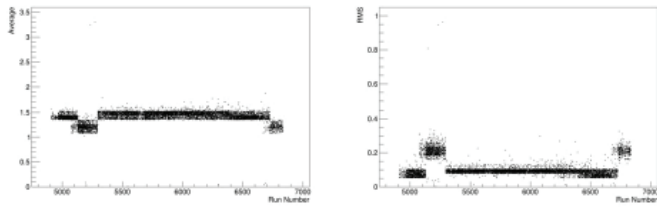


FIG. 10. Mean (standard deviation) of mis-configured channels 2016-2095 on the left (right).

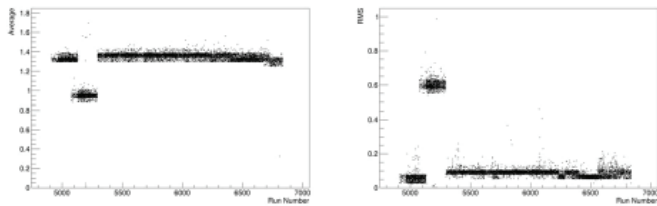


FIG. 11. Mean (standard deviation) of mis-configured channels 2192-2302 on the left (right).

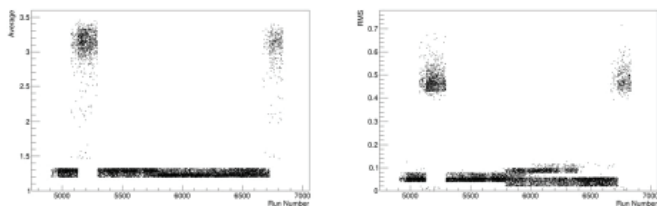


FIG. 12. Mean (standard deviation) of mis-configured channels 2352-2383 on the left (right).

nels are related to the change in noisy channels in the U plane. We also see that the whatever is causing the effects in the V plane noisy channels has the greatest correlation to the upstream V plane channels and the least in the downstream V plane, with the long wires being affected at an intermediate degree.

Plots of the FFT metrics averaged over the events in each run as a function of run number are given in Appendix B. We observe

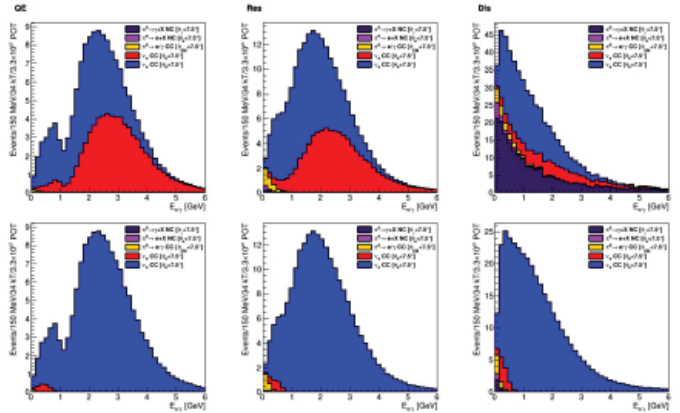


FIG. 13. Event rates defining bad signal events in terms of lepton angle for the standard and perpendicular wire plane configuration on the top and bottom.

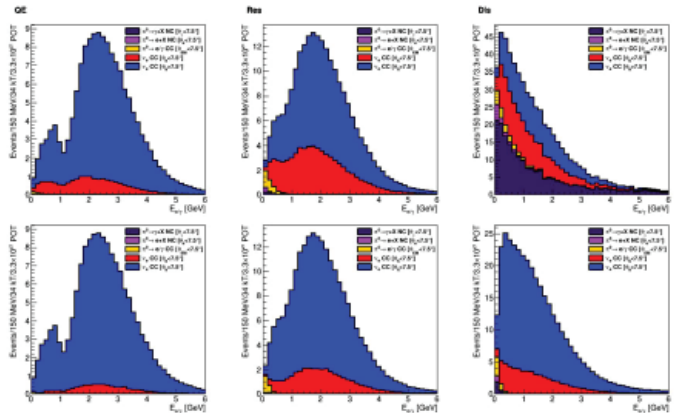


FIG. 14. Event rates defining bad signal events in terms of minimum hadron angle for the standard and perpendicular wire plane configuration on the top and bottom.

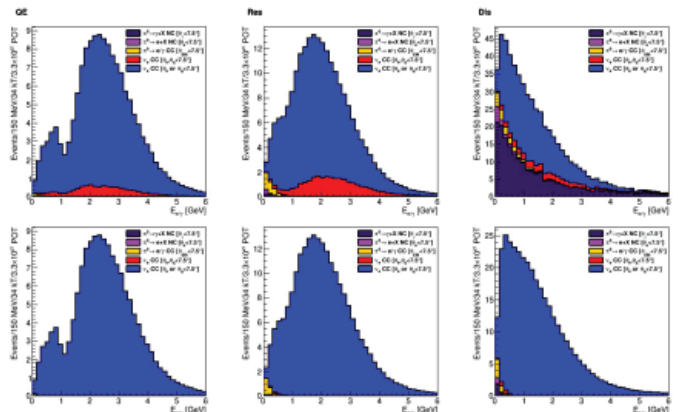


FIG. 15. Event rates defining bad signal events in terms of lepton angle and minimum hadron angle for the standard and perpendicular wire plane configuration on the top and bottom.

consistent magnitudes for these metrics except for the 36 and 108 kHz noise in the U plane. Since the U plane shields the other two wire planes from this noise, any fluctuation in the high voltage source would only be visible in the U plane. It is likely that this behavior is just a result of changes in the high voltage source on some level.

A. Parallel Event Rates

The event rates for nonparallel signal events and parallel signal and background events as a function of reconstructed energy using a parallel track angle of 7.5 degrees are given in Figures 13-15. The total event rates per channel are tabulated in Table II. The corresponding figures and tables using a parallel track angle of 5.0 and 2.5 degrees are given in Appendix C.

We observe a significant reduction in parallel electron tracks using a perpendicular wire plane configuration due to electrons carrying a large portion of the incoming neutrino's forward momentum. The number of problematic hadronic events are not as significantly reduced due to the fact that hadrons are produced more isotropically. By rotating the wire plane, we can reduce the number of degenerate events significantly. The reduction is nearly 100% above ~ 1 GeV.

The most problematic backgrounds are the NC π^0 decays, as was expected. Most of these degenerate events are due to photons, which is to be expected due to the very low branching fraction of $\pi^0 \rightarrow e^+e^-\gamma$.

IV. CONCLUSIONS AND FUTURE WORK

The sudden disappearance in very noisy channels in the V plane around run 5800 coincides with the replacement of MicroBooNE's cryogenic pump. If the pump that was taken out caused a lot of chirping in V plane wires, it would explain the effects we see in Figure 9. Therefore, we suspect this to be the case. By considering the various ADC pedestal metrics, we can see that there is a strong correlation between the jumps in the U plane noisy wires and the mis-configured channels' behavior. The effects seen in Figure 9 and the other metrics are consistent with the mis-configured channels' being properly configured for these periods of time. We are still investigating why the mis-configured channels are coming back as properly configured during these ranges. We are also investigating why there is a temporary decrease in the number of noisy channels in the Y plane.

Moving forward, the Electronic Detector Group will contin-

ue to study the MicroBooNE TPC noise. In particular, they will try to understand the causes of what we have observed in this study. They will be able to use the software that was developed for this study in order to extend the set of data studied as more is continually collected.

In studying simulated parallel track events in DUNE, we are able to understand on a more quantitative basis how problematic parallel track degeneracy will be for achieving sufficient data statistics and detector efficiency. We find that using a wire plane parallel to the beam yields a high number of degenerate background events from the NC channel, specifically in DIS. Almost all of these degeneracies can be avoided if a perpendicular wire plane is used. This information is useful for DUNE collaborators who are working to determine which of the two wire plane configurations should be used for the DUNE TPCs.

It can be argued that some of the background events studied can actually be discriminated from signal events using different physical properties of the event. When this is more thoroughly considered, DUNE collaborators may continue this study with more stringent event selection criteria. They may also study parallel track degeneracy using higher level simulation software, as the Fast MC used for this study only simulates neutrino interactions with LAr, which does not simulate a real detector and the physical processes that would affect measurement in a real TPC.

V. REFERENCES

- ¹The MicroBooNE Collaboration, "MicroBooNE, A Liquid Argon Time Projection Chamber (LArTPC) Neutrino Experiment," (2011), arXiv:hep-ex/1107.5112.
- ²The MicroBooNE Collaboration, "Noise Characterization and Filtering in the MicroBooNE TPC," (2016), MICROBOONE-NOTE-1016-PUB,.
- ³The MicroBooNE Experiment, "About the detector," (2016), <http://www-microboone.fnal.gov/public/aboutdetector.html>.
- ⁴X Qian, B Viren, C Zang, "Wire-cell," (2016), <http://www.phy.bnl.gov/wire-cell/>.

VI. ACKNOWLEDGMENTS

This project was supported in part by the U.S. Department of Energy, Office of Science, Office of Workforce Development for Teachers and Scientists (WDTS) under the Science Undergraduate Laboratory Internships Program (SULI).

	Standard Configuration			Rotated Configuration		
	QE	Res	DIS	QE	Res	DIS
NC $\pi^0 \rightarrow \gamma + X$	~ 0	0.6	192.2	~ 0	0.1	2.4
NC $\pi^0 \rightarrow e + X$	~ 0	0.5	11.0	~ 0	0.1	1.0
CC EM	0.4	3.3	16.5	0.1	2.1	4.4
Parallel Signal (θ_e)	70.5	88.0	83.4	1.5	2.7	9.9
Good Signal (θ_e)	79.2	131.2	259.0	148.9	216.6	332.5
Parallel Signal (θ_h)	18.3	66.9	159.6	8.6	35.8	59.1
Good Signal (θ_h)	132.1	152.3	182.9	141.8	183.4	283.3
Parallel Signal (θ_e, θ_h)	10.2	27.6	38.9	0.06	0.4	1.6
Good Signal (θ_e, θ_h)	140.1	191.6	303.6	150.3	218.8	340.9

TABLE II. Event rates for parallel tracks defined as being within 7.5° with respect to the wire plane.

VII. Appendix A: ADC Pedestal Metric

The metrics for the ADC pedestal as a function of run number are given in Figures 16-29. Each data point corresponds to one event, so there are multiple points for each run number.

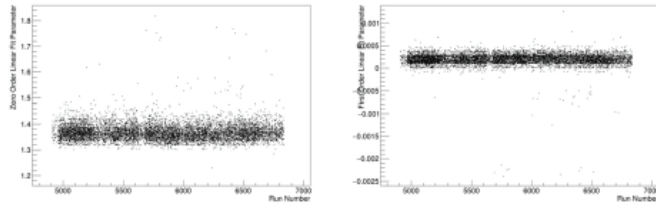


FIG. 16. Zero and first order fit parameter for the upstream U plane wires on the left and right, respectively.

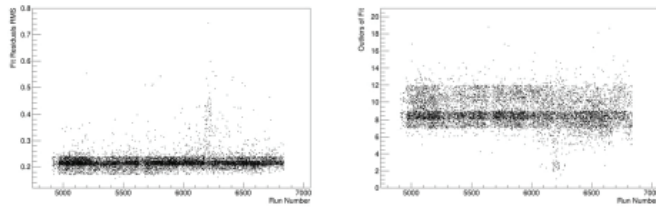


FIG. 17. Residual RMS and number of outliers for the upstream U plane wires on the left and right, respectively.

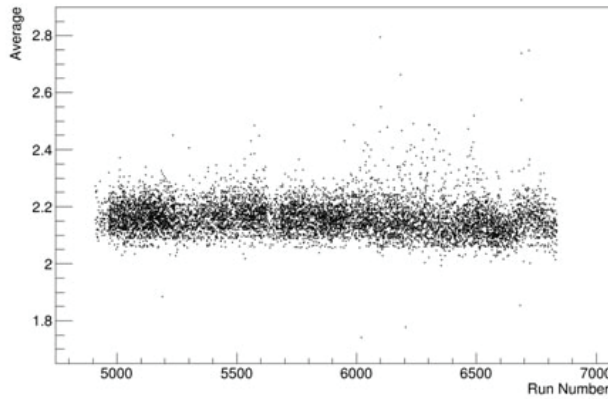


FIG. 18. Average of U plane long wires ADC pedestal

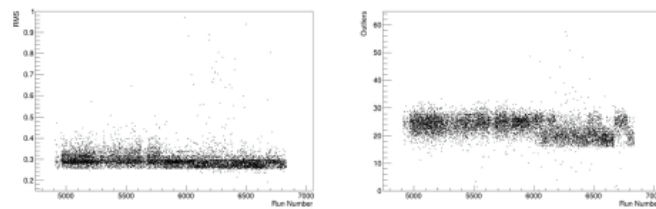


FIG. 19. Standard deviation and number of outliers for the U plane long wires on the left and right, respectively.

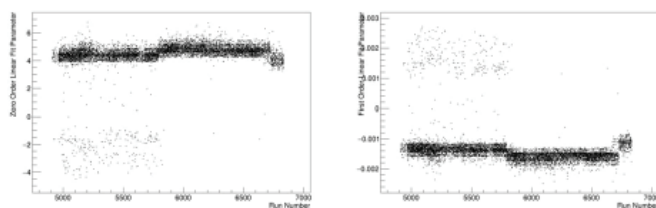


FIG. 20. Zero and first order fit parameter for the downstream U plane wires on the left and right, respectively.

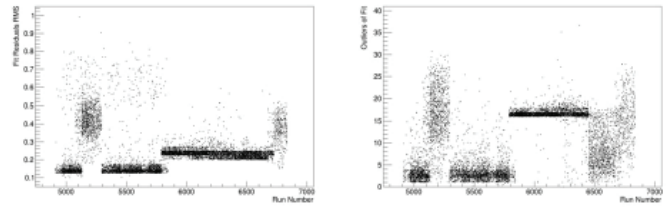


FIG. 21. Residual RMS and number of outliers for the downstream U plane wires on the left and right, respectively.

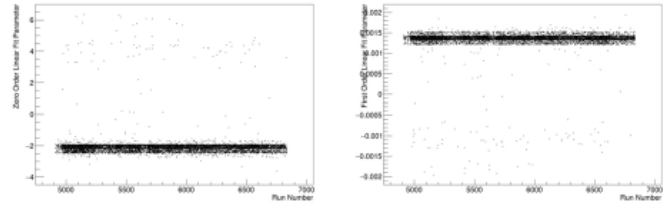


FIG. 22. Zero and first order fit parameter for the upstream V plane wires on the left and right, respectively.

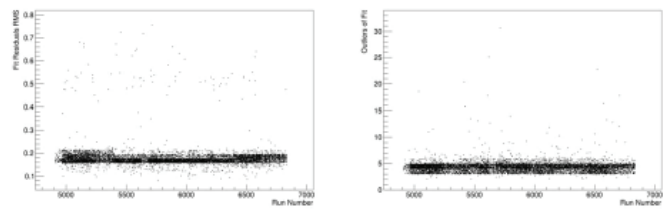


FIG. 23. Residual RMS and number of outliers for the upstream V plane wires on the left and right, respectively.

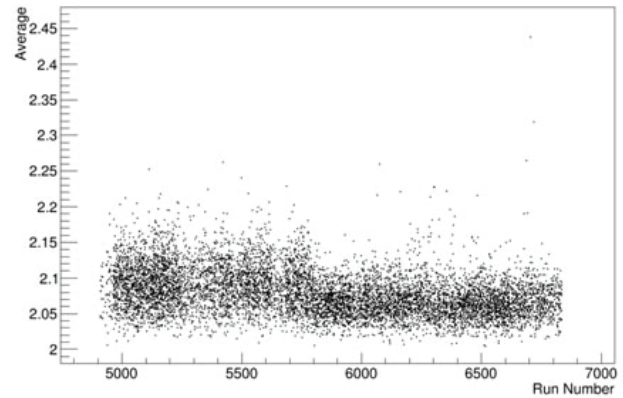


FIG. 24. Average of V plane long wires ADC pedestal

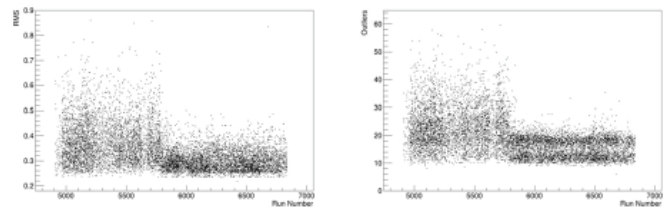


FIG. 25. Standard deviation and number of outliers for the V plane long wires on the left and right, respectively.

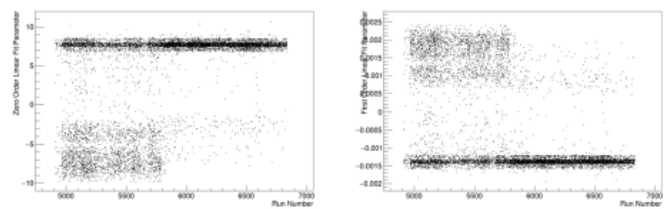


FIG. 26. Zero and first order fit parameter for the downstream V plane wires on the left and right, respectively.

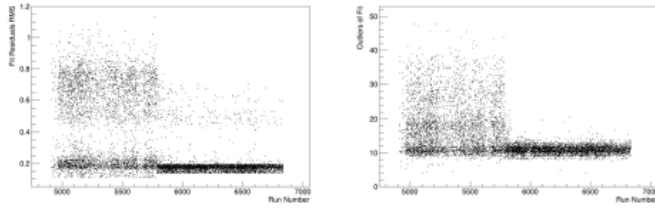


FIG. 27. Residual RMS and number of outliers for the downstream V plane wires on the left and right, respectively.

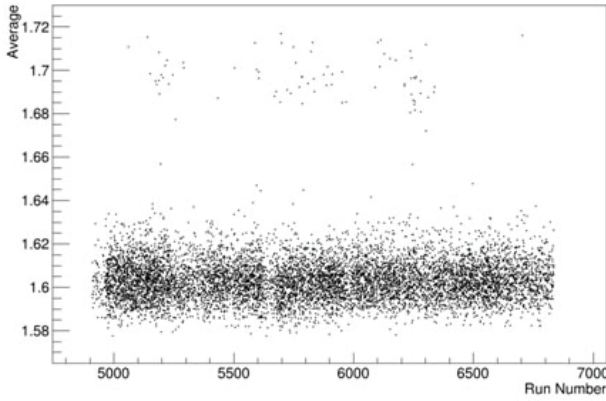


FIG. 28. Average of Y plane ADC pedestal

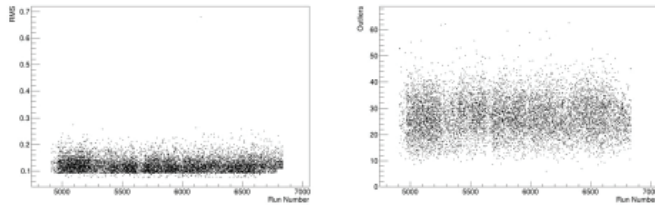


FIG. 29. Standard deviation and number of outliers for the Y plane on the left and right, respectively.

VIII. Appendix B: FFT Metrics

The plots of the FFT metrics as a function of run number are given in Figures 30-36.

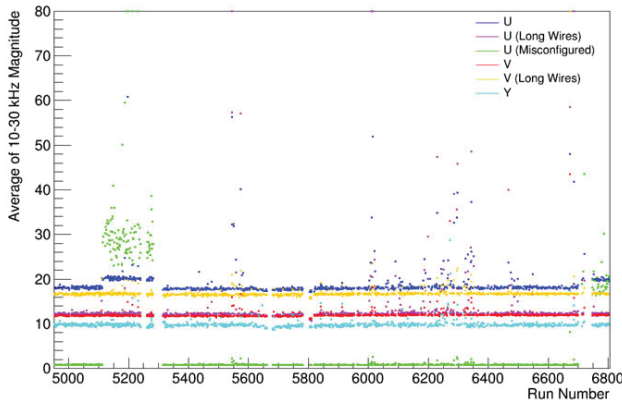


FIG. 30. Metric for the coherent noise averaged over the events in each run as a function of run number.

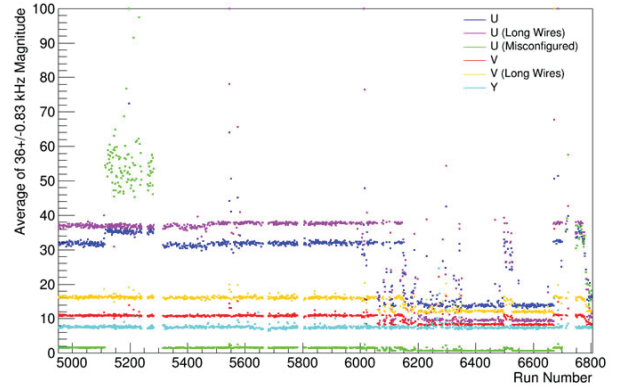


FIG. 31. Metric for the 36 kHz noise averaged over the events in each run as a function of run number.

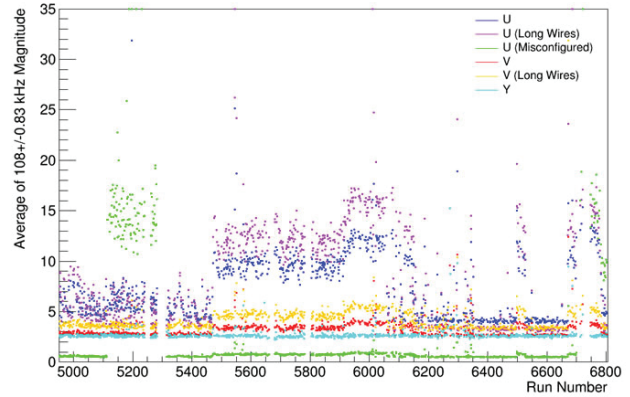


FIG. 32. Metric for the 108 kHz noise averaged over the events in each run as a function of run number.

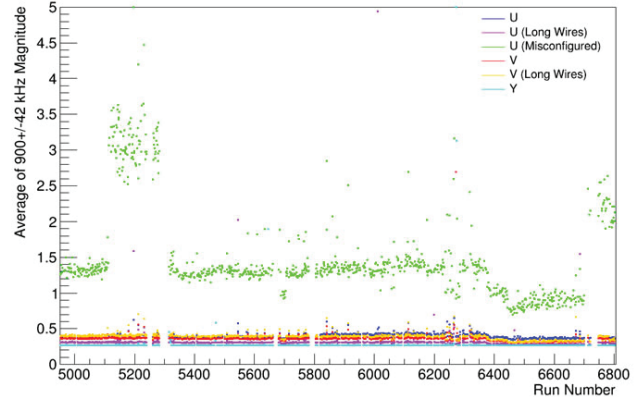


FIG. 33. Metric for the burst noise averaged over the events in each run as a function of run number.

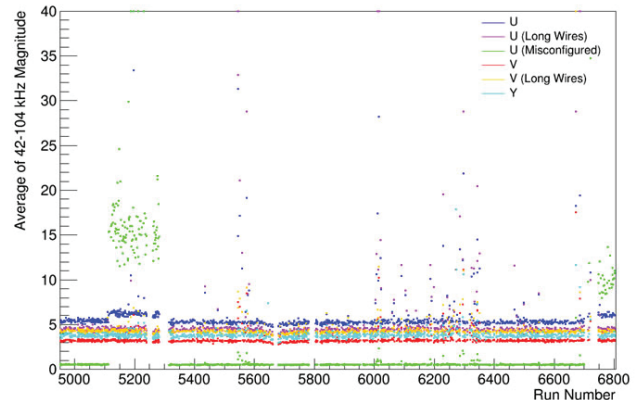


FIG. 34. Metric for the low frequency benchmark averaged over the events in each run as a function of run number.

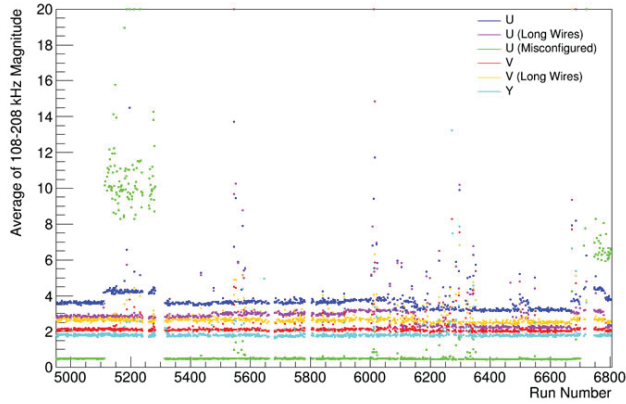


FIG. 35. Metric for the intermediate frequency benchmark averaged over the events in each run as a function of run number.

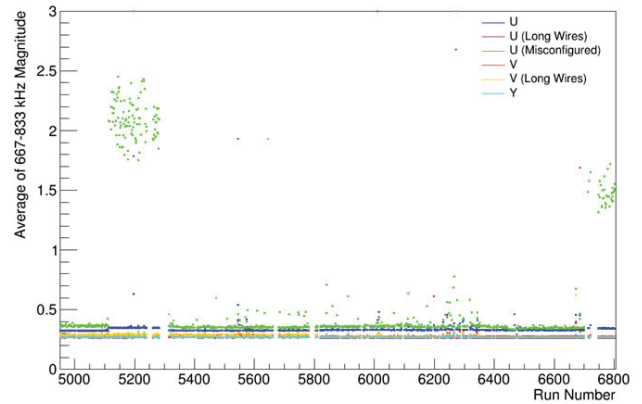


FIG. 36. Metric for the high frequency benchmark averaged over the events in each run as a function of run number.

IX. Appendix C: Event Rates for 5.0° and 2.5° Parallel Tracks

Figures 37-42 give the event rate for nonparallel signal events and parallel signal and background events as a function of reconstructed energy. Figures 37-39 use a parallel track angle of 5.0° and Figures 40-42 use a parallel track angle of 2.5°. Tables III and IV tabulate this.

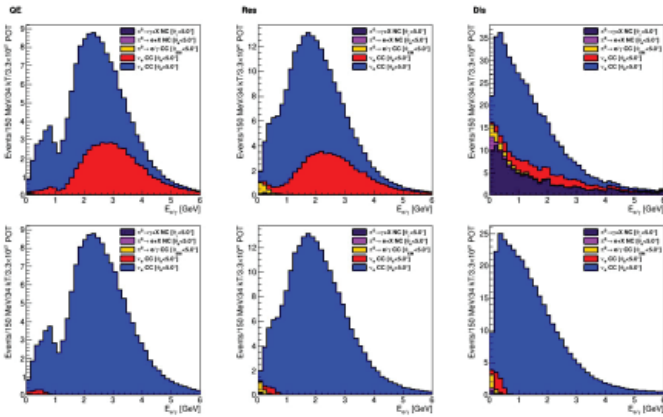


FIG. 37. Event rates defining bad signal events in terms of lepton angle for the standard and perpendicular wire plane configuration on the top and bottom.

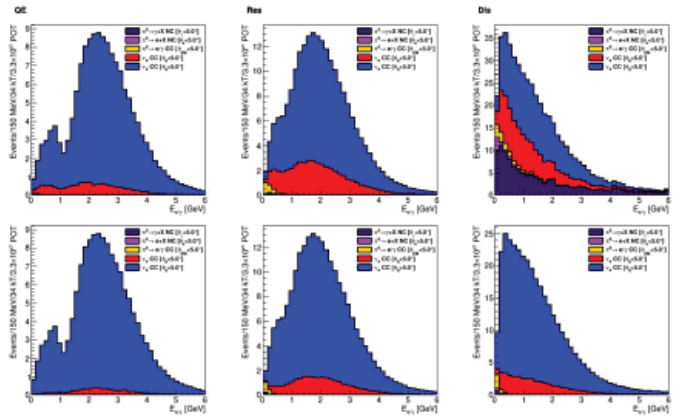


FIG. 38. Event rates defining bad signal events in terms of minimum hadron angle for the standard and perpendicular wire plane configuration on the top and bottom.

	Standard Configuration			Rotated Configuration		
	QE	Res	DIS	QE	Res	DIS
NC $\pi^0 \rightarrow \gamma + X$	~0	0.2	112.7	~0	0.2	0.9
NC $\pi^0 \rightarrow e + X$	~0	0.2	7.3	~0	0.1	0.5
CC EM	0.2	2.3	11.5	0.07	1.3	2.9
Parallel Signal (θ_ρ)	48.7	61.0	54.2	1.0	1.7	6.7
Good Signal (θ_ρ)	101.7	158.2	288.2	149.4	217.5	335.7
Parallel Signal (θ_h)	12.7	47.1	119.2	5.8	24.9	41.7
Good Signal (θ_h)	137.7	172.1	223.2	144.6	194.4	300.8
Parallel Signal (θ_ρ, θ_h)	5.9	13.8	19.1	0.03	0.2	0.7
Good Signal (θ_ρ, θ_h)	144.5	205.5	323.3	150.4	219.0	341.7

TABLE III. Event rates for parallel tracks defined as being within 5.0° with respect to the wire plane.

		Standard Configuration			Rotated Configuration		
	QE	Res	DIS	QE	Res	DIS	
NC $\pi^0 \rightarrow \gamma + X$	~ 0	0.07	38.4	~ 0	~ 0	0.07	
NC $\pi^0 \rightarrow e + X$	~ 0	0.1	3.2	~ 0	~ 0	0.2	
CC EM	0.1	1.2	5.9	0.03	0.7	1.5	
Parallel Signal (θ_e)	24.5	31.1	26.3	0.5	0.9	3.4	
Good Signal (θ_e)	125.9	188.2	316.1	149.9	218.4	339.0	
Parallel Signal (θ_h)	6.5	24.9	67.1	2.9	12.7	22.1	
Good Signal (θ_h)	143.9	194.3	275.3	147.5	206.5	320.3	
Parallel Signal (θ_e, θ_h)	2.1	3.7	5.4	0.01	0.05	0.2	
Good Signal (θ_e, θ_h)	148.3	215.5	337.1	150.4	219.2	342.2	

TABLE IV. Event rates for parallel tracks defined as being within 2.5° with respect to the wire plane.

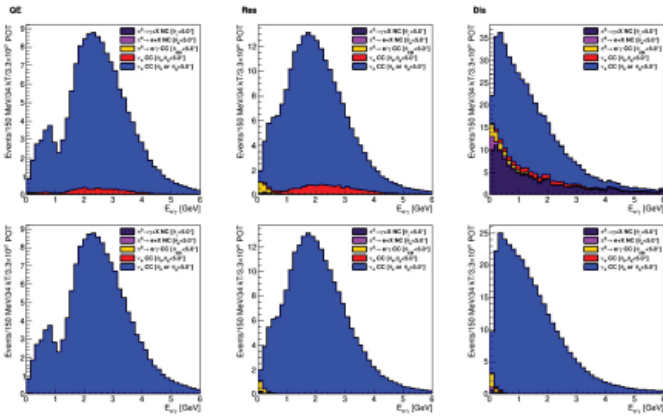


FIG. 39. Event rates defining bad signal events in terms of lepton angle and minimum hadron angle for the standard and perpendicular wire plane configuration on the top and bottom.

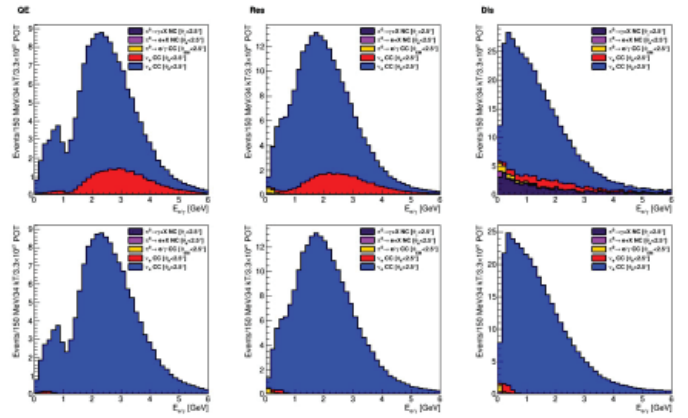


FIG. 40. Event rates defining bad signal events in terms of lepton angle for the standard and perpendicular wire plane configuration on the top and bottom.

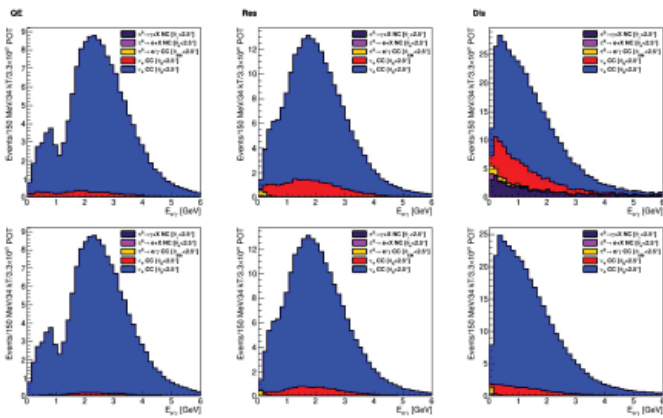


FIG. 41. Event rates defining bad signal events in terms of minimum hadron angle for the standard and perpendicular wire plane configuration on the top and bottom.

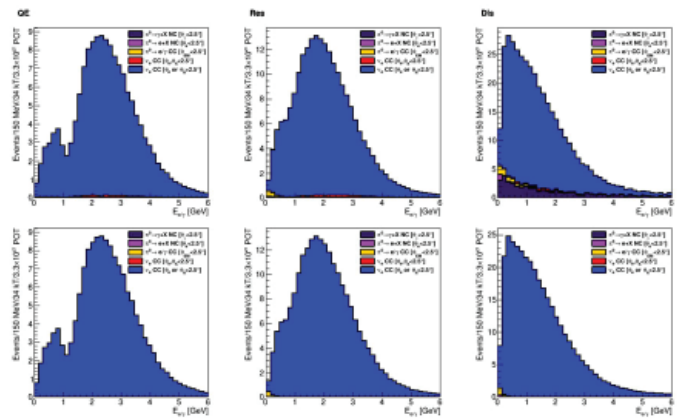


FIG. 42. Event rates defining bad signal events in terms of lepton angle and minimum hadron angle for the standard and perpendicular wire plane configuration on the top and bottom.

Design and analysis of the cradle support structure: Transportation components and alignment mechanisms for the sPHENIX Project at RHIC

Daniel Cacace, Engineering Department, Stony Brook University, Stony Brook, NY 11790

Donald Lynch and James Mills, Physics Department, Brookhaven National Laboratory, Upton, NY 11973

Abstract

At the end of the 2016 run, Brookhaven National Laboratory (BNL) began decommissioning the Relativistic Heavy Ion Collider's (RHIC) PHENIX detector, which has been in operation since 2000. The sPHENIX project, a new detector that is being designed to expand the scope of experimentation at RHIC, consists of several major components with a total weight of nearly 800tons. A critical portion of the current design proposal calls for designing a support structure, roughly weighing 200tons, that not only supports the detector, but also transports the assembly from the assembly hall (AH) into the interaction region (IR) and correctly positions it with respect to the beam-pipe. Modeling and analyzing a mechanism capable of completing the installation is mostly governed by physical phenomena, but is also influenced by intuition. Development of the support weldment and its alignment components has proven to be an iterative process consisting of several stages typical of engineering design. Generating designs for the cradle support structure consisted of conceptualizing potential solutions, detailing the more promising ideas, analyzing the results, and creating modifications where necessary to improve the design's capabilities. Creating parts in CAD software, researching commercially available components, and analyzing stress and deformation indicates where the design needs improvement and reveals potentially superior implementation with similar results.

I. Introduction

A. Background

sPHENIX is a proposed major upgrade to the current PHENIX detector at RHIC on BNL campus. This proposal is designed to address the fundamental questions regarding the nature of the strongly coupled quark-gluon plasma discovered from PHENIX's experiments at RHIC. In order to achieve the goal of further analyzing this relationship in finer detail the PHENIX infrastructure needs to be updated and modified. In addition to these modifications, new detectors and other sensing equipment need to be implemented. Part of the implementation process is the installation of the new detector.

RHIC recently completed its 16th run, over duration of 20 weeks, marking the beginning of the PHENIX removal and refurbishment. The 3000ton detector is getting a substantial upgrade with the sPHENIX project. Most of the detector components are being removed and replaced with an entirely new detector array. Having procured the solenoid utilized in the Babar experiments at SLAC, various new detector components are being designed in order to incorporate the magnet in the new detector. A crucial component for the proposed modifications is the cradle support structure. Considering the infrastructure will remain unchanged the detector will be erected in the assembly hall (AH), and trans-

ported into the interaction region (IR) where it will be aligned with respect to RHIC's beam pipe. Moving and aligning the detector poses a particular difficulty due to the sheer massiveness of the assembly and the geometry of the infrastructure.

B. Objective

Due to the geometric constraints created by the geometry of the infrastructure and current track system as well as the size and mass of the detector, manipulating its location and orientation poses a particular set of complications. In order to mitigate the complications a roller truck system needs to be designed that can both accommodate the geometry of the detector as well as the current track system. Determining what mechanisms are the most feasible, both in terms of application and expense, for such a roller truck system is an important part of the cradle design. Various "worst-case scenarios" should be considered in order to ensure stability and success of the proposal.

II. Market Research

A. Motion Mechanism

In order to move the detector components simultaneously with a total weight of 1000tons, traditional means are insufficient. Also, in order to align the detector on the current track system, the assembly needs to move from the AH into the IR, which is perpendicular to the beam pipe, and then move within the IR, parallel or along the beam pipe. Due to the pre-existing track structure, a roller assembly should be used. Likewise, because of the accuracy needed, the roller assembly should utilize an alignment system. The means of propulsion is also limited due to the amount of force

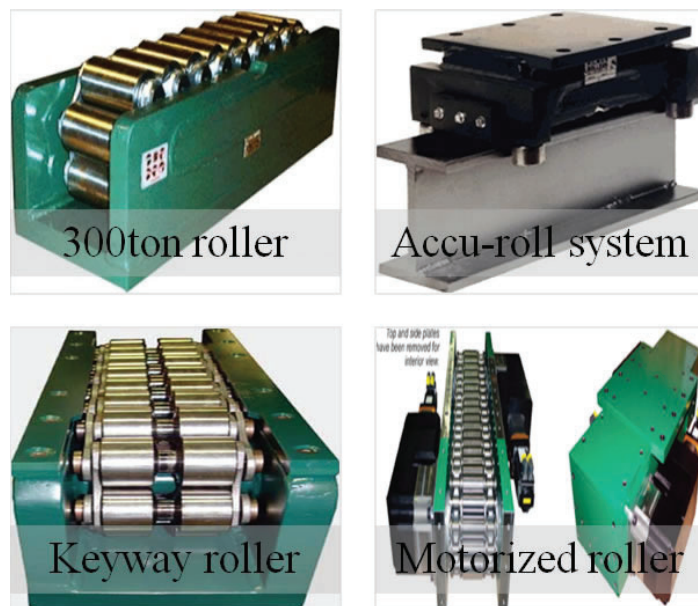


Figure 1. Roller options and configurations.

necessary to move such a massive detector. Hilman rollers offers a wide variety of options suitable for the intended application. Figure 1 shows a typical Hilman roller that has a maximum range of capacities from 100tons to 1000tons as well as two means of roller alignment and a motorized roller system that could potentially replace hydraulic rams.

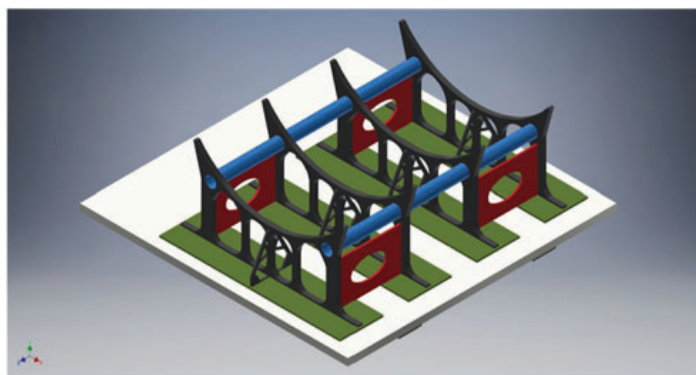
B. Alignment Mechanism

Once the detector is in the proper location, it's orientation needs to align with the beam pipe, such that the detector components point toward the collision location. In order to ensure that the alignment will be adequate, all six degrees of freedom are needed. The six degrees of freedom are translation: moving on the X-axis (surging), moving on the Y-axis (swaying), and moving on the Z-axis (heaving) and rotation: tilting on the X-axis (rolling), tilting on the Y-axis (pitching) and tilting on the Z-axis (yawing). Few mechanisms are capable of obtaining six degrees of freedom on their own and thus a combination of devices will most likely be utilized in order to create the alignment system. It may also be necessary to design a separate component to contribute one or more degrees freedom. Once the detector is positioned with respect to a degree freedom that positioning needs to be fixed in order to maintain the proper alignment. Figure 2 shows three potential mechanisms that can be used for alignment, the first being a six degrees of freedom motion platform, the second being a hydraulic cylinder in the third is a slewing bearing.

III. Design Specifications

In order for the motion and alignment systems to be acceptable for the intended application, there are several parameters for the design to meet or surpass. The components need to be able to withstand the entire weight of the detector, move the detector from the AH to the IR, correctly positions align the detector with respect to the beam pipe, properly mate with the track structure, fit within the dimensions of the infrastructure, etc. The following are desired design specifications:

- Figure 2. Alignment mechanisms. (top left)
- Figure 3. Cradle design. (bottom left)
- Figure 4. Cradle stress analysis. (top right)
- Figure 5. Cradle displacement. (bottom right)



- The rollers and the alignment mechanism should have a capacity of 500tons.
- The roller should use a mating cam follower system that is appropriate for the current cam on the tracks.
- Utilizing the current hydraulic rams or another means of propulsion, the roller should be able to transport the detector from the AH to the IR and along the beam line.
- The alignment system should be able to position the detector within a hundredth of an inch with respect to the beam pipe with respect to each degree freedom.
- The entire roller truck assembly and its corresponding support structure components should fit within the dimensioning determined by the infrastructure.
- The total cost of the truck assembly system should not exceed \$100,000.

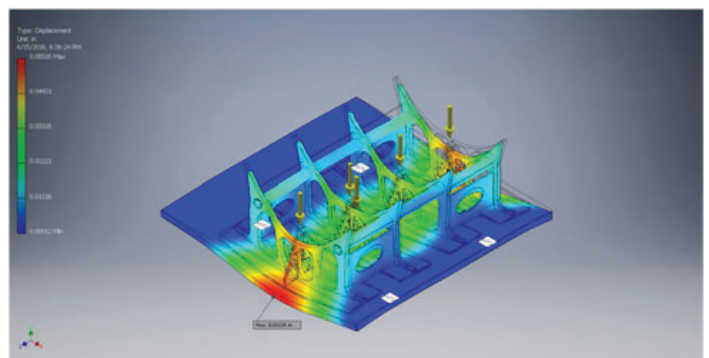
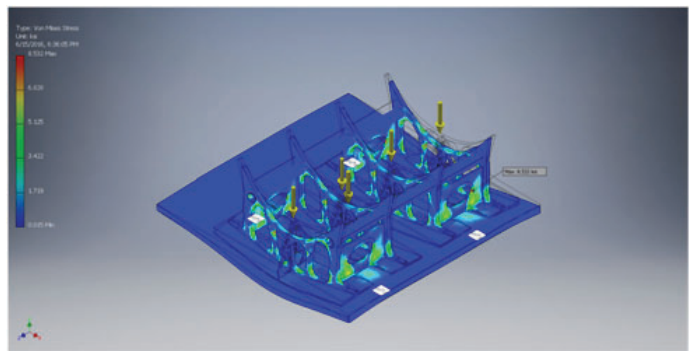
IV. Conceptual Processes

In order to meet the design specifications a conceptual procedure for the detector installation should be considered. First the detector should be assembled on the cradle support structure which is also comprised of the roller truck assemblies. Next the detector should be moved from the AH to the IR, at which point the roller assemblies need to be rotated 90° in order to move the detector along the beam pipe. Hydraulic tracking system embedded in the roller trucks will allow the rollers and alignment system to be rotated. Once the rollers move the detector to its final position the hydraulic jacks, rollers and hydraulic fluorogold boxes will allow the detector to be aligned with respect to every degree freedom.

V. Conceptual Designs

A. Cradle Support Structure

One of the first considerations when designing transportation and alignment systems is what will the corresponding cradle support structure look like. The detector itself is a series of nesting hollow cylinders. Thus the cradle support structure should consist



of curved plates to accommodate the detector and a flat platform to accommodate the roller truck system for the pre-existing track structure. Once the generalized structure is considered it should be optimized to reduce cost and increase material efficiency. Figures 3 through 5 show the cradle design, stress analysis and displacement respectively. Both the stress of approximately 8.6ksi and the displacement of approximately 0.06in are acceptable.

B. New Track Structure

There are number of potential problems utilizing the current track structure for the new sPHENIX detector. First of all, the current track structure does not lead straight into the IR from the AH. This means that the detector needs to be hydraulically lifted while the rollers are being rotated such that the detector can move along the beam line. If a new rail system was installed that entire difficulty could be eliminated. Another potential problem with the old track structure is that it may not be able to support the conservative loads of the sPHENIX detector. The PHENIX detector was composed of multiple carriages, the heaviest of which was about 600tons which is 100tons greater than half the approximate

sPHENIX detector weight of 1000tons. Figures 6 through 8 show the new potential track structure design, stress analysis and displacement respectively. Both the stress of approximately 20ksi and the displacement of approximately 0.007in are acceptable, however, a safety factor of 2 would be more ideal and thus a larger wide flanged beam may be used to reduce the stress to 15ksi.

C. Roller Truck Assemblies

One of the major problems with moving the cradle detector assembly from the AH to its final position in the IR is rotating the roller trucks 90 degrees. Currently the detector is hydraulically lifted such that the rollers are no longer under load and can easily be rotated. Once that is completed the hydraulics lower the detector back onto the roller assemblies. A further complication to the aforementioned methodology is that the cam followers need to be removed and reattached before and after the hydraulic lifting respectively.

1. Turntable Trucks

In order to mitigate the issue, the cross-sections of the track where the detector assembly would have been hydraulically lifted

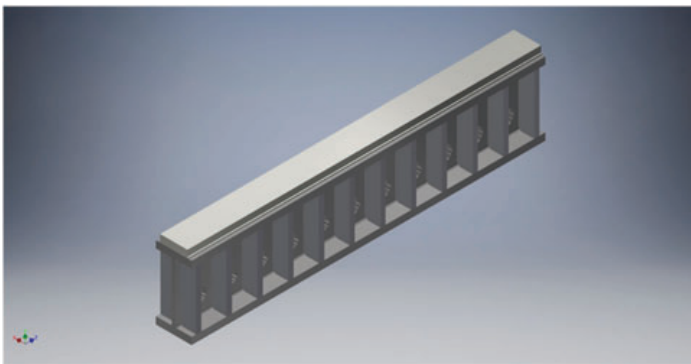


Figure 6. Generic new track structure section.

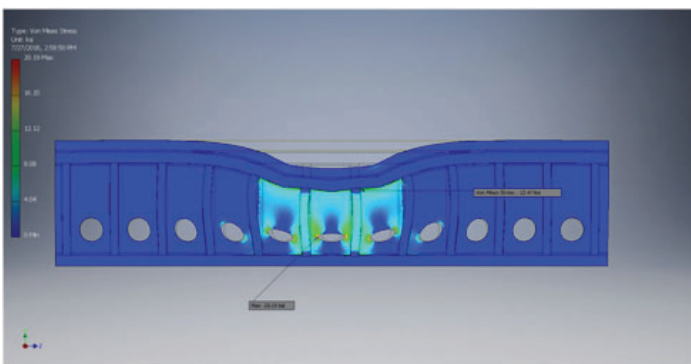


Figure 7. New track stress analysis.

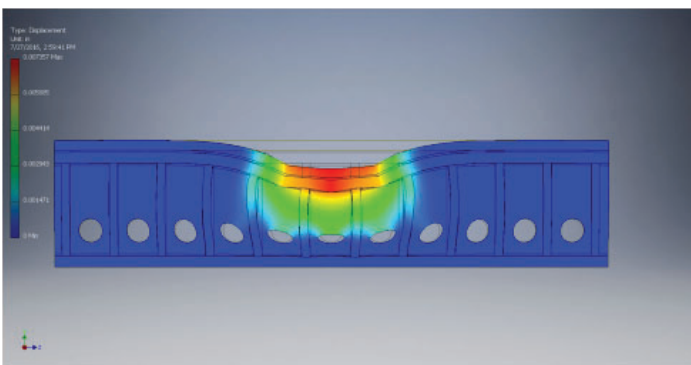


Figure 8. New track displacement.

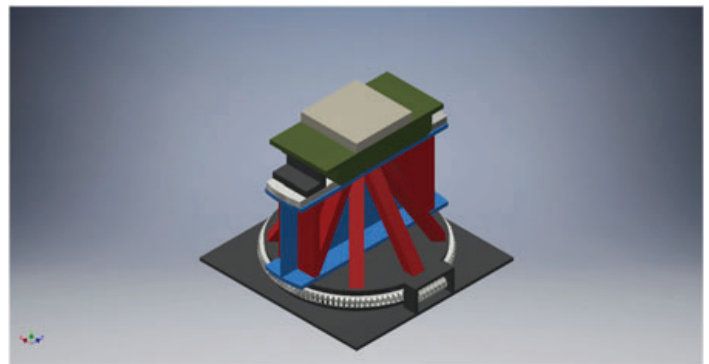


Figure 9. Turntable design.

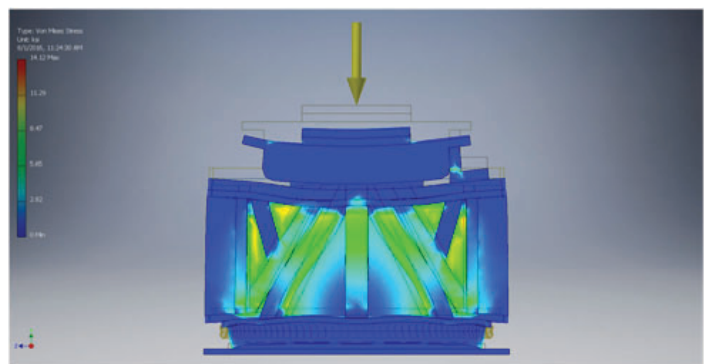


Figure 10. Turntable stress analysis.

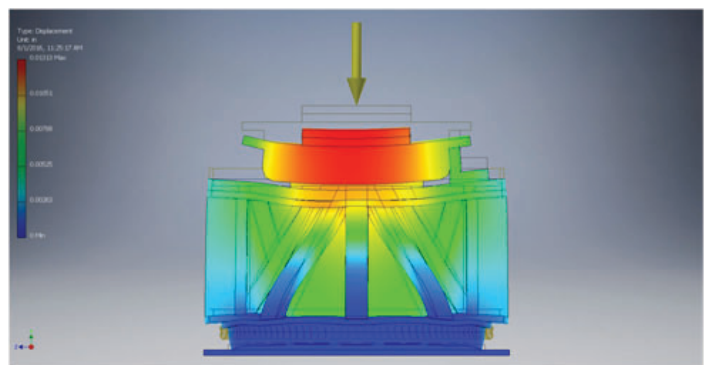


Figure 11. Turntable displacement.

are instead placed on heavy-duty slewing bearings in addition to the roller assemblies and thus can be rotated under loading. Figures 9 through 11 show the turntable design, stress analysis and displacement respectively. Both the stress of approximately 14ksi and the displacement of approximately 0.01in are acceptable.

2. Separate Rollers and Hydraulics

Another means of mitigating the issue of rotating the roller trucks, would be to utilize a hydraulic ram separated from the roller truck assembly to lift the detector high enough to surpass the cam follower system. Figures 12 through 16 show potential separated roller and hydraulic system design, roller loading stress analysis, roller loading displacement, hydraulic loading stress analysis and hydraulic loading displacement respectively. Both the stresses of approximately 37ksi and 41ksi are unacceptable, but both the displacements of 0.03in are acceptable. Due to the high stress concentrations, the load needs to be more distributed or the new track structure needs to be implemented.

3. Combined Rollers and Hydraulics

A third possibility to mitigate the issue of rotating the roller trucks is to incorporate the hydraulic jack in the truck itself, by utilizing a set of two rollers on either side of the Jack again where the Jack is able to lift the detector high enough to surpass the cam follower system. Figures 17 through 19 show the combined roller and hydraulics system design, stress analysis and displacement respectively. Note that in figures 18 and 19 the rollers aren't shown due to non-realistic stress concentrations. Both the stress of approximately 16ksi and the displacement of approximately 0.01in are acceptable. However, when the detector is jacked up,

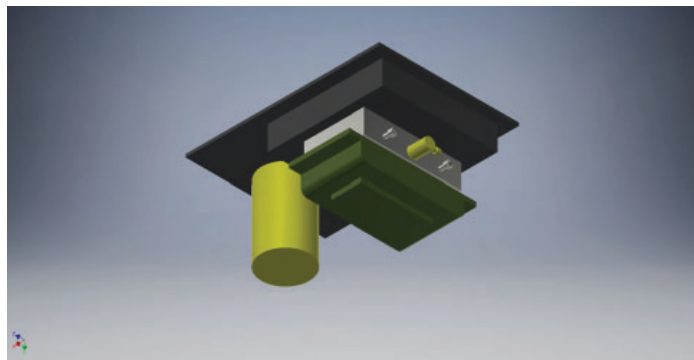


Figure 12. Separated hydraulic and roller system design.

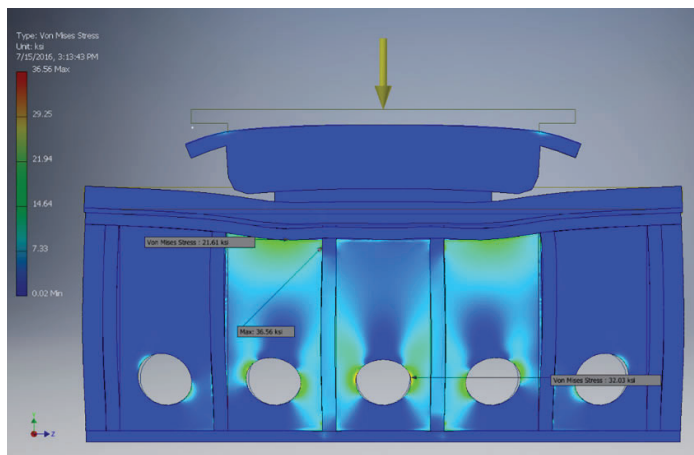


Figure 13. Roller loading stress analysis.

the hydraulics will be under load on the track structure and will experience similar results to those in section 5.3.2 shown in figures 20 and 21. The stresses are too high and thus that section of track may need to be stiffened.

D. Alignment Mechanisms

Once the detector is in the final position, the orientation needs to be adjusted such that the centerline of the detector is properly aligned with RHIC's beam pipe. Meaning that the support structure needs to be able to adjust each of the six degrees of freedom relatively accurately. The rollers have the potential to offer one degree of freedom with minor modifications or two degrees of freedom with major modifications. If hydraulic jacks are used to allow for the 90 degree rotation, they can provide three degrees of freedom.

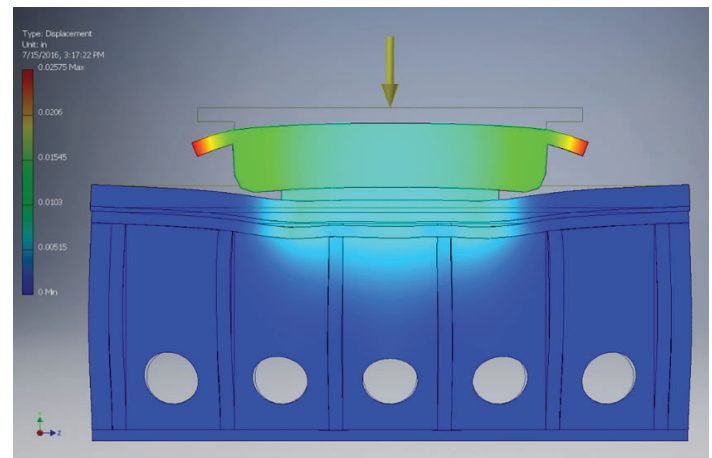


Figure 14. Roller loading displacement.

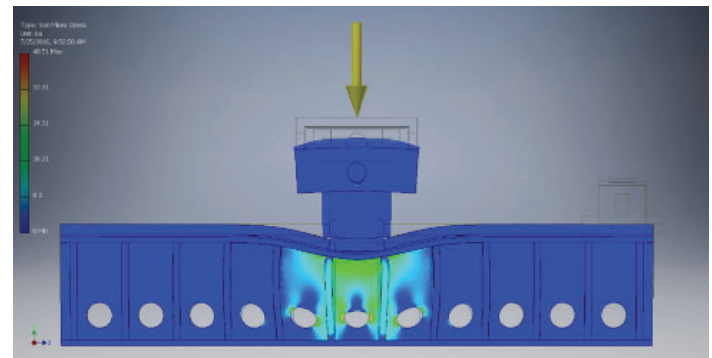


Figure 15. Hydraulic loading stress analysis.

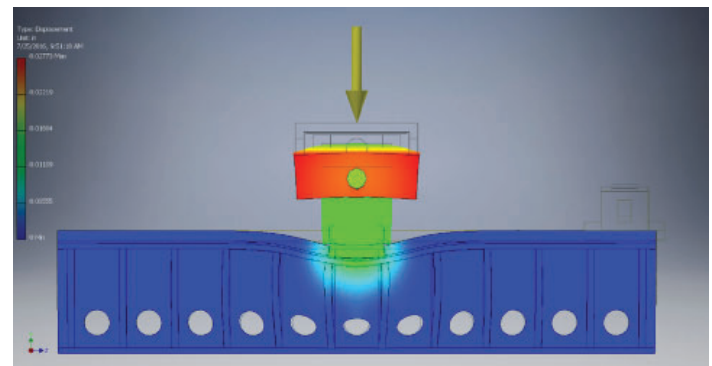


Figure 16. Hydraulic loading displacement.

1. Turntable Trucks

Utilizing turntables when the detector is in the final position, will allow for the rollers to provide two of freedom, translation along both the X and Z axis. This utilizes the slewing bearing discussed in section 2.2 and the design discussed in section 5.3.1.

2. Six Degrees of Freedom Motion Platform

Six degrees of motion platforms use hydraulic rams or electric linear actuators to manipulate a platform with various motions in order to produce all six degrees of freedom with one mechanism. This utilizes the six degrees of motion platform discussed in section 2.2.

3. Hydraulic Jack and Fluorogold Box

Hydraulic jacks can provide a translation in the Y axis and a rotation along the X and Z axis. A fluorogold box, which consists of fluorogold plates and hydraulic cylinders, complements the hydraulic jacks such that they provide translation in the X and Z axis and rotation in the Y axis. This utilizes the hydraulic cylinders discussed in section 2.2 and the design discussed in section 5.3.3.

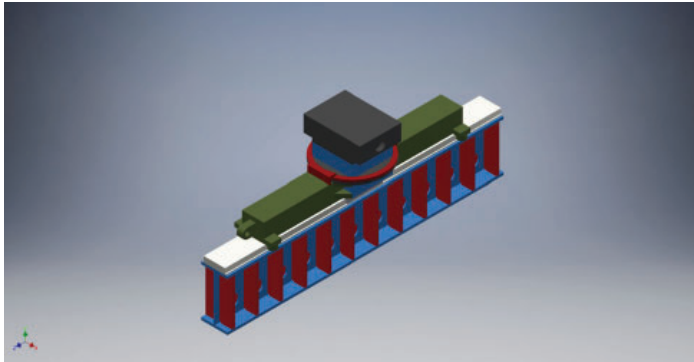


Figure 17. Combined roller and hydraulic system design.

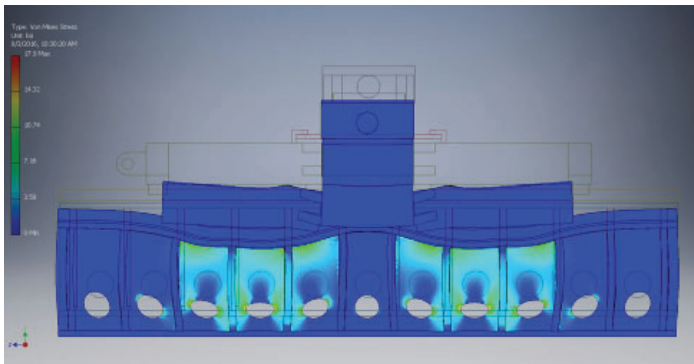


Figure 18. Combined roller and hydraulic system, roller loaded stress analysis.

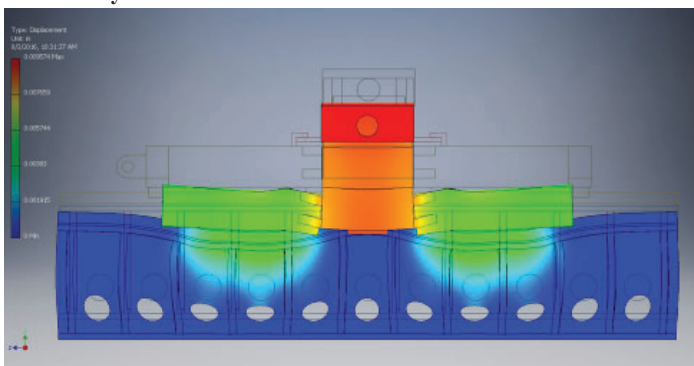


Figure 19. Combined roller and hydraulic system, roller loaded displacement.

VI. Final Design

The final design incorporates the conceptual design some sections 5.3.3 and 5.4.3. Utilizing a hydraulic track to not only allow for the rotation of the rollers but also to allow for three degrees of freedom is an efficient usage of the component. Furthermore, utilizing more rollers allows for the load and thus the stress to be distributed more evenly along the tracks and thus mitigates some problematic stress concentrations. Pairing the system with a fluorogold box contributes the remaining three degrees of freedom and allows for the rest of the components to function properly. The other various options such as the turntable design using the slewing bearings as well as the six degrees of motion platform were for various reasons such as cost, feasibility, ease-of-use, stress concentrations, etc.

VII. Conclusions

The final design is a feasible solution for the sPHENIX project detector support structure transportation and alignment mechanism. The roller truck assembly meets all of the design specifications. Each of the four truck assemblies consisting of two rollers, would meet the conservative load requirement of 500 tons. The final design but also utilize the same cam follower system that was used on the PHENIX central magnet and thus can meet with the track structure. Since the design is capable of using the same cam follower system, which houses the hydraulic mounts, the current hydraulic jacks will be sufficient for the sPHENIX detector. The proposed alignment system is capable of positioning the detector within a tenth of an inch with respect to each of the degrees of freedom as per the design requirements. The roller trucks are also small enough to be attached to the cradle structure and still fit within the infrastructure's accesses. Finally, the roller truck assemblies are within an acceptable range of the required budget.

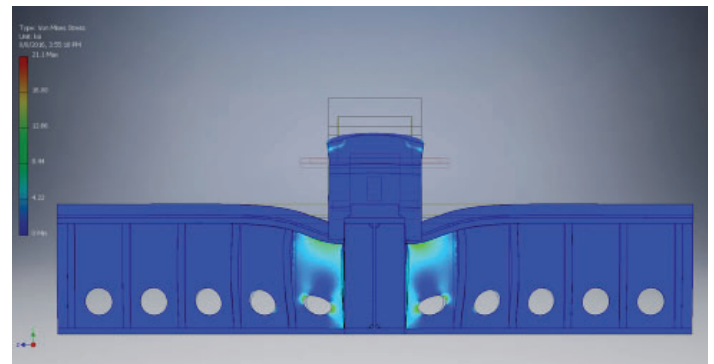


Figure 20. Combined roller and hydraulic system, hydraulic loaded stress analysis.

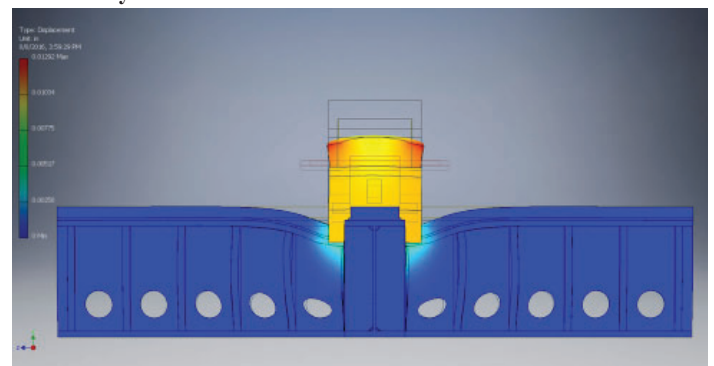


Figure 21. Combined roller and hydraulic system, hydraulic loaded displacement.

VIII. Acknowledgments

This project was supported in part by the U.S. Department of Energy, Office of Science, Office of Workforce Development for Teachers and Scientists (WDTS) under the Science Undergraduate Laboratory Internships Program (SULI). Also, a special thanks to Don Lynch (sPHENIX Chief Engineer), Jim Mills (sPHENIX Project Engineer), Rich Ruggiero (sPHENIX Chief Designer) and the PHENIX and sPHENIX technician, science and engineering teams for their guidance throughout the duration of the internship.

Coil assembly for direct current solenoid gun corrector magnets

Taylor Campbell, College of Engineering and Applied Science, Stony Brook University, Stony Brook, NY 11778
George Mahler, Collider Accelerator Department, Brookhaven National Laboratory, Upton, NY 11973

Abstract

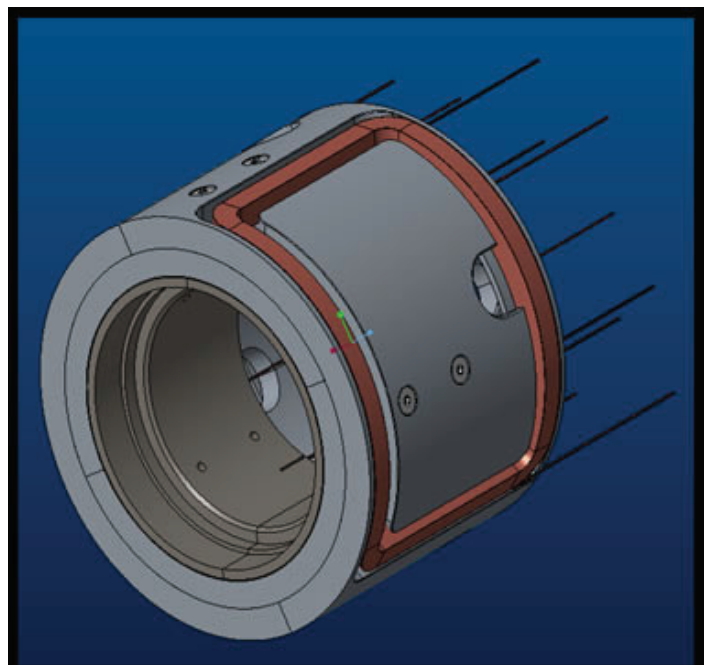
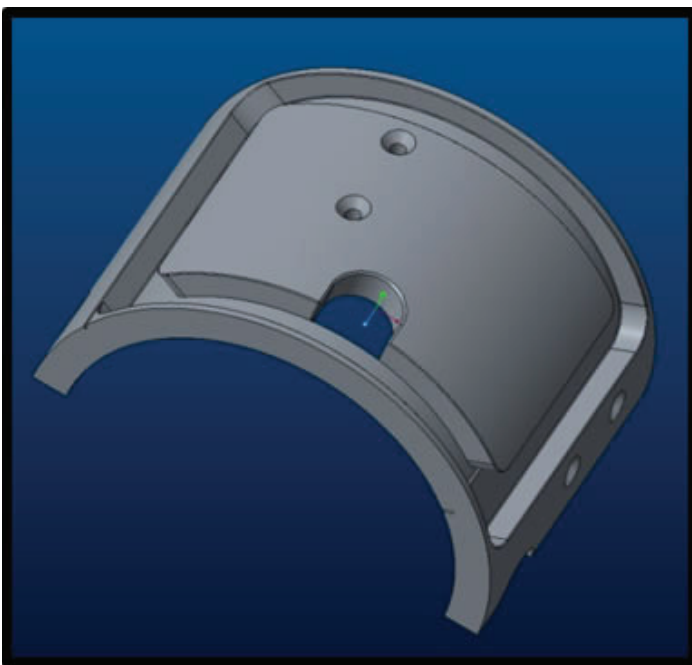
The Low Energy Relativistic Heavy Ion Collider (LeRHIC) is a project at Brookhaven National Laboratory which aims to use streams of electrons to cool adjacent ion beams during collider operation. At the core of the LeRHIC assembly is a direct current (DC) electron gun which injects the electrons into beamline at a slight angular offset. In order to correct this offset, a series of field inducing multipole magnets needs to be assembled in sequence with the DC electron gun for beam steering. My role in this project has been to design and manufacture the coils that need to be placed in a set of previously designed coil forms. Based on the size and shape of the existing forms, I had to design several different devices around which the coils would be wound and then removed. My models were created using Creo Parametric design software and then printed on an 'Ultimaker 2+' 3D-printer. Each design that I printed was tested with hand coil winding and compared by fit to the forms; once the right fit was observed, the device was fixed to a winding machine which allowed us to wind multiple coils with ideal accuracy and efficiency. At this time the coils are still being wound and the project is ongoing, but we can conclude that the coil production process which I developed has been successful. Once these coils are installed in our array of magnets, LeRHIC will be one step closer to full operation and BNL physicists will use the system in many future beam runs. Through completing this project I have gained experience in 3D modeling, plastic plotting, and

the general process of engineering design and testing. In addition, I have also learned more about superconducting magnet systems and engineering software programs such as Creo Parametric and Cura.

I. Background and Assignment

LeRHIC is a project at BNL which is intended to run alongside the existing RHIC experimental beamline. The LeRHIC assembly will consist of a main DC electron gun and a series of superconducting magnets to steer the beam of electrons which is produced. Since the electron gun tends to release electrons at a slight angular offset, it is necessary to install some of these magnets in close sequence with the end of the gun. This being the case, engineers have designed additional magnet fixtures to fit inside a pair of solenoid magnets which will already be installed next to the electron gun. The fixtures are organized into two sets of interlocking half-cylinder coil forms which will fit around the beam pipe and within each other. Each of the two sets will include six half-cylinder parts which fit together in mating pairs of two – creating the following complete three layer assembly around the beam pipe.

My role in this project has been to develop a method of winding coils to fit within these previously designed multipole fixtures. Using engineering design software and the various coil winding tools available to me, I have worked to create the most efficient and accurate method of winding these coils.



Figures 1 and 2: The above images show the previously designed coil forms as they appear individually and then assembled together.

II. Winding Assembly Design

In order to wind the correct coil sizes, a winding assembly had to be designed with dimensions matching the coil form slots in which they had to fit. The plan was to design a uniform winding assembly with variation in dimensions for the different size shell levels of the magnet. The assemblies were designed on 3D design software and plastic plotted as shown below, incorporating two separate parts to be attached by screws and through holes. Prior to winding, shims and radius attachments were taped to the edges around which the wire was to be wound; the detachable shims were intended to aid in coil removal, and the radius attachments were in place to maintain original curvature as shim width was added. Once fully prepared, the coil winding assembly was tested with hand wound trial wire and then moved toward a more automated process using a coil turning machine.

III. Coil Turning Machine

After initially winding test coils by hand, my mentor and I decided to increase production efficiency by seeking out a more automated method of coil winding. Acquiring a basic winding machine, we attached our assembly to the shaft, secured the spool of wire, and connected a turn counter for accuracy.

a. Attaching our winding assembly: The winding machine I was using consisted of a multi-speed motor and a rotating shaft with a circular metal base at the end. Our winding assembly would need to be attached to this winding base using through-holes and matching screws. To address this task, we measured the size of the four holes on the base and incorporated clearance holes into our printed models (in addition to the holes put in place to connect the two parts of the winding assembly). We then machined an additional plate with mating clearance holes to stand between the circular base and rectangular assembly in order to minimize potential stress. Below is an image of the attached assembly.

b. Configuring a turn counter: Since each coil needed to contain a specific number of turns with distinct cross-section geometry, accuracy was very important in this project; the outer and middle coils required 100 turns (10 x 10) and the inner coil required 25 turns (5 x 5). To ensure consistency among the coils,

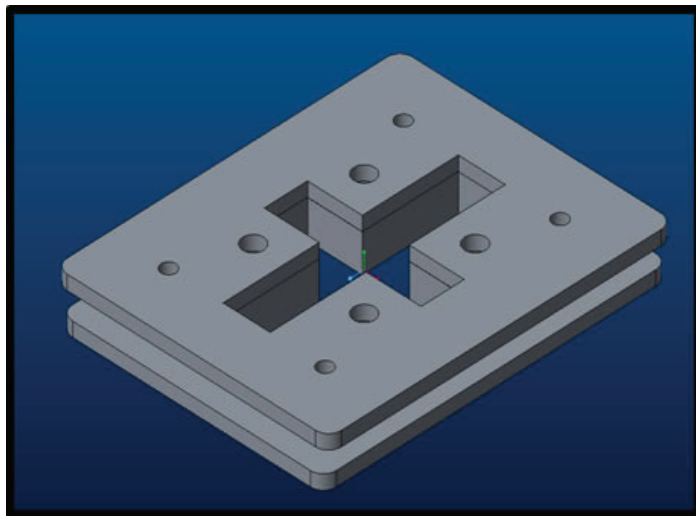


Figure 3: The adjacent image shows a sample of one of the fixtures used to wind our coils (outer layer). In this three dimensional representation you can see the through holes used for connection as well as the slots used to contain and control the wire.

we acquired a turn counter and attached it to the shaft of the coil turning machine. When mounting the counter, I had to design a small part to equate the radii of the counter shaft and turning shaft in order to create a one-to-one gear ratio. To complete the assembly, the two shafts were connected with a flexible O-ring as shown in Figure 4.

c. Installing the wire spool: For the composition of our coils, we determined that 20-gauge copper wire, with a square cross-section, would be appropriate for our intended usage. Areas around the coil turning machine were inspected for potential spool location, as the wire would have to be secured nearby and connected to the assembly during winding. A table next to the turning machine proved the ideal location to connect the spool. Existing holes in the table were used with threaded rods to create a bar assembly which suspended the wire at the correct location. In addition, we attached some brake springs to this fixture to ensure that slippage would not occur easily during winding.

IV. Coil Winding Process

As mentioned in previous sections, our coils were required to contain a specific number of coil turns and cross-section geometry based on the magnet layers which they correspond to. Since twelve sets of each coil size were needed, a crucial consistency among the products was maintained through a partially machine-automated winding process, designed specifically for this project.

a. Setup: Each time a coil was to be wound, the layer-specific winding assembly was constructed. The construction involved attaching removable shims and radius attachments to the



Figure 4: Pictured to the left is the entire assembly for our coil production process. Visible here are various components including the winding machine, winding fixture, stress relief plate, copper wire, and turn counter (the details of which will be discussed in the next section).

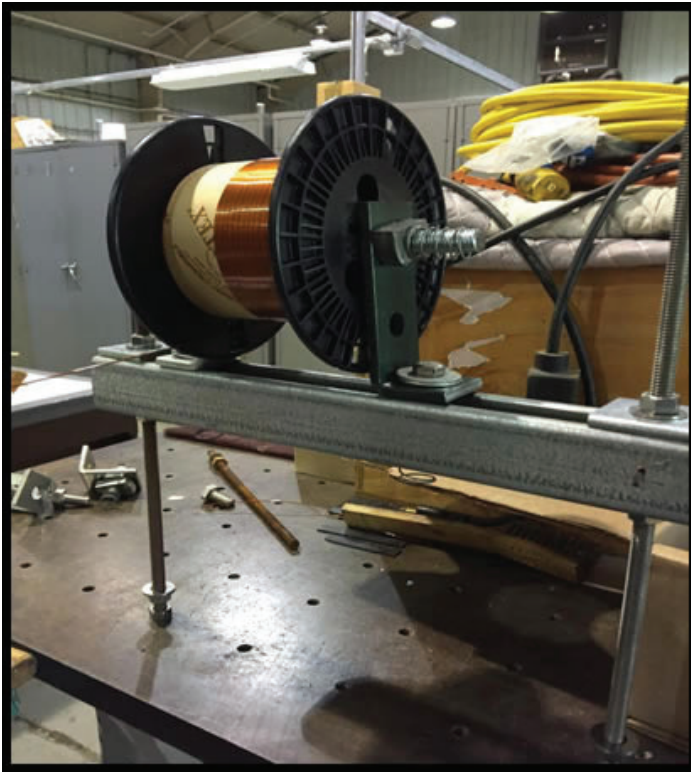
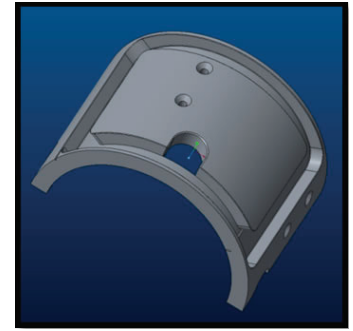


Figure 5: Shown in the adjacent image is our wire spool. As previously discussed, the spool was installed at a table near the winding machine and supported by threaded rods, nuts and tensioning breaks. The copper wire was then connected to the winding fixture over a short distance.

base, screwing the base and top together, and spraying the winding surfaces with mold release. After the mold release had dried, we would secure the winding assembly to the base of the machine shaft, on top of our stress relief plate. Connecting wire to the assembly through an entry slot, a considerable amount of excess wire was left at the start of the coil for connection purposes later on.

b. Winding and securing layers: Once the spool was connected to the assembly, coil winding began. The process required an operator to guide and physically manipulate the wire as it was laid in layers on the mold, using a foot pedal and speed knob to control wire deposition. After each layer of wire was placed, a coat of quick dry epoxy was applied to secure the coil. When the epoxy had set, the next layer of wire was deposited and the process repeated until the target number of turns was achieved in the desired cross-section geometry.

c. Removing and inserting the coil into its coil form: With the necessary number of turns on the coil and the final layer of epoxy set, the assembly was removed from the shaft and its wire cut. The assembly pieces were then disconnected, all shims removed, and the coil guided off its base; Kapton tape was used to wrap and further secure the detached coil. This finished coil was brought to a steel tube around which it was to be bent into proper shape and radius to match its mold. Once manipulated, the coil was placed in its corresponding coil form for size testing; if something was wrong with the coil fit, we would be able to slightly modify the part using 3D design software to control the slot sizes. As it turns out, some of the molds needed to be adapted with larger slots and reprinted to fit the coils. After making these changes, the coils were able to be secured in their fixtures for final preparations.



Figures 6 and 7: The images above show a sample of one of our bent coils and the mold that it fits into. Like this sample, all coils were consistently bent to match the radius and general shape of their corresponding coil form.

V. Summary of Progress

At the end of my term at BNL, I was able to successfully develop a coil production process for the DC solenoid gun corrector magnets. After multiple stages of design and testing, a system of partially machine-automated coil winding was developed to create consistent coils among the many layers of our intended magnet fixtures. With some of the magnets being assembled during my term here, the rest of the project will continue under the direction of other engineers at BNL until it is completed.

VI. Acknowledgements

This project was supported in part by the U.S. Department of Energy, Office of Science, Office of Workforce Development for Teachers and Scientists (WDTS) under the Science Undergraduate Laboratory Internships Program (SULI).”

Measuring inorganic aerosol composition with the Particle Into Liquid Sampler (PILS)

Mark Chan

Chemistry, Stony Brook University, Stony Brook, NY 11794

Thomas B. Watson

Environmental and Climate Sciences, Brookhaven National Laboratory, Upton, NY 11973

Abstract

The particle-into-liquid-sampler (PILS) is an instrument operated by the Environmental and Climate Sciences Department (EE) of Brookhaven National Laboratory (BNL) for the Department of Energy Atmospheric Radiation Program (ARM). The PILS is an instrument that measures atmospheric inorganic aerosols, by collecting particles in an aqueous solution. In 2013 and 2014, the instrument was operated in Cape Cod, but it has been idle for the past three years. This project consists restoring the instrument to operational condition by replacing critical components and then characterizing the performance of the instrument. The instrument will be calibrated and its limits of detection and quantitation determined. Calibration of the instrument was completed using standards prepared in the laboratory. Once operational and fully characterized, the instrument will be used to measure inorganic aerosols at BNL. Of particular interest is the concentration of sea salt aerosol seen at the site. In other settings, the PILS will be used to study the effect of inorganic aerosols on the global radiation budget.

I. Introduction

Atmospheric aerosols are fine particulate matter suspended in air, and are the result of natural and anthropogenic emissions. These suspended particles effect the global radiation budget by changing the the amount of solar energy reaching the surface of the Earth and the amount of energy emitted back into space. These particles can scatter and absorb sunlight, the aerosol direct effect, and change the properties of clouds, the aerosol indirect effect. Both these effects affecting the Earth's radiation budget and climate¹. An example of a particle with this effect is sulfate produced from power plants². Greenhouse gases (GHGs) have the same emission source as aerosols, but have different effects. GHGs directly absorb radiation to affect the global radiation budget, while aerosols both absorb and scatter radiation. They capture outgoing radiation within the atmosphere and contribute to the overall temperature increase of Earth's surface³. Cloud formation also effects the global radiation budget. Particles with diameters less than 1 μm scatter incoming solar radiation very well, and subsequently send a portion of the scattered solar radiation back into space. These particles and their scattering effect decrease the amount of solar energy that enters the Earth and results in decreasing temperatures³. The concentration of condensation nuclei increases as more aerosols are present in the atmosphere. A higher concentration of cloud droplets increases cloud reflectivity of solar energy, thus reflecting more radiation and shifting the Earth's radiation balance⁴. The PILS measures the inorganic component of atmospheric aerosols so we can better understand the effect of these species on the global radiation budget and therefore on global climate.

II. PILS

A. Theory and Operation

The components of the PILS are shown schematically in in Figure 1⁵. The PILS collects ambient particles by passing them through a reaction chamber filled with supersaturated steam. The particles are condensation nuclei and form liquid water droplets passing through the chamber. Ambient air flows through the steam chamber at 15 liters per minute (1min^{-1}), and is mixed with steam (). The aerosol particles form droplets in the supersaturated environment with a diameter of diameter $1\ \mu\text{m}$. These droplets strike an impactor and are the collected in a continuous flow of carrier solution washing over it. The carrier solution is concentrated on collection columns for 15 minutes. Ambient gas phase species also present in the air sample can be detected and may affect the accuracy of the particle measurements. Gas phases species are removed by denuders upstream of the PILS.

Purified, deionized (DI) H_2O is pumped through a heater at 100°C , causing the DI H_2O to change from liquid to gas phase. The steam is then directed into a reaction chamber and mixed with the ambient air stream. The inorganic aerosol particles form droplets which are collected on an impactor. Carrier solution flows over the impactor collecting the liquid droplets and transporting the sample to ion chromatographs for analysis.

B. PILS and Starburst Pattern

Figures 2 and 3 show the PILS body from the front and the side, respectively. Figure 4 shows the starburst pattern caused by the droplets formed from a mixture of ambient aerosol and steam hitting the impactor.

C. Components

The droplets are moved through the PILS by a carrier solution, 2.0 lithium perchlorate (LiClO_4) or lithium bromide (LiBr) (more details in section ii.) The analysis of the ambient species is completed using ion chromatography. Two ion chromatographs

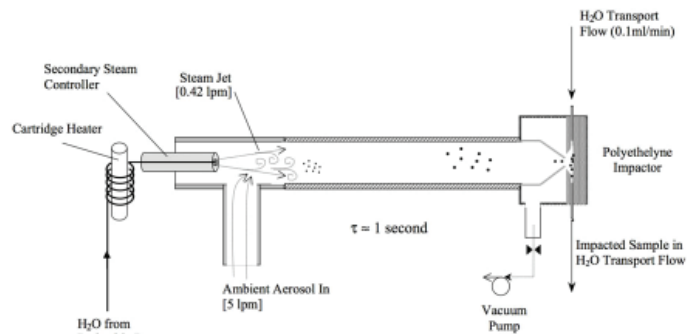


Fig. 1. 15 lmin^{-1} PILS design.

Solution	Use	Content	Preparation
Purified H ₂ O	Steam H ₂ O Supply	Purified H ₂ O	18 MΩ H ₂ O from EasyPure II H ₂ O Purification System
Carrier Solution	Wash off aerosol sample from impactor	2.0 μM LiClO ₄ or LiBr for internal standards	Dilute 2.0 mL of 1.0 mM LiClO ₄ into 1.0 L H ₂ O
Anion IC Eluent	Anion column elution	mM NaHCO ₃ 3.2 mM Na ₂ CO ₃	One packet of stock into 1.0 L H ₂ O
Cation IC Eluent	Cation column elution	2.5 mM oxalic acid	Dilute 5.0 mL of 0.5 M oxalic acid into 1.0 L H ₂ O
Anion IC suppressor solution 1	Suppressing anion IC background signal	100 mM H ₂ SO ₄	Purchased from Metrohm
Anion IC suppressor solution 2	Suppressing anion IC background signal	Purified H ₂ O	18 MΩ H ₂ O from EasyPure II H ₂ O Purification System
Calibration Standards	IC calibration	0.5 – 3.0	Prepared from 1mM intermediate standards

Table 1. All solutions used in the PILS instrument.

are used; one for anions chromatograph and one for cations chromatograph. These chromatographs separate the species of interest based on their affinity for the stationary phase of the column. A conductivity detector is used to determine when the separated ions elute from the column. The compounds are identified by their retention times.

D. Solutions

The instrument requires multiple solutions. These are listed in Table 1. All listed solutions are prepared from DI/purified H₂O with a resistance of 18 Mohm.

The PILS was characterized with calibration standards of ions we are interested in studying. Table 4 lists the ions and the compounds from which they were prepared.

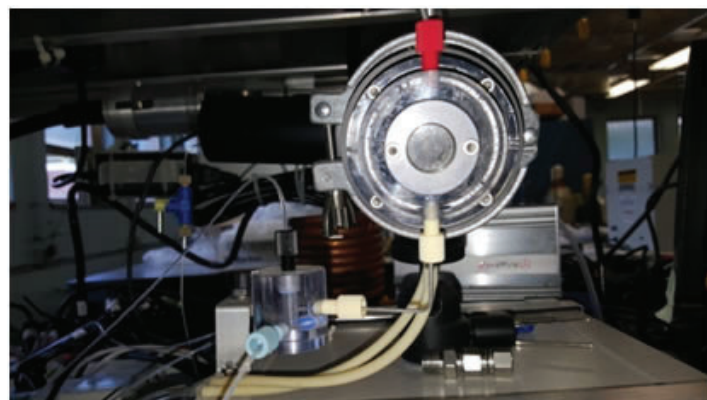


Fig. 2. Front view of the PILS.

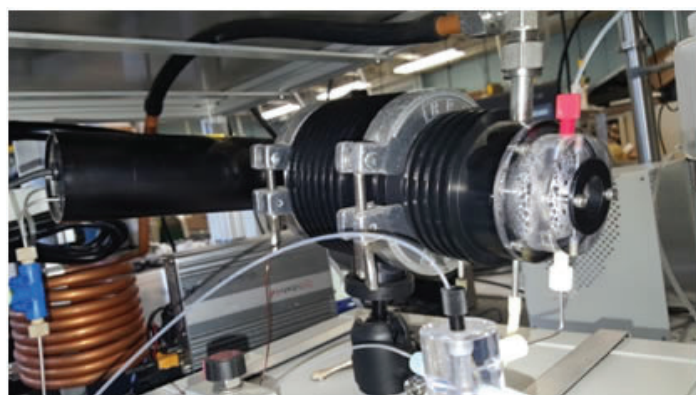


Fig. 3. Side view of the PILS.

Species	Source
Anions	
CH ₃ CO ₂ ⁻ (acetate, Act)	NaAct
Cl ⁻	CaCl ₂
Br ⁻	KBr
NO ₃ ⁻	NH ₄ NO ₃
H ₂ PO ₄ ⁻	KH ₂ PO ₄
SO ₄ ²⁻	MgSO ₄
C ₂ O ₄ ²⁻ (oxalate, Oxt)	Na ₂ Oxt
Cations	
Li ⁺	LiClO ₄
Na ⁺	NaAct, Na ₂ Oxt
NH ₄ ⁺	NH ₄ NO ₃
K ⁺	KBr, KH ₂ PO ₄
Mg ²⁺	MgSO ₄
Ca ²⁺	CaCl ₂

Table 2. Species used in calibration standards and source of calibration standards.



Fig. 4. Starburst pattern on the impactor of the PILS.

All solutions are prepared at 0.05 μM and then diluted to 1.0 mM by a 20 to 1 dilution series using a 1.0 mL Pipetman and a 100 mL plastic volumetric flask. Table 3 lists the final calibration standard concentration in 20 mL DI H_2O to X, where X is the volume to achieve the desired μM concentration.

Final nominal concentration (μM)	X (μL)
0.5	10
1	20
2	40
3	60

Table 3. Volume of 1.0 mM standard needed to create desired concentration in 20 mL DI H_2O .

1. Measurements

The ions are measured by anion and cation chromatography. The cation chromatograph analyzes all positively charged ions while the anion chromatograph analyzes all negatively charged ions. Table 4 contains the cations and anions we are interested in studying due to their effects within the atmosphere.

Cation	Li^+	Na^+	NH_4^+	K^+	Mg^{2+}	Ca^{2+}	
Anion	CH_3CO_2^-	Cl^-	Br^-	NO_3^-	H_2PO_4^-	SO_4^{2-}	$\text{C}_2\text{O}_4^{2-}$

Table 4. A complete list of measured ions.

2. Limits of Detection and Quantitation

The limits of detection and quantitation of the PILS is three times and ten times the noise⁶, respectively. Section IVC provides further details on how the values are calculated.

III. PILS Service: Replacement Parts

A. Past Operations

The PILS was previously operated at Cape Cod. Prior to returning to BNL, the instrument was not operated for three years. When the instrument returned to BNL, the first objective was to get it into working order by replacing the analytical columns and other critical components. We disassembled the PILS body to inspect the inner components, cleaned the impactor, and refitted the mesh that allows the carrier solution to flow over the impactor to collect the aerosol solution. The peristaltic pump tubing was replaced. The eight pump channels required different diameter tygon peristaltic pump tubing to account for different flow rates at 20% pump speed. Tubing was purchased from Cole Parmer, and Table 5 identifies the different tubing used for the peristaltic pump.

Pump Channel No.	Function	2-stop color identification	Diameter (mm)
1	Anion IC sample fill	Orange-yellow	0.51
2	Cation IC sample fill	Orange-yellow	0.51
3	Debubbler	Orange-Purple	2.54
4	Carrier flow	Green-green	1.85
5	Steam H_2O feed	Orange-purple	2.54
6	Impactor drain	Blue-blue	1.65
7	PILS body drain	Blue-blue	1.65
8	Flow drain	Blue-blue	1.65

Table 5. Tygon peristaltic pump tubing identification.

B. Service.

The ion chromatographs needed several replacement parts. They were all obtained from Metrohm USA. Columns and guard columns were replaced for both cation and anion systems. Inline filters are placed after the chromatograph pumps as well as before and after the injector were replaced. The anion chromatograph uses a suppressor that requires that requires a 0.1 M sulfuric acid (H_2SO_4) solution to suppress background chromatogram noise. It also requires a $\text{H}_2\text{O}/\text{CO}_2$ absorption cartridge to neutralize the used H_2SO_4 , which was replaced. There are pre-concentration columns inline with the injectors on both chromatographs, and both were replaced.

IV. PILS Characterization

A. Retention times

Determination of the retention times of all the ions of interest were determined by sampling individual compounds listed in Table 6 at 0.5 μM , 1.0 μM , 2.0 μM , and 3.0 μM . A minimum of six trials were ran for each concentration, and the results were used to determine the retention times of the ions.

1. Retention times

Cation							
	Li^+	Na^+	NH_4^+	K^+	Mg^{2+}	Ca^{2+}	
Mean	1.49	2.78	3.47	5.17	5.80	10.11	
STDEV	0.02	0.01	0.04	0.43	0.10	0.16	
SDOM	0.01	0.01	0.02	0.17	0.04	0.05	
RDEV	0.01	0.00	0.005	0.03	0.01	0.01	
%SDOM	0.58	0.20	0.45	3.36	0.67	0.53	
Anion							
	Act	Cl^-	Br^-	NO_3^-	H_2PO_4^-	SO_4^{2-}	Oxt
Mean	1.00	2.32	5.14	6.09	9.64	11.72	13.77
STDEV	0.02	0.07	0.02	0.04	0.08	0.02	0.08
SDOM	0.01	0.02	0.01	0.01	0.03	0.01	0.03
RDEV	0.01	0.01	0.00	0.002	0.003	0.001	0.00
%SDOM	0.66	1.00	0.15	0.24	0.28	0.08	0.24

Table 6. The average retention times of all interesting ions of six trials at 3.0 μM in minutes.

Abbreviations: STDEV: Standard Deviation

SDOM: Standard Deviation from the Mean

RDEV: Relative Deviation

%SDOM: Percent Standard Deviation from the Mean

2. Chromatograms

Figures 5 and 6 are chromatograms of 0.5 μM calibration standards that demonstrate the retention times of both cations and anions.

B. Calibration

1. Chromatograms

A minimum of six calibration trials were performed at each concentration. The following chromatograms were from 3.0 μM trials and they demonstrate previously stated problems with doubly charged ions.

2. Calibration Curves

The calibration curves are determined using the ion's concen-

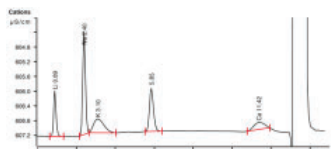


Fig. 5. 0.5 μM cation retention times.

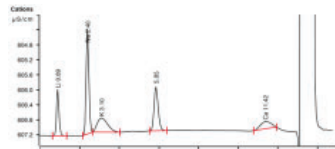


Fig. 6. 0.5 μM anion retention times.

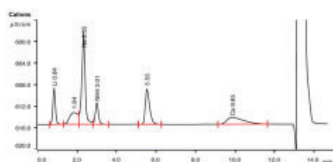


Fig. 7. 3.0 μM cation with all standards.

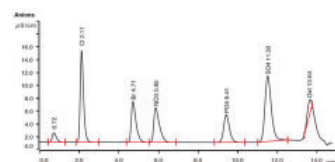


Fig. 8. 3.0 μM anion with all standards.

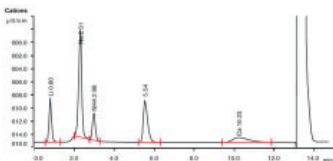


Fig. 9. 3.0 μM cation without MgSO_4 and CaCl_2 .

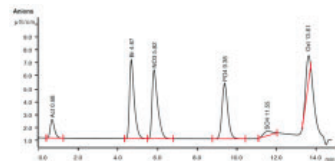


Fig. 10. 3.0 μM anion without MgSO_4 and CaCl_2 .

tration and the area underneath its peak. The concentrations of the solutions are 0.5 μM , 1.0 μM , 2.0 μM , and 3.0 μM . The areas peak areas are determined by the software, MagIC Net. Concentration is plotted in μM on the Y axis and area is plotted in $\mu\text{S}/\text{cm}$ on the X axis. A best fit line is superimposed on the graph and gives us a line with the equation $y = mx \pm b$. Figure 11 presents the acetate anion calibration curve. Table 7 presents all calibration coefficients.

Compound	m	b	
Li^+	10.77	-1.42	0.95
Na^+	6.30	-2.44	0.98
NH_4^+	4.63	-0.61	0.93
K^+	8.89	-2.42	0.9
Mg^{2+}	5.16	-0.64	0.97
Ca^{2+}	23.09	-3.28	0.99
CH_3CO_2^- (acetate, Act)	173.08	-0.54	0.95
Cl^-	5.91	-2.05	0.97
Br^-	9.22	-2.07	0.99
NO_3^-	5.14	-0.34	0.99
H_2PO_4^-	8.96	-0.73	0.92
SO_4^{2-}	4.54	-1.89	0.99
$\text{C}_2\text{O}_4^{2-}$ (oxalate, Oxt)	12.31	-2.90	0.99

Table 7. All calibration coefficients.

3. Standard Deviation v. Concentration Plot

The noise level of the instrument is determined by plotting the standard deviation of 6 measurements of the calibration standard at each concentration versus the concentration. These data are then fit with a line. The intercept, the extrapolated standard deviation at zero concentration, is then taken as the noise of the instrument. Figure 12 presents the standard deviation at each concentration versus concentration of the acetate anion. Table 8 shows the results of this analysis for all ions measured.

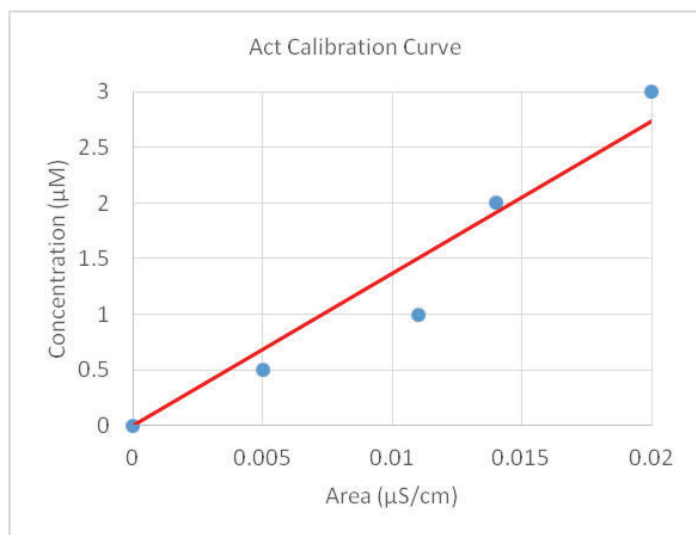


Fig. 11. Acetate anion calibration curve, Concentration (μM) v. Area ($\mu\text{S cm}^{-1}$).

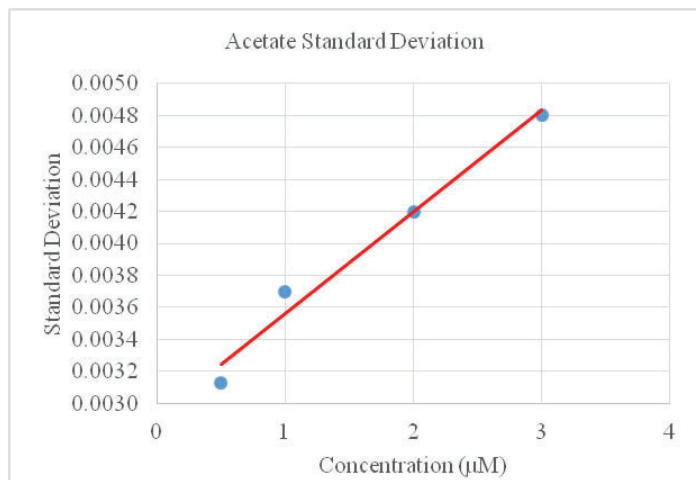


Fig. 12. Standard Deviation (Noise) of Acetate ion, Noise v. Concentration (μM)

Compound	m	b	
Li^+	0.04	0.03	0.86
Na^+	0.10	0.08	0.92
NH_4^+	0.07	0.07	0.86
K^+	0.07	0.05	0.99
Mg^{2+}	0.09	0.05	0.98
Ca^{2+}	0.04	0.15	0.99
CH_3CO_2^- (acetate, Act)	0.001	0.003	0.98
Cl^-	0.10	0.02	0.96
Br^-	0.08	0.02	1.00
NO_3^-	0.08	0.06	0.99
H_2PO_4^-	0.02	0.05	0.84
SO_4^{2-}	0.13	0.02	0.96
$\text{C}_2\text{O}_4^{2-}$ (oxalate, Oxt)	0.08	0.02	0.98

Table 8. All standard deviation coefficients.

C. Limits of Detection and Quantitation

The limits of detection and quantitation are three times the noise and ten times the noise, respectively. They are calculated by taking the intercept from Table 8 and substituting it into the calibration equation using the coefficients presented in Table 11. Table 9 presents the limits of detection and quantitation for all ions measured by the PILS.

	Limits of Detection	Limits of Quantitation
Li ⁺	3.29	10.97
Na ⁺	5.81	19.36
NH ₄ ⁺	0.86	2.86
K ⁺	5.93	19.76
Mg ²⁺	1.15	3.82
Ca ²⁺	0.55	1.84
CH ₃ CO ₂ ⁻ (acetate, Act)	0.06	0.21
Cl ⁻	5.80	19.32
Br ⁻	5.66	18.86
NO ₃ ⁻	0.09	0.32
H ₂ PO ₄ ⁻	0.85	2.82
SO ₄ ²⁻	5.40	17.99
C ₂ O ₄ ²⁻ (oxalate, Oxt)	7.96	26.54

Table 9. Limits of detection and quantitation for all measured ions ($\mu\text{g m}^{-3}$).

V. Discussions and Conclusions

The PILS is able to measure inorganic atmospheric aerosols with the detection and quantitation limits specified in Table 9. There are problems such as artefacts that can only be removed by flushing the instrument with DI H₂O and overlapping peaks, the latter of which is observed in figures 9 and 10. Magnesium (Mg²⁺) is the most prevalent ion to interfere with measurements because of its early elution time and peak broadening because of the fact that it is doubly charged. In this project we measured sodium (Na⁺) and ammonium (NH₄⁺) which both have similar elution times to Mg²⁺. Calcium (Ca²⁺) will behave similarly to Mg²⁺ if there is another ion of similar affinity and size measured in tandem. The peak present at the end of the cation chromatogram is due to the pressure change when the instrument switches from injection to fill.

VI. Results

We determined the instrument's limits of detection and quantification with calibration standards. The different ions have varying affinities for the columns that allow for separation in the chromatograms. Some of the ions cause problems because they do not elute consistently because of they carry a double charges. Fortunately, these species are not of atmospheric interest. Increasing the analysis time allows for better separation and more clear chromatograms. The PILS is able to measure aerosol concentrations with accuracy and precision at levels that are consistent with those found in the atmosphere.

VII. References

- ¹B. Allen. "Atmospheric Aerosols: What Are They, And Why Are They So Important?". NASA. N.p., 2016. Web. 8 Aug. 2016.
- ²E. J Liebsch and R. G. De Pena, *Atmo. Environ.* **16**, 1323 – 1331 (1982).
- ³J. H. Seinfeld and S.N. Pandis, *Atmospheric Chemistry and Physics: From Air Pollution to Climate Change*, 1st Ed. (John Wiley & Sons, New York, 1998), pp. 1113 – 1130.
- ⁴W. C. Hinds, *Aerosol Technology: Properties, Behavior, and Measurement of Airborne Particles*, 2nd Ed. (John Wiley & Sons, New York, 1999), pp. 311 – 313.
- ⁵D. A. Orsini *et al.*, *Atmo. Environ.* **37**, 1243 (2003).
- ⁶J. K. Taylor, *Quality Assurance of Chemical Measurements*, 1st Ed. (Lewis Publishers, Inc., Michigan, 1987).

VIII. Acknowledgments.

This project was supported in part by the Brookhaven National Laboratory (BNL), Environmental and Climate Sciences Department under the BNL Supplemental Undergraduate Research Program (SURP).

Developing an Arduino controlled datalogger for pyranometers

Daniel Christiansen

Chemical Engineering, Tulane University, New Orleans, LA 70118

John Heiser

Environmental and Climate Sciences, Brookhaven National Laboratory, Upton, NY 11973

Abstract

A pyranometer is a device used to measure and record the UV and solar radiation that solar panels are exposed to and produces data that is essential to knowing how much energy solar panels will produce. For the New York City solar projects, a single-purpose, low cost, data logger is needed that can sit with the pyranometer for elongated periods of time. For this reason, I developed and produced an Arduino (microprocessor) controlled data logger that is able to use Power Over Ethernet to power itself and record data from the pyranometers, then post this data to a web page that is also hosted by the Arduino. By using the Arduino's built-in voltage read capability, an attached ethernet shield, and an amplifying chip, the Arduino can take a voltage from the pyranometer and amplify it to an observable level that is then recorded. This device is able to convert the data into a usable form and also record its position from an accelerometer then store it on an SD card mounted to the board. This device has the ability to easily convert and transition for a variety of data collection needs with only a slight change in hardware and code. Through this project I was able to better my understanding of the programming software "Arduino IDE" and the research, design, and testing phases of product development. I also was able to use resources at Brookhaven National Laboratory to further my understanding of electrical engineering and networking.

I. Background

Devices known as "dataloggers" are common in any branch of STEM. From recording motor control to temperature reading, they are essential for recording accurate and specifically timed information. Well-known datalogging devices such as Texas Instruments, Logger Pro, and DataQ, are extremely diverse in usage and purpose but typically have a few things in common.

These would consist of being expensive, having more sensor ports than needed, and having many wires protruding from the box that need to be plugged into Internet, USB hub, power outlet, or some combination of the three. When it comes to large scale projects that could cover entire towns or counties at a time, and have a need for specifically localized sensors, these dataloggers are more than unnecessary.

II. Method

To address this over complication of a simple task, the ideal device would be "cheap" (for as many as possible in a large area), easily placed, and require as few wires as possible. These were my starting goals when beginning research into developing a datalogger and effective methods:

- Keep it inexpensive: There do exist devices that can handle the task at hand. However, these often cost hundreds to thousands of dollars and are bulky, or can not be placed

where the related projects would require them.

- Use a microcontroller: Arduino, BeagleBone, Raspberry Pi, etc. are all examples of microcontrollers and microcomputers that can easily take in sensor data and perform a myriad of tasks with it.
- Utilize Power over Ethernet (PoE): Sensors are often placed far from a computer that can communicate with and power the datalogger. PoE would make it so only one ethernet cable would be needed to complete both at once over the distance expected in NYC rooftop installations.

With these in mind, the following overview was constructed to visualize what we needed to accomplish to have a datalogger that could read a Kipp & Zonen SP Lite2 Pyranometer and process the readings. The "Server" in the image is where the data would be sent to and, presumably, further used.

The SP Lite2 works in a similar manner to a solar panel. Sunlight, carrying UV, solar, and other forms of radiation¹ "hits" the device and induces it to produce a voltage. For industrial and household solar panels, this energy is of such magnitude that it is considered "usable" and can be implemented into power grids and home electricity. The SP Lite2 on the other hand, even on the brightest day (most intense sunlight: $\sim 1100 \text{ W/m}^2$), can only produce a voltage around 54,000 microvolts (0.054 volts). Research and professional grade dataloggers accommodate for this, as any jukebox does to play a vinyl record, by amplifying the signal. Ergo, an amplification of some kind would be needed to make this signal on the scale that the microcontroller can handle and read accurately.

This voltage, now being on a more observable scale, still needs to be checked for accuracy, as the microcontroller may have a decent AC to DC (electricity) converter (ADC), but it may

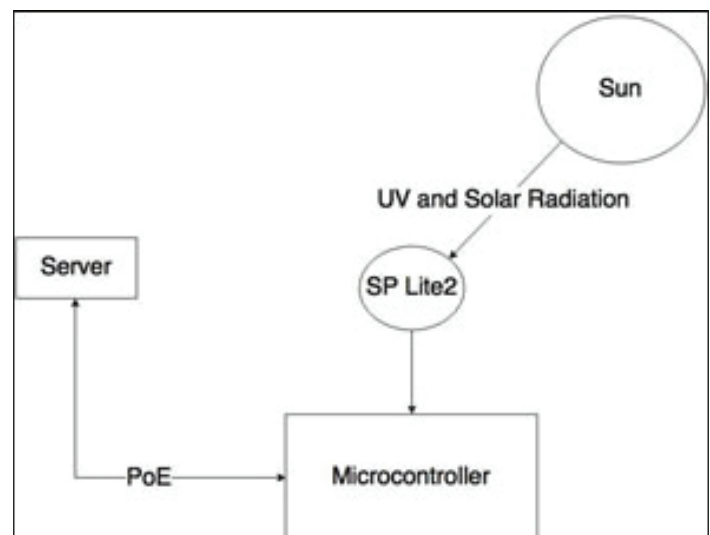


Figure 1: A simplified diagram of the data collection and transmission.

not be “up to snuff” for what we require. This is where a voltage reference comes in. A voltage reference is a chip or component that will always produce an exact voltage, with extremely low deviation. The received, amplified, signal from the pyranometer will be checked against the reference to see any drift in accuracy.

Having a web page to present all of this data is ideal as it would allow any user to view how the device is operating and what the most recent data is at any instant. A few microcontrollers have built-in ways to connect to the network and Internet via Ethernet (as mentioned earlier, PoE is desired). However, nowhere near all of them do. Microcontrollers such as arduino require an attachment that will allow communication to a network. Therein lies another concern over what additional parts may be needed.

Environmental and distance factors also play a role into how the whole device would receive power and be connected to the network, for presenting the data, and the internet, for accurate time stamps. PoE seemed the best alternative as it only requires one ethernet cable, an injector near the network connection for placing data on pins 1, 2, 3, and 6, and power on pins 4, 5, 7, and 8, and a splitter near the device to again split the PoE into signal and power.

After the device is turned on, and the first signal is sent from the pyranometer, the data has to go somewhere for future use. Our microcontroller has to be able to store data for a period of time and have it be retrievable on demand. Ideally, an SD card would be used for this purpose. Many microcontrollers have built-in microSD hubs or attachments that can serve the same need.

A recap of goals would include:

- Microcontroller to collect and move the data
- PoE
- Connect the pyranometer to the microcontroller
- Amplify the signal from the pyranometer
- Voltage Reference
- Store the data to an SD card
- Connect the microcontroller to the network/internet
- Server to present the collected data

III. Materials

With all of the above goals in mind, it was time to start making decisions on parts to fit each.

A. The Microcontroller

The most important part of this device is the “brain” that will control how it receives, processes, and sends out information. A

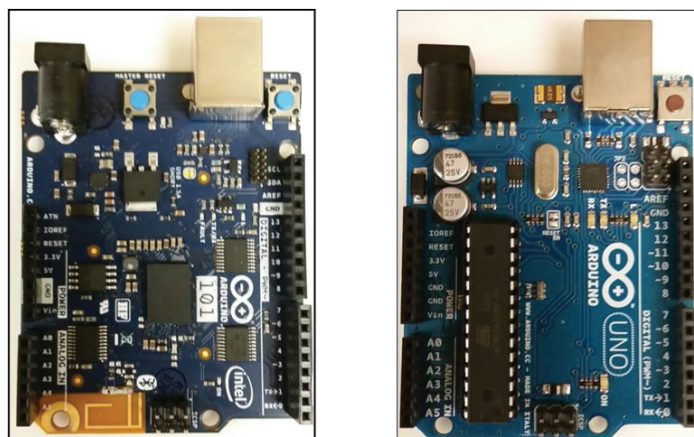


Figure 2: Arduino 101 (Left) and Arduino Uno (Right).

device that is cheap and can fit all of the needs we have was needed. My mentor and I have varying levels of experience with the Arduino microcontroller and its programming software “Arduino IDE,” so it only seemed appropriate to look at Arduino devices first and others afterwards. After some deliberation over the respective accuracy and benefits of different Arduino hardware, we decided on the Arduino 101 which would give us a high degree of accuracy with 10 bits of resolution, an internal gyroscope for checking the position of the datalogger and pyranometer (if the pyranometer is mounted to it), and all of the same pin layouts of the Arduino Uno (the current flagship product of the Arduino line), i.e. it can use all of the same “shields,” or attachments, that the Arduino Uno can.

B. The Shields (Attachable, stackable, specific purpose, boards)

The ethernet connection, SD hub, and prototyping board, to keep everything custom organized, are all shields for the Arduino that stack neatly on top of the main board (the Arduino 101 for this project). They attach by plugging in the pins of the shield into their respective plugs on the board below it. The ethernet shield used for this project was the Seeeduno W5500 Ethernet Shield. This was chosen due to it having a pre-existing library, or collection of software resources for a specific purpose, for programming, and an SD hub built into the shield. The prototyping shield is the Protoshield by Adafruit, which was used for the custom wiring needed for the amplifier, voltage reference, and connecting the sensor.

C. The Amplifier

For our purposes, an amplifier that can handle amplifications of 10, 100, and 1000 was desired. A programmable gain amplifier (PGA) could fit this task. The PGA204 from Texas Instruments fit our need and would only require a DC/DC converter, to produce a negative voltage, for operation. The RECOM RS3-xx05D series DC/DC converter accomplished this. The original plan was to have the amplifier on a static 100X amplification. However, due to the need for specific low-end ($<100 \text{ W/m}^2$) and high-end ($>600 \text{ W/m}^2$) data, it became essential to utilize the 10X and 1000X amplification settings for when the 100X could not provide enough detail. This became a tad daunting of a task, to program the Arduino 101 to detect when a switch in amplification would be needed, perform the switch, and then adjust data processing according. The PGA controls amplification via two pins, 15 and 16, on it.

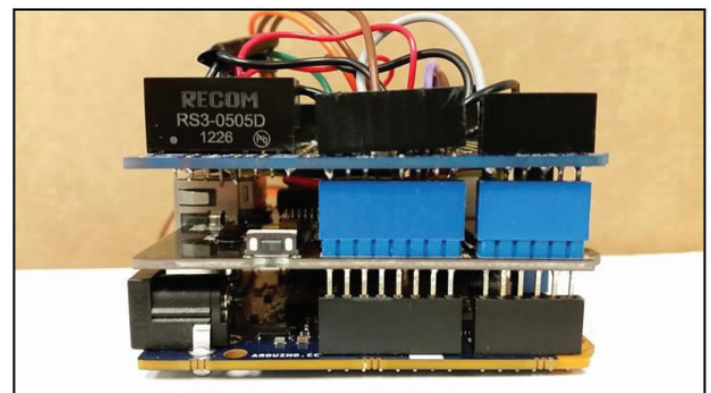


Figure 3: The device, fully assembled, showing the prototyping shield (Top), ethernet shield (Middle), and Arduino 101 (Base).

By changing the voltage of each pin, it is possible to control the amplification as so (HIGH means a voltage is provided, LOW means no voltage):

Amplification	Pin 15	Pin 16
10X	HIGH	LOW
100X	LOW	HIGH
1000X	HIGH	HIGH

Table 1: Chart demonstrating control of amplification through manipulation of the pins on the PGA.

The below diagram visualizes how the change in voltage and amplification occurs as the solar radiation intensity becomes greater. Notice how each amplification can cover exactly 10 times the W/m^2 values that the previous could.

D. Custom Wiring

A simple voltage reference was needed that produced an accurate reference between 0V and 3.3V (the operating voltage of the Arduino 101). The LM4040 Precision Voltage Reference board from Texas Instruments and Adafruit matches this with a precise voltage of 2.048V. This will be used to check the ADC for error and help to correct the readings from the pyranometer. A 3-pin connector to the pyranometer is also included on the prototyping board.

E. The PoE System

PoE has become as simple as can be in today's world. I was able to quickly find a few components that would perform what we needed and provide a voltage within what the Arduino 101 can handle. The system consists of a wall-mounted injector that takes in a cable from the Local Area Network (LAN) and power from the wall outlet, then combines them into an ethernet cable that is then connected to a splitter on the other end that breaks it back into a LAN connection and a power cable. This provides 12V power to the Arduino 101 and a connection to the network and Internet.

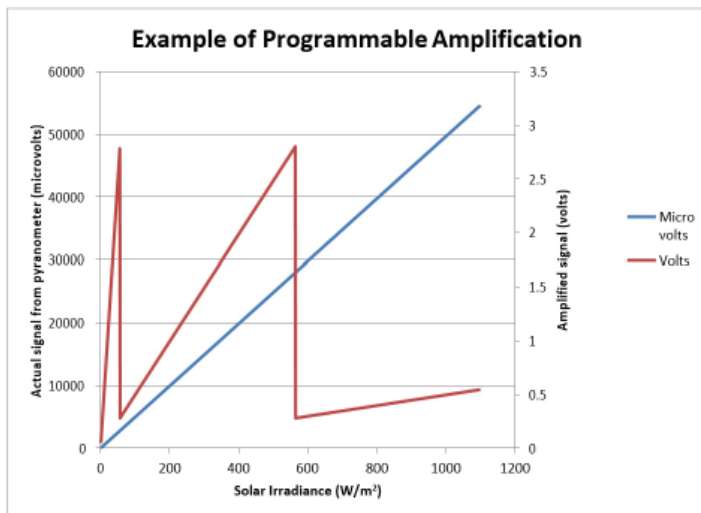


Figure 4: Diagram of changing amplification depending on irradiance observed by Arduino 101.

F. TheServer

The web server is a simple program built into the ethernet coding that allows the Arduino 101 to access the web, check it's time and date once a day against a Network Time Protocol (NTP) server, and present the most recent data. Any user on the network can access this page and see the data by using the IP address of the server hosted by the Arduino 101. A network administrator will be able to tell any future user what the current IP address is,

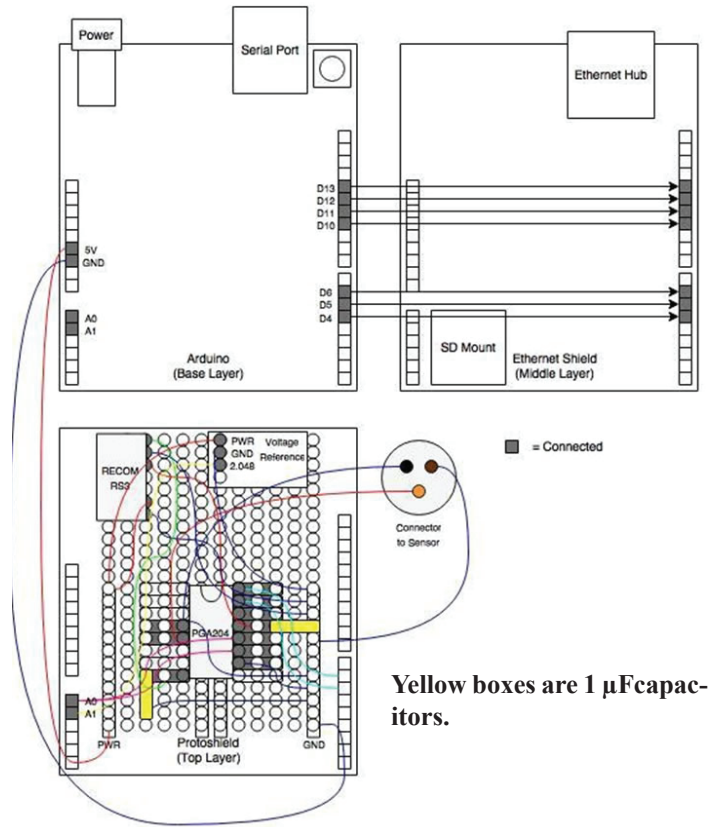


Figure 5: The wiring diagram of the boards. These boards stack as shown in Figure 3.

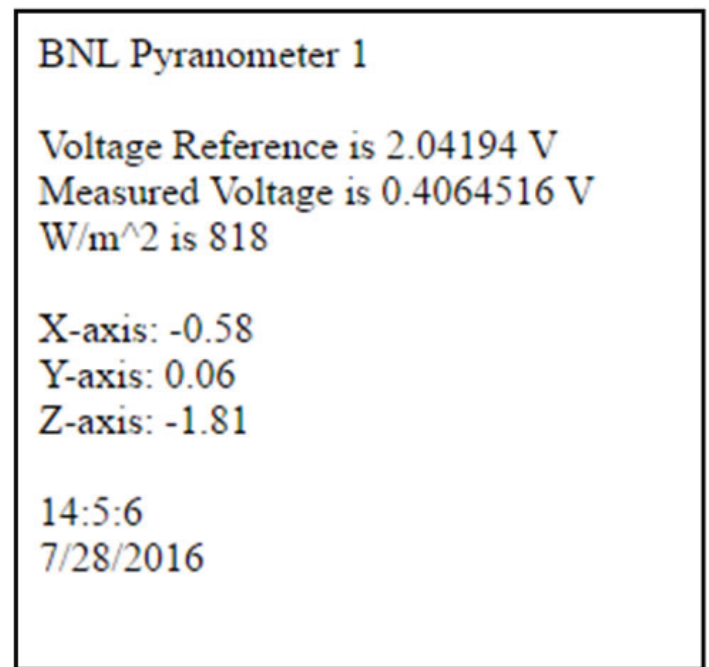


Figure 5a: An example of the web page displayed. The example shows some drift in the reference.

this will stay the same as long as the device is not moved to a new network subnet.

G. Coding

The programming for this project is specifically broken into 9 “parts” that each serve a specific purpose, but interact when needed. The first part is the “Setup” and initiates the device when it is first powered on. The other 8 parts belong to “Loop” and run continuously.

Setup:

Setup starts the gyro sensor, the web server, checks the SD card, gets the NTP time, and tells the Arduino 101 to check and correct the time on a daily basis.

CheckAmplification:

View the last W/m^2 value and determine what range that value falls in, and then tells the PGA which amplification to use.

Read ReferenceChip:

Read the reference chips voltage through analog pin A1 and convert the value (measured between 0 and 1023) to volts according to:

$$Voltage = MeasuredValue * \left(\frac{MaxVoltage[3.3]}{1023} \right)$$

Formula 1: The equation used for converting the data recorded from the sensor or reference to a real “voltage.” The [3.3] is the max voltage we used.

Measure Gyroscopevalues:

Check the gyroscope and convert the values received into degrees between -180° and $+180^\circ$.

Take a DataPoint:

Read the analog pin A0 and leave it in the simplified (0 - 1023) form. This is done every 6 seconds.

Average:

Once ten data points have been collected, take the total of them, divide by the number of points taken to produce an average over a minute’s time.

Conversions:

Convert the average into a voltage using the aforementioned formula and then take this voltage and perform the following equation on it to give W/m^2 .

$$\frac{W}{m^2} = \frac{AverageVoltage * 1,000,000}{Calibrationfactor}$$

Formula 2: The equation to convert the voltage from the pyranometer to W/m^2 .

Calibration factor is given in $\mu V/W/m^2$.

This also requires some manipulation before posting to the SD Card or the web page to account for which amplification was used.

Write to SDCard:

Write the date, time, and W/m^2 value to a text file on the SD card named “DATALOG.”

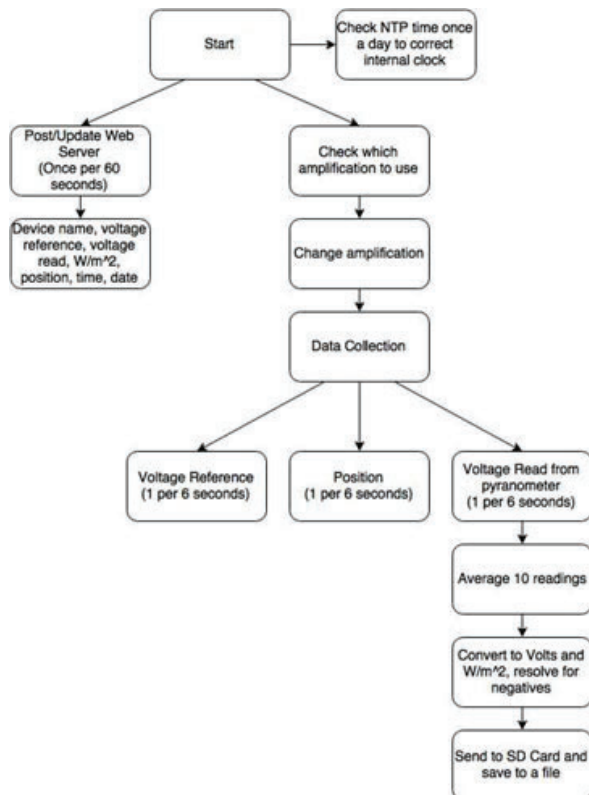


Figure 6: A flow diagram of how the device operates when in its loop stage.

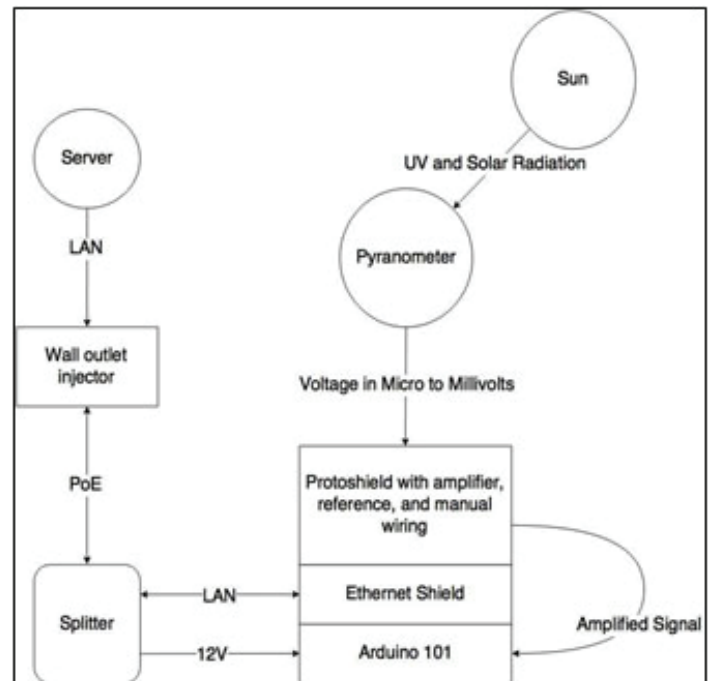


Figure 7: The more filled-in version of Figure 1 that shows all of the “sub-projects” that would come together to form the working device.

Present Webserver:

Present the device name, voltages, W/m^2 value, the gyroscope values, and the date and time to a web page. Then refresh this web page every 60 seconds.

Finalized Project

The final project now, following the same idea as in the beginning, would look like this:

IV. Results

The final product is a device that reads the voltage from the pyranometer, processes it by amplifying the signal and turning it into a usable W/m^2 , and presents it to a web page while also saving it to an SD card. It has undergone multiple field trials so far and has consistently shown above 94% (97% was highest) accu-

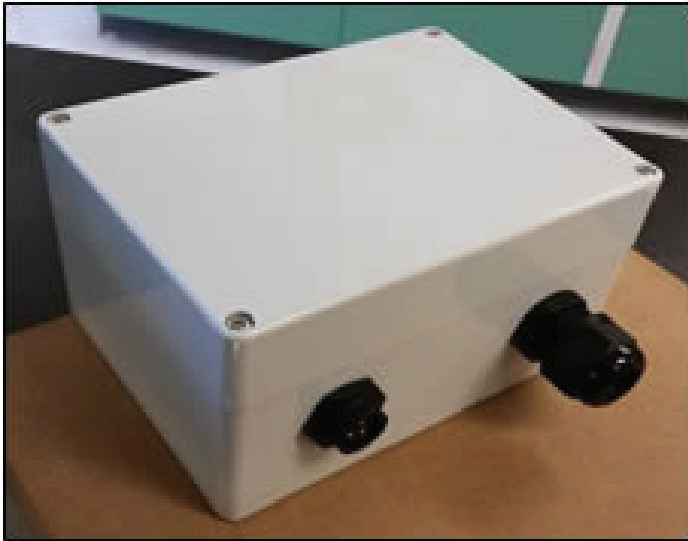


Figure 8: The finished device in its enclosure. The sensor port (left shorter plug) and the ethernet port (right longer plug).

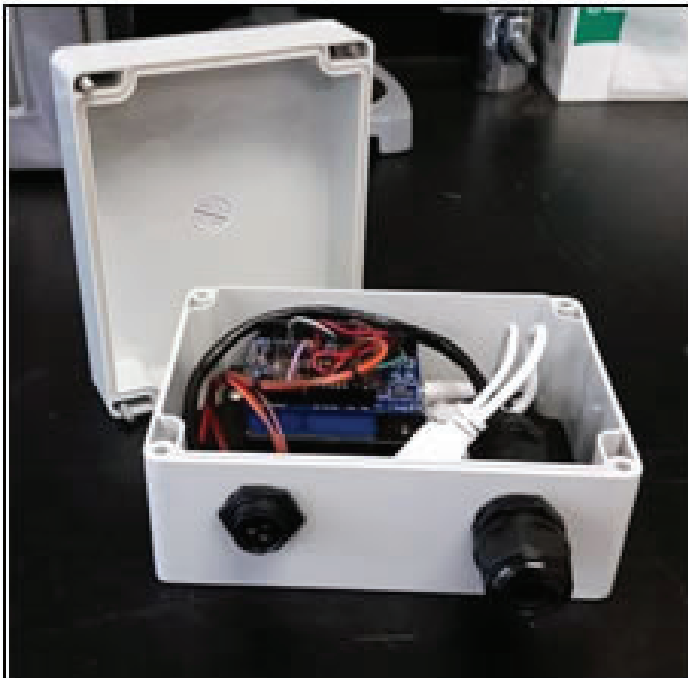


Figure 9: The finished device with its lid open showing the custom wiring and the PoE splitter (white).

racy compared to the research and professional grade dataloggers that are currently recording SP Lite2 data.

For now the device will be in an enclosure that is water and weather proof. This is a temporary housing and can be easily replaced by another, cheaper, alternative. Future enclosures should be able to be placed in any location and withstand the elements for an indefinite period of time.

Our goal was to keep this prototype under the \$200 range and operate as accurately as possible. For having a 97% (optimal) accuracy, this \$143.50 device has exceeded expectations. The cost breakdown is explained in the following table:

Cost of the Prototype in USD (\$)	
Arduino 101	\$30.00
W5500 Ethernet Shield	\$32.50
Protoshield	\$10.00
PGA204	\$18.14
RECOM RS3	\$17.84
Voltage Reference	\$7.50
Sensor Connector	\$7.89
Ethernet Connector	\$7.16
PoE Splitter	\$4.89
Wall Injector	\$7.58
Misc. Wire	\$0
Total	\$143.50

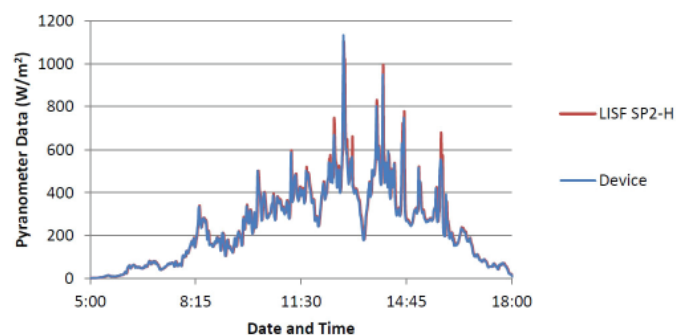
Table 2: Cost of the Prototype

The statistic of accuracy keeps being mentioned and this derived from trial runs where the device is left with a pyranometer for a number of days. The recorded and saved data is then compared to the professional and research grade dataloggers' data. An example of this from our July 29th to August 1st trial is the following image (Figure 10) showing the observable accuracy of the device:

This graph in particular shows part of an extremely cloudy day, which, as can be seen, produces extremely sporadic data that is very quickly moving up and down over short periods of time.

Even with this rapid shifting and changing, this device was able to match this with 96% accuracy. Another example of the accuracy of the device is from August 3rd when it was a clear and sunny day, except for one large cloud that changed the data from

Figure 10: Comparison of Pyranometer Data for 7-31-16



almost 1000 W/m² to under 200 W/m² (Figure 11).

Still, the device was almost entirely, sans the middle drop, matching to what the standard data is. This specific example had 94.5% accuracy to the professional and research grade data.

The device operates at a level of accuracy and is of a price that I would declare the goals set forth in this project accomplished.

V. Recommendations

My project was to design and produce an inexpensive, accurate, datalogger, which I feel I have completed. However, in finalizing the device, I have come to a few conclusions of how this could have been done in a different manner to be even cheaper, more accurate, and require almost entirely the same parts.

Primarily, bulk producing the device and using off-brand parts allows for much lower production cost. There are knock-off Arduino Uno's that can be bought for around \$3, which is a tenth of the cost of a genuine Arduino Uno. Every single part can be bought for less if buying in large quantities. This chart will explain how this device could be made for under \$100:

Optimized Cost in USD (\$)	
Seeeduino Uno	\$2.98
W5500 Ethernet Shield	\$24.65
Protoshield	\$8.96
PGA204	\$15.81
RECOM RS3	\$17.06
Voltage Reference	\$6.75
Sensor Connector	\$7.89
Ethernet Connector	\$7.16
PoE Splitter	\$1.64
Wall Injector	\$6.44
Misc. Wire/Solder	\$0
Total	\$99.34

Table 3: Optimized cost breakdown of the device.

Also, the Arduino 101 could do to be swapped for the Arduino Uno. Unfortunately, the 101 does not make use of the "Aref" pin which utilizes a precision voltage reference as the comparative "max voltage" instead of the built in 3.3V. The Uno uses this and can then correct the output of the ADC.

VI. Acknowledgements and Thanks

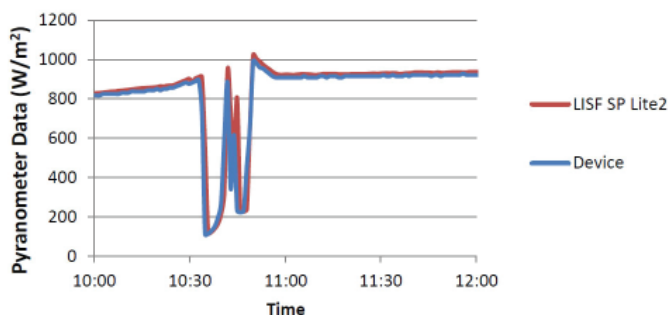
This project was made possible by the funding and support of the U.S. Department of Energy, Office of Educational Programs, and the Science Undergraduate Laboratory Internship Program.

I would also like to personally thank John Heiser and Andrew McMahon for their time and experience shared in helping me to complete my project.

VII. References

"How Solar Cells Work." *How Stuff Works*. Toothman, Jessica, and Scott Aldous. <http://science.howstuffworks.com/environmental/energy/solar-cell.htm>

Figure 11: Comparison of "Deep Drop" on 8-3-16



Reviving a demo synchrotron

Melissa De Jesus

Department of Mathematics/Computer Science, St. Joseph's College, Patchogue NY

Randy Smith

National Synchrotron Light Source II, Brookhaven National Laboratory, Upton NY

Abstract

The National Synchrotron Light Source II (NSLS-II) at Brookhaven National Laboratory (BNL) is a user facility that aids in scientific advances. Once a year, NSLS-II opens its doors to the public during BNL's Summer Sundays to explain some of these advances. Our task was to revive a model demonstration of a synchrotron to help illustrate how one works. To do this, we used a Raspberry Pi, its General Purpose Input Output (GPIO) pins, and a Hardware Attached to Top (HAT). We were able to reuse the existing control switches, and wired them to GPIO input pins. Because the wires were being reused, soldering had to be done to adjust the length of them after discovering which wires were connected. A python program manages what happens when a switch is flipped. The first switch uses the HAT to drive a DC motor that represents a vacuum pump extracting all air from inside the ring. The next switch turns on a relay switch that powers a string of lights symbolizing the electromagnets around the ring that steer the electrons. The third switch uses the HAT to drive a stepper motor that acts as the cluster of electrons circling around the ring. Lastly the X-ray switch, turns on a second relay for lights inside of a hutch to illustrate the light emitted. If the hutch door is opened while any of the switches are on, everything will stop because the hutch must remain shut whenever the beam is on. By using relay switches we insured that the demonstration accurately reflects how a synchrotron works, emphasizing the importance of the order of the steps. From this project, I learned how to integrate my programming skills and newly acquired soldering and circuitry skills to control hardware, along with learning the inner workings of a synchrotron.

I. Background

A. Synchrotron Light Source

A synchrotron light source is a particle accelerator that can be used to produce x-ray, ultraviolet, or infrared light. Producing these types of lights is beneficial to the science community because it allows us to see particles that may only be a few nanometers in size. The National Synchrotron Light Source (NSLS) II is currently the brightest synchrotron in the world, and scientist at Brookhaven National Lab (BNL) as well as outside users are able to use this powerful tool to help aid in their research.

Because a synchrotron can be a powerful tool in new research, it is interesting to understand how it works. The basic idea is that electrons are clustered together inside of a storage ring and accelerated causing them to reach high energy levels. When a magnetic field forces high energy electrons to change direction sharply they emit energy in the form of light. We first want the storage ring to be a vacuum to keep interference between electrons and air parti-

cles to a minimum. Then electromagnets are powered on around the storage ring to help guide the electrons. These magnets ensure that the electrons stay moving in a circular path. The radio frequency (RF) cavity gives energy back to the electrons and forces them to travel in a cluster even though their own electric charge repulsion would want electrons to spread apart from one another.

Before the electrons are inserted into the storage ring, they are accelerated in a smaller ring called a booster. Once the storage ring achieves a high vacuum and the electromagnets are powered on the boosted electrons can be injected into the storage ring. Electrons then circle around the ring and give off energy in the form of light. Because the electrons are losing energy there are RF cavities set up around the ring to reenergize the electrons. Tangent to the ring, are beam lines that extend into hutches. These hutches are where the experiments take place. At the end of the beam line is a shutter that remains shut when the hutch is not secured. If the shutter is shut scientists may enter there hutch as they please to setup their experiment. However, when they want the shutter to be opened to allow the x-ray light to enter into their hutch and onto their sample they must first secure the hutch. There are buttons set up around the hutch that must be pressed in a timely manner ensuring that the user has actually walked all the way around the hutch to be absolutely certain that no one is left inside of it. Once that is done, the hutch door can lock, and once it is locked the shutter can be opened. It is important that the hutch is secured and locked before the shutter is opened because the high intensity x-ray light can be extremely detrimental to the health of humans.

B. Jr. NSLS II

Because the process of a synchrotron can be hard to grasp for those without a scientific background, a tabletop demo of a synchrotron, that we call Jr. NSLS II, was built to help illustrate the inner workings of a synchrotron. The Jr. NSLS II would simplify the process of a synchrotron into four steps: turning the storage ring into a vacuum, turning on electromagnets, inserting electrons into the ring, and opening up a shutter. This display would then be used to show the general audience how a synchrotron works. More specifically the Jr. NSLS II was expected to be used at BNL's Summer Sunday, a day in July where BNL opens their doors to the public and allows them to visit NSLS II and learn about the facility.

Originally the Jr. NSLS II was controlled by a LabVIEW software and a National Instruments microcontroller that is capable of managing hardware as well as software. However, the LabVIEW based controller is an expensive piece of equipment and could be put to better use elsewhere. Still wanting to use the display during Summer Sunday, it was decided to rework the Jr. NSLS II so that it could run without expensive hardware/software. Still inside of the Jr. NSLS II, was a stepper motor that would move the "cluster of electrons," and a DC Motor with a propeller on it that could be

used as the “vacuum pump.” The control switches were still in our possession, so if we could somehow wire them to a microcontroller and use it to control the two motors the Jr. NSLS II would again be functional.

C. Raspberry Pi

We decided to use a Raspberry Pi to power the Jr. NSLS II. A Raspberry Pi is a microprocessor computer about the size of a credit card. It is a very inexpensive, costing around \$40. The Pi comes with a branch of Linux, called Raspbian, as its operating system, and thus uses common Linux commands in its command line to navigate through the computer. Though it is small, all the Raspberry Pi needs in order to serve as a full functioning computer is a monitor and keyboard to connect to. The Pi also supports Secure Shell sharing, which allows the command line prompt of the Raspberry Pi to be opened on another device wirelessly. This makes the Raspberry Pi useful for projects because the small computer can be mounted in one place and controlled somewhere else.

The Raspberry Pi has a set of 40 General Purpose Input Output (GPIO) Pins. These pins are used to either send or receive electrical signals. Amongst these pins, are some that are specifically 5V, 3.3V, or Ground Pins. Others have their own unique purpose. An example of this, is the SDA and SCL pins which are

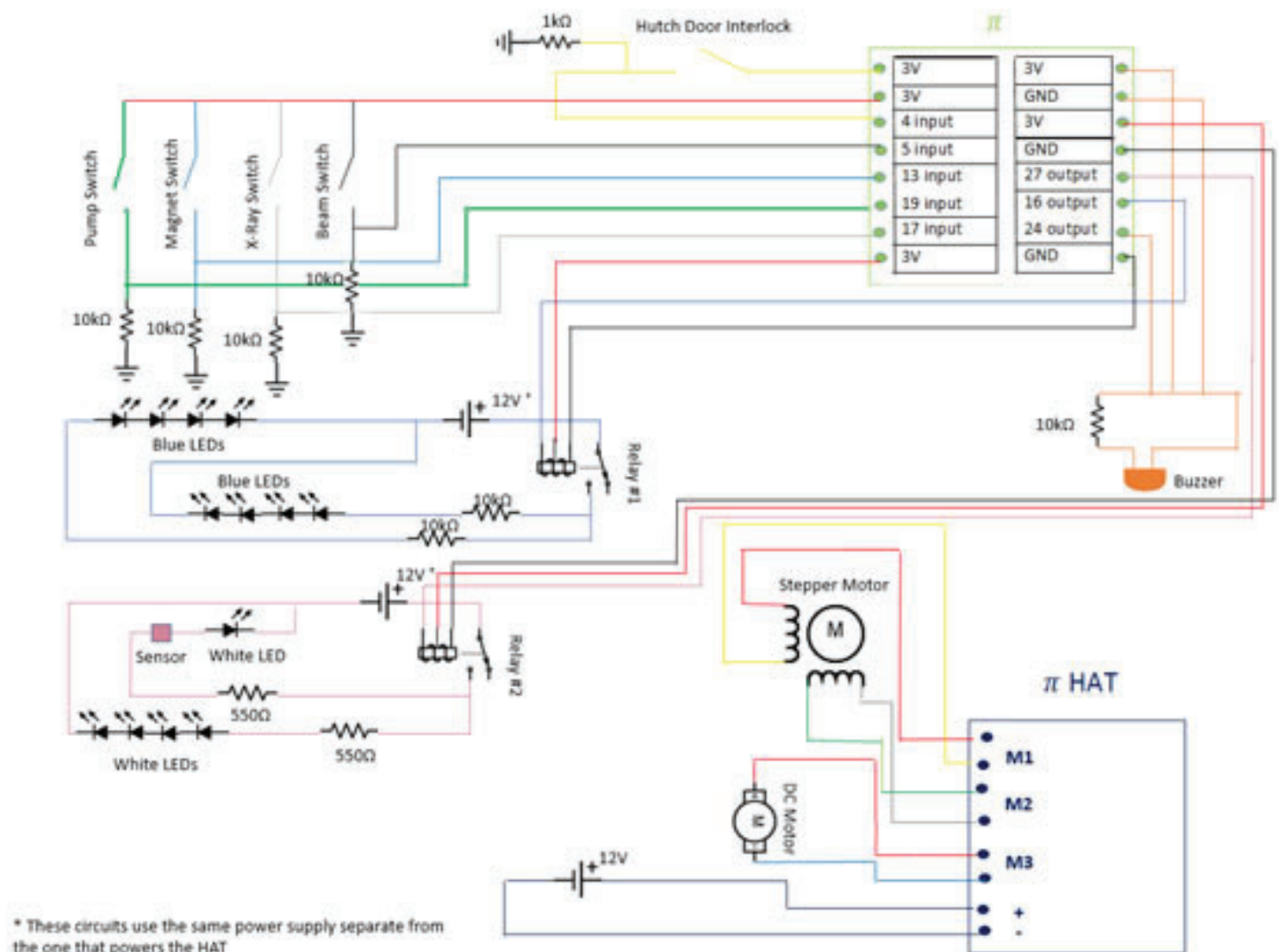
used to establish an Inter Integrated Circuit (I2C) connection. Most of these pins are without a specific purpose and can be set to either input or output depending on what they are needed for. Using GPIO pins, the Raspberry Pi is able to send power to lights, switches, and the like. For this reason a Raspberry Pi differs from an average computer because it is capable of controlling hardware as well as software.

Even though the Raspberry Pi has the ability to control hardware, the Pi only gives off a maximum of 5V and this is typically not enough to power larger types of hardware such as motors. In order to compensate for this Hardware Attached on Top or HATs are used to supply extra power, and are connected to the Raspberry Pi by plugging into their GPIO pins so that the Pi is still in control of the hardware. HATs may even be stacked so that a Raspberry Pi can control multiple different pieces of hardware at once, and all the pins that the HAT does not use may still be used to send or receive electrical signals the same way it would have if there was no HAT.

II. Methods

A. Design

The control panel that came with the Jr. NSLS II had a buzzer and four switches that read: “Pump,” “Magnets,” “Beam,” and



The circuit diagram of the Jr. NSLS II illustrates how the circuits were wired together. As is shown the circuit was very intricate because the Raspberry Pi was able to have so many different wires plug into it for various different reasons.

“X-Ray.” We were working towards reusing these switches, making sure something happened when each is flipped, and still have it accurately reflect the science of how a synchrotron would work. Because the DC Motor already had a propeller on it and was outside of the ring, it made sense to connect it to the pump switch and have it serve as our vacuum pump. The “fan” look to it helped show that air was coming out of the storage ring.

There was nothing already in the display that showed that the magnets were switched on. Because the magnets are an essential part of the synchrotron we wanted to have something that would visually show that the magnets were on instead of just the switch. We decided to solder together a string of blue LEDs and place them around the ring of the display. When the switch was turned on the lights would light up indicating that the magnets were on.

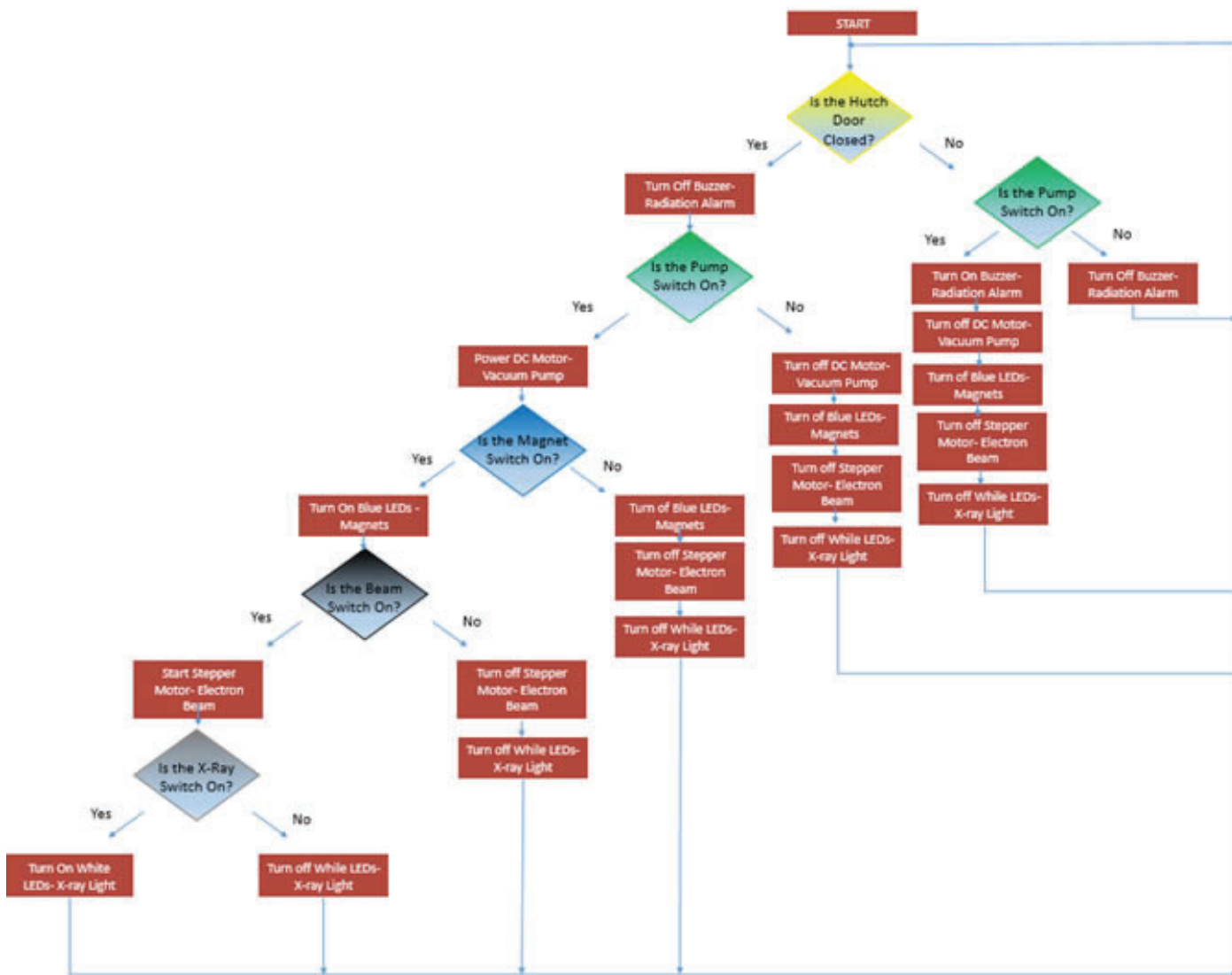
The stepper motor had already been mounted to the middle of the display. On top of it, a clear plastic arm was screwed on and at the end of it a green disk was epoxied onto it. This way when the top of the display was on only the green disk could be seen moving around the ring. This was our cluster of electrons, and would get wired with our Beam switch.

Lastly, our hutch needed some work. Originally, the “x-ray”

light came from the back of the hutch. Because this light should have been coming from the beam line, we 3D-printed a light holder with white LEDs and had it come from the side of the hutch so that it looked like an extension of the beam line. We also wanted to ensure that the light did not come on if the hutch door was opened, so we wired the hutch door interlock switch and the lights to the “X-Ray” switch. Wanting to incorporate a magnetic sensors that was already in the Jr. NSLS II, we placed an extra white LED inside of the light holder. This LED only went on when the cluster of electrons set off the sensor to show the light flashing into the hutch as the electrons went by. The buzzer would go off if x-ray switch was on while the hutch door was open to warn about exposure to radiation.

B. Procedure

In order to put our design plans into action we first needed to decipher which wires were connected. To do this we used a multi-meter’s continuity setting to check if wires were connected to each other. If they were, a beeping sound would go off to verify the connection. Once we knew which wires went to what we could wire the switches correctly to fit our needs.



The flow diagram for the python program that manages the Jr. NSLS II. Nested if statements inside of the code makes the program go through a checklist just like this to determine what is turned on and off depending on what else is on.

First the four switches were wired to GPIO input pins using a breadboard. Wires would be inserted into female headers on the HAT that connected to a specific GPIO pin. The other end of that wire was inserted into the breadboard. A wire that was from the switch associated with that pin was inserted in the same bus of the breadboard, this way if a switch was flipped the current would pass to the pin and the Pi would detect it. Output pins were wired the same way except instead of sharing a bus with a switch, they were connected to hardware that they were intended to power. The current would flow from the GPIO to either the LEDs, or the buzzer to turn it on.

A single line of python code was written per switch to set the pin. Once they were set up, a nested if statements in the python code determined when to send power to the different parts of the circuit. Then output pins were set to power on the lights for the magnets and the hutch. Instead of sending power to the lights directly power was sent to relay switches. This gave us more control over when the lights actually turned on. In addition to the switches and the lights, GPIO pins had to be set up for the buzzer and the hutch interlock door as well.

The two motors were wired into an Adafruit's DC and Stepper Motor HAT, instead of GPIO output pins because they needed more power in order to run. Adafruit wrote their own python library for their HAT. This library came equipped with easy to use functions that were used to start, stop, and set the speed of the DC and stepper motor. When either of the motor related switches were turned on, the signal would be received from an input pin, this would cause the code to enter an if statement, and within the if statement Adafruit's functions were invoked to get the motor to move. The lights and buzzer worked similarly, they waited for their signals, but instead of using a HAT, they received a signal from GPIO output pins which completed their circuit turning them on.

C. Logic

In order for a synchrotron to work the correct sequence of steps must be followed. That is to say that if the electrons were inserted into the ring before the magnets were on the electrons would not cluster together to form the bright light that is the benefit of a synchrotron light source.

This was reflected in the Jr. NSLS II by making sure that the previous switch was powered on before the next one could be. On startup, nothing is on. Once the Pump switch is on the DC Motor begins to turn. Then the Magnet switch can be turned on and the blue LEDs will light up. However, if the Pump switch is turned off, both the LEDs and the DC motor shut off. Likewise, if the X-ray switch is on but the Magnet switch is not, the only thing that will be on is the DC motor if that switch is on.

If the hutch door is opened, nothing will be powered on regardless of which switches are on. This emphasizes the importance of securing the hutch before we begin an experiment. To illustrate that this is done on purpose and not a software malfunction a buzzer goes off if the pump switch is on while the hutch door is open. We decided to use the Pump switch as our condition to sound the buzzer because only if the Pump switch is on can power be given to any part of the circuit.

D. Flow Diagram

The flow diagram for the python program that manages the Jr. NSLS II. Nested if statements inside of the code makes the

program go through a checklist just like this to determine what is turned on and off depending on what else is on.

III. Results

The Jr. NSLS II is now working as intended. It demonstrates the four basic steps of synchrotron and stresses that they must be done in the correct order for it to work. The Jr. NSLS II also uses a buzzer to signal an alarm when the hutch door is opened and the shutter is also opened to warn about the harmful radiation given off by the X-ray light. After the Jr. NSLS II was revived, it was used during BNL's Summer Sunday for the general public to see when they visited NSLS II. The audience enjoyed the display because it demonstrated the process that a synchrotron undergoes to produce X-ray light in such a way that was easy for people with little science background to understand.

The Jr. NSLS II is now not only working better and more accurately than it had before, but it is also much more cost efficient the way that it is running now. By using a Raspberry Pi the cost of running the Jr. NSLS II was significantly cut. On top of that, we were able to reuse enough of the previous design that no significant purchases needed to be made in order to revive the demo synchrotron.

IV. Discussion

With the Raspberry Pi still being so new to the world of technology there were many problems that arose along the way. The main issue that we had was overheating. The Raspberry Pi constantly monitors its own temperature and when it feels that it is getting too hot begins to slow itself down to avoid overheating. However, the Pi still managed to get up to 75°C. These high temperatures caused the Raspberry Pi to reboot itself which made the demonstration start to glitch. Trying to avoid this problem we put a heat sink on the Raspberry Pi to help cool it down. Though temperatures seemed to have dropped, the Raspberry Pi still reboots itself periodically, especially during BNL's Summer Sunday when the Python program that controlled the display had been on for hours at a time. However, even when the program is not running the Raspberry Pi still reboots itself after being on for a while. At this time, we are still looking into why this happens and how to fix it.

V. References

- Lady Ada. Adafruit DC and Stepper Motor HAT for Raspberry Pi. Adafruit.com. Lady Ada, 27 May 2016. Web. 2 Aug. 2016. <https://cdn-learn.adafruit.com/downloads/pdf/adafruit-dc-and-stepper-motor-hat-for-raspberry-pi.pdf>
- Monk, Simon. Programming the Raspberry Pi Getting Started with Python. 2nd ed. N.p.: McGraw Hill Education, 2016. Print.

VI. Acknowledgements

I would like to thank my mentor, Randy Smith, for taking me on this summer and for the knowledge and experience he has given me. I would also like to thank the Miller Research Group, especially Lisa Miller, Samantha Miller, and Adam Lowery, for all the support and guidance they have given me throughout the summer. This project was supported in part by the U.S. Department of Energy, Office of Science, and Office of Workforce Development for Teachers and Scientists (WDTS) under the Science Undergraduate Laboratory Internships Program (SULI).

Development of an electronic testing framework and procedures for protoDUNE

Amanda Depoian

Physics and Astronomy Department, Siena College, Loudonville, NY 12211

Matthew Worcester and Elizabeth Worcester

Physics Department, Brookhaven National Laboratory, Upton, NY 11973

The Deep Underground Neutrino Experiment (DUNE) at Fermi National Accelerator Laboratory (Fermilab) in Illinois will send neutrinos underground 800 miles to the Sanford Underground Research Facility (SURF) in South Dakota to measure the parameters governing neutrino oscillations and to search for differences between the oscillations of neutrinos and anti-neutrinos. The experiment is building a prototype detector (protoDUNE) at the European Organization for Nuclear Research (CERN). Front-end electronics containing Analog to Digital Converter (ADC) Application-specific integrated circuits (ASICs) are used inside the detectors to digitize and read out the signals from particle interactions. These 16-channel ADC ASICs need to be tested to make sure they are working correctly at room and cryogenic temperatures. My project was to help develop an automated testing procedure for these ASICs and create a new graphical user interface (GUI) to run it. The goal of the GUI is to validate these ASICs quickly without needing to execute a complicated series of tests by hand. I used Python with PyGTK and PyROOT to create the GUI. One GUI shows either the digitized waveform or the Fast Fourier Transform (FFT) of the waveform from a single channel of the ADC in real time. The second GUI au-

tomates the ADC ASIC validation process by collecting data over a range of DC input voltage, analyzing the data for all 16 channels, and reporting the outcome of the test in a simple format. Once the scripts are done, the GUI reports back to the user if the ASIC passed or failed the predetermined cuts. Through this project I have been able improve my Python skills, learn about electronics and the lab equipment, and I am now familiar with the process of creating a GUI.

I. Introduction

A. Neutrinos

Neutrinos are particles in the lepton family. There are three different flavors of neutrinos: electron neutrino, muon neutrino, and tau neutrino, as seen in Figure 1. The neutrino was first theorized by Wolfgang Pauli in 1930 to explain the violation of energy and momentum conservation in beta decays. According to the initial Standard Model, neutrinos have no charge or mass. However, recent experimental observations have shown with high confidence that neutrinos have a small non-zero mass.

Each neutrino flavor is superposition of different neutrino mass eigenstates, as shown in Figure 2.²

Neutrinos oscillate between flavors as they travel through space. Neutrino oscillations are a consequence of neutrino flavor mixing and non-zero neutrino masses.³ The matrix governing neutrino oscillations is

$$\begin{pmatrix} \nu_e \\ \nu_\mu \\ \nu_\tau \end{pmatrix} = \underbrace{\begin{pmatrix} U_{e1} & U_{e2} & U_{e3} \\ U_{\mu1} & U_{\mu2} & U_{\mu3} \\ U_{\tau1} & U_{\tau2} & U_{\tau3} \end{pmatrix}}_{U_{PMNS}} \begin{pmatrix} \nu_1 \\ \nu_2 \\ \nu_3 \end{pmatrix}$$

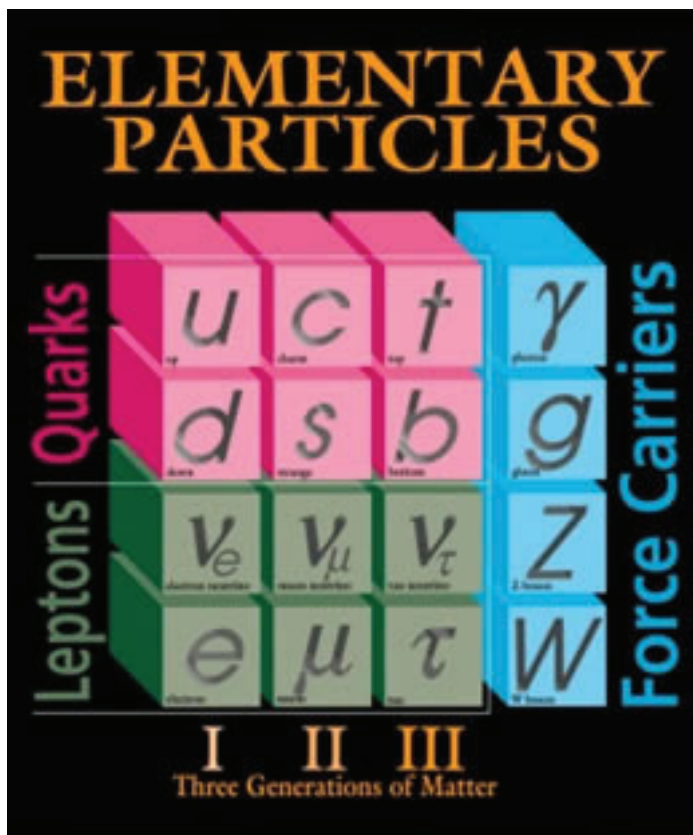


Figure 1.

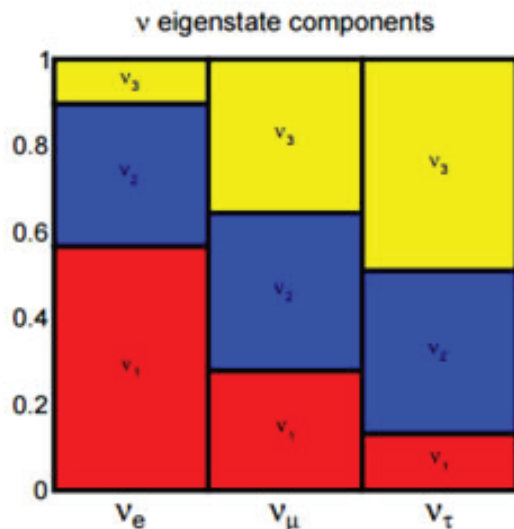


Figure 2: Mass eigenstates for the three different neutrino flavors

where U_{PMNS} is:

$$U_{PMNS} = \underbrace{\begin{pmatrix} 1 & 0 & 0 \\ 0 & c_{23} & s_{23} \\ 0 & -s_{23} & c_{23} \end{pmatrix}}_I \underbrace{\begin{pmatrix} c_{13} & 0 & e^{i\delta_{CP}} s_{13} \\ 0 & 1 & 0 \\ -e^{-i\delta_{CP}} s_{13} & 0 & c_{13} \end{pmatrix}}_{II} \underbrace{\begin{pmatrix} c_{12} & s_{12} & 0 \\ -s_{12} & c_{12} & 0 \\ 0 & 0 & 1 \end{pmatrix}}_{III}$$

Previous experiments have found $\theta_{12} \approx 34^\circ$, $\theta_{23} \approx 38^\circ$, and $\theta_{13} \approx 9^\circ$. However, the charge-parity (CP) violating phase, δ_{CP} , is unknown.²

Another open question about neutrinos is the mass hierarchy. It is still undetermined if the hierarchy is normal or inverted, as shown in Figure 3.

B. DUNE:

The Deep Underground Neutrino Experiment (DUNE) at Fermi National Accelerator Laboratory (Fermilab) in Illinois will send neutrinos underground 1,300 kilometers to the Sanford Underground Research Facility (SURF) in South Dakota to measure the parameters governing neutrino oscillations, to search for differences between the oscillations of neutrinos and antineutrinos, and to find evidence of CP violation in leptons.⁴

DUNE will consist of three main components: the beam line,

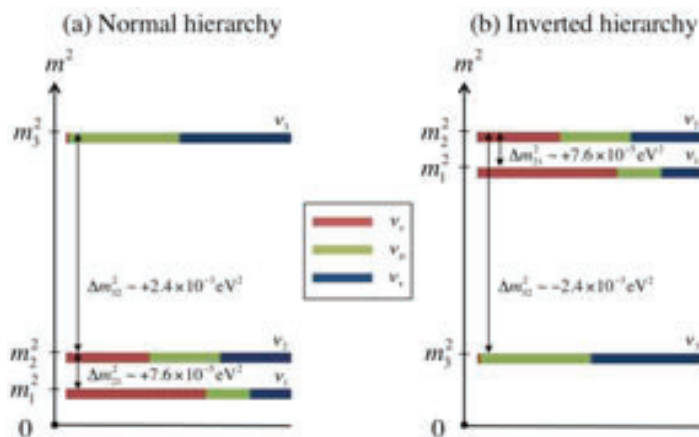


Figure 3: Normal and Inverted neutrino mass hierarchy.

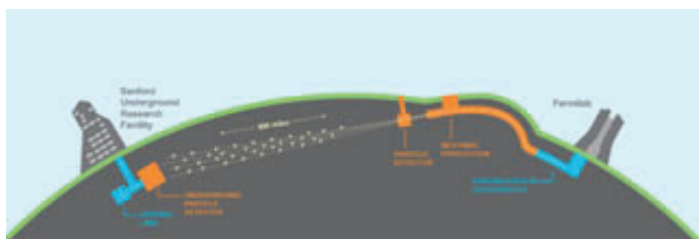


Figure 4: The dual-site long-baseline facility

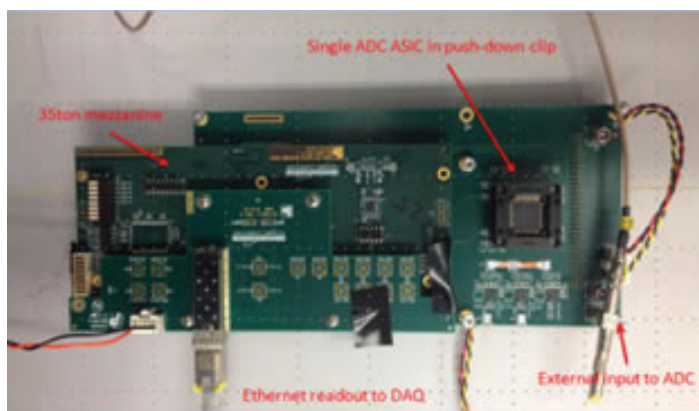


Figure 5: ADC test board

the near detector, and the far detector. The beam line at Fermilab will accelerate protons into a sheet of graphite. This collision will produce pions and kaons, which are then focused into a decay horn. This horn has a magnetic field that will focus the particles into a beam as they travel. As the pions and kaons travel in the horn, they decay into muons and muon neutrinos. The muons will be stopped, but the muon neutrinos will pass through as a beam of neutrinos. The energy of these neutrinos is 0.5 – 5 GeV.

The near detector will be located at Fermilab, 500 meters downstream of the beam. The near detector will be used to determine the unoscillated flux of . The near detector includes ionization chambers, Cherenkov detectors, and electromagnetic calorimeters, which are used to detect neutrinos.

The far detector will be located at SURF. It will consist of four modules, which will be used to measure the oscillated flux of neutrinos, make measurements on proton decay sensitivity, and make supernova observations. The detector will consist of Liquid Argon Time-Projection Chambers (LArTPC). There will be more than 10,000 metric tons of Liquid Argon (LAr) in each module. The LAr will be cooled to 87 K or -303 °F. LArTPC's are used to detect charged particles. In a LArTPC, there is an anode and a cathode that creates an electric field within the LAr. When a charged particle enters the detector, it ionizes the argon atoms and the loose electrons drift until they are collected within the wires. Front-end electronics are connected to the wires to readout the data.²

DUNE is building a prototype detector (protoDUNE) at the European Organization for Nuclear Research (CERN) that is set to begin collecting data in 2018. The reason behind the building of protoDUNE is to make sure that this size detector can be built, make sure all the components work correctly and to see how the detector reacts to different particles at different energies. Front-end electronics containing Analog to Digital Converter (ADC) Application-specific Integrated Circuits (ASICs) are used inside the detector to digitize and read out the signals from particle interactions. These 16 channel ADC ASICs need to be tested to make sure they are working correctly at room and cryogenic temperatures.

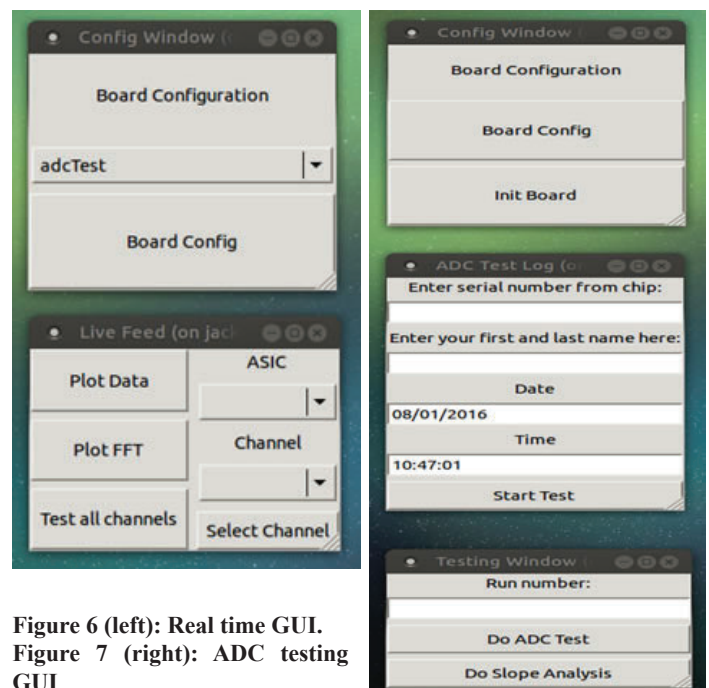


Figure 6 (left): Real time GUI. Figure 7 (right): ADC testing GUI

II. Methods

My project was to help develop an automated testing procedure for the ASICs and create a new graphical user interface (GUI) to run it. The goal of the GUI is to validate these ASICs quickly without needing to execute a complicated series of tests by hand.

I used Python, with PyGTK and PyROOT packages, to create a GUI that would automate the testing process of electronic ASICs, which will be used for ProtoDUNE. All of the code used for the testing process is hosted on Github. This allows for easy collaboration between different members of the research group.

One GUI I created shows either the digitized waveform or the Fast Fourier Transform (FFT) of the waveform from a single channel of the ADC in real time. The tester can change the channel they are looking at from a drop down menu found in the GUI. This GUI works with single ADC ASICs on the test board shown in Figure 5, or on a motherboard containing eight ADC ASICs with 128 channels of digitized readout.

The second GUI is specific to the ADC test setup. This GUI automates the ASIC validation process by collecting data over a range of DC input voltages, analyzing the data for all 16 channels, and reporting the outcome of the test in a simple format.

III. Results

The analysis script that tests the ASICs pulses through different DC input voltages, which are then sent to the ADC from a function generator. After the run is completed, the ADC value versus Voltage for each channel is plotted. The ADC response is expected to be linear as a function of voltage, so a linear fit is done, as shown in Figure 8, and the slope and χ^2 of the fit are extracted. If the slope and χ^2 for each channel is within the predetermined cuts, the ASIC is said to be functioning properly and we can classify it as a good ASIC.

To clearly report this information back to the tester, the GUI window will turn green and print out "This ASIC is good", as seen in Figure 9, or will turn red and print out "This ASIC is bad". Both return the mean slope of the ASIC in the window as well.

Additionally if the ASIC is classified as bad, the GUI will print the slope of the ADC value versus Voltage plot for each channel so that the tester can see which channels are out of range.

To determine the acceptance cuts for the ASIC, the slope and χ^2 for all the channels are plotted with data from multiple runs of several ASICs. We collected data for one ASIC ten different times and for another ASIC seven different times. The range of slope and χ^2 values observed in this data was used to make a preliminary definition of the cuts.

IV. Conclusions

A series of scripts to test ADC ASIC performance were developed and a simple GUI to execute them was created. To run the test it takes 8 minutes. There are 2000 ADC ASICs to test for the final detector electronics. If two testers work 8 hours a day, it will take 17 days to validate all the ASICs. The goal is to instrument protoDUNE with all 15,360 digital channels within the linearity parameters tested by this procedure.

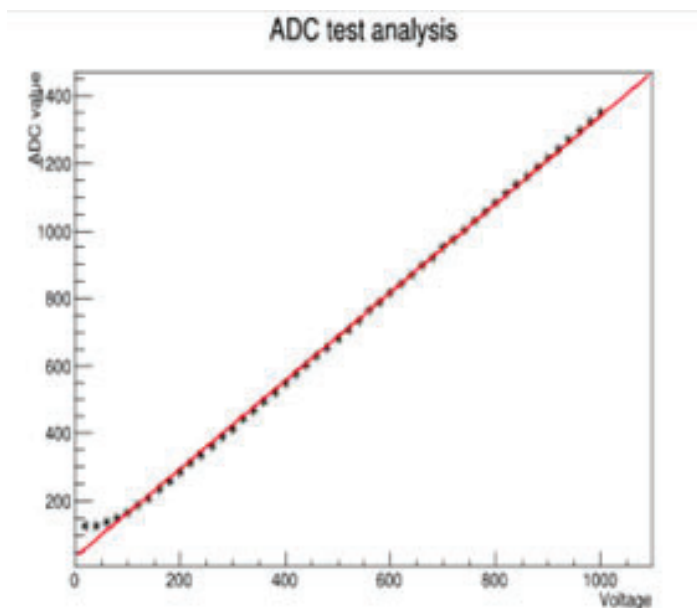


Figure 8: Plot of ADC values versus Voltage for one channel.



Figure 9: Output after analysis is done for ASIC.

V. References

¹<http://hyperphysics.phy-astr.gsu.edu/hbase/particles/neutrino.html>

² LBNE Collaboration, “The Long-Baseline Neutrino Experiment: Exploring Fundamental Symmetries of the Universe,” (2013), arXiv:1307.7335v3 [hep-ex].

³ Strassler, Matt. “Neutrino Types and Neutrino Oscillations.” *Of Particular Significance*. N.p., 05 Oct. 2011. Web. 04 Aug. 2016.

⁴<http://www.dunescience.org/>

VI. Acknowledgments

This project was supported in part by the U.S. Department of Energy, Office of Science, Office of Workforce Development for Teachers and Scientists (WDTS) under the Science Undergraduate Laboratory Internships Program (SULI).

Optimization of the LBNF/DUNE beamline for tau neutrinos

Michael Dolce

Department of Physics, University at Albany, Albany, NY 12222

Mary Bishai

Department of Physics, Brookhaven National Laboratory, Upton, NY 11973

Abstract

The Long Baseline Neutrino Facility (LBNF) and the Deep Underground Neutrino Experiment (DUNE) will create and detect mysterious particles known as neutrinos. Brookhaven National Laboratory (BNL) is a leading collaborator in the LBNF and DUNE projects, where physicists have simulated data to optimize the neutrino beam for detecting the transformation of the muon neutrinos into electron neutrinos. Our study focuses on the optimization of the tau neutrino appearance signal at the far detector in DUNE. To do this, magnetic focusing elements known as horns in the LBNF neutrino beamline were moved, the electrical current in the horns, and the size and location of the proton beam target were changed. We have concluded with four different optimal designs generating roughly 800 tau neutrino events with these ideal configurations. These four different compositions will allow for flexibility in the construction of the experiment because the optimized design for muon and electron neutrino signal appearance must be incorporated as well. With four optimized designs of the beamline, LBNF and DUNE will be able to understand the quantum mechanical nature of neutrino oscillations and the flavor changes of neutrinos when the experiment begins and data is collected.

I. Introduction

A. Neutrino Oscillation

The field of neutrino physics has become arguably the most popular subfield in particle physics in recent years. Its growth in popularity is largely due to the little understanding we have of neutrinos. For example, it was believed, according to the Standard Model, that neutrinos are massless particles [1]. However, in 1998 the Super-Kamiokande experiment revealed that neutrinos can oscillate, or change flavors, which implies that neutrinos must have mass [2]. The fact that neutrinos can oscillate between flavors is one of the most interesting and little understood characteristics of neutrinos. The three known flavors of neutrinos are the electron, muon, and tau neutrinos, where each type corresponds to a lepton in the Standard Model. As neutrinos travel they can change from one flavor to another, so that when it comes to measuring them, the probability that a different flavor is measured compared to the original flavor is much larger than it would be to measure the original flavor. This oscillation of flavors is due to the fact that the neutrino is a superposition of three different mass eigenstates. These mass differences cause the phases of the quantum mechanical mass states to propagate at a different rate. The result is a changing mixture of the neutrino's mass as it travels through space and thus oscillates. The probabilities for the neutrinos to oscillate are given by the following equations

$$P(\nu_\mu \rightarrow \nu_\tau) \cong \sin^2(2\theta_{23})\sin^2(1.27\Delta m_{32}^2 \frac{L}{E}) \quad (1)$$

$$P(\nu_\mu \rightarrow \nu_e) \cong \sin^2 2\theta_{13}T_1 - \alpha \sin \theta_{13}T_2 + \alpha \sin \theta_{13}T_3 + \alpha^2 T_4 \quad (2)$$

$$T_1 = \sin^2 2\theta_{23} \frac{\sin^2[1-x]\Delta}{(1-x^2)} \quad (3)$$

$$T_2 = \sin \delta \sin 2\theta_{12} \sin 2\theta_{23} \sin \Delta \frac{\sin(\Delta x)}{(x)} \frac{\sin[1-x]\Delta}{(1-x)} \quad (4)$$

$$T_3 = \cos \delta \sin 2\theta_{12} \sin 2\theta_{23} \cos \Delta \frac{\sin(\Delta x)}{(x)} \frac{\sin[1-x]\Delta}{(1-x)} \quad (5)$$

$$T_4 = \cos^2 \theta_{23} \sin^2 \theta_{12} \cos \Delta \frac{\sin^2(\Delta x)}{(x^2)} \quad (6)$$

with $\alpha \equiv \Delta m_{21}^2 / \Delta m_{31}^2$, $\Delta = \Delta m_{31}^2 L / 4E$, $x = 2\sqrt{2}G_F N_E E / \Delta m_{31}^2$, and where $\sin^2(\theta_{ij})$ are the mixing angles, $|\Delta m_{ij}^2| = |m_i^2 - m_j^2|$ are the absolute values of the squared difference of the neutrino mass states, L is the distance traveled by the neutrino, E is the neutrino's energy, and G_F is the Fermi coupling constant [1].

The DUNE experiment is the next generation of neutrino physics. It is an international collaboration created to understand the quantum mechanical nature of neutrino oscillations. Its primary objectives are to make precision measurements that govern $\nu_\mu \rightarrow \nu_e$ oscillations such as the mixing angle θ_{13} , measure δ_{CP} , the charge-parity (CP) violating phase, and understand the mass hierarchy by determining if the mass states are ordered by normal hierarchy (NH) $m_1 < m_2 < m_3$ or inverted hierarchy (IH) $m_3 < m_1 < m_2$. DUNE will also seek to make precision measurements of the mixing angle θ_{23} and the value of $|\Delta m_{23}^2|$ in $\nu_\mu \rightarrow \nu_{e\mu}$ oscillations [3].

B. LBNF/DUNE

A 1.2 MW, 120 GeV proton beam known as the Main Injector located at Fermilab in Batavia, Illinois, will direct 120 GeV protons down underground by 5.8° towards a fixed carbon target where mesons are produced such as positively and negatively charged pions and kaons. These scattered secondary particles are redirected by two magnetic focusing horns located several meters downstream of the target. The secondary particles then travel through a helium-filled decay pipe where they decay into neutrinos and pass through an absorber hall and continue towards the near detector 574 m downstream of the fixed target [4]. The absorber hall absorbs any secondary particles, like muons, that have not decayed into neutrinos so as to not fake neutrino interactions at the near detector. A longitudinal layout of the Near Site at Fermilab can be seen in Figure 1.

Once the neutrinos pass through the near detector hall they continue forward through the earth where 1,300 km later they reach the far detector site, 4,850-ft underground, housed in the Sanford Underground Research Facility (SURF) in Lead, South Dakota. The far detector at its full scope will consist of a 40-kiloton liquid argon detector time-projection chamber (TPC) where 34-kilotons will be used as the fiducial mass to detect neutrino in-

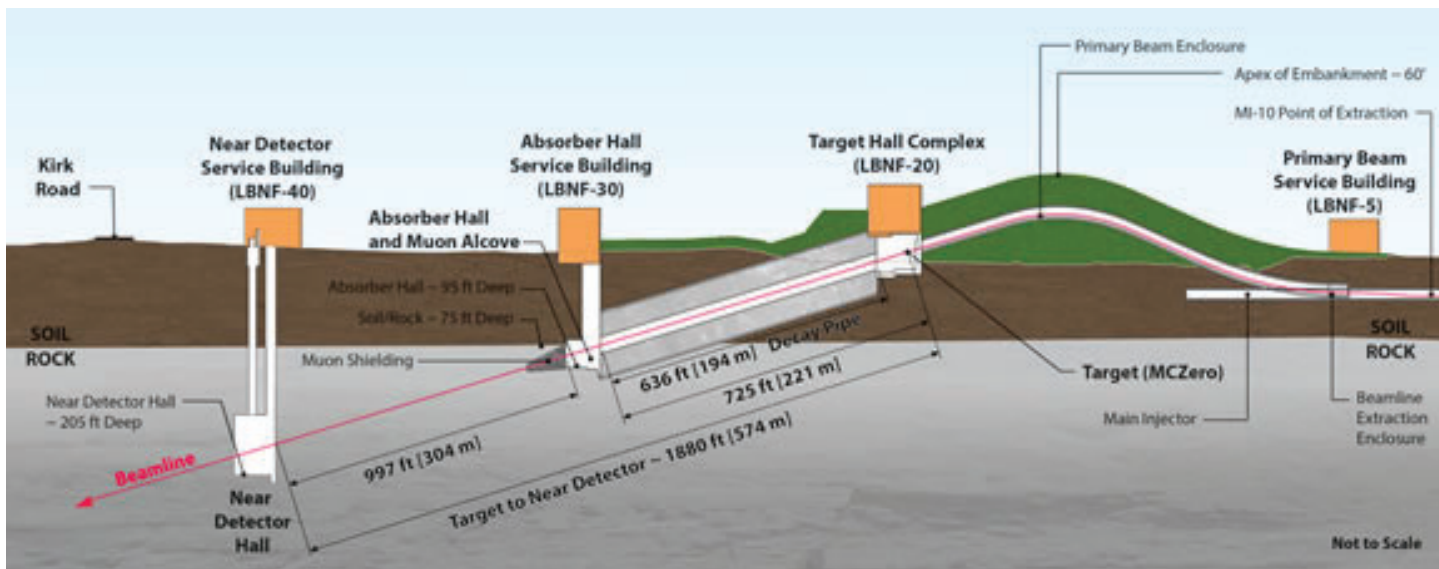


FIGURE 1. The longitudinal perspective of the LBNF design displays the surface buildings and underground facilities of the Near Site. Once the secondary particles travel through the target hall, they decay into neutrinos in the 194 m long decay pipe where the absorber hall at the end of the decay pipe absorbs any un-decayed particles. The near detector hall, 304 m after the absorber hall, then records the neutrinos passing through it and is ultimately used to compare the with the far detector for neutrino appearance and disappearance [4].

teractions within the nucleus of the argon atoms [4]. The focus of our research was on the configuration of the target hall in Figure 2. The objective was to optimize the components of the target hall to produce the largest amount of tau neutrino interaction events at the far detector.

The DUNE experiment will mostly focus on the appearance rate of the muon neutrino to the electron neutrino and of the disappearance rate of the muon neutrino. In addition, an understanding of how the muon neutrino will oscillate into the tau neutrino is also a priority as this will unlock a new level of understanding of the quantum mechanical nature of neutrino oscillations and the flavor changes of neutrinos. The primary objective of this study, through simulating the experiment, was to quantify the tau neutrino interaction events that would occur under various target design and magnetic horn configurations and to optimize the configurations for the most tau neutrino events.

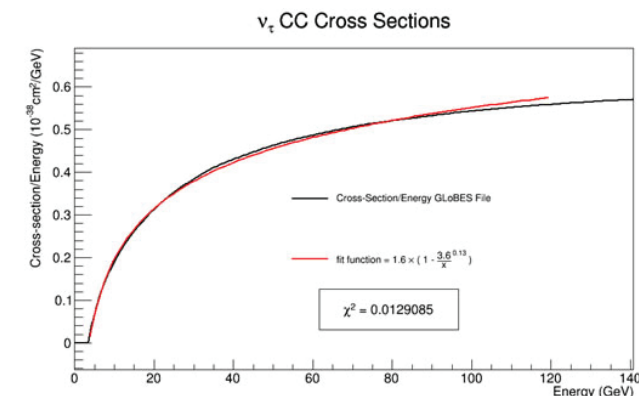


FIGURE 2. The neutrino cross section divided by its energy is plotted above. The cross sections were read in from a data file and plotted in ROOT. We then fitted a function to the cross section curve so the data could be parameterized. The χ^2 value achieved with the fit function was accurate, and then fit function was coded into the script to simulate the experiment.

II. Experimental Design and Procedure

A. Simulation

In order to optimize the configurations for the tau neutrino appearance signal, the probability function (1) was implemented into our simulation script. This would tell us the probability a muon neutrino would oscillate into a tau neutrino across the range of neutrino energies, 0-20 GeV, which would be observed at the far detector in South Dakota. However, when muon neutrinos oscillate into tau neutrinos, about 5% of them will oscillate to electron neutrinos (2). This 5% was neglected, and it was approximated that all muon neutrinos would oscillate into tau neutrinos. The study was carried out under the approximation of normal hierarchy where $\sin^2(2\theta_{23}) = 0.999$ and $\Delta m_{32}^2 = 2.44e-03 \text{ eV}^2$. Because the first and second mass states are similar in mass compared to the third, the approximation used was $\Delta m_{32}^2 = \Delta m_{31}^2 = 2.44e-03 \text{ eV}^2$. The probability of the neutrinos interacting with the liquid argon, or cross section, was then incorporated into the simulation. To do this, a function was fitted to the tau neutrino charged-current total cross section calculation. The equation of the function was parameterized and coded into the simulation. This plot can be

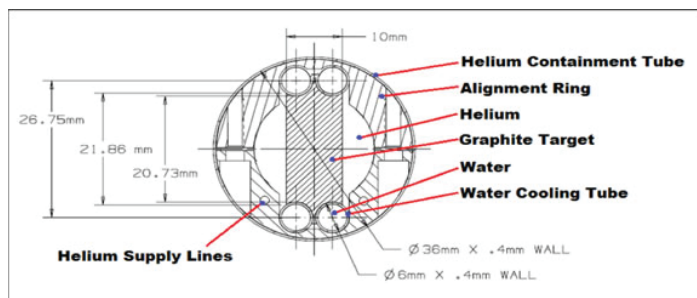


FIGURE 3. The image above is the cross section of the LBNF style target. The graphite target sits inside a helium containment tube. The significant difference of the LBNF style target to the NuMI style target is the width, where the LBNF style is almost twice as wide. In the true construction of the target, it is divided into multiple segments (47 segments for the 1 m target), where each segments is separated by a fin 0.2 mm long to reduce the density of the target to allow for pions and other secondary particles to exit the target easily [4].

seen below in Figure 2. Then by multiplying the cross section, the flux of the muon neutrino, and the probability a muon neutrino will oscillate into a tau neutrino together, the result calculated is the number of tau neutrino interaction events at the far detector.

To simulate the data, an extension of GEANT4, software created by CERN to simulate particles passing through matter, called G4LBNE, was used [5][6]. The software was used to simulate 900,000 protons on target (POT) for each configuration. Simulating the events requires editing an input file to make modifications to the configuration of the beamline and then submitting these jobs in parallel to a computing farm. Once the jobs are completed, the analysis on the tau neutrino events can be done. The results are then scaled up to 1×10^{21} POT for a year of proton beam in a 40-kiloton liquid argon detector. Therefore our results of the number tau neutrino events are in reference to a year of the experiment running at its largest far detector size.

B. Targetry

There was a caveat to these optimizations. There needed to be flexibility in the fixed target design due to engineering constraints and physics purposes. The target is expected to be made of graphite, which was the material used in this study, but in terms of the construction, engineers are not certain how large the fixed target can be in order to withstand a 1.2 MW beam [7]. While for physics, these optimized designs are focused only on the tau neutrino appearance signal, so a variety of target styles would allow for a better configuration of the muon and electron neutrinos appearances at the far detector in future work. As a result, four different target dimensions were examined. The two styles were the Neutrinos at the Main Injector (NuMI), from the Main Injector Neutrino Oscillation Search (MINOS) experiment, and the LBNF style target. The NuMI style target is 6.4 mm wide and 20.0 mm in height and two different lengths of 1 m and 2 m with a beam size of 1.5 mm in width and height of a Gaussian distribution. The LBNF style target is 10.0 mm wide, and 20.73 mm in height with the same target lengths of 1 m and 2 m with a 1.7 mm beam size Gaussian distribution. A visual representation of the LBNF style target can be seen in Figure 3.

However, the target is more complicated than a 1 m or 2 m long, single block. It is based off of the NuMI target design; it is actually segmented into short rectangular pieces oriented vertically. There are a total of 47 segments, each 2 cm long oriented to the beam, 10 mm in width, and 20.73 mm in height, which result

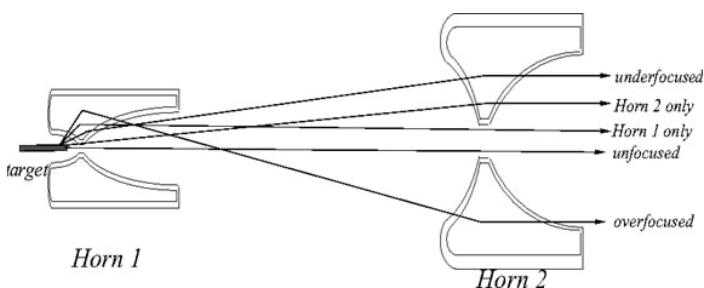


FIGURE 4. Above is a basic sketch of the trajectories of secondary particles once they exit the target. Depending on the angle at which a particle leaves the target, the magnetic horns will refocus that particle in different ways as seen above. The magnetic field of the horns work so that in the center of the necks of both horns the magnetic field is 0 T. Therefore, the a particle that is already traveling in the direction of the proton beam will continue traveling undisturbed through both horns to the near and far detectors [8].

in a total target length of 95 cm (1 meter LBNF target design) [4]. Splitting the target into segments reduces the density of the target, which allows for secondary particles like pions to exit easier and not re-interact with the nucleons in the target [7]. Due to the complexity in coding and simulating such an intricate design, the approximation that the target was a single, long block was used throughout the study. Therefore, in all of the simulations, regardless of the NuMI or LBNF target style, or the target length (1 m or 2 m), a single block for the target was used instead of the segmented design.

The location of the target was also a parameter of our choosing. The original distance of the target is located 1.5 m in front of the face of Horn 1. We had a limited amount of space to push the target upstream. The distances examined were 1.5 m, 2.0 m and 2.85 m. These locations were all tested in conjunction with the two different target dimensions and lengths to determine an optimized configuration for a 1 m and 2 m target length of the NuMI and LBNF styles.

C. Focusing Horns

The magnetic horn design consists of two NuMI style, parabolic shaped profiles: one facing upstream and one facing downstream. A narrow neck separates these parabolic shapes in between to create a focusing horn. Two of these magnetic focusing horns act as optical focusing lenses that redirect secondary particles back towards the beam axis; 230 kA of equal current flows through both horns to refocus the charged pions and kaons. Therefore, a larger current will redirect more secondary particles as it takes a stronger magnetic field to redirect more energetic particles. A sketch of the path of differently focused secondary particles traveling through the two horns can be seen in Figure 4 [8].

Aside from the current, the location of the second horn can be adjusted. The location of the first horn is fixed at 0 m while the second horn was moved further downstream in 1 m increments. The original location of the second horn was located 6 m away from the face of Horn 1 and could be placed as far as 17 m meters away from the face of Horn 1.

All parameters of our study were located in the target hall (Figure 5) of the LBNF (Figure 1). Figure 5 provides a visual description of the order of events in the target hall. The beam travels from right to left; the proton beam first comes in contact with

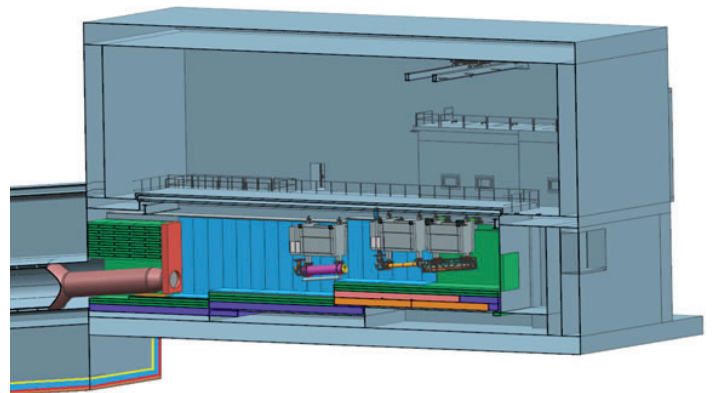


FIGURE 5. In this image, beam travels from right to left; the proton beam first comes in contact with the target (right) and creates secondary particles, then the secondary particles are refocused by the horns (middle & left), and then travel through the decay pipe (far left) with a snout facing upstream towards the horns and target [4].

the target (right) and creates secondary particles, the secondary particles are refocused by the horns (middle & left), and then travel through the decay pipe (far left) with a snout facing upstream towards the horns and target. The secondary particles then decay into neutrinos and finally pass through the near detector and ultimately the far detector 1,300 km later in South Dakota.

III. Results

Two parameters of the optimization were quickly understood. Moving Horn 2 further downstream produced significantly more tau neutrino events. Thus all four of the optimized designs are at the furthest distance, 17 m, from the upstream face of Horn 1. Therefore, we tested most of the configurations at the Horn 2's original location, 6 m, and distances at the far end of the hall, mostly 14 m and beyond. This can be seen on the NuMI and LBNF events plots to emphasize the increase in events at farther distances. The second parameter was the ideal electrical current running through the horns; at any distance, the maximum current available, 230 kA, would produce a larger quantity of events than a lesser current of 200 kA. This can be explained because a larger current creates a stronger magnetic field, which allows the mag-

netic horns to bend more massive secondary particles and redirects softer secondary particles that would otherwise be traveling in a nearly perpendicular direction from the beam axis, while the farther distance of Horn 2 allows for more secondary particles to focus itself along the beam axis before it passes through the near detector. Thus, the plots of the events of the NuMI and LBNF style targets only include 230 kA in Figures 6 and 7.

For both target designs of 1 m and 2 m, the optimal target location is 2.0 m in front of Horn 1. The results yielded the most tau neutrino interaction events in the NuMI style target with a target length of 2 m producing 827 events. The next best design is the NuMI style 1 m target length creating 809 events. For the LBNF target dimensions, the events were slightly less producing 764 and 721 events for the 1 m and 2 m target lengths respectively. Thus revealing 230 kA of current, with the horns 17 m away, a target 2.0 m away from Horn 1, and the NuMI style target 2 m in length would be the ideal configuration for tau neutrino interactions at the far detector. The four optimized designs were plotted together in Figure 8.

The muon neutrino flux plays a significant role in the tau neutrino appearance. As mentioned, tau neutrinos originate from an oscillating muon neutrino; therefore a large muon neutrino flux is advantageous for tau neutrino appearance. The muon neutrino flux plot reveals the 2 m targets of both styles produces a larger flux at lower energies, which explains the peaks of the tau neutrino events at lower neutrino energies for the 2 m targets. However, the 1 m targets have a slightly larger, but consistently higher muon neutrino flux at 8 GeV and above. This effect can be seen in the tau neutrino events plot where the peaks for the 1 m targets are at around 9 GeV, and have consistently more events at increasing neutrino energies (Figures 9 & 10).

IV. Conclusion

To obtain a maximal amount of tau neutrino events, the current should be at its maximum of 230kA, and the second magnetic focusing horn should be placed 17 meters from Horn 1, as far downstream as possible. With these two configurations, four different target dimensions were tested to allow for flexibility in construction of the target hall. We found the 1 m NuMI style target (809 events) offers about a 5% increase than the 1 m LBNF style target (764 events) while the 2 m NuMI target (827 events) offers about 13% more events than the 2 m LBNF target (721 events),

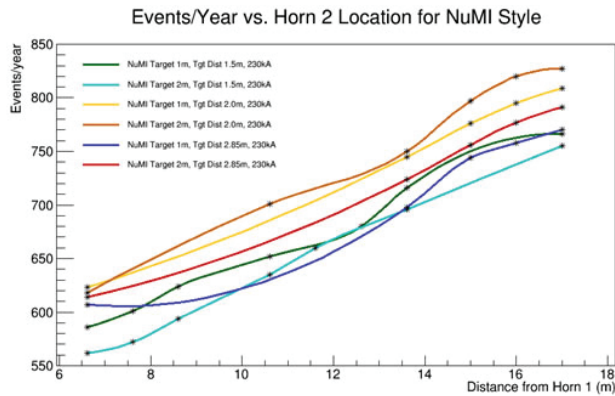


FIGURE 6. Events per year plotted against the distance from Horn 1 indicates that at further distances there will be a larger amount of tau neutrino events, regardless of the target design or target distance. The top two curves, brown and yellow, are the two optimized NuMI target designs. The 2 m NuMI target produced 827 and the 1 m target produced 809 tau neutrino interaction events at the far detector.

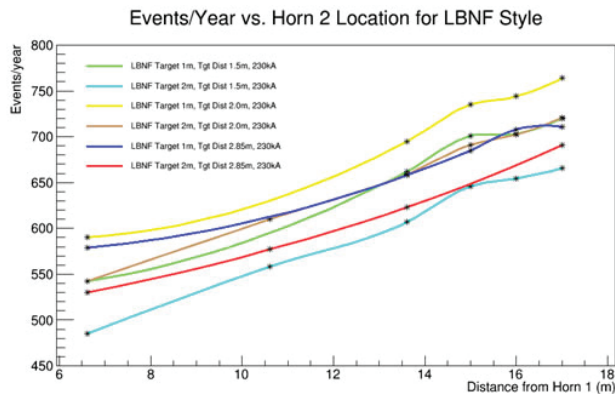


FIGURE 7. Events per year plotted against the distance from Horn 1. The top two curves, yellow and brown, are the two optimized LBNF target designs. The 1 m LBNF target produced 764 and the 2 m target produced 721 tau neutrino interaction events at the far detector.

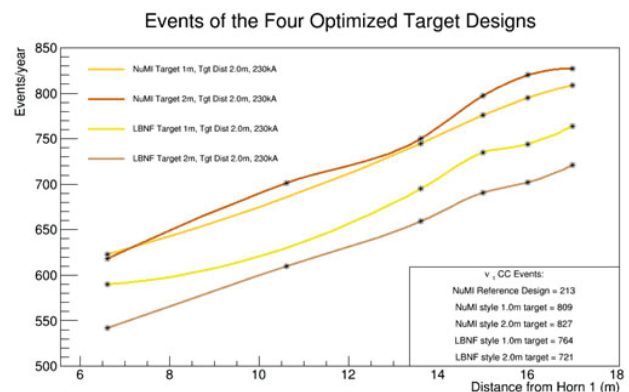


FIGURE 8. In the above figure are the four optimal target designs with the same color scheme from Figures 6 and 7. The top two curves are the NuMI style target that indicates the NuMI style is superior to LBNF design, which is primarily due to the narrower target.

all at a target distance of 2.0 m from the face of Horn 1. Thus, the NuMI style is preferred, however the LBNF style target would not significantly reduce the events. Of the four configurations optimized designs, the 1 m NuMI target in tandem with the other ideal conditions would be the optimal design for charged-current tau neutrino interactions at the far detector.

The next stage would be to incorporate background events into the calculated interaction events. This would optimize the signal to background ratio by identifying fake tau neutrino signals that are actually muon neutrinos oscillating into electron neutrinos. For example, the simulation could be refined to include the 5% of electron neutrinos that were approximated to be tau neutrinos. Incorporating this process into the simulation would reduce the tau neutrino events calculated in this project, but dramatically improve the accuracy of the events. The final step would be to automate the optimization process using neural networks to optimize features of the design like the magnetic horn shapes and target designs to even further maximize the number of tau neutrino interactions.

V. Acknowledgements

This project was supported in part by the U.S. Department of Energy, Office of Science, Office of Workforce Development for Teachers and Scientists (WDTS) under the Science Undergraduate Laboratory Internships Program (SULI).

VI. References

- [1] K.A. Olive et al. (Particle Data Group), *The Review of Particle Physics* Chin. Phys. C 38, 090001 (2014).
- [2] Y. Fukada et al. [The Super-Kamiokande Collaboration] *Measurements of the Solar Neutrino Flux From Super-Kamiokande's First 300 Days* arXiv:hep-ex/9805021 (1998).
- [3] The LBNE Collaboration *The Long-Baseline Neutrino Experiment, Exploring Fundamental Symmetries of the Universe* arXiv:hep-ex/1307.7335 (2013).
- [4] The LBNF/DUNE Collaboration *CDR Volume 3: The Long-Baseline Neutrino Facility for DUNE* (2015).

- [5] S. Agostinelli et al. *Geant4 – a simulation toolkit* Nucl. Instr. Meth. A 506, 250-303 (2003).
- [6] J. Allison et al. *Geant4 developments and applications* IEEE Transactions on Nuclear Science 53 No. 1, 270 (2006).
- [7] P. Adamson et al., *The NuMI Neutrino Beamline*, Nucl. Instrum. Meth. A806, 279 (2016).
- [8] Z. Pavlovic. *Observation of Disappearance of Muon Neutrinos in the NuMI Beam* University of Texas at Austin (2008).

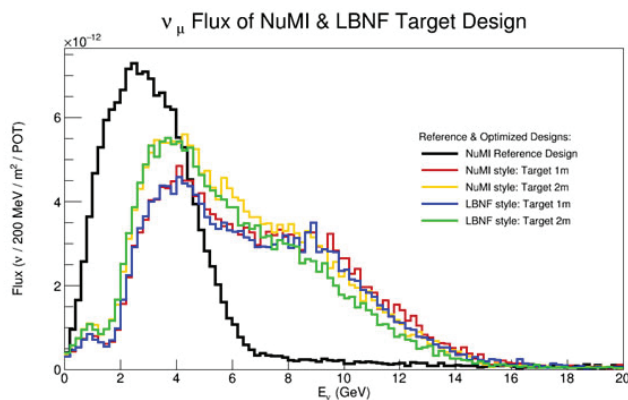


FIGURE 9. The 2 m targets, for LBNF and NuMI produce a larger muon neutrino flux at a lower energy range (about 4 GeV). Meanwhile, the 1 m targets produce a consistently larger flux at energies above 9 GeV.

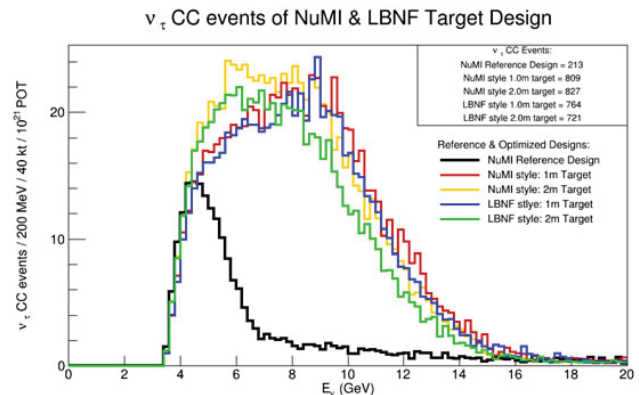


FIGURE 10. As a result in the larger muon neutrino flux at about 4 GeV, the 2 m targets for LBNF and NuMI yield a larger number of tau neutrino events at energies immediately after 4 GeV. Meanwhile, the 1 m targets produce consistently larger events at energies above 9 GeV due to the larger muon neutrino flux at these energies. These four optimized designs produce roughly four times more tau neutrino events than the original target hall configuration, which is a significant achievement.

Development of real time data visualization and analysis software for the National Synchrotron Light Source II X-ray Powder Diffraction Beam Line

Caleb Duff

Department of Physics, Brigham Young University Idaho, Rexburg, ID 83440

Eric Dooryhee

Photon Sciences, Brookhaven National Laboratory, Upton, NY 11973

Abstract

X-ray powder diffraction is an x-ray beam technique that allows scientists to gain information about the underlying crystal structure of materials. In one year of operation, the NSLS-II XPD beam line has already enabled a great diversity of experiments in areas such as next generation batteries, catalysis, ultra-high temperature ceramics, structural nuclear materials, pharmaceutical drugs and high-temperature superconductor flux growth. A long term software development plan is underway to make software that supplies the beam line's needs for data acquisition, analysis, simulation, and visualization. My project focused on creating software that enables beam line users to interact with their data acquired at the beam line in real time. The data can be presented in many ways, allowing the users to be confident in measurement that they are taking while working here at Brookhaven National Laboratory. By participating in this program I have gotten a real understanding of how programming works in a scientific setting. I have learned how to write python code that is useful to many different projects and can be reused for years to come.

I. Background

There are many materials around us that are formed by crystal structures. A crystal is simply any atomic pattern that repeats itself in building blocks to create a structure. Some great example of this are salt, sugar, metals, etc. Understanding how the structure of a material affects its properties is one of the driving reasons for XPD.

Before we can get into the specifics of how XPD works or what the software was trying to accomplish, we need to know why it works. Light when it enters some crystal structure is prone to diffract, or bend, based off of the spacing of the atoms. By sending in a beam of x-rays into some sample, light will come off in cone shapes that can be captured onto some detector.

Figure 1 gives a visualization of this idea.

The detector can then capture these light patterns in an image like the following (see figure 2).

It is important to note in the previous figure that this is a false color image. X-rays are not visible to the human eye, so this image has been given color. Darker regions show areas where light is not strongly diffracted to and brighter areas show regions where light is strongly diffracted to.

The brightest rings can tell us where the majority of atoms tend to be space from each other.

X-ray powder diffraction uses this idea to find out a variety things about some sample material. From this information we can learn about any symmetries found in the crystal, the coordinates

of each atom within its crystal lattice, and how well organized the atoms are.

Diffraction patterns with stronger rings refer to crystal structures that have more well defined crystal structures, or are in a more stable state.

Normally the rings are integrated azimuthally to create some 1D image that can display this information more clearly. These 1D integration patterns can look like this (Figure 3).

This is easier to obtain information from than the rings, in that we can infer from the radius through some mathematics what spacing the atoms appear to have most often.

The great thing about this technique is that the environment does not need to be static to gain this information. We can obtain this information in a variety of situations and that is where the beam line comes in along with the need for this software.

At the XPD beam line a variety of different environments can be simulated. The staff can increase the pressure the sample is under, change the composition of the atmosphere, and/or change the temperature of the hutch, or room the sample is kept in, to simulate the many kinds of environments that some material might exist in. The diffraction data can be recorded in all of these situations to see what happens to the crystal structure of the materials. These details of when the crystal breaks, when a phase change occurs, or even if any unexpected chemical reactions happen are important to know. This has led to improvements in batteries, nuclear reactor structural materials, and a growth of knowledge in many other fields that would otherwise not be possible.

The software that I worked on this summer allows all of this information to be gathered in one place and viewed by scientists who are asking a lot of different questions about their sample materials. The software allows them to see all of these diffracted image patterns together and answer the questions that they are seeking to answer about their materials.

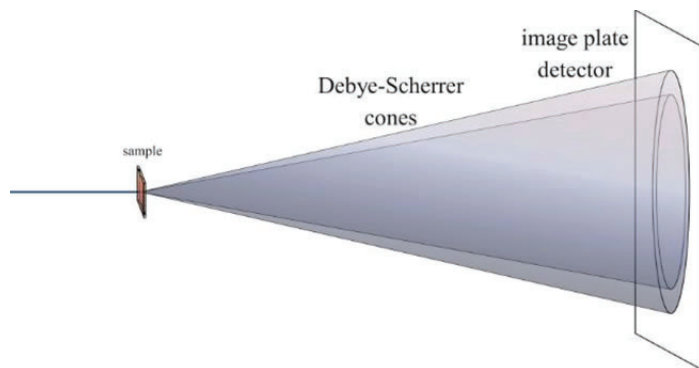


Figure 1. Example of diffraction

II. Methods

A long term software development plan is underway to provide software that can access the detector to save these images, process these images into useful data, display the data, and provide live analysis of the data. Much of the software is already developed that captures the images, but visualization has been tricky to do. I had the chance to meet often with the Data Acquisition, Management, and Analysis (DAMA) group and Professor S Billinge's Software Team, from Columbia University. These groups have been working on this long term plan for a few years now and I had to work closely with them to make sure that the software I developed synchronized well with what they had already accomplished. Another important part of the development process was to get input from beam line scientists in what they needed from the software. The constant reporting and demonstrating of developed code, allowed for a very positive development process that led to the results discussed in the next section.

This software has been coded in python. It relies heavily on the pyqt and matplotlib libraries found in the python language. These libraries allowed the software to be developed very effectively and quickly for the scientists.

III. Results

The following two figures will summarize the design and capabilities of the current software. Please note that in the table when it discuss level one and level two features these simply refer to when the option becomes visible. All level two's are tied to some inherently visible level one feature. Level one features are always visible to the user.

The software has been installed on the beam line and we have obtained optimal results. Since there was no previous version of the software it is difficult to draw comparisons. One of the main ways that I have defined success for this project has been the incorporation of the features desired by the scientists. Many of the fundamental features such as viewing 2D diffraction patterns and their corresponding 1D integrated patterns are already in the software. A variety of other options are also now available to users of the software as are discussed in the previous table.

The following specification for performance were found using a computer with an i7 processor at 2.9 Ghz that also had 8 GB of RAM. Images were read into the XPD View at a rate of

three 2048x2048 images every second. Refreshing took the same amount of time. Redrawing the image, when diffracted and integrated data are changed, took less than one tenth of a second. It took approximately half of a second to draw the reduced representation, the top right quadrant, for when we looked at a 400x400 pixel area on the 2D diffracted data.

IV. Conclusion

Software can always be built on. Currently many of the viewing features requested by the beam line staff have been implemented. As the title of this report however alludes to analysis is to be a main feature of the software. There are some basic analysis options available to users in the form of standard statistical parameters (mean, max, min, etc.), but analysis is the next major phase of the project to be worked on. Efforts are currently underway by myself and others to add new functionalities to the software such as real time streaming of data from NSLS-II servers, peak searching in 1D integrated patterns, and masking of data for further analysis. This will allow deeper real time analysis for beam line staff and users to create a more stream lined experimental experience.

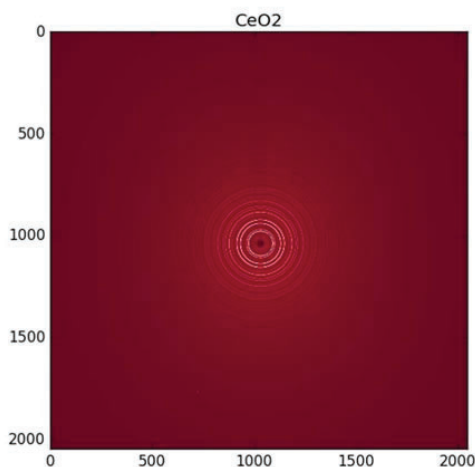


Figure 2. Example of diffraction data; This is Cesium Oxide

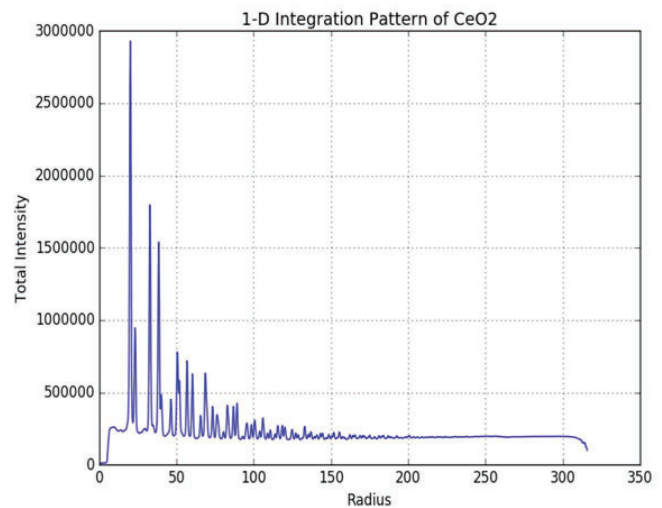


Figure 3. 1D integrated pattern of the previous 2D diffraction data; Radius refers to distance from center

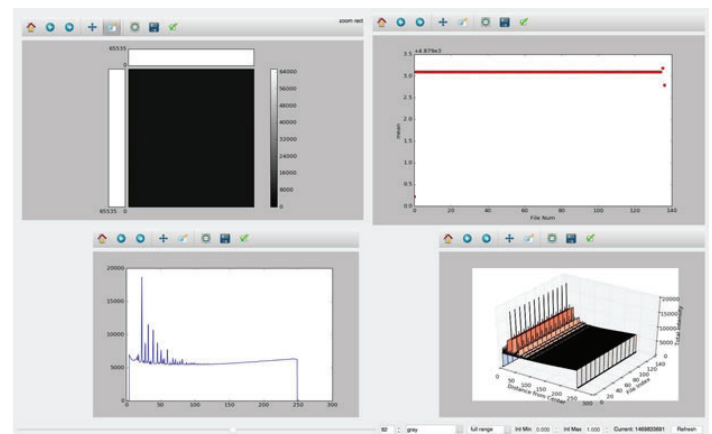


Figure 4. Current display window for XPD view (Top menu bar not visible in this snapshot)

Functionalities of XPD View GUI			
Region	Level One	Level Two	Description
Top Bar	File	Select Directory	Sets Directory for Software to search in
		Refresh	Searches for new files in directory
	Reduced Rep	Pop up window	Takes current zoom on 2D image and allows user to input the desired statistical parameter to observe in top right panel
For all four quadrants (Left to Right)	Home Icon		Takes user to original view of image
	Left and Right arrows		Takes user to previous or next view
	Blue cross shape		Allows user to move around within zoom region
	Magnifying Glass		Tool to give user option to define zoom
	Box w/ Green Arrows		Allows user to define size of image within relative frame
	Floppy Disk		Saves current image view as a separate file for future use
	Green check mark		Allows user to retile axes and title; Also allows user to set logarithmic scale
Top Left Quadrant	White Boxes		Display the data along the crosshair line; This is activated by clicking on the image
	Color bar on Right		Shows user what the intensity range is and what the corresponding colors are for the user
	Center Image		Shows 2D diffraction pattern obtained from the detector
Top Right Quadrant	Plot		Shows reduced representation of data; Clicking on specific point will pull up the corresponding image and 1D integrated pattern
Bottom Left Quadrant	Plot		Pulls up 1D integrated pattern of diffraction data
Bottom Right Quadrant	3D Plot		Shows all 1D integrated pattern stacked side by side ordered according to time data was taken
Bottom Bar (Going left to right)	Slider		Allows user to select diffraction pattern to be displayed in top and bottom left quadrants
	Spin box		Displays current frame number; Allows user to type in specific frame to use or parse through images one by one
	Combo box #1		Contains over 60 coloring options for top left quadrant
	Combo box #2		Determines intensity scaling user will use while viewing image; Options available are full range, percentile, and absolute
	Int Min Spin box		Sets the minimum intensity for diffracted data
	Int Max Spin box		Sets the maximum intensity for diffracted data
	Current File Label		Displays the name of the current file
	Refresh		Searches for new files

Figure 5. Table discussing all the tools of XPD View

V. Acknowledgements

I want to say thank you to all XPD beam line staff who helped me to make software for them. Chia-Hao Liu deserves special thanks for working with me on this project. Tom Caswell and Chris Wright as well for their computer savvy and advice. I want to especially thank my mentor for his patience and help in making

a platform that will be useful to the beam line.

This project was supported in part by the U.S. Department of Energy, Office of Science, Office of Workforce Development for Teachers and Scientists (WDTS) under the Science Undergraduate Laboratory Internships Program (SULI).

Cumulus congestus cloud growth during the Green Ocean Amazon 2014/5 campaign

Jordan Eissner

Meteorology and Physics, Valparaiso University, Valparaiso, Indiana 46383

Michael Jensen

Environmental and Climate Sciences, Brookhaven National Laboratory, Upton, New York 11973

Abstract

Despite the important role of convective clouds in the Earth's energy balance and hydrological cycle, climate models struggle to represent their lifecycle. Cumulus congestus clouds, which occur often in tropical locations, represent an intermediate state of convective development with cloud top heights near the freezing level. It is predicted that dry air entrainment in the mid-troposphere plays a role inhibiting these clouds from reaching greater heights, but freezing-level stability may also have an effect. The Green Ocean Amazon 2014/5 (GoAmazon2014/5) campaign collected cloud aerosol and atmospheric data at several sites in Brazil, South America. I analyzed observations from the Department of Energy's Atmospheric Radiation Measurement (ARM) mobile facility deployed at Manacapuru, Brazil, to determine the factors that limit convective cloud growth. Using W-band ARM Cloud Radar observations, cumulus congestus clouds were identified. The observations were used along with thermodynamic sounding observations in a simple plume model to estimate the level of neutral buoyancy (LNB) and entrainment rate. We tested our hypothesis by substituting thermodynamic profiles with a moist mid-troposphere and an unstable freezing level into the model to determine the new LNB and cloud-top height. The results show that the LNB increased significantly for most of the clouds when placed in a moist environment, and slightly increased for fewer clouds when in unstable freezing-level conditions. These results confirm the hypothesis that the cloud top heights depend more on the humidity of the mid-troposphere levels than the stability at the freezing level. By knowing the factors that limit growth, we can better represent the convective lifecycle in models and improve the simulation of their impacts on the radiative energy balance and hydrological cycle.

I. Introduction

Clouds play an important role in the global energy budget because they reflect incoming solar radiation (visible wavelengths) back to space and absorb and radiate at infrared wavelengths. The magnitude of the reflection, absorption, and radiation depends on the cloud macrophysical (fractional coverage, thickness, and height/temperature) and microphysical (liquid water content, particle size distribution and phase) properties, and it is important in determining the global and local energy budget and the resulting contributions to climate change. Cumulus congestus clouds, defined as having cloud top heights near the freezing level (~4-5 km in the tropics), have moderate shortwave albedos. These clouds occur often in tropical locations, but their lifecycles are not fully understood.

The general lifecycle of a convective cloud starts off with a "parcel" of air that is lifted through buoyant or mechanical pro-

cesses. The parcel will rise, sink, or stay where it is based on its density compared to the surrounding environment. If the parcel is warmer than the environment, it is less dense, and will rise. Under this condition, the environment is unstable. If the parcel is cooler than the environment, it is more dense, and so it will sink. This is a stable environment. If the parcel and environment are the same temperature, the parcel will not move, and it is defined as a neutral environment. To form a cloud, the parcel must rise and cool until its temperature equals its dew point temperature, at which time the water vapor condenses (given the availability of sufficient condensation nuclei). This point is the cloud base height. If the parcel is still warmer than the environment, it will continue to rise, and the cloud will grow vertically, until the parcel is no longer warmer than the environment. This point is defined as the level of neutral buoyancy (LNB) and can be considered a rough estimate of the cloud top height (CTH).

Cumulus congestus clouds have intermediate CTH. They do not grow into a deep convective state ($CTH > 9$ km) and are not shallow layer clouds. The purpose of this study is to better understand the factors that limit the growth of these clouds. Potential factors include dry air entrainment in the mid-troposphere, freezing level stability, and a lack of convective available potential energy (CAPE).⁶ When dry air mixes into the cloud, the water droplets evaporate, reducing in size or completely evaporating, which may limit further growth of a cloud. Cooling resulting from the evaporation decreases the buoyancy of the rising parcel, further limiting the growth. Previous studies (e.g. Mapes and Zuidema 1996) have found intrusions of dry air that originate in the subtropical latitudes (23.5°-40°) and mixes in at the mid-troposphere, around 5-7 km.⁵ Another important factor is the stability at the freezing level. Near the bases of anvils, clouds associated with deep convection, falling ice particles melt, removing latent heat from the air. This layer becomes cooler, and more stable, resulting in a loss of buoyancy of rising parcels. The CAPE is a measure of the stored potential energy in the atmosphere. A larger CAPE indicates that there is more potential energy available for convection.

We follow the methodology of Jensen and Del Genio (2006) to investigate the factors impacting cumulus congestus cloud growth during the GoAmazon 2014/5 field campaign in Brazil.² New techniques presented in Jensen et al. (2015) are incorporated to define the growth state of cumulus congestus at the time of their observation.³

II. Data and Methods

The purpose of the GoAmazon 2014/5 campaign was to study the interaction and lifecycle of anthropogenically generated aerosols from the city of Manaus and their impact on cloud and environmental properties. One important component of this campaign was the deployment of DOE's Atmospheric Radiation

Measurement (ARM) Mobile Facility at Manacapuru, Maunus, Brazil from January 2014 through December 2015. The W-band ARM Cloud Radar (WACR), a radar with high sensitivity to small cloud particles, took continuous data of the vertical profile of clouds as they advected over the site. Using the WACR reflectivities and Doppler velocities, cloud properties, including cloud base heights, CTH, and vertical velocities can be found. This cloud information was used to identify cumulus congestus clouds, based on the criteria of cloud base height less than 2 km and CTH between 3 and 9 km. For the 2 years worth of collected data, 792 cumulus congestus cloud cases were identified and used in the study. Figure 1 shows an example of one of these congestus clouds from May 14th, 2014. All calculations were completed in the Interactive Data Language (IDL) and all plots were done in the Python programming language.

The cumulus congestus clouds identified were further classified as either terminal (done growing) or transient (still growing)⁴, based on the vertical air motion near cloud top. In order to determine the vertical air motion, the hydrometeor fall speed needs to be estimated and removed from the observed mean Doppler velocity (MDV). We use a simple parameterization of the hydrometeor fall speed as a function of radar reflectivity.¹

$$v_f = aZ^b$$

where Z is the radar reflectivity and a and b are empirically derived coefficients. The vertical velocity of the air is then determined from

$$v_{air} = MDV - v_f$$

Two out of the following three conditions must have been met in order to be identified as transient: (1) The ratio of rising to sinking pixels greater than 1, (2) a positive mean velocity of the air (v_{air}), and (3) a positive slope of v_{air} in the upper 1 km of the cloud. The study should only use the cases where the clouds are terminal. The terminal cases have a better estimate of the entrainment rate, since the observed CTH is actually the max CTH with that amount of mixing. However, if the cloud is still growing, the air is not mixing as much, though the model assumes it is, so the entrainment rate will be overestimated. Though using the terminal cases is better, this study used both the terminal and transient cases because there were only 16 terminal clouds out of the 792 total congestus cases. The reason for so few terminal cases is likely

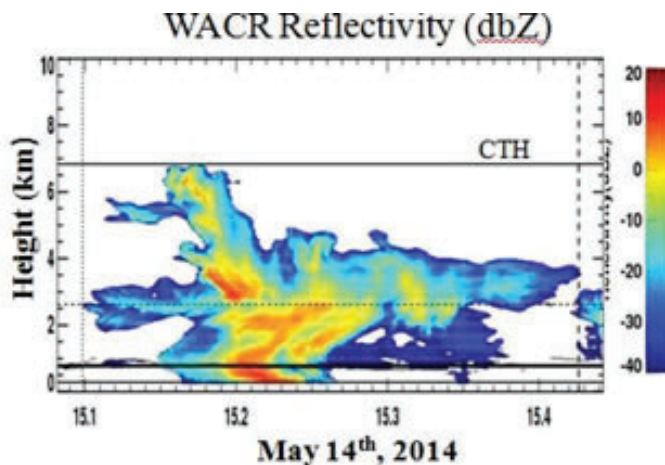


Figure 1: The WACR reflectivity of a cumulus congestus cloud, observed on May 14th, 2014. The lowest line is the cloud base height and the upper line represents the CTH.

due to an overestimation of v_f due to attenuation of the W-band radar signals.

For each day during the campaign, about four radiosonde launches took place at the site, in order to quantify the vertical thermodynamic profile of the atmosphere. Using the profile soundings nearest to the time of each cumulus congestus cloud, several variables could be calculated to help further understand the cloud properties. These variables include the CAPE, convective inhibition (CIN), mean relative humidity (RH) of the mid-troposphere, vertical shear of the horizontal wind, and LNB. The LNB can be considered a proxy for the CTH.

A simple “entraining plume” model used the CTH to estimate the entrainment rate for each of the clouds in the study. This model starts with an entrainment rate (σ) of 0.1 % km⁻¹, performs a linear mixing of the rising parcel and the environmental air, and then calculates a new level of neutral buoyancy (ELNB). This process is repeated for increments of 0.1 % km⁻¹, until the ELNB equals the radar-derived CTH (Figure 2). We assume a constant entrainment rate with height and pseudoadiabatic ascent.

Figure 3 shows the relationship between entrainment rate and CTH. The entrainment rates varies from 1.0 % km⁻¹ to 510 % km⁻¹. As expected, as the CTH increases, the entrainment rate and its standard deviation decreases.

In order to test our hypotheses on the factors that limit the CTH and convective cloud growth, we perform additional runs of our entraining plume model, substituting a sounding with a moist mid-troposphere and a sounding with an unstable freezing level for the environmental sounding. The mean RH of the mid troposphere and the mean instability of the freezing level were calculated for every sounding in the campaign. The 90th and 75th percentile values were found, and their corresponding soundings were substituted into a model to determine a new CTH in either a moist or unstable environment, using the calculated entrainment rate shown in Figure 3.

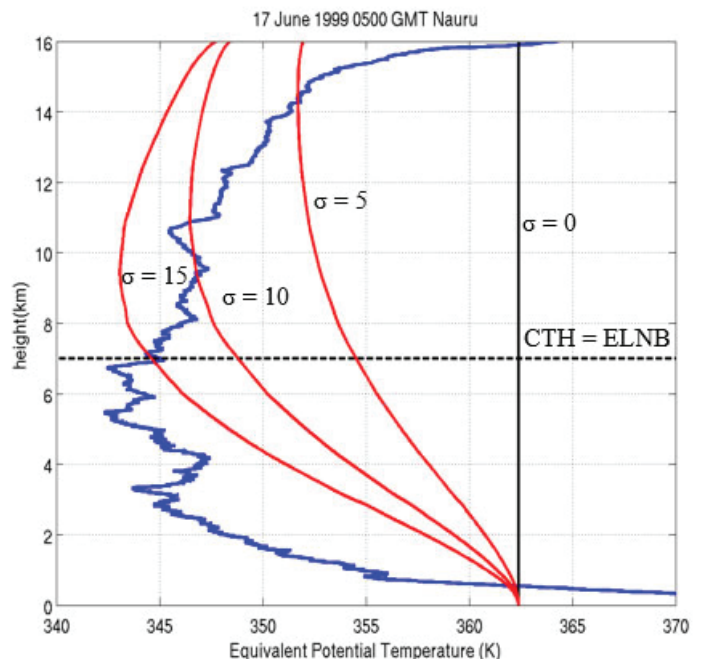


Figure 2: The “entraining plume” model used to find the entrainment rate. Here, the entrainment rate is 15 % km⁻¹, since that is the rate at which the CTH equals the ELNB.

III. Results and Discussion

Figure 4 shows a scatter plot of CAPE and CTH. There is little correlation between CTH and CAPE. The larger the CAPE does not necessarily mean that the CTH will be larger. This suggests that the environmental CAPE does not play a role in determining the depth of the cumulus congestus clouds.

After the sounding with an unstable freezing level was substituted, the CTH slightly increased for some of the clouds. For the 90th percentile substitution, 372 out of the 792 congestus clouds (47%) showed an increase in CTH, and 348 out of 792 (44%) increased when the 75th percentile sounding was substituted. The mean increase for the 90th percentile soundings was 2.95 km, and 1.73 km for the 75th percentile sounding (Table 1). The substitutions of the moist mid-troposphere have a greater effect on the CTH. The results are plotted for all substitutions in Figures 5 and 6. Both the 90th and 75th percentile substitutions show large increases for the moist case. For the 90th percentile soundings, 762 out of the 792 cumulus congestus clouds (96%) had an increase in CTH when substituted into a moist environment, and 723 out of 792 (91%) increased after the 75th percentile sounding. The mean increase of the CTH for the 90th percentile sounding is also

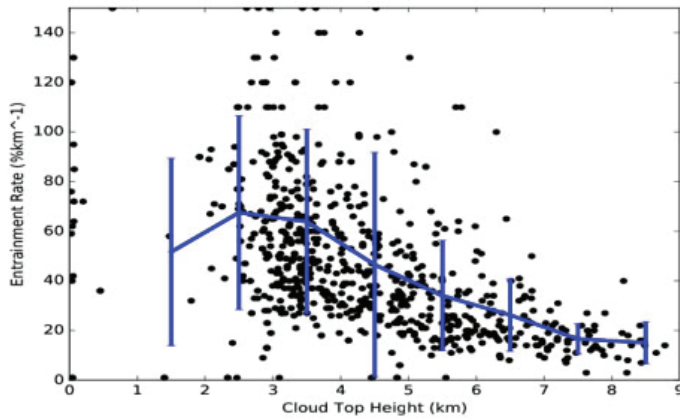


Figure 3: The entrainment rate vs. CTH. The line represents the mean entrainment rate for 1 km CTH bins and the error in those entrainment rates.

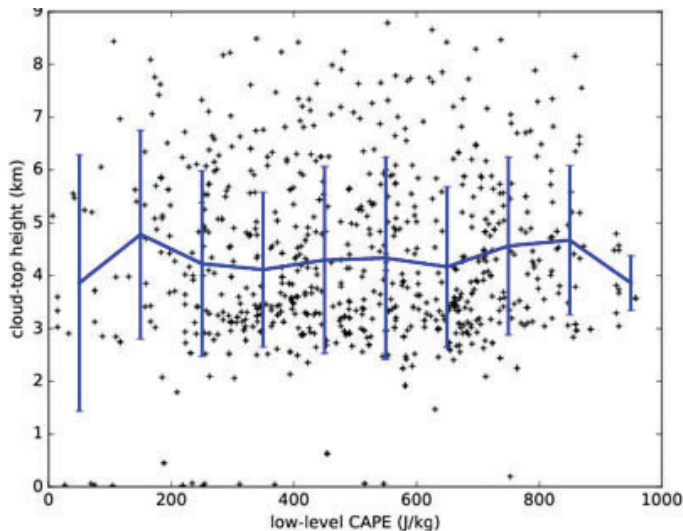


Figure 4: The CTH vs $\ln(\text{CAPE below } 5 \text{ km})$. The line represents the mean CTH of 100 J kg^{-1} sized bins and the error in those CTH. There is no apparent correlation between CTH and CAPE.

2.3 km greater for the moist case than the unstable case (Table 1). Though the numbers for the 75th percentile soundings are lower, they are not significantly lower, and the same conclusion remains. In addition, 429 out of 792 clouds (54%) had CTH that increased to the deep convective state ($> 9 \text{ km}$), compared to the unstable substitution case, which showed 50 clouds (6%) that grew into deep convective clouds. This suggests that the dry air entrainment in the mid-troposphere plays a more important role in limiting the further growth of cumulus congestus clouds. These results are also consistent with what was found at the Nauru ARM site in the tropical Western Pacific by Jensen and Genio (2006)² and Jensen et al. (2014).³

An analysis of the factors that cause variations in entrainment rate was done. Using a multiple regression, different environmental factors, such as CAPE, CIN, RH, shear, and combinations of

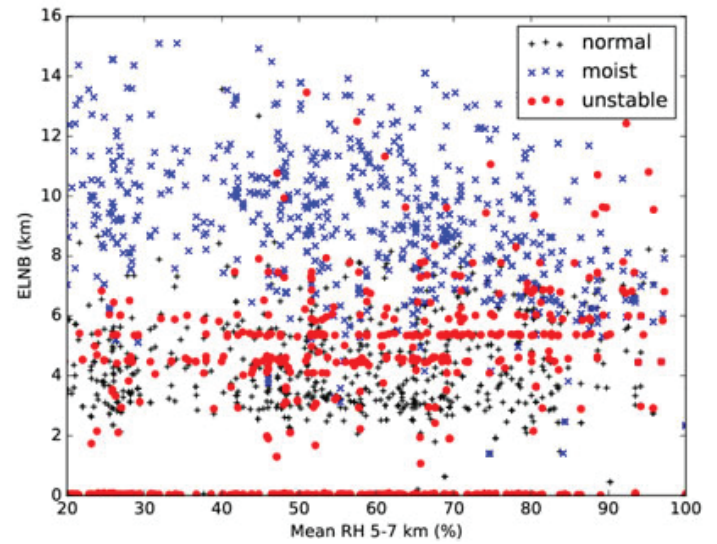


Figure 5: The ELNB as a function of mean mid-troposphere RH for the standard sounding (+), the moist sounding substitution (x), and the unstable sounding substitution (o), using the 90th percentile substitutions.

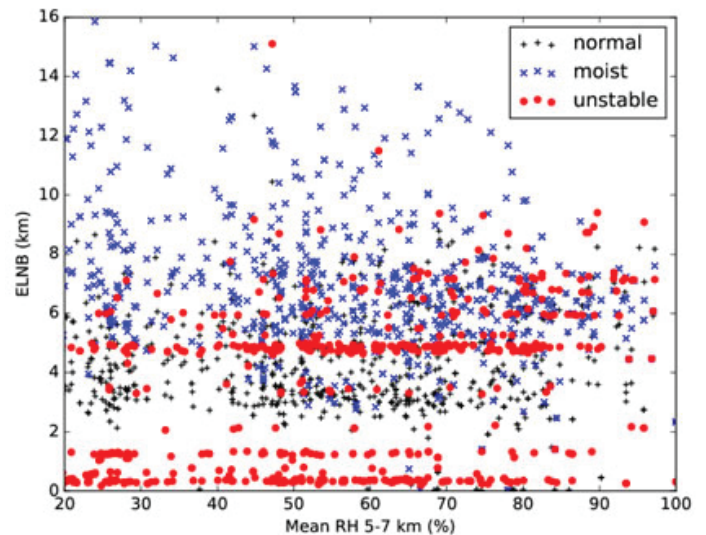


Figure 6: The ELNB as a function of mean mid-troposphere RH for the standard sounding (+), the moist sounding substitution (x), and the unstable sounding substitution (o), using the 75th percentile substitutions.

each, were tested to find a correlation. The regression analysis shows that there is little correlation between the entrainment rate and environmental variables (Table 2). This scatter can also be viewed in Figure 7, with plots of entrainment rate versus a few of the environmental controls (CAPE, CIN, and RH). Further investigation of the causes of the variation in entrainment rate is needed. For the study at the Nauru site, Jensen and Del Genio (2006) found that the entrainment rate correlated with CAPE and RH.² The difference in results from each study could suggest a real difference in the environmental drivers of entrainment rate between two different locations due to oceanic convection observed in Nauru compared to continental convection in Brazil. The role of

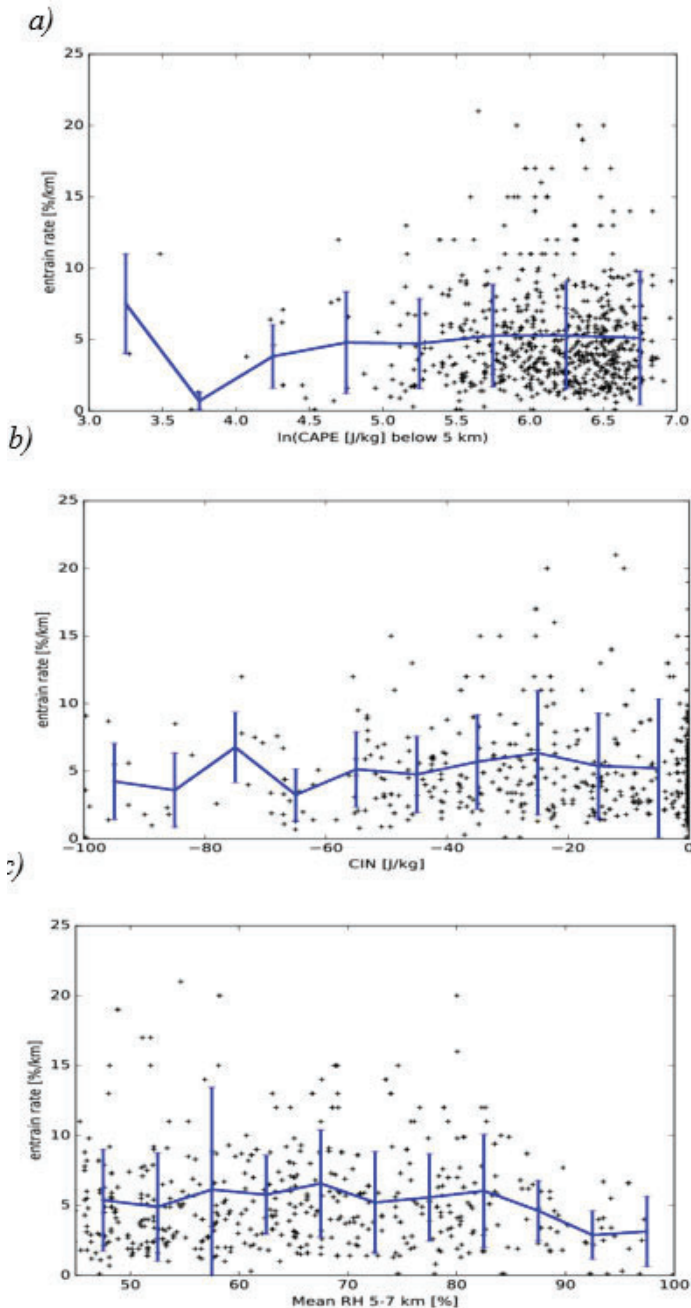


Figure 7: The entrainment rate as a function of a) natural log of CAPE below 5 km, b) CIN, and c) mean RH from 5 to 7 km. The line is the mean entrainment rate in appropriately sized bins and the error in those rates.

non-local forcing, such as sea and river breeze circulations may also impact the correlations. Another possible explanation is the impact of attenuation on the W-band reflectivity measurements, which may result in the underestimation of CTH and subsequent overestimation of entrainment rate. The relationships will require further analysis.

IV. Conclusions

After substituting soundings with a moist mid-troposphere and unstable freezing level, many CTH increased significantly when placed in a moist environment, and most clouds grew into deep convective clouds. Fewer clouds grew into deep convection, and the mean increase was much lower when the clouds were in an environment with an unstable freezing level. There was also no correlation between the CTH and CAPE. These results suggest that dry air entrainment in the mid-troposphere is the most important factor in limiting the growth of tropical cumulus congestus clouds.

A regression analysis was done to discern the environmental factors that have an effect on the entrainment rate. However, none of the environmental variables, like CAPE, CIN, RH, and shear, seem to be related to the entrainment rate. There is too much scatter in the plots to come to a conclusion. A more in depth analysis with more accurate data should be done to understand the factors that cause the variation in entrainment rate.

The results from this study can be used to improve cumulus congestus lifecycles in models. From the climate models, we will be able to better understand the global energy budget and the effects that clouds will have on global climate.

Substitutions	# of increase	Mean increase (km)	# of ELNB > 9 km
Moist (90)	762	5.25	429
Unstable (90)	372	2.95	50
Moist (75)	723	3.34	154
Unstable (75)	348	1.73	17

Table 1: A summary of the changes in ELNB after the sounding substitutions.

Variable	R ²
CAPE	0.002
CIN	0.006
RH	0.016
CAPE,RH	0.021
CAPE,RH,CIN	0.022
Wind shear	0.001

Table 2: The results of the coefficient of determination from the multiple regression analysis.

V. References

¹Giangrande, S. E., S. M. Collis, J. Straka, A. Protat, C. Williams, and S. Krueger, 2013: A summary of convective core vertical velocity properties using ARM UHF wind profilers in Oklahoma. *J. Appl. Meteor. Climatol.*, **52**, 2278-2295.

- ²Jensen, M. P. and A. D. Genio, 2006: Factors limiting convective cloud-top height at the ARM Nauru Island climate research facility. *J. Clim.*, **19**, 2105-2117.
- ³Jensen, M. P., K. Towey, and T. Toto, 2015: Entrainment and tropical cumulus congestus growth. Presented at the 6th Atmospheric System Research (ASR) PI Meeting. ASR-CONF-2015. Vienna, VA.
- ⁴Luo, Z., G. Y. Liu, G. L. Stephens, and R. H. Johnson, 2009: Terminal versus transient cumulus congestus: A CloudSat perspective. *Geophys. Res. Lett.*, **36**, L05808.
- ⁵Mapes, B. E. and P. Zuidema, 1996: Radiative-dynamical consequences of dry tongues in the tropical tropopause. *J. Atmos. Sci.*, **53**, 620-638.
- ⁶Redelsperger, J. L., D. B. Parsons, and F. Guichard, 2002: Recovery processes and factors limiting cloud-top height following the arrival of a dry intrusion observed during TOGA COARE. *J. Atmos. Sci.*, **59**, 2438-2457.

VI. Acknowledgments

I would like to thank my mentor, Michael Jensen for providing me with the knowledge and guidance to complete this project, Tami Toto and Karen Johnson for their assistance, and Brookhaven National Laboratory for their hospitality. This project was supported in part by the U.S. Department of Energy, Office of Science, Office of Workforce Development for Teachers and Scientists (WDTS) under the Science Undergraduate Laboratory Internships Program (SULI). I also would like to acknowledge the ARM Climate Research Facility for providing all of the data to do this study.

Comparing vegetative fuel loading and developing custom fuel models for Brookhaven National Laboratory

Sean Foote

School of Forest Resources, University of Maine, Orono, ME 04469

Julia Riley

Department of Forestry and Natural Resources, Clemson University, Clemson, SC 29632

Kathy Schwager

Environmental Protection Division, Brookhaven National Laboratory, Upton, NY 11973

Abstract

Where fire occurs, it shapes the form and function of ecosystems; however, as a method of ecosystem maintenance, fire has largely been suppressed. This study was conducted to collect and analyze fuel loading data in Brookhaven National Laboratory (BNL) and to assess potential fire behavior. Our study was focused on two stands (D and A) in the eastern complex of the northeastern corner of BNL. Vegetative surveys were conducted in 2006 and 2016, and the resulting fuel loading data was entered into BehavePlus 5.0.5 to create custom fuel models of the stands. The results showed that Stand D had a 17%, 77%, and 44% decrease in 1-, 10-, and 100-hour dead fuels respectively, and a 227% increase in live woody fuel from 2006 to 2016. Stand A had a 29% and 73% decrease in 1 and 10-hour dead fuels respectively, and a 2,886% increase in 100-hour dead fuels from 2006 to 2016. We believe that the herbivory of the orange striped oakworm (*Anisota senatoria*) and the gypsy moth (*Lymantria dispar*), in Stand D opened the canopy and increased live woody fuel values, thereby increasing rate of spread and flame length values. We also believe that the moderate-to-high intensity fire that top-killed many oaks in Stand A, in 2012, caused the increase in the number of 100-h dead fuels and the decrease in the 1- and 10- h dead fuels. The decrease in these fine fuels in Stand A would explain the lower predicted rate of spread and flame length values in 2016 as compared to 2006.

I. Introduction

Fire, from an ecological perspective, is a human induced or naturally occurring phenomenon that deals with the combustion and conversion of complex organic compounds (oxygenated fuels) to mineral and organic products.¹ It has shaped modern day landscape characteristics such as flora and fauna species composition, natural appearance, soil drainage categorizations, and trophic levels for centuries;² but, wildfires, or any non-structure fire other than prescribed fire that occurs in wildlands,³ now pose serious risks to the man-dominated environment including smoke introduction in to the atmosphere and jeopardizing human assets (land, home or business).

Wildfires are causal agents for ecosystems to adapt to or be altered by, and wildfires that aid in forest health are being suppressed due to human development protection.² As a limiting factor in forest succession and woody fuels on the forest floor, suppression shifts ecosystem species composition indefinitely. Long Island, New York, specifically has been suppressing fire for over 50 years due to large population increases and industrial devel-

opment in the tri-state area.⁴ The continual suppression of fire on Long Island has many social and ecological implications. The extent of fire suppression directly correlates to the accretion of fine and coarse woody fuel; therefore, increases in forest fuels pose an elevated risk for a larger, more intense, and more severe fire as opposed to letting natural fire initiate and end uninterrupted.⁵

By analyzing specific fuel complexes, we aim to quantify the risk of fire suppression and showcase the direct impacts on Brookhaven National Laboratory (BNL) land. Our specific objectives were to:

- Collect vegetation fuel loading data in the northeast corner of BNL land.
- Interpret the current fuel loading in the study site, and to compare the current data to the previous inventory conducted in 2006.
- Create custom fuel models in BehavePlus 5.0.5,⁶ and to analyze the predicted fire behavior between study site areas with different fire suppression histories.

II. Methods

A. Study Site

Our research was conducted on BNL, located in Upton, New York. BNL rests on 2,153.33 hectares (5321 acres) that are positioned within Long Island's Central Pine Barrens ecosystem and the Peconic River watershed.⁷ The Central Pine Barrens primarily consists of pitch pine (*Pinus rigida*), scarlet oak (*Quercus coccinea*), black oak (*Q. velutina*), white oak (*Q. alba*), and ericaceous shrubs. The soils for these areas were formed from the recession of glaciers less than 12,000 years ago, are medium to coarsely textured, and are well to excessively-well drained.⁸ Our research sites were specifically located in the northeastern corner of BNL that is divided into two subunits; north and east. The north complex consists of 45 hectares and the east complex consists of 23.88 hectares.⁹ Our specific analysis focused on stands D and A within the eastern complex that contained 5 and 6 plot points respectively. The southern 3.40 hectares of Stand D experienced a low intensity prescribed burn in 2006, and Stand A experienced a low intensity prescribed burn in 2011 and a moderate-to-high intensity wildfire in April 2012.⁹ These stands were chosen to be the focus of our research project because of the differing time periods in which fire was absent from the two sites. This allowed us to compare fuel loading between a stand 10 years without fire and a stand 4 years without fire.

B. Sampling Design.

Ninety-three points, each associated with unique GPS coordi-

nates, were established across the northern and eastern complexes using ArcGIS® (10.0). The fishnet tool was used to generate a grid of equally spaced points that were at least 22.86 meters from any edge and 30.48 meters from any other point. Each point was assigned a number, and a random number generator was used to pick the 93 points from that grid. A GPS unit was used to navigate to each point, a plot center was randomly chosen by throwing an object over the collectors shoulder. A modified Brown's transect¹⁰⁻¹¹ was used to inventory downed woody fuels, and a variable radius plot was used to assess the basal area and volume¹² at each plot center. Another object was randomly thrown from plot center, and at that point a 40x40cm² harvest plot was completed to measure the live and dead fuels including herbaceous. Sampling was done in accordance with vegetation and fuel monitoring protocols for the Long Island Pine Barrens Fire Management Demonstration Site Project adapted from the University of Massachusetts Project "Managing Fuels in Northeastern Barrens"¹¹ in order to assess the fuel loading of the two complexes by collecting a representative sample of fuel information. Data was collected starting June 2016.

C. Data Analysis.

Our data was recorded into macro-enabled Windows® Microsoft Excel (2007) spreadsheets provided by the University of Mas-

sachusetts website.¹¹ The data was then entered into BehavePlus 5.0.5⁶ to create custom fuel models for Stand D and A to compare the predicted fire behavior over time and between the two stands. The custom fuel models for stands D and A yielded predicted surface rate of spread (maximum) (m/min) and flame length (m) values for every 1-h moisture (%) value between 4-18% at midflame wind speeds (upslope) (km/h) between 3.218688 and 38.624256 in intervals of 3.218688. The moisture values of 4% to 18% were chosen because the BNL Prescribed Fire Plan⁹ requires the 1-h fuel moisture to be 6-18% inclusive for a burn to occur. The results of the BehavePlus 5.0.5⁶ runs were recorded and reorganized in Windows® Microsoft Excel (2007).

III. Results

The vegetation inventory yielded the fuel complex information for stands D and A, and the fuel complex information that was recorded for stands D and A, in 2006, was included for comparison. Stand D had a 17% decrease in dead 1-h fuel, a 77% decrease in dead 10-h fuel, a 44% decrease in dead 100-h fuel, and a 100% decrease in herbaceous fuel from 2006 to 2016. The live woody fuel load, however, increased by 227%, and the fuel bed depth increased by 125% from 2006 to 2016. Stand A had a 29% decrease in dead 1-h fuel, and a 73% decrease in dead 10-h fuel, but the dead 100-h fuel increased by 2,886%, the herbaceous fuel

Table 1. Table representing the fuel loading (tonne/ha) for two stands in the east block of Brookhaven National Laboratory, Upton, NY.

		Stand D 2006	Stand D 2016	Stand A 2006	Stand A 2016
1hr fuel load (dead)	tonne/ha	16.34	13.55	13.22	9.33
10hr fuel load (dead)	tonne/ha	1.28	0.29	0.7168	0.19
100hr fuel load (dead)	tonne/ha	3.09	1.72	0.22	6.57
Live Herbaceous fuel load	tonne/ha	0.52	0	0.36	1.39
Live Woody fuel load	tonne/ha	1.82	5.96	1.55	3.65
Fuel bed depth	m	0.12	0.27	0.12	0.15

Table 2a. Table representing the surface rate of spread (maximum) (m/min) for Stand D, in 2006, in the east complex of Brookhaven National Laboratory, Upton, NY.

1-h Moisture %	Midflame Wind Speed (upslope) km/h												
	3.218688	6.437376	9.656064	12.874752	16.09344	19.312128	22.530816	25.749504	28.968192	32.18688	35.405568	38.624256	
4	1.1	2.5	4.2	6.3	8.7	11.3	14.2	17.4	20.7	24.2	27.9	31.8	
5	1	2.3	3.9	5.8	8	10.5	13.2	16	19.1	22.3	25.8	29.4	
6	1	2.1	3.6	5.4	7.5	9.8	12.3	15	17.8	20.9	24	27.4	
7	0.9	2	3.4	5.1	7.1	9.2	11.6	14.1	16.8	19.6	22.7	25.8	
8	0.9	1.9	3.3	4.9	6.7	8.8	11	13.4	16	18.7	21.5	24.5	
9	0.8	1.8	3.1	4.7	6.4	8.4	10.5	12.8	15.3	17.9	20.6	23.5	
10	0.8	1.7	3	4.5	6.2	8.1	10.1	12.4	14.7	17.2	19.9	22.6	
11	0.8	1.7	2.9	4.3	6	7.8	9.8	12	14.2	16.7	19.2	21.9	
12	0.7	1.6	2.8	4.2	5.8	7.6	9.5	11.6	13.8	16.2	18.7	21.3	
13	0.7	1.6	2.7	4.1	5.6	7.4	9.2	11.3	13.4	15.7	18.1	20.6	
14	0.7	1.5	2.6	4	5.5	7.1	8.9	10.9	13	15.2	17.5	20	
15	0.7	1.5	2.6	3.8	5.3	6.9	8.6	10.5	12.5	14.7	16.9	19.3	
16	0.6	1.4	2.4	3.7	5.1	6.6	8.3	10.1	12	14.1	16.2	18.5	
17	0.6	1.4	2.3	3.5	4.8	6.3	7.9	9.6	11.4	13.3	15.4	17.5	
18	0.6	1.3	2.2	3.3	4.5	5.9	7.4	9	10.7	12.5	14.4	16.4	

increased by 286%, the live woody fuel increased by 135%, and the fuel bed depth increased by 25%. In 2016, Stand D has more dead 1-h and 10-h fuels (31% and 34% more respectively), 39% more live woody fuel, and a 44% increase in the fuel bed depth than Stand A, while Stand A had 282% more dead 100hr fuel and 139% more herbaceous fuel than Stand D (Table 1).

The BehavePlus 5.0.5 6 outputs indicated that the rate of spread (maximum) (m/min) and flame length (m) values for Stand D, in 2016, (Tables 3a and 3b) were more than double the values

for Stand D in 2006 (Tables 2a and 2b) at every 1-h fuel moisture value. Stand A had similar predicted rate of spread and flame length values in 2006 and 2016; however, predicted fire behavior, in the 2016 outputs, (Tables 5a and 5b) was consistently less than the 2006 outputs (Tables 4a and 4b). The rates of spread for Stand A, in 2006, increased at a faster rate than Stand A in 2016. Stand D, in 2016, had considerably higher (more than double) rate of spread values and flame lengths, at each moisture value, than Stand A in 2016.

Table 2a. Table representing the surface rate of spread (maximum) (m/min) for Stand D, in 2006, in the east complex of Brookhaven National Laboratory, Upton, NY.

1-h Moisture %	Midflame Wind Speed (upslope) km/h											
	3.218688	6.437376	9.656064	12.874752	16.09344	19.312128	22.530816	25.749504	28.968192	32.18688	35.405568	38.624256
4	1.1	2.5	4.2	6.3	8.7	11.3	14.2	17.4	20.7	24.2	27.9	31.8
5	1	2.3	3.9	5.8	8	10.5	13.2	16	19.1	22.3	25.8	29.4
6	1	2.1	3.6	5.4	7.5	9.8	12.3	15	17.8	20.9	24	27.4
7	0.9	2	3.4	5.1	7.1	9.2	11.6	14.1	16.8	19.6	22.7	25.8
8	0.9	1.9	3.3	4.9	6.7	8.8	11	13.4	16	18.7	21.5	24.5
9	0.8	1.8	3.1	4.7	6.4	8.4	10.5	12.8	15.3	17.9	20.6	23.5
10	0.8	1.7	3	4.5	6.2	8.1	10.1	12.4	14.7	17.2	19.9	22.6
11	0.8	1.7	2.9	4.3	6	7.8	9.8	12	14.2	16.7	19.2	21.9
12	0.7	1.6	2.8	4.2	5.8	7.6	9.5	11.6	13.8	16.2	18.7	21.3
13	0.7	1.6	2.7	4.1	5.6	7.4	9.2	11.3	13.4	15.7	18.1	20.6
14	0.7	1.5	2.6	4	5.5	7.1	8.9	10.9	13	15.2	17.5	20
15	0.7	1.5	2.6	3.8	5.3	6.9	8.6	10.5	12.5	14.7	16.9	19.3
16	0.6	1.4	2.4	3.7	5.1	6.6	8.3	10.1	12	14.1	16.2	18.5
17	0.6	1.4	2.3	3.5	4.8	6.3	7.9	9.6	11.4	13.3	15.4	17.5
18	0.6	1.3	2.2	3.3	4.5	5.9	7.4	9	10.7	12.5	14.4	16.4

Table 2b. Table representing the flame length (m) for Stand D, in 2006, in the east complex of Brookhaven National Laboratory, Upton, NY.

1-h Moisture %	Midflame Wind Speed (upslope) km/h											
	3.218688	6.437376	9.656064	12.874752	16.09344	19.312128	22.530816	25.749504	28.968192	32.18688	35.405568	38.624256
4	0.9	1.4	1.7	2.1	2.4	2.7	3	3.3	3.6	3.9	4.1	4.4
5	0.9	1.3	1.6	2	2.3	2.6	2.9	3.1	3.4	3.6	3.9	4.1
6	0.8	1.2	1.5	1.9	2.2	2.4	2.7	3	3.2	3.5	3.7	3.9
7	0.8	1.2	1.5	1.8	2.1	2.3	2.6	2.8	3.1	3.3	3.5	3.8
8	0.8	1.1	1.4	1.7	2	2.3	2.5	2.7	3	3.2	3.4	3.6
9	0.7	1.1	1.4	1.7	1.9	2.2	2.4	2.7	2.9	3.1	3.3	3.5
10	0.7	1.1	1.4	1.6	1.9	2.1	2.4	2.6	2.8	3	3.2	3.4
11	0.7	1	1.3	1.6	1.9	2.1	2.3	2.5	2.8	3	3.2	3.4
12	0.7	1	1.3	1.6	1.8	2.1	2.3	2.5	2.7	2.9	3.1	3.3
13	0.7	1	1.3	1.5	1.8	2	2.2	2.5	2.7	2.9	3.1	3.2
14	0.7	1	1.3	1.5	1.7	2	2.2	2.4	2.6	2.8	3	3.2
15	0.7	1	1.2	1.5	1.7	1.9	2.1	2.3	2.5	2.7	2.9	3.1
16	0.6	0.9	1.2	1.4	1.7	1.9	2.1	2.3	2.5	2.7	2.8	3
17	0.6	0.9	1.1	1.4	1.6	1.8	2	2.2	2.4	2.6	2.7	2.9
18	0.6	0.8	1.1	1.3	1.5	1.7	1.9	2.1	2.3	2.4	2.6	2.7

IV. Discussion

The orange striped oakworm (*Anisota senatoria*) is a moth that tends to deposit its young (up to 500 eggs per female) onto oak leaves.¹³ When the young hatch, the larvae consume the oak leaves, attacking the newest growth first for the most nitrogen, and move up the branches toward the trunk.¹⁴ As the orange striped oakworm is a fall defoliator, oak trees (*Quercus* spp.) are preparing for winter dormancy, and the defoliation should not impact the tree as much due to reduced photosynthesis. However, the

compounded stress and herbivory caused by the presence of the gypsy moth (*Lymantria dispar*) in the spring and summer, along with other stressful environmental factors, can cause oak death.¹³ We believe that the aggressive herbivory, and other environmental factors that occurred over time between the vegetation inventories of 2006 and 2016, caused oak death that opened the canopy and allowed understory vegetation (as seen in the live woody fuel values) to increase dramatically.

In addition to the orange striped oakworm and the gypsy

Table 3a. Table representing the surface rate of spread (maximum) (m/min) for Stand D, in 2016, in the east complex of Brookhaven National Laboratory, Upton, NY.

1-h	Midflame Wind Speed (upslope)											
Moisture	km/h											
%	3.218688	6.437376	9.656064	12.874752	16.09344	19.312128	22.530816	25.749504	28.968192	32.18688	35.405568	38.624256
4	2.4	5.6	9.6	14.3	19.6	25.5	31.8	38.6	45.8	53.4	61.4	69.7
5	2.3	5.2	9	13.4	18.4	23.9	29.9	36.3	43	50.2	57.7	65.5
6	2.2	5	8.5	12.7	17.4	22.6	28.3	34.3	40.7	47.5	54.6	62
7	2.1	4.7	8.1	12.1	16.6	21.6	27	32.7	38.8	45.3	52	59.1
8	2	4.5	7.8	11.6	15.9	20.7	25.9	31.4	37.2	43.4	49.9	56.7
9	1.9	4.4	7.5	11.2	15.4	20	25	30.3	35.9	41.9	48.1	54.7
10	1.9	4.2	7.3	10.9	14.9	19.4	24.2	29.3	34.8	40.6	46.6	53
11	1.8	4.1	7.1	10.6	14.5	18.8	23.5	28.5	33.8	39.4	45.3	51.5
12	1.8	4	6.9	10.3	14.1	18.3	22.9	27.7	32.9	38.4	44.1	50.1
13	1.7	3.9	6.7	10	13.7	17.8	22.2	27	32	37.3	42.9	48.7
14	1.7	3.8	6.5	9.7	13.3	17.3	21.6	26.2	31.1	36.3	41.7	47.3
15	1.6	3.7	6.3	9.4	12.9	16.8	20.9	25.4	30.1	35.1	40.4	45.8
16	1.5	3.5	6.1	9.1	12.4	16.1	20.2	24.5	29	33.9	38.9	44.2
17	1.5	3.4	5.8	8.7	11.9	15.5	19.3	23.4	27.8	32.4	37.3	42.3
18	1.4	3.2	5.5	8.2	11.3	14.7	18.3	22.2	26.4	30.8	35.4	40.2

Table 3b. Table representing the flame length (m) for Stand D, in 2016, in the east complex of Brookhaven National Laboratory, Upton, NY.

1-h	Midflame Wind Speed (upslope)											
Moisture	km/h											
%	3.218688	6.437376	9.656064	12.874752	16.09344	19.312128	22.530816	25.749504	28.968192	32.18688	35.405568	38.624256
4	1.9	2.8	3.7	4.4	5.1	5.7	6.3	6.9	7.5	8.1	8.6	9.1
5	1.9	2.7	3.5	4.2	4.8	5.4	6	6.6	7.1	7.7	8.2	8.7
6	1.8	2.6	3.3	4	4.6	5.2	5.8	6.3	6.8	7.3	7.8	8.3
7	1.7	2.5	3.2	3.8	4.5	5	5.6	6.1	6.6	7.1	7.5	8
8	1.7	2.4	3.1	3.7	4.3	4.9	5.4	5.9	6.4	6.8	7.3	7.7
9	1.6	2.4	3	3.6	4.2	4.7	5.2	5.7	6.2	6.7	7.1	7.5
10	1.6	2.3	3	3.6	4.1	4.6	5.1	5.6	6.1	6.5	6.9	7.4
11	1.5	2.3	2.9	3.5	4	4.5	5	5.5	5.9	6.4	6.8	7.2
12	1.5	2.2	2.8	3.4	3.9	4.5	4.9	5.4	5.8	6.3	6.7	7.1
13	1.5	2.2	2.8	3.4	3.9	4.4	4.8	5.3	5.7	6.1	6.5	6.9
14	1.5	2.1	2.7	3.3	3.8	4.3	4.7	5.2	5.6	6	6.4	6.8
15	1.4	2.1	2.7	3.2	3.7	4.2	4.6	5.1	5.5	5.9	6.3	6.6
16	1.4	2	2.6	3.1	3.6	4.1	4.5	4.9	5.3	5.7	6.1	6.5
17	1.3	2	2.5	3	3.5	3.9	4.4	4.8	5.1	5.5	5.9	6.2
18	1.3	1.9	2.4	2.9	3.3	3.8	4.2	4.6	4.9	5.3	5.6	6

moth, the southern pine beetle (*Dendroctonus frontalis*) has recently been detected on Long Island. Though the literature is inconclusive on the exact effects of forest pests on tree mortality and fire behavior, bark beetles can cause drastic pine mortality that could add woody debris to the fuel loading.¹⁵ The interactions between pests and forest fuel loadings have been addressed more in the western United States than the northeastern United States, with the conclusion that increased pest presence increases tree mortality and fuel accumulation.¹⁶ Despite current policies to

reduce or prevent the introduction of forest pests into the United States, their presence is increasing rapidly with a large concentration entering through the northeast.¹⁷ This lack of certainty and lack of literature on these interactions in the northeastern United States is alarming due to their increased presence and combined contribution to the fuel load in our study site. This should be further studied to truly ascertain forest pest impacts on northeastern ecosystems and fire behavior.

The moderate-to-high intensity wildfire that passed through

Table 4a. Table representing the surface rate of spread (maximum) (m/min) for Stand A, in 2006, in the east complex of Brookhaven National Laboratory, Upton, NY.

1-h Moisture	Midflame Wind Speed (upslope)											
	km/h											
%	3.218688	6.437376	9.656064	12.874752	16.09344	19.312128	22.530816	25.749504	28.968192	32.18688	35.405568	38.624256
4	1.4	3.1	5.3	8	11	14.4	18.1	22.1	26.3	30.8	35.6	40.5
5	1.3	2.8	4.9	7.4	10.2	13.3	16.7	20.4	24.3	28.5	32.8	37.4
6	1.2	2.7	4.6	6.9	9.5	12.4	15.6	19	22.7	26.6	30.6	34.9
7	1.1	2.5	4.3	6.5	9	11.7	14.7	17.9	21.4	25	28.9	32.9
8	1.1	2.4	4.1	6.2	8.5	11.1	14	17	20.3	23.8	27.4	31.2
9	1	2.3	3.9	5.9	8.2	10.7	13.4	16.3	19.4	22.8	26.3	29.9
10	1	2.2	3.8	5.7	7.9	10.3	12.9	15.7	18.7	21.9	25.3	28.8
11	0.9	2.1	3.7	5.5	7.6	9.9	12.5	15.2	18.1	21.2	24.5	27.9
12	0.9	2.1	3.6	5.3	7.4	9.6	12.1	14.8	17.6	20.6	23.7	27.1
13	0.9	2	3.4	5.2	7.2	9.3	11.7	14.3	17.1	20	23	26.3
14	0.9	1.9	3.3	5	6.9	9.1	11.4	13.9	16.5	19.3	22.3	25.4
15	0.8	1.9	3.2	4.8	6.7	8.7	11	13.4	15.9	18.7	21.5	24.5
16	0.8	1.8	3.1	4.6	6.4	8.4	10.5	12.8	15.3	17.9	20.6	23.5
17	0.7	1.7	2.9	4.4	6.1	7.9	10	12.2	14.5	17	19.6	22.3
18	0.7	1.6	2.7	4.1	5.7	7.4	9.3	11.4	13.6	15.9	18.3	20.9

Table 4b. Table representing the flame length (m) for Stand A, in 2006, in the east complex of Brookhaven National Laboratory, Upton, NY.

1-h Moisture	Midflame Wind Speed (upslope)											
	km/h											
%	3.218688	6.437376	9.656064	12.874752	16.09344	19.312128	22.530816	25.749504	28.968192	32.18688	35.405568	38.624256
4	1.1	1.6	2.1	2.5	2.9	3.3	3.6	4	4.3	4.6	4.9	5.2
5	1	1.5	1.9	2.3	2.7	3.1	3.4	3.7	4	4.3	4.6	4.9
6	1	1.4	1.8	2.2	2.6	2.9	3.2	3.5	3.8	4.1	4.4	4.7
7	0.9	1.4	1.8	2.1	2.5	2.8	3.1	3.4	3.7	3.9	4.2	4.5
8	0.9	1.3	1.7	2	2.4	2.7	3	3.3	3.5	3.8	4	4.3
9	0.9	1.3	1.6	2	2.3	2.6	2.9	3.2	3.4	3.7	3.9	4.2
10	0.9	1.2	1.6	1.9	2.2	2.5	2.8	3.1	3.3	3.6	3.8	4.1
11	0.8	1.2	1.6	1.9	2.2	2.5	2.8	3	3.3	3.5	3.8	4
12	0.8	1.2	1.5	1.9	2.2	2.4	2.7	3	3.2	3.5	3.7	3.9
13	0.8	1.2	1.5	1.8	2.1	2.4	2.7	2.9	3.2	3.4	3.6	3.8
14	0.8	1.2	1.5	1.8	2.1	2.3	2.6	2.9	3.1	3.3	3.6	3.8
15	0.8	1.1	1.4	1.7	2	2.3	2.5	2.8	3	3.2	3.5	3.7
16	0.8	1.1	1.4	1.7	2	2.2	2.5	2.7	2.9	3.1	3.4	3.6
17	0.7	1	1.3	1.6	1.9	2.1	2.4	2.6	2.8	3	3.2	3.4
18	0.7	1	1.3	1.5	1.8	2	2.3	2.5	2.7	2.9	3.1	3.3

Stand A in 2012 top-killed a large number of oaks. The 100-h dead fuel load increased radically in Stand A because of to the number of top-killed trees, and the reduction of the shrub layer allowed herbaceous fuels to increase. Oaks preferentially store resources in their roots before their shoots,¹⁸⁻¹⁹ and therefore responded well to the disturbances by resprouting.¹⁹ Many of the oaks that were top-killed have since coppiced.

1-hour and 10-hour fuels have the greatest impact on starting and carrying fires because of their lower heat capacities required

for combustion.²⁰ Stand D had not experienced fire for 10 years, and now has an increased live fuel load that is predicted to burn with high rate of spread and flame length values. The lack of fire is compounded by the herbivory and defoliation from the orange striped oakworm and the gypsy moth that caused tree mortality, opened the canopy, increased available sunlight to the forest floor, ultimately increasing the accumulation of live fuels. Stand D should be burned soon with increased precaution to reduce its 1 and 10-h fuels. Stand A's 1 and 10-h fuel load was reduced in

Table 5a. Table representing the surface rate of spread (maximum) (m/min) for Stand A, in 2016, in the east complex of Brookhaven National Laboratory, Upton, NY.

1-h Moisture	Midflame Wind Speed (upslope)											
	km/h											
%	3.218688	6.437376	9.656064	12.874752	16.09344	19.312128	22.530816	25.749504	28.968192	32.18688	35.405568	38.624256
4	0.8	1.9	3.2	4.8	6.6	8.6	10.8	13.1	15.6	18.3	21.1	24
5	0.8	1.7	3	4.5	6.2	8.1	10.2	12.4	14.7	17.2	19.9	22.6
6	0.7	1.7	2.9	4.3	5.9	7.7	9.6	11.7	14	16.4	18.8	21.5
7	0.7	1.6	2.7	4.1	5.6	7.4	9.2	11.2	13.4	15.6	18	20.5
8	0.7	1.5	2.6	3.9	5.4	7.1	8.9	10.8	12.9	15	17.3	19.7
9	0.7	1.5	2.5	3.8	5.2	6.8	8.6	10.4	12.4	14.5	16.7	19.1
10	0.6	1.4	2.5	3.7	5.1	6.6	8.3	10.1	12.1	14.1	16.3	18.5
11	0.6	1.4	2.4	3.6	5	6.5	8.1	9.9	11.7	13.7	15.8	18
12	0.6	1.4	2.3	3.5	4.8	6.3	7.9	9.6	11.5	13.4	15.4	17.6
13	0.6	1.3	2.3	3.4	4.7	6.1	7.7	9.4	11.2	13.1	15.1	17.1
14	0.6	1.3	2.2	3.3	4.6	6	7.5	9.1	10.9	12.7	14.7	16.7
15	0.6	1.3	2.2	3.2	4.5	5.8	7.3	8.9	10.6	12.4	14.3	16.2
16	0.5	1.2	2.1	3.1	4.3	5.6	7.1	8.6	10.2	12	13.8	15.7
17	0.5	1.2	2	3	4.2	5.4	6.8	8.3	9.8	11.5	13.3	15.1
18	0.5	1.1	1.9	2.9	4	5.2	6.5	7.9	9.4	11	12.7	14.4

Table 5b. Table representing the flame length (m) for Stand A, in 2016, in the east complex of Brookhaven National Laboratory, Upton, NY.

1-h Moisture	Midflame Wind Speed (upslope)											
	km/h											
%	3.218688	6.437376	9.656064	12.874752	16.09344	19.312128	22.530816	25.749504	28.968192	32.18688	35.405568	38.624256
4	0.8	1.2	1.6	1.9	2.2	2.5	2.7	3	3.3	3.5	3.7	4
5	0.8	1.2	1.5	1.8	2.1	2.4	2.6	2.9	3.1	3.3	3.6	3.8
6	0.8	1.1	1.4	1.7	2	2.3	2.5	2.7	3	3.2	3.4	3.6
7	0.7	1.1	1.4	1.7	1.9	2.2	2.4	2.7	2.9	3.1	3.3	3.5
8	0.7	1	1.3	1.6	1.9	2.1	2.3	2.6	2.8	3	3.2	3.4
9	0.7	1	1.3	1.6	1.8	2.1	2.3	2.5	2.7	2.9	3.1	3.3
10	0.7	1	1.3	1.5	1.8	2	2.2	2.5	2.7	2.9	3.1	3.2
11	0.7	1	1.3	1.5	1.8	2	2.2	2.4	2.6	2.8	3	3.2
12	0.7	1	1.2	1.5	1.7	1.9	2.2	2.4	2.6	2.8	2.9	3.1
13	0.7	0.9	1.2	1.5	1.7	1.9	2.1	2.3	2.5	2.7	2.9	3.1
14	0.6	0.9	1.2	1.4	1.7	1.9	2.1	2.3	2.5	2.7	2.8	3
15	0.6	0.9	1.2	1.4	1.6	1.8	2	2.2	2.4	2.6	2.8	2.9
16	0.6	0.9	1.1	1.4	1.6	1.8	2	2.2	2.4	2.5	2.7	2.9
17	0.6	0.9	1.1	1.3	1.5	1.7	1.9	2.1	2.3	2.5	2.6	2.8
18	0.6	0.8	1.1	1.3	1.5	1.7	1.9	2	2.2	2.4	2.5	2.7

the fire it experience 4 years ago, and has low predicted rate of spread and flame length values. This indicates that a prescribed burn could be potentially ineffective until there is a larger accumulation of these smaller fuels.

V. Conclusion

The fire suppression of Stand D has led to a potentially dangerous accumulation of fine woody fuels that should be remedied with a more frequent prescribed fire regime. Stand A's reduction of fuels from a fire that occurred 4 years ago is a testament to the effect of a single burn. This study has produced the most up to date fuel loading data for two of the eleven total stands in the northeastern corner of Brookhaven National Laboratory. This data will prove valuable for those trying to complete a prescribed burn in these areas, and could be potentially used in further pitch pine mixed oak forest research on Long Island. Not all of the data was able to be analyzed in time for this analysis because of the drying protocol for the 40x40cm² harvest plots; as such, our analysis was not as comprehensive as it would have been if granted more time.

VI. References

- ¹ Bond W. J., & Keeley, J. E. (2005). Fire as a global 'herbivore': the ecology and evolution of flammable ecosystems. *Trends in Ecology and Evolution*, 20(7), 387-394.
- ² Bento-Goncalves, A., Vieira, A., Úbeda, X., & Martin, D. (2012). Fire and Soils: Key concepts and recent advances. *Geoderma*, 191, 3-13.
- ³ Twisp, G. W. (1998). Fire and fuels management: Definitions, ambiguous terminology and references. Retrieved from <https://www.nps.gov/olym/learn/management/upload/fire-wildfire-definitions-2.pdf> Accessed on 7/19/2016.
- ⁴ Scheler, R. M., Tuyl, S. V., Clark, K., Hayden, N. G., Hom, J., & Mladenoff, D. J., (2008). Simulation of forest change in the New Jersey Pine Barrens under current and precolonial conditions. *Forest Ecology and Management*, 255, 1489-1500.
- ⁵ Brown, J. K., Reinhardt, E. D., & Kramer, K. A. (2003). Coarse Woody Debris: Managing benefits and fire hazard in the recovering forests. USDA Forest Service Gen. Tech. 1-17.
- ⁶ Heinsch, F. A., & Andrews, P. L. (2010). BehavePlus fire modeling system, version 5.0: Design and Features. General Technical Report RMRS-GTR-249. Fort Collins, CO: USDA Forest Service, Rocky Mountain Research Station.
- ⁷ Brookhaven National Laboratory (2016). Our Natural Resources. Sustainable Brookhaven. Retrieved from <https://www.bnl.gov/about/sustainability/naturalResources.php> Accessed July 18, 2016
- ⁸ Forman, R. T. T. (1979). Vegetational Gradients of the Pine Plains and Barrens of Long Island. In: Forman Richard T.T., ed. Pine Barrens: Ecosystem and Landscape, Academic Press, Pages 265-281.
- ⁹ Brookhaven National Laboratory (2016) Prescribed Fire Plan.
- ¹⁰ Brown, J. K. (1974). Handbook for Inventorying Downed Woody Material. General Technical Report INT-16. Ogden, UT: USDA Forest Service, Intermountain Forest & Range Experiment Station.
- ¹¹ Iwamoto, K. (2005) Sampling Methods. Managing Fuels in Northeastern Barrens. Retrieved from <http://www.umass.edu/nebarrensfuels/methods/index.html> Accessed July 25, 2016

<http://www.umass.edu/nebarrensfuels/methods/index.html> Accessed July 25, 2016

- ¹² Packard, K. C. & Radtke, P. J. (2007). Forest sampling combining fixed- and variable- radius sample plots. *Canadian Journal of Forest Research*, 37(8), 1460-1471.
- ¹³ Siegert, N.W. & McCullough, D. G. (1998). Identification and Management of Orange-striped Oakworm. Michigan State University Extension. Extension Bulletin E-2654.
- ¹⁴ Lawson, D. L., Merritt, R.W., Klug, M.J., & Martin, J.S. (1982). The utilization of late season foliage by the orange striped oakworm, *Anisota senatoria*. *Entomologia Experimentalis et Applicata*, 32(3), 242-248.
- ¹⁵ Hicke, J. A., Johnson, M. C., Hayes, J. L., & Preisler, H.K. (2012). Effects of bark beetle-caused tree mortality on wildfire. *Forest Ecology and Management*, 271, 81-90.
- ¹⁶ Parker, T. J., Clancy, K. M., & Mathiasen, R. L. (2006). Interactions among fire, insects and pathogens in coniferous forests of the interior western United States and Canada. *Agricultural and Forest Entomology*, 8,167-189.
- ¹⁷ Lovett, G. M., Weiss, M., Liebhold, A. M., Holmes, T. P., Leung, B., Lambert, K. F., ...& Weldy, T. (2016). Nonnative forest insects and pathogens in the United States: Impacts and policy options. *Ecological Applications*, 0(0), 1-19.
- ¹⁸ Dillaway, D. N., Stringer, J. W., & Rieske, L. K. (2007). Light availability influences root carbohydrates, and potentially vigor, in white oak advance regeneration. *Forest Ecology and Management*, 250, 227-233.
- ¹⁹ Rieske, L. K. & Dillaway, D. N. (2008). Response of two oak species to extensive defoliation: Tree growth and vigor, phytochemistry, and herbivore suitability. *Forest Ecology and Management*, 256,121-128.
- ²⁰ Byram, G. M. (1959). Combustion of forest fuels. In: Forest fire: control and use, 2nd edition. New York, McGraw-Hill, chapter 3, 61-89.

VII. Acknowledgements

This project was supported in part by the U.S. Department of Energy, Office of Science, and Office of Workforce Development for Teachers and Scientists (WDTS) under the Science Undergraduate Laboratory Internships Program. This project was also supported in part by the Brookhaven National Laboratory-Virginia Pond Scholarship Program under the VPSP-Supplemental Undergraduate Research Program (SURP). Thanks to the Environmental Protection Division for graciously helping us whenever we asked and allowing us to occupy a part of 528 for the summer. Many thanks to the other interns for their help and support.

Mass calibration for the PROSPECT shortbaseline reactor neutrino experiment

Nicholas Gabriel

Department of Physics, University of Mary Washington, Fredericksburg, VA 22401

David Jaffe

Physics Department, Brookhaven National Laboratory, Upton, NY 11973

Abstract

The Precision Reactor Oscillation and SPECTrum Experiment (PROSPECT) seeks to make a high precision measurement of the antineutrino spectrum produced by the High Flux Isotope Reactor at Oak Ridge National Laboratory using a segmented liquid scintillator detector. This measurement could definitively answer questions about the observed reactor flux and spectrum anomalies and search for neutrino oscillations with meterscale wavelengths. The optically separated segments of the antineutrino detector can vary in volume due to variations in the construction of the optical separators (i.e., there is a finite tolerance in their dimensions). As a result, the expected number of inverse beta decays in a specific detector cell has an uncertainty proportional to the uncertainty in the cell volume. This uncertainty can be estimated by measuring the number of alpha decays produced in a cell by a radioactive source that is uniformly distributed within the detector medium.

Timecorrelated alpha decays present in the decay chains of Actinium227 and Uranium232 have been investigated for this purpose. Monte Carlo particle transport calculations in conjunction with analytic calculations were used to calculate the observed distribution of alpha energies by the detector. Assuming uniform distribution of the calibration source, this method of calibration allows for an uncertainty in volume of less than 1%, allowing for variations in the antineutrino flux to be determined accurately at the cell level. Successful mass calibration could allow for more definitive conclusions to be drawn from neutrino oscillation data, and hence impact the design and implementations of next generation neutrino experiments.

I. Introduction

A. Background

Previous reactor neutrino experiments have observed a ~6% deficit between the expected electron antineutrino ($\bar{\nu}_e$) flux compared to theoretical predictions. In the process of making a high precision measurement of the $\bar{\nu}_e$ flux at the High Flux Isotope Reactor (HFIR), the PROSPECT collaboration seeks to achieve the following [1]:

- Search for signatures of eVscale sterile neutrinos (a proposed beyond the Standard Model particle);
- Test predictions of the $\bar{\nu}_e$ spectrum made using models of reactorsystems;
- Demonstrate new techniques for aboveground neutrino experiments;
- Develop techniques for use in nonproliferation;

The proposed detector design consists of two detectors, a Phase I and Phase II detectors. Both phases are ⁶Liloaded liquid scintillator (LiLS) detectors. Phase I is a mobile, optically seg-

mented detector that will survey a range of 712 meters from the HFIR core. Phase II will be stationary and will cover a range from 1620 meters. The optically segmented Phase I detector (Fig. 1.b) will allow for interaction topology cuts, and potentially, for the measurement of neutrino oscillations and relative flux between segments [2]. The latter functionality of the detector is limited by the precision to which the mass (or volume) of each segment is known.

B. Mass calibration motivation

Due to the low mass and composition of the optical separators, individual segments could have variations in mass at the ~1% level. It is not possible to mechanically measure the dimensions of each segment (e.g. with a ruler) once the detector is constructed. One way to make this measurement is to spike the LiLS with a radioactive source and measure the number of decays in a certain cell by that source. This decay has to be easily distinguished from backgrounds present in the detector, and hence the ideal radioactive source for mass calibration should have the following properties:

- time correlated decays (i.e. one decay right after another)
- highly localized energy deposit
- short range
- monoenergetic

Based on these criteria, timecorrelated α,α pairs can provide high precision calibration due in part to the fact that they have a range that is much smaller than the dimensions of the PROSPECT modules. The decay sequence $Rn \rightarrow Po \rightarrow Pb$ is present (and timecorrelated) in the decay chains of ^{227}Ac and ^{232}U , and have been investigated calibration. Though these α,α pairs are highly localized, their range does have some effect on the precision to which they can be used for mass calibration.

Decay	$t_{1/2}$	E_0 (MeV)	Branch. Ratio	R_α (μm)
$^{219}Rn \rightarrow ^{215}Po$	3.96 s	6.819	.794	59.95
		6.553	.129	55.56
		6.425	.075	53.87
Decay	$t_{1/2}$	E_0 (MeV)	Branch. Ratio	R_α (μm)
$^{215}Po \rightarrow ^{211}Pb$	1.78 ms	7.386	.999	67.07

Table I: ^{227}Ac α,α decay sequence, half life, initial energy, branching ratio, and cutoff range

Decay	$t_{1/2}$	E_0 (MeV)	Branch. Ratio	R_α (μm)
$^{220}Rn \rightarrow ^{216}Po$	55.6 s	6.288	1	53.1
Decay	$t_{1/2}$	E_0 (MeV)	Branch. Ratio	R_α (μm)
$^{215}Po \rightarrow ^{211}Pb$	1.78 ms	7.386	.999	67.07

Table II: ^{232}U α,α decay sequence, half life, initial energy, branching ratio, and cutoff range

C. Characteristics of ^{227}Ac and ^{232}U α,α pairs

The α,α sequences $^{219}\text{Rn} \rightarrow ^{215}\text{Po} \rightarrow ^{211}\text{Pb}$ of ^{227}Ac and $^{220}\text{Rn} \rightarrow ^{216}\text{Po} \rightarrow ^{216}\text{Pb}$ of ^{232}U have one major difference; whereas the ^{232}U sequence consists of two monoenergetic α 's, the first α of the ^{227}Ac sequence has 3 possible energies (Table 1). The cutoff range, R_α is defined as the distance that only 1% of α 's of a certain energy will exceed.

Notably, the range of all α 's listed is much less than that of the PROSPECT detector cell dimensions, i.e. α decays are highly localized. By a simple geometric argument, it can be shown that almost all α pairs will deposit all of their energy in the LS. This is the primary advantage of using an α,α coincidence over, for example, β,α coincidences. The number of coincidences detected in a certain cell, then, should be nearly proportional to the mass of the LS, and further, the expected number of inverse beta decays in that cell:

$$N_{\alpha,\alpha} \propto m_{LS} \propto \langle N_{IBD} \rangle.$$

Some uncertainty arises due to α 's that deposit some amount of kinetic energy in the cell wall rather than in the LS. These α 's and their effect on the mass calibration process is the primary concern of the following sections.

II. Methods

Before calculating the distribution of E_α (which from here on will denote the amount of energy deposited into the LS by an α particle with initial energy E_0), we can first calculate the number of α,α coincidences that are in the interior region of the 3 detector cell and thus will deposit all of their energy in the LS (i.e., $E_\alpha = E_0$) by nature of their location within the cell. The total volume of a detector cell is approximately $V_t = 120\text{cm} \times 14.4\text{cm} \times 14.4\text{cm} = 24883.20\text{cm}^3$, the interior region is then $V_i = (120\text{cm} - 2R_\alpha) \times (14.4\text{cm} - 2R_\alpha) \times (14.4\text{cm} - 2R_\alpha)$, where R_α is the maximum projected range of each α to be determined by a Monte Carlo transport simulation and the inequality $R_\alpha > \langle r_{proj} \rangle$ is always true due to range straggling. The maximum projected range of each energy of the α,α sources is tabulated below. The peripheral volume of an optical module is then $V_p = V_t - V_i$, the volume of a cell where some fraction of α 's will have $E_\alpha < E_0$. In order to understand the detector response to an α,α source, we must divide the active volume of a segment (Liquid Scintillator in Fig. 1.c) into several regions that will have different distributions of α energy, E_α in the active volume:

Optical module: Total active volume of a segment, denoted V_t

- **Fiducial volume:** the interior region of a segment where the α 's will deposit all of their energy into the LS, $V_i = V_t - V_p$
- **Peripheral volume:** region where an alpha can exit the LS; Has relation to other regions $V_p = V_f + V_e + V_c$ and $V_p = V_t - V_i$.
- **Face volume:** region where an alpha can exit the LS via one module wall only (6 total), denoted V_f . Comprises most of the periphery
- **Edge volume:** region where an alpha can exit the LS via two different module walls (12 total), denoted V_e . Comprises a small fraction of the periphery.
- **Corner volume:** region where an alpha can exit the LS via 3 different module walls (8 total), denoted V_c . Comprises a small fraction of the periphery.

The subregions of the peripheral volume can naturally be defined by the cutoff range, R_α . Due to the short range of α decays, the face volumes dominate the periphery and we have $V_f \approx V_p$.

Therefore, we need only to consider the distribution of E_α in V_f to understand the effect that the periphery has on mass calibration.

The distribution of E_α in the periphery was determined for each α in the ^{227}Ac and ^{232}U α,α decay sequences. This was

done by calculating the probability density function (pdf) for an α to travel a distance r before leaving the active volume of a segment,

$$f(r) = \frac{1}{6}r - \frac{1}{8}r^2$$

which was determined from the geometry of V_f .

In order to obtain the pdf $f(E_\alpha)$ via the transformation

$$f(E_\alpha) = f[r(E_\alpha)] \left| \frac{d}{dE_\alpha} r(E_\alpha) \right|$$

$E_\alpha(r)$ must be determined. This was done by interpolating the results of Monte Carlo simulations performed using SRIM [3] (Fig. 3 and 4). For each α energy under consideration, the outgoing energy of α 's was output after traversing sampled thicknesses of liquid scintillator. The thickness values of the LS were linearly spaced from 0 up to a thickness where no α 's would vacate the LS.

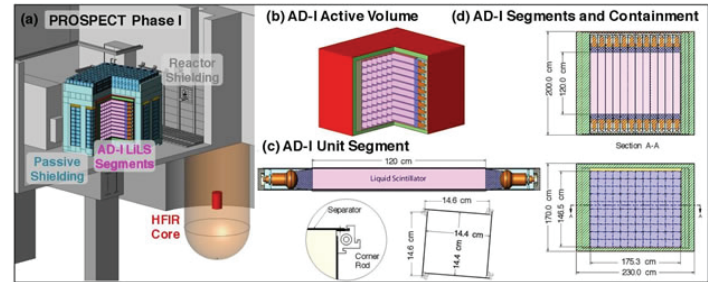


Fig 1: Various views of the PROSPECT Phase I antineutrino detector (a,b,d) and a single detector module (c)

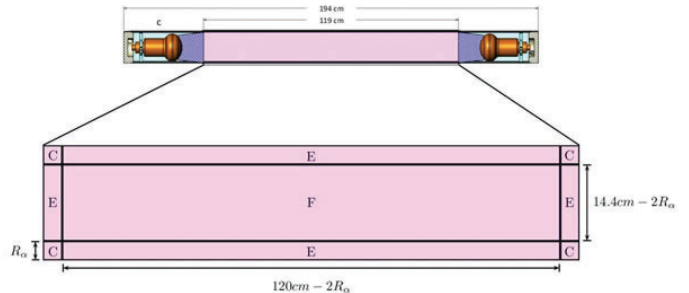


Fig. 2: Side view of the the periphery subvolumes, F=face, E=edge, and C=corner (Note: the magnitude of R_α is greatly exaggerated to show the different regions of the periphery)

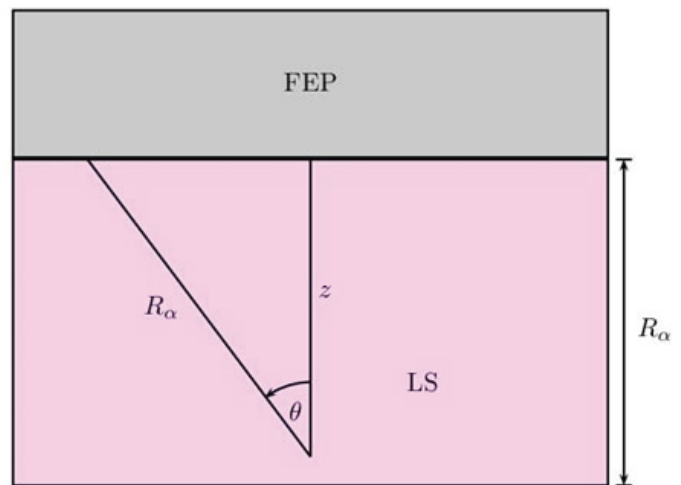


Figure 3: Diagram of a face region geometry, V_f

Additional thicknesses were then sampled near the end of range to allow for a reasonable cutoff range R_α to be determined. The value of R_α was taken to be where less than 1% of all α 's vacated the LS (and less than 1% of α 's vacated for thicknesses greater than that value). Xylene was used in simulations with a density set to that of EJ309 (.959 g/cm³). For compounds having a similar composition and bond structure, the difference in mass stopping power is negligible; even for compounds of dissimilar bond structure the difference in mass stopping power is small [4].

For each α energy under consideration the outgoing energy of α 's was output after traversing sampled thicknesses of liquid scintillator. The thickness values of the LS were linearly spaced from 0 up to a thickness where no α 's would vacate the LS. Additional thicknesses were then sampled near the end of range to allow for a reasonable cutoff range R_α to be determined. The value of R_α was taken to be where less than 1% of all α 's vacated the LS (and less than 1% of α 's vacated for thicknesses greater than that value).

When varying the thickness of the LS, the parameter that is truly being changed is z . It is unnecessary to also sample several values of θ at each z , because the radial spread of α 's due to multiple Coulomb scattering is extremely small for the values of E_α considered. The energy and range that corresponds to the largest radial spread of all considered is $E_0 = 7.386$ MeV through 68.79 μm of LS, which had an RMS spread of 0.97 μm .

III. Results

The proportion of the total volume made up by each of these regions depends on R_α , but for the α energies in question the face regions make up the majority of this volume (more than 99.9%, see the last column of Table III) The face regions comprise the majority of the peripheral volume of the optical modules, and are also geometrically much easier to work with, so we will assume that the entire periphery has the same distribution in E_α . It is quite easy to establish upper and lower bounds for the error that this assumption produces, but this effect is small enough for the calibration sources considered as to be negligible. This effect is not negligible when $O(R_\alpha) = O(L)$, where L is any dimension of an optical module (e.g. for β decays with range $O(1\text{cm})$).

Before a full calculation of the actual α distribution, we can determine the fraction of α 's in the periphery for which $E_\alpha < E_0$ by integrating over the solid angle where $0 < z < R_\alpha$ and $0 < \theta < \theta_{\max} = \arccos(z/R_\alpha)$, where we have used the fact that $R_\alpha = z \sec \theta_{\max}$ (or more generally that $r = z \sec \theta$). It is convenient to

let $R_\alpha = 1$ so that $0 < z < 1$ and $0 < \theta < \theta_{\max} = \arccos(z)$ before integrating:

$$\frac{1}{4\pi} \int_0^1 \int_0^{\theta_{\max}} \int_0^{2\pi} \sin \theta d\phi d\theta dz = \frac{1}{2} \int_0^1 \int_0^{\theta_{\max}} \sin \theta d\theta dz = \frac{1}{4}$$

The fraction of α 's that have $E_\alpha < E_0$ is then $V_p/4 V_t$. This tells us that only a small proportion of α 's will be affected at all. Since we are concerned with the probability that at least one of the α 's of an α,α coincidence will have $E_\alpha < E_0$, we must calculate the joint probability for each α in the decay chains considered. For the 232U α,α coincidence:

$$P\left(\bigcup_{i=1}^2 E_{\alpha,i} < E_{0,i}\right) = P(E_{\alpha,1} < E_{0,1}) + P(E_{\alpha,2} < E_{0,2}) - P(E_{\alpha,1} < E_{0,1})P(E_{\alpha,2} < E_{0,2}) \\ = \frac{1}{4} \left(\frac{V_{p,1}}{V_t} + \frac{V_{p,2}}{V_t} \right) - \left(\frac{1}{4} \right)^2 \left(\frac{V_{p,1}}{V_t} \right) \left(\frac{V_{p,2}}{V_t} \right) = .00083$$

For the α,α decay chain of 227Ac where there are three different branches for the 219Rn \rightarrow 215Po decay, we must sum over the j branches with weights w_j :

$$\sum_{j=1}^3 w_j P_j \left(\bigcup_{i=1}^2 E_{\alpha,ij} < E_{0,ij} \right) = .00094$$

So less than 0.1% of α,α coincidences will be affected for either source.

In order to calculate the fraction of α,α pairs that will pass a specific energy cut, we must integrate $f(E_\alpha)$ from 0 to an energy cut $E_0 - E_c$. Because the PROSPECT detectors operate by counting photoelectrons produced by scintillation light, the photoelectron yield can be calculated as

$$\text{Yield} = E_\alpha \times \text{quenching} \times \text{QE} \times \frac{\text{photons}}{\text{MeV}} = \\ E_\alpha \times .113 \times .2 \times 6000 = 135.6 E_\alpha$$

Because the photomultiplier tubes of the detector count photoelectrons, the distribution in the yield follows Poisson statistics, and hence the standard deviation in the number of photoelectrons (Yield) is the square root of the yield. The corresponding energy cut for n standard deviations is then

$$E_c = n\sqrt{\text{Yield}} = n\sqrt{135.6 E_\alpha}$$

IV. Conclusion

For both radioactive sources considered, it was shown that it is possible to use α,α sources for Phase I segment mass calibration

$\langle E_\alpha(r) \rangle$ vs. r

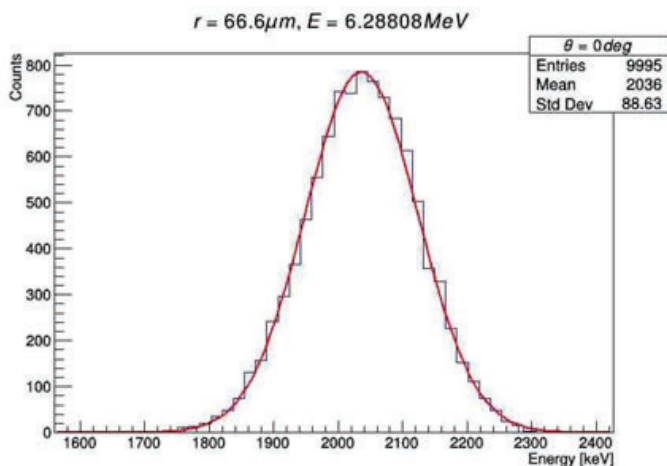


Figure 4: The output of a single Monte Carlo simulation

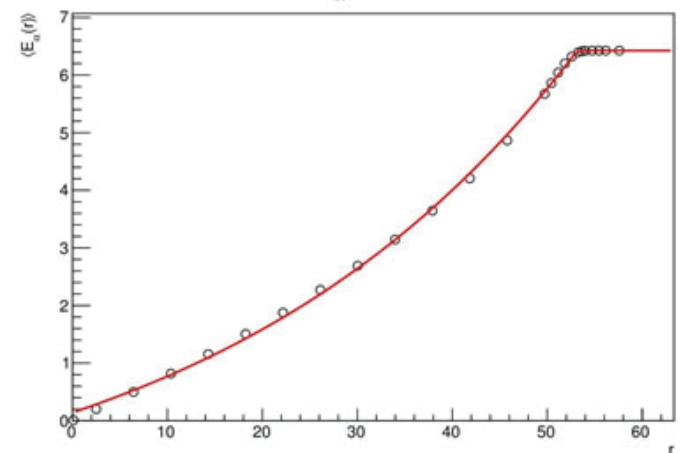


Figure 5: Plot of the mean alpha energy $E_\alpha(r)$ vs. distance traversed r

to better than 1%. This could allow for a more detailed picture of ν_e oscillations at short baselines. One possibility that still needs to be investigated further is whether or not the calibration source will stick to the inner surface of the optical modules.

V. References

- ¹ J. Ashenfelter et al. [PROSPECT Collaboration], arXiv:1508.06575 [physics.insdet].
- ² D. Norcini et al. [PROSPECT Collaboration], arXiv:1510.09082v1 [physics.insdet].
- ³ Z. F. Ziegler and J. P. Biersack, SRIM 201203, <http://www.srim.org>,(2012).
- ⁴ M. J. Berger et al., NIST ASTAR Database, <http://www.nist.gov/pml/data/star/>(1999).

VI. Acknowledgments

Special thanks to David Jaffe for his wisdom and guidance. This project was supported by the U.S. Department of Energy, Office of Science, as part of the Science Undergraduate Laboratory Internships Program (SULI).

E_0 (MeV)	R_α (μm)	V_p/V_t	V_f/V_p	C (MeV)	r_0 (μm)	k (μm^{-1})	ν
6.288	53.04	.00156	.99956	2.00	53.48	6.41	.003
6.425	54.81	.00161	.99955	2.00	54.6	8.52	.003
6.553	56.58	.00166	.99954	2.00	55.19	8.23	.003
6.778	59.75	.00176	.99951	2.00	57.3	7.87	.003
6.819	60.31	.00177	.99950	2.00	58.7	6.7	.003
7.386	68.79	.00202	.99944	3.00	67.0	6.05	.003

Table III: E_0 , cutoff range, ratio of peripheral volume to total volume, ratio of face volume to peripheral volume, and the four fit parameters for the logistic function.

A fundamental study and characterization of the surface structure of a Cs/TiO₂ (110) model catalyst

Isamar Garrido Rodriguez

Chemical Engineering, The City University of New York, NY, NY 10031
Rebecca Hamlyn, David Grinter, Sanjaya D. Senanayake, and Jose Rodriguez
Chemistry Department, Brookhaven National Laboratory, Upton, NY 11973

Abstract

Metal oxides catalysts are extensively used in industrial processes due to their enhanced lifetime, catalytic activity, and selectivity in response to growing energy and environmental demands. An in-depth understanding of the structure of metal oxides catalysts can lead us to design novel catalysts that remain stable and highly active under demanding reaction conditions. Modern-sensitive techniques have aided in the discovery of more efficient catalysts, yet there is still a gamut of novel catalysts to explore. A full comprehension of the structure of new metal oxides catalysts offers solutions to the current limitations in industrial catalytic processes, energy production and consumption, and environmental sustainability. This project focuses on imaging on the atomic scale a well-defined rutile Titania (TiO₂) single crystal under an oxygen (O₂) environment using Scanning Tunneling Microscopy (STM) in an ultra-high vacuum (UHV) environment to study how the structure, catalytic activity, and selectivity of TiO₂(110) is affected by the addition of alkali compounds such as Cesium(Cs). We hypothesized that the addition of Cs enhances the chemistry of the TiO₂(110) crystal. To carry out this project the surfaces were prepared with several sputtering and annealing cycles of the raw crystal before oxidation with O₂ and the subsequent vapor deposition of Cs. STM Images of the Cs/o-TiO₂(110) crystal was performed and further analysis was conducted using Scala Pro. Upon the complete characterization of the Cs/o-TiO₂(110) surface, other structures of Titania catalysts will be further explored. After the completion of this research, now I have a deeper understanding of how the surface atomic structure of metal/metal oxide catalysts may affect their reactivity and selectivity toward chemical reactions. Moreover, I am more familiarized with advanced in situ characterization techniques such as STM and XPS.

I. Introduction

Since the introduction of the term “Catalysis” by Jacob Berzelius in 1835 to the most recent advancements of the 21st century, heterogeneous catalysis has been fundamental to the development of promising materials in chemical industries, pharmaceutical industries, and academic research [1,2]. Metal and mixed metal oxides play an essential role in heterogeneous catalysis processes either as active phases or as supports [1]. They are employed in a variety of organic reactions, such as the selective hydrogenation and isomeration of olefins, water-gas shift (WGS) reaction, dehydrogenation of alcohols, oxidation of CO and alkenes, NO reduction, SO₂ destruction, photolysis of water, and others [3]. Their vast use is attributed to their reducibility, oxygen storage, acid-base and redox properties, high stability, and greater surface area, which improves the reactivity, stability and increases selectivity to yield of desirable products [1,3].

Oxides of transition and noble metals are widely used as catalysts for synthetic chemical conversions because of their enhanced catalytic activity [2]. The latter being slowly replaced by the formers owing to their abundance, low cost of production, easy generation and selectivity [1]. VO_x, RuO_x, CeO_x, WO_x and TiO₂ are common metal oxides used either as supports or as active phases, being titania the most investigated catalyst in the surface science of metal oxides [3,4]. Titania has a wide range of applications. In heterogeneous catalysis, for instance, it is used as a photocatalyst in solar cells for the production of hydrogen and electric energy [4]. Very commonly, alkali metals and metal oxides are deposited onto titania, often acting as promoters to enhance the overall activity of titania or to improve selectivity to it [1,4].

New research has been directed to study titania supported catalysts for the improvement of traditional catalytic processes and enhance selectivity towards desired reactions and/or to find pathways that proceed at milder conditions, give environmentally

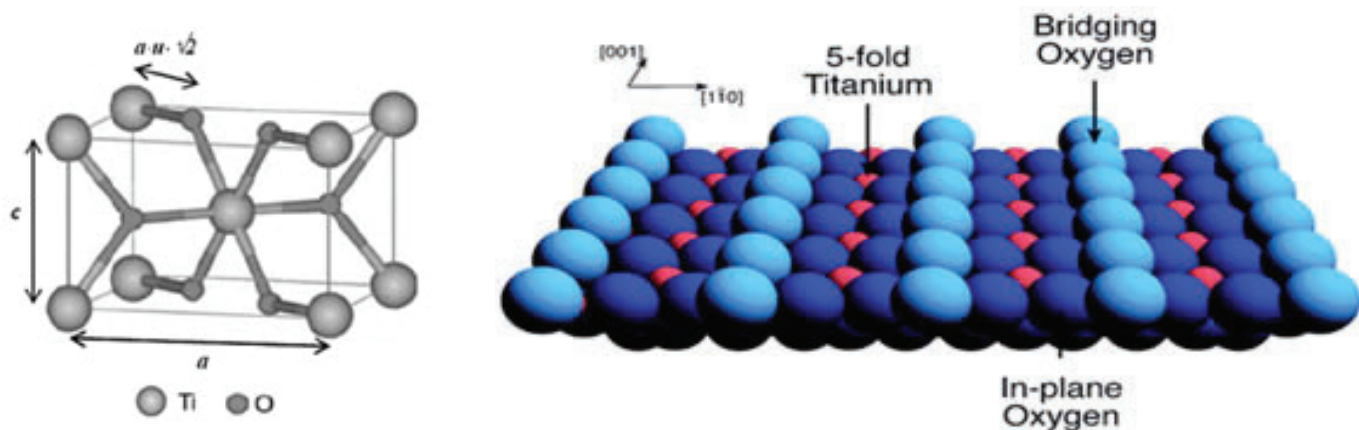


Fig.1. (Left) Figure of the rutile Titania unit cell. (Right) Model of the bulk structure of rutile TiO₂(110)-(1x1) surface. The blue and red spheres represent oxygen and titanium, respectively. There are no Oxygen Vacancies (missing oxygens) in the figure above. Chi Lun Pang et. al. “Chemical Reactions on rutile TiO₂(110)”. 2008. The university of Manchester. Royal Society of Chemistry. Web. July 2016.

friendly products and need less energy [1-4]. Despite the great progress, as stated in ref. 3, there is still a variety of fundamental science questions that need to be explored.

This research focuses on imaging rutile $\text{TiO}_2(110)$ (see fig.1) under an oxygen environment using Scanning Tunneling Microscopy (STM) (see fig. 2 and 3) in combination with X-ray Photoelectron Spectroscopy (XPS) to study how the structure, catalytic reactivity and selectivity of the $\alpha\text{-TiO}_2(110)$ catalyst is affected by the addition of other elements, such as Cs. We hypothesized that the addition of Cs enhances the overall activity of the $\alpha\text{-TiO}_2(110)$ crystal. A detailed understanding of the mechanism of the varied reactions to be investigated on the $\alpha\text{-TiO}_2(110)$ surface promises solutions to the current limitations of the exiting catalytic processes

II. Experimental procedure

We performed this experiment using an Omicron Scanning Tunneling Microscope (STM) (see fig. 3) under ultra-high vacuum (UHV) conditions ($\sim 5 \times 10^{-10}$ Torr). The first stage of the experiment consisted of the sample preparation. We prepared the $\text{TiO}_2(110)$ sample by sputtering the crystal with Argon ions for 10 minutes at a pressure of $\sim 4 \times 10^{-5}$ Torr and a drain current of ~ 5 nA. After the sputtering process, we annealed the sample in UHV with a supply current of ~ 3.1 A and bias of 0.7 kV. We annealed the sample for 10 minutes starting the timer when the emission current was at the desired value (for TiO_2 to appx. 600 C, this is 28.0 mA.) After the annealing process, we reported the temperature of the sample to be around 1000 K using an infrared thermometer. We repeated this processes several times until the crystal was in optimum conditions for imaging. Then, we let the crystal cool down for two hours before we transferred it to the sample holder and began the process of scanning. Following that, we approached the tip to sample (see fig. 2 and 4) and began imaging the clean $\text{TiO}_2(110)$ surface using Scala Pro 3.6. We took several images of the sample and compared the features shown in the structure depicted in the images to those previously reported in literature for rutile $\text{TiO}_2(110)$.

The second part of the experiment consisted of exposing the

crystal to an oxygen environment. Prior to the introduction of oxygen to the chamber, we filled the gas lines with oxygen and then pumped the gas lines out. This process was repeated several times until we confirmed that there was only oxygen in the lines. Then, we leaked some oxygen into the chamber and observed the mass spectrometer (MS) display looking for an increase in oxygen. When the MS reported oxygen in the chamber, the crystal was exposed to 1 L O_2 (100 seconds of 1×10^{-8} Torr) at room temperature. Subsequently, we started the scanning process for the $\alpha\text{-TiO}_2(110)$ crystal and took several images of the surface. These images were analyzed and compared to the ones taken of the clean surface.

The third part of the experiment consisted of the deposition of Cs on $\alpha\text{-TiO}_2(110)$. To initiate this process, we degassed the chamber with Cs for 15 minutes (@ 6.0 A and 0.7 V). Then, we placed the sample at the optimum position for sputtering and dosed with Cs for 10 seconds. After, we made the sample ready for scanning and took several images of the Cs/ $\alpha\text{-TiO}_2(110)$. Then, we moved back the crystal to the sputtering position and deposited Cs for another 20 seconds. Finally, we scanned the crystal and took images of it. These images we compared to the images taken for a 10 seconds Cs deposition.

III. Results and Discussion

The characteristics of the features identified on the raw $\text{TiO}_2(110)$ crystal such as Ti rows, step edges, terraces, Oxygen vacancies and others matched with those found in the literature. Fig. 4 is an STM image of the stoichiometric structure of $\text{TiO}_2(110)$. The bright lines correspond to Ti atoms instead of the bridging oxygen atoms (see fig.1). The average height of the step edges was found to be ~ 3.5 Å and the distance between two consecutive rows ~ 6.5 Å. Moreover, step edges were found to run parallel to the (001) and (111) directions. All these in accordance with reference 4. Also, several Oxygen vacancies perpendicular to the bright rows and with no apparent order were spotted on the raw crystal. However, no hydroxyls groups were identified on the surface of the of $\text{TiO}_2(110)$ surface (see fig.4).

Fig.5 shows the presence of possible reduced Titania rows on

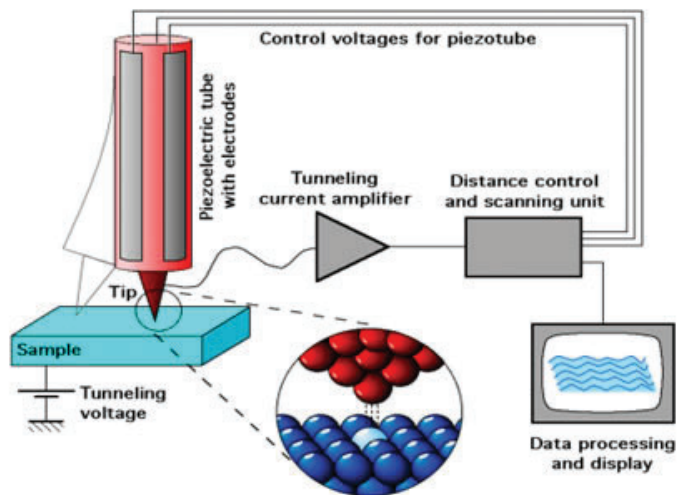


Fig.2. Diagram of the fundamental parts of the Scanning Tunneling Microscope that explains in brief how the STM functions. The STM works by registering the changes in current due to the changes in height from the tip to the sample. Michael Schmid. "The Scanning Tunneling Microscope".2011. IAP. Web. July 2016

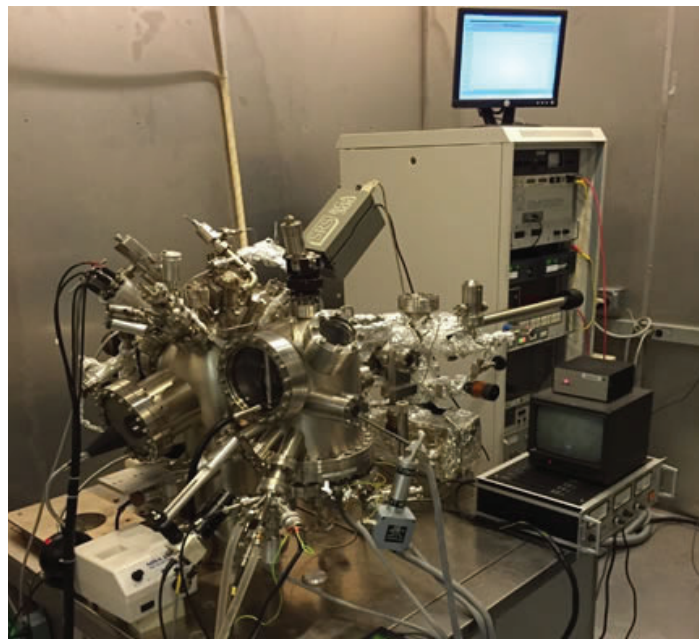


Fig.3. Picture of the STM used for this experiment

the $\text{TiO}_2(110)$ crystal that may have been caused by annealing the sample. Also, several point defects that have not yet been identified are depicted on the $o\text{-TiO}_2(110)$ surface. Further characterization of the $o\text{-TiO}_2(110)$ surface has to be carry out to identify these impurities. Moreover, no reduction in oxygen vacancies was identified after exposing the crystal to 1 L O_2 (see fig. 6), rather several depressions were seen on the surface (see fig. 7 left). Yet, there is not sufficient data to determine if these depressions were caused by oxidizing the TiO_2 crystal.

Finally, after a 10 seconds Cs deposition a decrease in impurities was seen on the Cs/ $o\text{-TiO}_2(110)$ surface (see fig. 7 right). This may have been caused by the adsorption of Cs atoms, however, better resolution images and further analysis using STM and other techniques such as XPS needs to be done on the crystal to verify this.

IV. Conclusion

The development of novel metal oxide catalyst offers solutions to the current catalytic processes limitations. Hence, developing more efficient catalysts is of great interest. The focus of this work was to study and characterize the surface of a Cs/ TiO_2 model catalyst to investigate its structure and chemical reactivity. At this point, there is not sufficient data to conclude whether or not the deposition of Cs on TiO_2 enhances the overall chemistry of the titania surface but we have established a fundamental understanding of its surface atomic morphology. Further investigation needs to be done on the Cs/ $\text{TiO}_2(110)$ surface using STM and other characterization techniques such as XPS to validate our hypothesis.

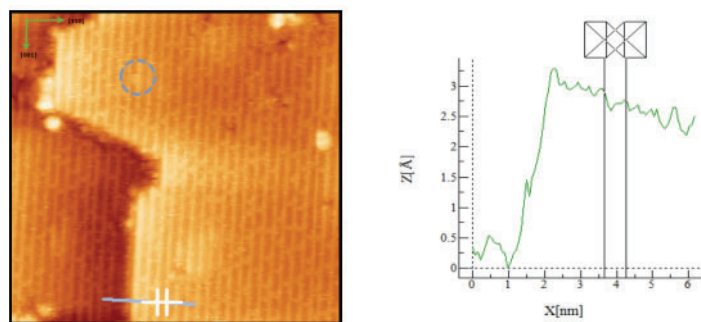


Fig.4. STM image of a $\text{TiO}_2(110)\text{-}(1\times 1)$ surface (30x30 nm, 1.5 V sample bias, 0.1 nA tunneling current) after sputtering and annealing to 1000 K for 10 minutes and its line profile. The blue dotted circle in the STM image shows the presence of an oxygen vacancy. The line profile shows the height of one step edge to be $\sim 3.5 \text{ \AA}$ and the distance between two consecutive rows $\sim 6.5 \text{ \AA}$.

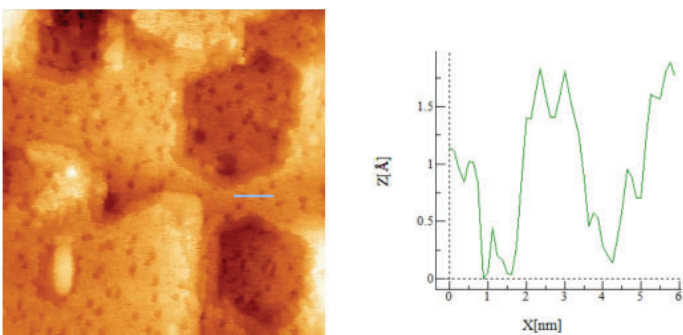


Fig.6. STM image of a $o\text{-TiO}_2(110)$ surface (50x50 nm, 1.0 V sample bias, 0.1 nA tunneling current) after dosing with 1 L O_2 and its line profile. Several depressions can be identified on the surface. The drop in height can be better visualized in the line profile.

V. Acknowledgements

“This project was supported in part by the U.S. Department of Energy, Office of Science, Office of Workforce Development for Teachers and Scientists (WDTS) under the Community College Internships Program (CCI).”

VI. References

- [1] Zaera, Francisco. *New Challenges in Heterogeneous Catalysis for the 21st Century*. Springer Link. Springer Science Business Media, 23 Mar. 2012. Web. 10 July 2016.
- [2] Gawande, Manoj B., Rajesh K. Pandey, and Radha V. Jayaram. *Role of Mixed Metal Oxides in Catalysis Science—versatile Applications in Organic Synthesis*. Royal Society of Chemistry. *Catalysis Science and Technology*, 03 Feb. 2012. Web. 15 July 2016.
- [3] Stacchiola, Dario J., Sanjaya D. Senanayake, Ping Liu, and Jose Rodriguez. “Fundamental Studies of Well-Defined Surfaces of Mixed-Metal Oxides: Special Properties of $\text{MO}_x/\text{TiO}_2(110)$ $\{M = \text{V, Ru, Ce, or W}\}$.” - *Chemical Reviews (ACS Publications)*. N.p., 4 Feb. 2012. Web. 30 July 2016.
- [4] Diebold, Ulrike. *The Surface Science of Titanium Dioxide*. Amsterdam: Elsevier, 2003. Science Direct. Jan. 2003. Web. 11 July 2016.

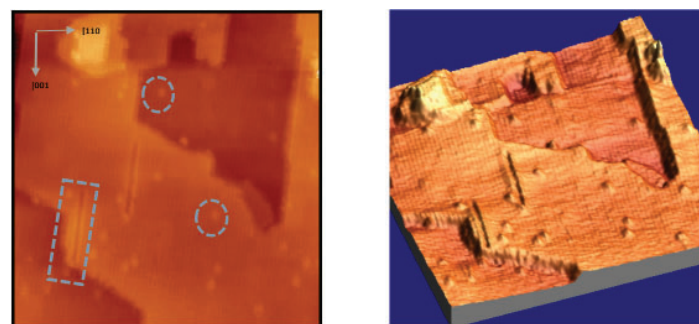


Fig.5. STM image of a $\text{TiO}_2(110)$ surface (50x50 nm, 1.03 V sample bias, 0.1 nA tunneling current) after sputtering and annealing to 1000 K for 10 minutes and image of its 3D surface. The blue dotted square in the STM image shows the presence of a possible reduced titania row along the $[001]$ direction and the blue dotted circles represents impurities that have not yet been identified.

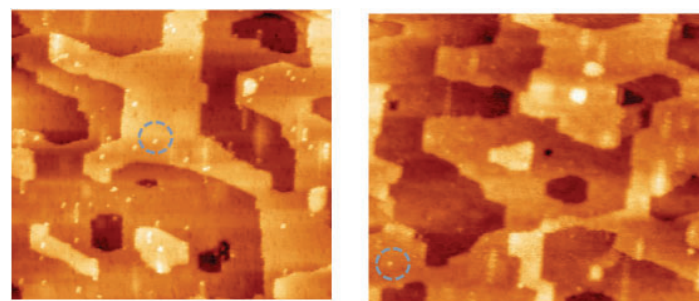


Fig.7. STM images of a $o\text{-TiO}_2(110)$ surface (100x100 nm, 1.0 V sample bias, 0.1 nA tunneling current) after dosing with 1 L O_2 (left) and Cs/ $o\text{-TiO}_2(110)$ surface (100x100 nm, 1.2 V sample bias, 0.1 tunneling current) after a 10 seconds Cs deposition (right). Impurities on the surface are marked with a blue dotted circles.

Nuclear structure studies of ^{202}Hg and ^{203}Tl using deep-inelastic collisions

E. J. Gass

Physics, Stony Brook University, Stony Brook, New York, 11794

E. A. McCutchan, A. A. Sonzogni

National Nuclear Data Center, Brookhaven National Laboratory, Upton, New York 11973, USA

W. Loveland, J. S. Barrett, R. Yanez

Chemistry Department, Oregon State University, Corvallis, Oregon, 97331

C. J. Chiara, J. L. Harker, and W.B. Walters

Department of Chemistry and Biochemistry, University of Maryland, College Park, Maryland 20742

S. Zhu, A. D. Ayangeakaai, P. Carpenter, J. P. Greene, R. V. F. Janssens, T. Lauritsen

Physics Division, Argonne National Laboratory, Argonne, Illinois 60439

Nuclei with a few valence nucleons outside ^{208}Pb are crucial for testing the nuclear shell model and guiding our understanding of single particle structure. Data in this region are also potentially relevant to nuclear astrophysics. This analysis focused on the high-spin structure of ^{202}Hg and ^{203}Tl . Excited states in these nuclei were populated through deep-inelastic reactions from a beam of ^{136}Xe and that was incident on a thick target of ^{208}Pb in the Gammasphere array at Argonne National Laboratory. The level schemes of ^{202}Hg and ^{203}Tl were extended by locating a new isomer in each nucleus and a number of new high-spin states built on top of the isomers.

I. INTRODUCTION

Doubly-magic ^{208}Pb has been studied extensively and is the basis for much of what is known about heavy nuclei, but nuclei removed from it by only a few nucleons are mostly unexplored. A reason for this is that nuclides in that region are difficult to access. They are not easily produced through fusion-evaporation or fission reactions [1] [2]. Transfer reactions have been used to populate excited states in nuclei that are not otherwise accessible, and causing these reactions is why the deep-inelastic collisions technique was used in this experiment. Large arrays of many gamma-ray detectors, combined with techniques for detailed gamma-coincidence analysis, are essential in studies of these reactions [1]. These nuclei are essential to testing and developing the nuclear shell model, which is useful for predicting the structures of exotic nuclides. Nuclei that are only a few particles away from closed shells, like ^{202}Hg and ^{203}Tl , tend to have fewer possible configurations that can lead to their excited states. This can lead to clear configuration assignments and simpler structures that the shell model describes well [3]. For example, pair approximations have been developed which reduce prohibitively complex shell-model calculations while maintaining much of the models predictive power. This applies well to ^{203}Tl because it is four neutrons and one proton away from the closed shells. In theory, the four neutron holes form pairs, leaving the proton hole to dominate the nucleus structure [4]. In particular, high-spin isomers have contributed much to the shell models development. Once they have been identified, they can be used to increase the sensitivity of deep-inelastic collisions studies and to measure a variety of more detailed properties like electromagnetic moment [1].

II. EXPERIMENT

The ATLAS accelerator and Gammasphere array at Argonne National Laboratory were used for the experiment. A 1 pnA beam of ^{136}Xe at an energy of 785 MeV was incident on a 50 mg/cm² target of ^{208}Pb . The targets thickness allowed it to stop all products of the reaction. Seventy-eight of Gammaspheres Compton-suppressed high-purity germanium detectors were included in the analysis, and the experiment used Gammaspheres analog electronics. Data were collected with both doubles and triples triggers for 48 hours each.

III. ANALYSIS

Data were divided into a prompt timeframe, which lasted a few nanoseconds after the beam reacted with the target, and a delayed timeframe, which began after the prompt and lasted several hundred nanoseconds. Data were sorted into γ - γ and γ - γ - γ histograms. These were gated using these time conditions to correlate gamma rays in coincidence with each other within either the prompt or delayed interval and between the two. There were four types of γ - γ - γ coincidence histograms, called cubes. The analysis began with the DDD cube, so named because it relates three γ -rays from the delayed time. This cube is best for constructing cascades below isomers. From there, one can proceed to the PDD cube, which contains data from both the prompt and delayed times. It is primarily used to gate on two γ -rays from the delayed time to find γ -rays associated with them from the prompt time, which allows structures above an isomer to be connected with structures below it. The PPD cube is similar to the PDD, but its gates relate one delayed γ -ray and two prompt ones. The PPP cube involves only prompt γ -rays and is best suited to examining cascades above isomers. Intensities of the γ -rays were also measured. Below the isomer, it is helpful to compare the flux through γ -rays in a cascade to make sure that flux is conserved as a way of confirming that levels are properly placed. Additionally, the relative intensities provide information on the ordering of the γ -rays within the cascade, as lower levels tend to have higher intensities. This method of determining the order of a cascade is particularly useful above the isomer, where less branching was observed. Time- γ -ray matrices were also created, which related the related the γ -rays coincident with a peak at a particular energy with the exact times that they were detected. This allowed the change in the intensities of the γ -rays over time to be measured, which was used to calculate the half-lives of the isomers. Data were analyzed using a modified version of Radware Gf3 and Levit8r.

IV. RESULTS AND DISCUSSION

In ^{203}Tl , a new isomer, a new cascade of seven γ -rays above the isomer, four new gamma rays, and four energy levels below the isomer were located. These are shown in figure 1. The positions in the level scheme of several previously-observed γ -rays were changed. The 264 keV γ -ray was moved to its position feeding the 2908 keV level because it was in coincidence with the 532 keV γ -ray and those below it but not with the 350 keV γ -ray. While the 10 keV γ -ray was not directly observed, its approximate position in the scheme can be inferred from the positions of the 477 keV, 497 keV, and 387 keV γ -rays, though the exact order of the 232 keV, 588 keV, and 10 keV γ -rays cannot be determined from this data. Gamma rays with a half-life of 7.9 nanoseconds had been observed in an earlier experiment, but it did not produce enough data to locate the isomer [4]. In this analysis, the isomers half-life was determined to be 7.5 ± 0.4 nanoseconds. This was determined by gating on a peak above the isomer, the 210 keV γ -ray, building time- γ -ray-matrices, and then measuring how the intensities of several peaks from below the isomer decayed as the time after the detection of the 210 keV γ -ray increased.

In ^{202}Hg , a new isomer and two cascades above the isomer were located. The position of the isomer at 2059 keV was determined when the 94 keV γ -ray was identified. The isomers half-life was determined to be 10.5 ± 0.3 nanoseconds. The previously-known levels and γ -rays below the isomer (as shown in the figure) were confirmed. Flux below the isomer is conserved when calculations for the conversion electrons are taken into account, for example the 222 keV γ -ray has an intensity of 53 with conversion electrons, the 872 has 50, and with the 351 their sum is within the uncertainty of the 195 of the 654 keV ray. These calculations were done using the theoretical values for the conversion coefficients [5]. The coincidence data suggests that the two cascades above the isomer have few, if any, γ -transitions connecting them, and they are connected to the isomer by the 163 keV and 598 keV γ -rays.

E_i	E_f	E_γ	I_γ
439	0	439	
960	0	960	9 (2)
960	439	520	85 (2)
1120	439	680	33 (6)
1182	960	222	33 (4)
1311	439	872	44 (6)
1311	960	351	100
1311	1182	129	13 (4)
1965	1311	654	173 (13)
1965	1120	845	32 (5)
1989	1120	869	24 (4)
2059	1965	94	19 (8)

Properties of γ -rays of ^{202}Hg below its isomer (all values are in keV, and intensities are corrected for efficiency and normalized to the 351 keV ray).

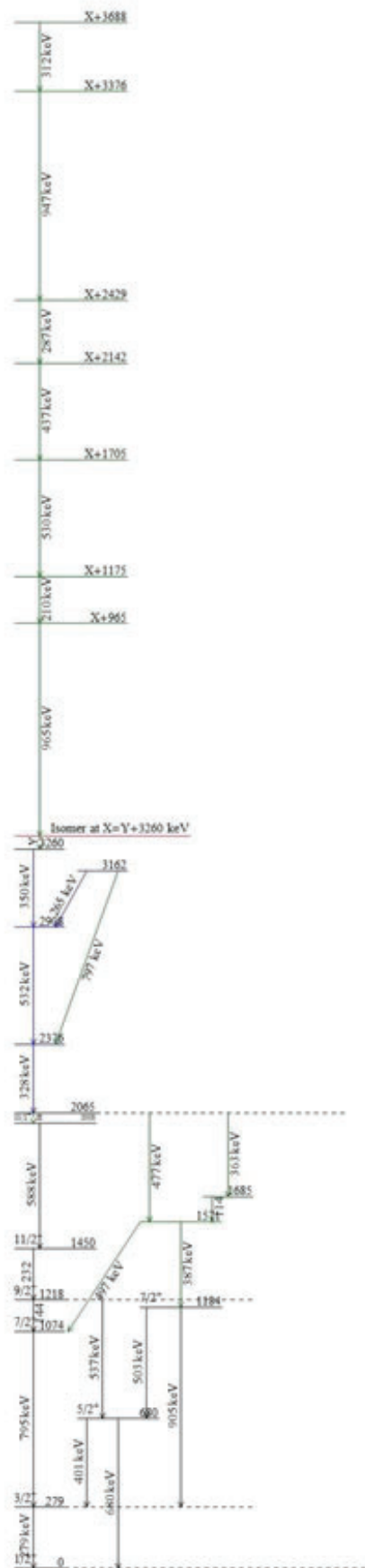


FIG. 1: The new level scheme of ^{203}Tl as determined from the present analysis. New levels are green, and previously observed γ -rays which have been moved to new locations are blue. The red line is the isomer.

Structural study of polycyclic aromatic ligands and salen-type metal complexes

Stephanie N. Ortiz Castillo Gellyz, N. Gonzalez Diaz, and Dalice M. Piñero Cruz

Chemistry and Department of Interdisciplinary Sciences, University of Puerto Rico-Río Piedras, San Juan, PR 00931

Eric Dooryhee

Photon Science, Brookhaven National Laboratory, Upton, NY 11973

Abstract

The goal of this project is to synthesize and characterize metal complexes from coronene and naphthalene ligands, which are polycyclic aromatic molecules, in order to test how well the products that are complexed can serve as assets of memory devices. The pi orbitals of these molecules have a high electron density which could turn them into good electron donors to serve as ligands and thus, coordinate with the metal centers. To accomplish our goals, we used the characterization technique PXRD (X-ray Powder Diffraction), at the National Synchrotron Light Source II (NSLS-II) at Brookhaven National Laboratory, a beamline facility dedicated to research in Materials Sciences. The PXRD serves for verifying the formation of metal complexes, studying their structural/chemical behavior, and determining the fingerprint structure of crystalline materials. Obtaining these structures is imperative for our research in order to confirm that the polycyclic aromatic compounds are coordinating with the transition metals (Mn^{+2} , Pd^{+2} , Fe^{+2} , Co^{+2} , Cu^{+2} , Ni^{+2} , Pt^{+2}). While obtaining the structures is still ongoing work, the obtained data was analyzed using programs such as Python and Fit2D. First results from this work exhibit different powder diffraction patterns of the complexes naphthalene and coronene with the metals. Also, once the graphs for these structures were obtained, the different displacements in the peaks of each product show that a coordination complex was produced. This study served as an opportunity to gain valuable knowledge on how to use different programs for data analysis the experience of working with the PXRD at the synchrotron beamline.

I. Introduction

Chemical compounds that contain metal and organic ligands are classified as metal complexes. For metal complexes that have a high number of unpaired electron and large axial anisotropies there is a category known as Single-molecule magnets (SMMs). SMMs exhibit superparamagnetic behavior below a certain blocking temperature which aids in the relaxation of the magnetization,

of molecular origin, in the absence of an applied magnetic field. The broad applicability of inorganic/organic synthesis has led to a series of SMMs. The use of Single Molecule Magnets (SMMs) over other magnetic materials present several advantages such as uniformity of magnetic domains due to their molecular nature and the ability to tune their properties through structural control.¹⁻⁵ Nevertheless, one of the issues encountered with the synthesis of SMMs is finding the appropriate building blocks to achieve structural control over the metal complexes to be synthesized. In order to overcome this problem, ligands with high charge delocalization like coronene and naphthalene (polycyclic aromatic compounds) are used.

These group of molecules consist of numerous carbon atoms joined together to form unique aromatic rings. These ligands are difficult to coordinate because their electronic density is compromised to its aromatic system of rings, however, their pi orbitals have a high electron density which could turn the ligands into good electron donors and thus, coordinate with the metal centers under a non-competitive ligand environment. Also, we synthesized this metals complexes using novel structures of salen-coronene and salen-naphthalene ligands. One of the goals of this work is to unravel the parameters controlling the formation of novel structures and frameworks from the new class of salen-based polycyclic aromatic metal complexes, which will allow the study of new magnetic hybrid materials.

The characterization technique PXRD (X-ray Powder Diffraction) is a rapid analytical technique primarily used for phase identification of a crystalline material that can provide information on unit cell dimensions and give structural information of the distribution of atoms in the unit cell. All diffraction methods are based on generation of X-rays in an X-ray tube. These X-rays are directed at the sample, and the diffracted rays are collected. This technique can be used for verifying the formation of metal complexes and study their structural/chemical behavior. Once the material is identified, its structure, packing of atoms, interatomic distances and angles may be determined using X-ray crystallography. Because of this, X-ray diffraction is one of the most important

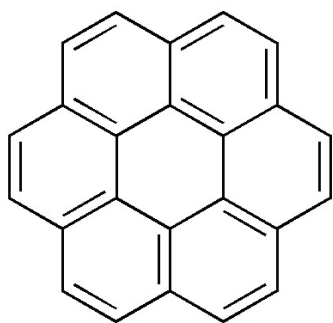


Figure 1. Coronene

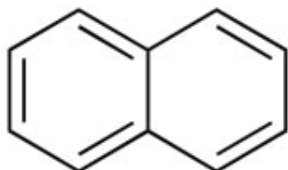


Figure 2. Naphthalene

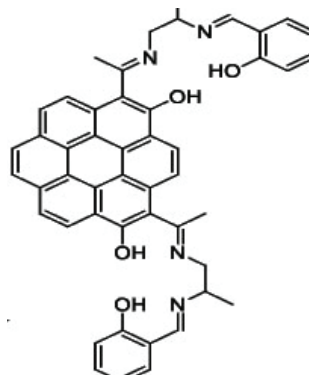


Figure 3. Salen-coronene

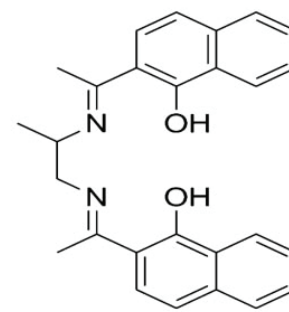


Figure 4. Salen-naphthalene

characterization tools used in solid state chemistry and Materials Science. NSLS-II beamline facility is dedicated to provide users with state-of-the-art instrumentation for performing research in many scientific fields that make use of monochromatic X- rays for diffraction and radiographic imaging of samples under *in-situ* settings, high pressures and/or different temperatures.

II. Experimental Section & Results

A. University of Puerto Rico Río Piedras Campus

The first part of this project began at The Piñero Research Laboratory at The University of Puerto Rico, Río Piedras Campus. The work that was done at the laboratory included the synthesis of the coronene and naphthalene metal complexes as well as the synthesis of the metal complexes with salen-functionalized coronene and naphthalene. The metallic salts used in this experiment were $\text{Fe}(\text{ClO}_4)_2$, $\text{Mn}(\text{ClO}_4)_2$, $\text{Co}(\text{ClO}_4)_2$, $\text{Ni}(\text{ClO}_4)_2$, $\text{Pd}(\text{ClO}_4)_2$, $\text{Pt}(\text{ClO}_4)_2$, and $\text{Cu}(\text{ClO}_4)_2$. Due to the hygroscopic nature of the salts, all the reaction sets were carried out in an inert atmosphere to prevent hydration and the oxidation of the metal ions. Thus, the reactions were performed using a glove box under Argon gas. For the coronene reactions, the ratio of metal to ligand used was 6 moles of metal per mole of coronene. This was done because an excess of metal was needed in order to increase the chances of a coordination between the metal and the ligand. Similarly, for the naphthalene reaction the ratio used was 3 moles of metal per mole of naphthalene.

B. Brookhaven National Laboratory National Synchrotron Light Source II (NSLS-II)

The samples were analyzed in an X-Ray Powder Diffractometer (XPD) localized in the National Synchrotron Light Source II, beamline 28-ID-2, at Brookhaven National Laboratory. This beamline is also equipped with several detectors in order to perform other types of diffraction experiments in addition to XPD, such as SAXS (small angle X-Ray scattering) and PDF (pair

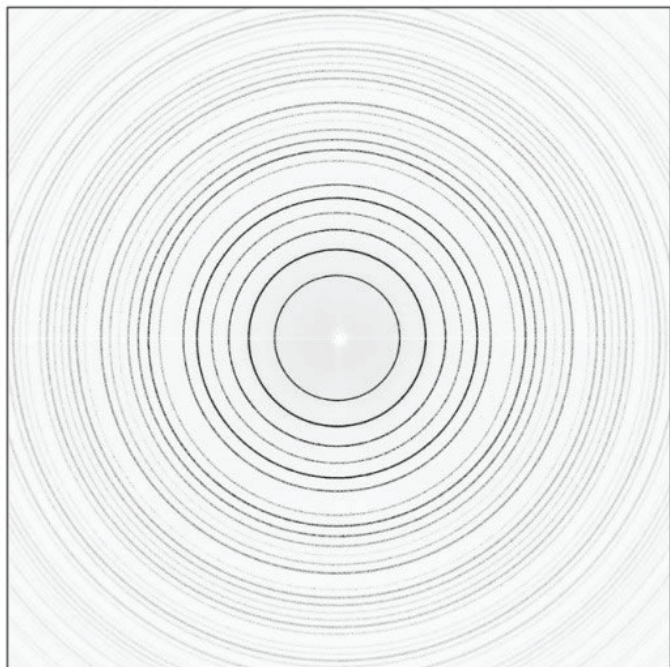


Figure 5. Powder Diffraction Pattern from the tiff file

distribution function experiments). In order to be measured, the samples must be mounted in capillary tubes which consists of a simple process. First the capillary tube must be dipped in some

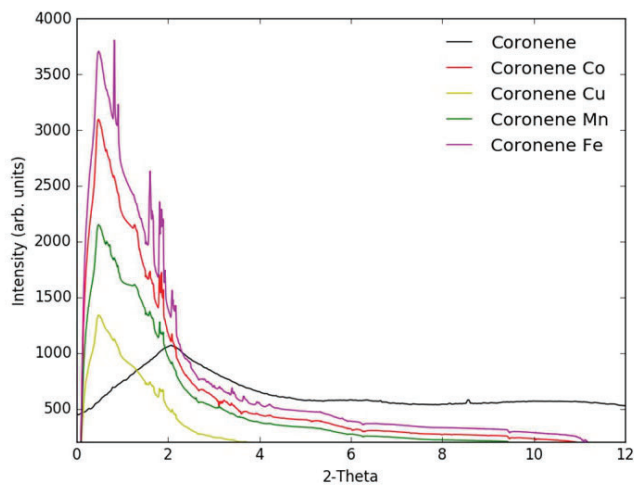


Figure 6. Graph that shows the Coronene metal complexes in comparison to the ligand alone.

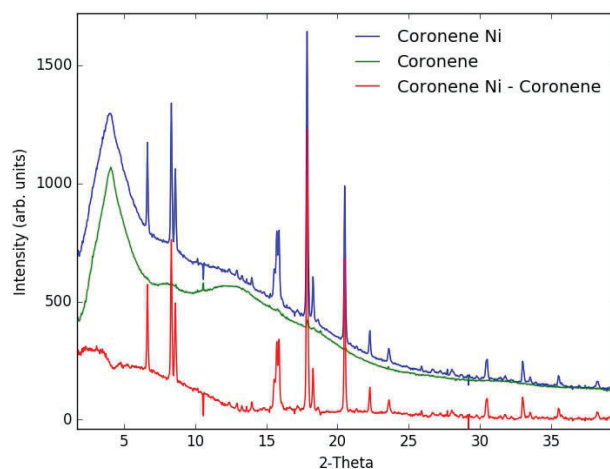


Figure 7. Powder diffraction pattern of the Coronene-Nickel Complex compared to the Coronene ligand.

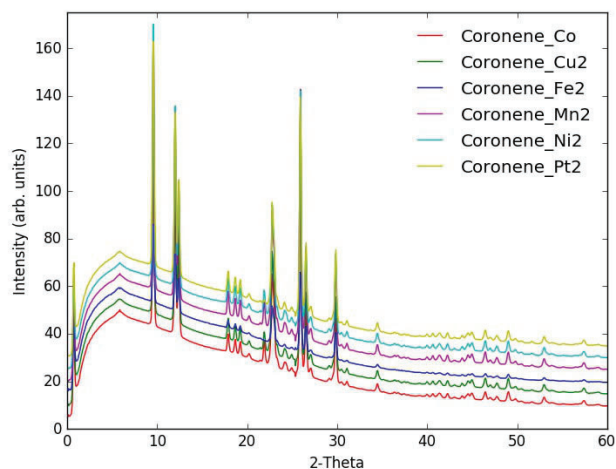


Figure 8. Second Graph of Coronene Metal Complexes

clay to ensure the sample does not come out of the other end of the tube, once the sample is transferred into the tube, the other end of the tube is dipped again in the clay to secure the sample. The cap-

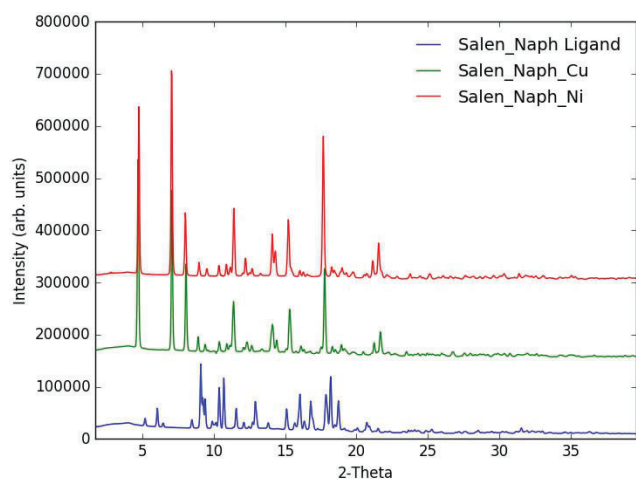


Figure 9. Graph of Salen-Naphthalene metal complexes

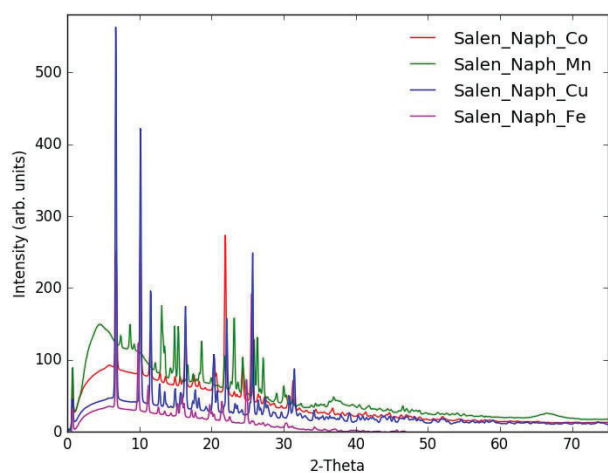


Figure 10. Second Graph of Salen-Naphthalene Metal Complexes

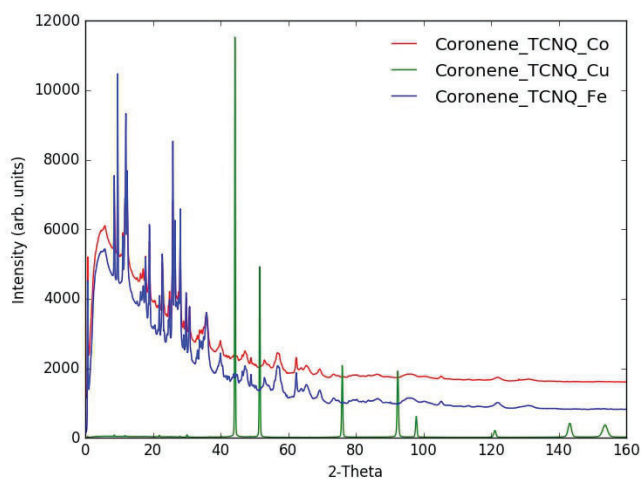


Figure 11. Graph of Coronene-TCNQ Metal Complexes

illary tube is then placed in a metal base that exposes the sample to the beam in the X-ray Powder Diffractometer. The process for obtaining the tiff files which contain the 2-D diffraction pattern takes 2 hours per sample.

This tiff files have to be converted to chi files using the program Fit2D to obtain the summation of all the files and then plot the graphs with the program Python.

III. Discussion and Results

The X-Ray patterns for the Coronene ligand and the Coronene-metal complex in figure 5 shows displacement of the bands and different peaks which indicate a coordination reaction between the metals and the ligand. In figure 6, the coordination reaction that occurred was between the coronene and Nickel.

The peaks of the Salen-naphthalene ligand and the Salen-Naphthalene Copper complex (figure 9) differ which indicates the formation of a new product. It can be observed that the diffraction patterns for the complexes are the same which indicates that these complexes recrystallize under the same spatial group.

The approach of this project was to synthesize and characterize metal complexes formed from polycyclic aromatic ligands such as coronene, naphthalene and the salen-type ligand, salen-naphthalene. This structural characterization were made by using the damping wiggler beamline X-ray diffractometer (XPD) at BNL, which is capable of collecting data at high energies (30 - 70 keV) for structurally characterizing the products from these reactions. Based on the displacements of the ligand peaks in comparison to the peaks of the complexes (figure 3), it is demonstrated that new coronene metal complexes were formed. Specifically in figure 4, the change in pattern can be seen for the complex Coronene-Nickel. In figure 5, a similar change is observed in the salen-naphthalene powder diffraction pattern in which new peaks appear, in comparison to the ligand spectrum, signaling the formation of a new compound. However, it can be observed that the diffraction patterns for the complexes are the same which indicates that these complexes recrystallize under the same spatial group. Ongoing work for this project involves the continuation of measuring and characterizing the samples and for future work, the incorporation of new techniques such as PDF with other transition metals. From the results obtained it can be concluded that, in effect, a coordination reaction between the ligands and the metal ions occurred. This can be seen in figures 3-5 where the diffraction patterns for the metal complexes are different from those of the ligands alone. These results demonstrate that the methods used for experimentation and data analysis were successful.

IV. Conclusion

From the results obtained it can be concluded that, in effect, a coordination reaction between the ligands and the metal ions occurred. This can be seen in figures 3-5 where the diffraction patterns for the metal complexes are different from those of the ligands alone. These results demonstrate that the methods used for experimentation and data analysis were successful.

V. References

- Beltran, L. M.; Long, J. R., Directed assembly of metal-cyanide cluster magnets. *Acc. Chem. Res.* 2005, 38, 325-34.
- Sessoli, R.; Tsai, H. L.; Schake, A. R.; Wang, S.; Vincent, J. B.; Folting, K.; Gatteschi, D.; Christou, G.; Hendrickson, D. N., High-spin molecules: [Mn12O12(O2CR)16(H2O)4].

J. Am. Chem. Soc., 1993, *115*, 1804-16.

³Christou, G., Single-molecule magnets: a molecular approach to nanoscale magnetic materials. *Polyhedron*, 2005, *24*, 2065-75.

⁴Gatteschi, D.; Sessoli, R.; Cornia, A., Single-Molecule Magnets based on Iron (III) Oxo Clusters. *Chem. Commun.* 2000, *42*, 725-32. 5. Milios, C. J.; Vinslava, A.; Whittaker, A. G.; Parsons, S.; Wernsdorfer, W.; Christou, G.; Perlepes, S. P.; Brechin, E. K., Microwave-assisted synthesis of a hexanuclear Mn(III) single-molecule magnet. *Inorg. Chem.* 2006, *45*, 5272-4. Jeon, Rang, Jesse G. Park, Dianne J. Xiao, and T. David Harris, An Azophenine Radical-Bridged Fe₂ Single-Molecule Magnet with Record Magnetic Exchange Coupling, *J. Am. Chem. Soc.*, 2013, *135* (45), pp 16845–16848.

VI. Acknowledgements

- This project was supported in part by the National Science Foundation, Louis Stokes Alliance(s) for Minority Participation (LSAMP) at the University of Puerto Rico Rio Piedras campus under the LSAMP Internship Program at Brookhaven National Laboratory and by the U.S. Department of Energy, Office of Science, Office of Workforce Development for Teachers and Scientists (WDTS) under the Visiting Faculty Program (VFP).
- This project was conducted under the mentorship of Dr. Dalice M. Piñero and Dr. Eric Dooryhee. We are grateful to Dr. Dooryhee for his mentorship and training during the time at NSLS II.
- We thank Keily Gutierrez and Wilfredo Pedreira for synthesizing part of the samples used in this project and Dr. Abeykoon Milinda during the measurements and for his mentorship using the programs Fit2D and Python.

Design and implementation of temporary beam pipes and their stands for sPHENIX

Howard Graham Giese

Mechanical Engineering, Cuesta College, San Luis Obispo, CA 93403

Donald Lynch

Physics Dept., Brookhaven National Laboratory, Upton NY 11973

Abstract

The Pioneering High Energy Nuclear Interaction Experiment (PHENIX) is designed to detect subatomic particle collisions inside The Relativistic Heavy Ion Collider (RHIC) at Brookhaven National Laboratory. Each year a series of experiments are conducted by the detectors over a six-month span and afterwards the facilities are shut down for repairs and updates. This year marks the final year of operation for the PHENIX Experiment and our team of engineers and technicians is in charge of designing a new and improved version of the detector, named sPHENIX. This will require the removal and repurposing of the existing PHENIX detector system. My task for the summer is to design temporary beam pipes and their support stands that will be present during the removal and repurposing portion of the project. The beam pipes are long stainless steel, vacuum-sealed pipes that connect the particle accelerator's main beam line and contain the beam particles. The pipes will be suspended sixteen feet up by the stands I'm designed in the PHENIX hall. I have researched what materials are needed, what equipment is already implemented or will be implemented, and the cost and manufacturing of making the stands. Other factors I need to take into account are the sizes of the beam pipes, how to connect the pipes, and how the pipes should be installed. This is essential for work in the facility to move smoothly and RHIC to continue to function while PHENIX is absent from the ring. From this summer experience I have grown in my technical, design, and communication skills as an engineer in the workplace. I have also expanded my networking skills and professional knowledge in programs such as: AutoCAD, Inventor, SolidWorks, and Microsoft Office.

I. Introduction

The PHENIX project runs annually and as of summer of 2016 is set for a major upgrade. This upgrade, named sPHENIX, is planned to be a more accurate and efficient detector on the RHIC ring. In order to efficiently detect things like high-energy particles and quark gluon plasma PHENIX requires a major upgrade. This is a very large undertaking, and an opportunity, for many scientists, engineers, and other BNL personnel. The sPHENIX detector is proposed to not only improve the detection of particles that the original PHENIX project had undertaken, but also add many more applied detectors and new implementations. For an upgrade to take place, the previous detector needs to be removed, dismantled, repurposed, and improved upon. The design and implementation of the sPHENIX project is planned to take a number of years, so for RHIC to continue its experiments without delays there needs to be temporary installments to the collider ring.

First and foremost, there needs to be a beam pipe in place to maintain the stream of particles, also referred to as the beam line,

in order for RHIC to function properly. This pipe would normally be part of the PHENIX or sPHENIX detector, but during the removal and refurbishing process, there will be a period of time where neither detector will provide a connection of pipe through the assembly hall. RHIC is scheduled to run once a year, so a temporary beam pipe needs to be implemented during the transition between the PHENIX and sPHENIX projects. The objective of this subsequent project is to research the design of standard RHIC beam pipes, research and design stand and supports to hold the beam pipes, and submit detailed drawings to the chief engineers, designers, and to the Collider Accelerator Department (C-AD) for review and approval. The project has produced resulting models

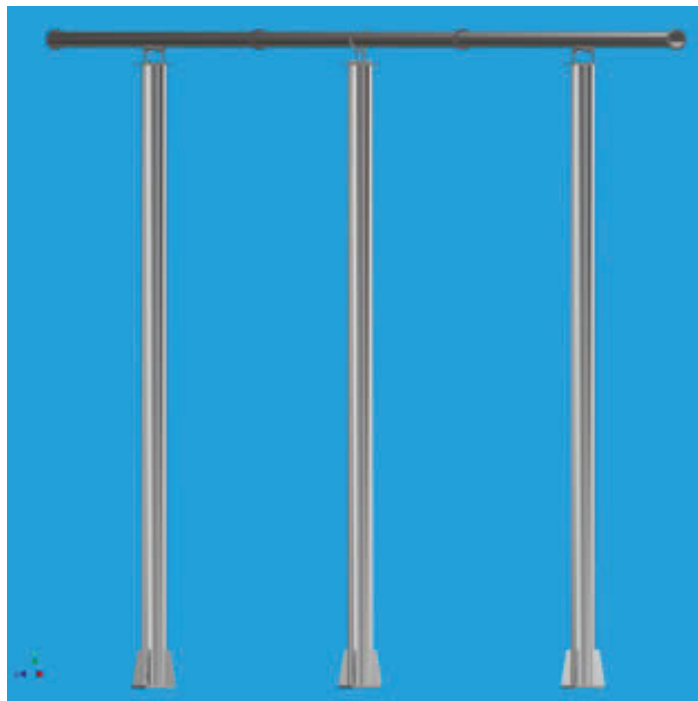


Figure 1. (top) full assembly of the temporary beam pipes Figure 2. (bottom) the three sections of stainless steel beam pipes

using Autodesk Inventor and detailed drawings as a basis for the fabrication of the pipes and stands. The design went through multiple changes and edits by the physics design team from meetings with individual engineers and technicians and group discussion in weekly meetings.

II. Methods and Design

A. Beam Pipes and Flanges

The most important parts of this project are the beam pipes that connect directly to RHIC. The beam pipes that house the particle beam need to withstand special conditions in order to properly function with RHIC. For the pipe, this requires a very strong material that is resistant to damage and can create a good seal. Stainless is chosen for the material of the temporary beam pipes to match the stainless steel in the rest of the RHIC beam pipes, but for a few other reasons as well. First, the pipes can withstand an Ultra-High Vacuum (UHV) environments so as to not add any extra collisions in the beam line. Using 5-inch diameter stainless steel pipes with a wall thickness of 0.109 inches meets the C-AD requirement for generic beam pipe that does not rest in the chain

of superconducting magnets inside the RHIC tunnels. Secondly, the pipes need to withstand temperatures up to 250°C, a process referred to as “baking-out”. When the pipe is baked-out, the pipe is fitted with heating jackets to raise the temperature. This allow some evaporation of moisture in the beam pipes that may be inside the beam pipes. Stainless steel also is a suitable material because it can support having a Non-Evaporable Getter (NEG) coating. This special coating that is applied at BNL help maintain the UHV by bonding any moisture that may be left in the pipes by creating a surface that doesn’t let water molecules escape back into the vacuum once they come in contact with the walls. The lengths of the beam pipes were chosen from two factors: how long the stainless steel tubing can be ordered, and where the pipes were to be placed. The pipes were limited to a length of 20 feet per pipe, per ordering. As the total length of the pipe needs to be 549.45 inches, the pipes are to be installed in three sections as shown in figure 1. Of the three beam pipes, the pipe in the north magnet may be required to stay in the hall during removal of original PHENIX, so the length needs to be 196.1 inches. As for the other two beam pipes, their lengths are both 183.18 inches, which span the rest of

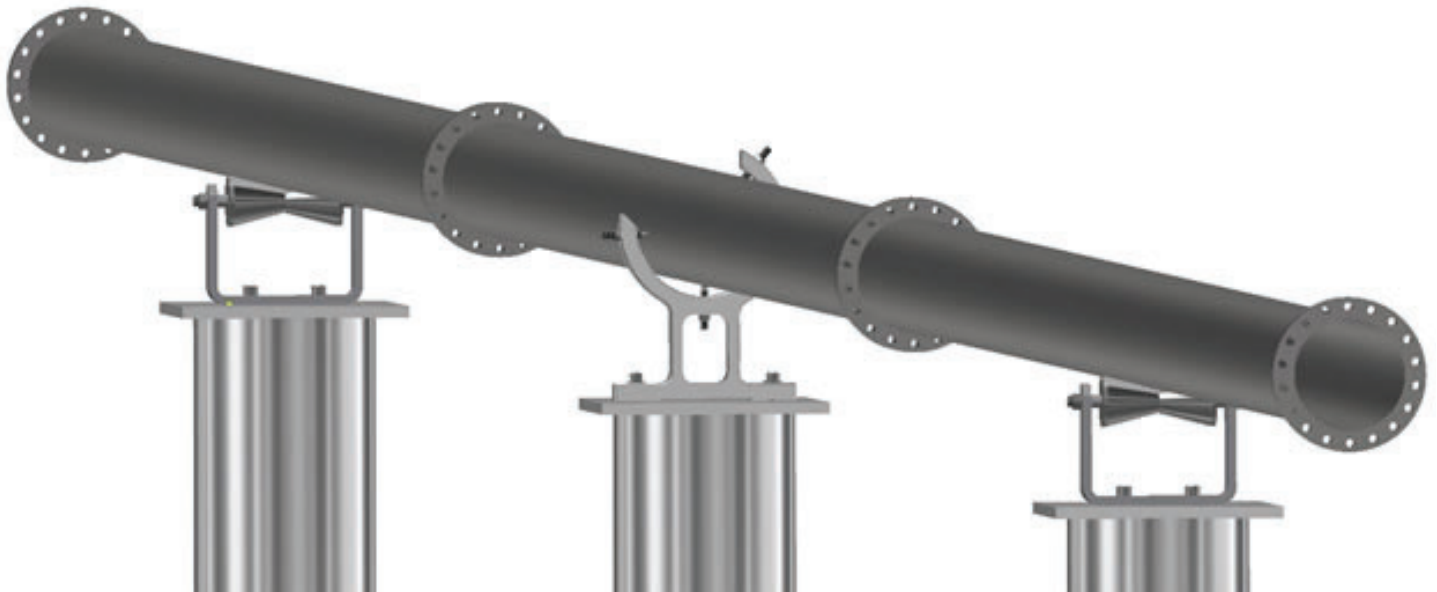


Figure 3. a close look at the beam pipes and attached flanges, along the top of the support stands

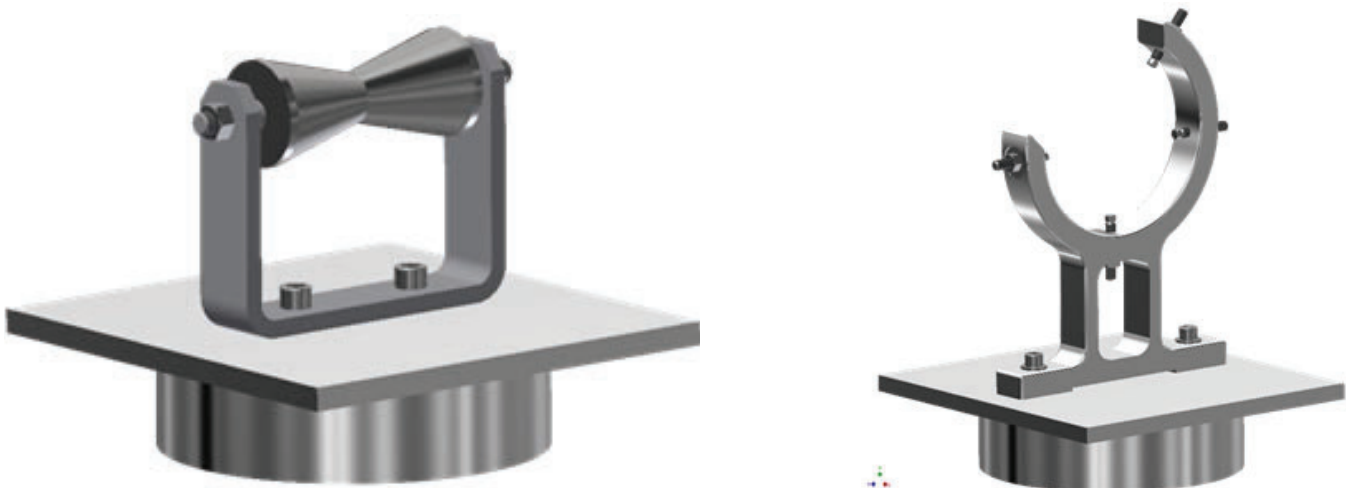
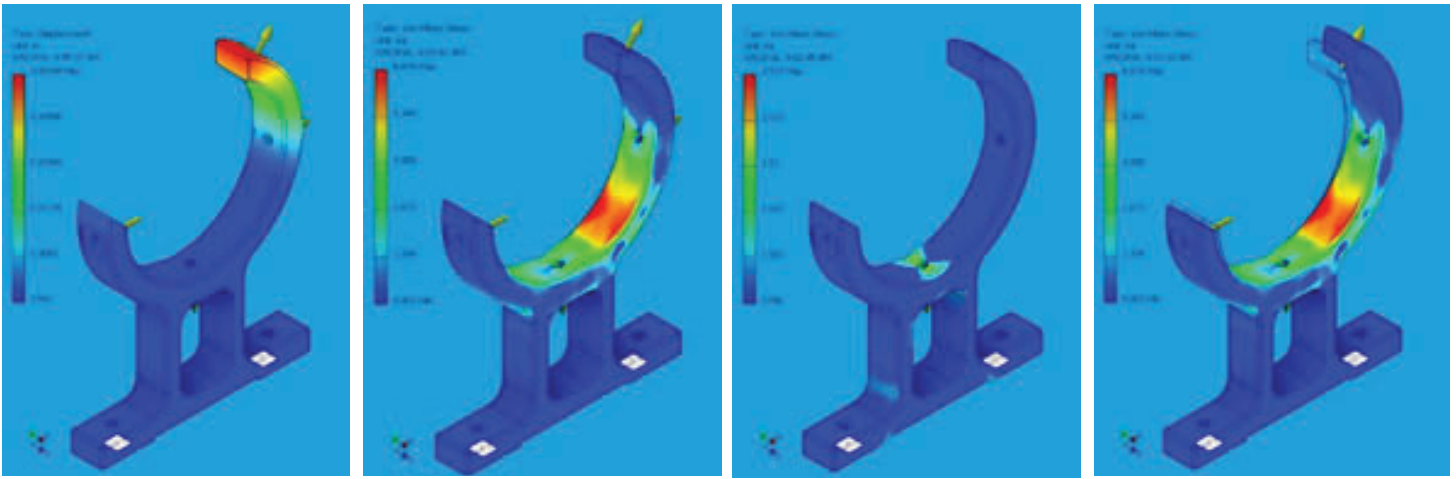


Figure 4 (left) rolling support stand designed by Gulf State Hangers [1], Figure 5 (right) the pipe bracket that was designed specifically for the beam pipes



Figures 6-9. Showing the displacement and Von Mises Stresses on the bracket model. Figures 6 through 8 have a factor of safety of 2.0, figure 9 has a factor of safety of 4.0 to show amplified deformation and stresses

the assembly hall. These values are subject to small changes, due to thermal expansion during testing and experimentation, and the two pipe bellows on either end of the beam pipe that can change the overall length of the pipe.

The way the pipes are held together are through stainless steel flanges. These flanges, which can be purchased through MDC vacuum fit around the ends of the pipes and connect to one another through bolts and a copper gasket [2]. As shown in figure 2, there are two flanges on each pipe, making a total of six flanges needed for assembly. To withstand the UHV needed, special C-AD welds are to be implemented when the beam pipes are fabricated so there are no leaks or breaks in the pipeline.

B. Support Stands

The design of the support stands, seen in figure 10 and 11, are designed to be stable and cheap to fabricate. The stands use aluminum tubing and plates, which give the structure strength, less weight and a cheaper cost to fabricate. The bottom of the stands will be bolted into a metal plate that lays on top of the bottom carriage section of sPHENIX, as opposed to the floor of the assembly hall. These bolts can be easily installed by following the holes in the bottom of the stand design. There are two separate sets of holes to be drilled and tapped at the top of the stands, see figure 10. These holes differ in size and distance from one another to account for the different support parts that attach to the beam pipe directly.

C. Bracket Support Clamp

The bracket support clamp, as seen in figure 5, is a design created to hold the beam pipes in place during the run. The bracket has a crescent shape so that it may be slipped on perpendicular to the pipe wherever needed. The material used for this part is aluminum. This is similar to the use in the support stands as it's strong, lightweight and cheap to use. The design of the bracket was also designed and drawn so that manufacturing the part would be more cost efficient, and possible to be done through the shops at BNL. The bracket implements four stainless steel socket swivel pad clamps, which can change the angle of attachment to the beam pipe and can be adjusted. The most notable part about these clamps is that they are the same material as the beam pipe. This will reduce any sort of damage that having separate materials might cause, such as scratching, breaking, structural integrity,

corrosion, and heating differences. The bracket has steel helical inserts where the four pad clamps are attached to account for the difference in hardness between the stainless steel and aluminum materials. Since this is a completely new part, some stress analysis is required to determine if it is adequate for the task of holding onto the pipe. Stress and displacement simulations can be shown in figures 6 through 9.

There will be one bracket implemented on the top of an aluminum stands, placed as the center of the three support stands, as seen in figure 3. There is only one bracket in use to account for the thermal expansion while in the bake-out process. If three brackets were implemented, then the expansion of the steel beam pipes may cause damage or misalignment to the stands. Having one bracket placed in the center allows the pipes to expand outward when heated to high temperatures, and expand into the beam pipe bellows at either end of the assembly hall.

D. Roller Supports

The roller supports were chosen for the two supports on either side of the bracket clamp. This is also to account for any thermal expansion that may occur during the experiment. The rollers allow for the pipe to be supported from the bottom, while still being able to move along the roller while keeping its general alignment with the bracket clamp and the rest of the attachment points. This roller was found through the Gulf State Hangers catalog and they meet the load requirements for holding the pipes, shown to meet MSS-SP-58 requirements [2]. The material of the rollers is specific to the beam pipe: stainless steel. This is to account for any transfer of heat through the metals and to provide similar surface metals. Another thing to note is the "V-shape" of the roller, as seen in figure 4. This keeps the pipe aligned if there happens to be any bending or shifting of the pipe.

III. Future Work

These designs and drawings are to be used in the fabrication and assembly of an actual Beam pipe with support stands in the near future. Once most of the equipment inside the PHENIX detector is taken out, then the beam pipes can be installed to continue test runs of RHIC. With time, the PHENIX team may change some of the values planned with sPHENIX and need to change similar values of the stands. There are plans discussed to adjust the length of the stainless steel pipes and placement of the support

stands to account for the heating jackets used during bake-out. Further edits and changes may also be made by the chief engineers and designers on the sPHENIX team to fit the needs of the project on the larger scale

IV. Impact on Laboratory Missions

The temporary beam pipe project directly impacts progress on multiple projects involving the particle collider at Brookhaven National Laboratory. Not only does this project plan out an important step towards completing sPHENIX, but after it's implemented it will help the function of RHIC and any experiments associated with it.

V. Conclusions

Utilization of these temporary beam pipes and supports provide a cheap and effective way to contain the beam line of RHIC while still being able to continue with the removal of the PHENIX project and the start of the sPHENIX project. Although it may not be the most aesthetically pleasing design, the strongest or cleanest, these models take into consideration the cost of having a temporary support structure for a large scale experiment such as RHIC, PHENIX, or sPHENIX.

VI. Acknowledgements

This project was supported in part by the U.S. Department of Energy, Office of Science, Office of Workforce Development for Teachers and Scientists (WDTS) under the Community College Internships Program (CCI). Also, a special thanks to Don Lynch (sPHENIX Chief Engineer), Rich Ruggiero (sPHENIX Chief Designer), and both the PHENIX and sPHENIX technicians and engineers for their help and guidance.

VII. References

- ¹"Pipe Support Catalog Part 75SS." Pipe Hangers, Pipe Supports, Clevis Hangers, Pipe Rollers, Beam Clamps - Gulf State Hangers. Web. 08 Aug. 2016
- ²"Nonrotatable Flanges & Fittings Del Seal CF 6-3/4 Inch OD." MDC Vacuum Products. MDC Vacuum Products LLC, Web. 08 Aug. 2016

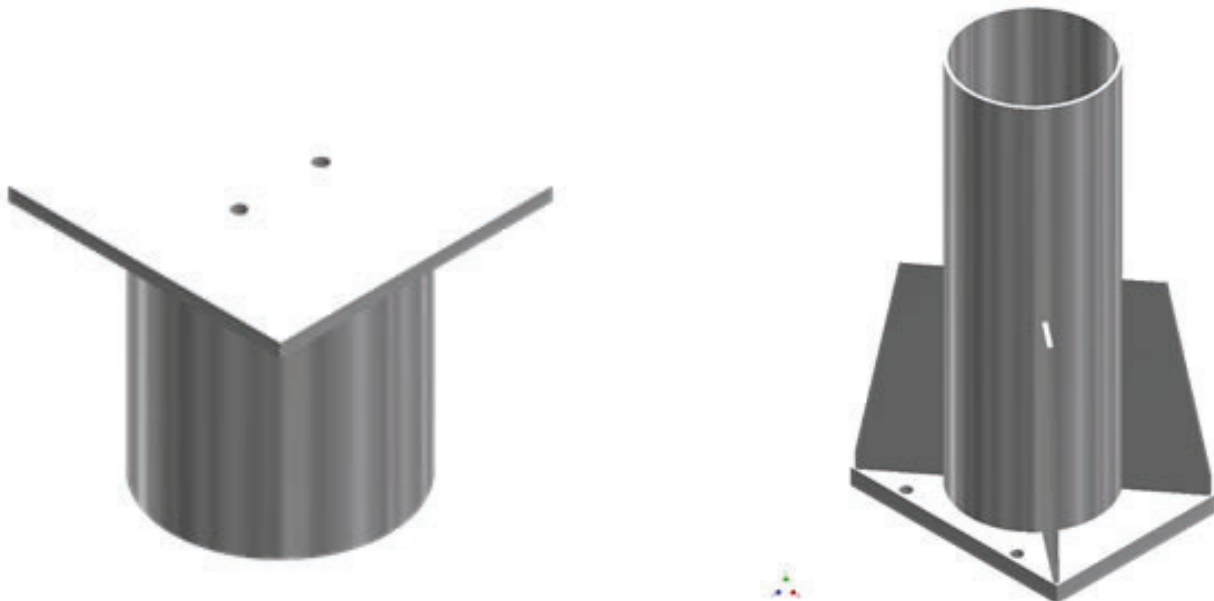


Figure 10. (left) view of the top of the aluminum support stand, Figure 11. (right) view of the bottom weldment of the aluminum support stand

Measuring techniques for detecting axions through photon splitting

Mal'Lica Gordon

Department of Physics, Florida A&M University Tallahassee, FL 32305

Marven Laborde

Department of Chemical Engineering, Florida A&M University and Florida State University College of Engineering,
Tallahassee, FL 32305

Carol Scarlett

Superconducting Magnetic Division, Brookhaven National Laboratory, Upton, NY 11973

Abstract

Axions were theorized to explain reactions in nuclear interactions that could not be understood. It is important to develop a way to measure axions since they potentially have all the right properties of dark matter which are believed to make up the vast majority of our galaxy. Since space behaves as a birefringent material as it is observed when light (photons) passes through the vacuum of space; those photons split (bifurcate). To determine the measurability of axions we simulated outer space by passing photons through a vacuum with an applied magnetic field. The magnetic field causes the birefringence of the vacuum. Since interactions between photons and axions will result in bifurcation or splitting, understanding all of the quantifiable effects caused by such splitting will enable us to design better experiments in the future. Photons in a beam are distributed in the shape of a Gaussian curve, therefore we can learn about the splitting process through careful measurements of the distribution. As the limits of this curve approach between 0 and 1, we gather perceptible information of birefringence using a photon detector. Analysis of the most infinitesimal changes in the beam as we rotate light along different degrees to its' axis. We understand that passing photons through several transversals, two polarizers and a birefringent material will give us an effect several orders of magnitude greater than what the vacuum of space will produce.

I. INTRODUCTION

A. Literature

Gravitational lensing is a phenomenon that helps describe the bending of photons or light with dark matter being the responsible agent. Dark matter is not fully understood and many studies have been conducted to further gain comprehension. In the Journal of High Energy Physics, Dr. Roszkowski, Kim, and Covi have suspected the axion to be the main component of dark matter. Axions are theoretical particles with low masses and has unobserved

interactions with electrons or protons. When they are produced they are non-thermal throughout out of equilibrium decays. Referencing the same journal axions would be the ideal particle make up of dark matter and be the possible solution to the strong charge parity (CP) confusion which highlights the violation of the CP symmetry when particles are inverted with its anti-particles. We also assume axions to be responsible and would want to further understand their behavior. We also concur that it is responsible for the major phenomenon in gravitational lensing.

B. Overview-Motivation

The more axion data that is collected is very important in the field of cosmology and particle physics. Dark matter binds galaxies to one another in bunches and it bends space around the galaxy bunches (Gravitational Lensing). To obtain a more concise understanding of dark matter, the component of it becomes an area of inquiry, and axions are the theoretical constituents.

Our efforts will consist of using an optical setup to simulate the space setting and using the birefringence concept and photon splitting as a vehicle to visually see behavior (noise) of the light source as it passes through a magnetically induced vacuum. In measuring the smallest amount of photon splitting we must decrease the number of photons in a beam. This is done by passing photons through a polarizer which will allow photons oriented towards a particular axis to pass through. The remaining photons then pass through a birefringent material which will split the beam according to the index of refraction of that material. We observe this by setting up a mirror cavity which emulates folded space. We know this splitting is how photons behave in space except it is much more drastic by several orders of magnitude. Since we cannot build a galactic sized model to pass photons through, we must try and emulate how light behaves in space by measuring the behavior of the smallest amount photons as they travel through unfolded space in a scaled environment. In further implementing a more sensitive system through each trial run we can eventually detect the conversion of light into axions, and obtain quantitative data.

Figures

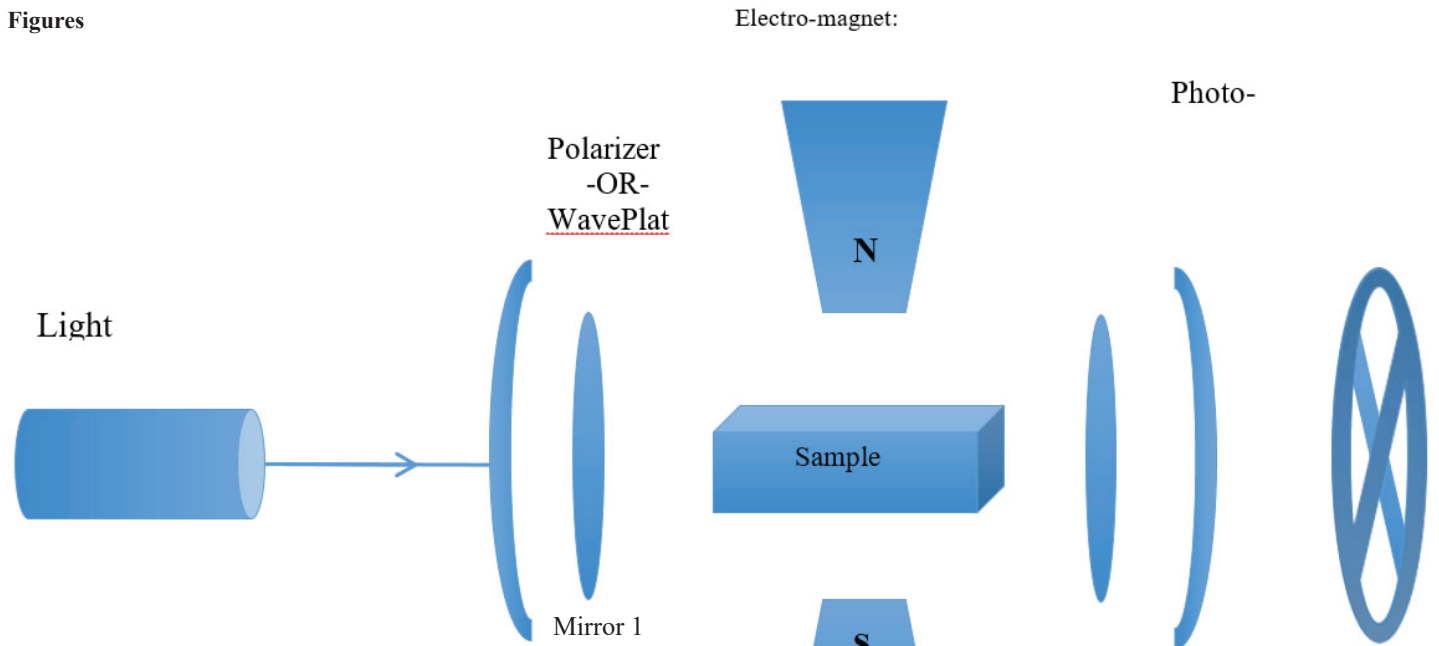


FIGURE 2. Modeled Cavity Setup.

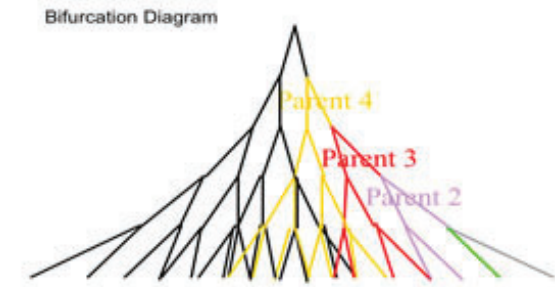
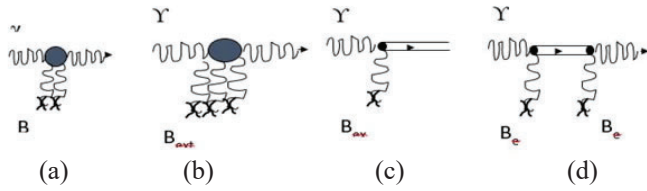


FIGURE 4. Splitting Effect

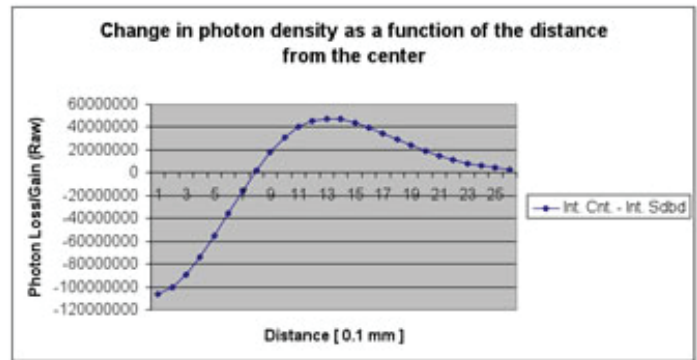


FIGURE 5. Change in Photon Density as A Function of the distance from the Center

Tables

Cavity Type	Cavity Length	Magnetic Field Length	∇B Strength	Laser Wavelength	Laser Energy	Mirror Radius	Number of Bounces	$\theta_{split} \sim 10^{-10}$ ($g_a = 10^{-6}$)	Injection Angle
Confocal	14 m	10 m	200 T/m	1064 nm	1 W	25 m	$1.2 \cdot 10^4$	$4 \cdot 10^{-10}$	$1.5 \cdot 10^{-2}$ rad
Convex-Concaved	14 m	10 m	200 T/m	1064 nm	1 W	25 m, -11 m	$1.2 \cdot 10^4$	$4 \cdot 10^{-10}$	$1.5 \cdot 10^{-2}$ rad
Planear-Planear	14 m	10 m	200 T/m	1064 nm	1 W	∞	$1.2 \cdot 10^4$	$4 \cdot 10^{-10}$	$1.5 \cdot 10^{-2}$ rad

TABLE 1: The real parameters of the involved cavities, magnet, and laser.

C. Experimental Equations:

Cavity experiments have been performed to search for optically induced rotation of the polarization of a laser beam, i.e. BNL – E840, PVLAS and BMV. These experiments have been limited, because rotation scales as the photon-axion coupling squared. To reach regions of axion phase space that are not otherwise ruled out and are important to several models, experiments have to look for effects that scale linearly in coupling strength. New measurable that scale with coupling strength, such as random noise, must be explored.

Below is the mathematical framework (Jones Matrix) which helps understand the light propagation as it passes through our optic system.

$$\begin{pmatrix} 1 & 0 \\ -\frac{1}{f} & 1 \end{pmatrix} \quad \begin{pmatrix} 1 & d \\ 0 & 1 \end{pmatrix} \quad \begin{pmatrix} 1 & 0 \\ \frac{\pm\theta_{split}}{X_0} & 1 \end{pmatrix}$$

Focusing:

Propagating

Splitting:

Below are the mathematical expressions which describe the changes in the beam profile due to splitting relative to the center of the beam.

$$P_D = Ae^{-\frac{1}{2} \frac{x^2}{r^2}}$$

$$P_D'' + P_D' = A \cdot \frac{r-\epsilon}{r} e^{-\frac{1}{2} \frac{x^2}{r^2}} \cdot e^{\frac{x^2}{r^2} \frac{\epsilon}{r}} \cdot e^{-\frac{\alpha^2}{r^2}} \cdot \cosh\left(\frac{x^2}{r^2} \cdot \frac{\alpha}{x}\right)$$

$$P_D - (P_D' + P_D'') = Ae^{-\frac{1}{2} \frac{x^2}{r^2}} \left[1 - \frac{r-\epsilon}{r} e^{\frac{x^2}{r^2} \frac{\epsilon}{r}} \cdot e^{-\frac{\alpha^2}{r^2}} \cdot \cosh\left(\frac{x^2}{r^2} \cdot \frac{\alpha}{x}\right) \right]$$

II. Data Analysis & Discussion

From experimentation it was noted that under the conditions of our experiment that we were not yet able to narrow down our optical setup to record the noise level to the desired magnitudes we sought after. We were however able to demonstrate birefringence effect with the unfolded space and tabulate the splitting effect (via mirror cavity and birefrigerence). Figure 4, describes the splitting effect as returning beams again couple to axions and continue to split with reflection. This experience also showed a greater understanding of the minor principles of photon splitting in the unfolded space.

Referencing Figure 2, there is an illustration of the modeled system. The photons from the laser propagate to the first polarizers which orients the beam to an assigned axis. Then it transfers over the birefrigerence sample which causes a splitting effect as stated above, and then reflects off of the mirror cavity back to the sample netting more splitting effect. This process repeats itself based on the strength of the signal. Then for more insight on the photon coupling effect as it progresses through the system reference Figure 3. This experimental setup was repeated for polarized angle of fifteen, thirty, forty five, sixty, seventy five, and ninety five as the one of axis remained fixed. The measurements and calculations consisted of the Jones Matrices which factored

in the focusing, propagating, and splitting effect of the elements in the optics system. The optics systems parameters is noted in Figure 1 as the cavity length, magnetic field strength, and a host of other variables were consistent to ensure high precision. From that it was reasoned that the splitting angle of the matter to axion was limited due to the strength of magnetic fields. There is a linear dependence and relationship.

It is known that most sources have slight fluctuations and do not yield consistent intensities as the photo detector recorded (for an unoccupied system) slight deviations/fluctuations. This would have probably been due to the circuit outlet at which the laser was connected, or the lighting in the setting. Despite, the fluctuations could be nullified as the beam splitting effect should net the same outcome. The beam resulted in a depletion of central intensity.

III. Conclusion

It is unknown exactly what the particles are that make up the vast majority of space. However, axions have the ideal characteristics of what this unknown material could possibly be. Therefore, determining a way to measure axions will bring us one step closer to determining components of dark matter and dark energy. After careful analysis of the running averages and standard deviations of data we observed that data deviations of photon randomize produces much more measurable data. This photon randomize is the same as noise. Therefore, we've concluded it is more useful to measure the noise of photon particles to determine behaviors of axions. The next to step will have to introduce a setup that has an enhancement in signal strength and the expansion upon the limits splitting. Also, modern and novel techniques will be needed to reach unique levels of precision in measurements in a magnetically induced vacuumed birefrigerence. A possible area of exploration is finding searches that are sensitive to photons coupling with a weakly interacting particle.

IV. Acknowledgements

• Louis Stokes Alliance(s) for Minority Participation (LSAMP) "This project was supported in part by the National Science Foundation, Louis Stokes Alliance(s) for Minority Participation (LSAMP) at Florida A&M University, under the LSAMP Internship Program at Brookhaven National Laboratory."

V. References

1. C. Scarlett, Optical Birefringence in the limit of photon Statistics (2016), p. 5,9,10,11.
2. See <http://arstechnica.com/science/2015/01/if-dark-matter-is-really-axions-we-could-find-out-soon/> for more information about axions; accessed 7 August 2016.
3. <http://adsabs.harvard.edu/full/1993ApJ...404..441K> for "Mapping Dark matter with Gravitational lensing" (last accessed 10 August, 2016).

Trending analysis of internal assessments within the radiological waste management division

Matthew Harris

Business Administration, St. Joseph's College, Patchogue, NY 11772

Steve Stein

Quality Assurance, Brookhaven National Laboratory, Upton, NY 11973

Abstract

Due to the many experiments occurring within Brookhaven National Laboratory (BNL), there are certain unsafe waste streams which require more care than standard waste. These hazardous chemicals and radioactive isotopes must be properly handled and transported away from BNL by the Radioactive Waste Management Division, in order to ensure the safety and health of the local community and the environment. Another support organization, the Quality Management Office, provides different services to the laboratory. The group develops programs which offer environmental and safety management principals among other things. Additionally, representatives are annexed out to different complexes. One of the departments in which quality management is interwoven is in Waste Management. I have had the opportunity to work at the intersection of these two departments, and to see the dynamic relationship between support organizations within BNL. A significant part of my summer internship involved performing a trending analysis on the internal assessments, completed on a rotational basis by Waste Management Personnel. The first step was to collect the assessments and extract the useful data, which was put onto an Excel spreadsheet. Once all of the data was input, causal codes were assigned to the different findings and observations were made through the assessments. From there, I isolated and compared the findings based on the causal codes in an attempt to find trends in the issues that are occurring within the department. Some common issues were found on a repetitive basis, and in response steps should be taken to ensure that they are eliminated or mitigated. Throughout the course of the summer, I have gained an in depth knowledge of Quality Management, a deeper understanding for the different Microsoft programs and their application functions, and valuable workplace experience which allowed me to apply the concepts taught to me throughout college.

I. Introduction

BNL's Waste Management Division focuses on handling radioactive, hazardous, or mixed waste. Radioactive waste is considered a waste stream which is emitting ionizing particles through radioactive decay. Hazardous waste can be considered materials that are highly flammable, volatile, should not be exposed to air/heat, or otherwise would be toxic to humans and the environment. Mixed waste can include both radioactive and hazardous waste streams. Waste Management is a part of BNL's Environmental Protection Division (EPD) whose main goal is to "[develop] and [deliver] environmental products and services for all Brookhaven stakeholders, including federal, state and local regulators, the public, the U.S. Department of Energy, and internal customers." (Brookhaven National Laboratory-Waste Management) Another support organization active within BNL is the Quality Manage-

ment Office, which employs quality representatives throughout the laboratory. One of the departments which have a Quality Representative placed within its operations is the Waste Management Division. Quality representatives facilitate event/issue fact finding, perform causal analyses, and write corrective action plans. These representatives provide quality assurance services which aide in perfecting processes and ensuring effectiveness and efficiency in the department's methods. As mentioned, the majority of my time has been spent performing a trending of causal codes for internal self-assessments regarding Waste Management standard operating procedures.

II. Methods

The internal self-assessment reports were collected from 2013 to the current year in order to effectively track long-term trends within the assessments. The assessments are conducted monthly by Waste Management staff. Standard operating procedures provide step by step processes for Waste Management. The assessment reports contain the following types of findings: noteworthy practices (performance that exceeds expectations), non-conformances (A lack of an element, procedure, or a non-fulfilled requirement that puts the process/system at jeopardy, observations (areas of concern, but not outright non-conformances), and opportunities for improvement (a suggestion for refining an activity). The assessments were reviewed and meaningful data was extracted in order to build a spreadsheet using Microsoft Excel. This data includes an assigned ID number, the date of the report, the title of the SOP, the finding(s), and the Occurrence Reporting Processing System (ORPS) causal code which was assigned to it.

Date	Document	Finding	Finding No.	Code	IDI	Finding Details
------	----------	---------	-------------	------	-----	-----------------

The ORPS causal code is a method of finding a root or apparent cause for findings. The system of coding is used throughout BNL, making it easily understandable. The ORPS codes have three nodes, starting with "A" which lists the major categories of problems. The "B" node lists subcategories, and "C" nodes provide the apparent cause of the problem.. The uppermost level (A) includes the following: (Design/Engineering Problems), A2 (Equipment/Material Problems), A3 (Human Performance), A4 (Management Problems), A5 (Communications Less Than Adequate aka LTA), A6 (Training Deficiency), A7 (Other). A common code found during the research was A3B1C01; this breaks down as the following: A3, Human performance /B1, Skill Based Error /C01, Check of work was less than adequate (LTA). This can be interpreted with the attachment 2 spreadsheet.

After all causal codes were placed on an Excel spreadsheet, a pivot table was made, allowing the user to manipulate variables in the data set in order to view graphs and charts with different focuses. Certain information was isolated through the pivot tables

including the count of each causal code, a pie chart of the popular “A” categories, and the ratio of each type of finding (noteworthy practice, nonconformance, observation, or opportunities for improvement).

III. Data/Results

First, the data was broken up into each type of finding. The graph below (1.1) depicts the distribution of each type of finding that was reported in the assessments by Waste Management Personnel: (N= Nonconformance, NP= Noteworthy Practice, O= Observation, OFI= Opportunity for Improvement)

The next pie chart (1.2) breaks down how many codes were assigned for each “A” section. It can be observed that A5, which deals with less than adequate communications (both verbal and written), encompasses almost 50% of the causal codes in the many reports throughout the three year period which was studied. Based on the prevalence of this A5 causal code, possible actions to reduce the occurrences would be beneficial.

Although a separate spreadsheet is attached to this report, the A5 section by itself will be posted below as well (note: all of these codes were not found):

The final graph (1.3) depicts a count of every ORPS causal code which was assigned to the findings. It is worth noting that the (blank) count is due to the numerous noteworthy practices that were reported; logically, a causal code is not necessary for an exemplary practice occurring within the department. Additionally, there were multiple assessments that had no findings to report at all, which contributes to the (blank) count on the chart. A few of the common codes found while studying the reports are also listed below chart 1.3:

Most common causal codes:

- **A3**, Human performance /**B1**, Skill based error /**C01**, Check of work was LTA
- **A4**, Management problem /**B1**, Management methods LTA /**C01**, Management policy guidance/expectations not well-defined, understood, or enforced.
- **A5**, Communications LTA /**B2**, Written communication content LTA /**C07**, Facts wrong/ requirements not covered
- **A5**, Communications LTA /**B3**, Written communication not used /**C01**, Lack of written communication
- **(Blank)**: Findings that are Noteworthy Practices are not assigned causal codes because it is not a problem being reported. Also, some internal-procedures did not have any findings at all to report.

IV. Conclusion and Recommendations

In summary, the ORPS causal codes assigned in the collective self-assessments were found to be in a few localized areas; Human performance errors, management policy and expectations, and problems with the written procedures and forms. In fact, these ORPS causal codes are not only ubiquitous, but also interwoven. Human errors are causing written procedures to be flawed, written errors are occurring because management may not be defining expectations well enough, and so on.

It should be noted that determining causal codes can be subjective, dependent on the person performing the causal code analysis. Additionally, some of the assessments date back to three years ago, and it was difficult to trace root causes from often basic finding details in the reports. Nevertheless, there are consistently recurring causal codes which point to a weakness in the opera-

A5 Communications LTA			
B1 Written Communications Method of Presentation LTA	B2 Written Communication Content LTA	B3 Written Communication Not Used	B4 Verbal Communication LTA
C01-Format deficiencies C02-Improper referencing or branching C03-Checklist LTA C04-Deficiencies in user aides (charts, etc.) C05-Recent changes not made apparent to user C06-Instruction step/infor- mation in wrong sequence C07-Unclear/complex wording or grammar	C01-Limit inaccuracies C02-Difficult to implement C03-Data/computations wrong/incomplete C04-Equipment identifica- tion LTA C05-Ambiguous instruc- tions/requirements C06-Typographical error C07-Facts wrong/require- ments not correct C08-Incomplete/situation not covered C09-Wrong revision used	C01-Lack of written com- munication C02-Not available or incon- venient for use	C01-Communication be- tween groups LTA C02-Shift communications LTA C03-Correct terminology not used C04-Verification/repeat back not used C05-Information sent but not understood C06-Suspected problems not communicated to super- vision C07-No communication method available
*Highlighted codes were found 3 or more times			

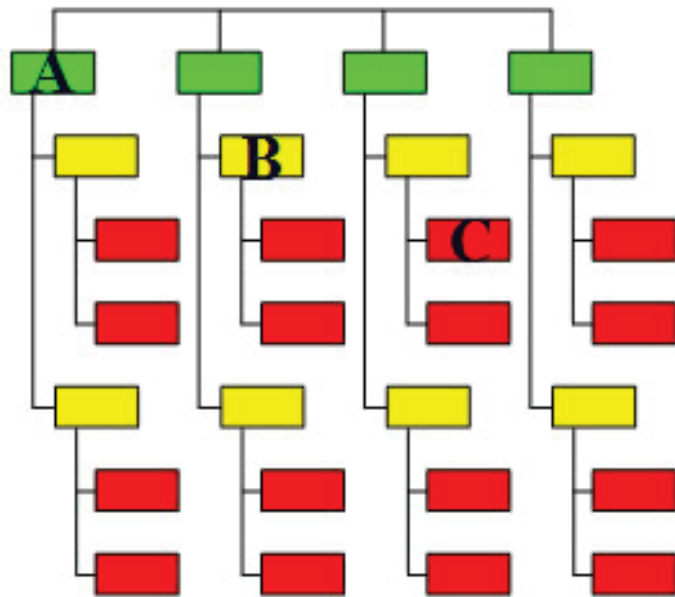
tions within the Waste Management Division, which should be addressed. One problem stems from the policies and procedures not being properly defined by management. Essentially, any occurrence that was reported which involves personnel not properly following procedures can be linked back to management, whose responsibility it is to communicate the necessary tasks to employees. It is recommended that the management within Waste Management ensures that the necessary objectives and regulatory requirements are communicated, and that responsibilities are assigned to specific personnel. This can be done through regular memos, or more frequent meetings in which there are discussions about what is needed and expected from personnel.

When dealing with human performance error, there can be additional training provided for changes in procedures and areas where specific problems are being found. However, re-training and focusing on procedural re-writes should not be the primary focus when looking at the self-assessments. The fact that employees are making mistakes and SOP's are lacking information points

to the fact that somewhere in the process there is a lack of communication. Another step that can be taken to increase transparency and provide clear instructions can involve increasing visual user aides, as is being done in Standards Based Management System (SBMS) documents. Interactive flow-charts can make processes easier to follow for workers.

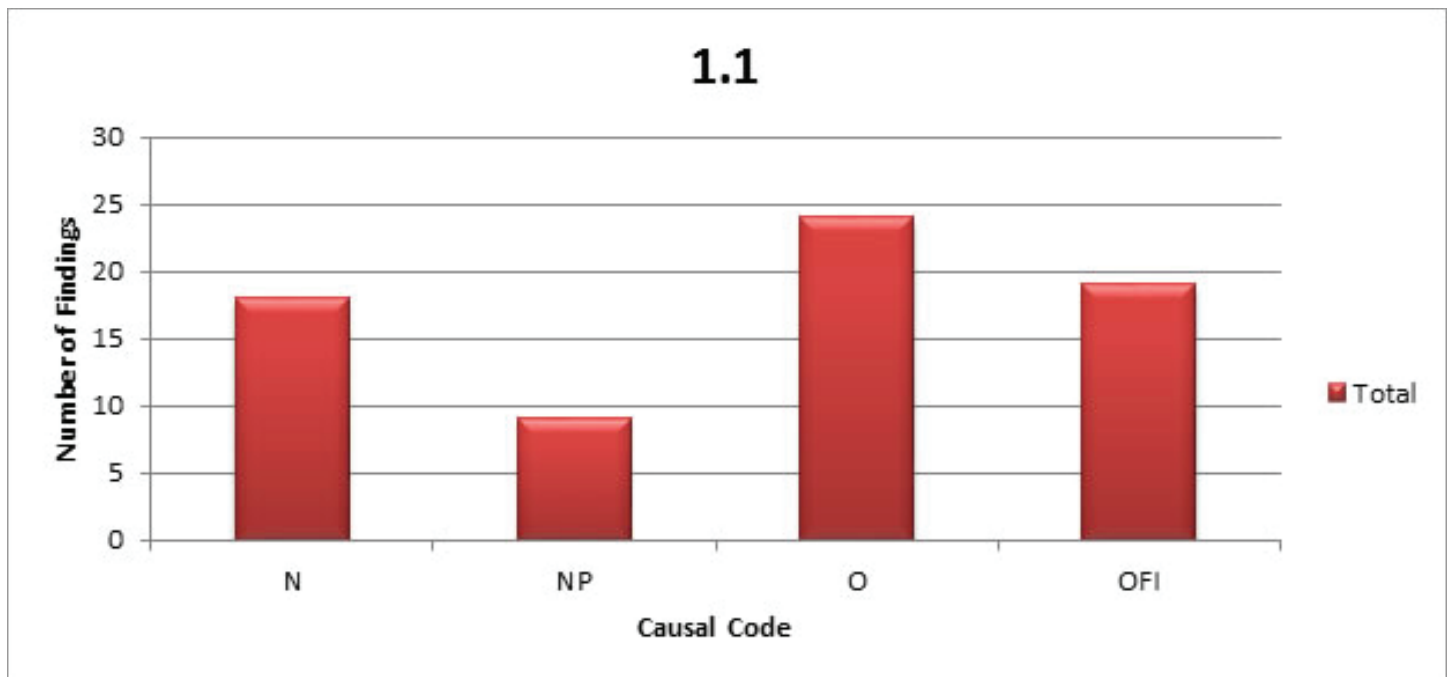
Since many of the codes are based on misinformation within the SOP's, it would be prudent to involve the staff in reviewing these procedures. This would ensure that the procedures will be implementable to those who need to follow them. This will also fix many of the gaps within the written procedures; when those using the SOP's are involved in the process there is a less likely chance that operations and steps will be missed. The best course of action would be to increase awareness of proper procedural practices by having more discourse between all levels of employees in the infant stages of development. This way, personnel will be more receptive to the changes since they have a say in how the plans are developed.

With these suggestions, along with the analysis that has highlighted the main problems occurring within the department, the Waste Management Division can now move forward with perfecting its processes to iron out procedural wrinkles which are causing non-conformances to occur. Additionally, the department can work towards preventative measures to mitigate future occurrences before they can happen.



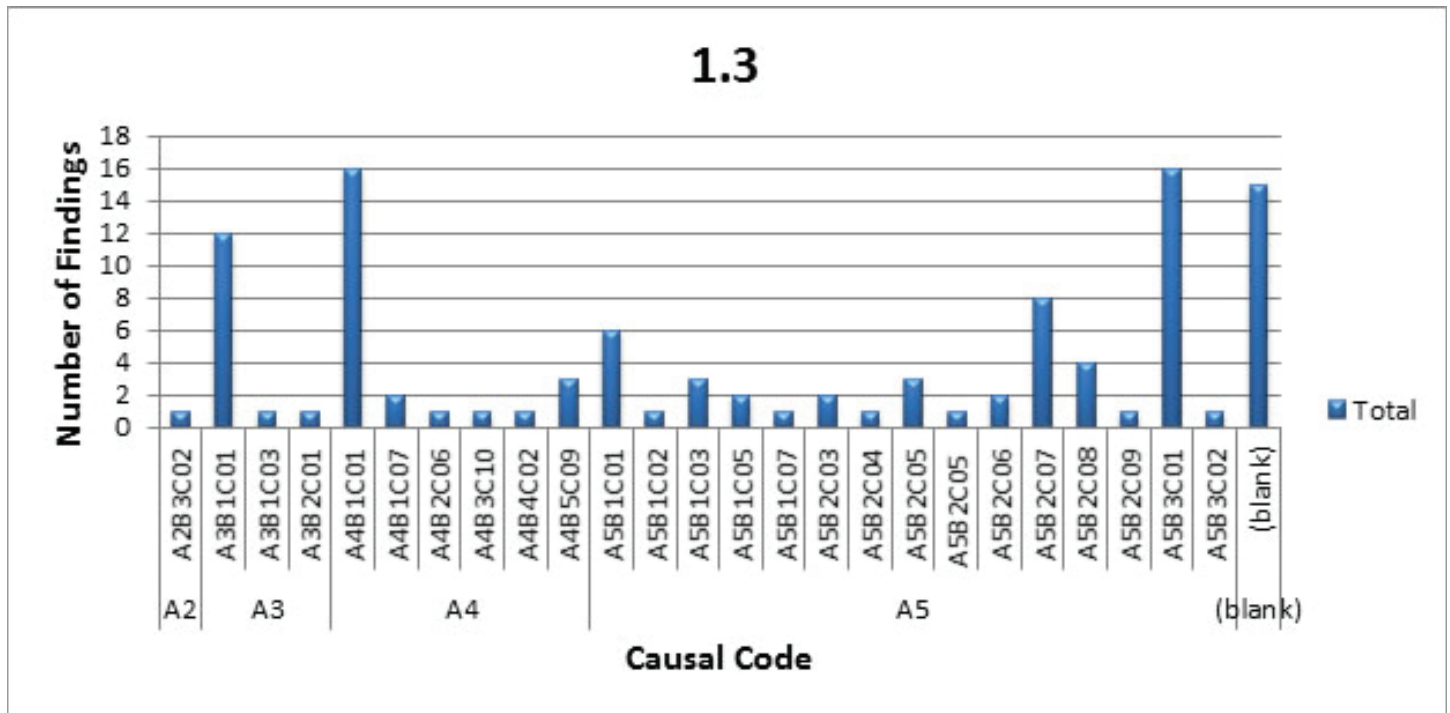
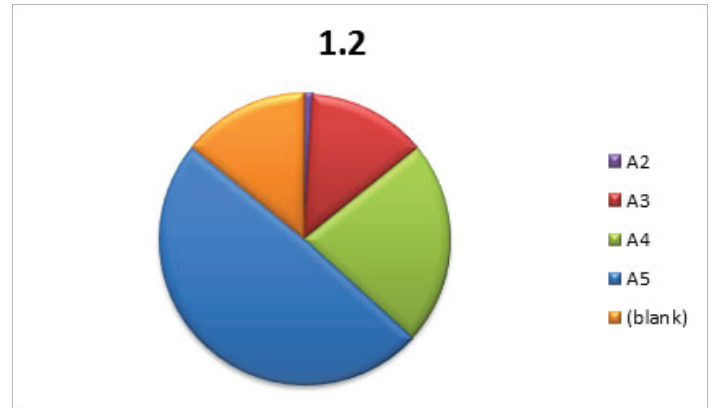
V. References

Brookhaven National Laboratory (Waste Management)- Brookhaven National Laboratory. (Environmental Protection Division). (U.S. Department of Energy), retrieved from <https://intranet.bnl.gov/esh/env/>
 Brookhaven National Laboratory (Quality Management Office)- Brookhaven National Laboratory. (Planning, Performance, and Quality Management). (US Department of Energy), retrieved from <https://intranet.bnl.gov/qmo/>



VI. Acknowledgments

I would like to thank my mentor, Steven Stein, for his help and guidance throughout the program. A special thanks as well to Marlene Mirabile, Charles Gortakowski, Jean Odin McCabe, and Roy Lebel for additional support. This project was supported in part by the U.S. Department of Energy, Office of Science, Office of Workforce Development for Teachers and Scientists (WDTS) under the Science Undergraduate Laboratory Internships Program (SULI).



Catalytic aromatization of methane: ex and in situ structural determination of metal exchanged zeolite catalysts

Tate Harvey, Sheima J. Khatib

Texas Tech University, Lubbock, TX 79409

Andrew Gamalski, Dimitriy Vovchok, T.-D. Nguyen-Phan, Sanjaya Senanayake, Jose Rodriguez
Brookhaven National Laboratory, Upton, NY 11973

ABSTRACT

The catalytic dehydroaromatization of methane which results in the production of benzene and hydrogen, using various metal-loaded zeolite catalysts, namely, Mo, Fe, or Ru, is a novel approach to adding economic value to methane, which is the main component of natural gas. The immediate concern of our research involves determining the presence and specific identity of different metal oxides, their state during reaction, and the influence they have on catalyst activity. It is believed that metal oxides transform to carbides in reaction conditions and that these carbides are the active species responsible for methane activation. To present, direct observation of these species in reaction has not been reported due to the limited number of techniques that can work at such high reaction temperatures. It is necessary to employ in situ characterization techniques that will allow monitoring of the species that are present under reaction conditions, which are likely directly involved in the reaction mechanism. In our work we employ state-of-the-art in-situ XRD measurements with an in situ reaction cell to monitor structural changes happening to a 6wt% Mo/ZSM5 catalyst in reaction. Rietveld refinement of the data indicate that after pretreatment, crystalline MoO₃ seems to re-disperse into the zeolite structure and that major changes occur to the zeolite unit cell parameters under gas flow at varying temperatures. These results are promising and lead to the hypothesis that apart from the zeolite pore structure and acidity, the zeolite lattice could also be playing a role in the reaction mechanism. These results are combined with ex situ measurements (Raman, XRD, DRIFTS, STEM-EDS) of the fresh catalysts, which indicate that for the three metals employed, the phases present are small metal oxide crystallites that are homogeneously dispersed in the zeolite support.

I. INTRODUCTION

The extraction and processing of fossil fuels is the largest source of methane production and expensive reforming processes prohibit alternatives to methane flaring at many well heads. The marginal market value of methane gas and high transportation costs also render many remote drilling sites stranded. The reported research targets the heterogeneous catalytic conversion of methane to value added products, namely, benzene and hydrogen, through the non-oxidative dehydroaromatization reaction: $6 \text{CH}_4(\text{g}) \rightarrow \text{C}_6\text{H}_6(\text{g}) + 9\text{H}_2(\text{g})$. Methane aromatization constitutes an alternative method for the sustainable and efficient use of natural gas, by cutting down on greenhouse gas production from flaring. One of the distinctive and most intriguing features of this reaction is that the formation of C-C bonds and subsequent oligomerization of the C1-C6 species, occurs in one direct reaction step, and

as proposed, may occur over a single multifunctional active metal site, a very challenging and remarkable process. The surface chemistry, reaction mechanism, and major contributing factors to catalyst deactivation are little understood as of yet, and make a promising case for the thorough examination and revelation of answer to these different unknowns.

The methane aromatization reaction is particularly attractive because of its single reactant requirements. With methane as the sole reactant, the presence of other oxidants and associated concerns for complete oxidation and combustion are removed, and the reaction can take place directly at the site of the well head. Disadvantages that currently impede the commercialization of methane aromatization are the rapid catalyst deactivation by coke deposition and low conversions (the most active catalysts tested so far give a methane conversion of only 14%). The removal of hydrogen from the product stream is necessary for moving equilibrium forward, but the high cost of membranes and low reproducibility make this a difficult task. Obtaining a better understanding of these catalysts' influence on methane aromatization, the predominant reaction pathway, and its distinction from deactivation pathways is crucial to minimizing coke formation and increasing selectivity to the desired product, benzene. The synthesis of benzene and hydrogen by methane aromatization is thus a viable reaction with a simple fundamental understanding of this process and subsequent testing of its catalytic limits.

With the use of the national facilities at Brookhaven National Laboratory (BNL) (Upton, NY), including the National Synchrotron Light Source –II (NSLS-II) and the Center for Functional Nanomaterials (CFN) which are user facilities of the U.S. Department of Energy and Office of Science: Basic Energy Science, we have compiled a thorough preliminary study of the methane aromatization process. Ex-situ characterization of the fresh catalysts was immediately important to identify the metal-oxide phases present and their relative dispersion throughout the zeolite support. A contrast between bulk composition techniques like STEM, Raman, and XRD, and surface studies such as XPS are crucial to understanding the location of active sites and the inclusion of these metals in the zeolite pore structure. We have also used in situ characterization techniques that allow monitoring of the species present under reaction conditions.

II. EXPERIMENTAL

A. Catalyst Preparation

A total of 15 different catalysts were prepared with different combinations of metal loadings, preparation methods, and precursors. For preparation using incipient wetness impregnation, Mo, Fe, and Ru were added to commercial ZSM-5 zeolites (Zeolyst International) using precursor solutions of ammonium heptamo-

lybdate tetrahydrate (AHM), iron (III) nitrate nonhydrate, and ruthenium (III) nitrosyl nitrate, respectively. Metal incorporation into the zeolite support through physical mixing was carried out using bulk MoO_3 and Fe_2O_3 . The ZSM-5 support used in all of the samples contained a Si/Al mole ratio of 30 (Si/Al = 30, Zeolyst CBV 3024E). The catalyst samples were calcined at 500 °C following impregnation.

B. Scanning Transmission Electron Microscopy

Crystalline size and surface morphology for (6%) Mo/ZSM-5 was studied with high resolution TEM imaging from an aberration corrected Hitachi HD2700C. The High Angular Annular Dark Field Scanning Transmission Electron Microscopy (HAADF STEM) instrument was run at 200 kV with a spatial resolution of 0.9 nm and energy resolution of 350 meV. STEM-EDS maps were collected using a Bruker Silicon Drift Energy Dispersive Spectroscopy detector. The powder samples were suspended in deionized water and sonicated for 20 min. Catalysts were allowed to settle for 10 min, before putting 1 droplet of solution onto a holey carbon TEM grid. The prepared samples were then air dried and transferred into the STEM.

C. Raman Spectroscopy

The Raman spectra were obtained using a WiTec Alpha combination microscope supplied with both 532 and 633 nm lasers as an excitation source. An integration time of at least 300 s provided more spatially resolved spectra. When samples were examined as fine powder, the high crystallinity of ZSM-5 scatters light too intensely to be properly focused. Zeolite samples pressed into thin

wafers had smoother surfaces, which diminished diffuse reflectance and allowed for smaller focal points.

D. X-ray powder diffraction

The metal-oxide phase identification and long range order determination of Mo, Fe, and Ru on ZSM-5 (6% loadings) were carried out by X-ray Powder Diffraction (XPD) with the Advanced Photon Source (APS) at Argonne National Laboratory. XRD patterns were collected both in operando and ex-situ under the beamlines 17 BM-B ($\lambda = 0.72768 \text{ \AA}$) and 11 BM-B ($\lambda = 0.41417 \text{ \AA}$). The former is equipped with a Perkin Elmer a-Si Flat Panel detector, while the latter uses a unique 12 analyzer detector system with 2 separation of $\sim 2^\circ$ Si(111) analyzer crystals and LaCl_3 scintillation detectors¹. Three different heating profiles and gas flow parameters were used for the in-situ experiments with 6 wt% Mo/ZSM-5. In experiment A, the temperature was initially at RT under pure He flow and was then ramped up to 700 °C and held for 30 min. After soaking, the gas was switched to 80% CH_4/He , while temperature remained at 700 °C for 200 min. Experiment B followed the same conditions as A, but after the 30 min soak at 700 °C in pure He, the temperature was brought back down to RT and gas flow was switched to 80% CH_4/He . Temperature was then increased stepwise to 700 °C, with 30 min soaks at every 100 °C. Upon reaching 700 °C, the temperature was held for 100 min. The sample in experiment C had no pretreatment in He and the temperature was increased stepwise in the same manner as in experiment B, under 80% methane flow to 700 °C, where it was held for 250 min. The ramp rate and volumetric flow rate for all experiments was 10 °C/min and 10 ccm, respectively. Spectra

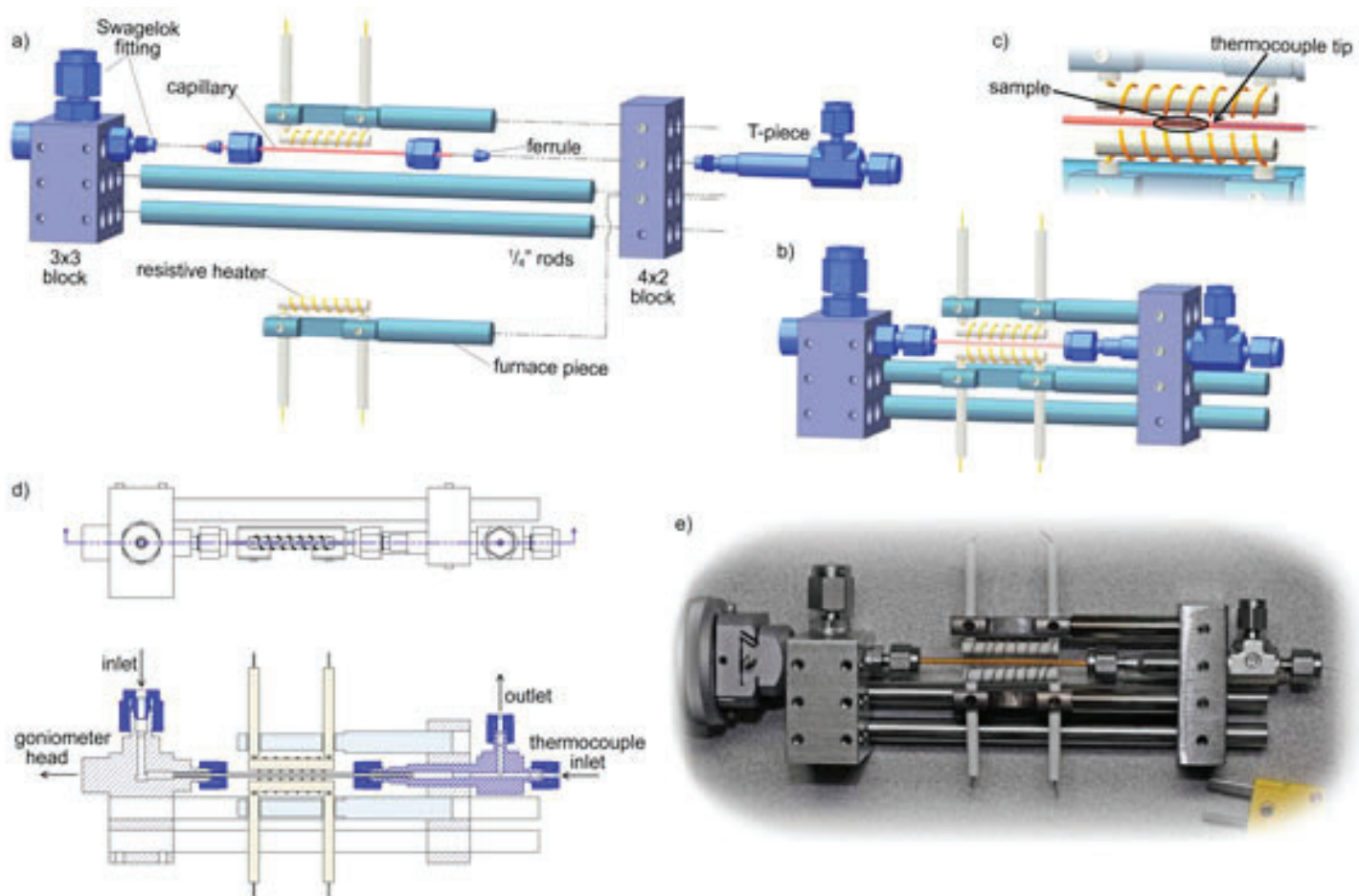


Figure 1: In-situ powder XRD Clausen cell with quartz capillary (ID 0.9 mm OD 1.1 mm)

were collected continuously throughout the experiments, with a 30 sec acquisition time per spectrum.

E. Diffuse Reflectance Infrared Fourier Transform Spectroscopy

DRIFTS data for the 6 wt% Mo/ZSM-5 and blank ZSM-5 samples were collected under reaction conditions on a Bruker Equinox 55 FTIR spectrometer with a Harrick Praying Mantis DRIFT cell. Sample spectra were collected against a KBr background and were outgassed for 20 min in pure He prior to reaction. Initially the temperature in the cell was ramped to 110 °C under 20% O₂/He flow at 20 ccm. The temperature was held at 110 °C for 1 hr, upon which gas flow was switched to pure He at 20 ccm and the temperature was further increased to 550 °C and soaked for 30 min before cooling down to RT. After the temperature in the cell was stabilized at RT, gas flow was again switched to 90% CH₄/He and the temperature was raised to 550 °C with soaks at 200, 300, and 400 °C for 10 min and at 550 °C for 30 min, before cooling again to RT. All ramp rates used in the experiment were set to 10 °C/min.

F. X-ray Photoelectron Spectroscopy

COULD NOT FIND EQUIPMENT INFORMATION

III. RESULTS

Initially, the preparation of the catalyst samples had not been verified as successful by any characterization techniques. General information regarding the very presence and relative dispersion of the different metals exchanged in ZSM-5 was obtained using an overlay of EDS maps on STEM images. STEM-EDS is a bulk technique that makes it difficult to draw conclusions as to the ac-



Figure 2: Praying Mantis™ High Temperature Reaction Chamber

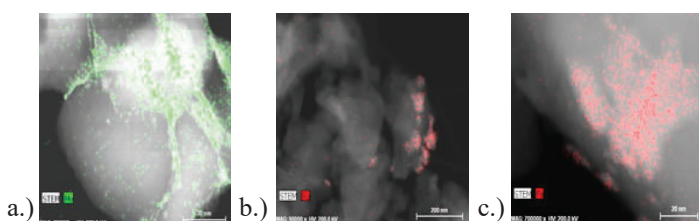


Figure 3: STEM images of 6 wt% Mo, Fe, and Ru overlaid with elemental EDS mapping.

tual location of the metals within the catalyst support. However, certain particle orientations allowed views of particle edges and down extended planes that suggest the bonding sites of metal-oxides are situated on the surface of the support. Contrast between elemental Al and the Mo, Fe, and Ru being imaged, shows that while the impregnated metals are homogeneously dispersed, they are found mostly in small crystallite colonies.

Identification of the crystallites seen in STEM was verified using Raman. As expected, the most prominent feature seen in all spectra came from the ZSM-5 Raman shift at 370 cm⁻¹. Various metal-oxides were identified on samples each prepared by incipient wetness impregnation at metal loadings of 6 wt%. Raman shifts at 520, 640, and 704 cm⁻¹ all correspond to RuO₂. Mo was present in its most common state Mo(IV)-O₃, as seen by the band at 820 cm⁻¹. The band at 957 cm⁻¹, is representative of various MoO_x oxidation states. Two bands in close proximity at 659 and 668 cm⁻¹ correspond to -Fe₂O₃ and Fe₃O₄ phases respectively.

The high spatial resolution of both STEM and Raman contributed to identification of crystalline metal-oxides. The ex-situ data showed no sign of any crystalline metal-oxides, except for MoO₃. XRD is subject to the long-range order and crystallinity of the species present and is blind to particles less than ~4 nm in size.

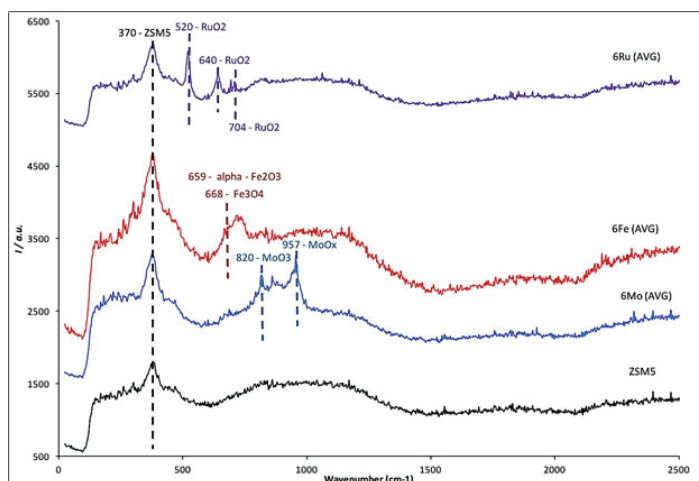


Figure 4: Raman spectra for 6 wt% Mo, Fe, Ru, and blank ZSM-5 showing various metal oxidation states present.

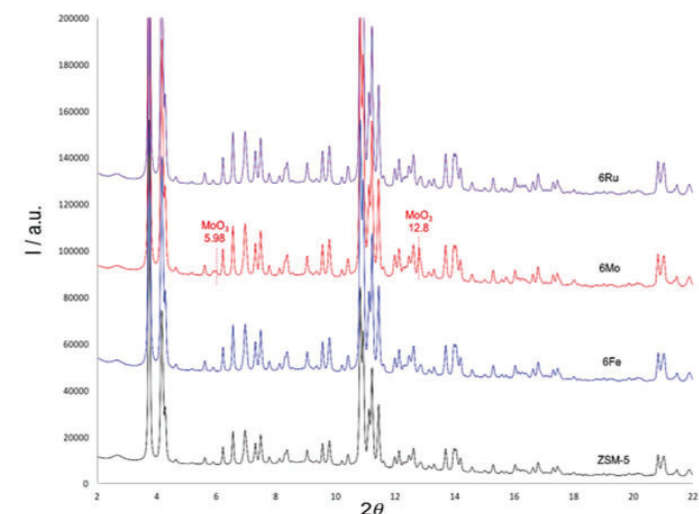


Figure 5: Ex-situ powder XRD patterns for 6 wt% Mo, Fe, Ru, and blank ZSM-5 show visible metal-oxides, except for the MoO₃ peaks of small relative intensity at 5.98° and 12.8°.

The small relative intensity of the MoO_3 peak and the absence of oxide species in other samples indicate that the crystallites, while present, are likely < 4 nm in diameter.

Methane aromatization over metal-exchanged ZSM-5 catalysts has been studied most extensively with Mo as a promoter, and with well established activity and selectivity our research aimed to verify the reproducibility of previous work with our own catalysts. An operando DRIFTS study of pretreatment conditions on 6Mo and ZSM-5 was conducted in order to track changes in framework and external $-\text{OH}$ groups, and understand the influence of Mo addition. The broad band corresponding to surface absorbed water between $2650\text{--}3500\text{ cm}^{-1}$ began to decrease under air flow at 110°C . However, water trapped inside the pore structure was not fully removed until temperatures reached $>200^\circ\text{C}$. The peaks at 3660 and 3783 are associated with externally located Al, at 1.127% . The minor amount of aluminum represented on the catalyst surface is a resultant of Al site removal during ion exchange and the high Si/Al ratio (30 at%). The peak positions were normalized using C(1s) as a reference, and the FWHM for O(1s) was positioned at a binding energy of 532.45 eV . The binding energies of Si(2s), Si(2p), and Al(2p) were found to be 153.95 , 102.95 , and 74.8 eV , respectively. The Si(2p) was an overlap of framework Si-O (103.214 eV) and external Si-OH (104.062 eV) peaks, with Si-O contributing to 68.675% of the total peak area.

$>500^\circ\text{C}$ the peaks at 3608 , 3660 , and 3745 are shifted down to 3590 , 3645 , and 3735 respectively. The presence of 6Mo can be seen by two clear peaks at 990 and 960 cm^{-1} that are representative to crystalline MoO_3 , and the external Al-OH peak at 3660 is split with new low intensity peaks at 3645 and 3655 cm^{-1} .

The informative and crucial understanding of the bulk composition of our samples is only one side the the ex-situ investigation needed for accurate catalyst characterization. XPS studies fill in the gap, providing surface information about present phases and composition. The zeolite support was scanned in an initial survey, which, after deconvolution, showed that surface oxygen comprised the majority of all the elements present, at 56.092% . The combined Si(2p) and Si(2s) regions accounted for an additional 42.781% , leaving room for a small fraction of elemental Al. The peak positions were normalized using C(1s) as a reference, and the FWHM for O(1s) was positioned at a binding energy of 532.45 eV . The binding energies of Si(2s), Si(2p), and Al(2p) were found to be 153.95 , 102.95 , and 74.8 eV , respectively. The Si(2p) was an overlap of framework Si-O (103.214 eV) and external Si-OH (104.062 eV) peaks, with Si-O contributing to 68.675% of the total peak area.

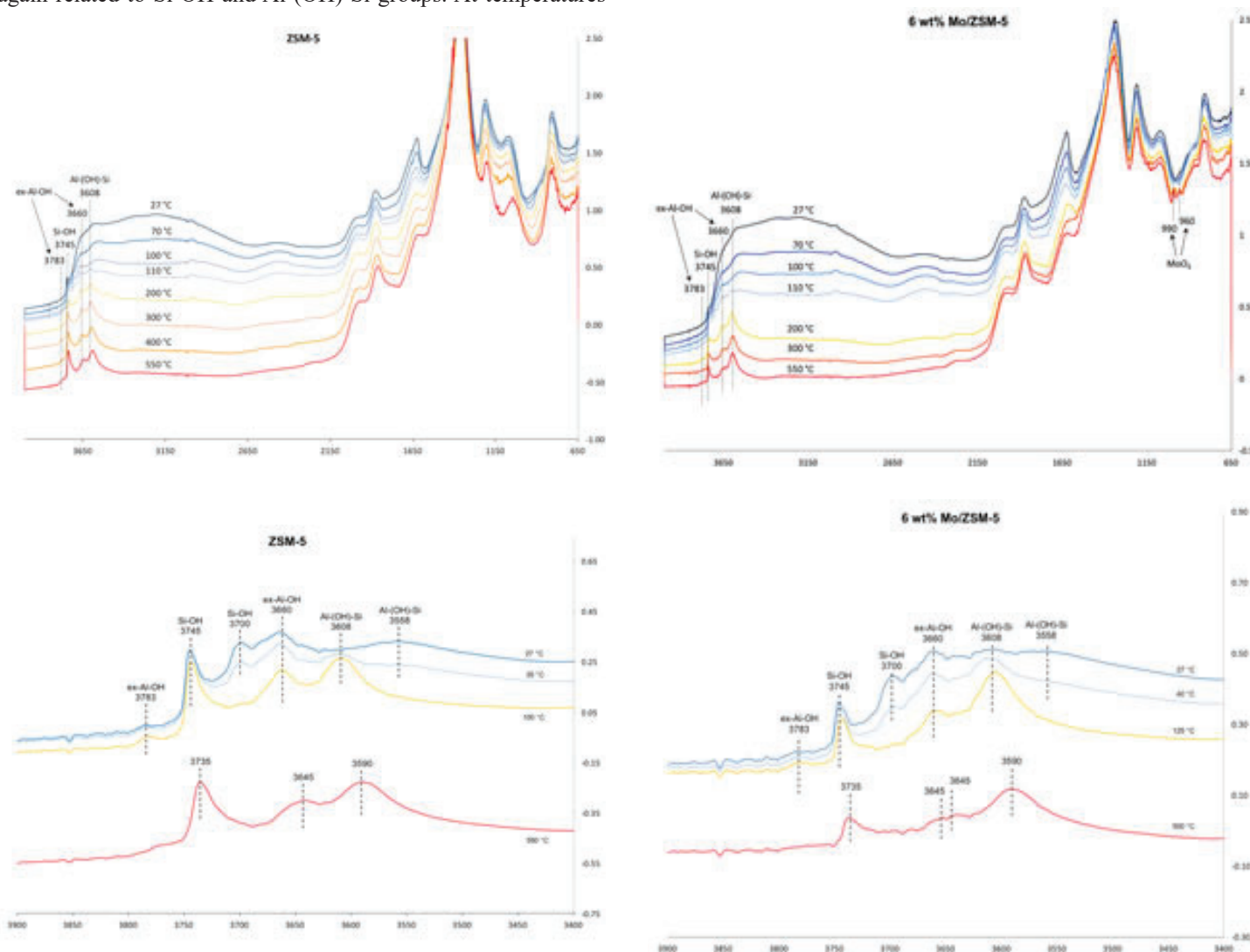


Figure 6: Operando DRIFTS spectra for 6Mo and ZSM-5 under pretreatment conditions, and the zoomed in hydroxide regions showing catalyst $-\text{OH}$ activity.

Phase	Position (eV)	Area %
Si-O	103.214	68.675
Si-OH	104.062	31.325
Al-2p	74.8	-

Table 1: XPS Phase compositions (denoted by peak area percentage) and peak positions given in terms of binding energy (eV).

Analysis and fitting of the Mo(3p) peak is dependent upon the dominant oxidation state present in the Mo(3d) split peak. The Mo(3d) region is mostly comprised of Mo⁶⁺, representing 90.515% of the total peak area with the remainder corresponding to the Mo⁴⁺ oxidation state. The Mo(3p) peak exhibited a left shoulder that was assigned to oxygen vacant (O_v) Mo based on the result that the Mo⁶⁺ oxidation was found to be the most prevalent phase.

Phase	Position (eV)	Area %
Mo ⁶⁺ (3p _{3/2})	397.966	40.457
Mo ⁶⁺ (3p _{1/2})	415.198	50.058
Mo(3p _{3/2})-O _v	401.779	3.865
Mo(3p _{1/2})-O _v	419.689	5.620

Phase	Position (eV)	Area %
Mo ⁶⁺ (3d _{5/2})	232.176	48.125
Mo ⁶⁺ (3d _{3/2})	235.333	46.084
Mo ⁴⁺ (3d _{5/2})	230.051	2.688
Mo ⁴⁺ (3d _{3/2})	233.587	3.104

Table 2: XPS Phase compositions (denoted by peak area percentage) and peak positions given in terms of binding energy (eV) for Mo⁶⁺ and Mo⁴⁺ oxidation states.

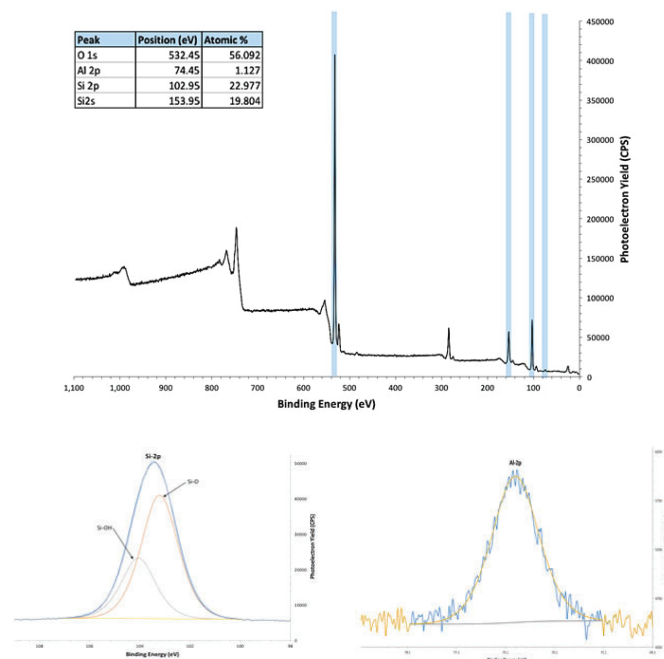


Figure 7: XPS sample survey for blank ZSM-5 and deconvoluted orbital regions for Si-2p and Al-2p.

The metal-oxide phases for Fe were present in comparable fractions, and were identified as Fe²⁺ and Fe³⁺. The peak positions and phase fractions for each region can be found in Table 2.

Phase	Position (eV)	Area %
Fe ³⁺ (2p _{3/2})	712.846	31.135
Fe ³⁺ (2p _{1/2})	726.410	24.282
Fe ²⁺ (2p _{3/2})	710.744	23.804
Fe ²⁺ (2p _{1/2})	724.270	20.779

Table 3: XPS Phase compositions (denoted by peak area percentage) and peak positions given in terms of binding energy (eV) for Fe²⁺ and Fe³⁺ oxidation states.

In-situ XRD results obtained at the Advanced Photon Source at Argonne National Laboratory underwent extensive Rietveld Refinement to monitor minor incremental changes occurring during reaction. Sample patterns were fit using a Si₂₄O₄₈ ZSM-5 unit cell and subjected to sequential refinement of all lattice parameters, particle size, and microstrain. After maintaining stable values for particle size and isotropic microstrain, these parameters were fixed at 0.2 nm and 2500, respectively. No atom positions, Uiso thermal factors, or occupancy fractions were refined in the process. After refinement, the zeolite unit cell was best defined as monoclinic and responded to changes in temperature and reaction progression with sizeable volume changes.

In addition, peaks at 12.00, 12.79, and 15.72 corresponding

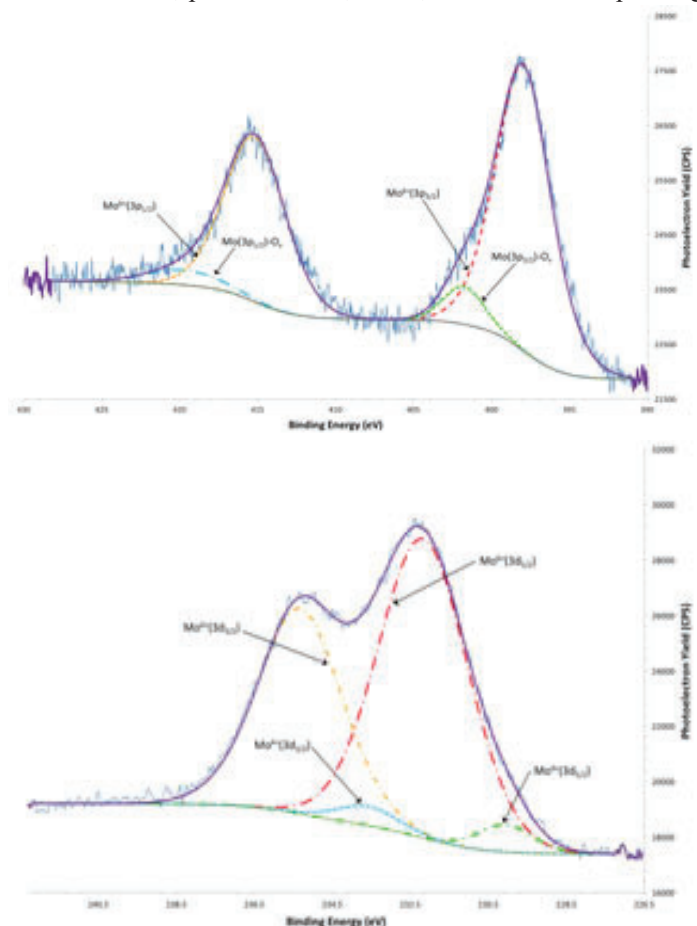


Figure 8: Deconvoluted XPS orbital regions for Mo(3p) and Mo(3d) and the representative oxidation states.

to crystalline MoO_3 disappeared at 700 °C under methane flow. The unit cell volume of the zeolite support was shown to expand and contract with temperature change, and maintained a consistent local maximum that occurred at ~ 200 °C. These volume changes were also seen to have a clear relation to product formation collected with RGA analysis - in specific, hydrogen.

A single sample of 6Mo reacted at 550 °C under 90% CH_4/He flow was examined after reaction using STEM-EDS. The majority of the images taken show significantly more dispersed MoO_3 crystallites and a perceived correlation between carbon formation and metal-oxide sites.

IV. CONCLUSIONS

A comparison of the Raman spectra (633 nm laser) with the XRD patterns for the different metals indicate that in the case of Fe and Ru, oxide crystallites are detected by Raman while they remain invisible to XRD. MoO_3 is detected in both techniques, the relative low intensity of the Raman bands corresponding to the metal oxides suggest that crystallites, while present, are likely < 4 nm in size. Mo-ZSM5 and H-ZSM5 were studied under pre-treatment conditions by DRIFTS to monitor the changes in external and inner pore hydroxide groups. When comparing the peaks in the OH region, at high temperature, the peak corresponding to Si-OH exhibits a lower intensity in the Mo-ZSM5 samples, suggesting that the Mo oxides are probably anchored to the external Si-OH sites of the zeolite. Changes in unit cell volume follow a uniquely different thermal trend before reaction occurs, which

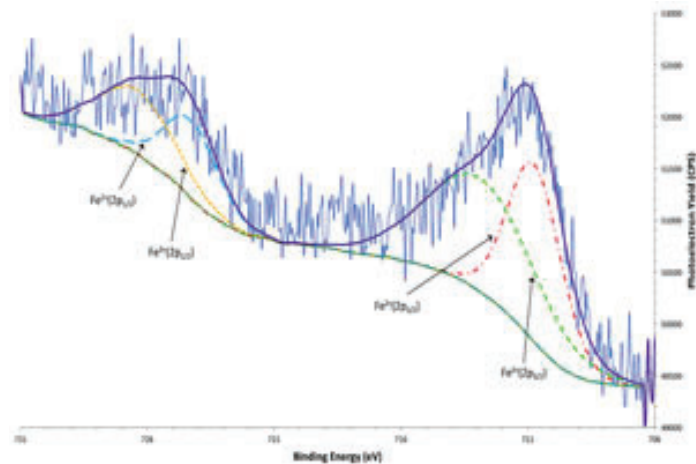


Figure 9: Deconvoluted XPS orbital regions for Fe(3p) and the representative oxidation states.

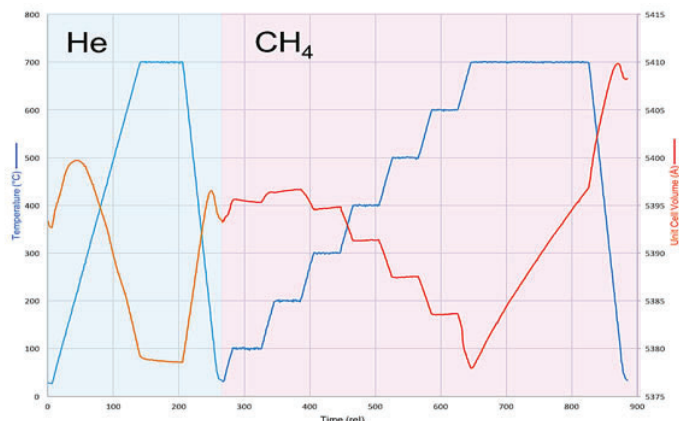


Figure 10: Plot of temperature (°C) and unit cell volume (vs. relative time). Cell volumes were obtained using Rietveld Refinement.

then dramatically increases upon exposure to the reactant gas, CH_4 , and reaction initiation, shown by peaks in H_2 and ethylene production.

The disappearance of MoO_3 XRD peaks at high temperature, in reaction conditions, suggest that dispersed metal-oxides may form active sites in reaction. Zeolite lattice cell parameters are shown to be a dependent of temperature and product formation, which leads to the new belief that, alongside zeolite pore structure and acidity, zeolite unit cell dimensions may also influence catalyst behavior in reaction.

V. REFERENCES

1. Lee, P. L., et al, (2008) Journal of Synchrotron Radiation, v 15, p 427

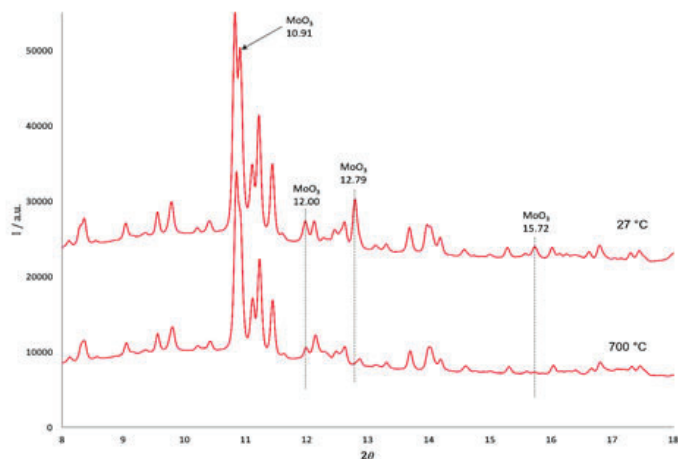


Figure 11: In-situ XRD patterns for 6 wt% Mo/ZSM-5 show the disappearance of crystalline MoO_3 peaks at 700 °C under reaction conditions.

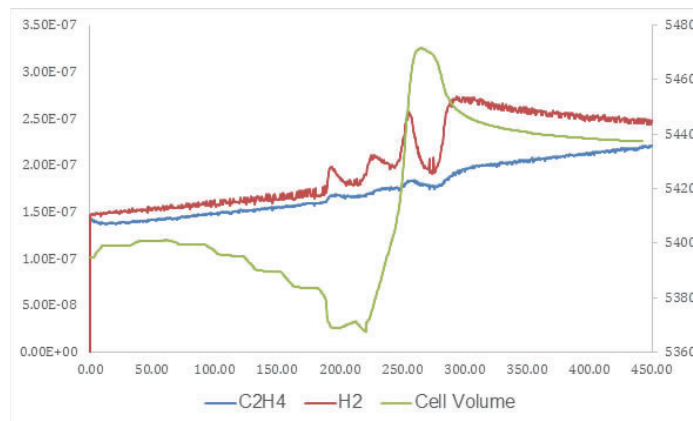
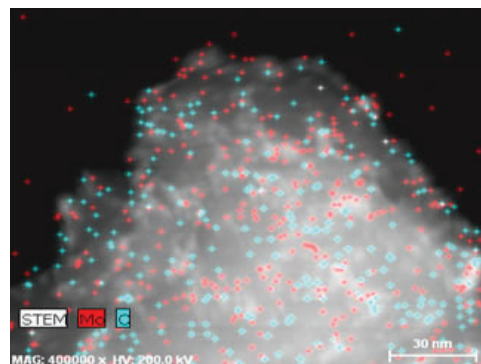


Figure 12: RGA data for ethylene and H_2 production and unit cell volume vs. relative time (reaction progression) and temperature.



Optimization of conductive carbon additive in Lithium-Sulfur (Li-S) battery

Jian Huang

Material Science and Chemical Engineering, Stony Brook University, Stony Brook, NY, 11794

Dong Su and Sooyeon Hwang

Center for Functional Nanomaterials, Brookhaven National Laboratory, Upton, NY 11973

Christina Cama, Kenneth Takeuchi, Amy Marschilok, and Esther Takeuchi

Department of Chemistry, Stony Brook University, Stony Brook, NY 11794

Ke Sun and Hong Gan

Sustainable Energy Technologies, Brookhaven National Laboratory, Upton, NY, 11973

ABSTRACT

For the Li-S battery, due to sulfur's and Li_2S 's insulative properties, conductive carbon additives have been necessary to improve overall cell performance and the electrode's structural integrity. By selecting the proper carbon material, higher sulfur loadings can be achieved to improve energy density in order to meet the DOE's cell level requirements (350 Wh/kg). We evaluated Li-S cells of seven commercially available carbon products of various particle and pore sizes including a control, Super C65. Thermal fusion was done to entrap the sulfur into the carbon and the cathode slurry mix was coated to produce the sulfur electrode. We observed that Ketjen Black and MP97 showed superior electrochemical performance compared to Super C65. Among them, MP97 can be processed to achieve sulfur loadings of greater than 4 mg/cm² without mechanical defects.

I. INTRODUCTION

With the rising demand for improved energy storage in technological applications, there is a major market need for a cost-effective battery chemistry to replace the currently leading choice, the Li-Ion battery while providing exceptional power and energy gains. One of the promising solutions is the Lithium-Sulfur (Li-S) battery that stands out for its high 2560 Wh/kg theoretical energy density and lower material cost due to the abundance of sulfur. This next generation lithium battery technology can be integrated into small electronics as well as used to achieve the current electric vehicle (EV) cell level criteria of the Department of Energy's Vehicle Technology Office.

A. Background and obstacles of the Li-S battery

The Li-S chemistry involves the movement of Lithium ions from the anode to the sulfur cathode where sulfur is reduced to polysulfides ($\text{Li}_2\text{S}_n, 4 \leq n \leq 8$) that are further reduced to Li_2S as shown in Figure 1 of the ideal voltage profile for Li-S discharge. The major challenges involved lie in the low sulfur utilization and the polysulfide dissolution resulting in shuttling effect which reduces the Li-S cell's Coulombic efficiency, cycle life, and cycle stability.¹ Furthermore, due to sulfur and Li_2S being non-conductive materials, there is need for conductive additives to increase the active material utilization. Carbon additives have been utilized to improve sulfur cathode material conductivity as well as to entrap the polysulfides.^{2,3} By containing the polysulfides in the carbon matrix instead of dissolution into the electrolyte, there is greater cycling retention of sulfur as well as minimization of undesired side reactions between the polysulfides, the electrolyte

and the lithium anode.^{4,5} The downside of the carbon content is that the total amount of active sulfur material decreases and thus the energy density of the cell is lowered.

B. Choice of carbon materials

For the Li-S battery, the ideal cathode needs to demonstrate superior conductivity as well as polysulfide trapping capabilities. These properties are highly dependent on the carbon material choice and therefore the focus of this study as we evaluated a selection of 7 carbon type candidates: Ketjen Black, Super C65, mesoporous (MP) carbons MP62, MP83, MP97, Fiber 150 and Fiber 200. They are commercialized carbons that can be obtained from different sources for their lower material cost and different characteristics. For instance, as shown in Figure 2, the materials have been found to have significantly different surface area and pore volumes which affects the mechanism of sulfur retention of each carbon and thus the electrochemical performance when the carbon additive is included in the cathode.

They are also found to have different particle sizes and pore sizes that distinguish each material as shown in Figure 3. These carbon properties would be expected to demonstrate different sulfur trapping capabilities which will provide detailed information about the impact of carbon structure on electrode mechanical integrity and performance.

Furthermore, in order to meet the DOE's vehicle criteria for cell energy density at 350 Wh/kg, modeling has shown that a greater than 4 mg/cm² sulfur loading is required in the cell's cathode. By increasing sulfur loading, the cell's energy density should increase due to the larger amount of active material present.^{5, 6} Cathodes with high sulfur loading are difficult to achieve due to the mechanical defects that form during the electrode prepara-

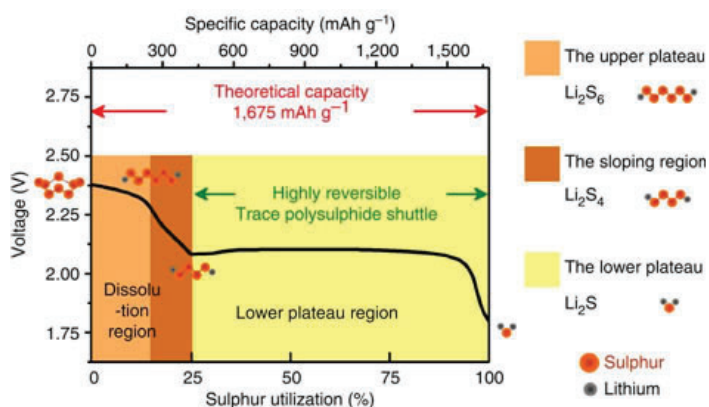


Figure 1. Theoretical discharge capacity vs voltage diagram of the Li-S chemistry. Su, Y.-S. *et al. Nat. Commun.* 4:2985 (2013).

tion process, such as cracking and delamination. This mechanical problem could be resolved by selecting an effective conductive carbon additive. The impact of several carbon additives on the Li-S cell electrochemical performance and electrode mechanical integrity is evaluated in this study.

II. METHODS

The thermal fusion method was used to make composite sulfur-carbon material using a 3:1 mixture of elemental sulfur powder (Alfa-Aesar) to each of the seven different commercially available carbon additive candidates: carbon blacks (Timical Super C65 Conductive Carbon Black and Ketjen Black), carbon fibers (150 micron long PAN-sourced and 200 micron long Pitch-sourced) or mesoporous carbons (MP62, MP83, MP97) that was sealed tightly inside a PTFE bottle, which was heated at 155°C for 24 hours. The cathode slurry which totaled 2g of material was made in a 62:30:8 ratio of sulfur to carbon to hydroxypropyl cellulose (HPC) binder, including 9.5% carbon black C65 added as make-up carbon to reach the desired ratio. This slurry was milled at 15 rpm using 30g of grinding media as well as 5g of n-methyl-2-pyrrolidone (NMP, Aldrich) with 2g of NMP added every hour until the mixture became homogenous and free-flowing totaling 15g to 17g of solvent depending on carbon material. It was

casted with a doctor blade at set gap width to spread the slurry out evenly onto aluminum foil using gaps of 250, 500, 750 μm. The coated electrode was air-dried for 12-24 hours, then oven-dried at 50°C for 24 hours. The dried electrode was stored for measurement and observations. Tape test was performed on electrodes using scotch tape that contacted the surface only through a punched circular hole on a piece of paper and weighed down by a total of 0.98 kg/cm² using a set of weights for 30 seconds and then pulled off in ten separate locations. For coin cell assembly, coated foil was punched into 1.27 cm diameter circular electrodes. They were assembled inside an Argon-filled glove box using CR2032 cell parts with a 1.6 cm diameter brushed lithium anode and Celgard 2325 film as the separator. The electrolyte used was 1.0M lithium bis(trifluoromethanesulfonyl)imide in a 1:1 solution of 1,3-dioxolane and dimethoxy ethane, containing 1% by weight lithium nitrate (1.0M LiTFSI/DOL:DME=1:1 + 1wt% LiNO₃). The internal contents of the cell are as follows: sulfur electrode, 80 μL of electrolyte, two layers of separator film, lithium electrode, two spacers and a spring; then the cell was crimped closed. The cells were electrochemical tested on Arbin coin cell testers at C/5 discharge and charge rates with a C/3 rate every 20th cycle.

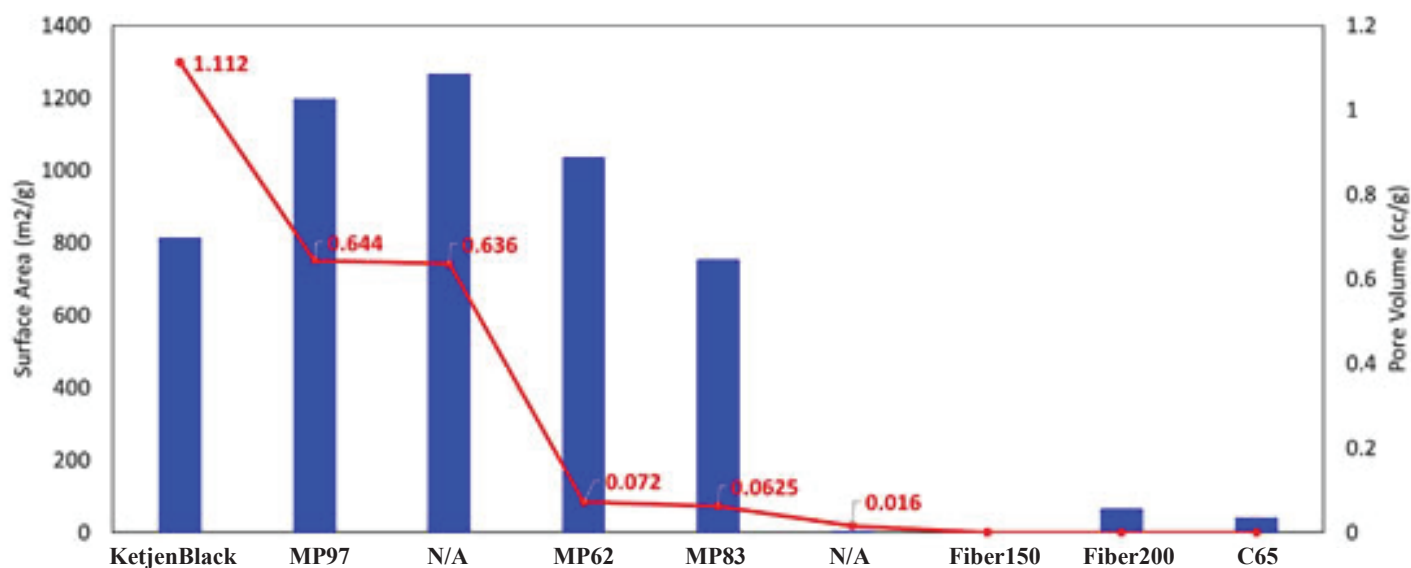


Figure 2. Surface area and pore volume of studied carbons calculated from BET analysis completed by SBU sub-team. The carbon fibers and Super C65 were found to have pore volume lower than the instrument's reading capabilities.

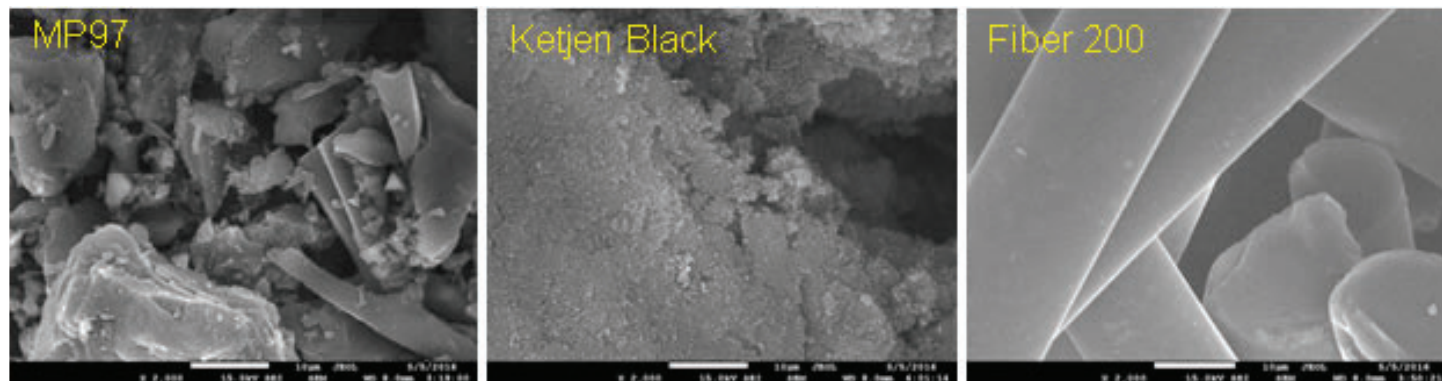


Figure 3. Images of several of the studied carbon materials' morphology taken with a SEM at the Center for Functional Nanomaterials (CFN).

III. RESULTS

A. Mechanical integrity of the electrodes

There is a significant impact on cohesion and adhesion properties of the electrode depending on the carbon material. As seen in Figure 4, Ketjen Black is completely removed showing severe delamination while MP97 remains on the foil indicating MP97 particles bind better to the Aluminum foil surface and to each other. In Figure 5, it is clear that the smaller particle size carbons, C65 and Ketjen Black, have much more material pulled showing poor adhesion that can affect cathode stability during cycling. Fiber 150 electrodes are not shown here or in following data because it was unusable as it was found to be trapped inside the PTFE bottle following thermal fusion.

B. The effect of carbon additive on electrochemical performance

The type of carbon additive has a very significant effect on the electrochemical performance of assembled coin cells of 1.3 mg/cm² loading. As shown in Figure 6, there are differences in



Figure 4. Electrodes of 1.3 mg/cm² sulfur loading after tape test, Ketjen Black (left) and MP97 (right).

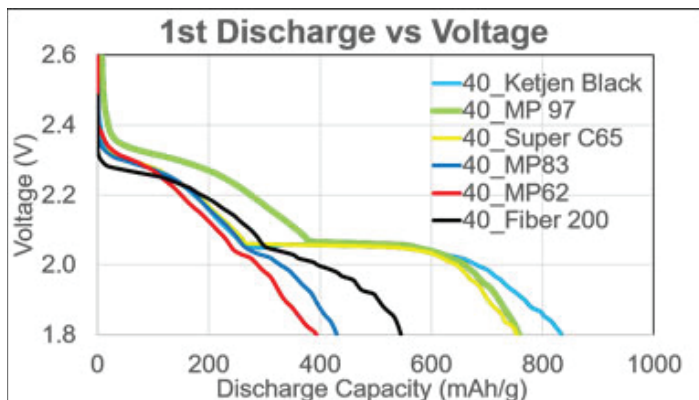


Figure 6. The 1st discharge vs voltage profiles for each carbon additive's coin cell with cathode sulfur loadings of 1.3 mg/cm².

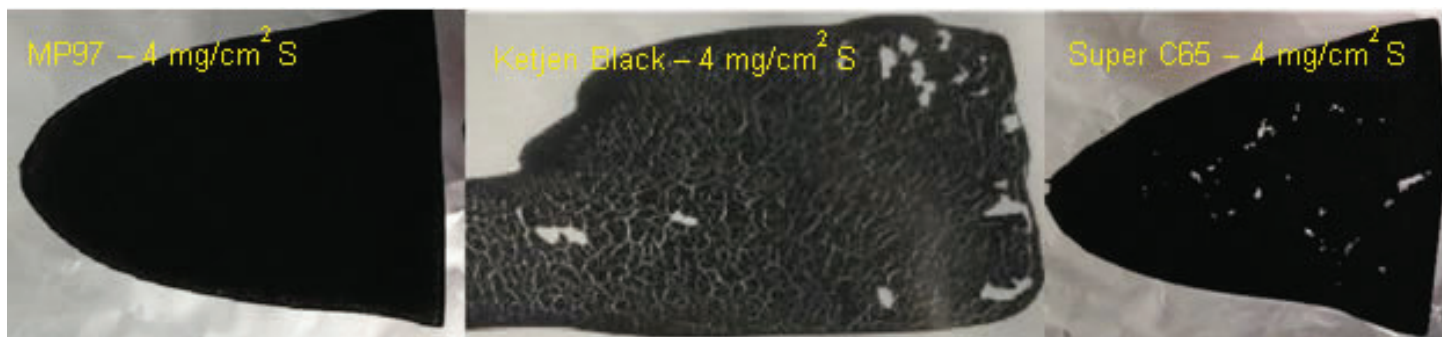


Figure 8. Images of electrodes of higher sulfur loading (4 mg/cm²) for the carbons that displayed good electrochemical performance.

the voltage profiles between the carbons that offer insight into the activity of the Li-S cell. The larger discharge capacities of Ketjen Black, MP97, and Super C65 is mainly distinguished with a 2nd voltage plateau. As seen in Figure 1, this 2nd plateau is critical in the Li-S battery as it represents the majority of the cell's specific capacity that is found between in the reduction of polysulfides into Li₂S. The absence of the 2nd voltage plateau in the poor performing carbons, MP62, MP83, and Fiber 200 shows that they do not exhibit significant polysulfide interactions with lithium ions and have low % sulfur utilization making them poor choices as a cathode additive. Correspondingly in Figure 7, the cycling discharge capacities show distinct performance differences between the carbon additives. Superior candidates are shown to have improved sulfur utilization and discharge capacities over many cycles. Only Ketjen Black exhibits significant capacity fade over time suggesting the smaller particle size carbon is having issues with sulfur material retention but nevertheless has extraordinary discharge performance likely from its high conductivity.

There also appears to be a strong correlation for electrochem-

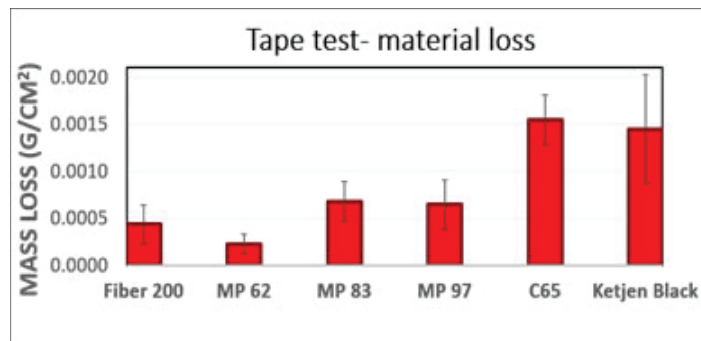


Figure 5. Average weight of material pulled during tape test for each electrode of different carbon material.

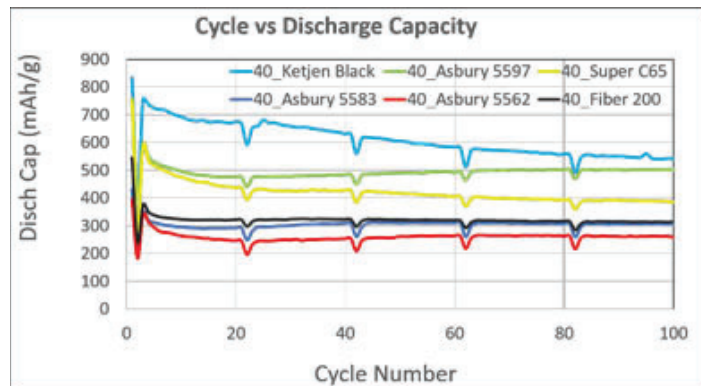


Figure 7. The cycle vs discharge capacities at C/5 with a C/3rate every 20th cycle for each carbon additive's coin cell with cathode sulfur loadings of 1.3mg/cm².

ical performance to the carbon's pore volume found in Figure 2 with exception of Super C65, suggesting the carbon's larger pores can trap polysulfides more effectively.

C. Achieving high sulfur loadings

These carbon additives were further investigated for their mechanical integrity with thicker coatings that produced higher sulfur loading electrodes that showed the mechanical difficulties to increase energy density in the cathode. As seen in Figure 8, Ketjen Black and Super C65 electrodes show mechanical defects in the form of delamination from the foil and severe cracking. These observations provided evidence that the smaller particle size carbons will fall apart from the cathode during preparation and cycling of cells, limiting their usability in their current state. However, the MP97 electrode remains intact at higher loading while also showing no mechanical defects and good cohesion and adhesion in the tape test. With its good mechanical stability and electrochemical performance, MP97 was selected for additional loading study with targeted sulfur loading ranging from 4 mg/cm² to 10 mg/cm² to determine the material's upper limit and physical characteristics.

Shown in Figure 9, the mesoporous carbon with larger particle size, MP97, was able to demonstrate extremely high sulfur loadings without mechanical defects on its surface up to 9.09 mg/cm². There is an observed large crack present on the thicker electrode on the right signifying the material has approached its physical boundary of remaining intact. However, the material is brittle and its surface is rough making it challenging to work with and requiring further optimization. It is likely that the rough surface of this electrode can be smoothed with addition of a 2nd carbon of smaller particle size which would improve the material's properties in formulation and electrochemical loading studies.

IV. CONCLUSIONS

The essential battery requirements in energy storage to be met are energy density, rate capability and long cycle life. For the sulfur cathode in the Li-S battery, there is a need for good conductivity and polysulfide trapping stability to achieve these criteria which has been widely approached using carbon additives. Other scientists have reported use of hollow carbon spheres, hierarchical ordered carbons and carbon nanotubes structures that produce

high discharge capacities and utilize different methods of encapsulating the sulfur material.^{7,8,9} Conversely, these specialized carbons come with higher production cost and procedures that restrict their mass-production. The materials must be cost efficient and demonstrate great mechanical integrity which can then allow the Li-S battery to be capitalized on for its improved energy performance. High sulfur loading cathodes are critical to achieve Li-S's high energy density to propel its widespread use in electronics.

As commercialized materials, the carbon candidates selected would demand a lower material cost and require fewer preparation steps. Using our methods to make cells with sulfur loadings of 1.3 mg/cm², it is shown that Ketjen Black, Super C65, and MP97 performed better electrochemically compared to other tested candidates. These carbons display the desired 2nd voltage plateau's high capacity showing better polysulfide reduction during operation and retain much higher energy capacities. However, the Ketjen Black and Super C65 electrodes fail to remain mechanically stable above 4 mg/cm² sulfur loading. Using MP97, sulfur loading of up to 9 mg/cm² was achieved making it a suitable candidate for future studies. In further work, the mechanical integrity as well as the electrochemical performance of the MP97 electrodes will need additional improvement through formulation and process optimization.

V. REFERENCES

- ¹A. Manthiram, Y. Fu, S.H. Chung, C. Zu, and Y.S. Su, *Chemical Reviews* 114 (23), 11751(2014).
- ²S.H. Kang, X. Zhao, J. Manuel, H.J. Ahn, K.W. Kim, K.K. Cho, and J.H. Ahn, *Physica Status Solidi A* 8, 1895(2014).
- ³Y. Fu, Y.S. Su, and A. Manthiram, *J. Electrochem. Soc.* 159, A1420(2012).
- ⁴K. Fu, Y. Li, M. Dirican, C. Chen, Y. Lu, J. Zhu, Y. Li, L. Cao, P. Bradford, and X. Zhang, *Chem. Commun.*, 50, 10277(2014).
- ⁵R. Sahore, B. Levin, M. Pan, D. Muller, F. DiSalvo, and E. Giannelis, *Adv. Energy Materials*, 1600134.(2016).
- ⁶J-S. Kim, T.H. Hwang, B.G. Kim, J. Min, and J.W. Choi, *Advanced Functional Materials*, 24, 5359(2014).
- ⁷N. Jayaprakash, J. Shen, S.S. Moganty, A. Corona, and L. Archer, *Angewandte Chemie*, 50, 5904(2011).



Figure 9. Electrodes of very high sulfur loadings achieved using MP97 as the carbon additive material only.

⁸B. Ding, C. Yuan, L. Shen, G. Xu, P. Nie, and X. Zhang Chem. Eur. J.,19, 1013(2013).

⁹X.B. Cheng, J. Huang, Q. Zhang, , H. Peng, M. Zhao, and Fei Wei, Nano Energy, 4, 62 (2014).

VI. ACKNOWLEDGEMENTS

This project was supported in part by the U.S. Department of Energy, Office of Science, and Office of Workforce Develop-

ment for Teachers and Scientists (WDTS) under the Science Undergraduate Laboratory Internships Program (SULI) as well as the Office of Energy Efficiency and Renewable Energy. Thanks to collaborators of the SBU sub-team for materials characterization. Also thanks to the CFN sub-team for assisting the SEM/TEM material analysis. Special thanks to Dr. Hong Gan, Dr. Ke Sun, and Brookhaven National Laboratory for the opportunity and guidance to conduct thiswork.

Developing the dipole corrector power supply beam permit system

Nida Imtiaz

Electrical and Computer Engineering Technology, Farmingdale State College, Farmingdale, NY 11735

Carl Schultheiss

Collider-Accelerator Department, Brookhaven National Laboratory, Upton, NY 11973

Abstract

The Relativistic Heavy Ion Collider (RHIC) at Brookhaven National Laboratory collides two beams of heavy ions that travel at nearly the speed of light. RHIC is 3.3 kilometers in circumference and has 468 dipole corrector magnets that fix the orbit of RHIC locally. These dipole corrector magnets are distributed around RHIC and are individually powered by dipole corrector power supplies. If a fixed number of corrector power supplies turn off, the beam could damage the machine. The beam permit system allows the beam to be injected and stored in RHIC. The beam permit system has several inputs, for example; beam loss monitor, vacuum and quench link, to sense the “health” of the beam. The dipole corrector power supply beam permit system will become another input to the beam permit system that will prevent the machine from being damaged. This paper describes the dipole corrector power supply beam permit system and how this system will react when a certain number of dipole corrector power supplies turn off. This system will monitor the signals coming from the dipole corrector power supplies and eject the beam safely into the beam dump when needed. This system is coded in Verilog High-Level Design Language (VHDL) and uses the Quartus Prime Standard Edition software to program the MAX 10 FPGA Development Kit.

I. Introduction

The Relativistic Heavy Ion Collider (RHIC) is one of only two operating heavy-ion colliders in the world and is located at Brookhaven National Laboratory (BNL) in Upton, New York. RHIC is the only operating particle collider in the United States that collides ions traveling at relativistic speeds. Physicists from around the world are using the RHIC to study the primordial form of matter that existed in the universe shortly after the Big Bang. The RHIC is one of the most commonly used research facilities at BNL and to conduct research and collect data, RHIC mainly uses gold ions, which is one of the heaviest elements. The beams in the RHIC travel around two rings in opposite directions at nearly the speed of light.

There are different types of power supplies in the RHIC and they all supply current to the superconducting magnets and these magnets bend the beam into a circle. One of these types of power supplies is called dipole corrector power supplies which power the 468 dipole corrector magnets that are spread around the two rings. The dipole corrector magnets locally correct the orbit. Therefore, if a fixed number of dipole corrector power supplies turn off, then the beam could hit the beam pipe and damage the machine.

The purpose of this project is to design a system that will shut down the beam when too many dipole corrector power supplies shut off. This project, the Dipole Corrector Power Supply Beam Permit System will be integrated into the higher level system

called the Beam Permit System. The Beam Permit System allows the beam to be injected into, and remain within RHIC. The Beam Permit System receives inputs from the services buildings and alcoves. These inputs have to be high in order to grant permission to RHIC to inset the beam into the beam pipe. The Dipole Corrector Power Supply Beam Permit System will be another input to the Beam Permit System and this system will be placed inside the alcoves.

The system prototype is built using the MAX10 FPGA Development Kit platform and the programming language being used is Verilog behavioral (procedural) language. We are using Quartus Prime Standard Edition software to upload the code to MAX10 FPGA Development Kit and to troubleshoot errors in the code.

II. Methods

The Dipole Corrector Power Supply Beam Permit System is designed to monitor all of the dipole corrector power supplies in RHIC, and to abort the beam when a fixed number of dipole correct power supplies shut off unexpectedly. There are six node cards connected to the RHIC and each node card has up to eleven dipole corrector power supplies. As described in Figure 1, each dipole corrector power supply has an on status which is an input to this system. These inputs go to a parallel adder called the Adder Tree that sums up all the “on” signals. These inputs can be masked to disable the signals coming from certain dipole corrector power supplies. The Power Supply Mask Adder register adds up all the “on” signals coming from the unmasked corrector power supplies, and subtracts a fixed number of dipole corrector power supplies that can be allowed to fail. Finally, the Adder Tree register gets compared with the Power Supply Mask Adder register and if the value in the Adder Tree is less than that of the Power Supply Mask Adder, the system will drop the corrector power supply beam permit input.

The system parameters can be programmed and read over the Ethernet. The Input Status register provides a way to record the state of the dipole corrector power supplies when the beam permit is pulled by this system; to help with diagnosing the cause. In Figure 1, the green dotted line separates this design into two modules, meaning they are working in different levels for the efficiency of the code. On the left hand side of this line is the Power Supply module and on the right is the Beam Out module. This system is written in Verilog HDL, which is a hardware description language use to design and document electrical systems.

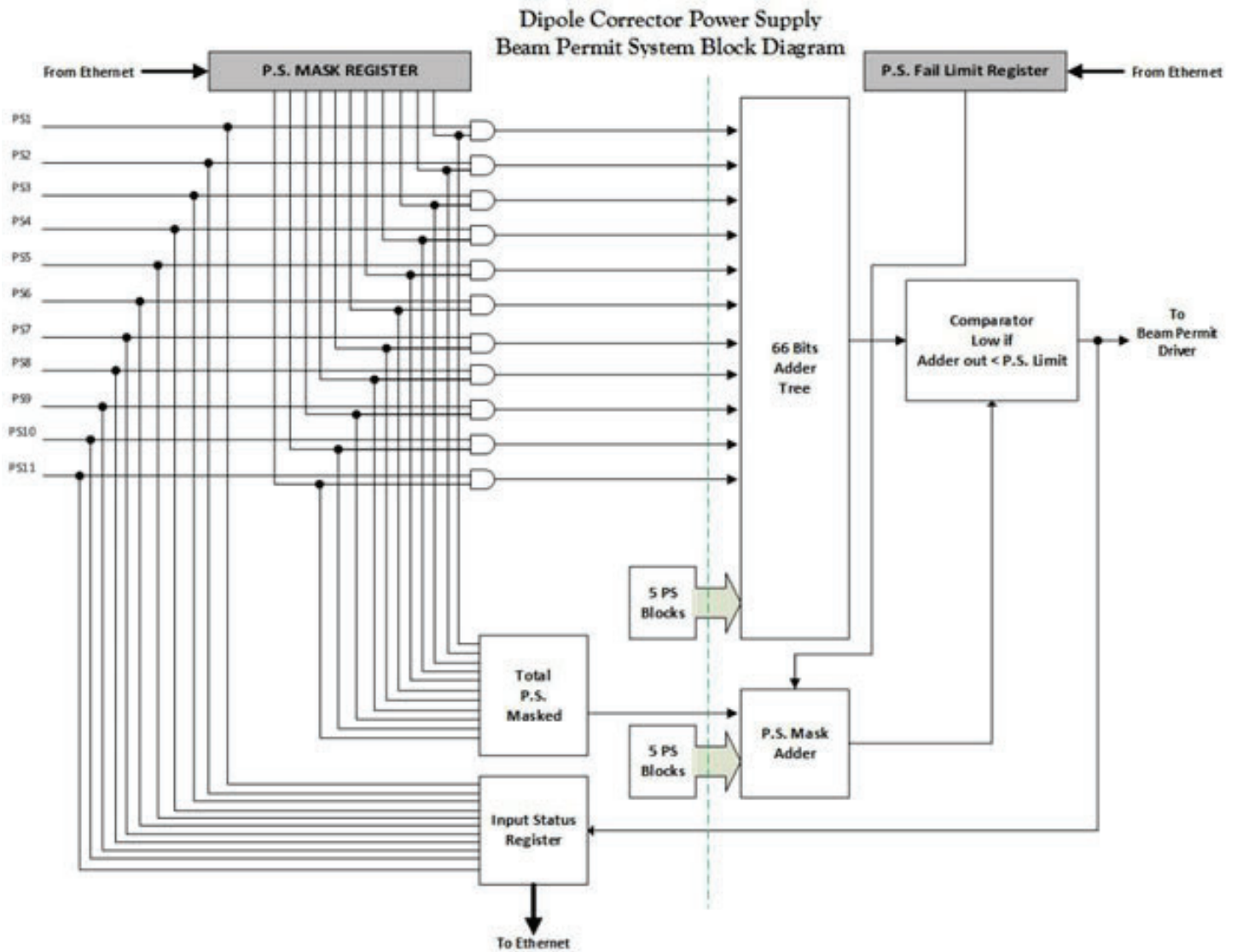


Figure 1. Overall design of the Dipole Corrector Power Supply Beam Permit System

The system has multiple modules:

- Corrector Power Supply Beam Permit
- Beam Channel
- Power Supply
- Beam Out
- Address Decoder
- MUX Power Supply
- Clock Divider
- MAC Configuration
- Ethernet Frame FSM
- Triple Speed Ethernet MAC
- Packets to Bytes
- Bytes to Packets

As described in Figure 2, each module has its own functionality but they all depend on each other for their inputs and that is how they are interconnected. The module, Corrector Power Supply Beam Permit is the top level module which connects the inputs and output of this system to the MAX 10 FPGA Development Kit's interface. All other modules instantiate inside this top level module. The module Power Supply and Beam Out are described in Figure 1 and the module Address Decoder and MUX Power Supply are described in Figure 3.

In this system, the data coming from the Ethernet is only be-

ing written to Mask Register in Power Supply module and Fail Limit Register in Beam Out module. On the other hand, the data read from the Ethernet is coming from Mask Register and Input Status Register in Power Supply module and Fail Limit Register is also being read from Beam Out module. Address Decoder module takes the data that is coming from the Ethernet and either latches the Mask Register in one of the Power Supply modules or Fail Limit Register in Beam Out module.

MUX Power Supply module is a 13 by 1 multiplexer that takes inputs from Power Supply module and Beam Out module. Based on the value that is coming from Address Decoder module, it selects the register and sends it as an output to the Ethernet. As Figure 3 elaborates more on the module Address Decoder and MUX Power Supply, the output of the Ethernet Frame FSM module is the manipulated data coming from the Ethernet. In other words, Address Decoder module selects one of the Power Supply Modules and, based on the data, it masks the "on" status of the dipole corrector power supply. The MUX Power Supply module is used to read back the data and the current status of the dipole corrector power supply.

In Figure 3, the green dotted line separates the two modules. The left hand side of the dotted line is the top level module called Corrector Power Supply Beam Permit module and the right hand

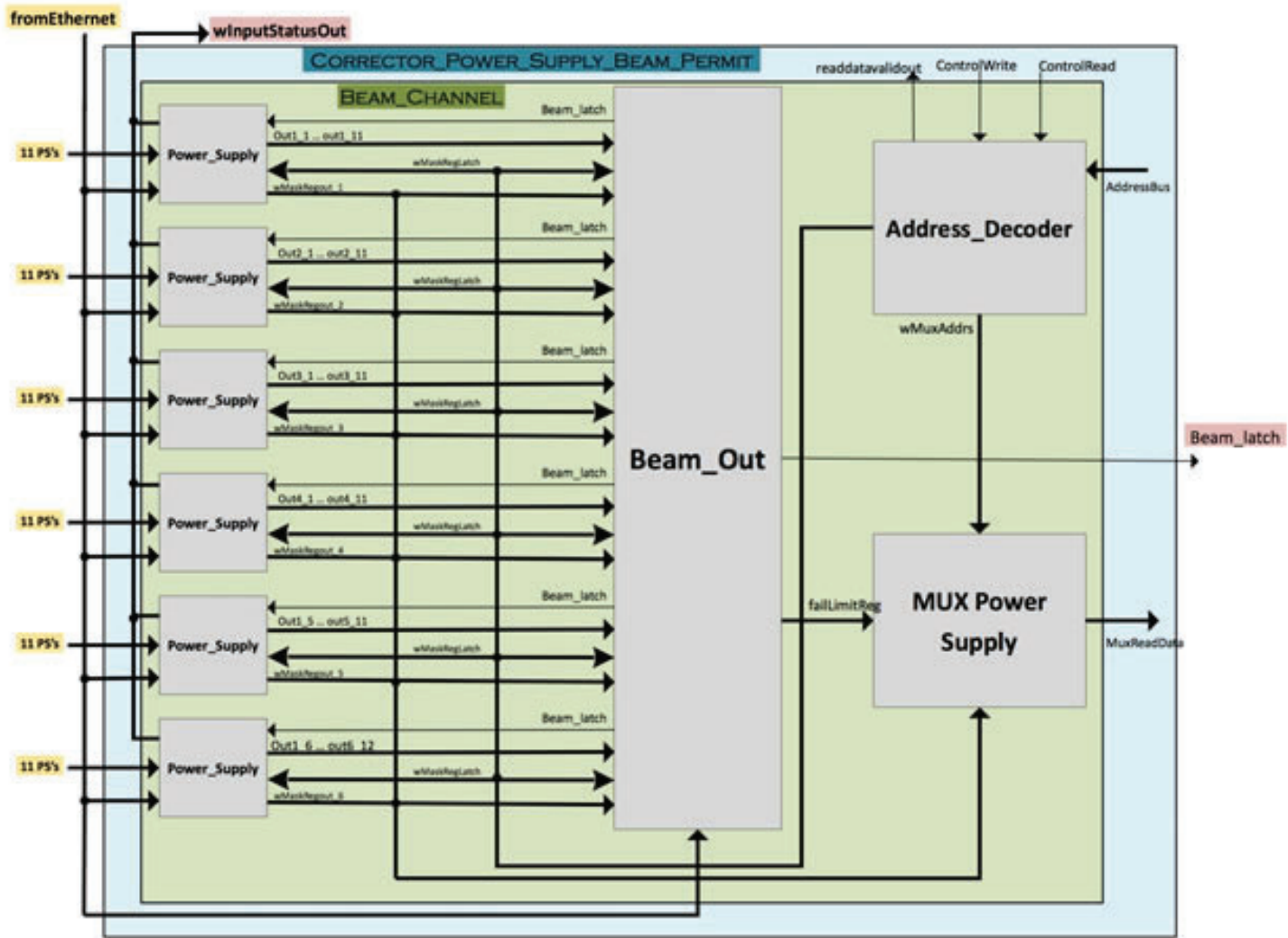


Figure 2. Coding Block

side is called Beam Channel module. The modules inside the Corrector Power Supply Beam Permit module are associated with formatting the data that is being transmitted and received from the Ethernet.

In order to transmit and receive data from the Ethernet, the Triple Speed Ethernet MAC module is configured by the MAC Configuration module. Triple Speed Ethernet MAC module receives the data in the form of Ethernet frames from the network, as shown in Figure 4. After receiving the Ethernet frames, it removes the preamble and SFD field and makes Avalon packets, which gets forwarded to the Packets to Bytes module. Packets to Bytes module transforms the Avalon packets into bytes and forwards only the payload data to the Ethernet Frame FSM module.

Ethernet Frame FSM module analyzes the incoming data and decides if this Ethernet packet belongs to this system. This module forwards the data to Address Decoder module if the incoming Ethernet packet belongs to the system. If it does not belong, it just drops that Ethernet packet.

On the other hand, when the system wants to send data to the Ethernet, the Ethernet Frame FSM module reads the data from MUX Power Supply module and aligns it in a manner that it can forward to the Bytes to Packets module. Bytes to Packets module receives bytes and transform them into Avalon packets and for-

ward those Avalon packets to Triple Speed Ethernet MAC module. Triple Speed Ethernet MAC module attach the preamble and SFD fields to the Ethernet packets and send them to the network as Ethernet Frames via a PHY Ethernet port.

III. CONCLUSION

This project will prevent costly downtime for RHIC. Past experience has shown the machine can be damaged if only a handful of the corrector power supplies unexpectedly shut off. The Dipole Corrector Power Supply Beam Permit System will be integrated into the main system called Beam Permit System. In order to protect the machine, the system will observe the “on” status of the dipole corrector power supplies in the RHIC and dump the beam into the beam dump in a case of a fixed number of dipole corrector power supplies shut off.

IV. ACKNOWLEDGEMENTS

I am most grateful to my mentor, Carl Schultheiss, for providing me an opportunity to work with him and his encouragement in carrying out this project work. I would also express my gratitude to the Office of Science Education, and other staff members of Collider-Accelerator Department who helped me during the period of my internship. Finally, I wish to acknowledge the

Communications Block Diagram

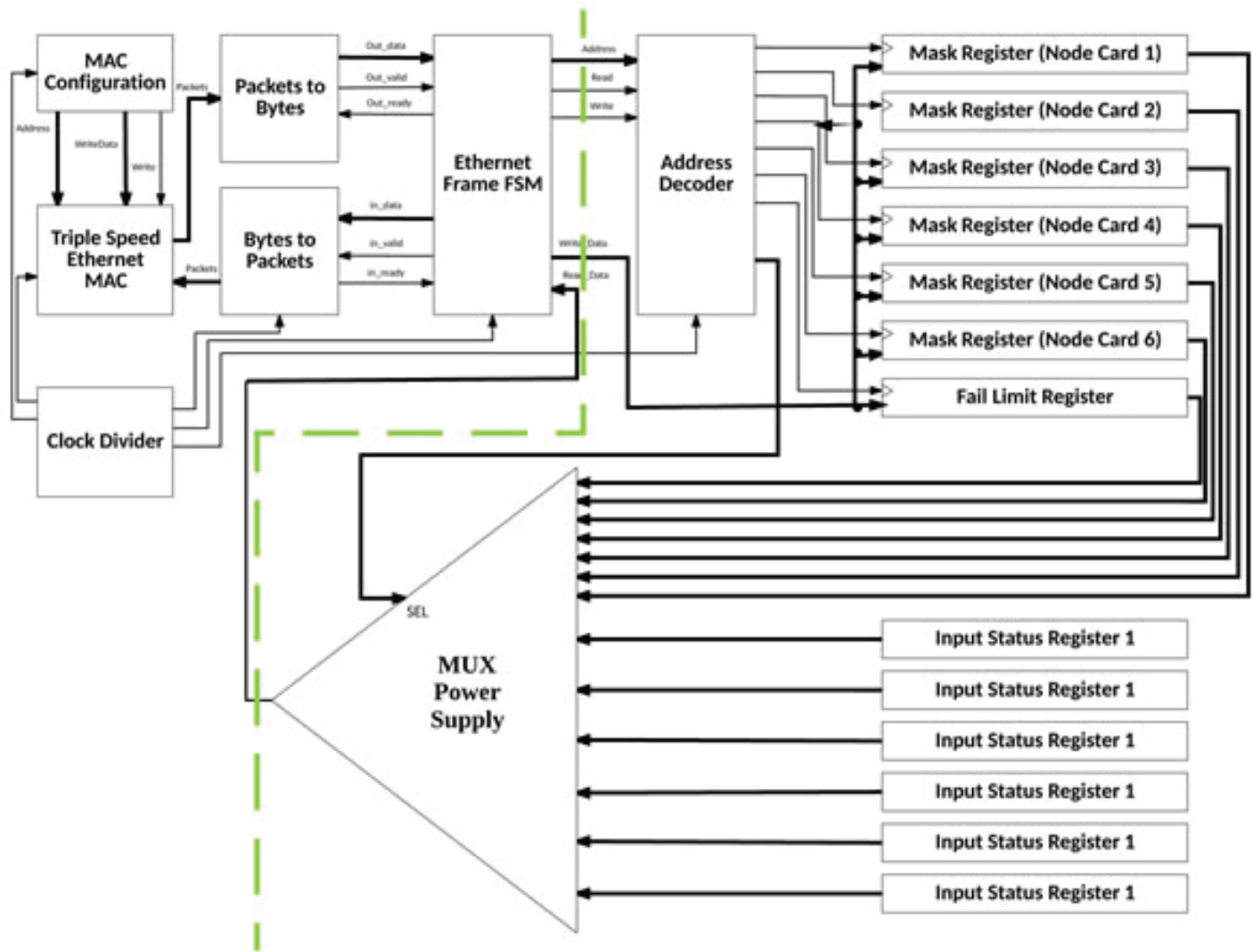


Figure 3. Communications Block Diagram

PREAMBLE	SFD	DESTINATION ADDRESS	SOURCE ADDRESS	LENGTH/TYPE	PAYLOAD DATA	PADDING	FRAME CHECK SEQUENCE

Figure 4. MAC Frame Format

hospitality and kindness of Brookhaven National Laboratory and the Department of Energy.

This project was supported in part by the New York State Collegiate Science and Technology Entry Program (CSTEP) at (Farmingdale State College) under the CSTEP- Supplemental Undergraduate Research Program (SURP) at Brookhaven National Laboratory.

This project was supported in part by the U.S. Department of Energy, Office of Science, Office of Workforce Development for Teachers and Scientists (WDTS) under the Science Undergraduate Laboratory Internships Program (SULI).

Developing growth procedure and measuring spectral response of NaKSb photocathodes.

Riley Joinnides

Chemical and Biological Engineering, Rensselaer Polytechnic Institute, Troy, NY 12180

Daniel Wines

Physics and Engineering Physics, Fordham University, Bronx, NY 10458

Triveni Rao

Instrumentation Department, Brookhaven National Laboratory, Upton, NY 11973

Abstract

The Relativistic Heavy Ion Collider (RHIC) at Brookhaven National Laboratory (BNL) requires photocathodes with a high electron yield and long lifetime that can reliably provide tens of mA of current to cool the charged particle beam for the Low-Energy RHIC electron Cooling (LEReC) project. Bi-alkali metal photocathodes have been considered suitable for such an application. Vapor deposition of alkali metals in an ultrahigh vacuum environment is one technique for fabricating bi-alkali cathodes. At BNL, a deposition chamber had been assembled and had reliably produced high performance cesium potassium antimonide (CsKSb) photocathodes. However, this material is short-lived if raised to temperatures $>100^{\circ}\text{C}$. Sodium potassium antimonide (NaKSb) photocathodes have been considered because of their ability to withstand higher temperatures [ref]. While at BNL we were tasked with the development of a procedure to reliably produce high performance NaKSb photocathodes. Procedures for developing such a photocathode exist in literature, but were not adaptable to the deposition chamber at BNL. In conjunction with BNL staff, we developed a preliminary procedure for the BNL deposition chamber by examining the stoichiometry, chemical properties and existing procedures of the NaKSb photocathode. The temperature of the photocathode substrate, the evaporation rate of the metal sources and the stoichiometric ratio of potassium to antimony are variables that greatly impact the performance of a photocathode and need to be fine-tuned. One measure of the performance of a photocathode is its quantum efficiency (QE), the number of emitted electrons per incident photon. By measuring the QE and the spectral response, we were able to measure the performance of each photocathode and come closer to developing a replicable procedure. During our appointment we gained experience with the vapor deposition process, measurement of photoemissive properties and the operation of an ultrahigh vacuum system.

I. Introduction

At RHIC, the ion beams heat up as they are accelerated. As the particles in the beam scatter off one another, there is a spread in their velocities, which heats up the beam and enlarges it. This makes it difficult for particles to collide. One method of increasing the likelihood that these particles will collide is by cooling down the beam. Cooling the particle beam can be done by accelerating a beam of electrons to the same speed as the ion beam and overlapping it with the ion beam.¹ The beam of electrons has an inherently cooler temperature than the beam of heavy ions and can essentially cool the ion beam when both are traveling together

at the same speed and in the same direction. In order to create this electron beam, Brookhaven scientists have designed an electron gun capable of accelerating bunches of electrons to match the speed of the ion bunches. The electron gun requires a photocathode capable of emitting mA levels of current when struck by a 532 nm laser.² These emitted electrons are accelerated by an electric field to the same speed as the heavy ions. Bi-alkali metal photocathodes have been considered for this application because of their high electron yield. These photocathodes are created by vapor deposition of the alkali metal sources. The alkali metals are much more sensitive to contamination by water vapor and oxygen than other photocathode materials. Because of this, these photocathodes must be fabricated, stored and transferred in an ultra-high vacuum system. Bi-alkali metal photocathodes must be replaced frequently due to the fact that they don't last as long as in the high current high field environment. In BNL's Instrumentation Division, a deposition system exists and a replicable procedure was in place to produce CsKSb photocathodes. However, NaKSb photocathodes have been shown to better withstand heat stress than CsKSb photocathodes.³ To produce such NaKSb photocathodes, a procedure needed to be developed that was adaptable to BNL's deposition system.

II. Experimental Setup

The ultrahigh vacuum deposition system consists of a transport suitcase, deposition chamber, storage chamber and load-lock chamber. To create a vacuum inside the system three types of pumps were used. A turbo pump is used to create an initial vacuum and is able to produce a vacuum levels on the order of 10-8 torr. Titanium Sputtering Pumps and ion pumps are then used reduce the vacuum to about 10-11 torr. The species present in the system are analyzed throughout the entire procedure by a residual gas analyzer (RGA). Saes Getter dispensers were used as sources for Na, K and Sb. Na, K and Sb sources were separated from the deposition chamber by ultrahigh vacuum gate valves. A quartz crystal monitor (QCM) was used to measure the thickness of the K and Sb films during deposition. A 532 nm, .5 mW laser was used to irradiate the photocathode during the Na deposition. A 2.5% transmittance filter was placed over this laser to reduce the beam power to 164 μW . The NaKSb photocathode was grown on a molybdenum puck that could be moved between the transport suitcase, deposition chamber, storage chamber and load lock chamber using manipulators that, when moved slowly, did not disturb the vacuum. The puck could be heated by a boron nitride heating element and cooled by a stream of gaseous N_2 . The stream of gaseous N_2 was cooled by passage through a cooling coil submerged in liquid N_2 . Liquid N_2 was replaced throughout the procedure as it evaporated. The molybdenum puck was biased

at -100 V during the deposition and the photocurrent emitted by the puck was measured by a Keithley 2400 source meter.

To develop a spectral response of the photocathode a setup consisting of a white light source, optical fibers, a focusing lens, an optical fiber holder and a spectrometer was used. The white light source consisting of halogen and deuterium lamps was attached to a spectrometer using optical fiber 600 μm in diameter. Optical fiber of the same diameter was attached to the output of the spectrometer and an optical fiber holder. A convex lens with a focal length of 3 cm was placed 8 cm from the optical fiber holder. The distance from the focusing lens to the photocathode was measured to be 26 cm. A 532 nm 164 μW laser was used to create a QE vs position plot of the photocathode. The laser was positioned on a table that could be translated in the horizontal and vertical directions. The spot size of the laser on the cathode was estimated to be about 1 mm in diameter.

To establish a power curve for the deuterium-halogen light source a similar setup for establishing the spectral response was used. The deuterium-halogen light source was connected to the spectrometer using 600 μm diameter optical fiber. Optical fiber of the same diameter was run from the spectrometer to an optical fiber holder. A convex lens with a focal length of 3 cm was placed 8 cm from the optical fiber holder. An optical power meter was placed 26 cm from the convex lens. The optical fiber holder, convex lens and optical power meter were enclosed in a box to isolate the setup from background light.

III. Methods

Measurement of photocurrent at different wavelengths was achieved using the setup shown in figures 1&2 and described previously. During photocurrent measurement the door to the deposition room was closed and the lights were turned off. Photocurrent from background light at each wavelength was noted before the shutter on the light source was opened. This procedure was repeated from a wavelength of 190 nm until no photoemission was observed in 10 nm increments. A QE scan of the photocathode was taken using the 532 nm laser in .5 mm vertical increments and .64 mm horizontal increments.

To establish the power curve of the deuterium-halogen light source a similar procedure for establishing the spectral response was used. Power was taken from wavelengths from 190 nm to 800 nm in 10 nm increments.

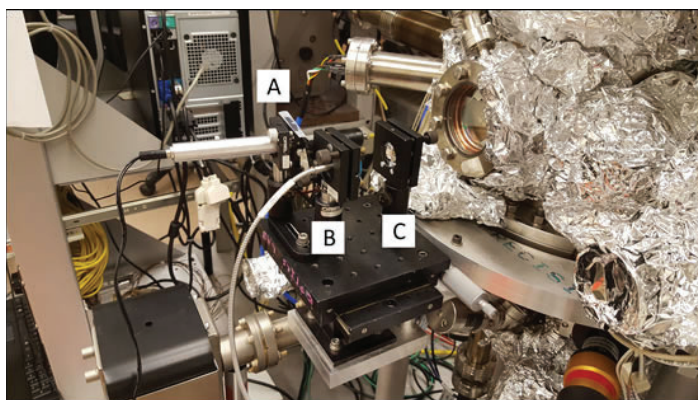


Figure 1. Pictured is the 532nm laser (A) used to scan the surface of the photocathode. Also pictured is the fiber optic holder (B) and focusing lens (C) used to establish spectral response of the photocathode.

IV. Results

During our time at BNL, three NaKSb photocathodes were produced. Out of these, two were successful. Procedures for the two successful photocathodes were not identical, however key similarities were found between the two procedures. An initial layer of Sb, K and Na was deposited. Following this layer a second layer of Sb, K and Na was deposited. An alternating deposition of Na and K during the second layer was used in both of the procedures. Temperature of the final Na deposition was found to be a critical factor for creating a successful photocathode. During the final Na deposition, the BN heater was shut off and Na continued to be deposited as the puck cooled.

Procedure 1

Heated the puck to 350 °C for 6 hours

Layer 1:

- Sb Deposition
 - 93.5 °C, 81 Å
- 1st K Deposition
 - 121.5-131.8 °C, 60 Å
- 1st Na Deposition
 - Very short amount of time, photocurrent rose slightly then fell
- 2nd K Deposition
 - 50 °C, 50 Å, no further photoemission

Layer 2:

- Sb Deposition
 - 96 °C, 90 Å
- 1st K Deposition
 - 143-146 °C, 180 Å, 2:1 ratio of K:Sb
- 1st Na Deposition
 - 95-200 °C
 - Deposited until photocurrent reached plateau and was about to fall
- 2nd K Deposition
 - 195-200 °C, 60 Å
- 2nd Na Deposition
 - 195-200 °C
 - Deposited until photocurrent reached plateau and was about to fall
- 3rd K Deposition
 - 195-200 °C, 30 Å
- 3rd Na Deposition
 - 195-200 °C
 - Deposited until photocurrent reached plateau and was about to fall, photocurrent started to rise more rapidly
- 4th K Deposition
 - 195-200 °C, 30 Å
- 4th Na Deposition
 - 195-200 °C
 - Rapid photocurrent rise, heater turned off and Na continued to deposit until a maximum was reached

Procedure 2

Heated the puck to 350 °C for 6 hours

Layer 1:

- Sb Deposition
 - 80 °C, 135 Å
- 1st K Deposition
 - 125-129 °C, 336 Å
- 1st Na Deposition
 - 190 °C
 - Very short amount of time, photocurrent rose slightly then fell
- 2nd K Deposition
 - 190 °C, 36 Å
- 2nd Na Deposition
 - 190 °C
 - Very short amount of time, photocurrent rose slightly then fell
- 3rd K Deposition
 - 190 °C, 18 Å
- 3rd Na Deposition
 - 190 °C
 - Very short amount of time, photocurrent rose slightly then fell

Layer 2:

- Sb Deposition
 - 160 °C which quickly fell to 143 °C, 75 Å
- 1st K Deposition
 - 140 °C which increased to 160 °C, 144 Å, 2:1 ratio of K:Sb
- 1st Na Deposition
 - 193 °C
 - Deposited until photocurrent reached plateau and was about to fall
- 2nd K Deposition
 - 193 °C, 36 Å
- 2nd Na Deposition
 - 203 °C
 - Photocurrent fell soon after
- 3rd K Deposition
 - 203 °C, 18 Å
- 3rd Na Deposition
 - 218 °C
 - Photocurrent started to rise more rapidly
- 4th K Deposition
 - 219 °C, 18 Å
 - Decided to pull back puck temperature slightly
- 4th Na Deposition
 - 208-210 °C
 - Rapid rise in photocurrent
 - *Temperature continued to rise because of lack of cooling, it rose to about 240 °C and killed the previous 4th deposition of sodium, drastically decreasing the photocurrent. We decided put another layer of K and try depositing sodium at a lower temperature
- 5th K Deposition
 - 230-240 °C
 - 18 Å
- 5th Na Deposition
 - Shut off heater during deposition
 - Photocurrent started increasing again at 220 °C and rapidly at 210 °C
 - Continued to deposit until photocurrent was at maximum

A QE scan was taken on one of the successful photocathodes and the results are shown below in figure 4. A spectral response of both successful photocathodes was taken. For the photocathode a QE scan was performed on, spectral responses were taken both at the center of the cathode and the high area of QE (the right side) and are displayed on figure 5.

A successful NaKSb photocathode underwent heat stress tests at 75, 100 and 125 °C. The results are shown below in figures

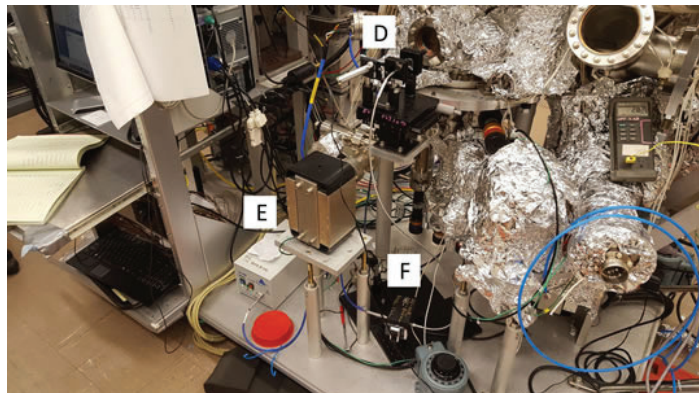


Figure 2. Setup used to measure the spectral response of the photocathodes. Pictured is the 532nm laser, fiber optic holder and focusing lens (D), light source (E) and spectrometer (F).

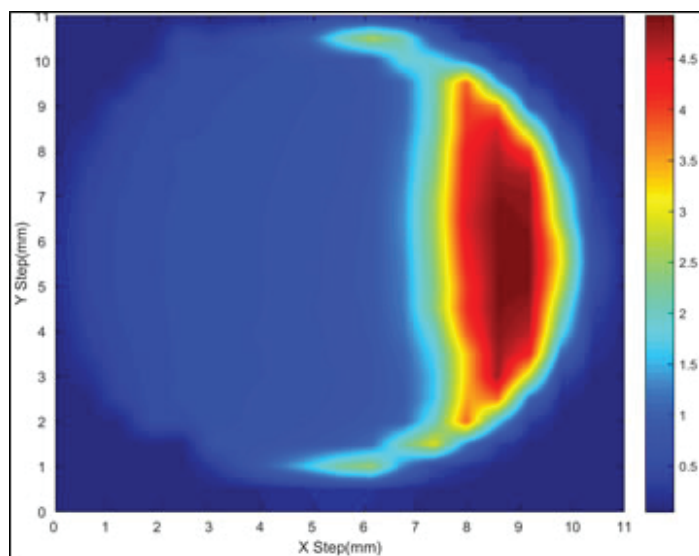


Figure 4. QE scan of asymmetrical photocathode.

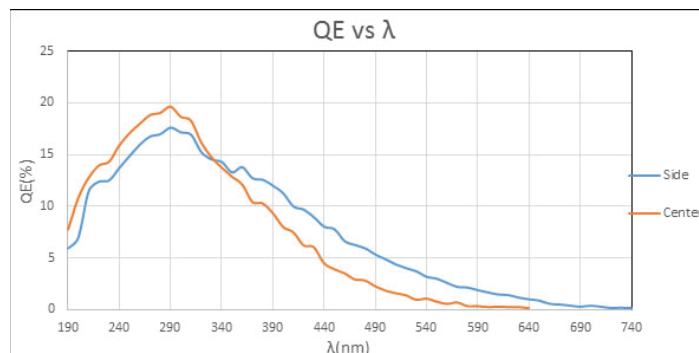


Figure 5. Spectral response of photocathode in high QE region and the center.

6-8. Heat stress tests were taken over the course of many days, on each day a baseline measurement was taken before the heating stress tests. The figures below represent a small portion of data taken from these tests.

V. Conclusion and Recommendations

It appears that the most critical factor for the growth of a NaKSb photocathode is the deposition of Na at high temperature and the lowering of the puck temperature as the Na deposition is completed. It is currently unclear whether the first layer of Na, K, and Sb is needed and unclear whether or not the 2:1 ratio of K to Sb in the second layer is correct. Further experiments need to be conducted to determine if these factors play a significant role. During the growth of the asymmetric photocathode, the puck was not centered on the Na source. This resulted in a photocathode with a disproportionate amount of Na deposited on the right side of the photocathode. We believe this misalignment is the cause of the high QE section on the right side of the asymmetric photocathode. From the preliminary data it can be seen that significant, but not total degradation occurs after NaKSb is exposed to temperatures above 100°C. Further analysis and experiments must be done in order to establish a relationship between temperature and QE of the NaKSb photocathode.

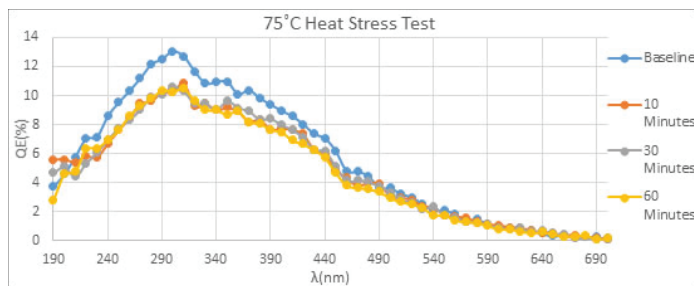


Figure 6. Spectral response of NaKSb photocathode after being heated at 75°C

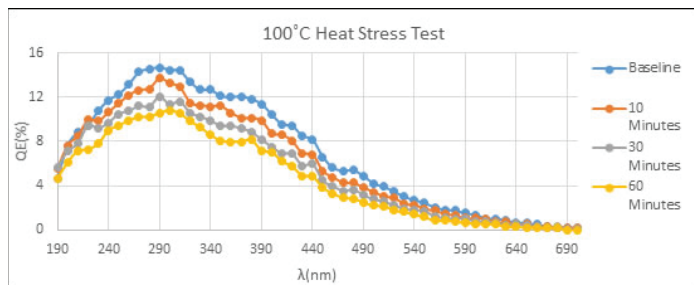


Figure 7. Spectral response of NaKSb photocathode after being heated at 100°C

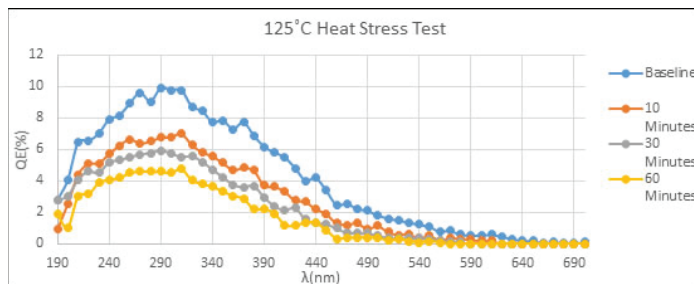


Figure 8. Spectral response of NaKSb photocathode after being heated at 125°C

VI. References

- 1 V. Parkhomchuk, I. Ben-Zvi, Electron Cooling for RHIC, Brookhaven National Laboratory (Unpublished).
- 2 K. Walsh, Producing Cold Electron Beams to Increase Collision Rates at the Relativistic Heavy Ion Collider, WWW Document, (<https://www.bnl.gov/rhic/news2/news.asp?a=5917> =today)
- 3 Hamamatsu Photonics, Photomultiplier Tubes: Basics and Applications, 3rd Ed. (2007), pp. 31

VII. Acknowledgements

We are grateful to everyone in the Instrumentation department that have assisted us during our time at Brookhaven National Laboratory. Specifically we would like to thank our mentor, Triveni Rao. Without her patience and expertise this project would have been impossible. We would also like to thank John Walsh for his assistance in operation of the ultrahigh vacuum system. We would like to acknowledge the Office of Educational Programs who have provided a well-organized intern experience. Finally we wish to express our gratitude to Brookhaven National Laboratory and the Department of Energy for this internship opportunity and the hospitality we received during our appointment.

Testing and troubleshooting of High Temperature Superconductor Dipole Magnet Coils

Shresht Joshi

Nanoscale Engineering, SUNY College of Nanoscale Sciences and Engineering, Albany, NY 12203

Ramesh Gupta

Superconducting Magnet Division, Brookhaven National Laboratory, Upton, NY 11973

William Sampson

Superconducting Magnet Division, Brookhaven National Laboratory, Upton, NY 11973

Abstract

This project revolves around testing and troubleshooting a High Temperature Superconducting (HTS) dipole magnet coil made with Yttrium Barium Copper Oxide (YBCO) tape. The HTS coil has a 30° bend angle to allow for a 4 meter bending radius.¹ Along with certain advantages, this neoteric design introduces many issues ranging from coil winding while manufacturing to Lorentz force distribution while the magnet is operating. Parts of the coil started to malfunction when installed and operated in a cryo-cooler. Upon further investigation, the issue was narrowed down to a specific region of the coil. This region was removed and rigged to be tested at liquid nitrogen temperatures (77K). After thermal cycling in liquid nitrogen, the defects became visible in the form of tape delamination. The defects were bridged and retested and performed within limits. This project gives great insight into how these HTS coils function in practice and how defects, whether intrinsic or due to thermal cycling, may be identified. These novel coils show great promise in applications ranging from medical gantries to high radiation environments to next generation particle accelerator systems.

I. Background

From Particle Accelerators to MRI machines, superconducting magnet design and manufacturing has been inhibited by Low Temperature Superconductors, which operate at liquid helium temperatures (~4K). Opposed to High Temperature Superconducting material, which is brittle, Low Temperature Superconducting material is malleable. This physical property allows manufacturers to draw Low Temperature Superconducting material into wires. These wires are then wound in different configuration to make conventional superconducting magnets.

Scientists at Brookhaven National Laboratory are developing superconducting magnet designs using novel High Temperature Superconductors. High Temperature Superconductors, which operate at sufficiently higher temperatures (30K – 70K) than Low Temperature Superconductors (4K), are also capable of producing very high magnetic fields. Higher operating temperature requires less elaborate equipment and is more cost effective to maintain.

The HTS dipole magnet being tested for this project was made using YBCO tape from SuperPower Inc. The YBCO HTS tape is fabricated by an automated, continuous process using thin film deposition techniques, such as those used in the semiconductor industry, to apply the superconducting material on buffered

Configuration of SuperPower® 2G HTS Wire

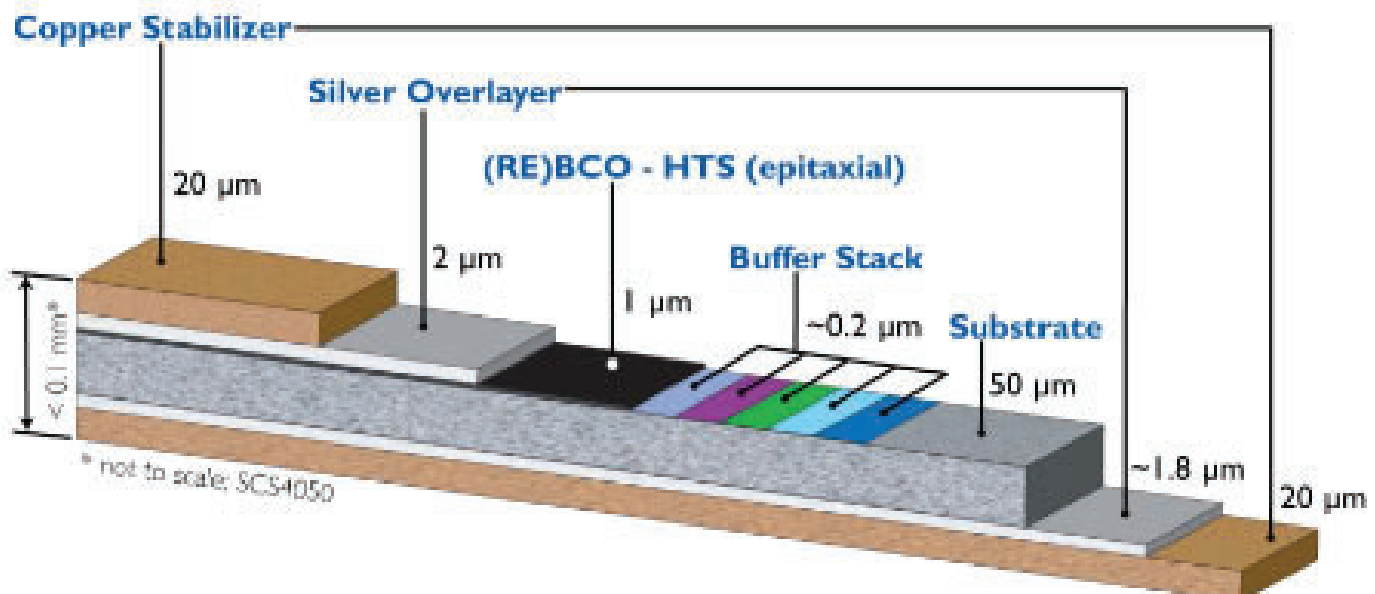


Figure 1: Second generation YBCO tape configuration²

metal substrates.² This novel deposition technique allows HTS tape manufacturers to circumvent the restrictions in HTS tape fabrication due to the physical properties of High Temperature Superconducting material, such as brittleness. The configuration of the YBCO HTS tape is shown in Figure 1.

The basic design for the YBCO HTS dipole magnet is a sector superferic magnet where the coils magnetize the iron yoke and the iron design dominates the field quality.¹ While the YBCO HTS dipole magnet was initially designed to operate in a high radiation environment, its ability to bend beams by 30° with a nominal magnetic field of 2 T gives it a wide range of applications; from medical gantries to next generation particle accelerators.³ The magnetic properties of the HTS dipole magnet are specified in Table 1.

II. Method

While being tested in a cryocooler, Figure 2, with a temperature of around 30K, a part of the YBCO HTS dipole magnet coil showed some readings that were out of limits. While in the superconducting state, the YBCO HTS tape should show no resistance. However, a section of the coil showed resistance. Multiple tests were ran to confirm that there was a malfunction within the coil. Through these tests, the malfunction was narrowed down to within the first 10 turns of a total of 140 turns of the coil.

For further troubleshooting and analysis, the YBCO HTS coil, Figure 3, was removed from the cryocooler and rigged to be tested in liquid nitrogen, at a temperature of 77K. The critical temperature for YBCO superconducting material is around 90K, thus, tests can be ran using liquid nitrogen.

Since tests in the cryocooler showed the defect to be within the first 10 turns, extra voltage taps were added every two turns for the first 10 turns of the coil. The coil was then submerged in a liquid nitrogen bath to make it superconducting and retested. The defective part of the coil was further narrowed down to a region between turns 8 and 10.

For further troubleshooting, the coil was taken out from the support structures, Figure 4, and the first 10 turns were removed to analyze the section of the HTS tape in more detail. Turns 8 through 10 of the YBCO tape were cut out and examined. Upon initial visual inspection, a slight variation in the physical uni-

formity of the tape was noticed in sections of the tape. Turns 8 through 10 were then installed onto a test cylinder, Figure 5. Voltage taps were installed every cylinder turn to pinpoint the defect. The cylinder was submerged in liquid nitrogen and tested.

III. Results and Discussion

For High Temperature Superconducting materials, the lower the cryogenic temperature past the materials critical temperature, the higher its current carrying capacity will be. Although the current carrying capacity of YBCO HTS tape will be less at liquid nitrogen temperatures, the SuperPower YBCO HTS tape used in this dipole magnet should be able to carry at least 300 A without showing resistance (going normal).

As can be seen from Graph 1 and 2, two sections in turns 8 through 10 of the YBCO HTS dipole magnet tape started to show resistance at lower currents than expected.

After the two tests confirmed two defective areas in turns 8 through 10 of the YBCO HTS dipole magnet tape, the tape was brought back to room temperature to check the physical integrity of the two defective areas. Upon visual inspection, the two areas that had previously showed a variation in physical uniformity now showed obvious tape delamination; approximately ¼ of an inch wide. The exacerbation of the physical deterioration of the YBCO HTS tape was most likely due to the thermal cycling of the tape into and out of liquid nitrogen.

We decided to bridge the defective areas to mend the defects. Bridging involves bypassing the defective areas by adding a strip of known good HTS tape, ideally the same part number tape as the one with the defect, over the defective site. This will allow another path for the current to flow. When done correctly, the effects of the defects will be greatly reduced.

A 3 inch long piece of SuperPower YBCO HTS tape was soldered over the defective sites using Indium. The tape was checked for integrity and reinstalled on to the test cylinder for testing in liquid nitrogen. Graph 3 shows the results.

As can be observed from Graph 3, one of the defects was mended while one persisted. Thermal cycling may have enlarged the size of one of the defective areas because even with a bridge, resistance was still prevalent for one of the sites. As can also be seen from Graph 3, other parts of the YBCO HTS tape form turns

Parameter	Value
Bending Radius	4 m
Bend Angle	30°
Effective Length along Design Trajectory	2.094 m
Max. Dipole Field	2.0 T
Variable Field Range	0 to 2.0 T
Field Non-Uniformity in Good Field Region	<0.7% for fields between 0.5 T to 2.0 T
Uniform Field Width in Bend Plane	0.3 m
Uniform Field in Non-Bend Plane	0.2 m

Table 1: Parameters describing the magnetic properties of the HTS dipole magnet¹

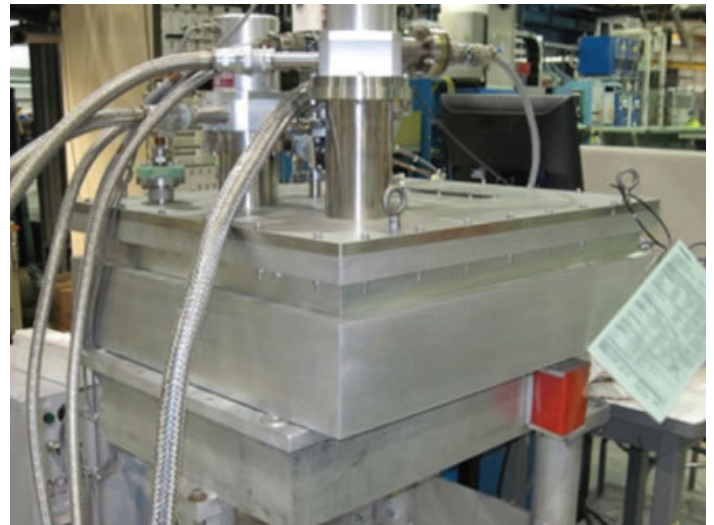


Figure 2: Cryocooler test structure⁴

8 through 10 were starting to develop defects. Multiple areas of resistance can be observed around 275 A; the prior tests showed no resistance in these areas of the tape at that current. Another interesting feature that can be seen in Graph 3 is that while the resistance in the main defective site increased with an increase in current, as the current was raised from 240 A to 250 A, the resistance in that particular defective area actually decreased. This phenomenon has been sporadically observed in multiple other HTS magnet coils. The phenomenon appears completely randomly and even with current cycling, it cannot be reproduced. There is no explanation as to why this happens or what makes it happen.

IV. Conclusion

Since the YBCO HTS dipole magnet coil passed all initial tests before being installed in the cryocooler and performed within limits for a duration of tests within the cryocooler, the defects were likely intrinsic to the YBCO tape. Thermal cycling contributed towards the deterioration of the sample after the defects were detected.

It was interesting to see and capture the sudden decrease of resistance in a defective area. Since this phenomenon is sporadic and cannot be reproduced, it will likely be very difficult to design an experiment to further investigate it.

This project gives great insight into how these HTS coils function in practice and how defects, whether intrinsic or due to thermal cycling, may be identified. It also shows that once a defect is detected, thermal cycling may increase the rate of degradation of YBCO tape.

V. References

- ¹S. A. Kahn and R. C. Gupta, "High Radiation Environment Nuclear Fragment Separator Dipole Magnet", *Proceedings of IPAC12*. Pp 3605-3607, 2012.
- ²<http://www.superpower-inc.com/content/2g-hts-wire>
- ³S.A. Kahn et al., "A Dipole Magnet for the FRIB High Radiation Environment Nuclear Fragment Separator", *IEEE Trans. Appl. Supercond.* **24**, Art. ID 4001004, 2013
- ⁴Hocker, H. et al., "Design, Construction and Test of Cryogen-Free HTS Coil Structure." BNL, 2011.



Figure 3: YBCO HTS dipole magnet coil with support structure (left) and YBCO HTS dipole magnet coil without support structure (right)

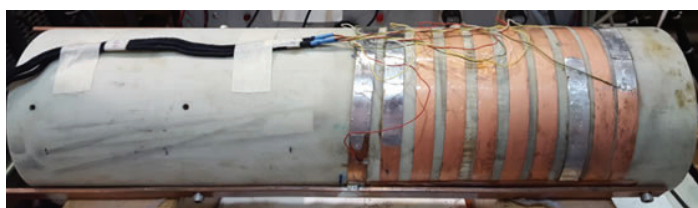


Figure 4: Turns 8 through 10 of YBCO HTS dipole magnet tape wrapped around test cylinder

VI. Acknowledgements

I would like to thank Dr. William Sampson and Dr. Ramesh Gupta for their unwavering support and guidance throughout this internship. This project was supported in part by the U.S. Department of Energy, Office of Science, Office of Workforce Development for Teachers and Scientists (WDTS) under the Science Undergraduate Laboratory Internships Programs (SULI).

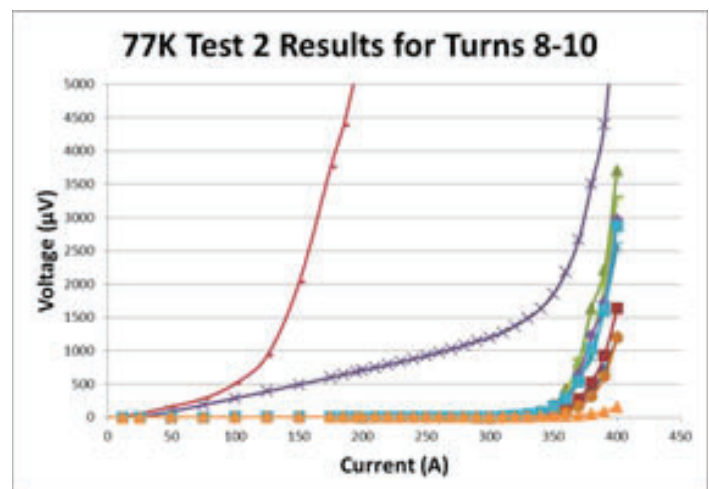
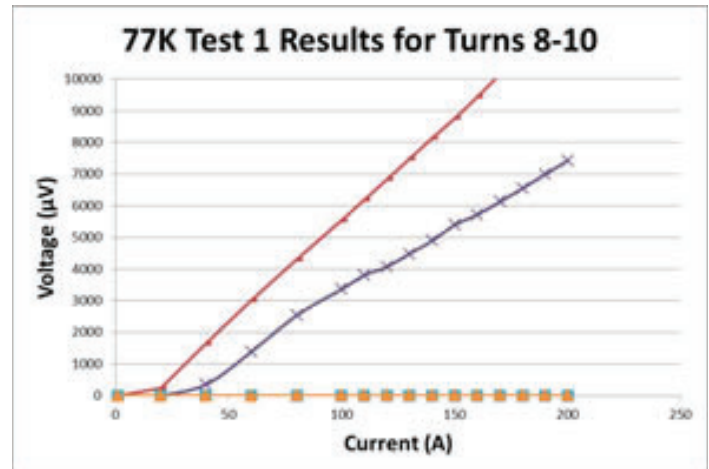


Figure 5: Voltage measured as function of current during the first test run (top) and during the second test run (bottom)

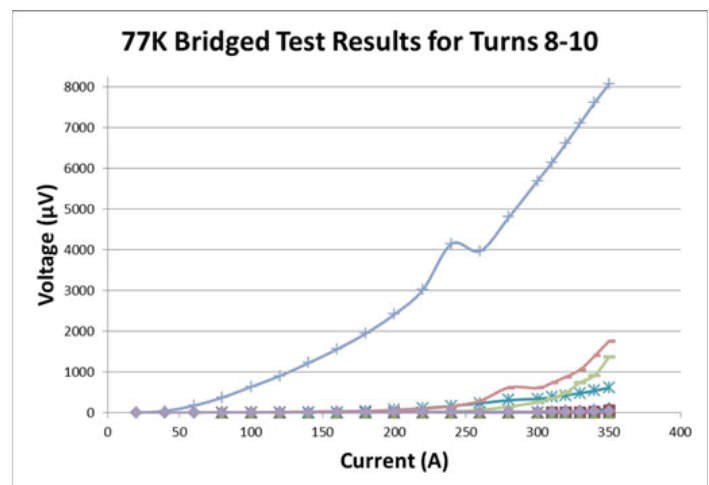


Figure 6: Voltage measured as function of current after bridging

Developing data process management routines in MATLAB for Thermo Gravimetric Analyzer experiments

Javier Joya

Mathematics Department, New York City College of Technology, Brooklyn, NY 11201.

Biays Bowerman

Non-proliferation & Homeland Security, Brookhaven National Laboratory, Upton, NY 11973

Abstract

The objective of this research is to expand the database of the vapor pressures for organic materials such as erythritol and penta-erythritol which are used as components in explosive devices. These organic materials are readily available and have sometimes been combined with oxyhalide oxidizers to make home made explosives (HME). Throughout the years, different ways have been developed to learn more about the physical characteristics of these solids with very low vapor pressures. Hence, we used a Thermo Gravimetric Analyzer Q5000 (TGA), which has a small oven capable of heating up the given material to temperatures up to 1000 °C. The basis of the analysis of the data relies on the Langmuir equation in conjunction with the Pseudo-Antoine equation to calculate the vapor pressure. The slope of the change in mass with time (also known as the instrumental constant, k , in our case) may be found by using the Claperyon plot. We are currently working on a MATLAB program to extract all the basic information from the TGA output file and calculate the vapor pressures. The program will also inquire if the user wishes to produce a “Claperyon plot.” The successful operation of the MATLAB routine will speed data processing from the research. The information collected in this type of research will provide data to help further development of explosive detection equipment.

I. Introduction

It is crucial to study the physical properties of materials in order to understand them, to develop uses for them, and to develop means to detect them. In particular, in this paper we will focus on vapor pressures of four organic compounds: Erythritol, Penta-Erythritol, Sucrose and Urea. As we may know, many materials release some sort of vapor at lower temperatures, even from the solid state. Detection equipment for vapors used in homemade explosives by terrorists have been developed to support law enforcement officials and it is important to identify their limitations in detecting a potential threat. Research laboratories have used a variety of methods when studying vapor pressures. Some of these techniques may not be sensitive enough to measure extremely low vapor pressures of some compounds. Hence we have used a Thermogravimetric analyzer (TGA) as an alternative method for this project. The instrument measures the mass loss over time as the temperature is raised [1] and these are correlated to a calibration constant which in our case, we have used Benzoic Acid. We wish to expand the available data by analyzing the vapor pressure of the Organic compounds stated above. Efforts to analyze the output data involve extensive manual spreadsheet manipulations. Here, we used MATLAB to write a program where one may pro-

cess the thousands of data that the TGA outputs in a excel format and process it in a more efficient and organized manner.

II. Methods

Every time an experiments finishes, the user running the TGA instrument extracts the data in a Microsoft excel format and stores it. This spreadsheet has crucial metadata regarding the experiment in addition to the experimental test results. Metadata includes the name of the compound, sample weight, date and time of the run as well as other parameters that set by the experimentalis so the TGA would execute the experiment as required. In the output spreadsheet, the experimental data of interest usually begins on the 40th row. We get three columns of data from the TGA: the time (m), the first derivative of mass over time ($\frac{mg}{sec}$) and the temperature (°C). The total number of rows varies from experiment to experiment. At times we may find ourselves dealing with hundreds or thousands of rows. This means that MATLAB is a very good candidate to analyze the data because we can use matrices. The analysis relies on the Langmuir equation in conjunction with the Antoine equation. The Langmuir equation is as follows:

$$\frac{1}{a} \frac{dm}{dt} = p\alpha \sqrt{\frac{M}{2\pi RT}} \quad (1)$$

Where the variables on the equation stand as:

a = Area of TGA pan (m^2)

$\frac{dm}{dt}$ = Mass loss with time ($\frac{kg}{s}$)

p = Pressure (Pascal)

α = Instrumental Calibration parameter I believe this is unit less.

M = Vapor molecular weight ($\frac{kg}{mol}$)

T = Temperature (K)

R = Gas constant ($\frac{J}{K \cdot mol}$)

By manipulating equation (1), it is possible to isolate the pressure. In other words we will end up with a modified version of the Langmuir equation.

$$p = \left(\frac{1}{a} \frac{dm}{dt} \sqrt{\frac{T}{M}} \right) \left(\sqrt{\frac{2\pi R}{a}} \right) \quad (2)$$

Furthermore, one may simplify (2) by breaking it into two parts

$$v = \left(\frac{1}{a} \frac{dm}{dt} \sqrt{\frac{T}{M}} \right) \quad (3)$$

and

$$k = \left(\sqrt{\frac{2\pi R}{a}} \right) \quad (4)$$

Therefore the equation to calculate vapor pressures have now taken a simplified form

$$p = kv \quad (5)$$

We mentioned Benzoic acid earlier because it was used to calibrate the TGA and to calculate the instrumental parameters since the vapor pressure for this compound is well characterized. The Antoine equation for Benzoic acid is:

$$\ln(p) = 34.14 + \frac{10381}{T} \quad (6)$$

The MATLAB program created will do all the required calculation in a timely, efficient style. The Microsoft excel spreadsheet output by the TGA is the input taken by the MATLAB program to extract crucial information such as the name of the sample and weight, and transfer it into a different output spreadsheet. The output spreadsheet will come after MATLAB executes the required calculations. This new file will consist of Temperature ($^{\circ}\text{K}$), Pressure (Pa), v , $\frac{1}{Temp}$, $LN(kv)$, weight of sample, name of sample, date (that it was run in MATLAB). Additionally, the program asks the user if a p vs v plot [Appendix 2] is needed for the given calculation. Whether the answer is “y” or “n” it will then ask if a $\ln(p)$ vs $\frac{1}{T}$ plot [Appendix 3] is needed. This last is of most interest since we will be able to extract information to create an Antoine equation for each organic compound we are studying. The charts below show the schematics on how the MATLAB program [Appendix 1] works to make calculations faster. Figure 1 shows the information to be entered by the user.

The third step of Figure 2 is a default setting in MATLAB. The data stored in the workspace is temporary and gets cleared every time the program is run due to the “clear all” command present in the script.

III. Data and Results

We found the instrumental constant, using Benzoic acid. From five runs of the compound’s weight loss on heating, and calculating pressure versus the v factor, we took the average slope

value to use as in equation (5) for all compounds studied in this project. Table 1 shows the range of temperatures we took and their respective slope as well as the R^2 values.

Tem. Range/ $^{\circ}\text{C}$	Slope/k	Intercept	R^2
55.02 - 88.97	153273	1.27	0.9964
55.41 - 89.62	151970	1.81	0.9923
56.03 - 88.82	162150	1.71	0.9958
55.28 - 88.30	147114	1.52	0.9918
55.03 - 88.07	152928	1.52	0.9967
AVERAGE	153487		

Table 1: Data required to estimate the instrumental constant k , for Benzoic Acid

Figure 3 shows p vs v over a certain temperature for Benzoic acid that was used to determine the instrument parameter k (slope).

Going back to Antoine equation for Benzoic acid (6), figure 4 agrees with the values since the linear fit for the slope and intercept are the same.

The instrumental constant value was used for all the compounds listed on Table 2. Values of v , which correspond to the change of mass over time multiplied by the temperature according to equation (3) were calculated first. By applying equation (5) to our compounds and plotting the natural log over the reciprocal of temperature, we achieved a linear fit and used it in the Antoine equation for each organic compound. Figure 5 shows all four Organic compounds plotted over a certain temperature range below their melting points. Table 2 shows the Antoine equation as well as the vapor pressure at 25°C for its respective compound.



Figure 1: Required input information by the user



Figure 2: MATLAB sequence of events of data

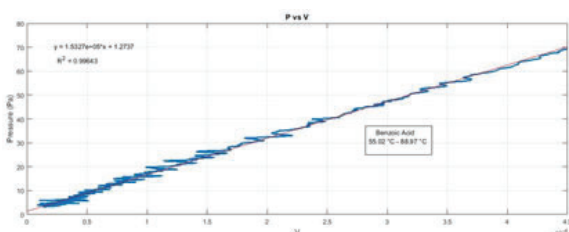


Figure 3: Plot of p vs v for Benzoic acid

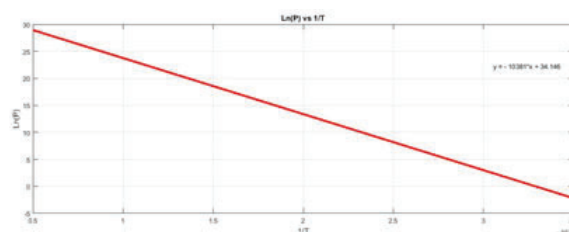


Figure 4: Plot of $\ln(p)$ vs $\frac{1}{T}$ for Benzoic acid

Compound	Antoine Equation	VP (Pa) at 25 °C
Erythritol	$y = -9328.15x + 24.78$	$1.42 \cdot 10^{-3}$
Penta-Erythritol	$y = -10423.35x + 26.65$	$2.54 \cdot 10^{-5}$
Sucrose	$y = -6927.4x + 13.38$	$4.62 \cdot 10^{-4}$
Urea	$y = -13337.54x + 35.62$	$1.06 \cdot 10^{-4}$

Table 2: Antoine Equations for the Studied Compounds based on linear fits

IV. Conclusion

We successfully wrote a program where MATLAB takes the output data from the TGA and calculates the vapor pressures for organic compounds below their melting points. Calculation time was considerably decreased due to the program since there is no longer a need to write formulas in excel to get the information needed. An important lesson learned in the process was to check and verify unit conversions throughout the program to avoid mistakes in the final analysis. At the beginning of the project, my mentor chose to use MATLAB to write this program, but we found that the software is expensive for new non-student users. Also, sometimes I noticed MATLAB was experiencing delays in processing the data. This could have been due to the very large size of matrices on some of the runs or to the old laptop with Windows 7 operating system assigned to me. If one needs to deal with hundreds of thousands of data points, I believe a different

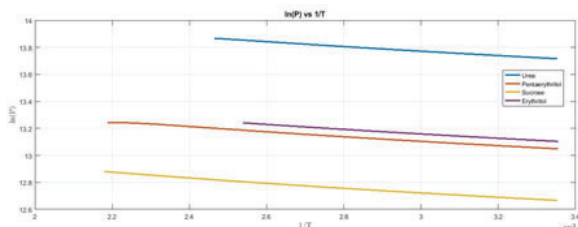


Figure 5. Plots of $\ln(p)$ vs $\frac{1}{T}$ for Organic compounds studied

programming language with more computer flexibility should be used. Hence the reason one may start looking into free and faster programming software such as Python or C++.

V. Acknowledgements

This project was supported in part by the U.S. Department of Energy, Office of Science, Office of Workforce Development for Teachers and Scientists (WDTS) under the Science Undergraduate Laboratory Internships Program (SULI).

VI. References

- [1] Brady, Joseph E., James L. Smith, Casuarina E. Hart, and Jimmie Oxley. "Estimating Ambient Vapor Pressures of Low Volatility Explosives by Rising-Temperature Thermogravimetry." *Propellants, Explosives, Pyrotechnics* 37.2 (2012): 215-22. Web.
- [2] Marchand, Patrick, and O. Thomas. Holland. *Graphics and GUIs with MATLAB*. Boca Raton, FL: Chapman & Hall/CRC, 2003. Print.
- [3] Oxley, Jimmie C., James L. Smith, Joseph E. Brady, and Austin C. Brown. "Characterization and Analysis of Tetranitrate Esters." *Propellants, Explosives, Pyrotechnics* 37.1 (2012): 24-39. Web.
- [4] Oxley, Jimmie C., James L. Smith, Joseph E. Brady, and Austin C. Brown. "Erratum: Characterization and Analysis of Tetranitrate Esters." *Propellants, Explosives, Pyrotechnics* 37.6 (2012): 735. Web.
- [5] Oxley, Jimmie C., James L. Smith, Wei Luo, and Joseph Brady. "Determining the Vapor Pressures of Diacetone Diperoxide (DADP) and Hexamethylene Triperoxide Diamine (HMTD)." *Propellants, Explosives, Pyrotechnics Prop., Explos., Pyrotech.* 34.6 (2009): 539-43. Web.
- [6] Steinkamp, Frank Lucus, Lauryn E. Degreeff, Greg E. Collins, and Susan L. Rose-Pehrsson. "Factors Affecting the Intramolecular Decomposition of Hexamethylene Triperoxide Diamine and Implications for Detection." *Journal of Chromatography A* 1451 (2016): 83-90. Web.

Appendix 1. MATLAB code to process initial TGA output data

```
% Import and export data from spreadsheet

% Clearing all the previous variables
clc
clear all
% First output sentence on the command window
disp('Please make sure to use single quotes')
% This is where you enter the FULL location of the file
loc = input('Enter the FULL location of the file (ex. Y:\\TGA\\Benzoic acid\\20160613 20C
to 1000C 1.xlsx): ');
% Here, you enter the name of the excel spreadsheet
sprd = input('Enter the name of the file (ex. 20160613 20C to 1000C 1): ');
% Not all file start neither end on the same cells
cells = input('Enter the range of cells you wish to consider (ex. A43:C1689): ');
% The command xlsread is being used since excel spreadsheets are being consider
wtg = input('Enter the Molecular Weight (in kg) ');
[~, ~, raw] = xlsread(loc, sprd, cells);
raw(cellfun(@(x) ~isempty(x) && isnumeric(x) && isnan(x), raw)) = {''};
raw = raw(:, [1, 2, 3]);

%% Create output variable
data = reshape([raw{:}], size(raw));

%% Allocate imported array to column variable names
Time = data(:, 1);
Temp_C = data(:, 2);
dmdt = data(:, 3);
Temp_K = (Temp_C + 273.15);
dMdT = dmdt/1e6;
Pan_Size = 7.85e-5;
Sample_mg = xlsread(loc, sprd, 'B14');
[~, Sample, ~] = xlsread(loc, sprd, 'B13');

q = (dMdT)/(Pan_Size);
w = sqrt(Temp_K/wtg);
v = q.*w;
% Calculating the Pressure
Pressure = exp(34.146-(10381./Temp_K));
% Calculates the reciprocal of the temperature
inverse_temp = (1./(Temp_K));
% Vapor Pressure equation
LogP = log(Pressure);
% Finds the k (Slope) value
k_value_slope = (Pressure./v);

Date = datetime('today');
M1 = table(Temp_K, Pressure, v, inverse_temp, LogP, k_value_slope);
M2 = table(Sample_mg, Date, Pan_Size, Sample);
name = input('Enter the name you wish to save the file as, use single quotes (ex. filename.
xlsx) : ');
writetable(M1, name, 'Sheet', 1, 'Range', 'A1');
writetable(M2, name, 'Sheet', 1, 'Range', 'G1');

disp(' ');
disp('-----')
disp('Please check the current folder for the output information')
disp('-----')
disp('-----')
```

```

plt = input('Would you like to create a LN(P) vs 1/T graph? If yes, press "y" if no press
"n": ', 's');

if plt == 'y'
    createlnpvsloverT(inverse_temp, LogP)
    second = input('Would you also like to plot a Pressure vs V? ', 's');
    if second == 'y'
        createpvsv(v, Pressure)
    elseif second == 'n'
        disp('Thank you, Goodbye');
    elseif second ~= 'y' || second ~= 'n'
        disp('Error, input was NOT a valid command');
    end
elseif plt == 'n'
    plt2 = input('Would you like to plot a Pressure vs V graph? ', 's');
    if plt2 == 'y'
        createpvsv(v, Pressure)
    elseif plt2 == 'n'
        disp('Thank you, Goodbye')
    elseif plt2 ~= 'y' || plt2 ~= 'n'
        disp('Error, input was NOT a valid command');
    end
elseif plt ~= 'y' || plt ~= 'n'
    disp('Error, input was NOT a valid command');

end
%% Clear temporary variables
clearvars data raw cellVectors;

```

Appendix 2. MATLAB code to generate p vs. v plot

```

function createpvsv(X1, Y1)
% Create figure
figure1 = figure('Color', [1 1 1]);

% Create axes
axes1 = axes('Parent', figure1);
hold(axes1, 'on');

% Create plot
plot1 = plot(X1, Y1, 'DisplayName', 'data1');

% Get xdata from plot
xdata1 = get(plot1, 'xdata');
% Get ydata from plot
ydata1 = get(plot1, 'ydata');
% Make sure data are column vectors
xdata1 = xdata1(:);
ydata1 = ydata1(:);

nanMask1 = isnan(xdata1(:)) | isnan(ydata1(:));
if any(nanMask1)
    warning('GeneratedCode:IgnoringNaNs', ...
        'Data points with NaN coordinates will be ignored. ');
    xdata1(nanMask1) = [];
    ydata1(nanMask1) = [];
end

% Find x values for plotting the fit based on xlim
axesLimits1 = xlim(axes1);
xplot1 = linspace(axesLimits1(1), axesLimits1(2));

```

```

% Preallocate for "Show equations" coefficients
coeffs1 = cell(1,1);

fitResults1 = polyfit(xdata1,ydata1,1);
% Evaluate polynomial
yplot1 = polyval(fitResults1,xplot1);

fittypesArray1(1) = 2;

coeffs1{1} = fitResults1;

% Plot the fit
fitLine1 = plot(xplot1,yplot1,'DisplayName',' linear','Tag','linear',...
    'Parent',axes1,...
    'Color',[1 0 0]);

setLineOrder(axes1,fitLine1,plot1);
showEquations(fittypesArray1,coeffs1,5,axes1);

% Create xlabel
xlabel({'V'});

% Create title
title({'Pressure vs V'});

% Create ylabel
ylabel({'Pressure'});

% xlim(axes1,[-0.0005 0.0025]);
box(axes1,'on');
grid(axes1,'on');
r = corrcoef(X1, Y1);
R_squared = r(1,2)^2;
text(0.25*10^-4, 65, ['R^2 = ', num2str(R_squared)])

function setLineOrder(axesh1, newLine1, associatedLine1)
% Get the axes children
hChildren = get(axesh1,'Children');
% Remove the new line
hChildren(hChildren==newLine1) = [];
% Get the index to the associatedLine
lineIndex = find(hChildren==associatedLine1);
% Reorder lines so the new line appears with associated data
hNewChildren = [hChildren(1:lineIndex-1);newLine1;hChildren(lineIndex:end)];
% Set the children:
set(axesh1,'Children',hNewChildren);

function showEquations(fittypes1, coeffs1, digits1, axesh1)

n = length(fittypes1);
txt = cell(length(n + 1) ,1);
txt{1,:} = ' ';
for i = 1:n
    txt{i + 1,:} = getEquationString(fittypes1(i),coeffs1{i},digits1,axesh1);
end
text(.05,.95,txt,'parent',axesh1, ...
    'verticalalignment','top','units','normalized');

function [s1] = getEquationString(fittype1, coeffs1, digits1, axesh1)

if isequal(fittype1, 0)

```

```

    s1 = 'Cubic spline interpolant';
elseif isequal(fittypel, 1)
    s1 = 'Shape-preserving interpolant';
else
    op = '+-';
    format1 = ['%s %0.', num2str(digits1), 'g*x^{%s} %s'];
    format2 = ['%s %0.', num2str(digits1), 'g'];
    xl = get(axesh1, 'xlim');
    fit = fittypel - 1;
    s1 = sprintf('y =');
    th = text(xl* [.95;.05], 1, s1, 'parent', axesh1, 'vis', 'off');
    if abs(coeffs1(1) < 0)
        s1 = [s1 ' -'];
    end
    for i = 1:fit
        s1 = length(s1);
        if ~isequal(coeffs1(i), 0) % if exactly zero, skip it
            s1 = sprintf(format1, s1, abs(coeffs1(i)), num2str(fit+1-i), op((coeffs1(i+1)<0)+1));
        end
        if (i==fit) && ~isequal(coeffs1(i), 0)
            s1(end-5:end-2) = []; % change x^1 to x.
        end
        set(th, 'string', s1);
        et = get(th, 'extent');
        if et(1)+et(3) > xl(2)
            s1 = [s1(1:s1) sprintf('\n      ') s1(s1+1:end)];
        end
    end
    if ~isequal(coeffs1(fit+1), 0)
        s1 = length(s1);
        s1 = sprintf(format2, s1, abs(coeffs1(fit+1)));
        set(th, 'string', s1);
        et = get(th, 'extent');
        if et(1)+et(3) > xl(2)
            s1 = [s1(1:s1) sprintf('\n      ') s1(s1+1:end)];
        end
    end
    delete(th);
    if isequal(s1(end), '+')
        s1(end-1:end) = [];
    end
    if length(s1) == 3
        s1 = sprintf(format2, s1, 0);
    end
end
end

```

Appendix 3. MATLAB code to generate ln p vs. 1/T plot

```

function createlnpvs1overT(X1, Y1)
% Create figure
figure1 = figure('Color', [1 1 1]);

% Create axes
axes1 = axes('Parent', figure1);
hold(axes1, 'on');

% Create plot

```



```

plot1 = plot(X1,Y1,'DisplayName','data1');

% Get xdata from plot
xdata1 = get(plot1, 'xdata');
% Get ydata from plot
ydata1 = get(plot1, 'ydata');
% Make sure data are column vectors
xdata1 = xdata1(:);
ydata1 = ydata1(:);

% Remove NaN values and warn
nanMask1 = isnan(xdata1(:)) | isnan(ydata1(:));
if any(nanMask1)
    warning('GeneratedCode:IgnoringNaNs', ...
        'Data points with NaN coordinates will be ignored.');
```

```

    xdata1(nanMask1) = [];
    ydata1(nanMask1) = [];
end

% Find x values for plotting the fit based on xlim
axesLimits1 = xlim(axes1);
xplot1 = linspace(axesLimits1(1), axesLimits1(2));

% Preallocate for "Show equations" coefficients
coeffs1 = cell(1,1);

% Find coefficients for polynomial (order = 1)
fitResults1 = polyfit(xdata1,ydata1,1);
% Evaluate polynomial
yplot1 = polyval(fitResults1,xplot1);

% Save type of fit for "Show equations"
fittypesArray1(1) = 2;

% Save coefficients for "Show Equation"
coeffs1{1} = fitResults1;
fitLine1 = plot(xplot1,yplot1,'DisplayName','    linear','Tag','linear',...
    'Parent',axes1,...
    'Color',[1 0 0]);
setLineOrder(axes1,fitLine1,plot1);
showEquations(fittypesArray1,coeffs1,5,axes1);

xlabel({'1/T'});
title({'Ln(P) vs 1/T'});
ylabel({'Ln(P)'});
box(axes1,'on');
grid(axes1,'on');
%-----%
function setLineOrder(axesh1, newLine1, associatedLine1)
% Get the axes children
hChildren = get(axesh1,'Children');
% Remove the new line
hChildren(hChildren==newLine1) = [];
% Get the index to the associatedLine
lineIndex = find(hChildren==associatedLine1);
% Reorder lines so the new line appears with associated data
hNewChildren = [hChildren(1:lineIndex-1);newLine1;hChildren(lineIndex:end)];
% Set the children:
set(axesh1,'Children',hNewChildren);

```

```

function showEquations(fittypes1, coeffs1, digits1, axesh1)
n = length(fittypes1);
txt = cell(length(n + 1) ,1);
txt{1,:} = ` `;
for i = 1:n
    txt{i + 1, :} = getEquationString(fittypes1(i), coeffs1{i}, digits1, axesh1);
end
text(.05, .95, txt, 'parent', axesh1, ...
    'verticalalignment', 'top', 'units', 'normalized');

%-----%
function [s1] = getEquationString(fittype1, coeffs1, digits1, axesh1)

if isequal(fittype1, 0)
    s1 = `Cubic spline interpolant`;
elseif isequal(fittype1, 1)
    s1 = `Shape-preserving interpolant`;
else
    op = `+-`;
    format1 = [`%s %0.`, num2str(digits1), `g*x^{%s} %s`];
    format2 = [`%s %0.`, num2str(digits1), `g`];
    xl = get(axesh1, `xlim`);
    fit = fittype1 - 1;
    s1 = sprintf(`y =`);
    th = text(xl* [.95;.05], 1, s1, 'parent', axesh1, `vis`, `off`);
    if abs(coeffs1(1) < 0)
        s1 = [s1 ` -`];
    end
    for i = 1:fit
        s1 = length(s1);
        if ~isequal(coeffs1(i), 0)
            s1 = sprintf(format1, s1, abs(coeffs1(i)), num2str(fit+1-i), op((coeffs1(i+1)<0)+1));
        end
        if (i==fit) && ~isequal(coeffs1(i), 0)
            s1(end-5:end-2) = []; % change x^1 to x.
        end
        set(th, `string`, s1);
        et = get(th, `extent`);
        if et(1)+et(3) > xl(2)
            s1 = [s1(1:s1) sprintf(`\n      `) s1(s1+1:end)];
        end
    end
    if ~isequal(coeffs1(fit+1), 0)
        s1 = length(s1);
        s1 = sprintf(format2, s1, abs(coeffs1(fit+1)));
        set(th, `string`, s1);
        et = get(th, `extent`);
        if et(1)+et(3) > xl(2)
            s1 = [s1(1:s1) sprintf(`\n      `) s1(s1+1:end)];
        end
    end
    delete(th);
    % Delete last `+`
    if isequal(s1(end), `+`)
        s1(end-1:end) = [];
    end
    if length(s1) == 3
        s1 = sprintf(format2, s1, 0);
    end
end
end

```

Analysis of the electron-ion timing resolution in a proportional gas chamber

Ian D. Kotler FRAS, Suffolk County Community College, Physics & Astronomy, Selden, NY 11784
John Blakley, Howard University, Engineering & Architectural Sciences, Washington, DC 20059
Robert Neblett II, Howard University, College of Arts & Science, Washington, DC 20059
Marcus Alfred, Howard University, Physics & Astronomy, Washington, DC, 20059
Mickey Chiu, Brookhaven National Laboratory, Physics, Upton, NY 11973

Abstract

At Brookhaven National Laboratory, physicists are using the Relativistic Heavy Ion Collider (RHIC) to collide heavy ions at high energies in order to create and study the Quark Gluon Plasma. An upgrade of the PHENIX detector to sPHENIX has been proposed. sPHENIX will have 2π hadronic and electromagnetic calorimetry. Some options for other upgrade detectors that have been proposed are a straw tube tracker, and multi-gap resistive plate chambers (mRPC) for time-of-flight particle identification. Both projects require running Garfield++ simulations for gas filled particle detectors. Garfield++ is a toolkit for the detailed simulation of the signal generation inside a gas filled detector. Gas filled detectors operate by utilizing the ionization produced by charged particles as they pass through the gas in order to create a signal. As an initial first step to simulating the proposed straw tracker for sPHENIX, we simulated in Garfield++ a straw tube filled with Argon gas. This project will help the sPHENIX collaboration to determine whether a straw tracker is a viable option. This work could also be useful for determining whether this straw tracker could be used in ePHENIX, an upgrade of sPHENIX for the Electron Ion Collider (EIC). As for me, I have benefited by learning how to program in C++ and gaining a much greater understanding of how gas-filled detectors work for detecting charged particles.

Ten weeks ago my team and I embarked upon an ambitious undertaking. For the past decade Brookhaven National Lab has played host to the Pioneering High Energy Nuclear Interactions Experiment, PHENIX. Utilizing the Relativistic Heavy Ion Collider, more commonly referred to as RHIC, the PHENIX team delved into the murky depths of particle physics, searching for a new elusive state of matter known as the Quark-Gluon Plasma. Reaching temperatures of over 250,000 times hotter than the center of the Sun, this mysterious substance has been deemed a perfect fluid due its agreeability with the complex equations of Fluid Dynamics as well as having a coordinated, collective flow.

sPHENIX is the first proposed upgrade to the PHENIX detector that will make high statistics measurements of jets, heavy flavor particles, and upsilons. It's unique features will help to determine the temperature dependence of transport coefficients and the color screening length in the Quark Gluon Plasma, thus helping to complete the science program at RHIC. sPHENIX will be a large acceptance detector with 2π hadronic and electromagnetic calorimetry over 2 units of pseudorapidity and a high rate DAQ (15 kHz). For tracking, an outer TPC with inner MAPS layers and intermediate silicon strip layers is being considered for the baseline detector. Another possible upgrade would be to add 10 ps TOF capabilities using mRPCs for particle identification. The

TOF wall is shown here with a straw tube tracker in lieu of the TPC. We have been tasked with optimizing the detection systems for S-PHENIX, in order to study the increasingly smaller phenomena with greatly improved precision.

In order to achieve this my team and I found it necessary to employ several software packages including Garfield++ & Root Primer, both of which are typically used in High Energy Particle physics simulations. We set out to model a Proportional Wire Pulse Chamber in an attempt to accurately measure the current produced from negatively charged electrons that would be released during the Primary & Secondary Ionization events. After studying the subtle intricacies of C++ over the first few weeks of our internship we began integrating our source codes onto a private server. The UNIX server that my team and I utilized was equipped with a Quad Core Processor, 1 Terabyte HDD, running an Ubuntu Desktop & a Linux 16.04 LTS OS.

In order to improve upon the existing detection systems it was first necessary to accurately model the environment in which the interaction would take place. A cubical container was created with dimensions of 1.46 cm^3 . With the region of interest created a cylindrical drift tube was then inserted within this virtual container with a radius of 1.46 cm, just barely fitting within our cubic region which was used to construct the Electric Field. Finally a co-axial wire was placed at along the central axis of the drift tube with a diameter 0.005 mm and a length proportional to the radius of the grounded cathode, the outer wall of the drift tube. 3,270 volts were applied to the co-axial wire to serve as the anode, attracting the electrons.

With our Proportional Gas Wire Chamber properly constructed we then needed a way to track the Primary & Secondary Ionization showers as well as the paths taken by the electrons as they made their way from their points of creation, to the negatively charged anode, the wire. Variables were introduced that would assist in the tracking of creation points, paths taken, as well as time required to travel to the wire.

The gas chosen for the experiment was Argon, and the "mixture" for the simulation consisted of what is referred to as Argon + Argon due to erratic & somewhat random nature at which the gas will ionize. Essentially some of the atoms will ionize, while other will remain inert and neutral. After virtually "filling" the our chamber a signal sensor was created to detect several important variables including evidence of Charge Transport as well as Ionization events with a time binning rate of 1,000 being applied upon ionization. The premise of the experiment relied on the fact that when electrons get near the wire they accelerate very quickly towards it while knocking into atoms within the argon gas. Moreover, these electrons have enough energy to start ionizing the argon atoms, causing an electron avalanche which corresponds to

the negative peak in the graph. Eventually all of the electrons get collected onto the anode and the trailing curve after the maximum current, corresponds to the few trailing electrons coming into contact with the anode wire. If one were to increase the voltage it would increase the electric field around the wire. This would cause the electrons to accelerate towards the coaxial wire with more force, since the electric field is larger, and an increase in the voltage would create more ionized electrons.

To successfully apply the aforementioned theory it would be necessary to employ a program known as Magboltz. Written by programmer Steve Biagi, Magboltz helps calculate the Electron Transport Properties. It does this through the use of a numerical integration technique known as Monte Carlo Integration which implements random numbers to off the set the very much so probability based world of Quantum Mechanics. This type of integration assists in determination of the distances of the ions upon creation with respect to the central wire.

The final third party software that was necessary to implement was a program named HEED, which implements something known as the Photo Absorption Ionization model. This allows my team and I to simulate the energy degradation of the δ electrons produced during the Primary & Secondary Ionization events. HEED is able to perform these complex calculations through the use of a phenomenological algorithm. Using the HEED class files we were able to set the type of charged particle we wished to send through the chamber as well as vary its initial energy level to examine how the behavior varies at different energies. In this experiment we have chosen the Muon, a cousin of the electron. Both have an identical charge & quantum number; however the Muon is about 200 times heavier than the much less massive electron making it much easier to detect.

With the Muon's energy set to 170 MeV we simply needed establish a few looping protocols to collect our data and a few more variables that would capture and record the paths taken by the ions as they, at least in a relative sense drift towards the central wire. We have chosen to only focus on the ions due to the incredible alacrity of electrons making them very difficult track and time while the much heavier ions would move thousands of slower.

The final bit of code that was needed was a method for viewing the output signal that would hopefully be created. For this we utilized the ROOT Primer tool kit. Developed and used extensively at the Large Hadron Collider at CERN in Switzerland, ROOT provided our team with a way to interpret the data into a analytical graph that we could use to interpret the massive amount data that we were to receive.

The final results from the simulations are depicted as in a graphical context. The graph shows the current in the wire produced by the electrons from the ionization of the argon gas particles caused by the muons traveling through the gas. The x axis on the graph portrays the time lapsed during the simulation ranging from 0 to 1000 nanoseconds. The y axis on the graph describes the current ranging from 0 to -0.08 femtocolumbs (fC). During the simulation, for 410 nanoseconds there was no current recorded as the electrons drift towards the coaxial wire. "One nanosecond later, at 411 nanoseconds, detectable current was recorded; this current was so small that it would require an amplifier. From 411 nanoseconds to 430 nanoseconds the current in the wire sharply increases as the electron avalanche occurs and the induced signals from the ion drift collects on the wire. At the 430 nanosecond mark, the maximum current was recorded in the system to

be -.084 fC. After reaching maximum current there was a rapid decrease with respects to ion interaction with the wire up until 1000 nanoseconds.

The simulated signal corresponds to a signal of a few microvolts which requires a large amplification to detect. The integrated charge for our signal is about -9 fC.

Having successfully simulated an argon drift tube using Garfield++, the next steps are to optimize the signal to achieve larger signals to get to 100 micron position resolution by studying the effects of different gasses and operating voltages. With simulations like this it is our hope that soon a physical upgrade to the current PHENIX detection system can be implemented to allow the many dedicated sPHENIX researchers to travel farther down the deepest rabbit hole in all of physics; where things are not always what they seem; the incredibly strange world of the very small.

With increased detection systems among the other upgrades we can see a potential boom in other fields of Science & Medicine as BNL physicists continue to diligently research many other unknown properties of nature, perhaps even determining what actually took place at the moment of the Big Bang. Another result of this upgrade could possibly lead to a better understanding of the spin properties of the proton.

Ultimately if we were to be given a chance to return to BNL and continue our research the next step would be to adjust the parameters and initial conditions, performing extensive simulations and data runs with many different monatomic & polyatomic gaseous mixtures to further optimize RHIC's detection systems leading to hopefully further breakthroughs in mankind's understanding of the Universe.

Finally I would like to acknowledge & thank my fellow researchers. Robert Neblett II & John Blakley, students from Howard University who worked with me extensively throughout the past 10 weeks; from learning to navigate through the various software packages, to unraveling the truth behind the many High Energy Physics lectures and successfully interpreting the complex data from the gas simulations. Next, my mentor Dr. Marcus Alfred, professor of physics & astronomy at Howard University, with a PhD in computational physics, for showing us how true research is conduct in a professional setting while also patient if we ever struggled with one of the many complex topics that he would present before us. Lastly I would to thank my sponsor Dr. Mickey Chui, Particle Physicist from BNL and one of the main proponents of the PHENIX & sPHENIX for giving me the chance to work with him over the passed ten weeks.

Simulating cosmic events in the protoDUNE detector

Jacob Larkin, Physics and Astronomy, University of Rochester, Rochester, NY 14627

Elizabeth Worcester, Physics, Brookhaven National Laboratory, Upton, NY 11973

Matthew Worcester, Physics, Brookhaven National Laboratory, Upton, NY 11973

The protoDUNE detector is a 400 ton prototype which will allow calibration measurements and provide data useful for reducing systematic uncertainties for DUNE. Before protoDUNE is complete, Monte Carlo simulations are used to test the reconstruction and analysis of the data the detector will produce. These simulations and reconstructions are carried out using LArSoft, a software package for simulating LArTPCs. Of particular interest are space charge effects, in which ionized argon atoms accumulate in the detector, distorting the electric field and thus the number and trajectories of drift electrons in the TPC. This effect can be calibrated by studying the space charge effect with cosmic rays and beam halo muons. It was found that muon counters placed on the front and back of the detector provide sufficient coverage to select muons which travel through the entire detector; however, additional counters placed on the top provide increased coverage and rate.

I. Introduction

The Deep Underground Neutrino Experiment (DUNE) is a planned neutrino experiment which will study neutrino oscillations. DUNE will consist of four modular liquid argon time projection chambers (LArTPCs); each module will have a fiducial mass of 10 kt of liquid argon. The detector will be constructed at the Sanford Underground Research Facility (SURF) and will observe neutrinos generated at Fermilab. DUNE will look for neutrino oscillations which will reveal information about the mass hierarchy of neutrinos and CP violation in the lepton sector.

LArTPCs are large containers filled with liquid argon with an electric field applied across them. Charged particles ionize the argon and the free electrons will move towards the anode while the argon ions move towards the cathode.¹

The anode plane consists of three planes of wires, a vertical collection plane behind two diagonal induction planes.¹ As the electrons pass the induction planes they induce a current which is picked up by electronics at the ends of the wires, and when they reach the collection plane they are collected by those wires with the resulting current again detected by electronics at the ends of the wires.

Large LArTPCs like those planned for DUNE will have many of these anode and cathode planes (APAs and CPAs) located throughout the length of the detector. DUNE will even have two layers of these planes, one on the top part of the TPC and one on the bottom. DUNE will have a total of 150 APAs and 100 CPAs. Each APA is m in size and each module in DUNE will be m in size.

ProtoDUNE will be a smaller prototype detector which will allow calibration measurements and provide data useful for reducing systematic uncertainties for DUNE.² Despite being smaller than the DUNE far detector, protoDUNE will use the same

APAs as DUNE, but fewer (only 6 instead of 150). ProtoDUNE will take data in a charged particle test beam. ProtoDUNE will be located on the surface at CERN, so the large rate of cosmic ray tracks in the detector induce a large space charge effect. Effective calibration of this effect is required to carry out the program of measurements planned for protoDUNE.

A. Space Charge

The space charge effect occurs because the positive ions from the ionization of the liquid argon move towards the cathode much slower than the electrons towards the anode due to their much greater mass.³ As a result, the electric field within the TPC is distorted by the positive ions from what is nominal, and the apparent track observed by the detector differs from the true particle track.

Cosmic ray tracks from high energy muons with a known start time provide a sample of straight tracks through the detector required to calibrate this effect. In order to fully resolve the field distortion in the detector we require two tracks which intersect at a large angle at points throughout the entire volume of the TPC. Using only a single track the direction of the distortion in the electric field is ambiguous, but using two tracks it is possible to compare the two distortions to find the direction.

Cosmic ray taggers (CRTs) are used to provide the start time for the cosmic rays as they hit the detector. We made a preliminary estimate of whether top counters are needed, in addition to counters on the front and back of the detector, for calibrating the space charge effect.

II. Methods

It was assumed that there is a uniform distribution of beam halo muons in the unit z direction with a start time provided by CRTs at the front, back and top of the TPC. The actual distribution

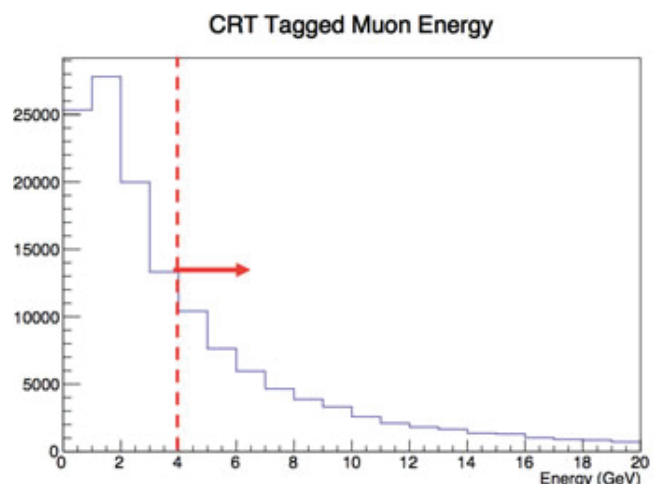
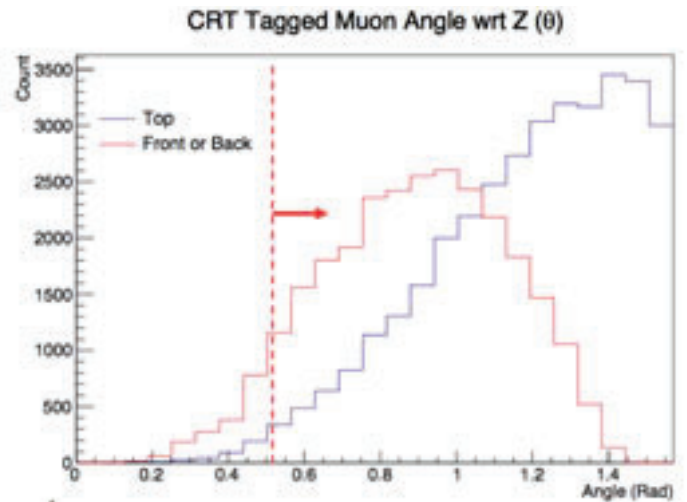
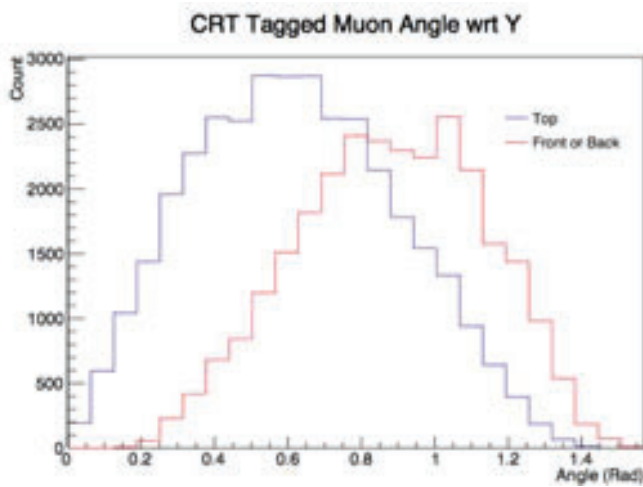


Figure 1: An $E > 4$ GeV energy cut was applied to the muons to ensure a straight track through the TPC.

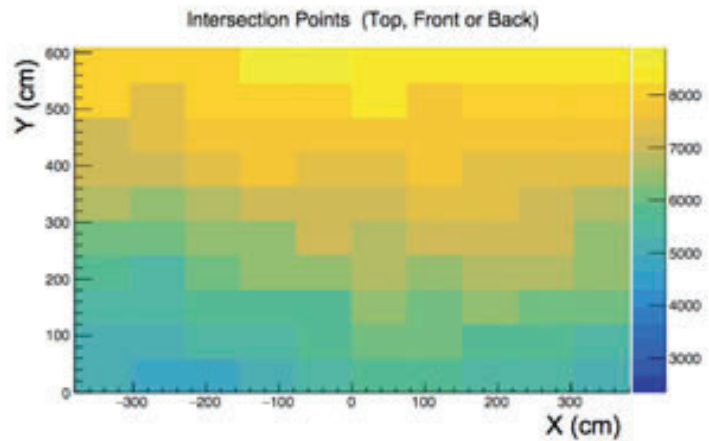
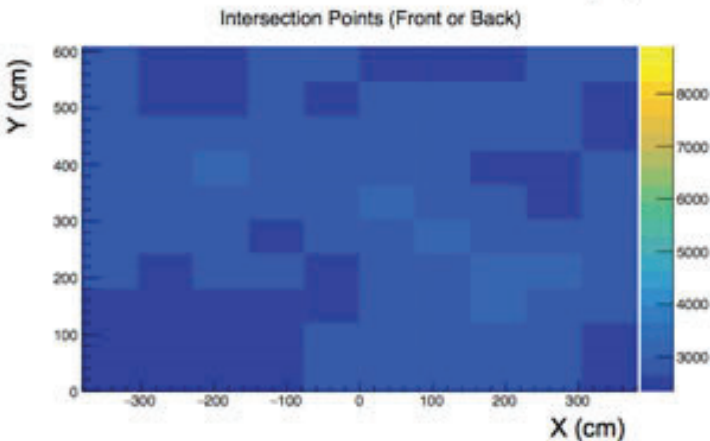
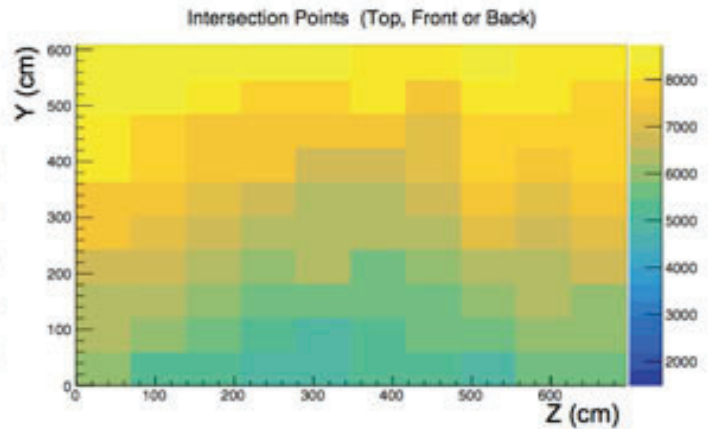
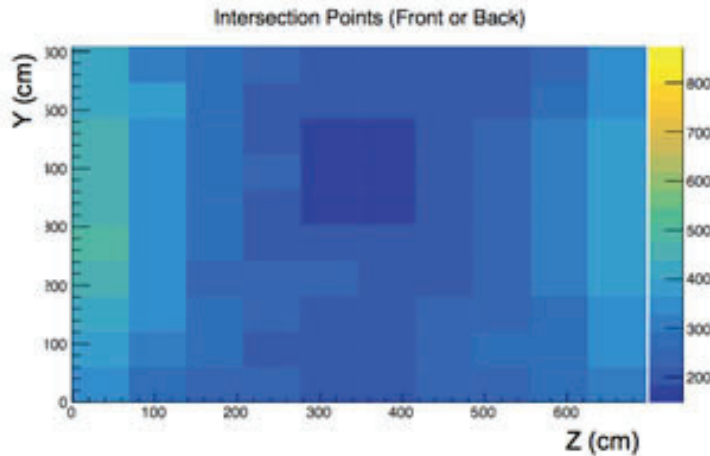
of beam halo particles is not expected to be uniform; simulations of the beam are underway that will allow future studies to use a more realistic distribution. Cosmic muons were generated by CORSIKA in LArSoft, and 1000 readout windows were used to give us a total of 145,997 cosmic ray muons. CORSIKA generates random samples of showers using a database. These samples are distributed over a shower area extending two meters beyond the cryostat and then projected to a greater height. Only those muons which hit the TPC are kept. A sample of tagged muons was extracted from the generated sample with a geometric simulation of the CRTs run with counters on the top ($y = 861$ cm), front ($z = -202$ cm) and back ($z = 944$ cm) of the cryostat. The results were

saved to a ROOT ntuple. Any track with a generated trajectory passing through one or more of the CRT modules was included in the analysis.

An algorithm was run which found the intersection points and angle between the assumed beam halo distribution and the tagged cosmic ray sample in $71 \times 61 \times 70$ cm bins. In order to find the intersection points, the point where the muon hit the CRT was used to calculate an infinite line representing the path of the muon. If the muon hit two CRTs, only the first CRT was used to calculate this line. The x-axis was then split into 100 points and the y and z coordinate on this line were calculated. The bins were then filled with these points.



Figures 2 and 3: The angular distributions of muons which hit a CRT after the energy cut.



Figures 4 – 7: The intersection points between the assumed beam halo distribution and the tagged cosmic ray sample.

III. Results

We first selected a sample of cosmic ray tracks with the $E > 4\text{GeV}$ cut shown in figure 1. This cut ensures that the tracks we are considering are straight since high energy muons follow a straight path through the argon.

Figure 2 shows that the top counter configuration selects more vertical muons than the front or back counters. The angle with respect to the beam halo muons for the different counter configurations is shown in figure 3. We applied a $\theta > 30^\circ$ angular cut to ensure a sufficiently large angle for the space charge calibration as shown in figure 3.

Figures 4 and 5 show the intersection points in the YZ plane before and after the top CRTs were added. Figures 6 and 7 show the intersection points in the XY plane before and after the top CRTs were added.

IV. Conclusions

The Front and Back configuration provides space charge intersection points over the entire TPC. However, from these plots it is clear that there is an advantage in using the Top counters since there are more tracks intersecting the beam halo over the whole volume of the TPC.

Increased statistics from further cosmic ray muon samples will need to be considered. For example, considering anode to anode cosmic ray tracks will increase statistics without the need for additional CRTs on the top of the detector. This would allow a cost savings, since this configuration uses fewer CRTs, without sacrificing utility.

This study shows promising results of the capability of the front and back CRTs to provide useful data for calibrating the space charge effect in protoDUNE, even without CRTs on the top.

V. Acknowledgements

This project was supported in part by the U.S. Department of Energy, Office of Science, Office of Workforce Development for Teachers and Scientists (WDTS) under the Science Undergraduate Laboratory Internships Program (SULI).

VI. References

- ¹ LBNE Collaboration, *The Long-Baseline Neutrino Experiment: Exploring Fundamental Symmetries of the Universe*, arXiv:1307.7335v3 [hep-ex], (2013).
- ² M. A. Leigui de Oliveira, et al., *Proposal for a Full-Scale Prototype Single-Phase Liquid Argon Time Projection Chamber and Detector Beam Test at CERN*, No. CERN-SPSC-2015-020, (2015).
- ³ M. Bass, M. Mooney and S.R. Soletti, *Space Charge Effect Measurements and Corrections*, MicroBoone Note-1018-INT-v6, (2016).

Evaluation of ^{86}Kr cross sections for use in fusion diagnostics

A. Lewis

Department of Nuclear Engineering, University of California, Berkeley, Berkeley, CA 94720

D. Brown

National Nuclear Data Center, Brookhaven National Laboratory, Upton, NY 11973-5000, USA

The National Ignition Facility at Lawrence Livermore National Laboratory uses ^{86}Kr as a diagnostic tool to measure the neutron flux produced by fusion reactions. As krypton is chemically inert, it can be implanted directly into the fuel capsule, and the reaction products can be measured to determine the flux of fusion neutrons. ^{86}Kr cross sections are also a valuable tool for studying both the ^{85}Kr branching point in the s-process and determining the neutron flux in stars. In this work, experimental data on the neutron production, radiative capture, inelastic scattering and total cross sections of ^{86}Kr were used in conjunction with the fast region nuclear reaction code EMPIRE and a new resonance region evaluation to produce a new evaluation of neutron-induced reactions on ^{86}Kr . For the EMPIRE calculations, the Koning-Delaroche global spherical optical model potential with a slight deformation was used, along with several additional reaction models. Two pre-equilibrium models were included for the high incident neutron energy region, direct and semi-direct capture models were used to correct the calculation of the radiative capture cross sections, and an approximation of the soft rotator model was made in order to accurately calculate the direct inelastic cross section. With these models and corrections to the structure of ^{86}Kr , the evaluated cross sections matched the experimental data. The new evaluation will be incorporated in the next release of the ENDF/B nuclear reaction library.

I. INTRODUCTION

^{86}Kr is an isotope with important applications for both fusion technology and astrophysics. As a chemically inert noble gas, krypton can be frozen and implanted in the fuel capsules used at the National Ignition Facility (NIF) at Lawrence Livermore National Laboratory [1], as shown in Figure 1. During a shot, the Kr nuclei are directly exposed to the neutron flux at the location of the burn, providing the most accurate picture of the fuel areal density. The RAGS (radiochemical analysis of gaseous samples) detector is then used to collect the krypton gas and analyze it for certain decay products that are produced by neutron-induced reactions with the fusion neutrons. The $^{86}\text{Kr}(n,2n)^{85m}\text{Kr}$ and $^{86}\text{Kr}(n,\gamma)^{87}\text{Kr}$ reactions are of particular interest for this application, as the resultant nuclei of both reactions de-excite with half-lives and energies that are convenient for measurement. The RAGS detector allows for the determination of the number of each isotope produced in the shot, which can be used to calculate the flux of neutrons caused by the fuel burn if the cross sections of the reactions are well understood. The $^{86}\text{Kr}(n,2n)^{85m}\text{Kr}$ and $^{86}\text{Kr}(n,\gamma)^{87}\text{Kr}$ reactions are also of importance in the astrophysics. ^{85}Kr is an important branching point in the slow-neutron capture process (s-process) that occurs in asymptotic giant branch (AGB) stars, which are thought to produce about half of all elements heavier than iron [2]. Branching points in the s-process occur at isotopes with decay half-lives that are long enough to allow the neutron capture reaction to compete with the radioactive decay. In the case of ^{85}Kr , with a half-life of 4.48 h, neutron capture is competitive in typical AGB star environments, as shown in Figure 2. The $^{86}\text{Kr}(n,2n)^{85m}\text{Kr}$ reaction provides a check for the modeling of the

$^{85}\text{Kr}(\gamma,n)^{86}\text{Kr}$ reactions that have been measured to study the ^{85}Kr radiative capture cross section. The $^{86}\text{Kr}(n,\gamma)^{87}\text{Kr}$ reaction cross section is also important for the calculation of the abundance of ^{87}Kr isotopes in AGB stars [3]. For the use in these applications, a new evaluation of the neutron-induced reactions on ^{86}Kr has been performed, using a new resolved resonance region evaluation and the fast region nuclear reaction code EMPIRE [4] which employed several physical models, described in Appendix A.

II. RESOLVED RESONANCE REGION

The resonance region evaluation was updated by converting the resonance parameters in the most updated ATLAS of Neutron Resonances [5] from the Multi-level Breit-Wigner format to the Reich-Moore format [6]. Two resonances were also added to the evaluation, as the resonance at 188.89 keV which was missing from the current evaluation, and a fake resonance at -20 keV was needed to match the thermal cross section value of 3 mb given in the ATLAS [5]. The contribution of the primary capture gammas to the thermal and resonance region cross sections were also calculated for ^{86}Kr , and in the process it was determined that their contribution to fast region capture cross section was negligible.

III. NEUTRON PRODUCTION CROSS SECTION

The $^{86}\text{Kr}(n,2n)^{85m}\text{Kr}$ reaction is important for both the NIF diagnostics and for understanding the ^{85}Kr branching point in the s-process. The first excited state of ^{85}Kr is an isomer, and the decay of this isomeric state also provides a convenient method to measure the total (n,2n) reaction rate in RAGS detector, providing information on the primary fusion neutrons. Two sets of experimental data are available for the $^{86}\text{Kr}(n,2n)^{85m}\text{Kr}$ isomer reaction. One set was measured at the Triangle Universities Nuclear Laboratory (TUNL) by Bhike *et al.*, in the energy range between 10 MeV and 15 MeV [3]. A single measurement of the $^{86}\text{Kr}(n,2n)^{85m}\text{Kr}$ cross section was taken by Kondaiah *et al.*, at the Georgia Tech accelerator at 14.4 MeV [7]. Figure 3 presents the experimental data for the isomer reaction, along with the evaluated cross section, which was calculated with EMPIRE using Hauser-Feshbach, multi-step compound (MSC) and multi-step direct (MSD) models. The final evaluated cross section follows the shape of the Bhike *et al.* data very closely, indicating that this was an accurate combination of physical models for this energy region.

IV. RADIATIVE CAPTURE CROSS SECTION

The $^{86}\text{Kr}(n,\gamma)^{87}\text{Kr}$ reaction is important for studying the low energy component of the NIF flux, and for calculating the abundance of ^{87}Kr in AGB stars. Bhike *et al.* measured the radiative capture cross section in the energy region between 0.5 MeV and 15 MeV in 2015 [3], and a single measurement was made by Hughes *et al.* in 1953 at Argonne National Laboratory at an incident neutron energy of 1 MeV [8]. Both sets of experimental data

are presented in Figure 4, along with the calculated and evaluated cross sections. It can be seen that the EMPIRE calculation of the radiative capture cross section does not have the correct energy dependence, indicative of the importance of the direct contribution to the cross section. The EMPIRE calculation only includes the compound contribution, so the direct and semi-direct (DSD) capture cross sections were calculated with the model by Chiba *et al.*[9] and were added to the EMPIRE calculations to obtain the evaluated cross section. The direct and semi-direct components are each shown in Figure 4, and it can be seen that the semi-direct component is actually the most significant portion of the cross section above 10 MeV. The evaluated cross section fits the shape of the data very well above 2 MeV, the region over which the energy averaging method used in the calculations is valid.

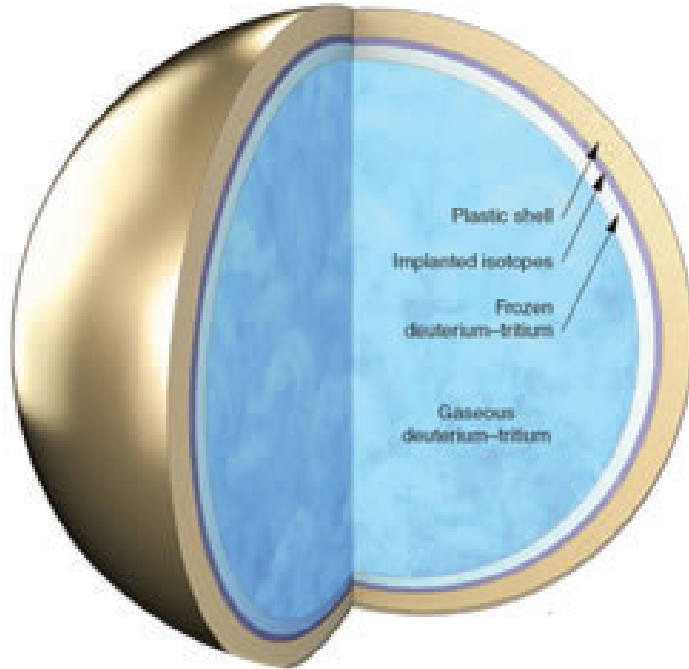


FIG. 1. Diagram of the NIF fuel capsule, with a layer of implanted Kr isotopes shown. The Kr, located very near the fuel burn, provides an accurate picture of the areal density of the fuel as it burns[1].

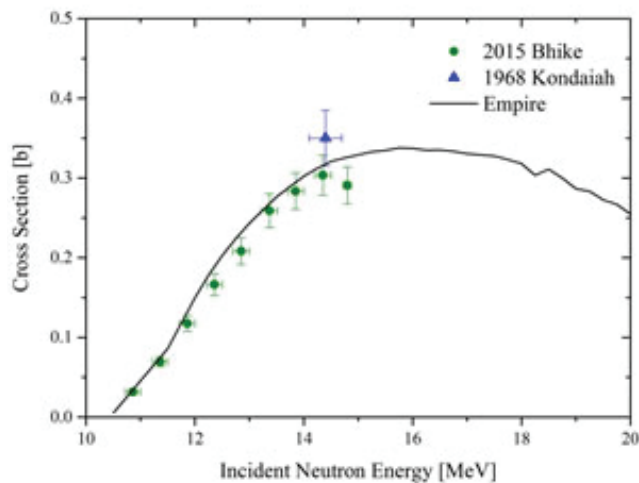


FIG. 3. Plot of the (n,2n) isomer cross section. Two sets of experimental data are presented along with the evaluated cross section, which was calculated using the Hauser-Feshbach, MSD and MSC methods.

V. INELASTIC SCATTERING CROSS SECTION

The inelastic scattering reaction provides valuable insight into the nuclear structure of the target nucleus. The compound nucleus decays by emission of a neutron, leaving an excited ^{86}Kr nucleus that de-excites by gamma emission. The inelastic scattering gammas are the energy given off as the nucleus transitions from one level to another, and therefore can be used to study the nuclear structure. Partial gamma cross sections for thirteen such transitions were measured by Fotiades *et al.* with the DANCE array at the Los Alamos Neutron Science Center for incident neutron energies up to 20 MeV[10]. The gamma transitions that were measured are shown on a partial level scheme of ^{86}Kr in Figure 5, which also indicates how well the initial EMPIRE cross section calculations matched the experimental data. The level scheme

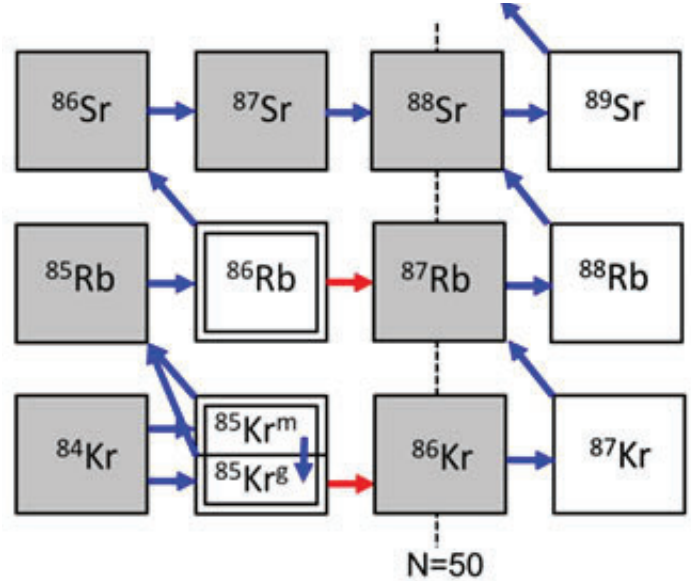


FIG. 2. Branching diagram of the s-process showing how ^{85}Kr can either undergo beta decay to become ^{85}Rb or neutron capture to become ^{86}Kr , and how the $^{86}\text{Kr}(n,\gamma)^{87}\text{Kr}$ cross section is important for calculating the abundance of ^{87}Kr [2].

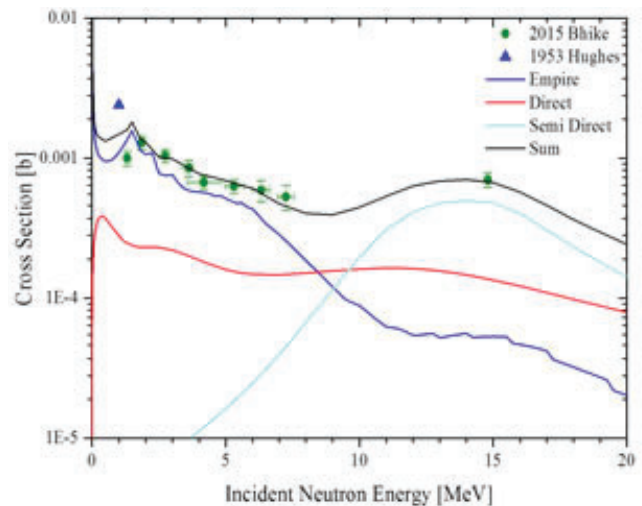


FIG. 4. Plot of the (n, γ) cross section. Two sets of experimental data are presented along with the evaluated cross section, which is the sum of the compound cross section, the direct and semi-direct cross sections.

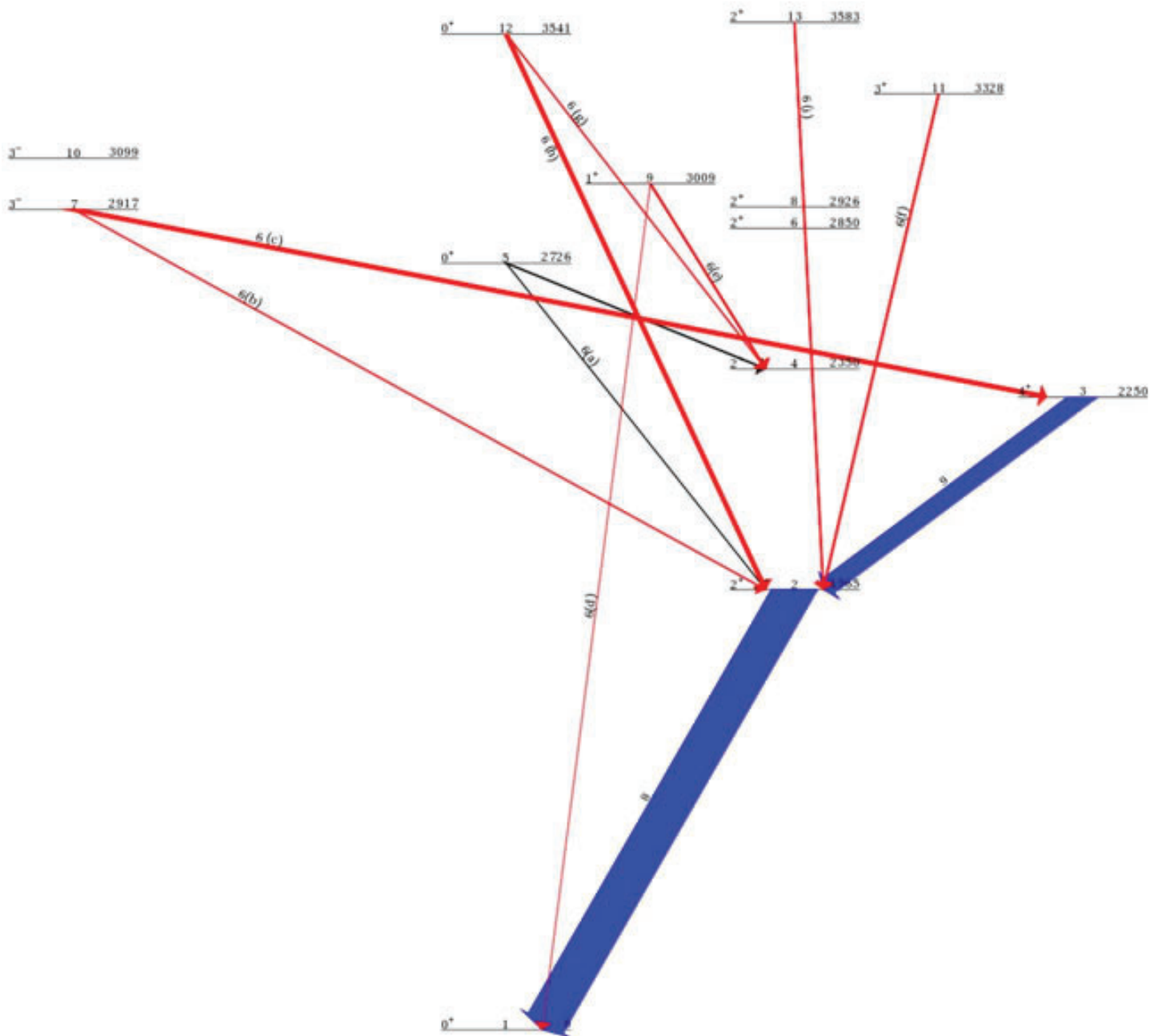


FIG. 5. Partial level scheme for ^{86}Kr for the original EMPIRE runs. The experimentally measured gamma transitions are shown, and are labeled by the figure that shows their cross section plot. The transitions in red indicate calculated energy dependencies that did not match the experimental data, the transitions in blue indicate calculated cross sections that were the right shape but were underestimated in magnitude, and the black transitions indicate good fits. The size of the arrows represent the relative cross section magnitudes, and show how the population of the lowest three levels is largely from the direct reactions and that the gamma transitions from the first two excited states are the largest contribution to the total inelastic cross section.

shows that the three lowest levels are fed mostly by the direct inelastic reaction, but that the cascade from higher levels does contribute. This indicates that the higher levels need to be fixed in order to properly evaluate the inelastic cross section, but that most of the effect will come from fixing the direct contribution to the lower three levels.

Empire allows for the direct component of the inelastic scattering reaction to be calculated either by the coupled-channels method or by the Distorted-wave Born Approximation (DWBA). The strongest coupling in a nearspherical nucleus is in the ground state vibrational band, which for ^{86}Kr is the first three levels, so the direct cross sections to the three lowest levels needed to be

treated with coupled-channels method. The coupling strength decreases with level energy, so DWBA was used for the rest of the levels up to 16, and the direct contribution for the levels above this was neglected[11].

For the gamma transitions from the DWBA-treated levels, the calculated cross sections all had magnitudes that were close to the experimental data, but all of the transitions except those from level 5 did not have correct energy dependencies. This is illustrated in Figure 6, in which the red cross sections were calculated by EMPIRE in the original run. For levels 9, 11 and 13, a specific spin and parity (J^π) assignment was not given in Evaluated Nuclear Structure Database Files (ENSDF)[12], but rather a range of

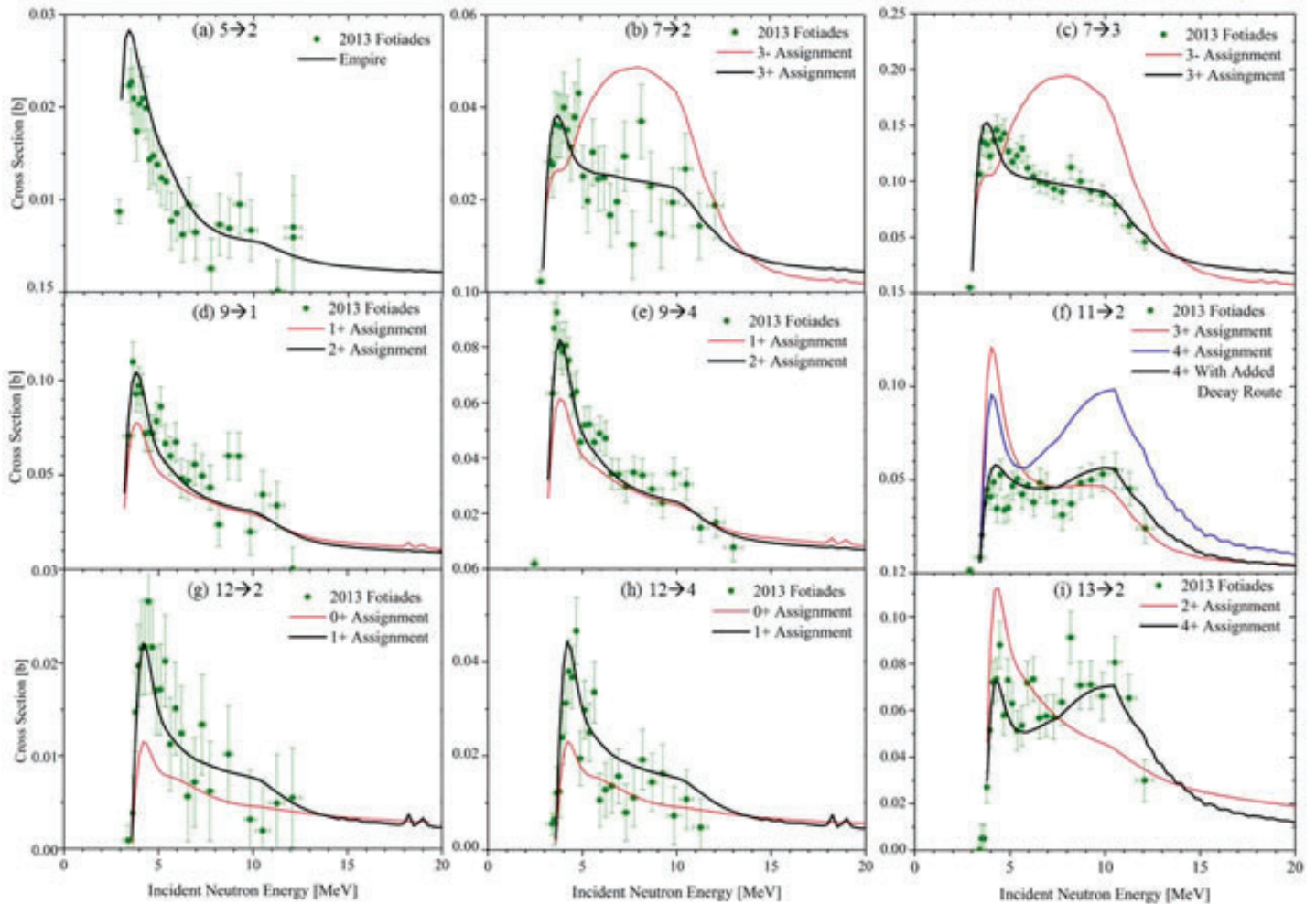


FIG. 6. Plots of the partial gamma cross sections for nine of the experimentally measured gamma transitions, all of which were treated with DWBA. The plots correspond to the labels in Figures 5 and 7, and each is labeled by the initial and final levels of the transition.

possible assignments was given. The ENSDF J^π assignments are determined based on radioactive decay, inelastic scattering measurements, stripping reactions and known gamma transitions, but for these three levels there was no conclusive choice, and so in the original EMPIRE run one of the options had been chosen at random for each of these three levels. For levels 7 and 12, a single J^π assignment was given in ENSDF, but experiments had suggested other possibilities as well. The J^π assignments for these five levels were changed based on patterns in the energy dependence of the experimental data, and for each level a new assignment was found which produced calculated cross sections with energy dependencies that fit the experimental data. For level 11, the change in spin opened up a new M1 gamma transition of comparable strength with the known transition, and so the branching ratio for this decay route was calculated using the Weisskopf single-particle estimates[13] using previously calculated systematics[14]. The J^π assignment changes are summarized in Table I and a revised level

TABLE I. ^{86}Kr level spin assignments

Level	ENSDF J^π	Original J^π	Final J^π
7	(3 ⁻)	3 ⁻	3 ⁺
9	(1,2) ⁺	1 ⁺	2 ⁺
11	(3 ⁺ ,4 ⁺)	3 ⁺	4 ⁺
12	0 ⁺	0 ⁺	1 ⁺
13	(0 ⁺ ,1 ⁺ ,2 ⁺ ,3 ⁺ ,4 ⁺)	2 ⁺	4 ⁺

el scheme is presented in Figure 7. The cross sections calculated with the new J^π assignments are presented in Figure 6 in black.

The three lowest lying levels are fed by both the gamma cascade and by direct inelastic reasons, and so were improved slightly by the correction of the structure above them. The largest contribution to the population of these levels, however, is the direct inelastic scattering and so these improvements were not enough to fix the under-estimation of the population of the gamma transitions from the second and third levels. The direct inelastic scattering for these levels was calculated by the coupled-channels method using the rigid rotator model. The soft rotator model is much more accurate for isotopes in this mass region, but the input data required for soft rotator calculations in EMPIRE was not available for ^{86}Kr [15]. The soft rotator model was therefore approximated by introducing spin-dependent dynamic deformations into the rigid rotator calculations in EMPIRE. This approximation increased the direct population of the second and third levels and brought the gamma transition crosssections up to the magnitude of the experimental data. With the corrections in the spin and parity assignments and the addition of the dynamic deformations for the coupled-channels levels, the calculated cross sections for all of the partial gammas matched the experimental data.

The evaluated cross sections for the total inelastic reaction could not be verified by experimental data, but the accuracy of the evaluated partial gamma cross sections supports the conclusion that the total inelastic cross section is also accurate.

3° 10 3099

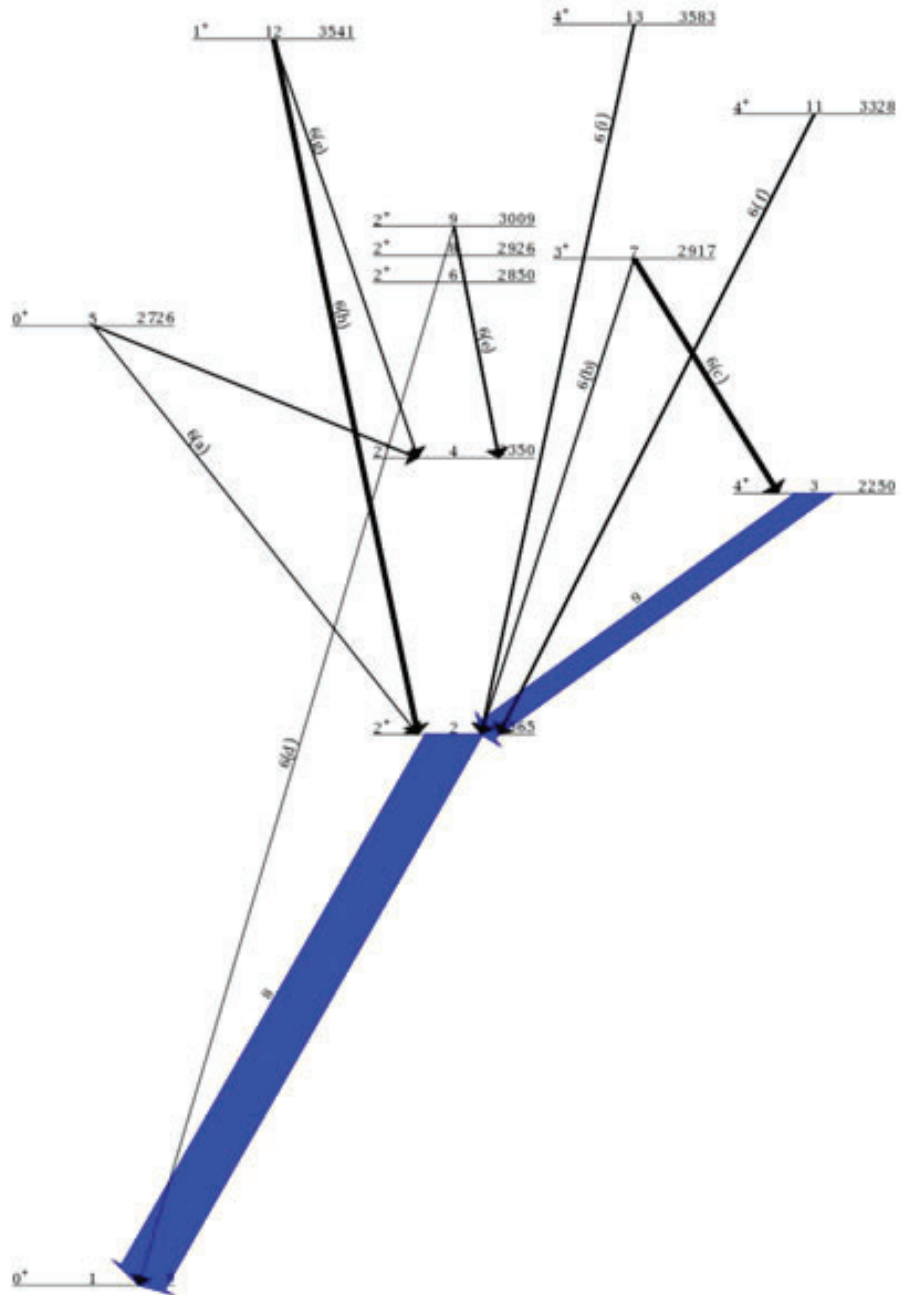


FIG. 7. Revised level scheme based on the final J^π assignments. The corrected assignments led to calculated cross sections that matched all of the DWBA-treated levels.

VI. TOTAL AND ELASTIC CROSSSECTIONS

The elastic scattering cross section is the strongest constraint on the optical potential, as it is entirely dependent on the chosen potential. For ^{86}Kr there is no experimental elastic scattering data, but as the elastic scattering is the largest contribution to the total cross section, the calculated total cross section can also be used to check the optical potential. It can also act as a weak constraint on all other physical models used, as the calculated total cross section is the sum of all channel cross sections. The total cross section is the simplest cross section to measure experimentally, and so usually provides the most accurate data. In this case, two sets of total cross section data were used to check the slightly deformed Koning-Delaroche optical model potential [16] that was used for the EMPIRE calculations.

Two measurements of the total cross section of ^{86}Kr were

performed by transmission at the Oak Ridge Electron Linear Accelerator (ORELA). In 1983 Raman *et al.* measured the total cross section in the energy region between 4 keV and 5 MeV [17], and in 1988, Carlton *et al.* measured the cross section in the energy region between 1 MeV and 25 MeV [18]. The experimental data were energy averaged because of the overwhelming number of data points, to provide a more accurate comparison with the calculated cross sections. The averaged total cross section data is presented in Figure 10, along with the EMPIRE calculation of the total cross section. The calculated total cross section accounts for all reaction mechanisms except for the (DSD) capture, which could not be calculated within EMPIRE. The DSD capture cross section, however, is on the order of mb and so is not significant in the comparison of the total cross section to the experimental data. It can be seen that the evaluated total cross section stays well

within the uncertainty of the experimental data, and is similar in shape over the entire optical model region (below 20 MeV, the resonance region begins and the cross section averaging process used here is no longer valid). This fit indicates that the optical potential and the combination of reaction models used in this evaluation are a good fit for ^{86}Kr .

VII. CONCLUSIONS

A new ^{86}Kr reevaluation was performed based on a new resolved resonance region evaluation and several sets of experimental data. The calculation of the neutron-induced reactions was performed using a deformed Koning-Delaroche optical model potential in addition to multi-step direct, multi-step compound, direct and semi-direct capture models and an approximation of the soft rotator model. Several level J^π assignments and branching ratios were also fixed in the ^{86}Kr structure, leading to an overall evaluation that fits the experimental data. The accurate evaluation of the neutron production and radiative capture reactions will improve the modeling and calculations for the RAGS detector at NIF and understanding of the ^{85}Kr branching point in the s-process. The new inelastic partial gamma evaluation provides insight into the nuclear structure of ^{86}Kr and may be used in future structure evaluations. This new evaluation of the neutron-induced reactions on ^{86}Kr will be included in the ENDF/B-VIII.0 library.

VIII. Appendix A: NUCLEAR PHYSICS MODELS

The total reaction cross section for a neutron-induced reaction is the sum of the cross sections of each individual channel,

$$\sigma_{\text{tot}} = \sum_c \sigma_c. \quad (\text{A1})$$

The cross section of each reaction can be described by the scattering matrix (S-matrix), where the matrix element $S_{cc'}$ represents the amplitude of the reaction with incoming channel c' and outgoing channel c . The channel cross section can be described by the real part of the scattering matrix,

$$\sigma_c = \frac{2\pi}{k_c^2} g_c [1 - R(S_{cc})] \quad (\text{A2})$$

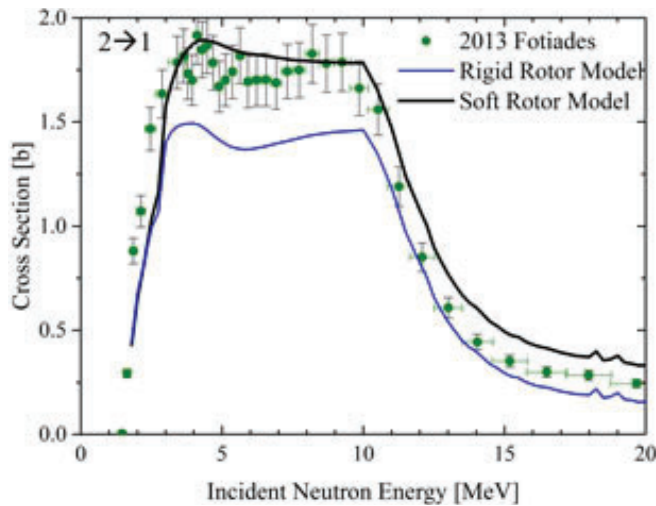


FIG. 8. Cross section of the gamma transition from the second level to the ground state, which was treated with the coupled-channels method. The rigid rotator model underfitted this level, leading to a calculated cross section that was well below the experimental data. The inclusion of the spin-dependent deformations of the soft rotator model improved the fit.

and the cross section of a reaction with incoming channel c and outgoing channel c' is defined as

$$\sigma_{cc'} = \frac{2\pi}{k_c^2} g_c |S_{cc'}|^2 \quad (\text{A3})$$

The S-matrix can be split into a smooth, or average, component and a fluctuating component,

$$S_{cc'} = \langle S_{cc'} \rangle + S_{cc'}^f \quad (\text{A4})$$

allowing the reaction cross section to be written as

$$\sigma_{cc'} = \frac{2\pi}{k_c^2} g_c |\langle S_{cc'} \rangle + S_{cc'}^f|^2 \quad (\text{A5})$$

or

$$\sigma_{cc'} = \frac{2\pi}{k_c^2} g_c (|\langle S_{cc'} \rangle|^2 + |S_{cc'}^f|^2 + 2\text{Re}(\langle S_{cc'} \rangle \cdot S_{cc'}^f)). \quad (\text{A6})$$

For convenience in calculations, the T-matrix is defined in terms of the S-matrix as,

$$T = 1 - S \quad (\text{A7})$$

and can be calculated using the Lippmann-Schwinger equation, which projects the interaction potential on the channel of interest using the inverse of the interaction Hamiltonian.

A. Energy Averaged Cross Sections

For fast region calculations, the fluctuations in the cross sections are spaced too closely to be seen experimentally and only the average cross section can be measured, allowing for the calculated cross sections to be energy averaged as well. Averaging

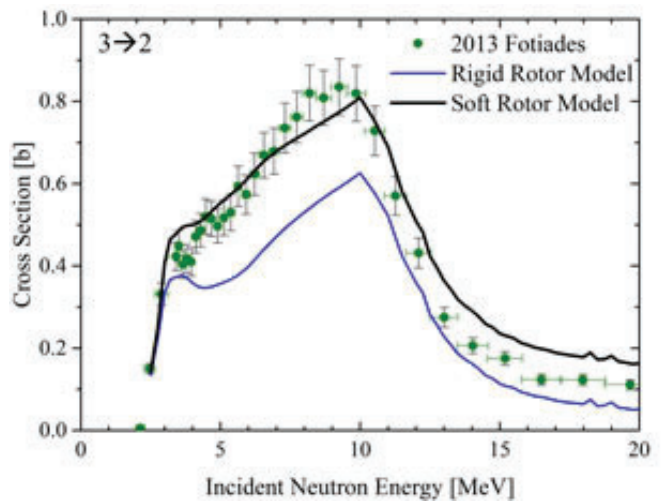


FIG. 9. Cross section of the gamma transition from the third level to the second level, which was treated with the coupled-channels method. The inclusion of the spin-dependent deformations of the soft rotator model improved the fit.

the cross section in Equation A6 causes the final term to vanish, leaving

$$\langle \sigma_{cc'} \rangle = \frac{2\pi}{k_c^2} g_c \left(\langle |S_{cc'}| \rangle^2 + \langle |S_{cc'}^{\text{fl}}|^2 \rangle \right) \quad (\text{A8})$$

as the energy-averaged reaction cross section. The first term in Equation A8 represents the direct contribution to the cross section, and the second term represents the compound contribution[19].

B. Compound Reactions

Compound reactions are reactions in which the neutron is absorbed into the nucleus and the excess energy is shared among the nucleons, creating an excited compound nucleus. The compound nucleus must de-excite by some means, but the time between the creation and decay is very long compared to the time it would take a neutron to traverse the nucleus, and in the process of sharing the excess energy most of the information about the original configuration is lost.

The compound reaction cross section for a specific reaction, from Equation A8, is

$$\langle \sigma_{cc'}^{\text{cmp}} \rangle = \frac{2\pi}{k_c^2} g_c \langle |S_{cc'}^{\text{fl}}|^2 \rangle \quad (\text{A9})$$

The fluctuation part of the scattering matrix can be rewritten in terms of the average scattering cross section by squaring Equation A4,

$$\langle |S_{cc'}^{\text{fl}}|^2 \rangle = \langle |S_{cc'}|^2 \rangle + \langle |S_{cc'}^{\text{dir}}|^2 \rangle \quad (\text{A10})$$

and solving for the fluctuation term. This allows for the compound reaction cross section to be written in terms of the scattering matrix and the average scattering matrix,

$$\langle \sigma_{cc'}^{\text{cmp}} \rangle = \frac{2\pi}{k_c^2} g_c \left(\langle |S_{cc'}|^2 \rangle - \langle |S_{cc'}^{\text{dir}}|^2 \rangle \right) \quad (\text{A11})$$

which can be solved for based on the desired model.

1. Hauser-Feshbach Calculations

The Hauser-Feshbach model for compound cross sections is a first order approximation of the interaction between the neutron and the target nucleus system. Under this assumption, the transmission coefficient (not to be confused with the T-matrix) for each channel can be calculated as

$$T_c = 1 - |S_{cc'}|^2 \quad (\text{A12})$$

allowing the fluctuation term of the S-matrix to be written as

$$\langle |S_{cc'}^{\text{fl}}|^2 \rangle = \frac{T_c T_{c'}}{\sum_i T_i} W_{cc'} \quad (\text{A13})$$

This gives the final Hauser-Feshbach formula,

$$\langle \sigma_{cc'}^{\text{cmp}} \rangle = \frac{2\pi}{k_c^2} g_c \frac{T_c T_{c'}}{\sum_i T_i} W_{cc'} \quad (\text{A14})$$

in which $W_{cc'}$ is the with Width Fluctuation Correction, which accounts for the elastic scattering enhancement and the high energy cross section fluctuations[20].

2. Multi-Step Compound Calculations

If the incident neutron energy is high enough to allow for multiple neutron emissions, a higher order interaction approximation must be made. This can be done using the multi-step compound (MSC) model. With MSC, the cross section is calculated with a sum of n transmission coefficients, where the n^{th} coefficient represents the excitation of n particle-hole pairs[4].

C. Direct Reactions

Direct reactions happen on a much faster time scale than compound reactions, as the incoming neutron does not get absorbed to create a compound nucleus, but rather interacts with individual states in the nucleus. The direct reaction cross section for a specific reaction, from Equation A8, is

$$\langle \sigma_{cc'}^{\text{dir}} \rangle = \frac{2\pi}{k_c^2} g_c \langle |S_{cc'}^{\text{dir}}|^2 \rangle \quad (\text{A15})$$

and the S-matrix is calculated based on the desired model.

1. Distorted-Wave Born Approximation

The Distorted-Wave Born Approximation (DWBA) is a first order approximation of the direct interaction, in which the incoming and outgoing channels are represented as plane waves and the interaction is distorted to account for elastic scattering. This model accounts for coupling between channels, but as it is first order it is only valid when the coupling is weak[20].

2. Coupled-Channels Calculations

In the case of strong coupling or a target that is a strong absorber, the coupled-channels method (CCM) is more appropriate.

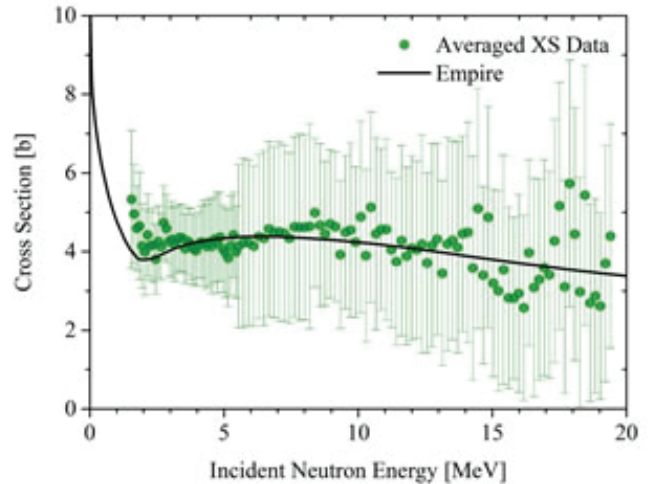


FIG. 10. Plot of the total cross section. The experimental data was averaged to allow for easier comparison to the evaluated cross section.

The CCM Hamiltonian is the sum of the optical model term and a coupling term, which accounts for coupling between channels. The dependence on the channel creates a set of coupled equations that can then be solved for the S-matrix and the transmission coefficients[11].

The coupling term of the CCM Hamiltonian can be calculated by several models, including the rigid rotator model and the soft rotator model. The rigid rotator model is not as accurate, as it does not include dynamic deformations of the excited levels. The soft rotator model accounts for the centrifugal force on the level deformations, and includes spin-dependent dynamic deformations caused by the angular momentum. The spin-dependent deformations are usually larger than the ground state static deformation, and so have the effect of enhancing the excitation of those levels which increases the direct cross section to those levels[15].

3. Multi-Step Direct Calculations

The multi-step direct (MSD) pre-equilibrium model is analogous to the MSC model in that it is a higher order interaction approximation that should be used at higher energies. With the MSC model, the cross section is calculated from the sum of n transmission coefficients, of which the n^{th} coefficient represents n interaction steps[4].

4. Direct/Semi-Direct Capture Calculations

The direct radiative capture reactions are calculated separately from the inelastic scattering cross sections, and can be split into direct capture and semi-direct capture in the fast incident neutron energy region. Direct capture is modeled as a single-step electromagnetic transition and is calculated using a first-order perturbation on the potential. Semi-direct capture is modeled as a two-step process, in which the giant-dipole resonance in the target nucleus is excited and then decays by gamma emission. The T-matrix components for direct and semi-direct capture can be calculated using these models, allowing for the calculation of the scattering matrix and the cross sections[21]. In this energy region, the capture gammas form a continuous spectrum, as the neutron kinetic energy is comparable to the binding energy.

In the thermal and epithermal region, the incoming neutron does not bring a significant amount of kinetic energy into the reaction and so the nucleus is always excited to the neutron separation energy. This leads to discrete de-excitation gammas, called primary gammas. The energy dependence of the cross section of a specific primary gamma, as developed by Lane and Lynn[22], is given as

$$\sigma_{\gamma}(ch) = \sum_s \sigma_{\gamma}^{\text{dir}} \left[1 + \frac{R - a_s}{R} \frac{y(y+2)}{y+3} \right], \quad (\text{A16})$$

which is the sum of both the compound and direct cross sections. The direct cross section is given by

$$\sigma_{\gamma}^{\text{dir}} = \frac{0.062}{R\sqrt{E_n}} \left(\frac{Z}{A} \right)^2 \frac{2J_f + 1}{6(2I + 1)} S_{dp} \frac{(y+3)^2}{(y+1)^2} y^2 \quad (\text{A17})$$

where the factor y ,

$$y^2 = \frac{2mE_{\gamma}}{\hbar} R^2 \quad (\text{A18})$$

contains the dependence on the gamma energy[23]. The Lane-Lynn formalism allows for the extension of the primary gamma cross section calculations from thermal energies, where most primary gamma cross sections are experimentally measured, up into the resonance region.

D. Optical Model

1. Generalized Optical Potential

In all of the preceding models, the basis of the potential is the generalized optical potential (GOP). The GOP is a complex potential that accounts for scattering, absorption and coupling between the target and projectile. The GOP is calculated by projecting the reaction state onto the channel of interest using the projection operator P and defining the projection operator Q as $1 - P$ (the projection onto all other channels). This projection is used to determine the potential by accounting for coupling with all other possible channels, leading to the definition of the GOP[20],

$$V_c^{\text{GOP}} = \langle c | V_{\alpha} | c \rangle + \left\langle c \left| V_{\alpha} Q \frac{1}{E + i\eta - QHQ} Q V_{\alpha} \right| c \right\rangle. \quad (\text{A19})$$

The GOP is the full optical potential and is too complicated to use in calculations, so to actually calculate the scattering matrix, an approximated optical potential is necessary. Most proper optical potentials share three terms- a real potential well, an imaginary potential term and a spin-orbit potential term. The real potential term is the scattering potential and is proportional to the nucleon density, the imaginary potential term is the absorbing potential and is usually modeled as a surface potential, and the spin-orbit potential term is the coupling potential and is proportional to the derivative of the nucleon density[24].

2. Koning-Delaroche Spherical Potential

For ^{86}Kr , the Koning-Delaroche spherical potential is used. The Koning-Delaroche neutron potential has five terms- real and imaginary volume terms, real and imaginary spin-orbit terms and an imaginary surface term. The volume terms have the Woods-Saxon form,

$$\rho(r) = \frac{1}{1 + e^{(r-R)/a}}, \quad (\text{A20})$$

in which R is the nuclear radius and a is the diffuseness of the nucleus, and the form of the surface and spin-orbit terms is a derivative of Woods-Saxon.

The Koning-Delaroche potential models the nucleus as spherical, but it can be modified to account for ground state static deformation as outlined by Nobre *et al.*[25]. This modification was used in this work, as ^{86}Kr has a slight static deformation.

IX. ACKNOWLEDGEMENTS

The authors would like to thank Michal Herman, Gustavo Nobre, Ian Thompson and Said F. Mughabghab for their assistance with this project, and Toshihiko Kawano for the calculations of the DSD cross sections. The authors would also like to thank Elizabeth Rubino for the initial development of the evaluation in a previous SULI project. This project was supported in part by the U.S. Department of Energy, Office of Science, Office of Work-

force Development for Teachers and Scientists (WDTS) under the Science Undergraduate Laboratory Internships Program (SULI).

X. REFERENCES

- A. Heller, "A New Detector for Analyzing NIF Experiments", Science and Technology Review, Lawrence Livermore National Laboratory, Dec 2012
- R. Raut, A.P. Tonchev, G. Rusev et al, "Cross-section measurements of the $^{86}\text{Kr}(\gamma, n)$ reaction to probe the s-process branching at ^{85}Kr ", Phys. Rev. Lett. 111, 112501 (2013)
- M. Bhihe, E. Rubino, M.E. Gooden et. al., "Measurements of the $^{86}\text{Kr}(n, \gamma)^{87}\text{Kr}$ and $^{86}\text{Kr}(n, 2n)^{85}\text{Kr}$ reaction cross sections below $E_n = 15$ MeV", Phys Rev C 92, 014624(2015)
- M. Herman, R. Capote, B.V. Carlson, et. al., "EMPIRE: Nuclear Reaction Modeling Code System for Data Evaluation", Nucl. Data Sheets, 108, Issue 12 (2007) 2655- 2715
- S.F. Mughabghab, "Atlas of Neutron Resonances: Resonance Parameters and Neutron Cross Sections, $Z = 1-100$ " (Elsevier, Amsterdam 2006).
- Cross Sections Evaluation Working Group, ENDF-6 Formats Manual. National Nuclear Data Center, Brookhaven National Laboratory, June 2009. BNL-90365-2009
- E. Kondaiiah, N. Ranakumar, R. W. Fink, "Neutron activation cross sections at 14.4 MeV for Kr and Xe isotopes", Nuclear Physics A120, Issue 2, (1968) 337-341
- D.J. Hughes, D. Sherman, "Fast Neutron Cross Sections and Nuclear Shells" Phys Rev **78**, 632(1950)
- S. Chiba, H. Koura, T. Hayakawa, et. al., "Direct and semi-direct capture in low-energy (n, γ) reactions of neutron-rich tin isotopes and its implications for r-process nucleosynthesis", Phys Rev C, 77, 015809(2008)
- N. Fotiades, M. Devlin, R.O Nelson, et. al., "Low-spin states in ^{86}Kr from the (n, n') reaction", Phys Rev C 87, 044336(2013)
- T. Tamura, "Analysis of the scattering of nuclear particles by collective nuclei in terms of the coupled-channel calculation", Reviews of Modern Physics **37**(1965)
- Evaluated Nuclear Structure Data File, National Nuclear Data Center, Brookhaven National Laboratory
- M.J. Martin. *Reduced Gamma-Ray Matrix Elements, Transition Probabilities and Single-Particle Estimates.* [Memorandum] September 27, 1982. Oak Ridge, Tennessee: Oak Ridge National Laboratory.
- E. Rubino, "The use of EMPIRE to simulate the neutron induced reactions on ^{86}Kr ", Brookhaven National Laboratory(2015)
- E.S. Soukhovitskii, S. Chiba, "Soft-rotator model and coupled-channels approach for Consistent description of the nuclear collective levels and their excitation by nucleons", Journal of Nuclear Science and Technology, 39 (2002)697-702
- A.J. Koning, J.P Delaroche, "Local and global nucleon optical models from 1 keV to 200 MeV", Nuclear Physics A, Volume 713, Issue 3-4(2003)
- S. Raman, J.A. Harvey, R.L. Macklin, et. al., "Overlapping β decay and resonance neutron spectroscopy of levels in ^{87}Kr " Phys Rev C 28(1983)
- R.F. Carlton, R.R. Winters, C.H. Johnson, et al., "Total cross section and resonance spectroscopy for $n+^{86}\text{Kr}$ " Phys. Rev. C 38(1988)
- P.A. Moldauer *Statistical Theory of Neutron Nuclear Reactions* February 1978, Argonne National Laboratory, ANL/NDM-40
- P. Fröbrich and R. Lipperheide, *Theory of Nuclear Reactions* (Oxford, New York, 1996)
- I.J. Thompson, J.E. Escher, G. Arbanas, "Coupled-Channel Models of Direct-Semidirect Capture via Giant-Dipole-Resonances", Nucl. Data Sheets 118 (2014) 292-294
- A.M. Lane, J.E. Lynn, "Theory of radiative capture in the resonance region", Nuclear Physics 17(1960)563-585
- S.F. Mughabghab, "Verifications of the Lane-Lynn theory of direct neutron capture", Phys Lett **81** (1979)
- A. Foderaro, *The Elements of Neutron Interaction Theory* (MIT Press, Boston, 1971)
- G.P.A. Nobre, A. Palumbo, F.S. Dietrich, et. al., "Derivation of an optical potential for statically deformed rare-earth nuclei from a global spherical potential", Phys Rev C 91, 024618(2015)

Designing and prototyping the electromagnetic calorimeter for sPHENIX

Spencer Laddy-Locks

Mechanical Engineering, Stony Brook University, Stony Brook 11790, OEP Intern

Donald Lynch

Physics Dept., Brookhaven National Laboratory, Upton, NY 11973

Rich Ruggiero

Physics Dept., Brookhaven National Laboratory, Upton, NY 11973

Abstract

An electromagnetic calorimeter (EmCal) is going to be one type of calorimeter in the sPHENIX detector at Brookhaven National Laboratory. Starting this year, the PHENIX project will be undergoing removal and repurposing to make room for the newest upgrade to the Relativistic Heavy Ion Collider (RHIC). The sPHENIX project includes the EmCal, which will allow scientists and physicists to analyze the electromagnetic particles that are emitted by quarks and gluons after a collision. The detector will do this by utilizing 6,144 triple tapered tungsten blocks which, internally, have 2,400 scintillating fibers each. My engineering focus this summer was to design and test how these blocks would be packaged inside of the detector. The EmCal is made up of 64 sectors, each containing 96 blocks. Each sector is the same; however, in order to eliminate any interferences or gaps within a sector, 24 unique types of blocks are needed. This requires a significant amount of design work, and the blocks could be expensive to produce. To reduce costs, CAD software was used to model and assemble different blocks in a sector. The blocks' geometries were then analyzed to see if a slightly modified machining process could produce the 24 unique blocks. This could result in only one type of mold, which would reduce costs significantly. I used Autodesk Inventor to design and 3D print prototype blocks and molds. The resulting 3D printed assembly is currently being used for test fitting, and as a visual aid. The 3D printer allowed for quick changes in design. Understanding the geometric complexities of this triple taper design would be significantly more difficult without those tools. The work that I have done over this summer will continue and may be implemented in the January beam test. While working with great engineers and scientists, I have not only increased my understanding of mechanical engineering and collaboration, but I have also made a contribution to a large project that has and will continue to help push this project forward. Additionally, while working on the sPHENIX project at BNL I have gained experience that will carry through my career and invaluable connections that will last a lifetime.

I. Background

The electromagnetic calorimeter converts electromagnetic particles into photons. These photons can then be read by a sensor which converts the light into an electronic signal. This is used to calculate the energy of the particle. To do all of this in sPHENIX, the proposed EmCal will use 6,144 tungsten epoxy composite blocks. These blocks are produced by filling screens with scintillating fibers and then pouring tungsten powder into a mold, epoxy is then infused to solidify the block. These blocks have

complex geometric features which makes designing the mold and the screens to produce the blocks a challenge.

To assemble the EmCal inside of the detector, an EmCal block must be triple tapered. The first two tapers allow for the blocks to point towards the interaction point when the blocks are rotated about the phi and eta direction. The third taper permits the block to fit inside of the stainless steel sector assembly box, which has a taper of its own. To help make the complex geometry more understandable, a 3D printer was used to create prototype blocks. Due to the non-square nature of these blocks, screens and light guides also had to be designed with tapered geometry.

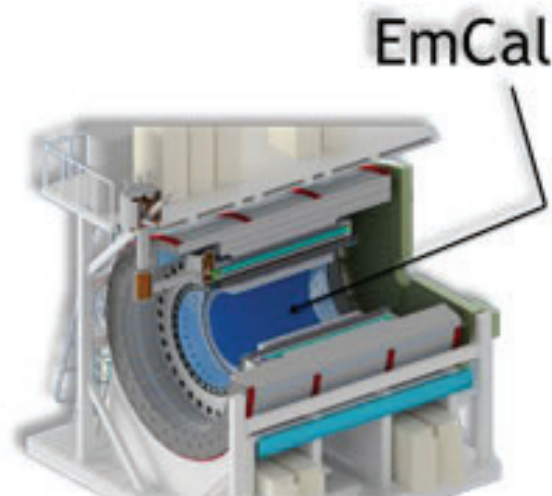
II. Design Considerations

A. Block Geometry

The geometry of the EmCal blocks allows for each block to point towards the interaction point. To do this a triple taper design was implemented. The EmCal blocks will be assembled inside of a stainless steel box, which can be seen in figure 3. This box is tapered to allow for a polar array of 32 sectors along the interaction axis. The EmCal block geometric profile can be seen in figure 4.

B. Module Geometry

A module is comprised of four blocks which are glued together using epoxy. To allow for easier attachment of each module to its light guides, electronics board and metal strong back, each module will be machined flat on top and bottom. The blocks must therefore be originally oversized in length, and then assembled as a module to be machined. This process will also provide a more desired finish on the ends of each block.



C. Screen Geometry

Each EmCal block will contain around 2,400 scintillating fibers. To ensure consistent fiber density within each block, placement of the fibers must be closely controlled. To do this, brass screens will be used to guide each individual fiber. These screens, which can be seen in figure 5, have a hole pattern that follows the outer profile of their respective block. A program was written using matlab to calculate where each hole must be located to maintain a constant area between any three adjacent holes. A half millimeter tolerance was provided between the tangent of a fiber and the wall of the block, this gap is present to protect the fibers during the machining process. These screens will be produced by an etching process. Currently there are a few ideas for the perimeter geometry of the screens. Previously square screens with the same overall dimensions has been used when making blocks, however there are some inconveniences with this design that can be resolved by utilizing tapered screens. These tapered screens would have an identical profile of the block profile, just offset on the order of a few millimeters. These screens would allow for faster filling of the fibers, as well as simplification of the mold and machining process.

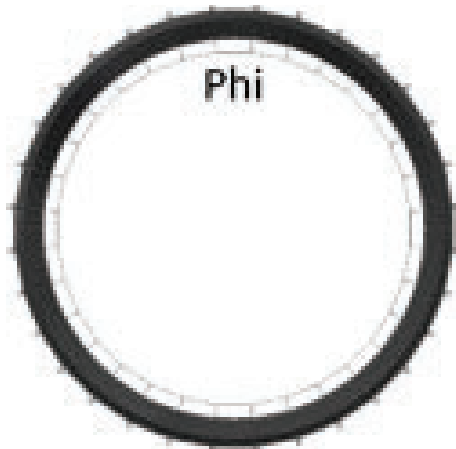


Figure 1.

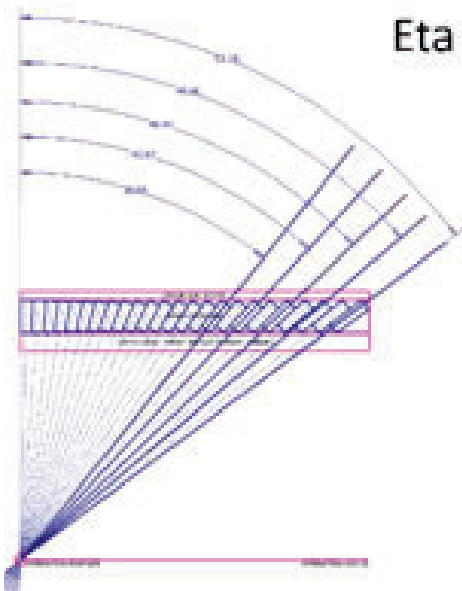


Figure 2.

D. Mold Design

To produce each block, a mold will be used to hold the screens in place while tungsten powder and epoxy are poured into the mold. The mold must have tapered sides to accommodate the final block shape. The mold design is also an important part of the machining process. When machining the blocks, references planes are needed to zero out the milling machine. Designing the mold to incorporate these compound angled planes will decrease machining time and costs. One way of creating these molds is to 3D print all 6,144 disposable molds. Another possible method to produce these molds would be to machine 24 different metal molds, however this would be expensive, and would slow production.

E. Light Guide Geometry

Light guides are used to funnel the light transmitted by the scintillating fibers into a silicon photo multiplier (SiPM). These light guides are made from acrylic and must be polished in order to properly internally reflect the light. Due to the taper of the blocks, these light guides need to be of a different geometry to reduce any dead space. Prototyping is currently underway to try and produce these light guides quickly and cost effectively. Currently, each light guide is machined and polished by hand, which is both time consuming and expensive. One possible technique to produce these light guides more efficiently is through a casting process. This process will utilize a silicon mold that is cast as a negative, which is then filled with the acrylic. Once set, the acrylic should have a polished finish that will allow for proper internal reflectivity.

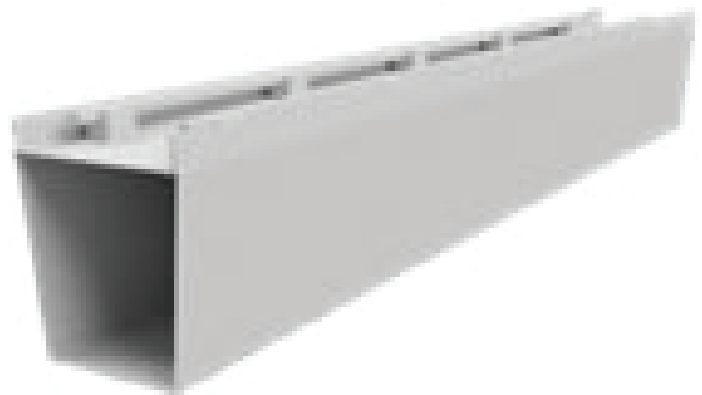


Figure 3.



Figure 4.

III. Results

Through the process of designing and prototyping the EmCal blocks, many geometric complexities were found. The geometry of the blocks has now been specified in more detail regarding the triple taper, and by prototyping many of the modules it has been confirmed that the stainless steel box is a viable solution to assembling the detector. It is also now known that in order to eliminate any gaps or interferences, 24 different blocks must be used.

By utilizing programs such as matlab, it was possible to write a program that computes the position of all the holes in the screens. The program was able to design screens that maintain the same area between any three adjacent holes to within 0.7% relative error, which is less than the maximum of 2.0%. This result is promising, and will help to improve the performance of the detector.

IV. Recommendations

After working with the complex geometry of the EmCal blocks, I have found that the 3D printer is an invaluable tool that provides fast prototype parts and fixtures. These parts have been utilized to not only visually display and convey important information about the complex geometry, but it has also helped in manufacturing prototype towers (1/4 block).

In the future I would suggest looking into other equipment such as laser cutting machines, which would help us develop and test different configurations of screens and mold design quickly. This would increase productivity exponentially, and move the project forward at an accelerated pace.

After some experience from last summer, I have come to the conclusion that to optimize the manufacturing process to make a block, tapered screens should be utilized. These tapered screens would not only provide faster fiber filling, but also a simplified machining process from start to finish. The screen design is an important aspect of the EmCal design and manufacturing process. Therefore, I feel that the design of these screens should be looked at more thoroughly before making a final decision, and testing should be done to provide insight as to the efficiency of the process.

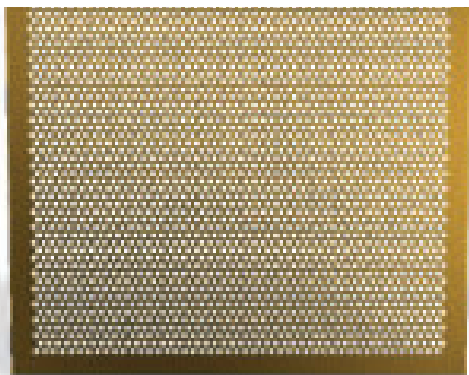


Figure 5.

Designing new magnets for future circular colliders

Nicholas Maineri

Department of Physics, State University of New York at Geneseo, Geneseo, NY 14454

Ramesh Gupta

Superconducting Magnet Division, Brookhaven National Laboratory, Upton NY 11973

Abstract

The magnets used in the Relativistic Heavy Ion Collider at Brookhaven National Laboratory (BNL) are based on a magnet design operating at 3.5T. Researchers at BNL are currently designing high field magnets to be used in the next generation of circular colliders which will operate with a field at 16-20T and be based on the common coil design. The main challenge for these magnet designs is to obtain good field uniformity while minimizing the overall magnet cost. We used a program called ROXIE to design the accelerator magnet cross section. These magnets consist of superconducting coils and of an iron yoke. The placement of each turn of a conductor has a significant impact on the error harmonics of the magnetic field. These error harmonics must be as close to zero as possible in order to produce a uniform field. When the iron yoke is introduced, the values of the harmonics change as a function of the magnetic field. In order for the accelerator to work, this change has to be minimized by optimizing the iron cross-section. I focused on optimizing the iron so the error harmonic b_3 is less than 10 and the error harmonic a_2 is less than 20. This was done by changing different design parameters, like the size of the inner chamber and by putting holes in the iron at specific locations. For one coil design the error harmonics were 6.4 for b_3 and 5.6 for a_2 . These common coil magnet designs could use both Low Temperature Superconductors and High Temperature Superconductors. From the work I have accomplished, I have learned how to use the magnet design program ROXIE. In addition, I have developed my skills in interpreting data and on optimizing the complex magnet design.

I. Introduction

Researchers at BNL are designing magnets for circular colliders that operate at 16T. The circular collider at BNL, RHIC, operates at ~ 3.5 T. The challenge with creating such a powerful collider is to ensure a uniform magnetic field in the center of the track, while minimizing the overall magnet cost. The specific locations of the magnet coils and the design on the iron yoke that surrounds the coils have an effect on the uniformity of the magnetic field. In order to create a design that produces a uniform magnetic field of 16T and minimize the design cost, the design will be based on the common coil design. The common coil design has simple race track shaped coils placed next to each other,¹ as seen in Figure 1. This design produces less strain on the coils while they are under larger Lorenz forces. Thus reducing the need for many expensive support structures.¹ This design also allows an easier process to create hybrid coils using both HTS and LTS coils.² Eventually designs will be produced using only HTS coils. HTS are much more brittle than LTS and can be cooled using liquid nitrogen instead of liquid helium.² Liquid nitrogen is significantly less money than

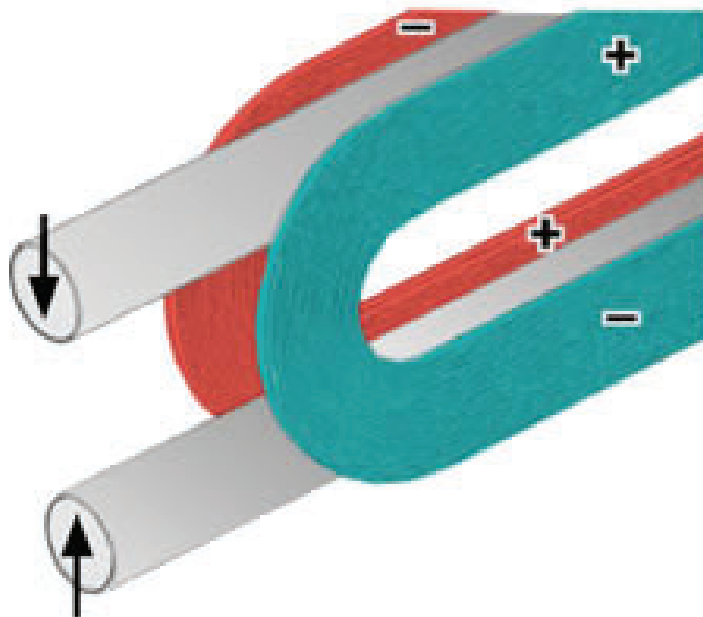


Figure 1. Common coil design

liquid helium, so the cost to operate the collider will be much less. The harmonics of the coil determine the uniformity of the magnet field. The harmonics of a coil are related to the position of a point in comparison to the origin and expressed in terms of normal and skew harmonics, b_n and a_n . These harmonics are defined with the expansion of the horizontal and vertical components of the magnetic field (B_x, B_y):

$$B_y + iB_x = 10^{-4} \times B_1 \sum_{n=1}^{\infty} (b_n + ia_n) [(x + iy) / R]^{n-1}$$

where x and y are the horizontal and vertical components, B_1 is the dipole field strength at $x=R$, and R is the reference radius.¹ The closer the harmonics are to zero the more uniform the magnetic field will be. I focused on the design of the iron yoke to optimize the error harmonics of the coil. The error harmonics of a coil is the difference between the absolute maximum harmonic and absolute minimum harmonic as the magnetic field increases as a function of current. By changing the dimensions of the iron yoke around the magnet coils and adding in specific details like holes in the iron at specific locations the error harmonic can be changed.

II. Specifications

Our designs must meet the correct specifications for them to be acceptable. The main specification is that the entire coil design must be able to produce a magnetic field of at least 16 T.³ All the designs have to have a beam-to-beam distance of 250-350 mm.³ The maximum outer diameter of the iron yoke must not exceed 800 mm.³ Specific values for the geometric harmonics or normal

harmonics have to be met when the coil is operating at its greatest magnetic field strength. The geometric harmonics are caused by the specific location of the magnet coils and the shape of the iron. For these design the b3, b5, and b7 geometric harmonics have to be as close to zero as possible because they have the greatest effect on the magnetic field. The b3 and b7 geometric harmonic must be less than 3.0 and the b5 geometric harmonic must be less than 5.0. The skew harmonics, a2, a4, a6..., occur when the iron is introduced. There is no specification for these harmonic for when the coil operates at its greatest magnetic field strength, but the closer that they are to zero the more uniform the magnetic field will become. The error harmonics, which are the focus for these designs, are the b3 error harmonic and the a2 error harmonic. The b3 error harmonic is the contribution due to iron as it saturates with the magnetic field and the a2 harmonic is the main skew harmonic.³ The b3 error harmonic must be less than 10 and the a2 error harmonic must be less than 20.³

III. Optimizing the iron design

A. Process

We know that if a coil design was optimized to ensure low geometric and skew harmonics it will change dramatically when the iron yoke is introduced. When the iron yoke changes the error harmonics change as well, but when the coil is optimized again, with the addition of the iron yoke, the error harmonics will only change slightly. By knowing this, the studies focused on creating iron yoke designs and test different possible parameters to observe the different effect they had on the error harmonics. We started with a coil that has been optimized with a basic iron shape,

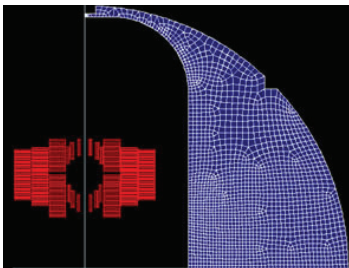


Figure 2. basic starting design

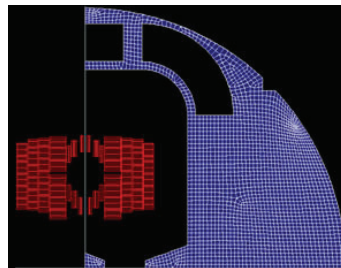


Figure 3. Teeth and holes in iron yoke

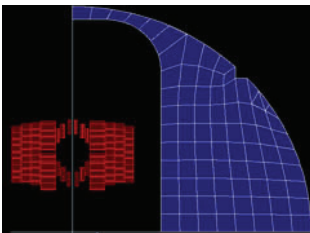


Figure 6 and 7. Picture of design and evaluation of harmonics

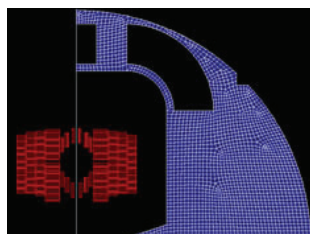
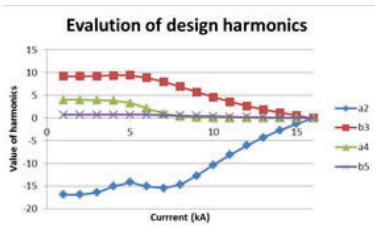
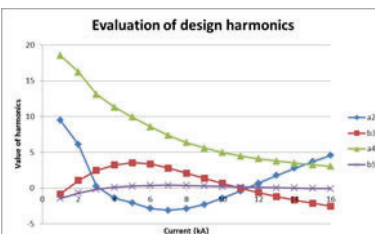


Figure 10 and 11. Picture of design and evaluation of harmonics



seen in Figure 2. Using the basic design the height, width, out radius, and the radius of the round corner was changed. We noticed the coil produced a magnetic field barely strong enough to meet the specifications. Another coil design was created and used for the rest of the studies. For the second study we added a protrusion to the insider chamber, which we called a tooth. By changing the shape and size of this tooth we studied the effect it had on the error harmonics. A hole was then added in the iron where the iron tends to saturate with the magnetic field. A study was conducting where the size, shape, and location of the hole affected the error harmonics. Finally another tooth was added to the center of the inner chamber and the effect on the error harmonics was studied again. Figure 3 shows an example with both teeth and holes in the iron yoke design.

B. Effects on the error harmonics

The original design, shown in figure 4, did not meet the specifications necessary. All the geometric harmonics and skew harmonics were 0.0, it produced a magnetic field of 16.0 T, and the b3 error harmonic was 8.6. These specifications were all met, but the a2 error harmonic was 25.9, as seen in figure 5.

With the first study it was clear that the size and shape of the inner chamber played an important role in the management of the error harmonics. As the height of the inner chamber increased the b3 error harmonic generally increased, while the a2 error harmonic generally decreased. As the inner width increased the b3 error harmonic decreased but the a2 harmonic increased. The change in the inner radius and the outer radius didn't have much of an impact on the b3 error harmonic. When the outer radius increased

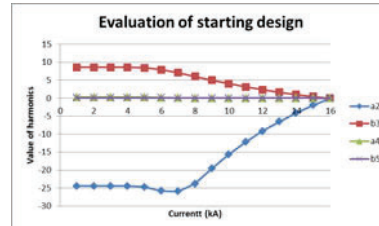


Figure 4 and 5. Picture of original design and elevation of harmonics

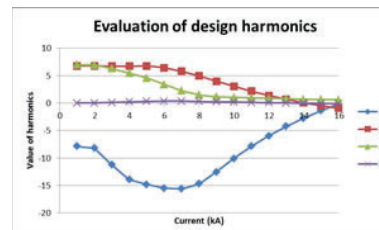
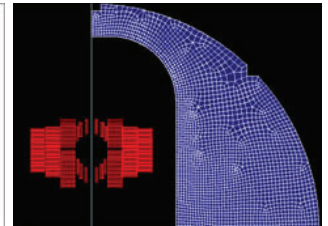


Figure 8 and 9. Picture of design and evaluation of harmonics

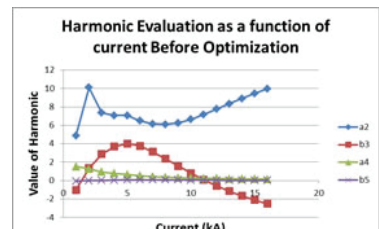
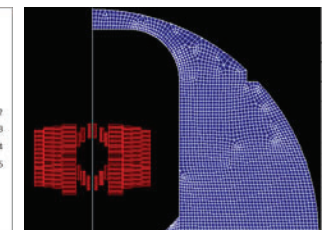
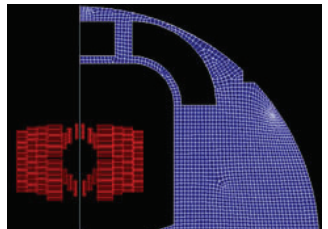


Figure 12 and 13. Picture of final design and evaluation of harmonics before optimization.



when there are no holes in the iron the a2 harmonics decreased dramatically. In comparison when the inner radius of the round corner got changed there was not much effect on the a2 error harmonic. When the test concluded a design where the b3 error harmonic was 9.4, the a2 error harmonic is 16.8, and the magnetic field is 16.0 T, as seen in figure 6 and 7. This design meets all the requirements, but it could be made much better.

The addition of the first tooth had a huge impact on the error harmonics. At first it was a rectangular shaped and later given a slant. Regardless of the exact shape of the tooth relationship between the size of the tooth and the error harmonics remained the same. The slanted tooth shape did generate better results in comparison to the rectangular shaped ones. Generally as the height of the tooth got larger the b3 harmonics got worse and the a2 got better. As the width of the tooth increases the b3 error harmonics slightly increased, but decreased as the study continued. The opposite occurred for the a2 error harmonic. It decreased at first but then dramatically increased. From this study two relationships were discovered. The error harmonic was affected more by the overall volume of the tooth more than the actual shape of it and that the distance away from the coils has a dramatic effect on the error harmonics. In comparison to the original design the addition of the tooth slightly increased the b3 harmonic, but decreased the a2 error harmonic. A design for further studies was created where the b3 error harmonic was 7.7, the a2 error harmonic was 14.6, and a magnetic field of 16.0 T, as seen in figure 8 and 9.

There was an immediate difference when a hole was added to the iron yoke. When a small hole was added the b3 error harmonic

slightly increased, while the a2 error harmonic decreased by a value of ~ 1.0 . By making this hole bigger and adding a second hole in another location the b3 error harmonic increased again and the a2 error harmonic decreased by ~ 2.0 . By going through many different designs we concluded to make two larger holes, one rectangular and one quarter circle, instead of putting many circular holes, as seen in figure 10. By changing the dimensions of the holes and what was learned from the previous studies a design was created where the magnetic field was 16.0 T, the b3 error harmonics was 6.1, and the a2 error harmonics was 12.6, shown in figure 11.

After some time of trying different iron designs it seemed like nothing would drive the error harmonics any lower. Gupta suggested adding a tooth to the center of the inner chamber and study the effects of the addition. With this addition the b3 error harmonics slightly increased again, but the a2 decreased dramatically by about half its value. The closer this tooth got to the magnet the worse the b3 error harmonic got because it would saturate quicker. After changing the dimension of the tooth we noticed more of a relationship between the harmonics and the distance between the two teeth, than the harmonics and the width of the center tooth. Further studies will be conducted to learn more about this relationship.

From looking at all these studies a final design was created. It is simple but very effective, as seen from figures 12 and 13. The b3 error harmonic was 6.5, the a2 error harmonic was 5.2, and the magnetic field was 16.0T. Since this coil structure was not optimized for the specific iron yoke the b3 geometric harmonic

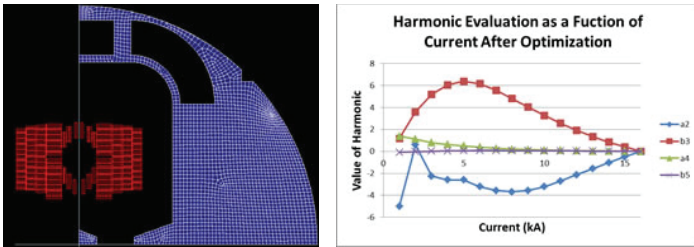


Figure 14 and 15. Picture of final design and evaluation of harmonics after optimization.

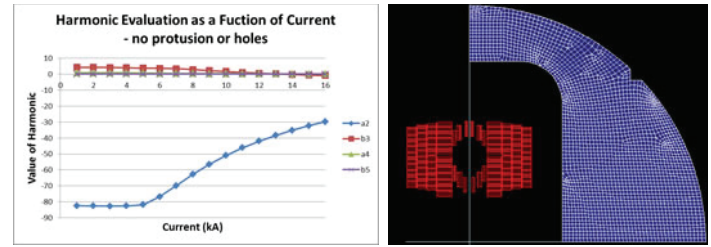


Figure 16 and 17. Final design without details.

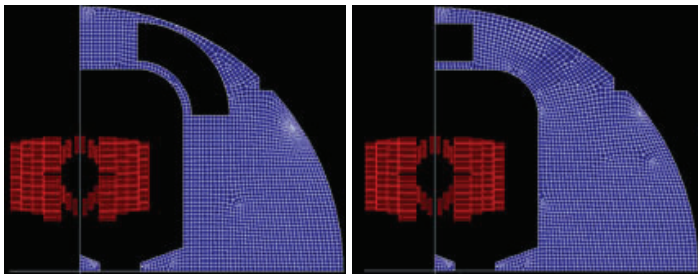


Figure 18. Removal of hole1 Figure 19. Removal of hole2

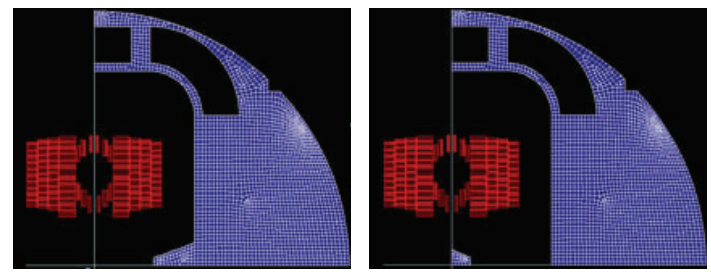


Figure 22. Removal of tooth1 Figure 23. Removal of tooth2

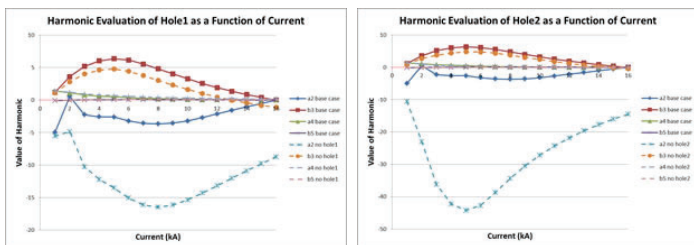


Figure 20 and 21. Comparison of harmonics of design with missing details to final design.

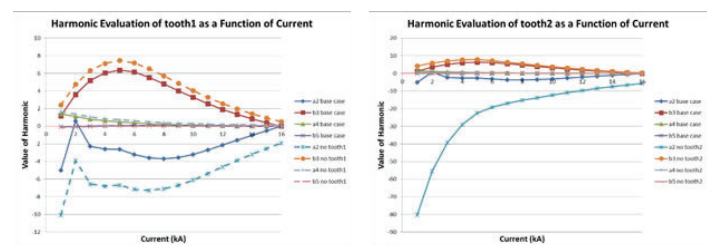


Figure 24 and 25. Comparison of harmonics of design with missing details to final design.

was -2.5, the b5 geometric harmonic was 0.0, the b7 geometric harmonic was 0.0, the a2 skew harmonic is 10.0, and the a4 skew harmonic was 0.2. The harmonics do meet specifications, but they could be much better.

Using the ROXIE program the coil design was optimized for the new iron yoke. During the optimization the magnet coils change slightly but this causes the net harmonics to change, as seen in figure 14 and 15. The resulting b3 error harmonics was 6.4, the a2 error harmonic was 5.6, and the magnetic field was 16.0 T. All the geometric harmonics were 0.0 and both a2 and a4 skew harmonics were 0.0. This is all well within the specification needed for the design. Other research groups have developed acceptable design, but their results have been closer to the minimum specifications.

IV. Break down of final design

After a final design is created all the details are examined to see what contribution it has on the entirety of the design. An iron yoke was created that had the same dimensions as the final design, but it did not include the teeth and holes. Without these details the b3 error harmonics actually got better, but the a2 error harmonic got significantly worse. The b3 error harmonic was 5.2 and the a2 error harmonic was 52.8. Figure 16 and 17 show how much has been changed and how crucial the teeth and holes are to this design.

Next just hole1 was removed, as seen in figure 18. The b3 error harmonic changed to 5.9 and the a2 error harmonics changed to 11.6. Even though the b3 error harmonic becomes worse, the effect on the a2 error harmonic is significant enough to keep hole1. The same effect happened when hole2 was removed, seen in figure 19. The b3 error harmonic changed to 5.3 and the a2 error harmonic was 33.8. Figure 20 and 21 show the comparison between the final design, which is called the base case, and when the holes were removed.

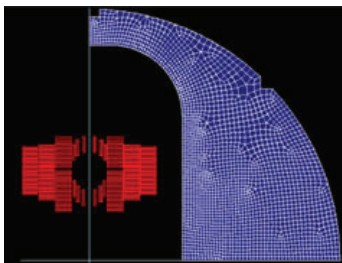


Figure 26. Starting design

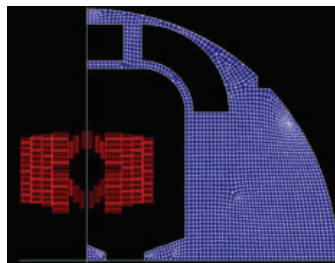


Figure 28. Final design

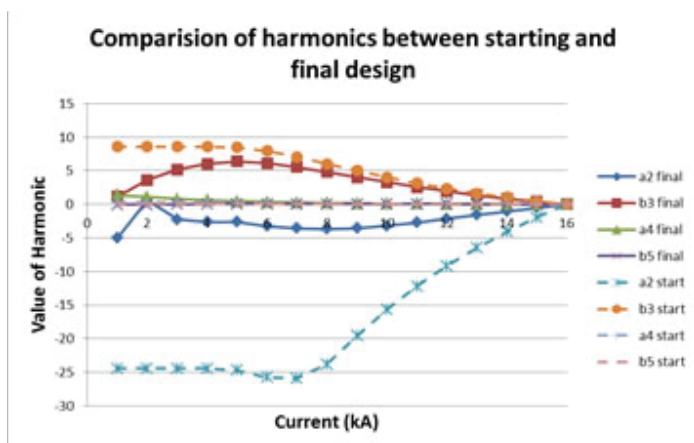


Figure 29. Comparison of harmonic between the starting and final design

The removal of tooth, as seen in figure 22, didn't change the error harmonics much, but this shows that it can be used to "fine tune" the harmonics to make them better. The b3 error harmonic changed to 6.9 and the a2 error harmonic changed to 8.2 when tooth1 was removed. The removal of tooth2, as seen in figure 23, was very different from tooth1. Both error harmonics increased significantly without tooth2. The b3 error harmonics increased to 7.5 and the a2 error harmonics increased to 74.5. Tooth2 is a significant factor to the overall design. These changes in harmonics can be seen in figure 24 and 25.

V. Conclusion

Each part of the iron plays a crucial role in the overall success of the design. This design is successful at meeting all the specifications laid out. The maximum magnetic field of the coil is 16.0 T. The beam separation is 250 mm and the outer diameter of the iron yoke is 680 mm. All of the geometric and skew harmonics are 0.0, which is well within the specifications. In addition the contribution of b3 due to the saturation of the iron (b3 error harmonic) is 6.4 and the skew harmonic (a2 error harmonic) is 5.6. Figure 26 and 27 show how much of the original iron structure was changed. Figure 28 shows how much the harmonics have changed from the original design. Looking at the design structurally there may be a problem with it. Since the holes are so large and the iron is thin at certain points it may bend, changing the harmonics, and possibly break while it is under such large Lorenz forces. Also there may be too high of a magnetic field on the outside of the iron. This will be further studied in the future in order to better the design.

VI. Looking towards the future

This is just a stepping stone for this project. New designs using a different magnet coils and iron yokes based off of this one design have already been created. The main specifications for the design have been already tested. Other specifications like quench protection and stress limit still need to be studied. Using what was learned better designs will be created. The next design being studied is one which would hopefully provide more structural support so the iron doesn't bend. If these designs could be perfected the potential for these future circular colliders would be extraordinary. Many new tests could be done studying how the universe was like moments after the big bang.

VII. References

- ¹R.C. Gupta, A Common Coil Design for High Field 2-in-1 Accelerator Magnets, Presented at the 1997 Particle Accelerator Conference in Vancouver, Canada (1997).
- ²R. Gupta, et al., Field Quality Optimization in a Common Coil Magnet Design, International Conference on Magnet Technology (MT16) at Ponte Vedra Beach, Florida, USA (1999).
- ³FCC Week 2016, <https://indico.cern.ch/event/438866/>

VIII. Acknowledgements

This project was supported in part by the U.S. Department of Energy, Office of Science, Office of Workforce Development for Teacher and Scientists (WDTS) under the Science Undergraduate Laboratory Internships Program (SULI).

eRHIC 18 GeV electron storage ring: Magnet design with water cooling system, support facilities, and power supply analysis

Lisa Marone

Engineering, Clarkson University, Potsdam NY 13699

Joseph Touzollo

Collider-Accelerator Department, Brookhaven National Laboratory, Upton NY, 11973

Abstract:

Modern advances in accelerator technology will make the next electron-ion collider less expensive to build and operate, as well as more reliable. An electron-ion collider has the potential to reveal deeper insights into the underlying quark-gluon regime of individual particles which can help fill gaps in our understanding of the structure and behavior of atoms. The existing infrastructure at Brookhaven National Laboratory's (BNL) Relativistic Heavy Ion Collider (RHIC) is under consideration to be utilized and supplemented so the facility can function as a one of a kind electron-ion collider. In order to do so additional electron accelerator systems and a storage ring need to be constructed inside the existing RHIC Tunnels. Using existing 3D layouts of the tunnel structure in PTC Creo, supplemented with my own 3D models of the magnets and lattice, I was able to present layouts on the space available for equipment and develop component performance spreadsheets for each of the magnets based on given sheets from SLAC and performance specifications from physicists. These spreadsheets aided in the team's accelerator component detail designs and helped defined engineering requirements for the system's water cooling and electrical power requirements needed to operate a single arc of the storage ring.

I. Introduction:

Previous hadron collision experiments in hadron collider accelerators have shown the promise of a quantum field theory, Quantum Chromodynamics (QCD). The Quantum Chromodynamics theory describes the strong force as a result of the interactions of force carrier particles-quarks and gluons. Hadron collisions have revealed "a richness of nature" in this theory, but have difficulty gaining the required energy to penetrate so deeply into the atomic structure. The construction of an electron-ion collider (EIC) is believed to broaden our ability to study the subatomic gluon regime of particles more thoroughly, providing insights into their "QCD substructure".¹ Part of the considerations of operating

an electron-ion collider inside the RHIC tunnels includes not only evaluating the space availability of the tunnels, but also looking at water cooling systems for the storage ring, additional pumps and power supplies as well as the complimenting support structures to store the equipment. Since existing magnets are cheaper to employ for the storage ring, it's cost-effective to be able to utilize the existing magnets from SLAC's PEP-II despite the fact the magnets will have to be tailored to operate at the proposed higher magnetic fields. The existing magnets come with their own derived component spreadsheets, which can be modified to reflect the effects of the increased magnetic fields. Using these spreadsheets a water cooling system was evaluated and data on power supplies collected will aid in future design decisions and evaluations for the possibility of implementing eRHIC on the BNL campus. A floor model of a support facility along with spreadsheet specifications on the amount of power and water needed aided in early resource estimates and designs for the civil structure requirements of the project.

II. Methods:

A. Space Availability

A focus area was narrowed down to a single arc that could be duplicated throughout the ring structure due to the symmetry of RHIC's 6 arcs. By utilizing magnets from SLAC's PEP-II, the given specification sheets and diagrams made it possible to use values for things like magnet core length and pole width length to find the physical dimensions of each magnet type. Given and calculated dimensions can be seen in table 1.² Physical dimensions made it possible to model basic structures that represent the physical space the magnets would take up without worrying too much about the tedious mechanisms of its overall design.

Each magnet was modeled in PTC creo, and then assembled into a single lattice as well as a whole 60 degree arc. These models, overlaid with the existing models of the RHIC tunnels and beam lines, provided visual aids in determining the amount of space available for new equipment in the existing RHIC tunnels.

	Dipole	Sextupole (10SD,HER)	Quadrupole (4Q17,LER)
Magnetic Length (in)	212.83*	10.041	16.93
Pole Width (in)	8.425	---	---
Conductor Length/Pole (ft)	----	49.6	176
Cooling hole diameter (in)	0.25	0.125	0.25
Conductor Cross section (in ²)	1.63	0.127	0.198
Coil Length (m)	89.66	90.66	215

Table 1: list of magnet specifications from SLAC's PEP-II component detailed performance sheets (unless noted).

*Calculated based on split dipole design (eRHIC Ring-Ring design report)³

B. Dipole Magnets

The original lattice design given at the beginning of the project was modeled from SLAC's

PEP-II 2.8 C212 dipole. 3D models given in this report reflect that magnets design and physical appearance. However, upon farther research and development of the project design, physicists and engineers changed the dipole to a split dipole design due to complications they had found with the existing magnet design. Calculations and spreadsheet values reflect this design change using values given in the eRHIC Ring-Ring Design Report.³

C. Water pumps

In order to size water pumps some of the specifications needed to first be adjusted to depict how the magnets would perform at the proposed higher magnetic fields. Quantities like current and power, that affect the water flow rate, changed along with the increasing magnetic fields. Current drawn by the dipole was recalculated using a given field value at 20 GEV, the values for the other magnets were scaled by a factor of 2.22 to account for the energy increase from 9 Gev (given in the SLAC specification sheets) to 20 Gev. I created excel spreadsheets in order to consolidate data and aid in the constant iterations of calculations for values of pressure drop and water flow rate, which were first done by hand and compared with values determined by numerous other spreadsheet calculators.

To determine the piping diameter needed for the water cooling system a guess and check method was used with an online calculator⁴. Values for water flow rate, length of piping and pipe diameter were evaluated. The pressure drop calculated across the pipe was examined by knowledgeable team members to determine whether the guessed diameter had to be bigger or smaller based on the overall head loss of the system, which effected the pump size and power. High pressure and low pressure water

systems were under consideration and it was widely preferred to maintain a pressure drop below 100 Psi to be able to implement a low pressure system for the magnets.

To address the dipole bus, we used the same cross section as specified on the dipole's performance sheet from SLAC and assumed a 60ft supply line length from the supply building to the ring for all calculations. In order for the pressure drop across the bus to be in the same range as the pressure drops from the dipole or quadrupole the number of sections the bus is divided into was changed to decrease the distance and therefore the pressure drop.

Several trips were made out to some of the tunnel support structures to compare and evaluate the equipment being used for RHIC to equipment that may be needed for eRHIC. After getting input from knowledgeable team members, an online pump sizing system from Bell and Gossett was ultimately used to find a specific pump for the system so a floor print could be obtained.⁴

D. Power Supplies

The power supplies were analyzed using the same spreadsheet data with the addition of calculations on voltage drops, and the resistance of the wires that may be used alongside the magnets. The spreadsheets compiled voltage drops per arc along with listings of currents to help in future considerations of the number of power supplies needed, the amount of power they'd draw as well as the type of cable and cooling that would supplement them.

III. Data and results:

A. Space Availability

Space availability of the tunnels was the first thing that was addressed. Two different views used as visual aids for space evaluations are shown in figures 1 and 2.

Preliminarily these models show the magnets can fit in the tunnels without intercepting equipment or walls, they also show a

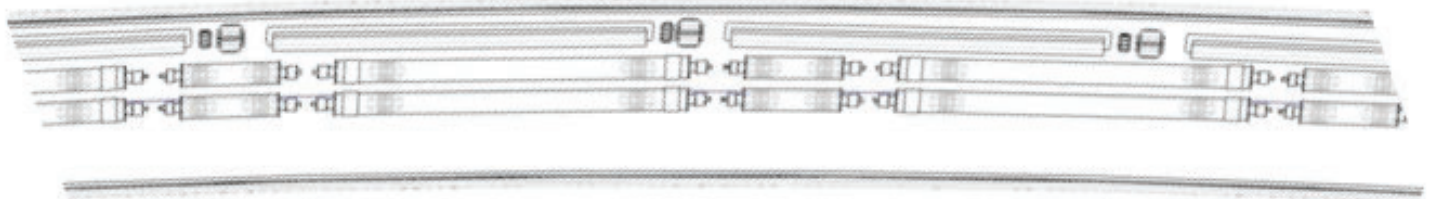


Figure 1: Aerial view of magnet lattice (top row) inside the RHIC tunnel structure.

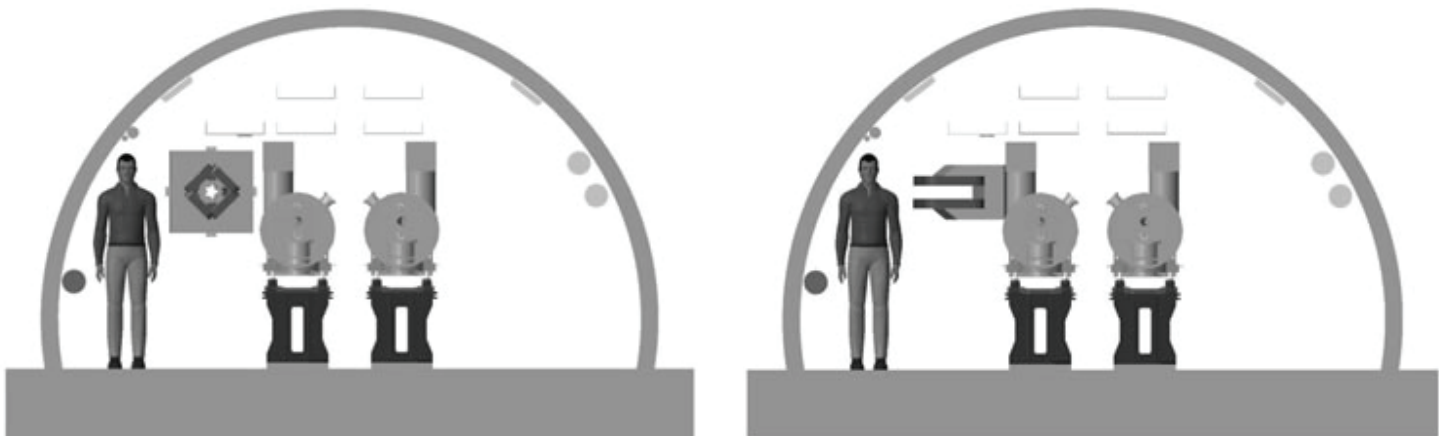


Figure 2: Cross sectional views of the lattice inside the tunnel structure. (Left) Quadrupole cross section (right) Dipole cross section

	<u>Quadrupole</u>	<u>Sextupole</u>	<u>Dipole (outer)</u>	<u>Dipole (inner)</u>	<u>Dipole Bus</u>
Total Flow Rate/Arc	36.6	19.4	85.8	1.5	
Total (GPM)					143.4
Pressure Drop/Magnet (PSI)	289.0	1112.3	158.9	1.6E-02	473.7
Pressure Drop/pole(PSI)	72.2	185.4	79.5		

Table 2: Water flow rate and pressure drop per magnet as calculated using an excel spreadsheet.

	<u>Quadrupole</u>	<u>Sextupole</u>	<u>Dipole (outer)</u>	<u>Dipole (inner)</u>	<u>Dipole bus</u>
Operating Current (Amps)	376.4	395.6	2070.0	2070.0	2070.0
Voltage drop/magnet (V)	10.7	7.5	3.0	0.1	4.5
Voltage Drop/Arc (V)	385.4	270.8	223.4	3.8	4.5
# per Arc	36.0	36.0	72.0	36.0	

Table 3: Data that was calculated regarding magnet power specifications.

standard person can fit alongside them- even after some of additional piping and cable trays have been placed. Both views have to be farther evaluated for regulations regarding the space required for human traffic, as well as the space needed for maintenance and maneuvering of the magnets and excess tunnel equipment but these models have helped establish baselines for the amount of room project engineers and scientists will be working with to fit additional equipment.

B. Water pumps and Power Supplies

Based on the spreadsheet data regarding water flow rate and pressure drop for the magnets, it was determined that one pump per arc is needed, leading to the need for six pump houses for the entire ring. The system sizing program from Bell and Gossett suggested an e-1510 series 1.5 AD pump size for a 150 Gpm total flow rate and 90 Psi pressure drop across the arc.⁴ A breakdown of the contributing flow rates and pressure drops per magnet can be seen in table 2. It was found that the sextupole, due to its smaller cooling hole, had a much larger pressure drop than the dipole, 185 psi per pole compared to 80 psi per pole. To address this issue it was decided a booster pump would be used to save space and power but still provide the necessary pressure boost across the sextupoles. PTC creo models of a 56 motor frame pump provided by Bell and Gossett were used for modeling the interior of the support building (Figure 3) and evaluating the space availability of a building that size compared to the total floor print of equipment that would be needed. The booster pump was modeled to be a quarter of the size of the main pump, based on the water flow rate ratio between the dipole and sextupole.

There are other variables that contribute to the overall water flow rate that were overlooked for the basis of this project due to their relatively small effect on the quantity or lack of time to compile details on its contribution. The dipole magnet design was changed more than half way through the project but it was assumed dimensions of the coils and cooling hole stayed the same as what was listed on the component sheets from SLAC.

Operating currents for each magnet, the number of magnets per arc and the voltage per arc were determined to aid in decisions regarding the amount of power supplies that would be needed and

how big they'd need to be. Ultimately, the power supplies would need to supply 714 kW per arc for the magnets and 884 volts. Table 3 shows a table of these attributes by magnet.

Though a quantity could not be determined, because of the compiled component spreadsheets that were created many other elements of the project have been affected since previous evaluations done by team members in March. Supplementing cables and wires need to be reevaluated to match the increased current and power; Air conditioning systems need to be sized to compensate for the increased heat load, as well as the equipment houses may need to be reconfigured to fit larger power supplies than expected.

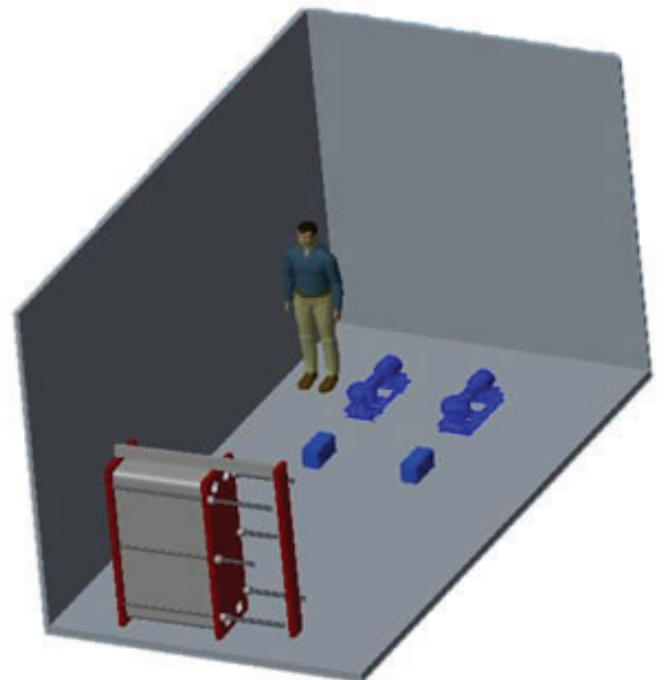


Figure 3: 3D model of support structure with water/booster pumps (blue) and heat exchanger (red)

IV. Conclusion:

As farther research and analysis on the project is completed by physicists and engineers the spreadsheets can continue to be adjusted to accommodate the changing lattice design and magnet specifications. As these change it's easy for fundamental things like water flow rate and pressure drop to change as well, which drive the sizing of the water cooling pumps and pipes. The work-in-progress nature of this design project prevents anything from being definitive, though my work has laid a foundation for early resource estimates and system evaluations, and provided tools to team members to continue and expand on that work.

V. References

- ¹E.C. Aschenauer, M.D. baker, A. Bazilevsky, K. Boyle, S. Belomestnykh, I. Ben-Zvi, S. Brooks, C. Brutus, T. Burton, S. Fazio, A. Fedotov, D. Gassner, H. Hao, Y. Jing, D. Kayran, A. kiselev, M.A.C. Lamont, j-H. Lee, V.N. Litvinenko, C. Liu, T. Ludlam, G. Mahler, G. Mcintyre, W. Meng, F. Meot, T. Miller, M. Minty, B. Parker, R. Petti, I. Pinayev, V. Ptitsyn, T. Roser, M. Stratmann, E. Sichterman, J. Skaritka, O. Tchoubar, P. Thieberger, T. Toll, D. Trbojevic, N. Tsoupas, J. Tuozzollo, T. Ullrich, E. wang, G. Wang, Q. Wu, W. Xu, and L. Zheng, ERhic Design Study-An Electron Ion Collider at BNL (2014).
- ²“Collider Components.” in PEP-II Conceptual Design Report (1993), pp. 229–483
- ³G. Bassi, J. Beebe-Wang, J.S. Berg, M. Blaskiewicz, J.M. Brennan, A. Fedotov, W. Fischer, H. Hahn, Y. Hao, A. Hershcovitch, Y. Luo, C. Montag, R. Palmer, B. Parker, S. Peggs, V. Ptitsyn, S. Seletskiy, T. Shaftan, V. Smaluk, K. Smith, S. Tepikian, F. Willeke, O. Wu, and W. Zhang, ERhic Conceptual Design Report: Ring-Ring (To be Published, n.d.), pp. 35–40.
- ⁴Xylem Applied Water Systems United States < http://bellgossett.com/pumps-circulators/end-suction-pumps/e-1510/?cid=cp_bm_e1510_1-1_2ad > Web. 29 July 2016.

VI. Acknowledgments

This project was supported in part by the U.S. Department of Energy, Office of Science, and Office of Workforce Development for Teachers and Scientists (WDTS) under the Science Undergraduate Laboratory Internships Program (SULI).

I'd like to thank my mentor Joseph Touzollo for the opportunity to work with him on this project, which I am very appreciative for. I'd also like to thank other members who stepped up to help me throughout this project and who it's also been a privilege to work with: Christoph Montag, Robert Lambaise, Joseph Scaduto, Don Bruno, John Halinski and Rick Porqueddu.

Thermal characterization of organic and inorganic compounds used in homemade explosives

Morgan Matthews

Chemistry and Chemical Engineering, Saint Mary's College and University of Notre Dame, Notre Dame, IN 46556

Dr. Biays Bowerman

Non-proliferation & Homeland Security Department, Brookhaven National Lab, Upton, NY 11973

Abstract

Homemade explosives (HME) can be created using oxidizers and fuels. Understanding the characteristics and behavior of the explosive components will assist in planning for and mitigating the threat of HME preparation and destruction. In general, chemical materials should be sufficiently stable in order to allow long-term storage with minimal risk to the safety of makers and users. Using a thermogravimetric analyzer (TGA), the mass loss of various materials was measured while heating to determine the thermal stability of HME materials. Eleven materials were analyzed: inorganic compounds – potassium chlorate (KClO₃); potassium bromate (KBrO₃); potassium iodate (KIO₃); potassium perchlorate (KClO₄); sodium chlorate (NaClO₃); sodium perchlorate (NaClO₄); as well as organic compounds – benzoic acid; meso-erythritol; urea; pentaerythritol; sucrose. The thermal stability of the material also allows for further research regarding the required handling of the explosive. The decomposition of each oxidizer, whether alone, as a mixture, or in the presence of a fuel, was analyzed and its data collected. The use of transition temperatures for inorganic oxidizers as well as the vapor pressures obtained based on the rate of mass loss of organic fuels described the stability properties of each material. The data for each compound analyzed will be used further in future research, experimentation and procedures.

I. Introduction

HMEs are a special concern because they can be prepared from easily obtained materials and used by anyone. HMEs are extremely convenient compared to commercial or military explosives, which are difficult to obtain and are extremely expensive. They can be made from common household chemicals that are easily available and can be legally purchased. Homemade explosives are able to be mixed at home or in a workshop. It is not necessary for those creating HMEs to have a background in chemistry to be successful in the field.

However, HMEs also have their disadvantages. Certain explosive mixtures require an instructor or detailed and complex recipes to improvise. These recipes can contain multiple steps and they directions for the HME's assembly may be difficult to follow for those who are inexperienced. A very frequent disadvantage is accidents from premature detonations due to unstable precursors. In addition, many individuals can be injured or even killed while making HMEs due to health hazards from harmful precursors. Lastly, by buying certain precursors or a certain amount, an individual increases their chance of interdiction.

The components of HMEs are readily available chemical precursors and can be common household products. They can be bought, stolen or made by an individual easily. Precursors include an oxidizer and a fuel. The oxidizer of a HME reacts rapidly with

the fuel to achieve detonation velocities that characterize explosives. Due to the jobs of the components, it is imperative for both to be extremely stable in order to prevent premature detonation.

A popular type of HME is peroxide-based, which are a growing area of concern. This category can include triacetone triperoxide (TATP), hexamethylene triperoxide (HMTD), and methyl ethyl ketone peroxide (MEKP). These oxidizers are made by mixing a concentrated hydrogen peroxide, the oxidizer, with a fuel such as acetone or ethanol, and a strong acid. HMEs with either TATP or HMTD are extremely dangerous due to their instability, which makes them hazardous to make and handle. This creates a danger for many officials and police officers during searches

For this specific research project, the oxidizers analyzed included a collection of inorganic compounds such as Potassium Chlorate (KClO₃) and Sodium Chlorate (NaClO₃). In addition, the fuels analyzed included four organic compounds including pentaerythritol (C₅H₁₂O₄) and urea (CH₄N₂O).

II. Methods

Using a TGA, the mass loss percentage of each compound was analyzed versus temperature in degrees Celsius (°C). The TGA measures the stability of materials by measuring their weight loss while they are heated to a maximum of 1000°C. Slow, regular weight loss is indicative of evaporation. Sudden and rapid weight loss indicates a decomposition reaction, or, if air is present, a reaction with oxygen. The thermogravimetric analysis used is the TA Instrument TGA Q50.

The experiment was run solely by the TGA Q50 using its software, Thermal Advantage for QSeries. The software allows for an individual experiment procedure to be customized based on the compound as well as the accuracy of the data. The accuracy is determined based on the method chosen. In the cases included in this specific research project, the TGA would equilibrate at 25.00°C and continue with Ramp at a tailored temperature increase per minute. The Ramp rates and end points are also customizable. Most often, the run sequence finished once the TGA reached 1000°C. However, for some compounds whose mass was completely lost at a much lower temperature, the Ramp end was changed to complete in a shorter amount of time, increasing trial efficiency.

For each inorganic compound, 15 trials were run. This included five trials at a ramp of 20°C/min, five at a ramp of 10°C/min and five at a ramp of 5°C/min. This incorporates the inclusion of determining differences in accuracies and minor details in each run. Five trials were run for each organic compound, all five at a ramp of 10°C/min. For each run, the completed graph from the Thermal Advantage program is opened in the program TA Universal Analysis for the data to be evaluated. With this software, the graphs were used to determine the step transitions for each trial. From there, the data was tabulated for each material in order

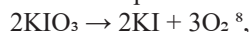
to calculate the averages and standard deviations for each compound's data.

Most inorganic materials exhibited either two or three transitions and required heating to the 1000°C limit. For example, Potassium Perchlorate underwent two step transitions, the first around 600°C with about 50% mass loss, and the second around 820°C with the remaining 50% mass lost. This agrees with the decomposition mechanism of Potassium Perchlorate reported by reference 5:



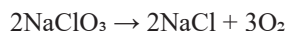
The first transition corresponds to the initial breakdown of potassium perchlorate to potassium chloride with the loss of oxygen. The second transition corresponds to the evaporation of potassium chloride until it is gone.

The decomposition of potassium iodate, KIO_3 , goes through the same decomposition around 540°C:



Like potassium perchlorate, the first transition indicates the initial breakdown of potassium iodate into potassium iodide with the loss of oxygen and the second transition indicated the evaporation of the compound until it is gone.

The decomposition of potassium bromate, potassium chlorate, sodium chlorate, and sodium perchlorate all follow the same pattern respectively, whose data can be found in the appendices A-F:



By comparing the current data to past data and analyses, the validity of the data can be determined. For example, data for the organic compound, Urea ($\text{CH}_4\text{N}_2\text{O}$) was collected, analyzed and

compared to previous data. Based on a previous experiment, the decomposition of Urea includes three transitions. The first transition occurs from 135°C to 220°C and indicates the formation of biuret ($\text{C}_2\text{H}_5\text{N}_3\text{O}_2$)⁹, with a corresponding 78% mass loss. The second transition occurs between 224°C and 257°C, indicating the loss of an additional 20% mass and formation of cyanuric acid ($\text{C}_3\text{H}_3\text{N}_3\text{O}_3$)⁹. The last transition occurs from 307°C to 372°C. This indicated the decomposition of cyanuric acid⁹.

Based on the data researched as well as the data collected, the higher the initial transition temperature of the decomposition of an inorganic compound, the more stable the compound. For example, the initial transition temperatures, in Celsius, for potassium chlorate, potassium perchlorate, potassium bromate and potassium iodate are 290°C, 600°C, 300°C, and 540°C, respectively. The most stable compound out of the four is potassium perchlorate with the highest initial transition temperature measured. For organic compounds, the data was used to calculate the vapor pressures for the solid below its melting point. (This was another student's project). No transitions were observed for these materials other than a linear loss of weight corresponding to evaporation (or sublimation from the solid phase). Each graph and table that proves each of these results can be found in the Appendix.

III. Conclusions

Information on the assembly and distribution of HMEs is readily available to the public. For instance, methods of constructing explosives and the placements are described in al-Qaeda and jihad training manuals and videos.⁶ This information and instruction can also be found in books that give a 'how-to' in using improvised materials and commercial products in HMEs. Military manuals can also be used as a source of construction and deployment.

The data collected can be used for future research as well as guides for individuals. For example, additional studies are planned for testing mixtures of oxidizers and fuels using a differential scanning calorimeter (DSC). This machine is used to study reactions of mixtures, and determine energy release. This is done by heating a sample pan and a reference pan simultaneously. The heater under the sample pan must work harder than the heater under the reference pan. The DSC then measures how much more heat the heater under the sample pan has to put out, producing a plot of heat capacity. This plot is used to study the thermal transitions (the changes that take place in a material while heated) of a material.

In a TGA, each component's stability is measured individually. The data from the studies using the DSC indicate the stability of the components of a HME together. This allows individuals to obtain a better understanding of how stable a HME is as a whole.

IV. References

¹Central Valley Arson Investigators. (n.d.). Homemade

Graph 1 - Potassium Perchlorate TGA at 20°C/min

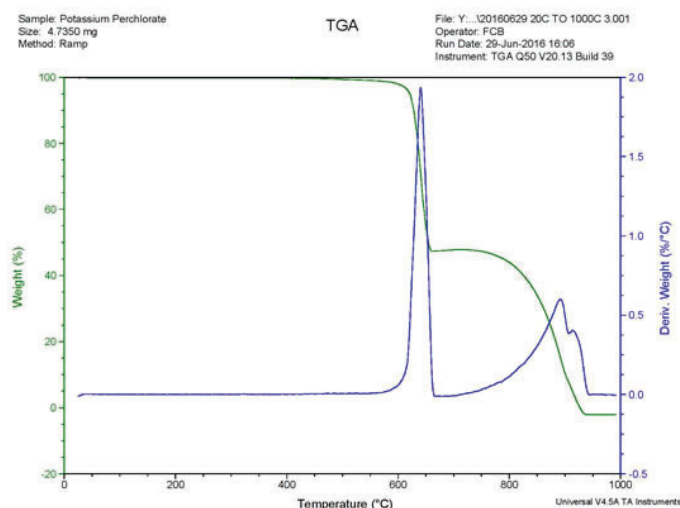


Table 1 – Potassium perchlorate transition data (average of five runs each)

Ramp (°C/min)	Transition 1 Temp. (°C)		Transition 1 mass loss (%)	Transition 2 Temp. (°C)		Transition 2 mass loss (%)
	Start	Finish		Start	Finish	
20	626 ±3	651 ±4	54 ± 3	855±8	918±4	50±1
10	601±8	623±8	50±1	811±2	877±4	51±1
5	574±5	586±6	47±3	785±3	841±2	51±1

Explosives (HME) Unclassified. Retrieved August 4, 2016, from <http://www2.bakersfieldcollege.edu/cfeer/Forensic Evidence/CBRNE/Explosives/1 CVAI Home Made Explosives PP.pptx>

²Devlin, D. J., & Herley, P. J. (1987). Thermal decomposition and dehydration of sodium perchlorate monohydrate. *Reactivity of Solids*, 3(1-2), 75-84. doi:10.1016/0168-7336(87)80019-0

³Diefallah, E. M., Basahl, S. N., & Obaid, A. Y. (1987). Kinetic analysis of thermal decomposition reactions. *Journal of Radioanalytical and Nuclear Chemistry, Articles Journal of Radioanalytical and Nuclear Chemistry Articles*, 109(1), 177-181. doi:10.1007/bf02117534

⁴Glasner, A., & Weidenfeld, L. (1952). Thermal Decomposition of Potassium Chlorate and Chlorate—Chloride Mixtures 1. *J. Am. Chem. Soc. Journal of the American Chemical Society*, 74(10), 2464-2467. doi:10.1021/ja01130a006

⁵Johnson, W. H., & Gilliland, A. A. (1961). Heat of decomposition of potassium perchlorate. *J. RES. NATL. BUR. STAN. SECT. A. Journal of Research of the National Bureau of Standards Section A: Physics and Chemistry*, 65A(1), 63. doi:10.6028/jres.065a.005

⁶Homemade Explosives: Current and Emerging Threats | Firehouse. (n.d.). Retrieved August 04, 2016, from <http://www.firehouse.com/article/10456558/homemade-explosives-current-and-emerging-threats>

⁷Law Enforcement Publications and Conferences. (n.d.). Retrieved August 04, 2016, from http://www.hendonpub.com/resources/article_archive/results/details?id=3544

⁸Muraleedharan, K. (2011). Thermal decomposition kinetics of potassium iodate. *J Therm Anal Calorim Journal of Thermal Analysis and Calorimetry*, 109(1), 237-245. doi:10.1007/s10973-011-1711-6

⁹Schaber, P. M., Colson, J., Higgins, S., Thielen, D., Anspach, B., & Brauer, J. (2004). Thermal decomposition (pyrolysis) of urea in an open reaction vessel. *Thermochemica Acta*, 424(1-2), 131-142. doi:10.1016/j.tca.2004.05.018

V. Acknowledgements

This project was supported in part by the U.S. Department of Energy under the Science Undergraduate Laboratory Internships Program (SULI).

VI. Appendix

Available upon request.

Graph 2 - Urea TGA at 10°C/min

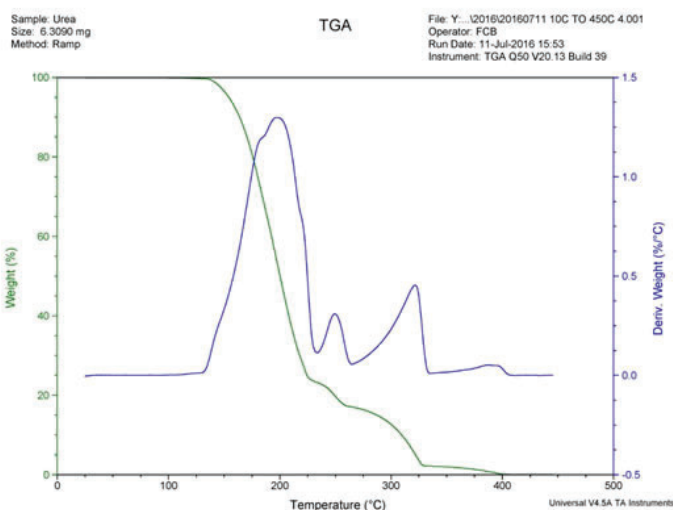


Table 2. Urea transition data

Ramp (°C/min)	Transition 1 Temp. (°C)		Transition 1 mass loss (%)	Transition 2 Temp. (°C)		Transition 2 mass loss (%)	Transition 3 Temp. (°C)		Transition 3 mass loss (%)
	Start	Finish		Start	Finish		Start	Finish	
10	164±4	214±7	78±1	281±30	301±30	21±1	366±4	398±7	2±0.5
5	154±3	201±6	85±3	284±3	309±5	13±1	356±5	383±3	2±0.5

Mechanism for CO oxidation over a CuO_x catalyst: An in situ XRD and DRIFTS study

Nataniel Medina Berríos

Department of Chemistry, University of Puerto Rico Río Piedras Campus, San Juan, Puerto Rico 00931

José Rodríguez

Department of Chemistry, Brookhaven National Laboratory, Upton, New York 11973

Jonathan Hanson

Department of Chemistry, Brookhaven National Laboratory, Upton, New York 11973

Abstract

Catalysts are known to play an important role in the production of fuels, accelerate reactions and even help in environmental remediation processes. Within this field of study, copper oxide (CuO) catalysts were discovered to promote carbon monoxide (CO) conversion into carbon dioxide (CO₂). However, determining the catalytic mechanism involved is still difficult because of the complex dynamic processes that occur. To better understand the catalytic process of CO oxidation using bulk CuO catalysts, a synchrotron-based time-resolved X-ray diffraction (TR-XRD) combined with simultaneous spectroscopic measurement of the gases observed was done at the Argonne National Laboratory Advanced Photon Source to obtain a fingerprint of the compounds present while the reaction occurs. In our experiment at National Synchrotron Light Source II, we used a low H₂ flow rate to be able to observe the behavior of CuO catalyst in bulk form using in situ-XRD. By utilizing all these characterizations, we were able to understand catalytic processes under the used parameters and thus now have a wider knowledge necessary to optimize these catalysts.

I. Introduction

The mechanism for carbon monoxide (CO) oxidation using copper oxide (CuO) as a catalyst has been studied as part of an effort for its usage in many technical applications such as energy production, environmental remediation and pollution control.^{1,2} However, determining the catalytic mechanism involved is still difficult because of the complex dynamic processes that occur. To better understand the catalytic process of CO oxidation using bulk CuO catalysts, techniques such as the synchrotron-based time-resolved X-ray diffraction (TR-XRD) combined with simultaneous spectroscopic measurement of the gases observed can be done to obtain a fingerprint of the compounds present while the reaction occurs.

After refining the data and analyzing the graphed results, we could determine of the changes to the catalyst during the carbon monoxide oxidation reaction. This was done by observing the graphed peaks and correlating the x-axis coordinate (in 2θ units) with a standard XRD pattern specific to each compound. Theoretically, the CO oxidation reaction mechanism with a copper oxide catalyst should happen in 4 reduction steps, visible as changes in the catalyst's composition: CuO → Cu₄O₃ → Cu₂O → Cu. However, in the conditions of the reaction in which the in situ-XRD study was done, the catalytic process of CO oxidation with CuO showed three visible steps in our XRD patterns: CuO → Cu₂O → Cu. The Cu₄O₃ compound has been observed in the copper oxidation process in which the CuO catalyst is regenerated with O₂ for subse-

quent use and CuO nanoparticle catalysts^{2,3}.

There are three different mechanisms considered for the CO oxidation reaction utilizing a CuO catalyst. The first mechanism is the Eley-Rideal where one of the reactants is adsorbed on the catalyst's surface and afterwards a unit of the reactant, while still in gas phase, interacts with the adsorbed molecule and the product desorbs from the surface. In this case, the rate is given by the equation $R_{ER} = k \theta_1 p_2$ (Eq. 1.1), which in turn, when substituting for the Langmuir adsorption isotherm gives:

$$R_{ER} = k \frac{K_1 p_1}{1 + K_1 p_1} p_2 \quad \text{Eq. 1.2}$$

For this mechanism, the higher rate is given when there is a maximum coverage of the catalyst's surface with reactant number one and a high pressure of the second gaseous reactant⁴.

A second mechanism to be considered for the CO oxidation reaction is the Langmuir-Hinshelwood mechanism, which describes a surface reaction as two atoms, one of each reactant, adsorbing first in the surface, then the surface diffusion facilitates the interactions between the two adsorbed reactants, enabling them to form a molecular bond. In the Langmuir-Hinshelwood mechanism, the susceptibility to react is at its peak when the reactants are adsorbed in stoichiometric amounts on the catalyst's surface. The behavior of this mechanism may be described by the derived Langmuir adsorption isotherm, illustrating its dependence on gas pressure⁴.

$$\theta = \frac{Kp}{1 + K} \rightarrow R_{LH} = k \frac{K_1 p_1 * K_2 p_2}{(1 + K_1 p_1 + K_2 p_2)^2} \quad \text{Eq. 2.1}$$

Third is the Mars and Van Krevelen mechanism. In contrast with the other two aforementioned mechanisms, the surface plays a role in the reaction. One of the reactants forms a chemical bond with the catalyst's surface and creates a reactant-metal layer which serve as the catalytic site for the second reactant to act on as a gas phase. The rate of the reaction is given by a similar equation as the Eley-Rideal mechanism $R_{MVK} = k \theta_{1a} p_{1b}$ (Eq. 3.1) which addresses the adsorption of the reactant bonded to the metal and the pressure of the gaseous second reactant. When the product desorbs from the catalyst, a vacancy is left behind in the surface of the catalyst⁴. This vacancy, as described by Mars and Van Krevelen, is stabilized and filled by a reactant unit from the catalyst bulk instead of an atom or molecule of the gas phase reactant⁵.

To gain a better understanding of which mechanism applies to the CO oxidation reaction on a CuO catalyst in bulk form, a series of experiments were done: Residual Gas Analysis (RGA), Syn-

chrotron-based X-Ray Diffraction (XRD) and Diffuse Reflectance Infrared Fourier Transform (DRIFT). Residual Gas Analysis is a technique that is used for analyzing the composition of high vacuum systems, such as analyzing the chemistry that is occurring⁶. For the purpose of determining surface chemistry mechanisms, RGA is a valuable tool for identifying the behavior of the catalyst during a phase reaction. In an experiment where gases of reducing and oxidation agents are pumped through a sample in alternating cycles, we obtain data that can be graphed as gas pressure data versus time. This graph enables us to understand the behavior of the reaction in an in-situ manner, and correlated with the Mass

Spec data from the RGA, the identity of the species formed and present during the catalytic reaction can be confirmed. This is extremely important for the determination of the mechanism of CO oxidation with a CuO catalyst.

One of the techniques that compliments the RGA is the Synchrotron-based X-Ray Diffraction (XRD). This technique serves to carry out in-situ x-ray diffraction measurements, which lets us obtain the powder diffraction patterns of the species forming while a reaction is ongoing. The powder diffraction patterns are specific to every compound, which is why this technique is useful to characterize the steps in the CO catalyzed oxidation reaction.

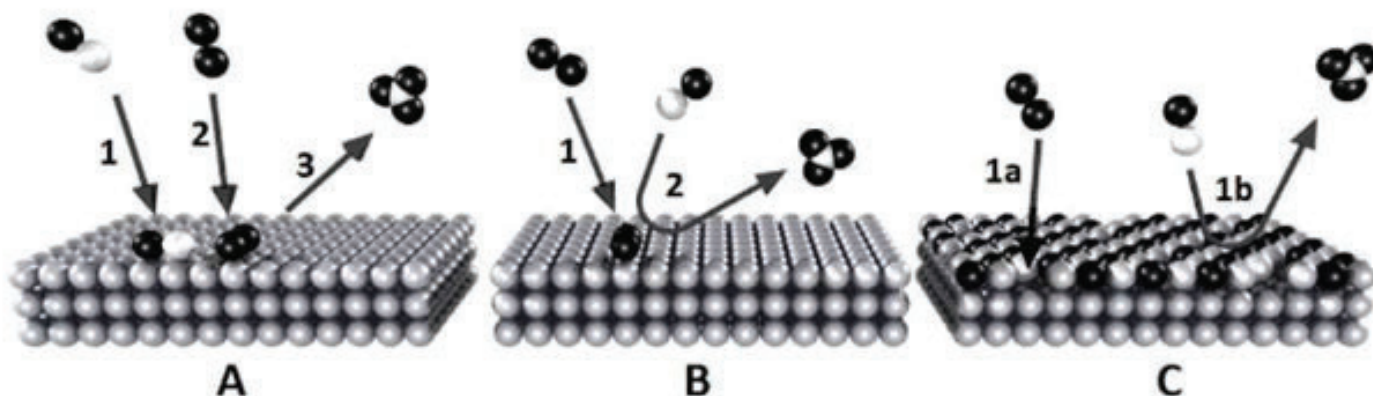


Figure 1: a) Langmuir-Hinshelwood mechanism, b) Eley-Rideal mechanism, c) Mars and Van Krevelen mechanism⁴.

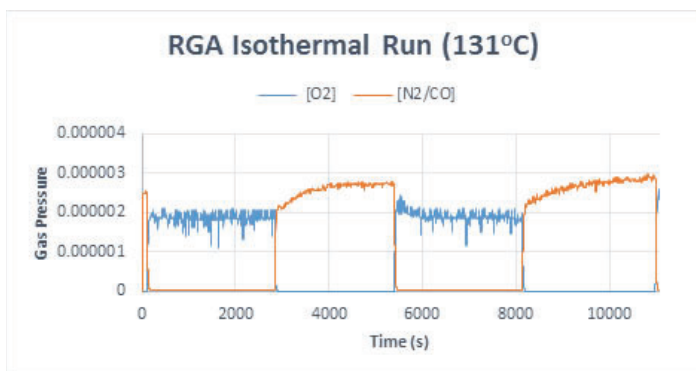


Figure 2: RGA isothermal run at 131°C with a CuO catalyst in bulk form. O₂ and CO pulses.

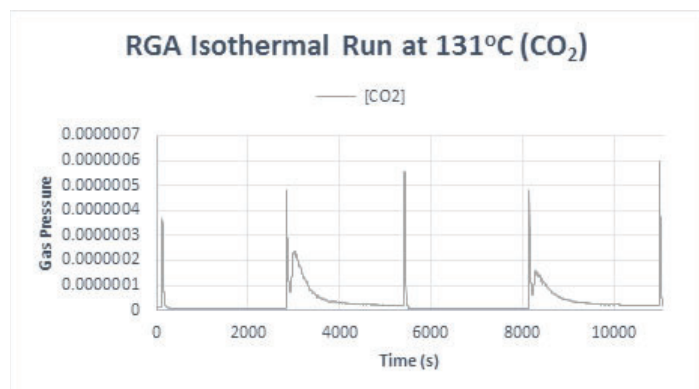


Figure 3: RGA isothermal run at 131°C with a CuO catalyst in bulk form. Carbon dioxide (CO₂) production

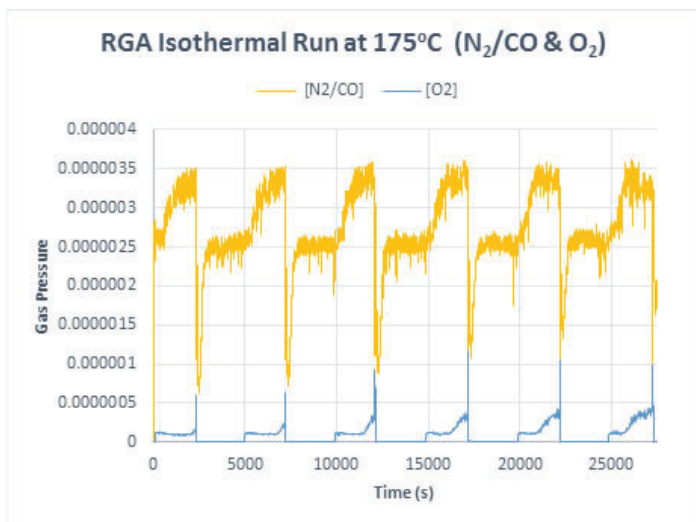


Figure 4: RGA isothermal run at 175°C with a CuO catalyst in bulk form. O₂ and CO pulses.

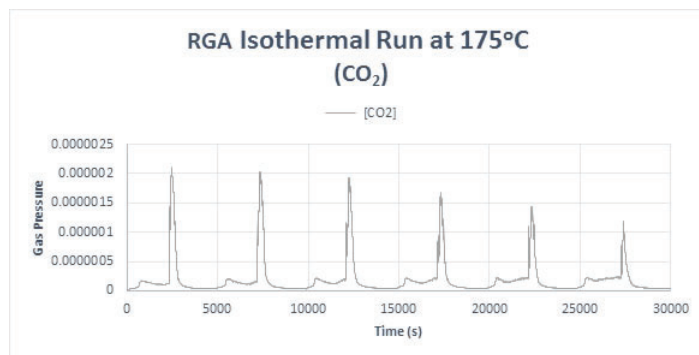


Figure 5: RGA isothermal run at 175°C with a CuO catalyst in bulk form. Carbon dioxide (CO₂) production

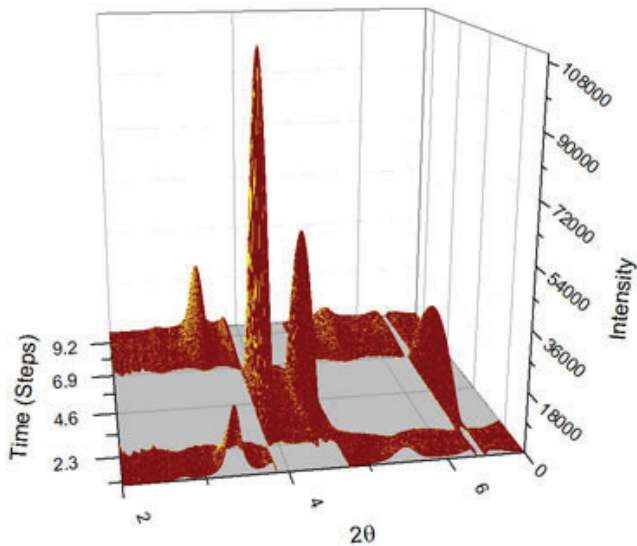


Figure 6: In-situ XRD Pattern for isothermal run at 131°C

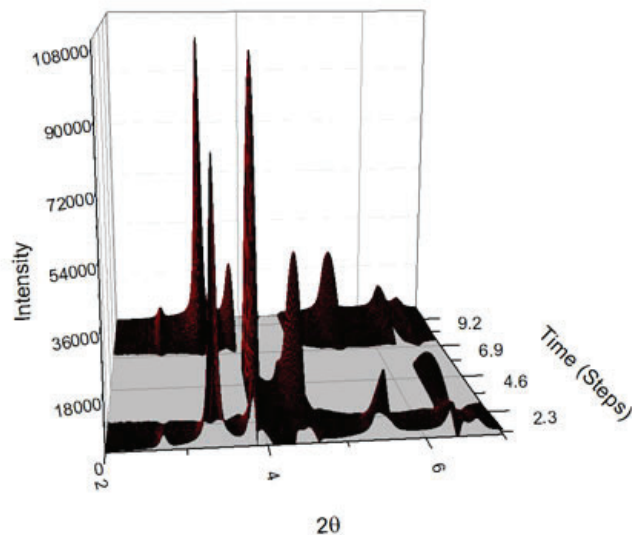


Figure 7: In-situ XRD Pattern for isothermal run at 175°C

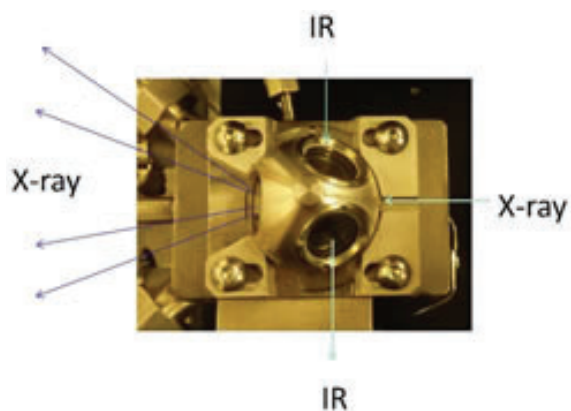


Figure 8: Simultaneous XRD and DRIFT setup.

DRIFT Plot for Isothermal run (131°C)

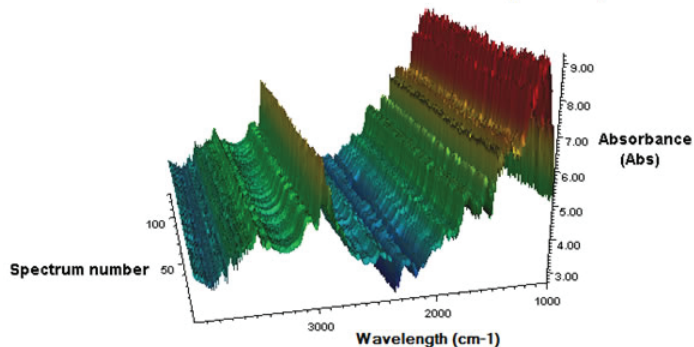


Figure 9: DRIFT Plot for Isothermal run (131°C). CO/Cu⁺ appears negative because of background subtraction.

DRIFT Plot for Isothermal run (175°C)

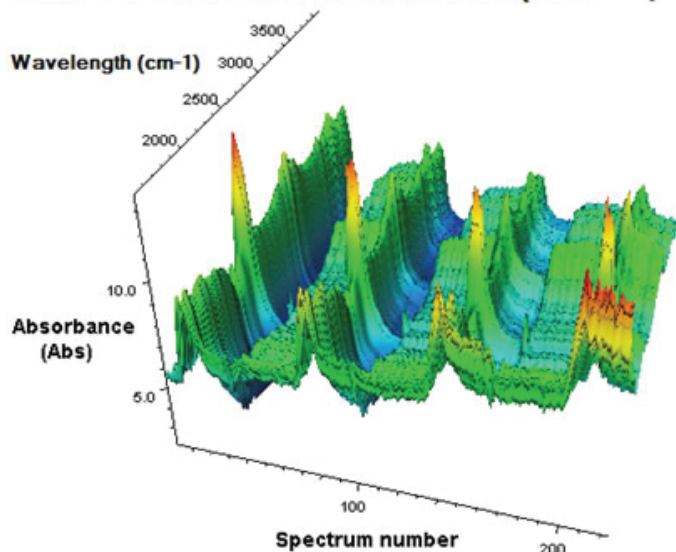


Figure 10: DRIFT Plot for Isothermal run (175°C)

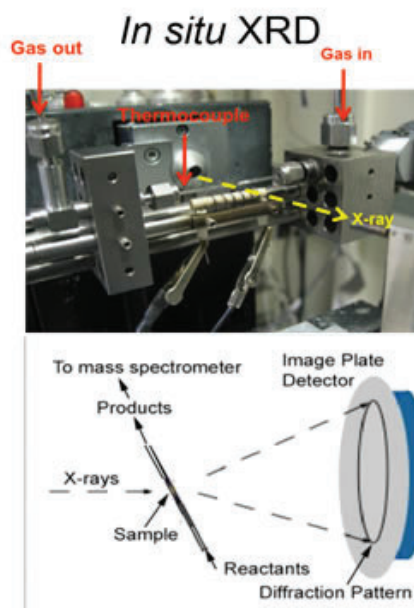


Figure 11: In-situ XRD Setup

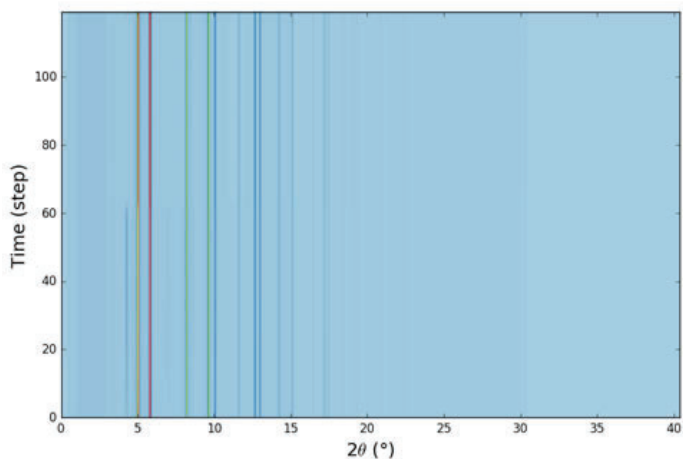


Figure 12: Averaged and Normalized XRD data

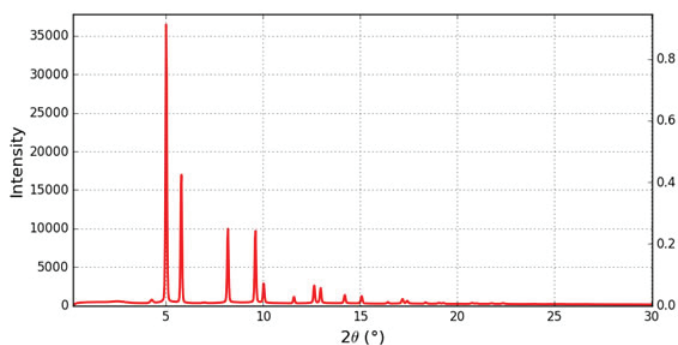


Figure 13: Averaged and Normalized XRD data 1D Pattern of starting phase (CuO)

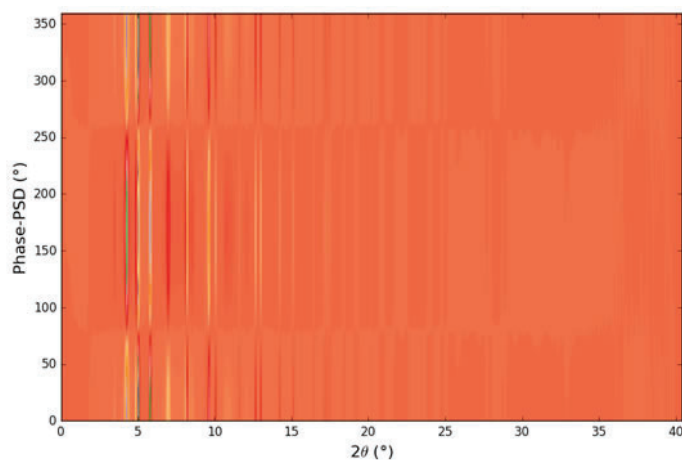


Figure 14: Demodulated XRD Data

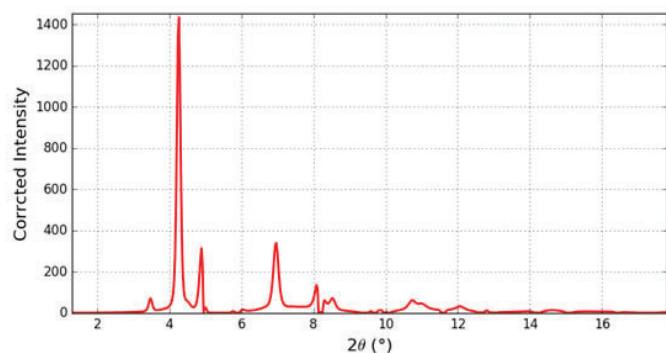


Figure 15: Demodulated XRD Data 1D Patterns at demodulation phase 0. Positive peaks are from CuO chemical phase and negative peaks are from Cu chemical phase.

Different from Single Crystal X-Ray Diffraction, Powder X-ray is done on polycrystalline materials. If the crystallites are very small, the signals obtained in the powder X-ray diffraction are not sharp peaks but distributed bumps associated with the angle of diffraction (2θ). Since catalysts work on the surface on the material and Powder X-Ray Diffraction only gives the structure of the bulk sample, other techniques are necessary to confirm the mechanism of the surface reactions.

To back up the data from the RGA and XRD studies the Diffuse Reflectance Infrared Fourier Transform (DRIFT) serves as an in-situ infrared scan that gives the peaks of functional groups of compounds that appear during the progress of the surface reaction, giving a confirmation of the species present at a certain time on the surface of the catalyst. By correlating and analyzing RGA, XRD and DRIFT data it is possible to determine the behavior of a surface catalytic reaction.

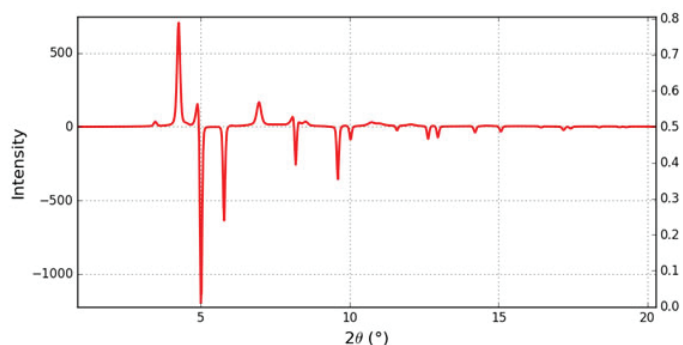
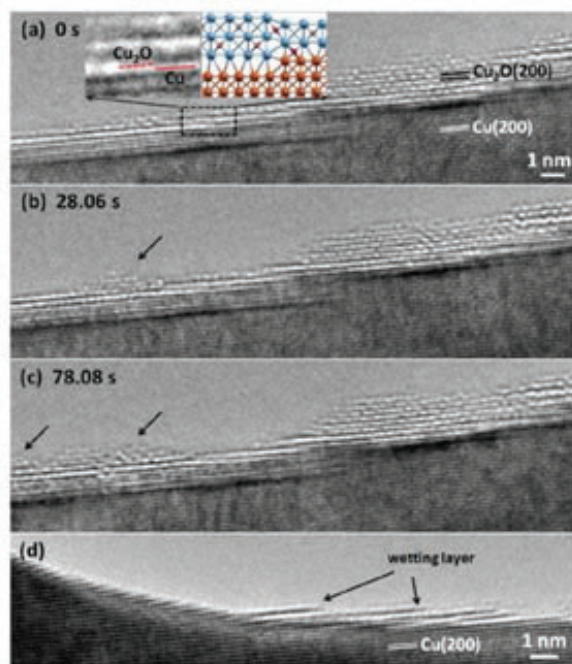


Figure 16: Demodulated XRD Data Corrected Patterns at phase=0 (during the O_2 pulse)



(a-c) *In situ* TEM observations of the nucleation and growth of a Cu_2O island on the oxide wetting layer during oxidation of $Cu(100)$ at $350\text{ }^\circ\text{C}$ and $pO_2 = 5 \times 10^{-3}$ Torr (see *in situ* TEM movie S1 in the ESi†). Inset in (a) shows the formation of a disconnection at the buried $Cu-Cu_2O$ interface due to the presence of an atomic Cu surface step. (d) TEM image revealing that the oxide wetting layers initiate at Cu surface steps.

Figure 17: In-situ TEM observations of island formation during initial Cu oxidation. Image from: *Chem. Commun.* 2013, 49 (92), 10862.

II. Experimental Section & Results

A. Argonne National Laboratory

1. Residual Gas Analysis (RGA)

An RGA isothermal run at 131°C and 175°C were done at Argonne National Lab's Photon Source (APS), pulsing between 5% oxygen (O₂) and 5% carbon monoxide (CO) in He in 30 minute cycles, as observed in Figure 2. A flow of reactant gases was allowed into the cell and the reactant gases were passed to a Dycor Mass Spectra analysis system. The flow rate of the input gases was controlled with Brooks mass flow controllers. A Valco switching valve was used for switching between oxidizing and reducing gases. Data of cycles was graphed and analyzed as a function of time vs. gas pressure. Here are the results of these studies:

2. Time-Resolved X-Ray Diffraction (TR-XRD)

TR-XRD was done at Argonne National Lab's Photon Source (APS) with a wavelength of 0.1430Å. The pulsing was of 30 minutes O₂, 30 minutes CO per cycle plus two empty frames as marker during all process of collection of XRD, IR and RGA data. In addition to the 60 minutes of gas cycles, 1 minute before collection and 1 minute between collections were added for a total time of 62 minutes per cycle. Each image was of 30 seconds, to a total of 120 images, including dark images for one minute before each 122 image collection. Data corrections were done using python script programs such as 2dftjch.py and 2dmed_2.1.py. Processed data was then graphed using the Origin program. Images obtained represent the diffraction patterns of the species present throughout the reaction.

3. Diffuse Reflectance Infrared Fourier Transform (DRIFT)

DRIFT data was collected along the XRD data simultaneously for the isothermal runs at 131°C and 175°C. Presence of CO and CO₂ was confirmed throughout the runs by correlating wavelength number associated with the presence of CO double bonds (2958 cm⁻¹ for monodentate formate and 2108 for CO/Cu⁺) in the obtained graphs.

B. Brookhaven National Laboratory

1. Synchrotron-based X-Ray Diffraction

To better understand the behavior of the CuO catalyst, a Synchrotron-based X-Ray Diffraction experiment was done at the National Synchrotron Light Source II facility at Brookhaven National Laboratory. Wavelength of x-ray beam used was 0.18730 Å, the temperature was held at 250°C while flowing 3% H₂ in helium, and was kept switching between H₂ and O₂ overnight.

Data collected was then extracted from its metafile and converted to chi files. Data corrections were done using python script programs such as 2dftjch.py and 2dmed_2.1.py. X-Ray powder patterns were analyzed to determine the species formed during the reaction. (See Figures 12-16)

III. Discussion

From the results obtained in the experiments done at Argonne National Laboratory (ANL), we can observe that the CO oxidation proceeds well when utilizing CuO at relatively low temperatures (131°C and 175°C). The RGAs data show the reduction of the CuO bulk at the time the CO gas is flowing (Figures 2 & 4), consistent with the time of the CO₂ production in the system (Fig-

ures 3 & 5). After the regeneration of the CuO catalyst with O₂, the copper oxide can be reutilized for further production of CO₂ with consistent efficiency, as observed by the symmetry of the peaks between the CO & O₂ cycles. The X-Ray Diffraction patterns were compared with published patterns obtained from the International Centre for Diffraction Data. The 2θ values obtained in the XRD studies showed the clear presence of the species CuO, Cu₂O and Cu throughout the CO & O₂ cycles. No definite presence of the intermediate Cu₄O₃ was spotted in the XRD patterns. To complement the data on the CO catalyzed oxidation reaction, XRD studies were done at the NSLS-II facility at Brookhaven National Laboratory. In contrast with the experiments done at ANL, where the focus was on observing the CO oxidation reaction's behavior, the experiment executed at BNL's NSLS-II focus was observing the behavior of the catalyst during H₂ oxidation. The XRD patterns obtained in this experiment showed a step-wise reduction mechanism for the CuO catalyst in bulk form. The demodulated data (Figure 15) shows the appearance of Cu₂O as CuO is consumed and the formation of Cu⁰ when all the oxygen in the copper oxide lattice is consumed by the reducing agent in gas phase. No distinguishable signal for the intermediate Cu₄O₃ was detected under these reaction parameters. The DRIFT confirmed the presence of both the monodentate formate and CO/Cu⁺ species on the surface of the catalyst in the same time offset as when the CO gas was flowing.

When analyzing the three surface chemistry mechanisms described previously {Eley-Rideal, Langmuir-Hinshelwood and Mars and Van Krevelen}, the in-situ XRD patterns, DRIFT data and the nature of the catalyst were taken into account to determine which mechanism applies best to the CO oxidation reaction utilizing a CuO catalyst in bulk form under these reaction conditions. The Eley-Rideal mechanism involves the adsorption of one of the reactants on the surface of the catalyst, then the second reactant interacts with the adsorbed reactant and the product desorbs from the surface. Given the nature of the CuO catalyst and that it contains one of the reactant chemically bonded in its lattice, the Eley-Rideal mechanism does not apply. For the Langmuir-Hinshelwood the two reagents are adsorbed on the surface and interact via diffusion on the surface, for which the same reason as the Eley-Rideal mechanism to rule this mechanism out applies, one of the reagents is chemically bonded to the catalyst. In addition, the conditions at which the reaction was done in this work's experiments does not include simultaneous gas flow of both O₂ and CO. It is possible that by doing so the Langmuir-Hinshelwood mechanism would be feasible, as long as there are stoichiometric amounts of reactants adsorbed on the surface, which is when the Langmuir-Hinshelwood mechanism has its highest activity⁴. Last, but not least, the Mars and Van Krevelen mechanism works by one of the reactants chemically bonding to the surface of the catalyst, creating a thin metal-reactant layer in which the second reactant interacts while in gas phase and forms the product. Moreover, the vacancy created on the metal-reactant layer by desorption of the product is filled by a reactant atom from the bulk, instead of a gas phase or the catalyst's lattice relaxes into a more stable conformation^{3, 4, 5}. Because of this, the mechanism fits the CO oxidation reaction utilizing a CuO catalyst in bulk form since the reactant, the oxygen, is chemically bonded to the copper in the form of a metal oxide, forming islands in the surface during the initial oxidation⁷.

The Mars and Van Krevelen mechanism is further supported

by the stepwise apparition of XRD signals belonging to the CuO intermediates going from $\text{CuO} \rightarrow \text{Cu}_2\text{O} \rightarrow \text{Cu}$ when CO is flowing and from $\text{Cu} \rightarrow \text{Cu}_2\text{O} \rightarrow \text{CuO}$ when oxygen is flowing.

IV. Conclusions and Recommendations

In this work, the behavior of the CO oxidation reaction utilizing a CuO catalyst in bulk form and the copper oxide catalyst were observed. With these observations, it was determined that the most suitable mechanism for this gas-solid reaction, within the parameters studied in, is the Mars and Van Krevelen mechanism. Further studies should be made to support and evidence this mechanism, such as in-situ TEM measurements of the CO oxidation reaction utilizing a CuO catalyst in bulk form. Determining the mechanism in which the the CO oxidation reaction utilizing a CuO catalyst in bulk form occurs with substantial evidence, will bring a great contribution in understanding heterogeneous catalysts' mechanism and will open the door for improvements in creating more efficient and cost-effective catalysts.

V. References:

- ¹Yao, S.; Mudiyansele, K.; Xu, W.; Johnston Peck, A. C.; Hanson, J. C.; Wu, T.; Stacchiola, D.; Rodriguez, J. A.; Zhao, H.; Beyer, K. A.; Chapman, K. W.; Chupas, P. J.; Martínez Arias, A.; Si, R.; Bolin, T. B.; Liu, W.; Senanayake, S. D. *ACS Catal.* **2014**, *4* (6), 1650–1661.
- ²Svintitskiy, D. A.; Kardash, T. Y.; Stonkus, O. A.; Slavinskaya, E. M.; Stadnichenko, A. I.; Koscheev, S. V.; Chupakhin, A. P.; Boronin, A. I. *J. Phys. Chem. C* **2013**, *117* (28), 14588–14599
- ³Wang, X.; Hanson, J. C.; Frenkel, A. I.; Kim, J. Y.; Rodriguez, J. A. *J. Phys. Chem. B* **2004**, *108* (36), 13667–13673.
- ⁴Herbschleb, C. T. Reactor STM: Imaging Catalysts Under Realistic Conditions. Thesis, 2011.
- ⁵Mars, P.; Krevelen, D. V. *Chemical Engineering Science*, **1954**, *3*, 41–59.
- ⁶Stanford Research Systems, *Vacuum Diagnosis with an RGA Application Note #7*. http://www.thinksrs.com/downloads/PDFs/ApplicationNotes/Vac_diag_RGA.pdf (Accessed: July 27, 2016)
- ⁷Zhou, G.; Luo, L.; Li, L.; Ciston, J.; Stach, E. A.; Saidi, W. A.; Yang, J. C. *Chem. Commun.* **2013**, *49* (92), 10862.
- ⁸Pašti, I. A.; Skorodumova, N. V.; Mentus, S. V. *Reac Kinet Mech Cat* **2014**, *115* (1), 5–32.

VI. Acknowledgements

This project was supported in part by the U.S. Department of Energy, Office of Science, Office of Workforce Development for Teachers and Scientists (WDTS) under the Science Undergraduate Laboratory Internships Program (SULI).

Special thanks to José Rodríguez, Jonathan Hanson, Dmitry Vovchok and Sanjaya Senanayake from the Catalysis Group at BNL's Chemistry Department for helping and guiding me with their knowledge throughout this summer.

Tools for the characterization and improvement of the electron beam orbit stability for the National Synchrotron Light Source – II storage ring

Jessica Mele

Applied Mathematics and Statistics, Stony Brook University, Stony Brook, NY 11794

Timur Shaftan

Photon Sciences, Brookhaven National Laboratory, Upton, NY, 11973

Abstract:

The National Synchrotron Light Source – II (NSLS-II) is a 792 meter-long state-of-the-art storage ring designed to run 500 mA of a 3-GeV beam that will serve high-brightness X-rays to approximately 60-70 beamlines in its final buildout. The low beam source size drives tight requirements on maintaining the high stability of the beam orbit. Various noises, ranging from slow ground motion to high frequency jitters, need to be suppressed in order to maintain beam orbit stability. This stability is of critical importance to X-ray beam users who depend on the high brightness X-rays to conduct ground-breaking research at the NSLS-II. Beam position is monitored by 180 beam position monitors (BPMs) located around the entire storage ring. I designed a complex Python program that measures signals from all 180 BPMs and runs an elaborate Fourier analysis of the beam position in horizontal and vertical planes. My program suppresses spectral noise by the use of filtering algorithms, analyzes spectral data to retrieve significant maxima including their frequencies and bandwidths, coordinates processing of multi GB data sets for efficient diagnostics of the noise sources, and interfaces processed spectral data to the facility archive. My program will enable scientists at NSLS-II to locate and characterize the sources of noise that could compromise the low emittance of the storage ring thus allowing them to increase beam orbit stability.

I. Introduction

NSLS-II is a third generation 3GeV storage ring with ultra-low emittance, which delivers high brightness X-rays to beamlines. The circulating bunches of electrons around the storage ring are focused via the use of focusing magnets (quadrupoles and sextupoles). The low emittance feature of the storage ring requires an extremely stable beam orbit, along the lines of submicron beam orbit stability. There are various noises that need to be suppressed in order to maintain this stability, ranging from low frequency ground motion to high frequency mechanical vibration.⁵

The unwanted ground vibrations that could cause disturbances in the storage ring can be classified into one of two groups: technical noise and cultural noise. The category of technical noise encompasses noise generated by the operation of the accelerator facility. Technical noises can arise from electric motors, compressors, workshops, etc. Some examples include pumps, crane activity, site traffic and even people walking about the facility. Cultural noise describes other human generated vibration noise that comes from outside of the facility, which means that it cannot be controlled by the accelerator operators. Some examples of cultural noise include traffic on roads around the facility, nearby railways and even airplanes flying overhead.⁴

It is imperative that these noises be suppressed in order to maintain beam orbit stability. Facility scientists at NSLS-II need a way to characterize and analyze the beam orbit stability to determine areas being affected by noise so that they can investigate the area and make adjustments to improve the beam orbit stability. The analysis of the power spectral density of the electron beam orbit allows facility scientists to view how the strength of a signal is distributed in the frequency domain, relative to the strengths of other ambient signals. This is necessary to extract or suppress the unwanted noises.³

II. Methods

To provide an efficient way of analyzing and characterizing the beam orbit stability for NSLS-II scientists and users I created a Python program that analyzes BPM readings and interfaces the results to the facility archive. My program views the power spectral density of the electron beam orbit position and calculates important maxima information for the use of maintaining and improving the beam orbit stability.

There are 180 BPMs located around the storage ring and through the use of a fast order feedback system, each can be utilized to retrieve horizontal and vertical spectra of the electron beam orbit positions around the entire storage ring. At NSLS-II there are 120 nondispersive BPMs and 60 dispersive BPMs. The difference between the dispersive and nondispersive BPMs is that the dispersive BPM readings depend on the electron beam's energy whereas the nondispersive BPM readings do not. I decided to show them in separate 3D graphs for visibility reasons. If you take a look at (Figure 5) and (Figure 7) then you can see that the peaks from the dispersive BPM readings are much more profound. If I were to place these readings in the same graphs then it would be difficult to analyze the nondispersive BPMs as their peaks may become overshadowed. The 3D graphs can show the power spectral density of the electron beam position for any requested BPMs, allowing facility scientists to view trends and investigate sufficient maxima which may be jeopardizing the electron beam orbit stability.

A. BPM Readings

My program takes in readings from all 180 BPMs from the control system of the NSLS-II. The program reads in BPM information for both fast acquisition (FA) data and slow acquisition (SA) data. The difference between the FA and the SA data is the sampling rate at which the samples were taken. The sampling rate for the FA data is 10^{-4} seconds whereas the sampling rate for the SA data is 0.1 seconds. The readings are available for both horizontal and vertical planes.

B. Fourier Analysis

In order to compare the signals from the BPMs around the storage ring relative to the strengths of other signals we need to perform a Fourier analysis on the BPM data in both horizontal and vertical planes. Using the Fast Fourier transform (FFT) of the positions from each BPM, we can view the signals in the frequency domain.

The FFT $y(k)$ of length N of the length- N sequence $x(n)$ is defined as:

$$y(k) = \frac{1}{N} \sum_{n=0}^{N-1} x(n) e^{-\frac{2\pi i k n}{N}} \text{ for } k = 0, \dots, N-1 \text{ (Discrete Fourier transform)}$$

In general, the transform into the frequency domain is a complex valued function with magnitude and phase. For my program, we are only concerned with the magnitude components, which can be obtained by taking the absolute value of the result of the FFT.

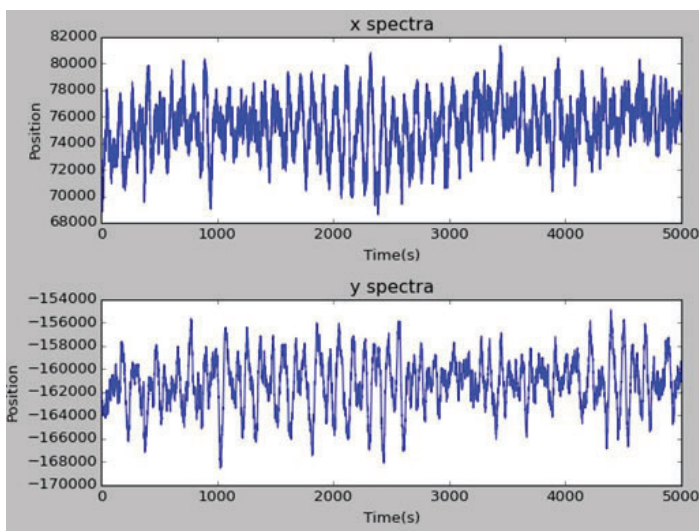


Figure 1: This is a graph of the beam position versus time for a specific BPM in the NSLS-II storage ring for both the horizontal and vertical planes.

C. Filtering/ Suppressing Spectral Noise

Once we have computed the FFT of beam orbit positions for each BPM, we need to apply a filtering algorithm in order to suppress spectral noise. The signals that come in can be very noisy, which can make analysis difficult. I implemented a running average filtering algorithm in order to facilitate the location of significant maxima from the signals.

The running average algorithm is implemented as follows:

I have different sized windows ranging from five to twenty. I begin to iterate along the horizontal axis and compute the running averages for data points that fall in these windows. The window sizes changes after each average is computed so that we can best handle the noise in the signals. This method gets applied to both the frequency values as well as the FFT values so that we have a new set of data points that can be viewed in an elegant graph once the filtering is complete.

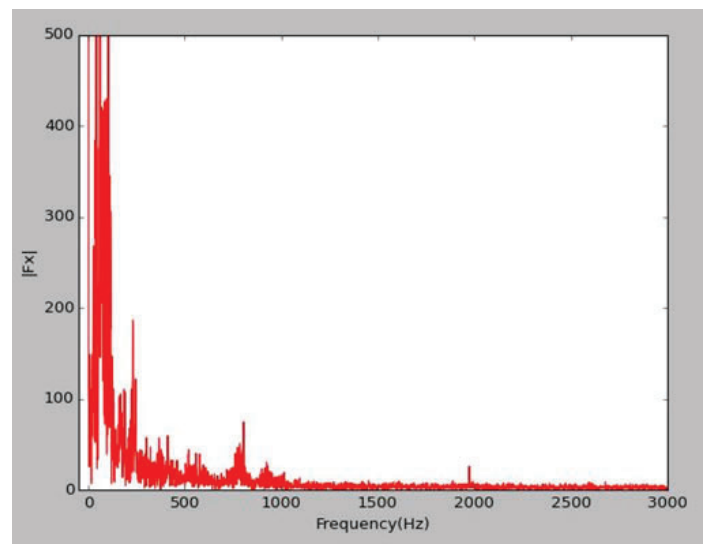


Figure 2: This is a graph of the Fourier transform of a single BPM reading in the horizontal plane.

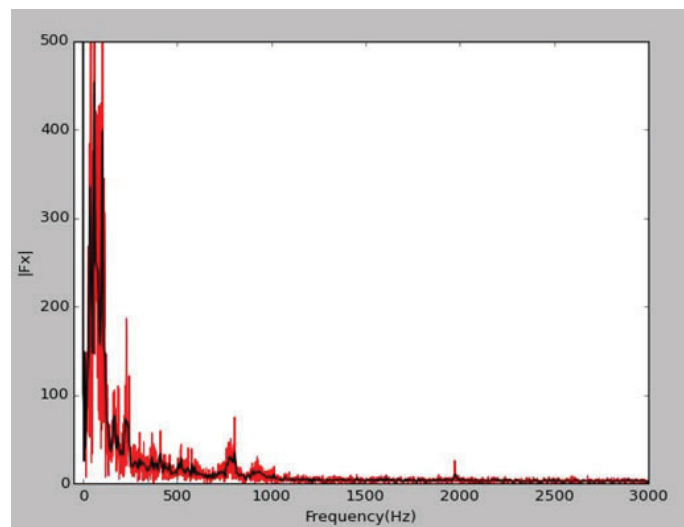


Figure 3: This is a graph of the same FFT as in (Figure 2). The black line represents the FFT after the smoothing algorithm is implemented.

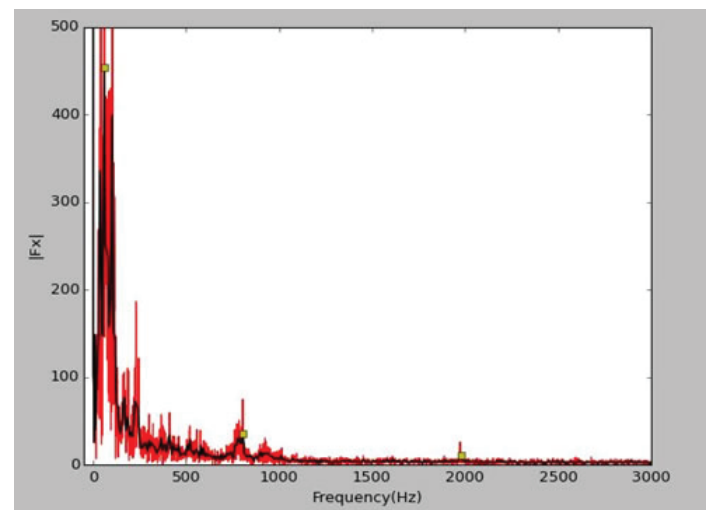


Figure 4: This graph shows the same FFT as in (Figure 2) with the filtering algorithm and here the yellow squares represent the significant maxima.

D. Locating Significant Maxima

Locating significant maxima is crucial to the investigation and suppression of noise around the storage ring. Maxima peaks that feature exceptionally high amplitudes and/or large bandwidths indicate areas that could possibly be affected by unwanted noise sources.

In order to locate significant maxima that are not considered noise I iterate through the smoothed data with moderate changes being made between locating maxima for FA and SA data separately.

To locate maxima for the FA data I begin by determining whether a specific point could be a potential maximum. This is done by comparing the height of this point with the points directly before and after it. If this middle point is located higher than its neighbors then it has the potential to be a maximum. Despite the filtering efforts, the data is still comprised of some noise which means that there a lot of points that can be considered maxima from just this method alone, which would also encompass points that are considered noise. In order to prevent this from happening I added additional components to the algorithm. I take the potential maxima and check it with a number of data points before and after it. Depending on how dense the area is around the specific point I am checking, the points must be higher than a certain number of data points to the left and right of it in order to be considered a significant maxima.

Similarly with the SA data, I check for potential maxima and rule out noise by checking a number of neighboring points. However, for the SA data I found that this still led to noise in the maxima for some BPMs. I added a threshold such that each point had to be higher than its neighbors by this value in order to be considered a significant maximum.

Once significant maxima are found, my program returns the BPM location, frequency and full width at half maximum of each peak.

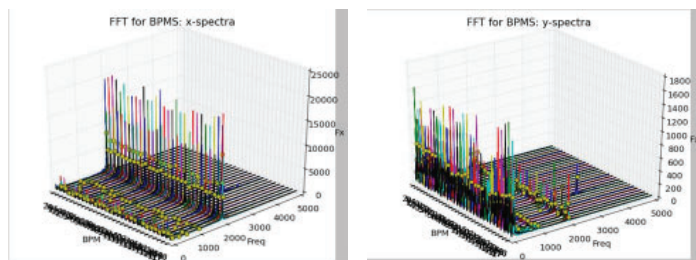


Figure 5 (left): This is a 3D graph of dispersive BPMs taken from fast acquisition (FA) data in the horizontal plane.

Figure 6 (right): This is a 3d graph of dispersive BPMs taken from fast acquisition (FA) data in the vertical plane.

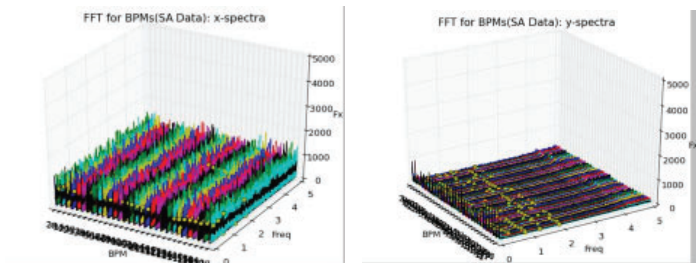


Figure 9 (left): This is a 3D graph of dispersive BPMs taken from slow acquisition (SA) data in the horizontal plane.

Figure 10 (right): This is a 3D graph of dispersive BPMs taken from slow acquisition (SA) data in the vertical plane.

E. Interfacing to Facility Archive

Once the significant maxima are located and values of interest are computed, my program outputs the information to facility users. My program saves the found and computed values into the facility archive. It also interfaces several useful graphs to assist in the analysis of the noise. These graphs can be found below in the results section of this paper.

III. Results

My program outputs a variety of graphs for facility users to perform analysis with.

The graph of beam position versus time for a single BPM in the storage ring showcases the need for the FFT for analysis of the beam position. The readings are complex signals that are difficult to compare or analyze without the use of the FFT. (See Figure 1)

The graph of the FFT (See Figure 2) gives a useful way to characterize the amplitude versus the frequency content of the signals being read in from the BPMs. The FFT still encompasses some spectral noise, which is why I then implemented a filtering algorithm. You can see the result of this algorithm in (Figure 3), where the black line represents the smoothed data. Next, in (Figure 4) you can see the yellow squares which are the significant maxima that my program detects.

The graphs that are most interesting to facility scientists are my 3D plots of each BPM around the storage ring. (See Figures 5-12) Split into dispersive, nondispersive and fast acquisition (FA) versus slow acquisition (SA) data, you can take a look at trends that are happening all along the storage ring.

After the 3D graphs are created, the significant maxima information is saved to the facility archive. The important information that NSLS-II scientists and users wish to view include the BPM number in which in the maxima was located, the peak height, the frequency and the bandwidth. An example of what is saved can be found in (Figure 13). Scientists can then view this information

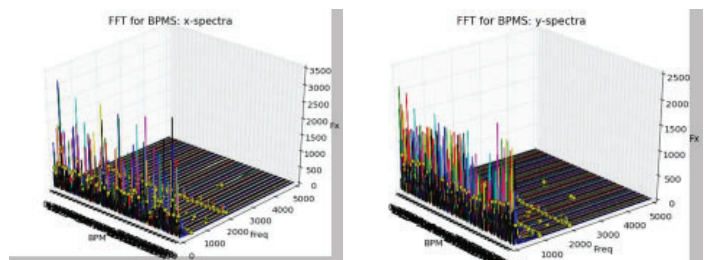


Figure 7 (left): This is a 3D graph of nondispersive BPMs taken from fast acquisition (FA) data in the horizontal plane.

Figure 8 (right): This is a 3D graph of nondispersive BPMs taken from fast acquisition (FA) data in the vertical plane.

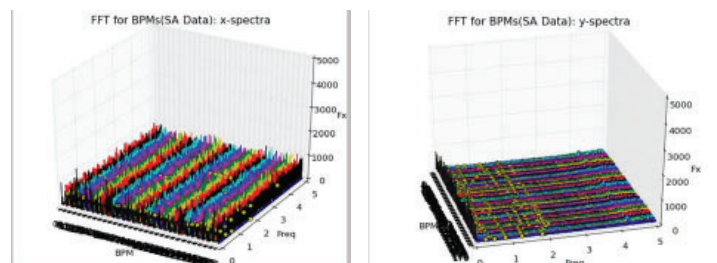


Figure 11 (left): This is a 3D graph of nondispersive BPMs taken from slow acquisition (SA) data in the horizontal plane.

Figure 12 (right): This is a 3D graph of nondispersive BPMs taken from slow acquisition (SA) data in the vertical plane.

and determine if there are areas of the storage ring which require investigation. If a peak's amplitude or bandwidth is too large then this could be an indicator that the area is being affected by noise. After further investigation I found that every BPM has an unusually high peak around a frequency of 0 Hz and has no impact on the rest of the data. My algorithm has been improved to exclude these values from the calculations.

The last graph is the "noise finder". (See Figure 14) Taking a look at amplitudes around the storage ring at a specific frequency, we can easily analyze where the largest source of noise of a specific frequency is coming from. This will make it a lot easier for facility scientists to pinpoint exactly where the noise is coming from and what frequency of noise they should be investigating. For the graphs in (Figure 14), I chose these specific frequencies because of the trends that I noticed in the 3D plots of the FA data. These three frequencies seem to be the location of most maxima for a large number of BPMs. The trends in these "noise-finders" indicate that for certain BPMs, these frequencies indeed encompass a lot of noise, which is why these graphs show a lot of maximal peaks along the entire storage ring.

Below in (Figure 15), you can see a labeled figure with the known noise sources for the specific labeled frequencies. These

are the frequencies in which NSLS-II scientists have already investigated and are looking at for noise suppression. Generally, they have an idea about what is causing the current noise in the BPM readings, but my program will help highlight areas in which they have not yet looked. It will also help locate new areas affected by noise as they arise throughout the future runtimes of the facility.

IV. Future Work

In the future I would like to be able to optimize my algorithms. I would like further investigate ways to locate significant maxima so that we can be sure that we are locating only the most significant peaks every single time regardless of if the data is FA or SA. I would also like to look into ways of improving the efficiency of my program. Currently, it takes approximately fifteen minutes to compute one of the 3D graphs shown in the results and approximately twenty minutes to compute of the noise finder graphs. Since these graphs are the most useful for facility scientists, I would like this information to be as easily accessible as possible.

BPM Number	Peak Height	Frequency	FWHM
1	150636.951904	0.0	294.832348518
1	608.360062385	58.6080586081	14.2360116628
1	168.27753523	1970.6959707	29.1507272577
2	126870.264893	0.0	1590.54534531
2	454.402522304	58.6080586081	14.5875337846
2	109.709958753	1970.6959707	29.3997369145
5	70328.2670898	0.0	132.911234853
5	388.5622074	58.6080586081	16.0565556523
5	28.8502876915	512.820512821	14.4205106256
5	77.1019271128	1970.6959707	28.5127626652
6	277553.860352	0.0	3025.0878361
6	291.076324675	58.6080586081	20.5406176017
6	25.0490847319	461.538461538	20.2542773323
6	76.2588244293	1978.02197802	15.4036219388
7	25525.1201172	0.0	154.039442664
7	732.778394712	58.6080586081	15.5063980768
7	177.777112087	183.15018315	30.9793830534
7	35.5898543031	512.820512821	12.8440069341
7	6.65254217016	1970.6959707	10.1317134936

Figure 13: This figure shows the information that gets saved for maxima found in the data from the power spectral density of the BPMs.

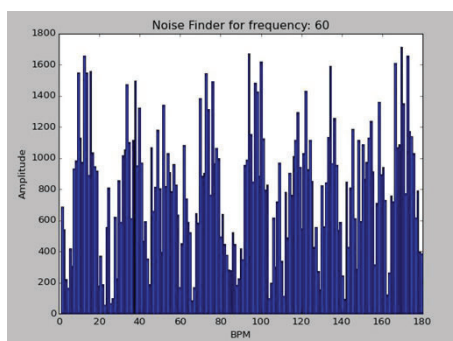


Figure 14 (a): These are graphs of my noise finding algorithm. Here we are looking at the full storage ring (BPM by BPM) at the specific frequency 60 Hz.

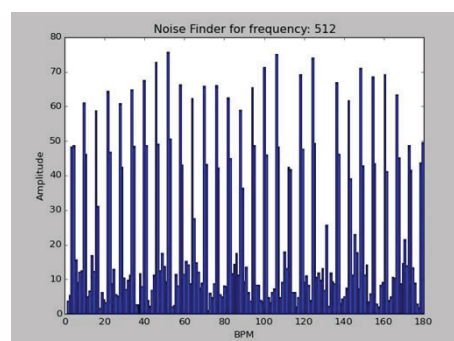


Figure 14 (b): Here we are looking at the full storage ring (BPM by BPM) at the specific frequency 512 Hz.

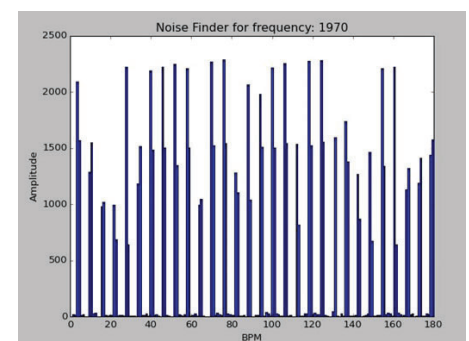


Figure 14 (c): Here we are looking at the full storage ring (BPM by BPM) at the specific frequency 1970 Hz.

V. Acknowledgments

I would like to thank my mentor Timur Shaftan for his guidance and support throughout my entire two summers here at Brookhaven National Laboratory. He has taught me so much and has helped prepare me for a professional future in the research industry. I would also like to thank Reid Smith and Guimei Wang for their assistance in testing my program for accuracy as well as being readily available to answer any and all of my questions.

This project was supported in part by the U.S. Department of Energy, Office of Science, and Office of Workforce Development for Teachers and Scientists (WDTS) under the Science Undergraduate Laboratory Internships Program (SULI).

VI. References

- ¹Bruel & Kjaer. *PSD (Power spectral density) - description*. n.d. June 2016.
- ²Emery, L. *Advanced Photon Source Storage Ring Orbit Correction Overview*. 4 December 2002. June 2016.
- ³MIT. *Chapter 10: Power Spectral Density*. n.d. June 2016.
- ⁴Sahoo, Gajendra Kumar. *Ground Motion*. n.d. June 2016.
- ⁵Y. Tian, et al. "NLSL-II Fast Orbit Feedback System." *Proceedings of ICALEPCS2015 - Pre-Press Release*. Melbourne, 2015.

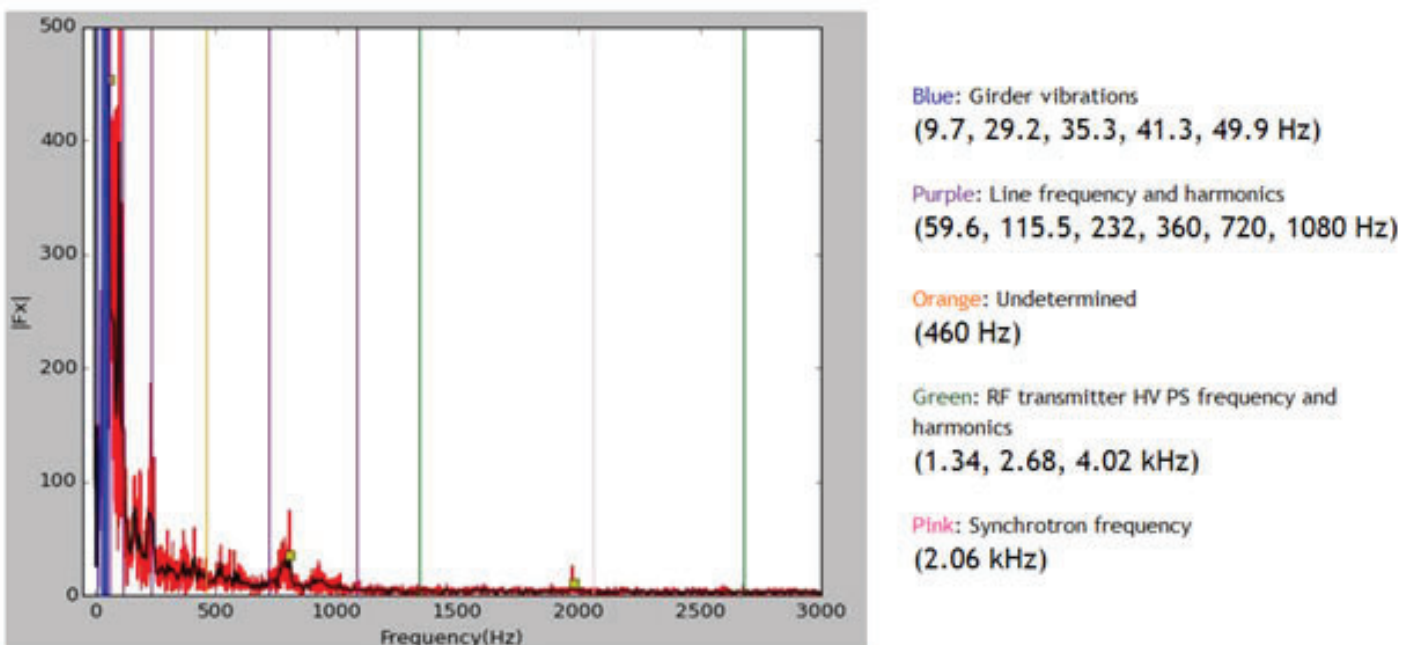


Figure 15: Here is a graph of the FFT from (Figure 2) with known frequencies labeled by color indicating their noise sources.

Pulsed reactant in-situ studies of copper doped ceria redox catalysis for CO oxidation using DRIFTS, XRD, and PSD

Shane Michtavy

Chemistry Department, Monroe Community College, Rochester, New York, 14623

Jose Rodriguez

Chemistry Department, Brookhaven National Laboratory, Upton, New York, 11973

Abstract:

The structural and mechanistic properties of copper doped ceria (CuO/CeO_2) being used to oxidize CO were analyzed by simultaneous in situ Powder X-ray Diffraction (PXRD) and Diffuse Reflectance Infrared Fourier Transform Spectroscopy (DRIFTS). The diffraction data was processed using Phase Sensitive Detection (PSD). A residual gas analyzer (RGA) was used to probe the presence of reactant and product gases. The reactivity of the CuO/CeO_2 was examined through pulsing CO and O₂ gases (5% concentration, balance He), giving insight of specific $\text{CuO} \leftrightarrow \text{CeO}_2$ interactions that favor CO oxidation catalysis. Pulsing of CO and O₂ reactant gases over the CuO/CeO_2 catalyst under isothermal conditions gave insight into the kinetics of the reaction process and the relationship between the redox behavior of CuO/CeO_2 and the catalytic production of CO₂. The use of PSD, RGA, and simple time conversions, helped produce evidence of the phase-transition intermediates starting from CuO transitioning to Cu₂O and finally to metallic Cu $\{\text{CuO} \rightarrow \text{Cu}_2\text{O} \rightarrow \text{Cu}(0)\}$ on the surface of the catalyst during pulses. The DRIFTS data further confirm this relationship, and in addition provides information about intermediates not easily seen through the previously mentioned methods which may play a role in the oxidation as well. This investigation gives a more complete understanding of the copper doped ceria's synergetic catalytic properties and may aid in the understanding of metal-oxide, redox catalysis a/cross the field.

I. Introduction/Background

Carbon monoxide (CO) present in reformat gas feeds has been found to eventually degrade the performance of many catalysts used in industrial applications. The selective oxidation of CO to produce carbon dioxide (CO₂) would lead to increased longevity and efficiency of the catalyst. Optimizing CO oxidation offers the ability to meet demands in efforts towards minimizing pollution as well as enabling more efficient and cleaner energy production such as hydrogen. Fuel cells which offer an alternative to internal combustion engines using hydrogen rich gas mixtures

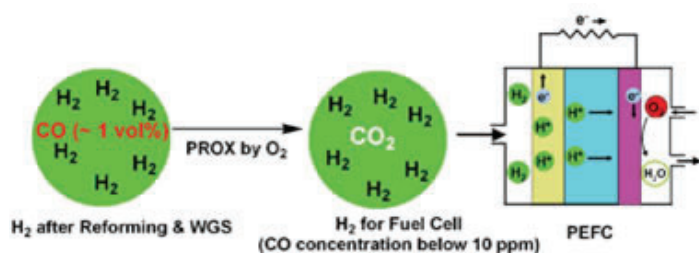
produced from steam reforming with concentrations of even 1-2 vol% of CO present, poisons the electrode. With precious metals like platinum commonly used as the catalyst in the reaction recently seen pricing at \$1,158.00 an ounce, the development of a cost effective and efficient catalysts is essential for enabling promising reactions such as CO oxidation and the Water-gas Shift ($\text{CO} + \text{H}_2\text{O} \rightarrow \text{CO}_2 + \text{H}_2$). This shifts a notable amount of attention to other transition metals and their oxides.

The defined role of the catalyst is to lower the necessary energy for the reaction to occur, in doing so speeding up the reaction, and all without the compound being consumed in the reaction. Most industrial catalyzed reactions are heterogeneous and have respective key traits. A distinctive positive aspect of hetero vs. homogenous catalysis in industry is ease in separation of product from the catalyst. Also, maximizing surface area and the ability for the catalyst to be fixed in place are attributing factors to the reactions efficiency and selectivity.

Copper doped ceria (CuO/CeO_2) has shown 100% CO to CO₂ conversion at temperatures of 150 degrees and shows a much higher selectivity than even commercial catalysts such as Pt/Al₂O₃. Cu is used for its catalytic activity in many reactions including CO oxidation ($2\text{CO} + \text{O}_2 \rightarrow 2\text{CO}_2$), CO oxidation under H₂-rich steam (CO-PROX), methanol synthesis ($\text{CO} + \text{H}_2 \rightarrow \text{CH}_3\text{OH}$) and the Water-Gas Shift (WGS: $\text{CO} + \text{H}_2\text{O} \rightarrow \text{CO}_2 + \text{H}_2$). Cu proven ability to convert CO is what attracted the exploitation of its properties over oxides as typically found in industrial processes like Al₂O₃. The reason in the decision to explore CuO on the ceria (CeO_2) is due to ceria's unique properties for ready reducibility, oxygen storage, and its distinctive ability to anchor Cu resulting in its lesser tendency to sinter. These properties holds reason towards its valued selectivity. CuO supported on CeO_2 has attracted attention for research and application across the board for CO oxidation and preferential CO-PROX.

Active sites have been located at the interface between the ceria and CuO nanoparticles.

Also in earlier studies using X-ray Diffraction (XRD) experiments observations of partially reduced ceria ($\text{Ce}^{4+} \rightarrow \text{Ce}^{3+}$) showed at the same time CuO was reduced to Cu(0). In order to gain more insight to the more active components in the unsteady state of the catalyst, pulsing technique was used for perturbation. Because of the complex nature of the catalytic reaction dynamic in situ observation was necessary.



Example h₂ gas mix used of fuel cell.

Determining the fluorescence quantum yield of a water-based liquid scintillator

Henry J. Nelson

Department of Physics, Grinnell College, Grinnell, IA 50112

Lindsey Bignell and David Jaffe

Department of Physics, Brookhaven National Laboratory, Upton, NY 11973

Abstract

Particle detectors that study weak interactions must contain large amounts of a detection medium to produce a large enough event rate for research purposes. While water and liquid scintillators (LS) are both effective detection media, there is still no cost effective alternative that combines the angular resolution of water with the sensitivity of LS to low energy interactions. Brookhaven National Laboratory (BNL) is developing a water-based liquid scintillator (WbLS) that combines the two in order to bridge this gap. The purpose of this research is to determine the fluorescence quantum yield or re-emission probability (RP) of WbLS in order to investigate its effectiveness as a detection medium. To find the RP we make both absolute measurements of the RP as well as relative measurements comparing the WbLS to standard solutions whose RP are well known. Our preliminary results suggest this is a viable method of measurement, but more testing is needed to produce quantitative results. Once results are obtained, this information will be crucial to constructing models of WbLS to predict how it will perform in large-scale particle detectors. Using the information obtained in this study, it will be possible to determine what aspects of the WbLS require more development and it may even be used in the next generation of particle detectors allowing benefits over current water and LS detectors.

I. Introduction

In order to model how WbLS will behave in large scale detectors and to evaluate whether or not it will be an effective detection medium, the quantum yield must be accurately known. Quantum yield is the number of events triggered by each absorbed photon. In this context, the event we are looking for is the emission of a photon meaning that quantum yield is equivalent to the emission efficiency or re-emission probability. In particle detectors, the motion of an energetic particle produces photons either through Cherenkov radiation or by transferring energy to the medium which may then fluoresce. The light given off from these processes can then be detected by photomultiplier tubes (PMTs) giving evidence that a particle passed through our detector. Since WbLS is a mixture of a few different things, it would be helpful to measure the quantum yield of each component independently so that we can have some idea of how the resulting quantum yield will change if we change the concentration of one of the components as WbLS is still in development.

As with any process that requires the counting of small events like photon absorption or photon emission, this becomes difficult as systematic and equipment biases are very significant and must thus be accounted for. To ensure then that our measurements of WbLS are accurate we will first make these measurements for simpler scintillators and the components of WbLS whose quan-

tum yields are already well known. This will allow us to validate our equipment and methodology before testing WbLS to ensure the accuracy of our measurements.

II. Methods

To measure the quantum yield we utilize two different approaches: an absolute measurement and a relative measurement. Both measurement techniques are reasonably straightforward and are considered standard methods of measuring a quantum yield [1]. With both methods a fluorescence spectrometer is used as the main instrument for collecting data. A diagram of our fluorescence spectrometer setup is shown in figure 1. Since both methods involve the fluorescence spectrometer we first describe the methods and equipment corrections used with it. After that we fully describe each of the two methods in detail.

A. The fluorescence spectrometer

As can be seen in figure 1, the fluorescence spectrometer is made up of a Xenon lamp, three monochromators, a PMT, a standard sample container (box), a photo-diode, and an integrating sphere. These components are connected by a series of gates shown as small rectangles in the diagram with which the size of the opening in the gate may be set using an attached micrometer. The lines connecting to the integrating sphere are fiber optic cables.

The light generated in the Xenon lamp first passes through a series of two monochromators and gates (often called a double monochromator) in order to reduce the stray light level. It then enters the standard sample container where it encounters a beam splitter which redirects part of the beam onto a photo-diode to measure and correct for fluctuations in intensity caused by the lamp spectrum and power fluctuations. The rest of the beam continues on to the small sample stage in the standard sample container or integrating sphere where the sample is excited at the wavelength selected by the previous monochromators. Both the standard container and integrating sphere have a wavelength dependent response functions that must be accounted for. To do this, the manufacturer of the fluorescence spectrometer supplies a correction file that may be applied to data to remove this dependence. Light that is then emitted by the sample will pass through another monochromator to a PMT where the light is detected. The second monochromator allows us to know the wavelength of the light being detected by the PMT at a given setting, thus giving us the ability to record the emission spectra of samples.

In order to improve the accuracy of the measurements produced by the fluorescence spectrometer we calibrated the monochromators each time before taking measurements. Since there are differing light paths into the emission monochromator from the standard container or integrating sphere, each of these scenarios must be calibrated for separately and must be only used

independently because when the fluorescence spectrometer is calibrated for one, it is necessarily not calibrated for the other.

We begin by calibrating the emission monochromator. To this end an emission scan is taken of the fluorescent room lights in the lab. In order to scan the spectrum of the room lights the standard container lid is left slightly ajar when calibrating for that container while the fiber optic exiting the box is removed and faced upwards when calibrating for the sphere. In either case the resulting scan shows the spectrum of the fluorescent lights which have some stable features we can calibrate to. Many fluorescent lights contain Mercury (Hg) which when excited produces well known spectral lines in the wavelength range we will use. This allows us to identify these spectral lines in our scan and compare them to the accepted values to find the inaccuracies of this monochromator. For this purpose we use the three Hg lines shown in red in figure 2. A typical spectrum is shown on the plot as well. Once we know the differences between where we see the spectral lines and where they should be, the calibration of the emission monochromator can easily be produced.

We then use the calibrated emission monochromator to calibrate the double monochromator used to choose the excitation wavelength. To do this, at least three wavelengths are chosen in the range we wish to calibrate and these are used as the excitation wavelengths for three emission scans. Since we know the wavelength that the excitation monochromators were set to and that the emission monochromator is accurate, we are able to see how the wavelengths seen in these scans differ from the excitation setting and calibrate to correct for any discrepancy. After calibration, the instrument typically gets a much stronger signal as even a correc-

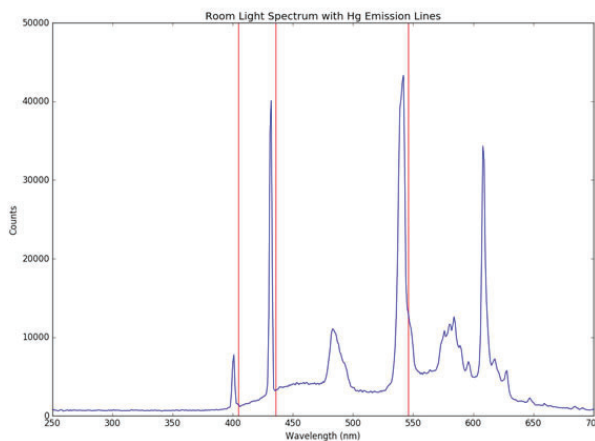


Figure 2: Spectrum of fluorescent lights with marks of Hg emission lines

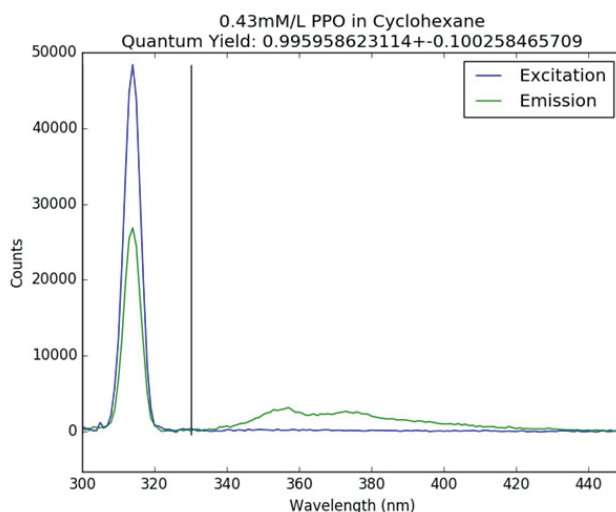


Figure 3: Fluorescence spectra used to determine an absolute quantum yield

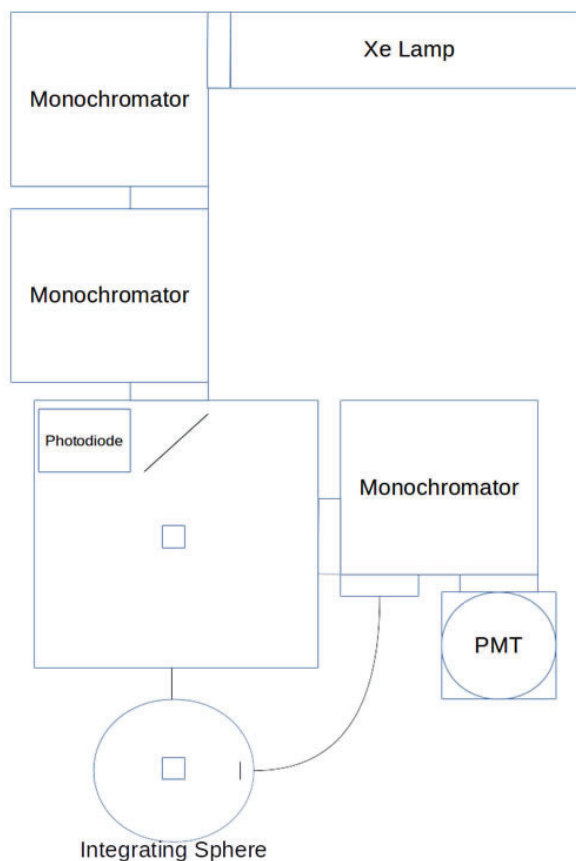


Figure 1: Diagram of the fluorescence spectrometer and its components.

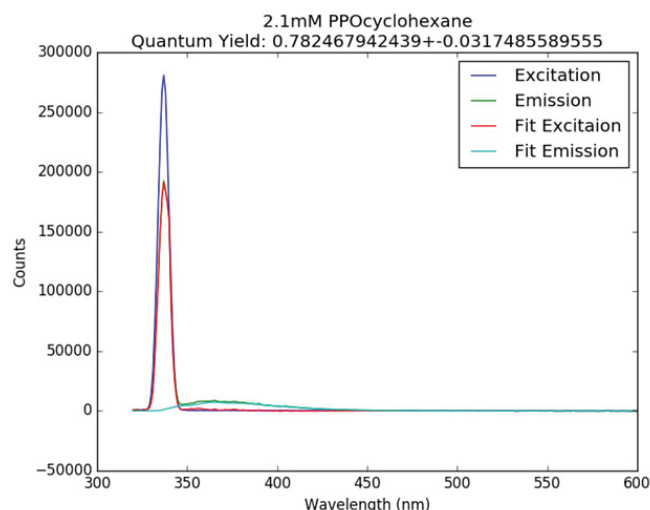


Figure 4: Fluorescence spectra used for absolute measurement with overlapping peaks

tion of 2nm can increase the number of counts at a given wavelength setting by a factor of 2-3. We next move on to correcting other inaccuracies in the fluorescence spectrometer.

As was mentioned previously, the box and sphere have wavelength dependent transfer functions which must be corrected for in order to obtain accurate data. It was noticed though that the files provided by the manufacturer did not produce a constant, flat signal as was expected. For this reason, we attempted to produce our own correction files but we were unable to produce one that performed better than those provided by the manufacturer so we continued using the provided corrections. During this investigation, however, we did learn that the changing of slit widths in the gates effected the signal enough where the corrections should take this into account while they are currently independent of them. We have thus contacted the manufacturer to inquire about what slit-widths the correction file is for in order to make sure our measurements are accurate but we still have not heard back. Because it matters so much then what corrections we use, the 'ExCorr' correction and a gain of 6.8V are used for all scans while 'emcorri' and 'emcorr-sphere-quanta' are used for box scans and sphere scans respectively. The slit widths used were either 2mm for excitation and 1mm emission or 1mm excitation and 0.5mm emission depending on the nature of the scan. Slits that are narrower improve the wavelength resolution of the instrument but also allow fewer photons to pass through resulting in a diminished signal.

B. Absolute Measurements

Measuring absolute quantum yield requires an instrument known as an integrating sphere which is shown as part of the fluorescence spectrometer in figure 1. This instrument reflects light uniformly in all directions inside the sphere in order to get a measurement of all the light given off by the sample. With the sample we want to measure inside the integrating sphere, we take emission scans of both the scintillator solution and a pure sample of the solvent at the same excitation wavelength. We can then compare these two scans to see the number of photons absorbed (on the excitation peak) and the number of photons emitted (on the emission peak). This is done by taking the integral of the difference of the two curves. We are then able to calculate the quantum yield by taking the ratio of these quantities because re-emission probability is the number of photons emitted per photon absorbed.

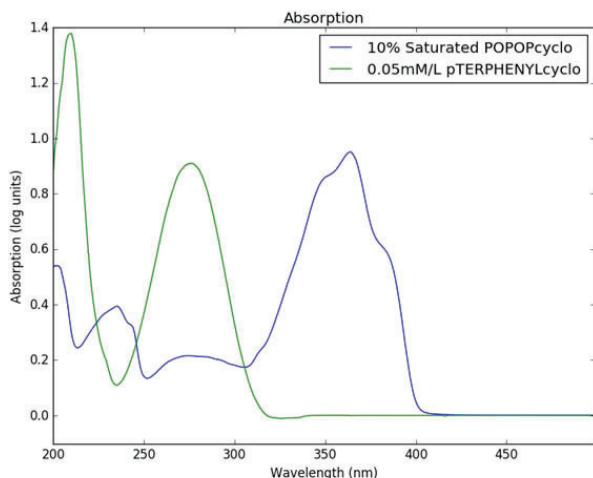


Figure 5: Two absorption spectra with intersecting points where a measurement may be done.

A plot of the two required measurements for one tested sample are shown in figure 3. The black vertical bar separates the excitation area on the left from the emission area on the right.

As can be seen in figure 3, we are fortunate in this case that the excitation and emission peaks are so far apart, but this is not always the case. Sometimes they overlap making it difficult to separate the peaks. To combat the problem of overlapping excitation and emission peaks, a third scan can be taken. This scan is taken from the standard sample chamber meaning the excitation peak is severely diminished as any light not going straight out the exit gate of the box is quickly absorbed. We then fit this signal to our original scan to achieve a good approximation of the emission peak which we can then subtract from the sample scan to get the excitation peak as well. A plot using this method is shown in figure 4.

Overall, the absolute method is extremely straightforward but is also incredibly prone to error. This propensity for error could come from a variety of sources such as the response functions described earlier, difficulty in separating excitation and emission peaks, or the small number of photons used for each measurement. To get around some of these difficulties we can also do a different kind of measurement.

C. Relative Measurements

When measuring the relative quantum yield, we make measurements in relation to a standard whose quantum yield is well known. To make a relative measurement we measure the emission spectrum (photons emitted), absorbance (A), and index of refraction (n) of both the sample we would like to measure and the standard at a given wavelength. We can then plug these values into the formula shown below in order to calculate the quantum yield of our sample [2]. In equation 1, values with the R subscript are for the standard and all the others are for the test sample.

$$\Phi = \Phi_R \frac{\text{photons emitted} (1 - 10^{-A_R}) n^2}{\text{photons emitted}_R (1 - 10^{-A}) n_R^2} \quad \text{Eq. 1}$$

Since values of absorbance can differ greatly, we measure the absorption spectra of both the standard and the test sample and choose a wavelength at which to measure all the other parameters such that the absorbance values of the two are as close as possible. To do this we use an absorption spectrometer and record the absorbance values for a wide wavelength range and look for wavelengths where the two absorption spectra intersect. An example of these absorption spectra is shown in figure 5.

Once we know the wavelength to use we can then measure the emission spectra and index of refraction at this wavelength and plug these into the formula to calculate the quantum yield.

Because we are comparing data from one instrument to another, we must know the difference between wavelengths measured with either system if one exists. To know the wavelength scale difference between the absorption spectrometer and fluorescence spectrometer, we take a scan of a bandpass filter. In the absorption spectrometer the bandpass filter is placed in the measurement beam line directly covering the light source and a measurement was taken, results shown in figure 8. Similarly, in the fluorescence spectrometer we place the filter inside the standard sample container directly covering the aperture allowing light into the box (before the beam splitter). We can then scan through wavelengths with the excitation monochromator and track the signal of the photo-diode. The signal from the photo-diode is used as it is not

effected by the emission monochromator and thus produces a much cleaner signal. This signal is shown in figure 7. We can then compare these scans to find the relative wavelength difference.

In the future, a bandpass filter with a narrower band should be used as in our data it is not precisely clear where the center of the passing band is so simply the average of a fitted Gaussian was used and compared with the other system.

III. General Methodology

While the previous two methods are relatively straightforward, because we are essentially counting photons both methods are effected greatly by instrumentation error. In order to be confident in the accuracy of our measurements we must validate our instruments and methods. To do this, we measure the quantum yield of a few scintillators whose quantum yield is well known using both methods. If we are able to accurately measure the quantum yield of our standards then it means that our measurements of WbLS and its components will also be accurate. Since the relative measurements are slightly less sensitive to minute errors, these were favored when making measurements for validation and results.

In general, the solutions we are able to measure with these methods must be very dilute. The samples being extremely dilute helps us to avoid certain sources of error and allows us to make a few simplifying assumptions. If the samples are very dilute we mostly avoid quenching by re-absorption or self-absorption which allows us to disregard these effects. Also, if solutions are dilute enough, the index of refraction of the solution is approximately the index of refraction of just the solvent which can typically be found to a higher accuracy than we could measure. Having a low concentration of scintillators also makes the absorption measurements easier as with higher concentrations the signal on the absorption spectrometer often saturates and thus does not produce accurate values.

IV. Difficulties

As we have pointed out, many aspects of these measurements are hard to accomplish accurately. This section lists a few of the problems we encountered in hopes that others can avoid them in the future. The most common problem we encountered

was sample contamination. Because each of the samples must be put in the same cuvette when being scanned in both the fluorescence and absorption spectrometer, contamination is likely unless the cuvette is thoroughly washed. It was often helpful to compare a measurement to previously published spectra of the same substance to check for consistency and avoid working with contaminated samples [3]. Towards the end of our project we started using sealable cuvettes with a screw top so that we no longer had to move a sample between containers as often and could simply leave it in the same container for all tests which seemed to help with the contamination problem. At one point, the Xe lamp in our fluorescence spectrometer began to fail and drew power inconsistently. This caused the intensity of the lamp to fluctuate wildly (by 70-80%) so that even the photo-diode signal could not compensate and the fluctuations became apparent in our measurements. This problem was remedied after the lamp was replaced. In another instance, it appeared that the fluorescence spectrometer was contaminated as it seemed to give an emission signal with no sample in the chamber. In the end though, the signal we were seeing was simply Raman scattering which had produced peaks and then those peaks had been spread out through the wavelength range by scattering through the solvent.

V. Results

So far, we have only been able to partially validate our equipment and methods. While we hope to eventually validate with three to four standards we have thus far only completed a preliminary estimate of one, 2,5-Diphenyloxazole (PPO) in ethanol. To do this measurement we used the relative method and compared it against 1,4-Bis(2-methylstyryl)benzene (Bis-MSB) in Linear Alkyl Benzene (LAB) at a few different wavelengths. A plot of these results is shown in figure 8 along with the same value determined in a different study [4].

As can be seen in figure 8, there does appear to be a slight wavelength dependence although with three data points it is difficult to be certain. We do expect to see some dependence on wavelength as a higher excitation wavelength means lower energy photons and thus less energy absorbed by the sample. From this plot we can also see that the uncertainty ranges of the reference [4] and our measurements do overlap so they are reasonably close. It will,

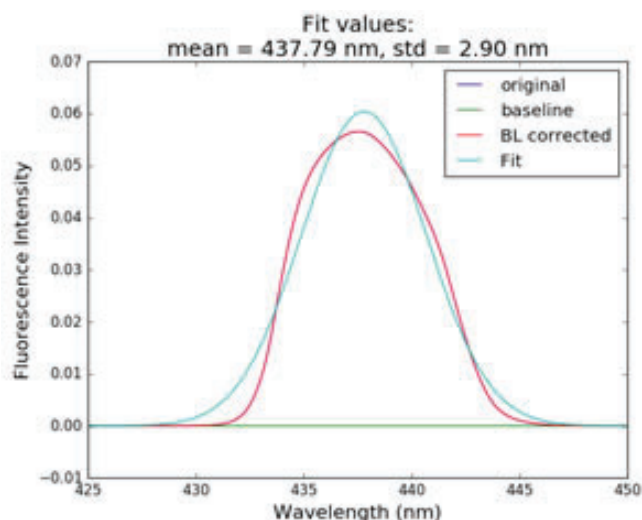
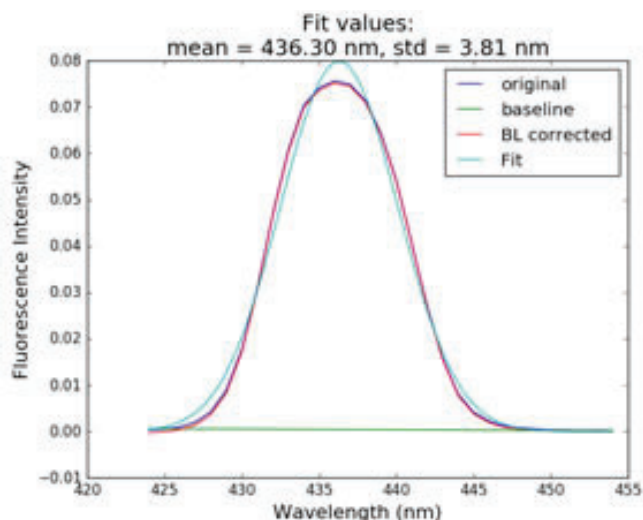


Figure 6 (left) and 7 (right): The transmittance of the bandpass filter in the fluorescence spectrometer and absorption spectrometer on the left and right respectively. A Gaussian was fitted to each in order to determine the mean value.

however, require a few more reference samples to be measured and a few trials of each to test reproducibility before we can say satisfactorily that our equipment and methods are validated.

VI. Future work

In the future, we will continue to measure more quantum yield standards to fully validate our equipment and methods while trying to refine our accuracy. Once the setup has been validated, we will use this same process to measure the quantum yield of each component of WbLS independently as well as measuring the quantum yield of WbLS itself. This means we will make quantum yield measurements of LAB, PPO, Bis-MSB, and the surfactant used in producing WbLS. After all of these measurements, WbLS may be optimized further and tested in simulations of large-scale particle detectors.

VII. Acknowledgements

I would like to thank Dr. Minfang Yeh and Richard Rosero for the use of their lab space, equipment, and time in helping with this project.

I would also like to thank Lauren Capelluto for her previous work in this area with the same equipment which provided a solid foundation for this work.

This project was supported in part by the U.S. Department of Energy, Office of Science, Office of Workforce Development for Teachers and Scientists (WDTS) under the Science Undergraduate Laboratory Internships Program (SULI).

VIII. References

- ¹Wurth et al., Relative and absolute determination of fluorescence quantum yields of transparent samples, 18 July 2013, doi:10.1038/nprot.2013.087
- ²Albert M. Brouwer, Standards for photoluminescence quantum yield measurements in solution, Pure Appl. Chem., Vol. 83, No 12
- ³Scott Prahl, Oregon Medical Laser Center (OMLC), August 2016 <http://omlc.org/spectra/PhotochemCAD/html/020.htm>
- ⁴Berlman, Handbook of Fluorescence Spectra of Aromatic Molecules, Academic Press (1971)

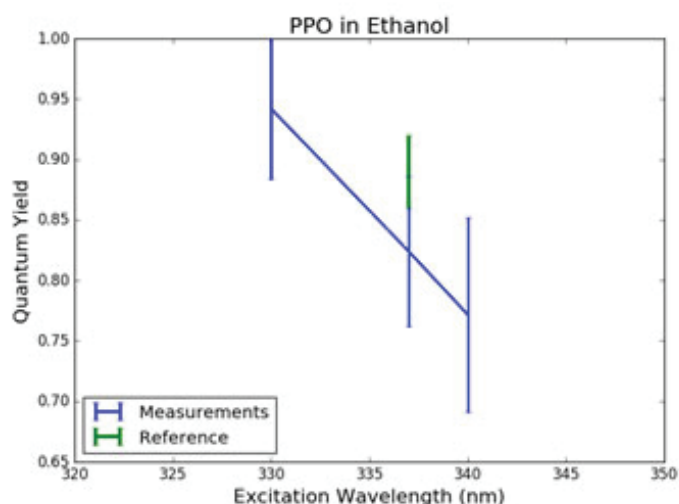


Figure 8: Quantum yield measurements of PPO in Ethanol (part of the validation set).

Imaging ultrafast single photon events using the Timepix camera

Jayke Nguyen

University of California – Davis, Davis, CA 95616

Andrei Nomerotski

Brookhaven National Laboratory, Upton, NY 11973

ABSTRACT

The Timepix camera is an ultrafast optical imager capable of 50 MHz readout speeds (20ns timing resolution) with high quantum efficiency between the 500nm-850nm wavelength range. Similar cameras have been limited to less than 1MHz readout speeds (1 μ s timing resolution). Each pixel on the Timepix sensor requires 1,000 photons to trigger an event; however, by utilizing an image intensifier, Timepix can become sensitive to single photons. Using a combination of a photocathode, a two-stage microchannel plate, and a phosphor screen, photons incident on the entrance window are multiplied to produce thousands of photons upon exiting the image intensifier. The triggered pixels hold information on the time that they were triggered, storing information on “timecodes.” Using timecode measurements, novel methods were used to construct a pipeline for data reduction and analysis. Furthermore, I performed a thorough characterization of the upgraded Timepix system. The extreme sensitivity of the new Timepix system allows for expanded applications in ultralow light regimes, but requires that the system be placed in complete darkness to ensure the image intensifier is not damaged. The system was upgraded with single photon detection capabilities for experiments at Stony Brook University using entangled photon pairs. By studying the Timepix camera, I have learned useful data analysis techniques in addition to expanding my Python programming experience

I. BACKGROUND

Ultimately, the greatest limitation of the ultrafast Timepix camera is its lack of sensitivity to light. The bump bonded silicon sensor requires, at minimum, 1000 photons to trigger a single hit. To rectify this, an image intensifier can be used with the system. These devices are commonly used in low-light imaging. The typical drawbacks for an image intensifier are its monochromatic output, high voltage requirements, and low quantum efficiency. However, in the Timepix setup, using an image intensifier comes at little cost to the efficacy of the system.

II. METHODS

The Timepix camera uses a 50mm f/1.2 Canon lens focused on the phosphor screen of the image intensifier. The front photocathode was covered, with only a small opening 2 millimeters in diameter as a cutout for incident light. This is to reduce the total number of photons incident on the photocathode. The test source is a red LED that is pulsed in sync with a trigger signal that activates the camera shutter. This system ensures that the camera is only activated when the source emits light. Data is offloaded via USB connection from the camera to a laptop.

Each pixel of the Timepix sensor records the timecode of when the pixel was first triggered. Each timecode corresponds to

20 nanoseconds. A limitation of Timepix is that once a pixel is hit and activated, the same pixel cannot take another reading until a new frame is started. However, this should not impact the study.

It should be noted that the image intensifier is extremely sensitive to light. Because of this, only very low light sources were used with the image intensifier. Furthermore, any sources of ambient light are also amplified by the image intensifier, therefore making the system more susceptible to noise from external sources. To combat this, the system was enclosed in a dark box sealed with tape and covered with a black cloth, blocking any external sources in the visible to infrared ranges.

In general runs were about 500-5000 frames, depending on the statistics needed. For example, low LED voltages tended to have fewer hit pixels on the sensor (due to less incident light), and therefore required more frames to increase the statistical certainty of the measurement. Similarly, high LED voltages required less frames due to the high number of hit pixels.

For the main dataset, the red LED is pulsed at 200 Hz, but the voltage was changed from 0v to 10v in increments of 1v for

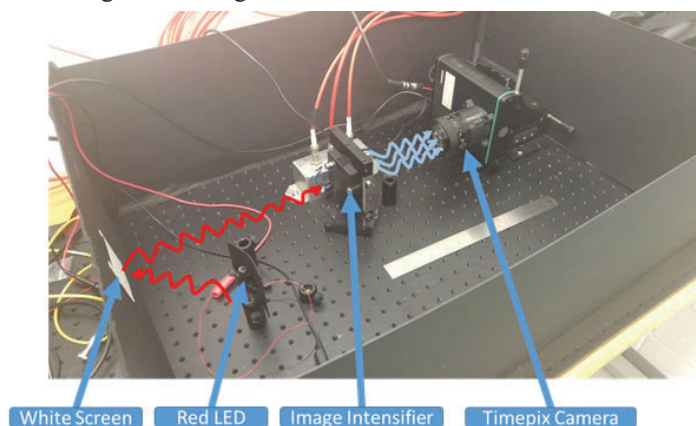


FIG. 1. General setup of the experiment.

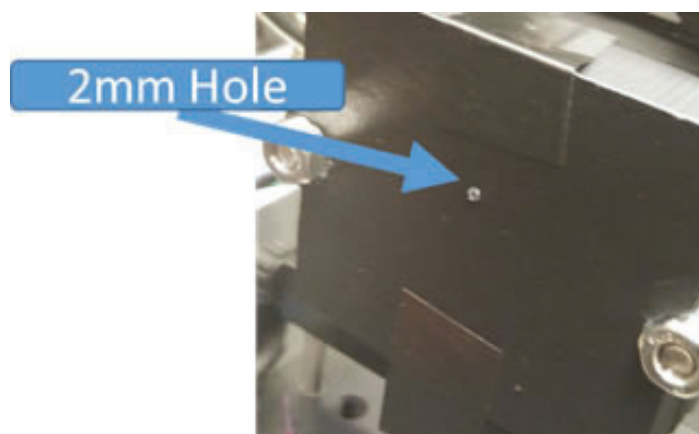


FIG. 2. Image of the small cutout on the PhC screen side of the image intensifier.

each run. Other data was taken that explored changing the gain of the system, running the LED at extremely low voltages, and completely uncovering the photocathode.

Data was analyzed and graphed using purpose-written Python code. A sizeable Python module was specially written to handle Timepix data. Functions included in the module helped consolidate data, automate graphing, and find clusters.

The cluster finding algorithm checks for adjacent activated pixels in a single frame of data. Figure 4 displays example results of the cluster finding algorithm. For our purposes, looking at cluster data was much more useful than looking at individual pixels. Timecode measurements were not the main result we were analyzing in this study, but are a main aspect of the abilities of the Timepix camera.

III. DATA AND RESULTS

Figure 5 shows the photon transfer curve that was generated. At voltages from 0v to 3v, the PTC curve is linear with a slope of roughly one. Additionally, figure 6 was created to display Poissonian distributions overlaid with the cluster distribution, corresponding to the first four points on the PTC curve. These two figures show that the data is indeed Poissonian, as expected. Therefore, the statistics show that at low voltages we are seeing single photon hits, not simply noise. If significant noise were present, we would expect a super-Poissonian distribution.

The low noise can be attributed to the surprisingly powerful effect of synchronizing the light source and the trigger for the camera. This synchronization means that the timecode of the pixels can show which photons were in sync with the generator. Additionally, noise is further reduced by removing the hits that aren't inside the pre-selected timecode window. However, as evidenced by figure 7, only at lower voltages, does the timecode window



FIG. 3. Single frame hits corresponding to a specific LED voltage.

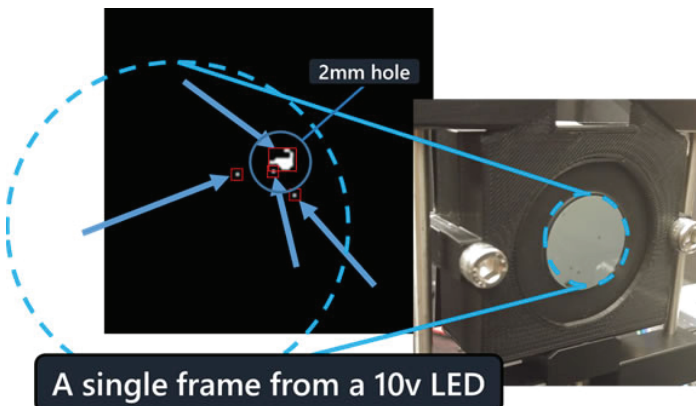


FIG. 4. Results of the cluster finding algorithm are pointed to in red boxes. The blue outline is the approximate size of the image intensifier phosphor screen on the Timepix sensor.

play a significant role. At higher voltages, out of sync photons are far less than one percent of recorded pixels.

Further characterization shows the relationship between the voltage and the cluster size, and the relationship between the voltage and the number of pixel hits. In both instances the cluster size increases and the number of pixels also increases as you increase voltage. A notable feature is the point of saturation in figure 8, where the average of the number of clusters per frame seems to increase at low to middle voltages, then decrease and flatten at high voltages. The hole (corresponding to the cutout on the cover) is saturated, and the size of that particular cluster does not change much from frame to frame.

Further exploration of the parameter space was done by varying the three voltages applied to the image intensifier with an LED run at 5v as the light source. Figure 11 shows a various measures of performance after changing three variables: microchannel plate (MCP) voltage, microchannel-photocathode voltage (MCP-PhC) voltage, and phosphor screen (P47) voltage. As expected, as the

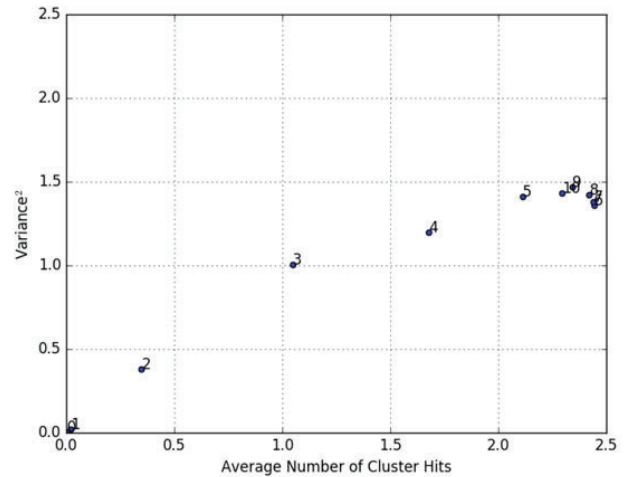


FIG. 5. Photon Transfer Curve (PTC) generated from collected data.

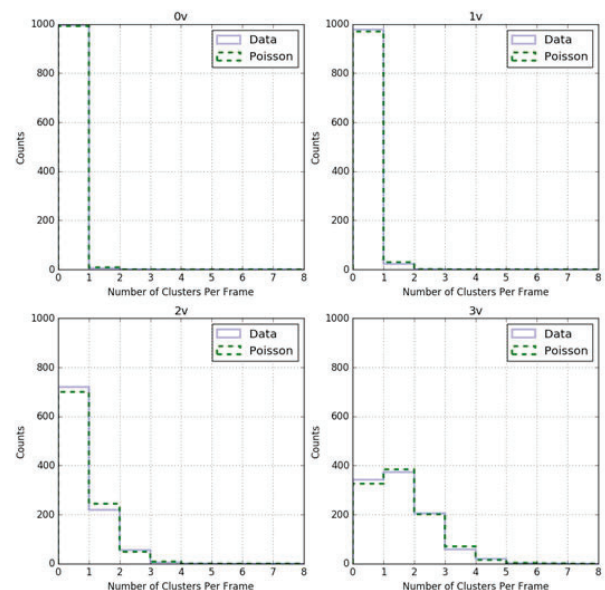


FIG. 6. Histogram of number of clusters, overlaid with a random Poissonian distribution with the same mean.

MCP voltage increases, the average across all measures increases. Increasing the MCP voltage is effectively increasing the gain of the image intensifier. Furthermore, decreasing the MCP-PhC and P47 voltage decreases the gain. This dataset was taken to confirm expected trends and presents no surprising results. It serves as a qualitative analysis of the image intensifier parameter space.

Lastly, figures 12-23 is another analysis of the dataset taken for the PTC curve. In this format, three measures of performance are displayed: number of clusters per frame, cluster size per frame, and number of pixels per frame. The area under these graphs correspond to points on figures 8-10.

IV. CONCLUSION

By using an image intensifier, the Timepix camera can be reliably used with single-photon light sources. The pulsed source in tandem with the timecode window is proven to be an effective method for removing noise from the data. Some final tests are being done to determine the absolute dark noise of the system, but are not yet conclusive. Lastly, the Timepix camera used in this study is the first generation of camera. It is soon to be replaced by its third generation successor, but this study serves as a proving ground for the usage of image intensifiers with ultrahigh time resolution cameras.

V. ACKNOWLEDGEMENTS

I would like to thank my mentor Andrei Nomerotski for graciously allowing me to work on the Timepix project. This project was supported in part by the U.S. Department of Energy, Office of Science, Office of Workforce Development for Teachers and Scientists (WDTS) under the Science Undergraduate Laboratory Internships Program (SULI).

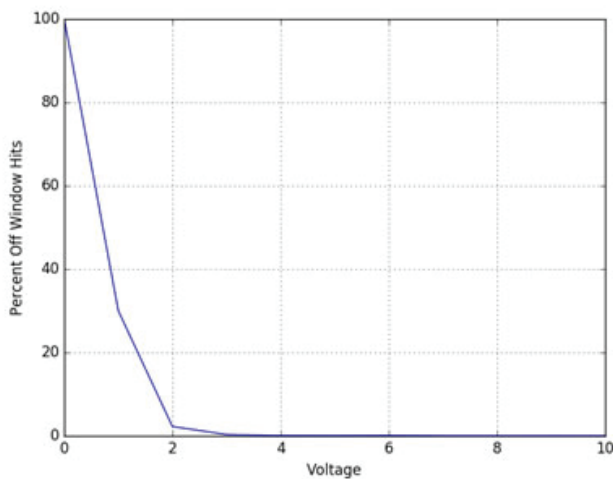


FIG. 7. Percentage of pixels not inside the predefined timecode window.

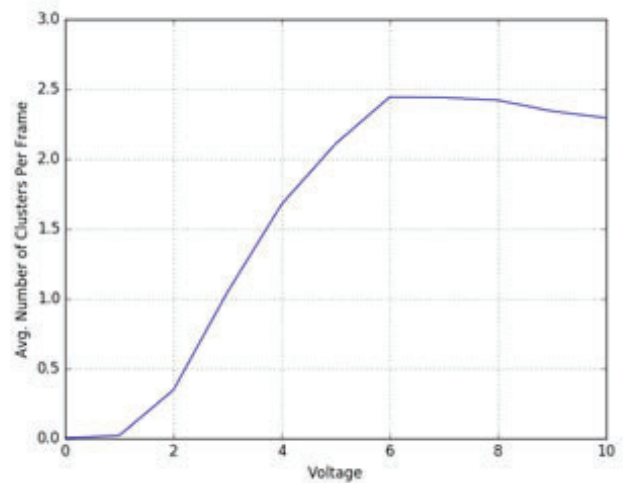


FIG. 8. Average Number of Clusters per frame vs. LED

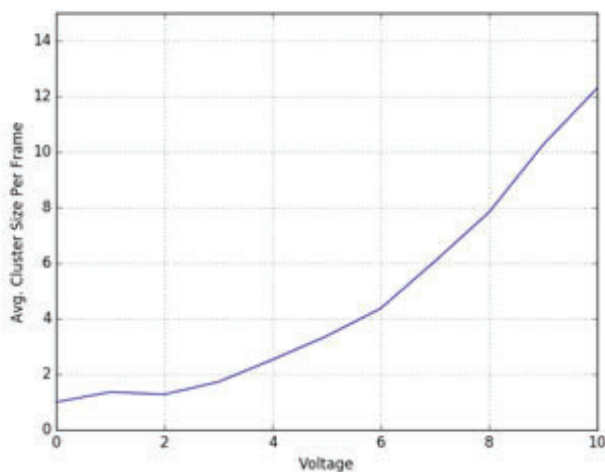


FIG. 9. Average Cluster Size Per Frame vs LED Voltage

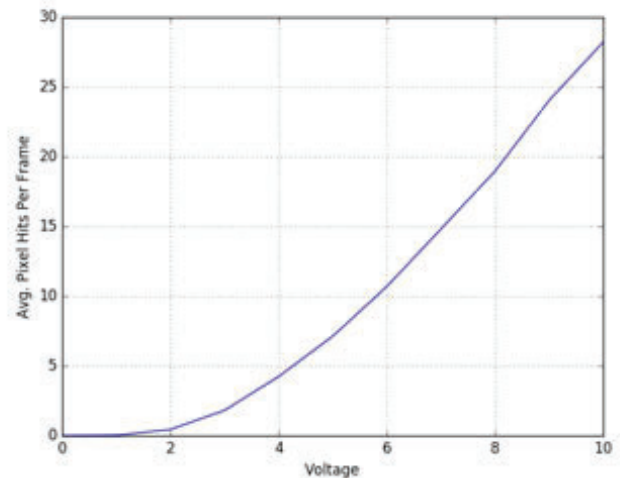


FIG. 10. Average Pixel Hits Per Frame vs. LED Voltage

VI. APPENDIX

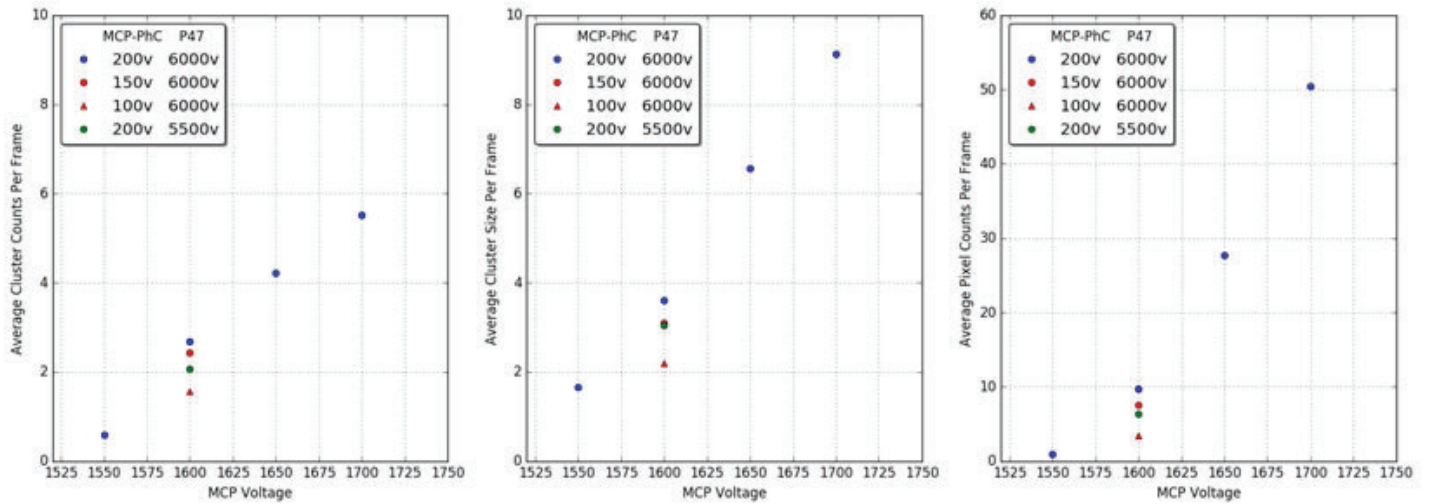
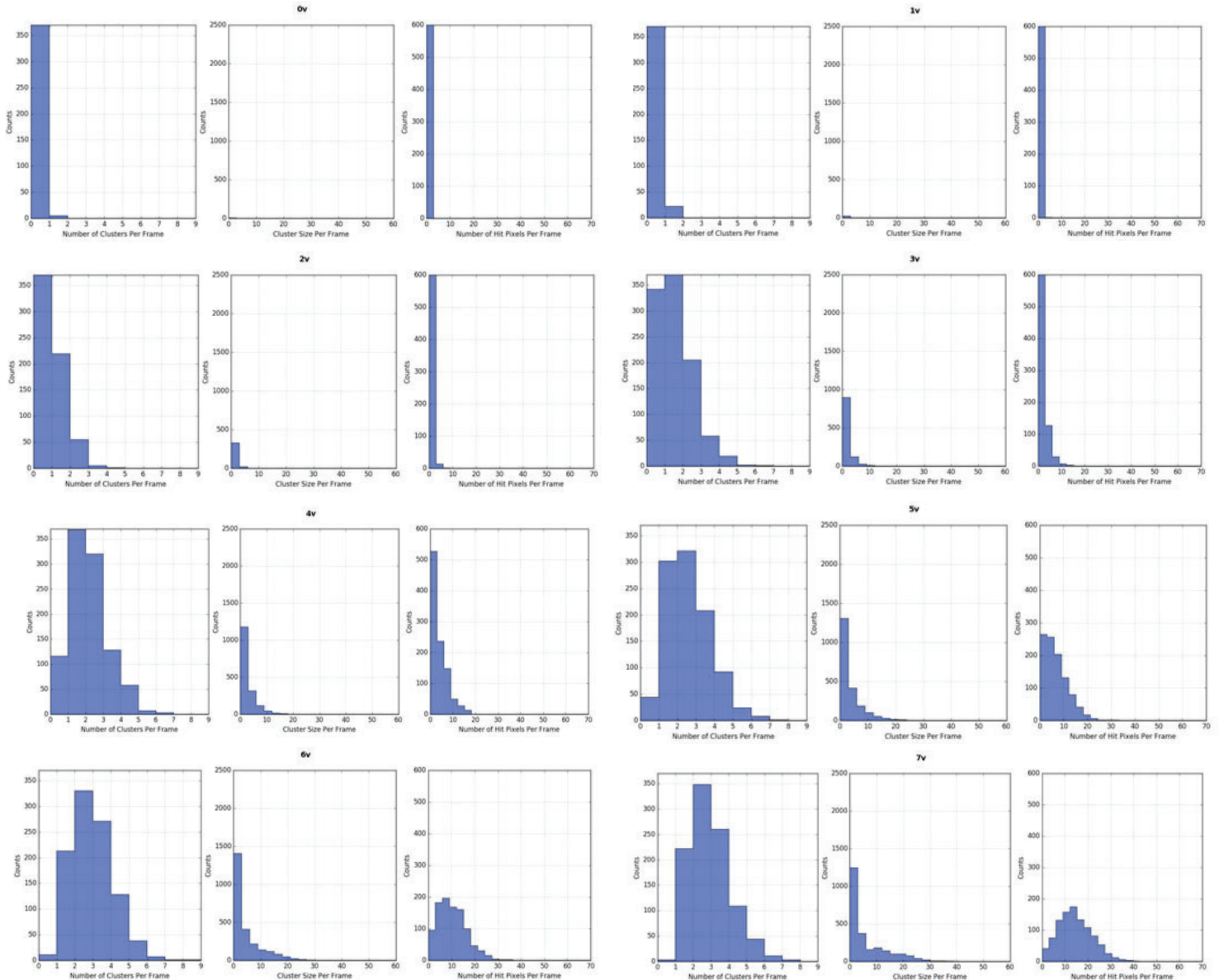
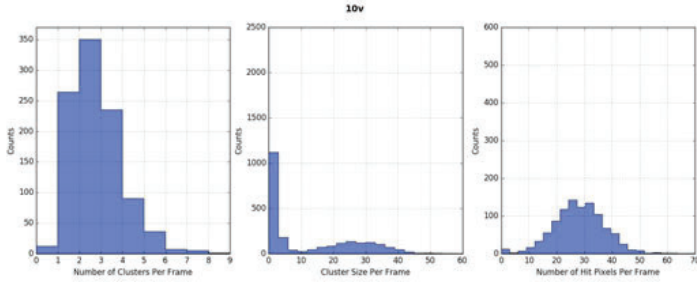
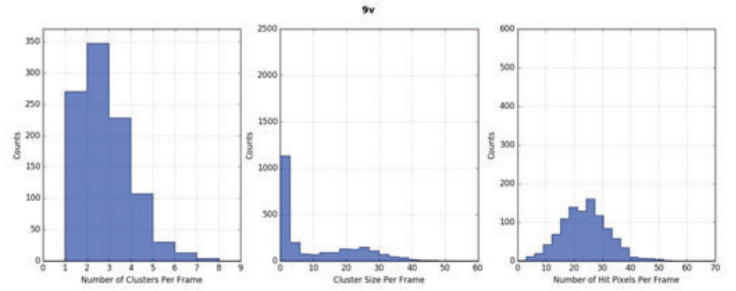
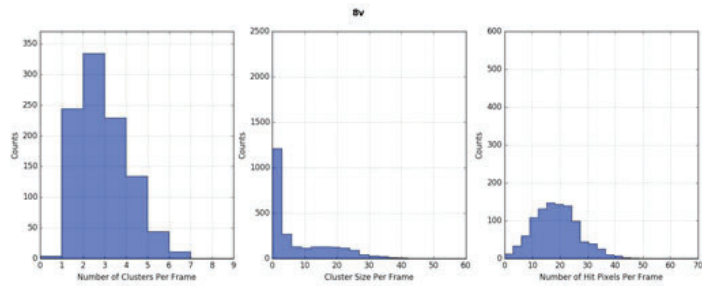


FIG. 11. Various averages vs. MCP Voltage. Light source was a 5v LED. Meant to explore how performance is affected by changing settings on the image intensifier.

FIGS. 12-22. Histogram of three measures of performance: number of clusters per frame, cluster size per frame, and number of pixels per frame. Titles correspond to LED voltage.





Analyzing photographs of solar flare on a fish-eye camera lens

John Pavacic

Environmental Sciences, long Island University, Brooklyn, NY 11201

John Heiser

Environmental and Climate Sciences, Brookhaven National Laboratory, Upton, NY 11793

I. Background and Project

Solar energy is a clean, replenishable source of power that is becoming more prevalent in today's fossil fuel dependent market. A solar farm is a large area of unshaded land that is covered with solar panels that harness the sun's energy. The more solar farms built the more need there is for solar forecasting accurate cloud coverage over the farms. Solar forecasting allows solar farms to be shut down on days that would not run efficiently and use another source of power to keep costs low. Solar forecasting uses algorithms to analyze clouds using cameras to see their size, shape, thickness, speed and other characteristics. This allows the forecaster to know what time it would be necessary to shut down the solar panels if a given day is going to be cloudy. My project designs a python script used for a FE-8391-v camera that takes snapshots of the sky at different exposure times and levels. The FE-8391-v is a regular security camera typically found on ceilings in stores and malls that track movement of people. Here we use the camera to look at clouds and take pictures using different exposure levels and times. The difference between the exposure level and time is that exposure time is the amount of time the camera takes the photo for, while exposure level is adjusted by a small aperture around the camera which closes and opens depending on how much light the user wants to be allowed. These pictures will focus directly on the movement of the sun and its interaction with clouds around it. The camera will try to focus on the sun flare which many of the cloud algorithms mistake as parts of cloud coverage in photographs. My camera will take photos of that sun flare which will be analyzed in another algorithm that identifies what is sun and what is cloud. When the sun brightens up the middle of the photograph it also darkens the horizon creating the dilemma of depicting what percent of the sky is covered in cloud.



The pictures can also be used to track the aerosol content in the air, a large solar glare means higher aerosol content, and smaller solar glare means lower aerosol content.

II. Setup of Camera

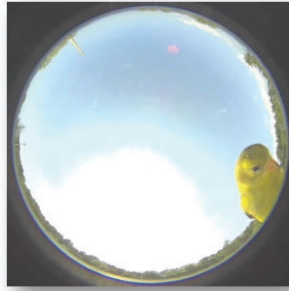
On top of building 490 my mentor and I created a stand that allows the camera to look directly at the sky without being moved.^[1] It is above anything that would block its view on the roof and it runs wires to a lab on the first floor of 490. The camera itself is powered through the subnet box of the lab and is accessed remotely using a VPN from my computer in building 815. In the picture you can see the stand attached to the side of the railing so that it has no interference from other objects that could block its view

III. Network Setup

It is The Camera is set up on a server that allows it to be seen all the time on a web page named 130.199.208.28 which is its ip-address. The settings can all be changed to set different exposures levels and time manually. Python is a programming language which was used to create the script which controls the camera's settings. The python script sends commands to the URL of the camera which tells the camera to take a picture, change the exposure time, change the exposure level and change the Rgain and Bgain. I can set it so the camera takes multiple snapshots almost simultaneously (within around one second of each other) and this allows us to take different exposures of relatively the same portion of the sky. Originally Vivotek sent me a script which ran off of a FTP server that would take the snapshots every 6 seconds. FTP servers (File Transfer Protocol) is used to file and store files on a computer. The script that Vivotek sent was far too slow for what I needed. The reason, for being so slow, was because the script had to upload the snapshots taken to that server which took about 4 seconds. So instead I took some of the code from Vivotek's script and built off an existing script in python which just saved and stored photographs and made it so it changes the camera's exposure and took the actual snapshots.^[2] I can now execute the script and let it run for several hours so that it takes hundreds of photos as the sky passes through its view. Each set of photos has a 10 second break in between but I made it so that each photograph is labeled with the time it was taken down to the seconds.

IV. Experimental Error

Some experimental errors that occurred were animals or water droplets would be seen in the snapshots. Sometimes a fly would land on the camera. We've also had birds land on the camera which makes the pictures useless. An example below shows a Golden Finch landing on the camera. Another example shows a bird flying through the camera's field of view while it was taking snapshots. These occurrences do not happen often, but enough to find them while sifting through the photographs.



at a longer exposure time as there is more flare around the sun in the photo and the outer horizon darkens distorting how much cloud we can depict. The third and fourth snapshots represent what the solar flare looks like when the sun illuminates the clouds that are blocking it. These two snapshots will help the camera detect what is the sun and what is the cloud with the help of a few algorithms.

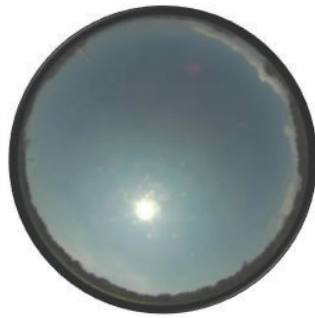
VI. Future Use and Long Term Goal

The long term purpose of the camera is to set up a grid of 12 cameras in the city on top of buildings. The cameras will triangulate to accurately forecast incoming clouds that could shade the buildings with solar panels on them. Using the script to store snapshots for the cloud algorithms will make the cameras able to identify solar flare more accurately, making the forecasts precise. If this grid does well then it will help create a foundation for even larger scale solar farms across states, to create large grids of these cameras that will be able to more accurately predict solar forecasts. The grids will then have solar panels that will be used more efficiently and help decrease the consumption of fossil fuels in the United States.

V. Data Collection

The camera is set to take sets of five pictures, each picture being at a different exposure time from a very dark photo to an extremely bright photo. This allows us to see a wide range of solar flare on the camera lens.

The set of four photos above is a few of the snapshots taken by the camera. The first photograph has an extremely short exposure time which shows the sun's position in the sky very clearly allowing us to calculate where the sun will be and help determine when clouds are being illuminated by it. The second snapshot is



Visualizing cesium on hydrated titanium dioxide at the nanoscale

Allison Pereira

Chemical and Biomolecular Engineering, Cornell University College of Engineering, Ithaca, NY 14853

Rebecca Hamlyn, Sanjaya D. Senanayake, David Grinter, and José Rodriguez

Chemistry Department, Brookhaven National Laboratory, Upton NY 11973

Abstract

The structure and morphology of alkali metals on oxide surfaces is important because alkali metals have been discovered to be promoters in catalytic chemical reactions. Titanium dioxide is a well-known oxide to study because it is a versatile support material and also compatible with many experimental approaches. The objective of this project is to determine if the adsorption of high coverage cesium on a hydrated titanium dioxide Cs/h-TiO₂ (110) surface would be beneficial. The images of the atoms on the Cs/h-TiO₂ surface were obtained at the nanoscale level with scanning tunneling microscopy, -("STM") under ultra-high vacuum conditions. By using this instrument, we can unravel atomic structure and identify even the movement of oxygen vacancies at the surface of titanium dioxide. This knowledge could reveal several important properties of catalyst surfaces such as its chemical reactivity, morphology and stability. Also we can study if the adsorption of high coverage cesium on a hydrated titanium dioxide surface may result in a stable configuration to enable a good catalyst surface. This research project is ongoing, but a few preliminary observations have been made through my work this summer. Throughout the last few weeks, we have performed cesium adsorption onto a hydrated titanium dioxide surface, and scanned them using STM to examine the change in structure and identify surface states on titanium dioxide. We have been able to identify oxygen vacancies on the surface and show that electrons from the oxygen atom result in titanium being reduced from Ti⁴⁺ to Ti³⁺. In addition, by understanding the reduction, role of Cs, and stability of surface species we have been able to determine if the adsorption of high coverage cesium on a hydrated titanium dioxide surface would result in a stable catalyst. With this experience I have added important chemistry research skills and learnt analysis using surface science tools of different specimens to my repertoire of laboratory techniques and critical thinking.

I. Introduction

Catalysis is essential because it enables a chemical reaction to occur faster when approaching chemical equilibrium and it promotes the generation of products selectively by interacting with reactants and avoid getting consumed. There many types of catalysts but one class are heterogeneous catalysts, in which the catalyst is in a distinctly different phase from the reactants (solid-gas, solid-liquid). Heterogeneous catalysts are used in many chemical process including organic synthesis, oil refining, and pollution control. Specific properties of these materials include porosity, surface area, dispersion, high reaction rates, selectivity, and activity.²

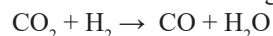
The catalyst is often metallic and needs to be dispersed on an appropriate support to maintain size, morphology, and stability as

nanoparticles which will thus achieve optimal chemical performance. A strong heterogeneous catalyst support is often reducible oxides such as titanium dioxide TiO₂, which is commonly used in fuel processing, solar cells, photocatalyst, and in mineralizing toxic and nonbiodegradable environmental wastes. It is well known for its reducibility, electronic, chemical, and thermal stability, activity, Lewis acidity, and redox properties.²

Titanium dioxide exists in several crystalline forms: anatase, rutile, and brookite. Rutile structure is the most common because it is the most thermally stable and has the best chemical reactivity and stable properties.

Many aspects of these systems have been studied to date. One important recent finding on the surface chemistry of titanium dioxide is evidence for direct propanol synthesis from carbon dioxide, ethylene, and hydrogen over cesium-gold/titanium dioxide rutile surface.¹ This proves how important the structure of the titanium dioxide's crystal structure is and which alkali metal is utilized on titanium dioxide's surface.

Reverse Water-gas Shift reaction for CO generation:



Hydroformylation of C₂H₄ with CO and H₂ to propanal:



Hydrogenation of propanal to propanol:



The reactants used in this reaction are more active and generate two times higher propanol yield than potassium-gold titanium dioxide and cesium-gold titanium dioxide catalysts. Since new products could be formed with cesium-gold titanium dioxide rutile catalysts, it is important to understand what role each component of this catalyst plays in the chemistry. With this motivation we have started to study the atomic structure of the Cs adsorption on h-TiO₂(110) surfaces.

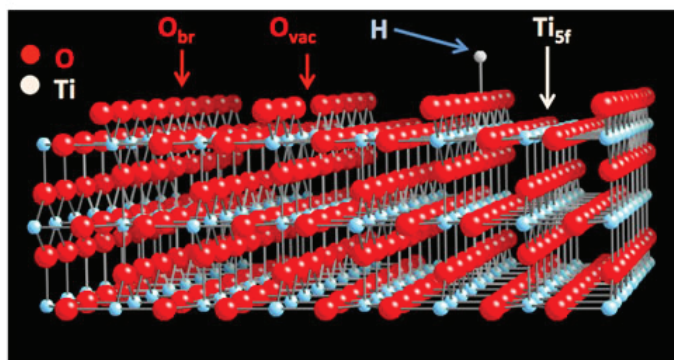


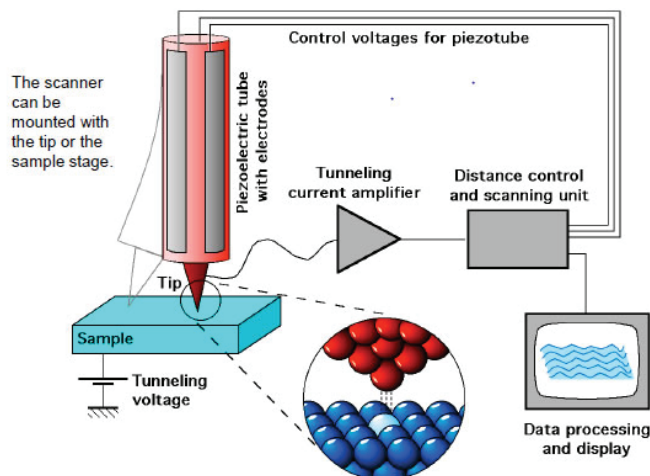
Figure 1: Titanium dioxide (110)

II. Experimental

To study the adsorption of high coverage cesium on a hydrated titanium dioxide surface Cs-h-TiO₂ (110), the scanning tunneling microscope is needed to obtain atomic resolution of the surface. The scanning tunneling microscope visualizes the surface at the nanoscale and images local regions, defects, and active sites, surface specific, electronic states, and specific states. The scanning tunneling microscope has five basic components: metal, conducting tip, piezoelectric scanner, current amplifier, bipotentiostat, feedback loop (current).⁴

The scanning tunneling microscope contains two chambers and two instrumental racks nearby. The instrumental racks have eleven separate layers- ion gauge which measures pressure, high voltage power supply, omicron sample heater, power supply, ion gauge which gives pressure reading, power supply for ion pump, omicron power supply system, turbo controller power supply, high voltage calibrated DC power source, ion pump controller and sublimation controller, and omicron controller.

The sample is scanned by a very fine metallic tip and is controlled in 3D by a piezo scanner either bound to the tip or attached under the sample stage which is either positive or negative. Once an electrical voltage is applied between sample and tip, a tunneling current is produced if there is an electron wavefunction overlap and bias. The tunneling current is strongly influenced by electron flow between last atom on tip and nearest atom in sample and is the sum of tip to sample and sample to tip currents. This tunneling current is thus intensified and calculated.⁴ Both the tunneling current and feedback electronics keep the distance between the surface of titanium dioxide and tip the same. If the tunneling current falls short of previous value, distance decreases and if current exceeds original value, distance increases due to the mathematical relation that current varies exponentially with distance. The tip is scanned line by line above sample surface after topography of sample.⁴ To map out the contours of the surface and to image the surface the current is either kept constant and then height of tip is measured or height is kept the same and current of the tip is determined to see if atoms are the same. If current is maintained the same, the heights for the same atoms can be found and since the atoms are the same, the surface topography at atomic resolution is imaged. If the height is kept constant, it can be determined if the atoms are the same and thus the different surface atoms due to their disparate work functions can be imaged to reveal the surface composition and defects.⁴



To obtain atomic resolution images of different specimens in the scanning tunneling microscope, each specimen goes through a cycle of sputtering and annealing. In sputtering, the particles of surfaces are ejected from a solid target material due to bombardment of the target by energetic gaseous ions which happens when kinetic energy of entering particles is much greater than thermal energies. In annealing the specimen is heated and then cooled slowly to harden it.

To sputter the atoms in a scanning tunneling microscope, the position of instrument must be read, the scroll pump must be turned on, the valve to the turbo pump must be opened, and the turbo pump must be turned on by pressing the power button on the small Pfeiffer power supply. The "Turbo On" button on button on system controller must be pressed. After fifteen minutes, the "Open AN" button must be pressed so the gate valve can be opened to the chamber. The gas tank on top must be opened, regulator should be adjusted to 30 psi, and swagelok valve to the gas line should be opened. The emission on pressure gauge must be changed by turning off the filament, opening panel, flipping the switch from ten to one, and then the filament must be turned back on. The red BNC cable to the picoammeter on top of small control rack must be connected to monitor drain current, and then sputter gun ion source must be plugged in. The emission should slowly be increased to twenty, then voltage knob should be set to one, and then voltage switch should be switched on. The gas leak valve should be slowly opened and drain current and chamber pressure should be monitored. The current should increase to about five to ten nanoamperes and pressure should be at 4×10^{-5} torr. The timer should be started for ten to fifteen minutes. After the waiting time, the leak valve should be closed, the emission should be turned down, and voltage should be switched off. The HV BNC cable should be reconnected from the picoammeter to the power source. If there are to be no more cycles of sputtering to be done, the gun power supply should be unplugged, valves on gas tank should be closed, and picoammeter should be turned off. The ion pump should be turned on and gate valve to turbo pump should be closed. Since this system has no ion pump valve, high pressure can only enter the machine if the ion pump is turned off and pumping be turned over to the turbo.

For the annealing process, the sample should be turned toward the viewing window to monitor temperature. The filament power, and high voltage power supply should be turned on and the red BNC cable should be connected to the HV supply. The "HV on" button should be turned on so voltage can increase to 700 Volts. The filament current should increase slowly and at around

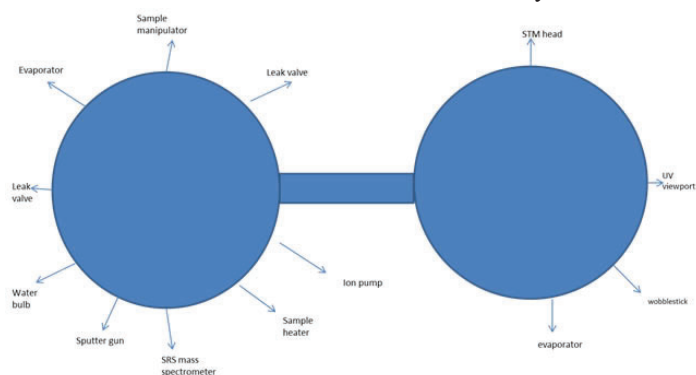


Figure 2 (left). The five basic components of the scanning tunneling microscope.

Figure 3 (above)

2.4 Amperes the emission current should be increasing so filament voltage would be 6 Volts. The emission current should be monitored and slowly brought up to expected value: 600 C and 28 miliamperes. Then the timer should be started again for fifteen minutes. After waiting time the filament current should be turned down slowly. The button “HV on/off” should be pressed to turn off high voltage and then power of filament and high voltage supplies should be turned off. Once the sputter and anneal cycles are completed and pressure in chamber is staying constant, the turbo can be turned off. The valve to the scroll pump should be closed and switched off.

III. Sample Preparation and Scanning

Since the hydrated surface of cesium on rutile titanium dioxide Cs/h-TiO₂ (110) was being studied, the chamber was dosed with two liters of water. When the images were scanned, the x, y, and z positions could be changed, current, voltage, loop gain, scan speed, width/height could be altered, and voltage pulses could be added anywhere to the surface. These images showed hydroxyls but there was streaking, more spots, and step edges could be detected. However once the tip was stuck in a mode and needed to be moved. Morphology could be seen at a smaller scale and thus there was poor image quality due to noise. From these images the electrochemical reactivity, special atomic geometries, functionality, surface, and hydroxyl count could be seen and understood in great detail. One main necessity to get images with the STM was to get a sharp metallic tip to obtain clearer and better images. In addition the crystal needed to be clean, have longer deposition, and needed to pick up hydroxyls. The forward and backward scans had to be the same because if they were not or if there were numerous diagonal lines the images were not real. The images would improve if titanium dioxide was cleaned and if there was no cesium. The better images would be at higher width/height dimensions.

After a couple days, cesium was added to the titanium dioxide surface. So cesium was dosed on to the surface three different

times and at different conditions. Cesium was degassed on h-TiO₂ (110) at six amperes and at 0.8 volts for ten seconds at x=10, y=20, and z=137 and no angle. For the second dosage of cesium was degassed for twenty seconds at six amperes and 0.8 Volts. Then the images of cesium looked different, could be covering much of the surface, looked more textured and reduced titanium lines could be seen. There was a possibility for the tip to be heated since it could remove any impurities off tip and thus the tip would be sharper to give better images. Nevertheless, this was not done but the titanium dioxide crystal was heated for ten minutes at 2 amperes, 2.8 volts at twenty-eight degrees Celsius. After ten minutes the temperature rose to forty-one degrees Celsius. Swirls on images were seen and the surface looked grainy which was unusual so the crystal was heated again for twenty minutes at 2.5 amperes and 4 Volts so the temperature rose to 71.2 degrees Celsius. There was some drift and there was no distinction between titanium dioxide terraces and edges from cesium.

The images were then studied and analyzed in depth by using the WSxM solutions software which is the powerful and user-friendly Windows application for Data Acquisition and Processing in Scanning Probe Microscopy and a wide range of microscopy or spectroscopy techniques. The images needed to be leveled, flattened, extracted and loaded. The terraces were made flat by global/local plane features and color and brightness were altered. The heights of vertical step edges were measured and compared to detect ends of terraces, the scanning tunneling microscopy needed to be calibrated, line profiles needed to depict

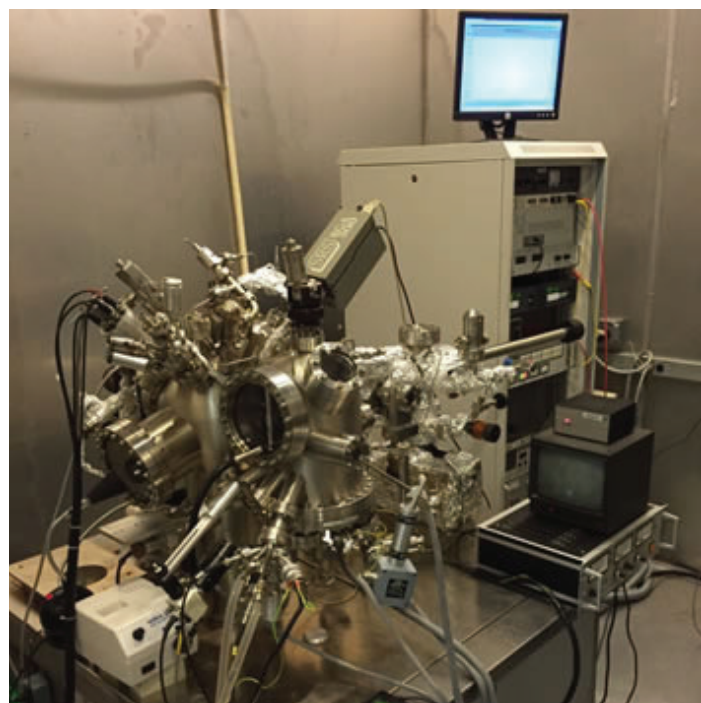


Figure 4: Scanning Tunneling Microscope in Chemistry Department of Brookhaven National Laboratory

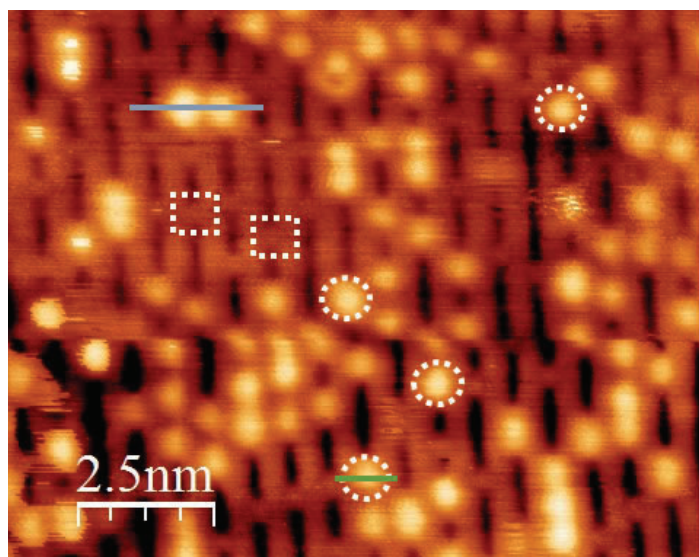


Image of h-TiO₂ (110) with no cesium

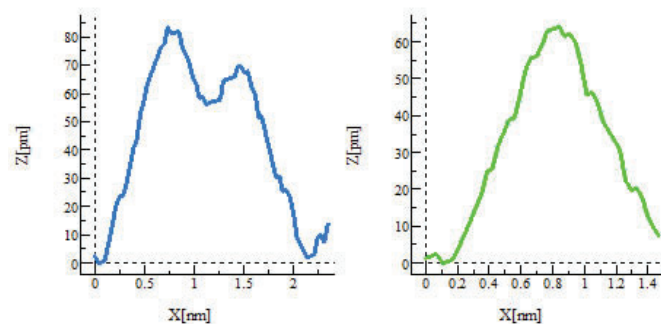


Figure 5.

the height at certain points on surface for oxygen vacancies and hydroxyls. Oxygen vacancies were useful to find because they can show where the metal can rest on a titanium dioxide surface. A hydroxyl and oxygen vacancy count can tell how reduced the titanium dioxide surface is. Each vacancy holds two hydroxyl groups.

IV. Results

The circles which are on all the yellow bright spots represent hydroxyls. The square represents oxygen vacancies. The black and orange background is titanium dioxide with the orange being titanium atoms and the black are the oxygen rows. The hydroxyls and oxygen vacancies are defects that interrupt the titanium dioxide surface. It is at 1.4 Volts and its dimensions are fourteen nanometers by fourteen nanometers. The area of the surface is $1.96 \times 10^{-16} \text{ m}^2$. Profiles were done on hydroxyls of the surface and the peaks represent how many hydroxyls were present. The hydroxyls range from 80 picometers to 60 picometers- 8×10^{-11} to 6×10^{-11} meters. There appears to be about 90 hydroxyls and thus 45 oxygen vacancies on the entire surface. (Figure 6)

Image of Cs/h-TiO₂; Cesium on hydrated titanium surface

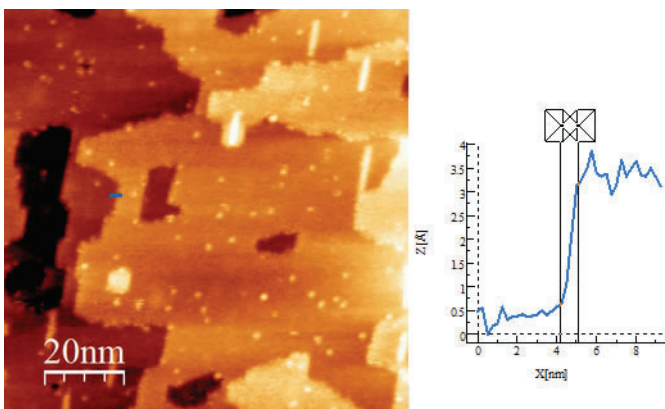


Figure 6:

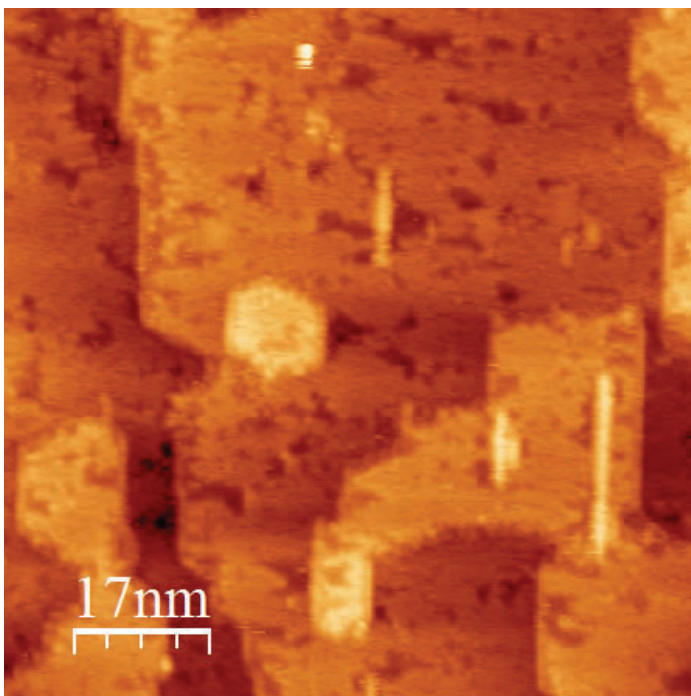


Figure 8:

The dimensions are one hundred nanometers by one hundred nanometers and the surface is at 1.6 Volts. Thus the area is $1.0 \times 10^{-14} \text{ m}^2$. A profile was done on cesium atoms on the surface. The atoms are around 3.5 angstroms high or 3.5×10^{-10} meters. There appears to be about 90 cesium atoms on the entire surface. The cesium atoms are one nanometer in width and two nanometers from tip. This image also identifies step edges and terraces on the surface. (Figure 7)

These next few images (figures 8,9, and 10) show how different voltages alter the surface.

At 1.03 Volts: Cesium is covering much of the surface; image looks textured and reduced titanium lines can be seen. (Figure 8)

V. Discussion and Conclusions

The results give much information about the cesium adsorbed onto the hydrated surface of rutile titanium dioxide. It seems hydroxyls are not as mobile on a hydrated surface as they are on an oxide surface. Various defects such as oxygen vacancies, reduction of titanium lines, and line profiles to indicate the number of cesium and hydroxyl atoms can give information on what type of catalyst Cs-h/TiO₂ can be. More research will be done in the future to see how this catalyst can be an assist to different innovations and applications.

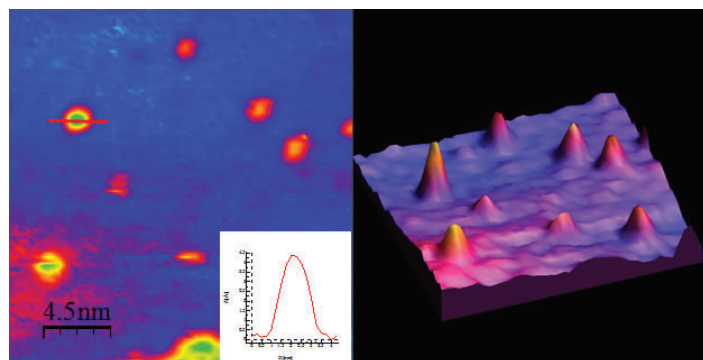


Figure 7: The image on the left is a 2D image of cesium on h-TiO₂ rutile with a line profile for one cesium atom and the image on the right is a 3D image.

At 1.58 Volts:

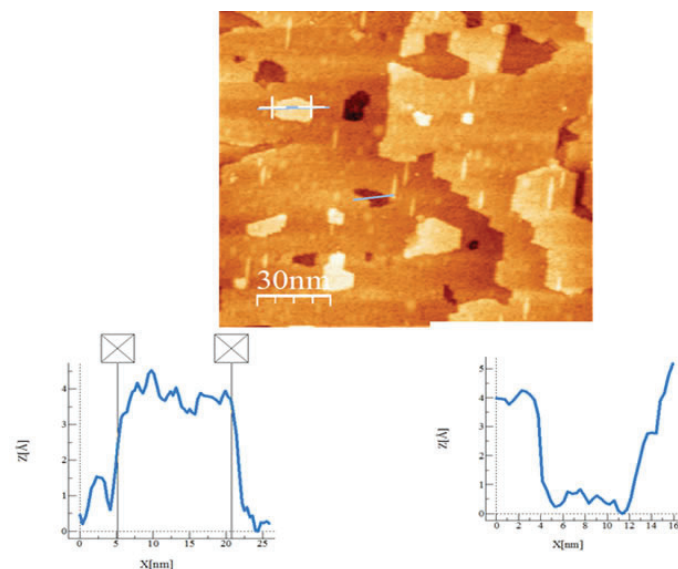


Figure 9: Line profiles compare the heights of cesium and hydroxyls. Cesium line profile is on the left and hydroxyl profile is on right.

VI. Acknowledgements

This project was supported by the U.S. Department of Energy. All research was performed at Brookhaven National Laboratory under the Science Undergraduate Laboratory Internships Program (SULI).

VII. References

- ¹Ahlers, S. J., M.-M. Pohl, M. Holena, D. Linke, and E. V. Kondratenko. "Direct Propanol Synthesis from CO₂, C₂H₄, and H₂ over Cs–Au/TiO₂ rutile: Effect of Promoter Loading, Temperature and Feed Composition." *Catal. Sci. Technol.* 6.7 (2016): 2171-180. Web.
- ²Bagheri, Samira, Nurhidayatullaili Muhd Julkapli, and Sharifah Bee Abd Hamid. "Review Article Titanium Dioxide as a Catalyst Support in Heterogeneous Catalysis." *The Scientific World Journal* Volume 2014 (2014), Article ID 727496, 21 Pages (2014): n. pag. Web.
- ³Diebold, Ulrike. "The Surface Science of Titanium Dioxide." *Surface Science Reports* 48.5-8 (2003): 53-229. Web.
- ⁴"Lecture 6 Scanning Tunneling Microscopy (STM)." *Lecture 6 Scanning Tunneling Microscopy (STM)* (n.d.): 1-23. Web.
- ⁵Pacchioni*, Gianfranco. "Oxygen Vacancy: The Invisible Agent on Oxide Surfaces." *Oxygen Vacancy: The Invisible Agent on Oxide Surfaces* 4.10 (2003): 1-7. Brookhaven National Laboratory. Web.
- ⁶Postma, Henk. "Scanning Tunneling Microscopy, Introduction." *Scanning Tunneling Microscopy, Introduction* (n.d.): n. pag. Web.

At 2.3 Volts: The green mark on surface corresponds to bottom right profile. The tall, thin, narrow white streak on surface corresponds to left bottom profile.

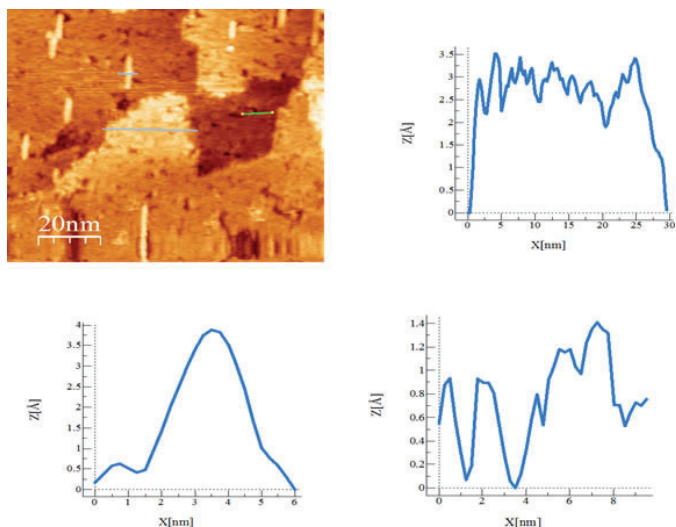


Figure 10: The line profiles with higher peaks represent cesium and the downward peaks represent hydroxyls.

An in situ examination of copper/ceria catalysts' properties and effects on the water-gas shift reaction mechanism

David Salazar

Engineering, Queensborough Community College, Bayside, NY 11364

Jon Hanson and Senjaya Senanayake

Chemistry, Brookhaven National Laboratory, Upton, NY 11973

Dimitriy Vovchok and José A. Rodriguez

Chemistry, Brookhaven National Laboratory, Upton, NY 11973

Chemistry Department, Stony Brook University, Stony Brook, NY 11794

Abstract

The catalysis behind the Water-Gas Shift (WGS) reaction, $\text{CO} + \text{H}_2\text{O} \rightarrow \text{CO}_2 + \text{H}_2$, plays a critical role in the removing of CO from CO and H₂ mixtures. One of the current limitations of industrial WGS catalysts is their high temperature active phase requirements (300 – 500 °C). Various Cu/CeO₂ catalysts are being studied in order to better understand their properties, and a better understanding on these catalysts can result in the development of more efficient catalysts that have active phases at lower temperatures. (20:80) Doped Cu/CeO₂, and (60:40) Inverse Cu/CeO₂ are the focus of this investigation to understand their properties and to determine how each catalyst behaves under WGS reaction conditions. X-Ray Diffraction (XRD), Residual Gas Activity (RGA), and Diffuse Reflectance Infrared Fourier Transform Spectroscopy (DRIFTS) are used in this study in order to study catalyst composition. In situ ramp WGS data was analyzed in order to compare the active copper phases of the doped and inverse Cu/CeO₂ catalysts. Phase Sensitive Detection (PSD) with 2-Dimensional Modulated Excitation Demodulation (MED) was applied to the X-Ray Diffraction powder patterns too look for structural changes of the catalysts, and DRIFTS analysis was used in order to look for chemical changes on the surface of the cat-

alysts that affect the WGS reaction mechanism. It was found that the active phase of the catalyst is composed of metallic copper on a partially reduced oxide support (CeO₂). The active metallic copper phase of the inverse catalyst was found to be higher than the metallic copper phase of the doped catalyst. The different types of software used to analyze the data of my research project such as 2D-MED with PSD for structural property characterization in powder XRD, and OMNIC for DRIFTS analysis have expanded my knowledge on catalysis research.

I. Introduction:

The Water-Gas Shift (WGS) reaction, $\text{H}_2\text{O} + \text{CO} \rightarrow \text{H}_2 + \text{CO}_2$, is used in industry for the production of hydrogen. Currently, the production of clean hydrogen is very costly, and one of the many reasons is that the industrial WGS catalysts that are being used, such as CuO/ZnOx/Al₂O₃, are not stable in long term operations. When compared to CuO/ZnOx/Al₂O₃, Cu/CeO₂ catalysts show a very different chemical structure which employs only one oxide support system. Copper/Ceria catalysts show a high catalytic activity for the oxidation of Carbon Monoxide (CO), and they are very active and stable in the temperature range of 200-300 °C. This investigation focuses on understanding and comparing some of properties of (60:40) Inverse Cu/CeO₂, and (20:80) Doped Cu/CeO₂ in their active states in order to characterize their multiple phases to obtain more information on the WGS reaction mechanism (Figure 1).

Copper/Ceria catalysts under WGS conditions undergo a series of chemical transformations. During the WGS reaction, there is reduction of the copper component of the catalyst when Carbon Monoxide reacts with the catalyst. This leads to Copper Oxide (CuO) being present, and the Copper gains a +2 oxidation state. As the reaction proceeds, the CuO is then reduced to metallic Copper with a 0 oxidation state. This Copper +2 → Copper 0 (metallic) transformation marks the time when catalytic activity is seen which is when hydrogen and carbon dioxide get produced in the WGS, $\text{H}_2\text{O} + \text{CO} \rightarrow \text{H}_2 + \text{CO}_2$, as this reaction goes to completion. The highly active metallic copper phase is seen on partially reduced oxide support. In this case Ceria is partially reduced from a +4 oxidation state to a +3 oxidation state which results in a Ceria cell dimension that is larger in size than when it had its +4 oxidation state.

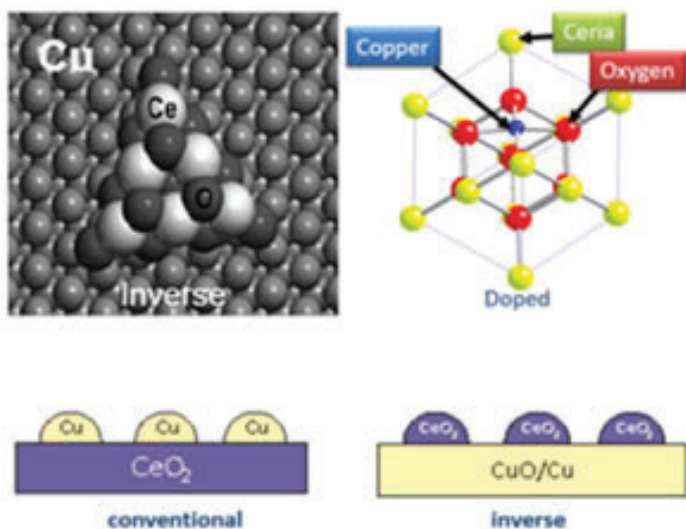


Figure 1: Structural differences between the Inverse and Doped Copper/Ceria catalysts¹

II. Experimental:

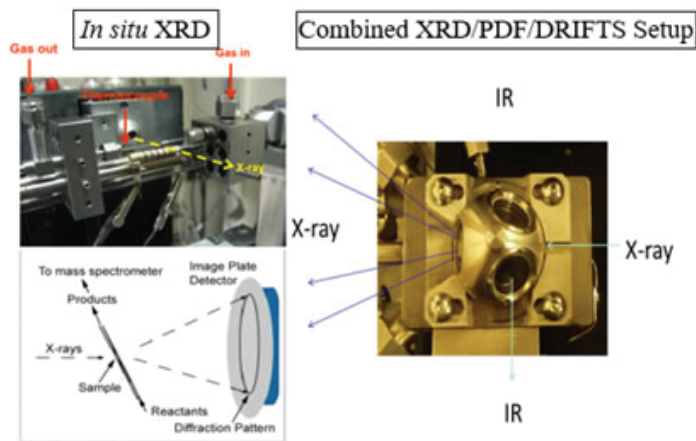


Figure 2: Experiments were conducted at Advanced Photon Source (APS) at Argonne National Laboratory at Beamline 11ID-B. (Photon energy: 90KeV) ($\lambda=0.13702 \text{ \AA}$) XRD, DRIFTS, RGA. 2% CO/3% H₂O / He He 6 cc/min 5% CO/ He 4 cc/min

III. Results:

A. In situ XRD: Structural Properties of the Inverse and Doped Copper/Ceria Catalysts

1. (60:40) Inverse Catalyst WGS Ramp 300 °C

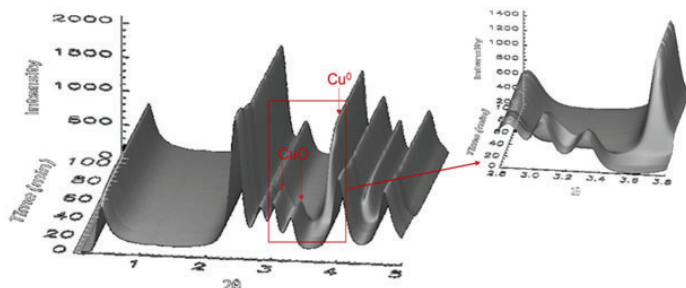


Figure 3a: WGS temperature ramp for the inverse catalyst. Heating up the reaction to 300 °C starting from 35 °C at 5 °C / min shows In situ measurements with time-resolved X-ray diffraction of the reduction of CuO (Cu⁺²) to metallic Cu (Cu⁰) for the inverse catalyst.

2. (20:80) Doped Catalyst WGS Ramp 300 °C

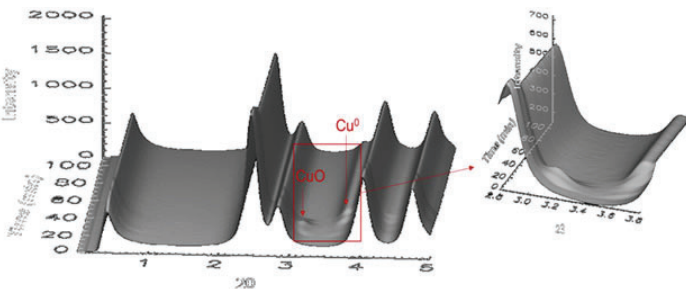


Figure 3b: WGS temperature ramp for the doped catalyst. Heating up the reaction to 300 °C starting from 33 °C at 5 °C / min shows In situ measurements with time-resolved X-ray diffraction of the reduction of CuO (Cu⁺²) to metallic Cu (Cu⁰) for the doped catalyst.

B. 2D-MED & PSD: Active Copper Phases

1. Inverse Catalyst

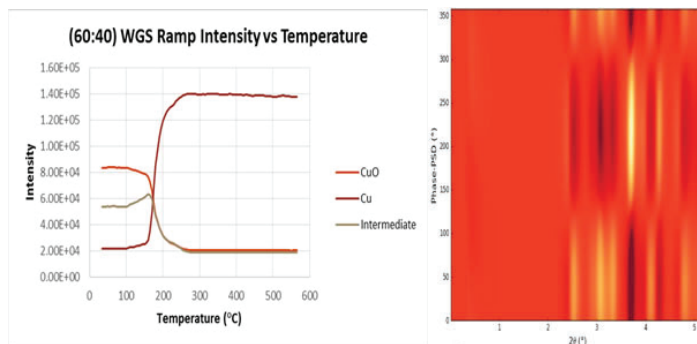


Figure 4a: 2D-MED & Phase Sensitive Detection (PSD) to look for important features of the active phases of the inverse catalyst. The three active features of copper seen for the inverse catalyst are CuO (Cu⁺²), Cu₂O (Cu⁺¹), and Cu. The CuO phase seems to coexist with the Cu₂O phase, and they both decrease at a similar rate at around 170 °C. This could have been caused by a smaller amount of Cu⁺² intermediate being present when compared to the Doped catalyst (Figure 4b).

C. 2D-MED & PSD: Active Copper Phases

1. Doped Catalyst

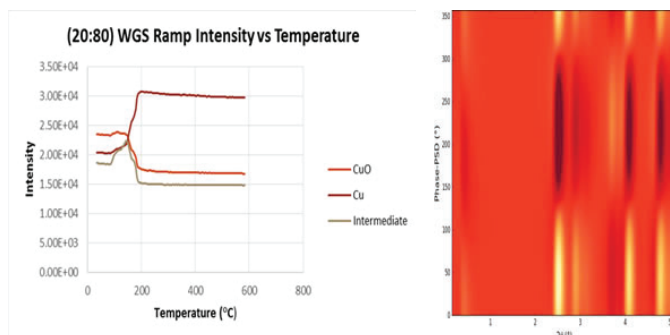


Figure 4b: 2D-MED & Phase Sensitive Detection (PSD) to look for important features of the active phases of the doped catalyst. Intermediate intensity is lower, and decreases in intensity at a much faster rate than the CuO phase. One possibility is that the CO bound on the catalyst's surface, and the Cu⁺¹ intermediate species was used up fast because there is not much of a CuO phase. In the Doped Catalyst there is not as much CuO phase when compared to the Inverse catalyst, and this could correlate with how much metallic copper phase is being produced.

D. Chemical Properties of the Inverse and Doped Copper/Ceria Catalysts

1. DRIFTS: Product Formation, and Surface Intermediates

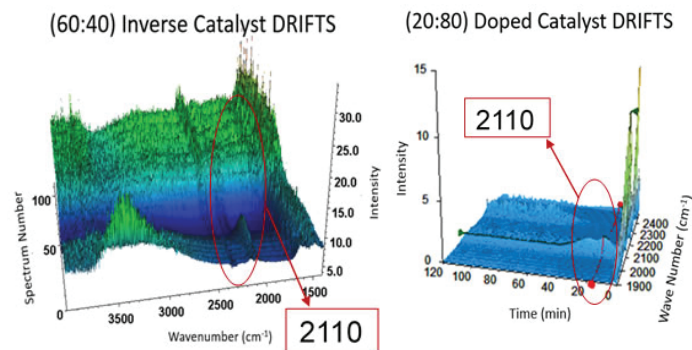


Figure 5a: The 2110 line shows CO is binding on the Cu^{+1} . CO_2 formation begins after CO binds on the surface of Cu^{+1} .

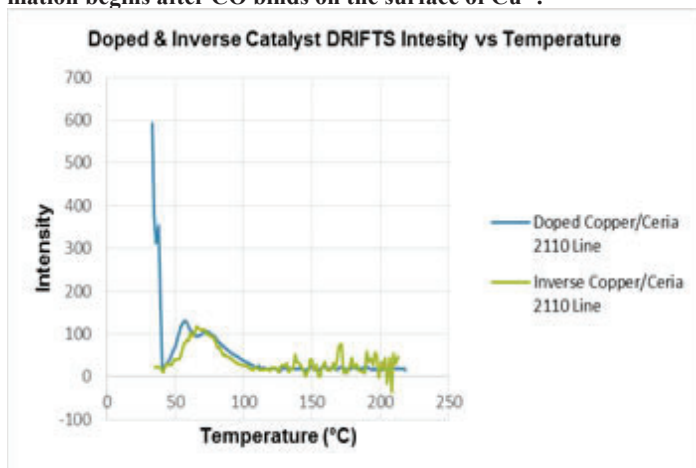


Figure 6: Information from previously integrated 2110 lines for the doped and inverse copper/ceria catalysts showing the binding of CO on Cu^{+1} .

CO on Cu^{+1} has the highest intensity at 58 °C for the doped catalyst, and it reaches its highest intensity at 67 °C for the inverse catalyst.

2. Residual Gas Activity (RGA): Monitoring H_2 and CO_2 formation

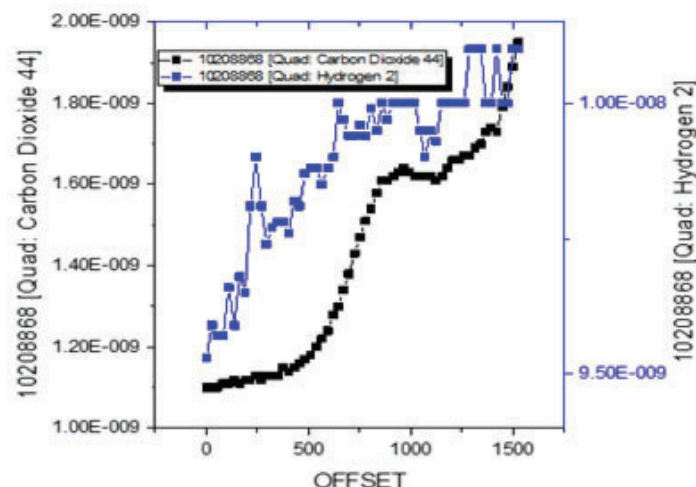


Figure 7a: Doped catalyst RGA analysis of CO_2 and H_2 formation for the (20:80) doped Copper/Ceria catalyst. Hydrogen begins to form before CO_2 after 5 minutes or 58 °C, and this coincides with the DRIFTS results.

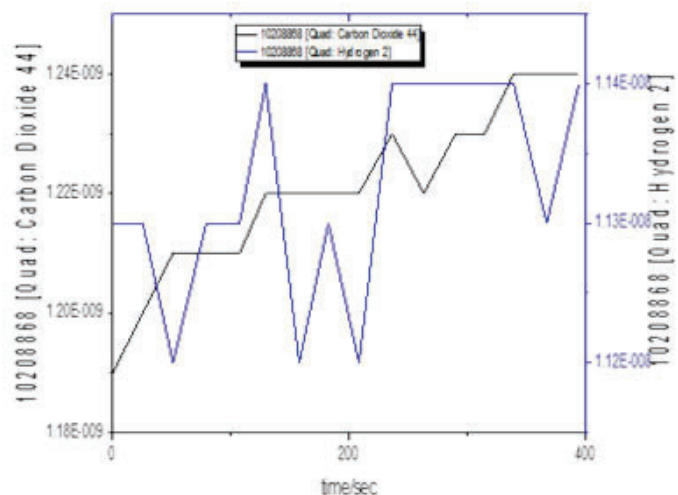


Figure 7b: Inverse catalyst RGA analysis of CO_2 and H_2 formation for the (60:40) Inverse Copper/Ceria catalyst. Hydrogen forms before CO_2 after 6 minutes or 65 °C, and this coincides with the DRIFTS results.

IV. Conclusion

Increased presence of copper in the (60:40) inverse catalyst corresponds with increased catalytic activity. It was found that the active phase of the catalyst is composed of metallic copper on a partially reduced oxide support (CeO_x)₂ (Figures 3a,3b,4a,4b). The active metallic copper phase of the inverse catalyst had much higher intensity than the metallic copper phase of the doped catalyst. For the Doped catalyst, H_2 began to form before CO_2 at around 58 °C which supported the DRIFTS results obtained. Also, for the Inverse catalyst, H_2 began to form before CO_2 at around 65 °C.

V. References

- ¹José A. Rodriguez, Water-Gas Shift Reaction on a Highly Active Inverse $\text{CeO}_x/\text{Cu}(111)$ Catalyst: Unique Role of Ceria Nanoparticles
- ²Jos A. Rodriguez, In-Situ Studies of Active Sites and Mechanism for the Water-Gas Shift Reaction on Metal/Oxide Nano catalysts

VI. Acknowledgements

This project was supported in part by the U.S. Department of Energy, Office of Science, Office of Workforce Development for Teachers and Scientists (WDTS) under the Community College Internships Program (CCI).

Radiological surveying and monitoring of laboratories at Brookhaven National Laboratory

Rachel Sanders

ES and H, Alabama A&M University , Huntsville, AL 35811

John Shlonsky

ES and H, Carnegie Mellon, Pittsburgh, PA 15213

Steve Coleman and Andrew Levine

Radiological Control, Brookhaven National Laboratory, Upton, NY 11873

Abstract

The Radiological Control Division at BNL is responsible for ensuring the radiological safety and health of personnel, the public and the environment. The activities of Radiological Control apply to most of the lab. Our project included site wide radiological surveys to identify or verify the presence of historical fixed contamination. A radiological survey is used to document what the level of fixed contamination present in a given area. For each building we conducted multiple surveys. The surveys must be thorough because the locations will be continually monitored. The result of this was the discovery of a few unmarked fixed contamination locations in two separate buildings. Through this research, I have gained experience in the use of radiation monitoring devices, such as a floor walker and a frisker, and in the procedure to identifying and marking contamination.

I. Objective

For our project, we intended to survey historical fixed contamination in order to verify the presence of it. We also planned to gain experience and knowledge in the operation of radiation monitoring devices as well as the procedures used with them.

II. Introduction

Radiation is emitted by all the radioactive elements of the periodic table according to their isotope. The radiation can be a result of an unstable nucleus being stabilized. Some isotopes have extremely short half-lives (secs) or extremely long half-lives (billions of years) which makes it very important to determine which isotope is present. The half-life is the rate at which the radioactive element will decrease by half. The four basic types of radiation are alpha, beta, gamma and neutron. Each type of radiation has a different mass and energy which changes the properties. Due to their properties, each one requires different type of material for shielding and different equipment for monitoring. For example, alpha radiation can be shielded by aluminum foil whereas gamma radiation would require much more shielding like concrete. Shielding is crucial because radiation can cause damage to the living organisms. Radiation safety guidelines are in place to avoid contamination but sometimes it still occurs. Contamination can be fixed which means it cannot be readily removed. In order to detect a specific type of radiation, the contamination monitoring device must be designed and built to detect it. Contamination monitoring devices are routinely calibrated and source checked to ensure accuracy.

Contamination is defined as the count rate or the amount of disintegrations per minute in a defined area above the background count rate. The count rate is the counts of radiation a person will

receive at a certain distance over a certain time. There is a limited total dose for a person over a given time. The dose a person receives at work is monitored by a TLD, Thermo luminescent dosimeter. To ensure people are aware of a dose they will be receiving, an area with above background dose will be marked as such. BNL has been around for almost 70 years and buildings are constantly being modified for different uses. Some laboratories and buildings utilize radiation in their experiments that may leave contamination. The contamination is only detected by monitoring devices and can last for a while, depending on the isotope. As a result of this, it is very important to have correct markings for the contamination to ensure safety.

III. Methods and Materials

In order to begin our project, we had to complete several lab wide training courses as well as some job specific one such as compressed gas safety. To survey the inactive labs and rooms, we used a floor walker (*figure 5*) as a screening tool and frisker (*figure 6*) to quantify the fixed contamination when it was detected. The contamination monitoring devices were response checked with a sealed radioactive source before each use and constantly monitored to make sure they were operating correctly. A handheld frisker was used to survey fume hoods, sinks, and other places that could not be surveyed by the floor walker. The floor walker was used to survey large areas such as the floor. The procedures used for these were FS-SOP-2020(1) and FS-SOP-1000(3) which prescribes the process of using the floor walker and radiological surveys. When observed counts per minute on the frisker read above 500, the location was considered fixed contamination. The Thermo Scientific "Identifinder" was used to determine the radio-isotope associated with the contamination. For certain rooms, a TLD was required for entry; the TLD was required to monitor the occupational dose a person will receive. Personal protective equipment (PPE) is mandatory for entry into many of the labs that we surveyed. Some of the PPEs that we used were safety glasses, lab coats, work boots, and gloves. After each survey of a room, the results had to be documented to maintain a history or establish



Figure 6: Image of Ludlum frisker monitor model 3

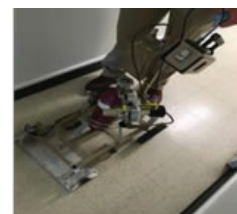


Figure 5: Image of Ludlum floor walker monitor model 239-1f

one. A temporary marking was used to identify the area of fixed contamination to allow for proper marking in accordance with Radiological Control Procedures. For us, this was either black marker or yellow and black tape.

IV. Results

After surveying several buildings with between five to thirty labs per building, we found only two labs with unmarked fixed contamination locations. The unmarked fixed contamination in one case was not near any radiological posting, building 197, and in the other case it was near the sign but not within the boundary, building 830. In building 830, we surveyed several labs and did not find any unmarked contamination in all but one lab. In *figure 1*, there are visible black markings to indicate where the unmarked fixed contamination was observed to be 1500 counts per minute.

In *figure 2*, there are more visible black markings just below the hood where the unmarked contamination was observed to be 11,000 counts per minute. Also in *figure 2*, the previously labeled contamination is seen with the magenta trefoil and yellow background posting. In *figure 3*, the two black markings are visible just below the hood and on the far left cabinet hinges. The fixed contamination radio-isotope found in building 830 was identified using the Thermo Scientific Identifinder. All of it was determined to be Cesium-137. In building 197, we found another unmarked fixed contamination with 300 counts per minute. This was not near any known elevated count rate areas and can be seen in *figure 4*.

While surveying building 197 using the floorwalker instrument, we started to notice that the counts per minute were uniformly high in a few rooms, appearing to indicate a malfunction. The instrument was taken to the Instrumentation and Calibration group that services them. Their diagnosis indicated the detector window had numerous holes. While they were repaired, our surveys were delayed for a couple of days.

V. Discussion/Conclusions

After surveying several buildings with inactive labs, we found only two instances of unmarked contamination where the count rate was above the threshold for posting. The instance in lab 3 of building 830 was an area that was already known to have marked fixed contamination in the area. The lab itself is also posted as a Radioactive Material Area. We found two spots of higher count rate near the previously identified fixed contamination. This would lead us to conclude that the contamination we found was from the same source as the previously identified contamination. The contamination found in building 197 lab 5 was not found near any other known fixed contamination or radiological work. We believe that this lab was not previously surveyed and we were the

first to find this fixed contamination. When the floorwalker began displaying uniformly high readings, we suspected that it was not operating correctly. To verify this, we source checked the floor walker. However, the source response indicated it was working properly. After the floor walker continued to malfunction, we took it to the RCD Instrumentation and Calibration laboratory who determined there was a masslinn cloth inside of the count rate meter that did not belong there, holes in the mylar window, and low gas bottle pressure.

Although source check readings are a way to determine whether an instrument is working correctly, the instrument must be monitored for proper performance. Fixed contamination count rates change over time because of decay and therefore should be continually monitored to verify its presence and quantity. Throughout the project, we became more familiar with operating contamination monitoring devices as well as correct procedures in using them.

VI. Acknowledgements

This project was supported in part by the U.S. Department of Energy, Office of Science, Office of Workforce Development for Teachers and Scientists (WDTS) under the Science Undergraduate Laboratory Internships Program (SULI). We would like to thank our sponsor Steve Coleman and our mentor Andrew Levine for all the guidance and professionalism. We would also like to thank other members of the radiological control division, Tim Welty, Chuck Schaefer, Dennis Ryan, Deana Buckallew and Andrea Epple, for giving us more knowledge and experience on the site. We wish to thank members outside of radiological control, Eric Dooryhee, Woody Fintan, Benny Hooda, Charlie Rose, Joe Moskowitz and Paul Bergh, for showing us operations in other facilities. Finally, we appreciate the support and opportunity given to us by Brookhaven National Laboratory, Office of Educational Programs and the Department of Energy.

VII. Literature Cited

- ¹Zak, Bill. Environment, Safety and Health Directorate Brookhaven National Laboratory Radiological Control Division. Upton: Brookhaven National Lab, 2014. Print. FS-SOP-2020.
- ²"Google Images." Google Images. N.p., n.d. Web. 29 July 2016.
- ³Zak, Bill. Environment, Safety and Health Directorate Brookhaven National Laboratory Radiological Control Division. Upton: Brookhaven National Lab, 2014. Print. FS-SOP-1000.



Figure 1: Building 830 lab 3. Temporary black markings for contamination on hinge



Figure 2: Building 830 lab 3. Temporary black markings for contamination just below hood and permanent marking of previously known contamination



Figure 3: Building 830 lab 3. Overall picture of temporary and permanent markings.



Figure 4: Building 197 lab 5. Overall picture of temporary and permanent markings.

Radiation damage studies in silicon photomultiplier with gamma rays and neutrons

Taylor Shimek

Physics, Texas State University, San Marcos, TX 78666

Craig Woody and Sean Stoll

Physics, Brookhaven National Laboratory, Upton, NY 11973

Abstract

Silicon photomultipliers (SiPMs) are used to detect light/photons and other charged particles for various types of detectors used at the Relativistic Heavy Ion Collider (RHIC) at Brookhaven National Laboratory (BNL). These include Electromagnetic Calorimeters (EMCAL), Hadronic Calorimeters (HCal), and other types of scintillator detectors. Previous research suggests that SiPM's detection characteristics suffer from gamma and neutron radiation, which is the type of radiation that SiPMs will be exposed to at RHIC. My project was to study this radiation damage in SiPMs and determine its causes in order to help improve SiPM performance so that future research at BNL will be able to address new challenges in nuclear physics. Three different types of SiPMs with four different types of epoxy/silicone window materials were irradiated to various levels of Cobalt (^{60}Co) and neutron radiation and tested for radiation damage by measuring the change in transparency of the window, and the change in the SiPM's dark current and saturation level. The results showed that the transparency of the window worsened with higher levels of gamma radiation, but not with neutron radiation. However, neutrons cause a much larger increase in dark current than gammas, and SiPMs with larger pixels showed more damage than those with smaller pixels. We also observed that the dark current decreased with time after the exposure. In conclusion, we determined that gammas and neutrons produce different types of radiation damage in SiPMs. The amount of damage depended on the size of the pixels in the SiPMs, and the radiation induced dark current partially decreased over time.

I. Background

A. Use of SiPMs in sPHENIX

SiPMs are solid-state photodetectors that (have?) provide single photon detection capability, high gain $\approx 10^6$, and good time resolution (< 1 ns). They are also small sized, insensitive to magnetic fields and relatively cheap. They are increasingly used in fields that require efficient photon detection and are being proposed for use at the Relativistic Heavy Ion Collider (RHIC) at Brookhaven National Laboratory (BNL) for the sPHENIX experiment. SiPMs could be used in detectors such as Electromagnetic Calorimeters (EMCAL), Hadronic Calorimeters (HCal), and other types of scintillator detectors. These experimental detectors at RHIC are exposed to various levels of gamma irradiation and neutron radiation. Previous research[1] suggests that SiPM's detection characteristics suffer from gamma and neutron radiation, which is the type of radiation that SiPMs will be exposed to at RHIC. Research is being done to find out what is exactly being damaged in the SiPMs by the radiation and if there is any way to prevent this damage in the future.

B. SiPMs

SiPMs are single photon sensitive devices made of avalanche photodiodes (APDs) on a silicone substrate as seen in Figure (1). APDs are highly sensitive semiconductor electronic devices that use the photoelectric effect to convert light to electricity. SiPMs consist of an array of APDs (also known as pixels), pointed out in Figure (1), that operate in a Geiger avalanche mode. Geiger avalanche mode is essentially a built-in first stage of gain by applying a high reverse bias voltage, which shows an internal current gain effect due to impact ionization (avalanche effect). The pixels on the SiPMs amplify the charge from a single electron produced by the conversion of a single photon by a factor of typically a few $\times 10^5$.

1. Optical Transmission

The SiPMs are covered by either an epoxy or silicone, which coats the silicon wafer and wire bonds from mechanical damage. The epoxy/silicone are normally transparent materials, which allow for photons to move through and be detected by the APDs. Radiation can create atomic defects in the material where electrons can get stuck. The energy level to move these electrons is now closer to the energy of optical photons. Thus, the probability

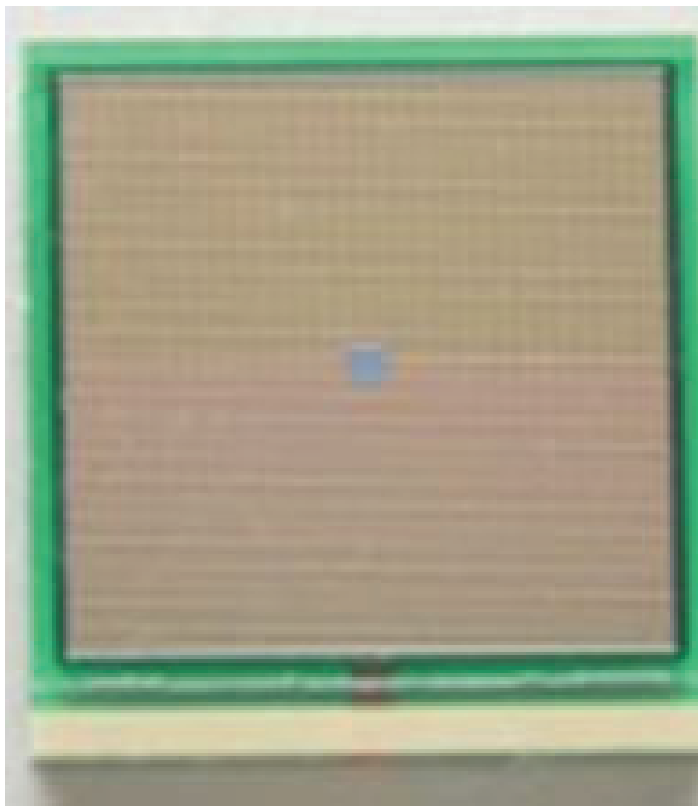


Fig. (1) Hamamatsu's 50 um SiPM from their catalog. [3] The lines point out one row of the APD (pixel) array.

of a photon hitting these electrons and getting absorbed gets higher the more atomic defects there are in the material. The optical transmission is affected by how many photons are absorbed instead of passing through the material.

2. Dark Current (Internal Noise)

Besides photon-generated carriers, other carriers from thermal noise can also fire the avalanche process that can produce signals in SiPMs. These pulses are called dark current because they can be detected when the SiPM is in complete darkness. Dark current can create noisy signals produced by photons. All SiPMs have a dark current at their operating voltage. If the dark current increases at the SiPMs operating voltage, particles with low energy could potentially become undetected because the dark current is too high. Radiation can change the atomic levels of these materials by moving electrons to the conduction band. As the conduction band begins the fill up, the dark current goes up.

3. Photon Counting

When light enters SiPMs, each photon that a pixel detects creates an output pulse with the same amplitude. For one event, all output pulses are superimposed onto each other, where the measured amplitude reflects how many pixels detected a single photon. This can be seen in Figure (2), different events show different output pulse heights depending on the number of photons detected. Measuring the height of each pulse allows estimating the number of detected photons. Photon counting is made easy by how high the output pulse is compared to the dark current. As the dark current is affected by radiation, so can the output pulses thus making photon counting difficult.

The optical transmission can also affect the probability that a photon is detected, changing the SiPMs PDE, but not the total

number of pixels that can fire. Thus, the radiation damage to the epoxy/silicone coating can affect saturation curve of a SiPM by lowering the PDE.

4. Saturation Curves

Each pixel only outputs one pulse at a time regardless of how many photons are incident on this pixel at the same time. The output signal is linearly proportional to the number of incident photons up to a level. This linearity can be described by the SiPM's photon detection efficiency, better known as the PDE. However, it begins to depart from a linear relationship with incident flux as the number of incident photons increases due to the finite number of pixels in the SiPM. This is called the saturation curve. The count rate reaches a maximum defined by the number of pixels in the SiPM. The theoretical formula for the saturation, which is given in the Hamamatsu Tech Note [3]:

$$N_{\text{fired}} = N_{\text{total}} \times \left\{ 1 - \exp \left(\frac{-N_{\text{photon}} \times \text{PDE}}{N_{\text{total}}} \right) \right\} \dots$$

N_{fired} : number of excited pixels
 N_{total} : total number of pixels
 N_{photon} : number of incident photons
 PDE: photon detection efficiency

II. Methods and Set-up

A. Epoxy/Silicone Window Samples

Eight window samples were tested along with four controlled window samples. The window samples are made of four different materials: Potting Epoxy, Potting Silicone, Molding Epoxy, and Molding Silicone. The samples are sandwiched between two quartz windows as seen in Figure (4). The window samples are 0.3 mm thick with a 25 mm diameter and were produced by

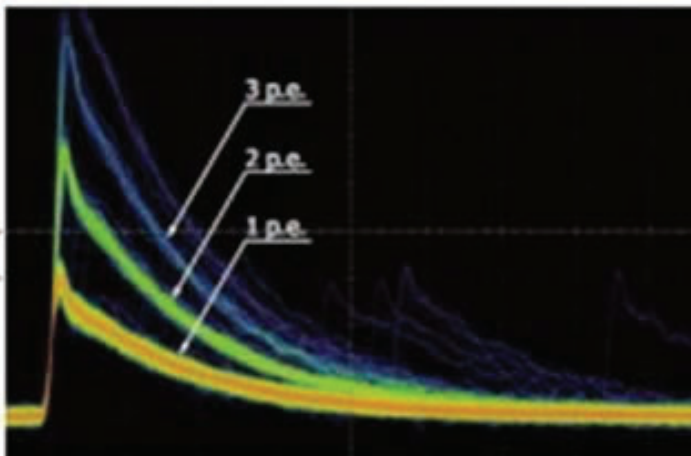


Fig. (2) SiPM output pulses with height describes the number of pixels fired. Taken from Hamamatsu's SiPM description. [2]

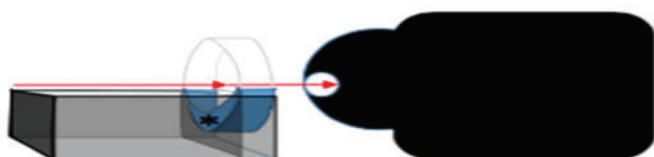


Fig. (3) Epoxy Sample Set-up in the Hitachi U3210 Spectrophotometer for the optical transmission measurements.



Fig. (4) Epoxy sample sandwiched between two quartz windows.

HAMAMATSU. As seen in Figure (4), these samples are labeled to describe what material is in this sample and what radiation the sample was exposed to. All the samples were first measured for their initial optical transmission using a Hitachi U3210 Spectrophotometer, as seen in Figure (3). To ensure the measured region as seen in Figure (4) stayed the same, the position and orientation of the samples were noted so that the opening of the spacer faced upward, the labeling faced toward the laser in the spectrophotometer, and the samples were marked on the side where the samples' holders top stopped on the window sample as demonstrated in Figure (3).

1. Gamma Irradiated Samples

Four samples of each different material were irradiated with different cumulative exposures to 1.17 MeV and 1.33 MeV Cobalt (⁶⁰Co) gamma rays. Between each cumulative exposure, their optical transmissions were measured again, making sure to not change the measured region. The cumulative exposures were of magnitude: 1 kRad, 10 kRad, 100 kRad, and 1 MRad. After the final cumulative exposure, their optical transmission was measured several times, immediately after the exposure, and once more a couple of days later to test for any recovery.



Fig. (5) The set-up for SiPMs irradiated at BNL's Solid State Gamma Irradiation Facility (SSGRIF) using a ⁶⁰Cobalt gamma source.



Fig. (7) SiPMs Dark Current measurements were taken using a Keithley K657 Picoammeter and a voltage source. The setup can be seen here with the SiPMs inside the light tight box.

2. Neutron Radiated Samples

Four samples of each different material were radiated with cumulative exposures to 14 MeV Neutrons. The same procedure for the gamma irradiation was repeated, but with the cumulative exposures of magnitude: 108 n/cm², 109 n/cm², and 1010 n/cm².

3. Control Samples (No Radiation)

Four samples of each different material were not radiated, but still had their optical transmissions measured at the same time as the radiated samples to test for controls and to ensure the spectrophotometer was working correctly. The optical transmission measurements were then used to make plots and for data analysis.

B. SiPMs Measurement Set-up

Three SiPMs were tested along with one controlled SiPM. They are squared devices with three different micro pixel sizes: 15μm x 15μm, 25μm x 25μm, 50μm x 50μm. They each have the same area, making their total micro pixel amounts 40,000 for the 15μm, 14,400 for the 25μm, and 3,600 for the 50μm. These SiPMs were produced by HAMAMATSU, called Multi Pixel Photon Counter or MPPC.

During the tests, the SiPMs were biased with a voltage pro-



Fig. (6) The set-up for SiPMs irradiated at BNL's Solid State Gamma Irradiation Facility (SSGRIF) using a 14MeV neutron generator.



Fig. (8) SiPMs Saturation curves were measured using a pulsed LED and a charge integrating ADC. This is the setup. (It will be)

vided by a different voltage source for the different tests. For each SiPM, the bias voltage reported by the manufacturer was used for each test and during radiation exposures. The devices we studied had an operating voltage (V_{op}) between 55-70 V. Also between

and after testing and exposure, the SiPMs were left in the dark box at a controlled temperature of 25 oC at their bias voltage with their change in current measured from the beginning of the experiment until the end.

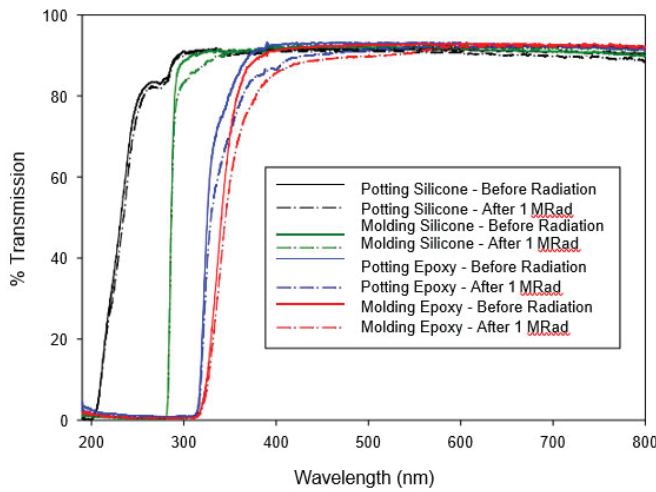


Fig. (9) Measured Optical Transmission of Silicone and Epoxy/Samples Before and After 1 MRad Gamma Irradiation

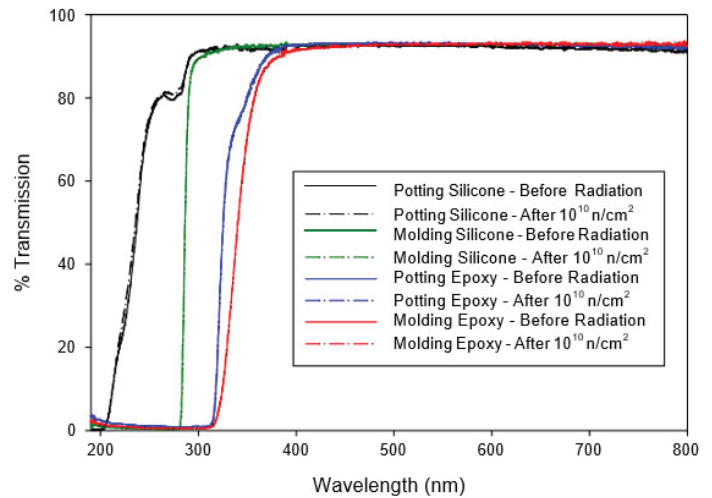


Fig. (10) Measured Optical Transmission of Silicone and Epoxy Samples Before and After Exposure to 10^{10} n/cm² of 14 MeV Neutrons

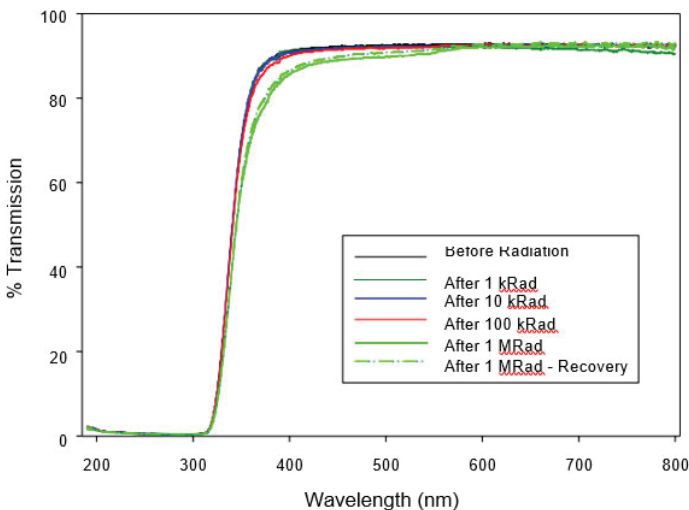


Fig. (11) Optical Transmission of Molding Epoxy with Different Cumulative Gamma Irradiation Exposures

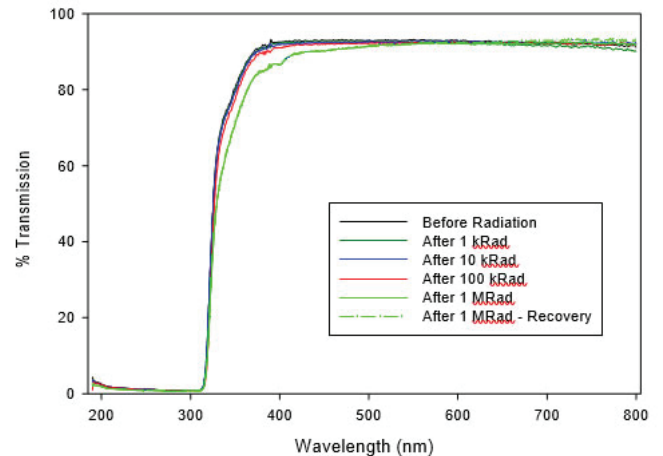


Fig. (12) Optical Transmission of Potting Epoxy with Different Cumulative Gamma Irradiation Exposures

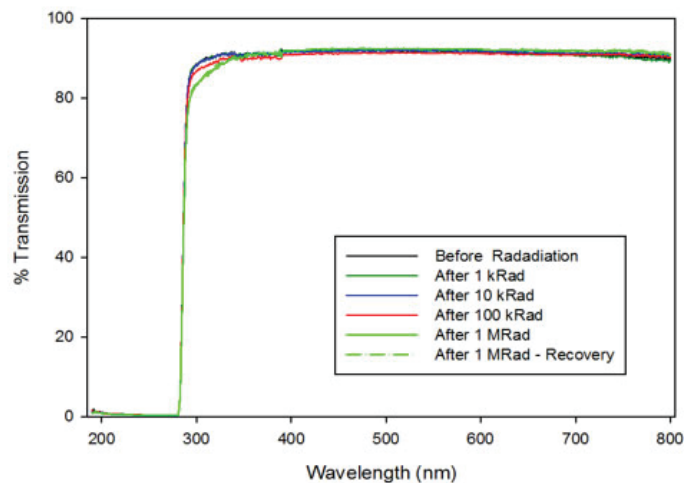


Fig. (13) Optical Transmission of Molding Silicone with Different Cumulative Gamma Irradiation Exposures

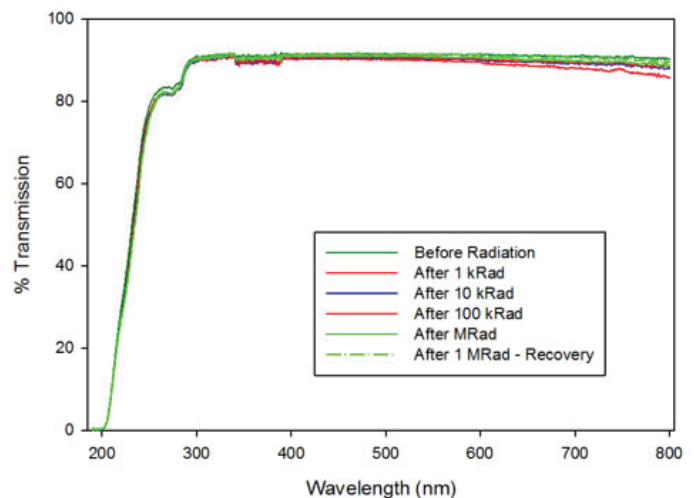


Fig. (14) Optical Transmission of Potting Silicone with Different Cumulative Gamma Irradiation Exposures

1. Radiation

Three SiPMs, each of different pixel size, were irradiated with different cumulative exposures to 1.17 MeV and 1.33 MeV Cobalt (^{60}Co) gamma rays with the cumulative exposures of magnitude: 1 kRad, 10 kRad, 100 kRad, and 1 MRad. Additionally, three different SiPMs, each of different pixel size, were irradiated with 14 MeV Neutrons with the cumulative exposures of magnitude: 108 n/cm², 109 n/cm², and 1010 n/cm². The SiPMs and Epoxy/Silicone samples were irradiated at BNL's Solid State Gamma Irradiation Facility (SSGRIF) using a ^{60}Co gamma source and a 14MeV neutron generator. Both of these set ups can be seen in Figures (5) and (6). The SiPMs dark current, saturation curves, and initial output pulses images were measured/taken before radiation, between accumulative radiations, and after. Some measurements were repeated after some time to measure for any recovery. The controlled SiPM for each type of radiation sets was not radiated, but was measured for each test at the same times as the radiated samples to test for controls and make sure all measurement devices were working correctly.

2. Dark Current Measurements

The SiPMs dark currents were measured using a Keithley K647 Picoammeter and a Voltage Source where the temperature was controlled at 25 oC and light was controlled by

being in the light tight box as seen in Figure (7). The measurements were performed manually where the voltage was only increased in increments as to where the dark current graphs were easily readable. After the final cumulative exposure of each radiation, their dark currents were measured several times, immediately after the exposure and once more a couple of days later to measure any recovery.

3. Initial Output Pulses Images for Photon Counting

The SiPMs initial output pulses were imaged when it was illuminated with the pulsed light at photon counting levels and then amplified with a linear amplifier and observed on an oscilloscope. The SiPMs initial output pulses were integrated using an oscilloscope, and sense the SiPM's gain is high enough to produce a large amount of charge, the distribution can show discrete peaks according to the number of detected photons. This is the diagram of the photon count was also included in these images. All instruments, besides the oscilloscope, were in the light tight box to control the light as illustrated in Figure (8).

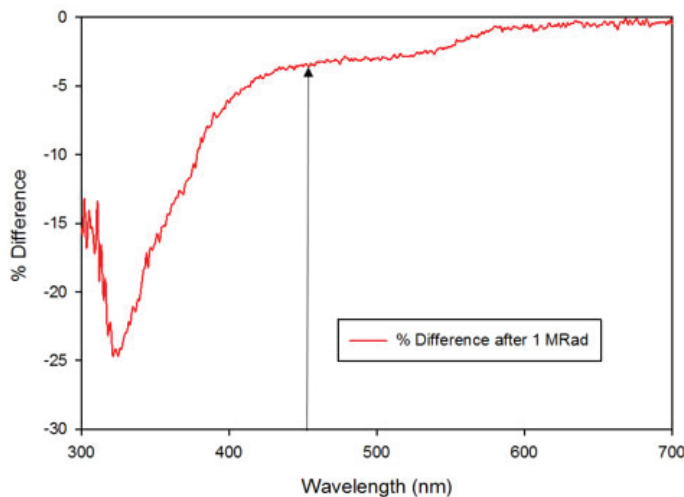


Fig. (15) Change in Optical Transmission of Molding Epoxy With 1 MRad Gamma Irradiation

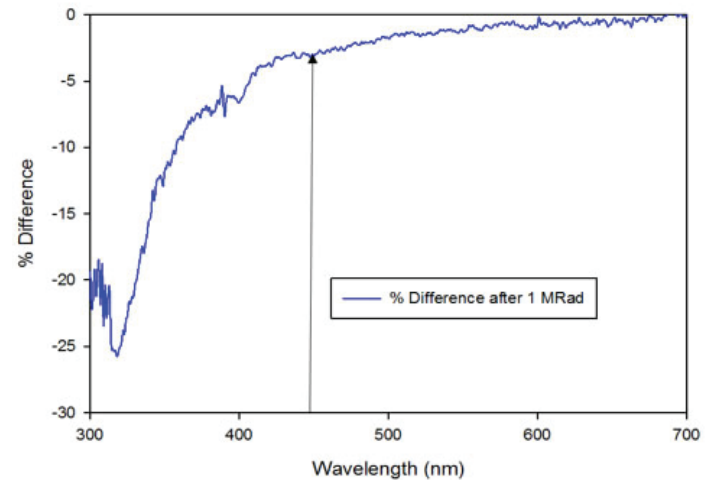


Fig. (16) Change in Optical Transmission of Potting Epoxy With 1 MRad Gamma Irradiation

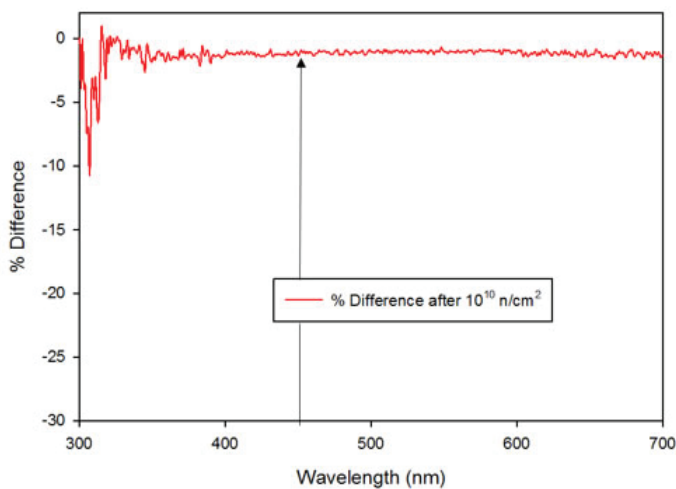


Fig. (17) Change in Optical Transmission of Molding Epoxy With Exposure to 1010 n/cm² of 14 MeV Neutrons

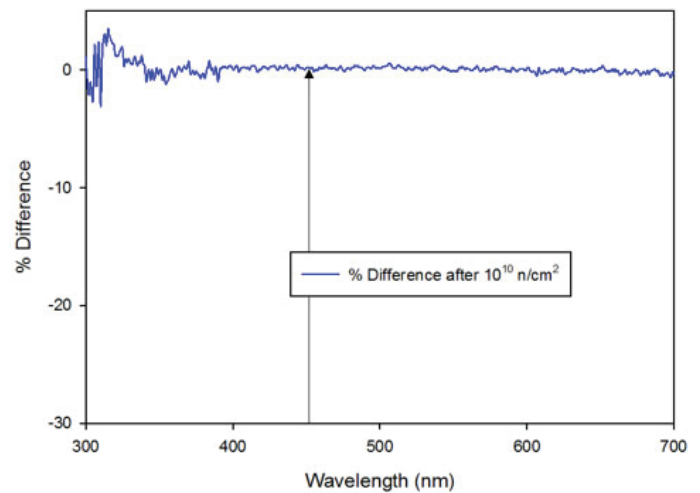


Fig. (18) Change in Optical Transmission of Potting Epoxy With Exposure to 1010 n/cm² of 14 MeV

4. Saturation Curve Measurements

The SiPMs saturation curves were measured using a pulsed LED and a charge integrating ADC, where all instruments were in the light tight box to control the light as illustrated in Figure (7). This is the same set up used to take the SiPMs initial output pulse images. The measurements were performed manually where the pulsed LED increased the incident photon flux at different increments determined from the initial measurements where the saturation curves were easily readable. The conversion of the pulsed LED to Incident Photons was given by Hamamatsu. The conver-

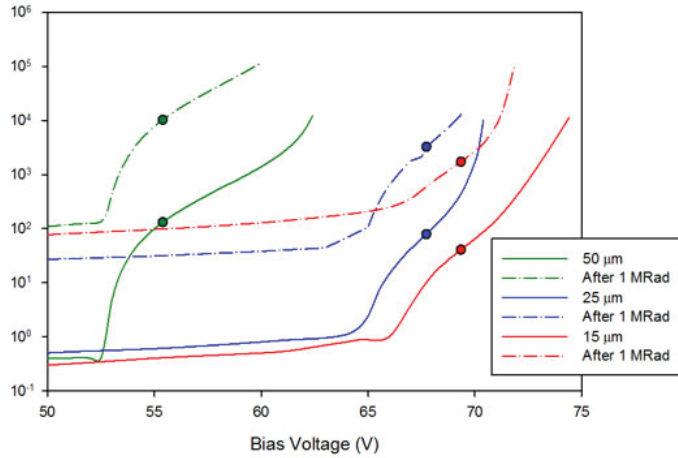


Fig. (19) Dark Current Measurements of SiPMs Before and After Exposure to 1 MRad Gamma Irradiation

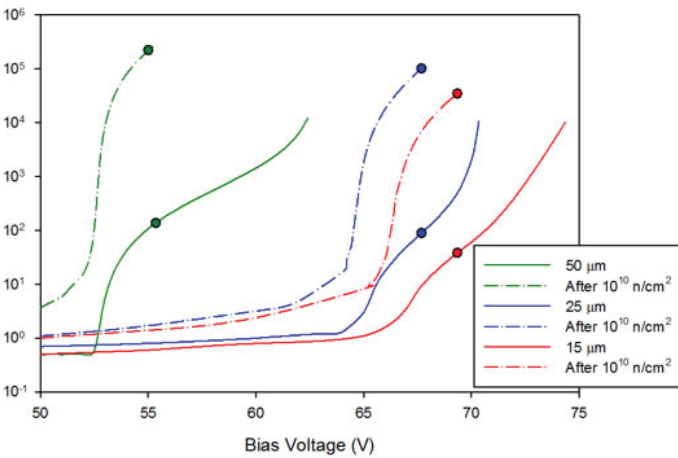


Fig. (20) Dark Current Measurements of SiPMs Before and After Exposure to 10^{10} n/cm² of 14 MeV Neutrons

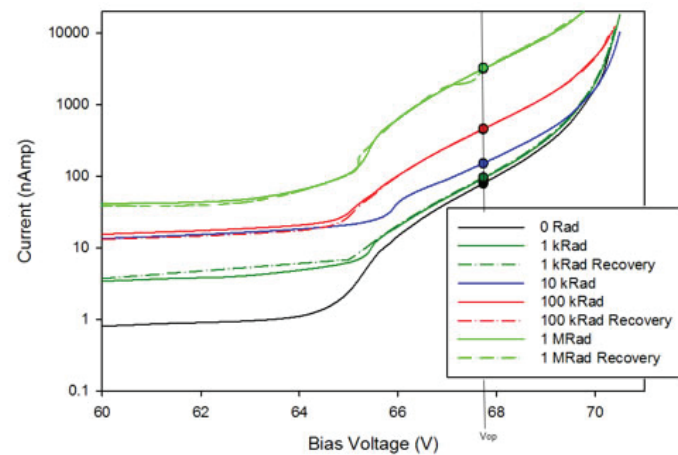


Fig. (22) Dark Current Measurements of the 25um Pixel Sized SiPM with different cumulative exposures to Gamma Irradiation

sion from the measured current to the measured photons was provided by the manufactures. Both conversions are what were used for data analysis.

III. Experimental Results

A. Optical Transmission

The change of the silicone/epoxy sample window's optical transmission as a function of wavelength is plotted in Figure (9) and (10). Figure (9) illustrates the difference between the optical transmission of the samples before and after being exposed to 1 MRad Gamma Irradiation. Figure (10) illustrates the difference between the optical transmission of the samples before and after being exposed to 1010 n/cm² of 14 MeV Neutrons. By comparing the trends before and after the exposure to neutrons, one can observe that the optical transmission does not change. By comparing the trends before and after the gamma irradiation, one can observe that the optical transmission decreases. Figure (11), (12), (13), and (14) illustrates the difference between the optical transmission of the Molding Epoxy, the Potting Epoxy, the Molding Silicone, and the Potting Silicone samples before and after different cumulative gamma irradiation exposures. By comparing the trends before and after each cumulative gamma irradiation, one can observe that the optical transmission decreases the most after 1 MRad and not significantly after smaller exposures. The wavelength of light being read out in the EM Calorimeter is marked with an arrow at

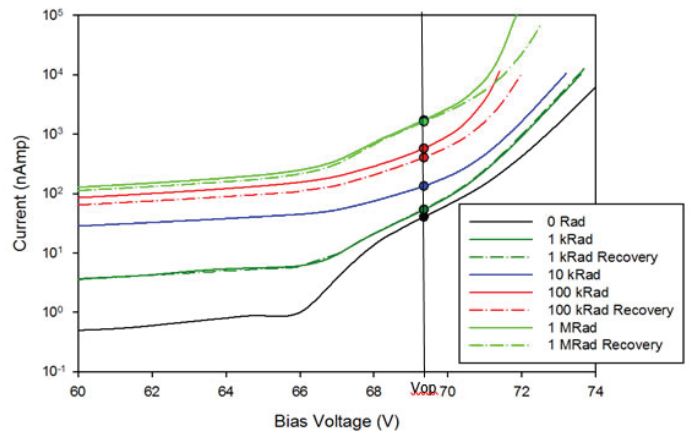


Fig. (21) Dark Current Measurements of the 15um Pixel Sized SiPM with different cumulative exposures to Gamma Irradiation

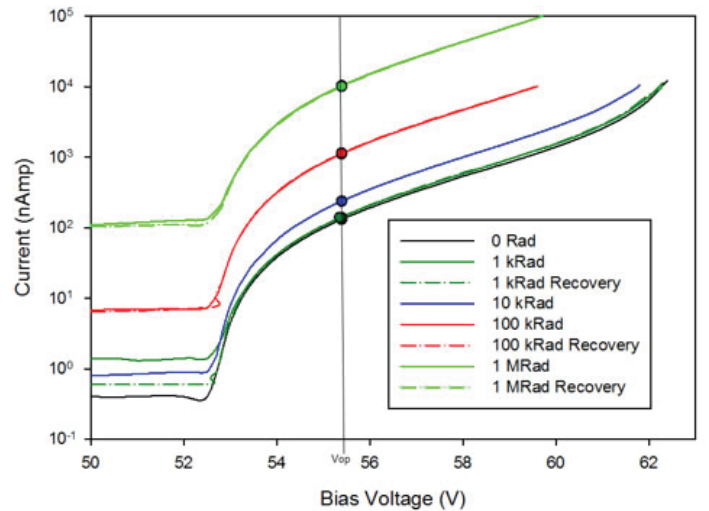


Fig. (23) Dark Current Measurements of the 50um Pixel Sized SiPM with different cumulative exposures to Gamma Irradiation

450nm. One can observe that the materials mainly affected at this wavelength by the gamma irradiation are the Molding Epoxy and the Potting Epoxy. For that reason, Figure (15)-(18) illustrates the percent difference versus the wavelength between the 'before and after' radiation optical transition measurements. Figure (15) illustrates that at 450 nm, approximately 5% of the signal will be lost after this much gamma radiation damage to the Molding Epoxy sample. Figure (16) illustrates less than 5% of signal will be lost after this much gamma radiation damage to the Potting Epoxy sample. Further, Figure (17) and (18) both indicate that approximately no signal will be lost after this much neutron radiation damage to either the Molding or the Potting Epoxy samples.

B. Dark Current Measurements

The SiPM's dependences of the dark current on the bias voltage measured before and after exposure to 1 MRad gamma irradiation and to 1010 n/cm² of 14MeV neutrons are shown in Figure (19) and Figure (20). The points are plotted to indicate the SiPM's operating voltage. By comparing the trends before and after the gamma irradiation and neutron radiation, one can observe that

the dark current increases significantly more as a result of neutron radiation damage to the SiPMs. Figures (21) - (23) illustrates the difference between the 15um, 25um, and 50 um pixel sized SiPMs before and after different cumulative Gamma irradiation exposures. Figures (24) - (26) illustrate this difference with different cumulative neutron irradiation exposures. By comparing the

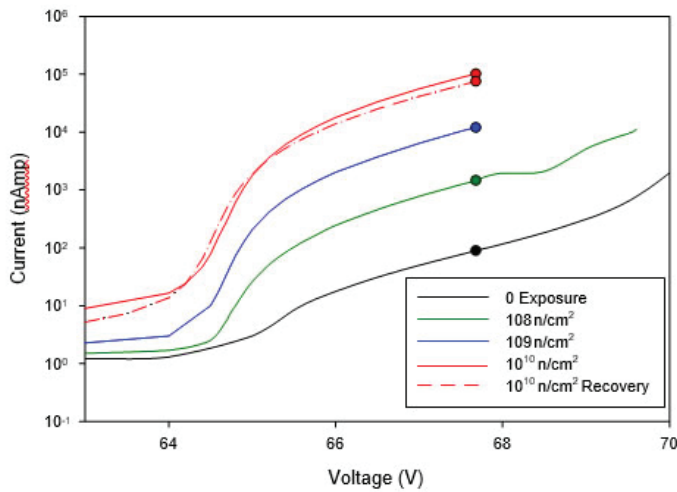


Fig. (25) Dark Current Measurements of the 25um Pixel Sized SiPM with different cumulative Exposures to 14 MeV Neutrons

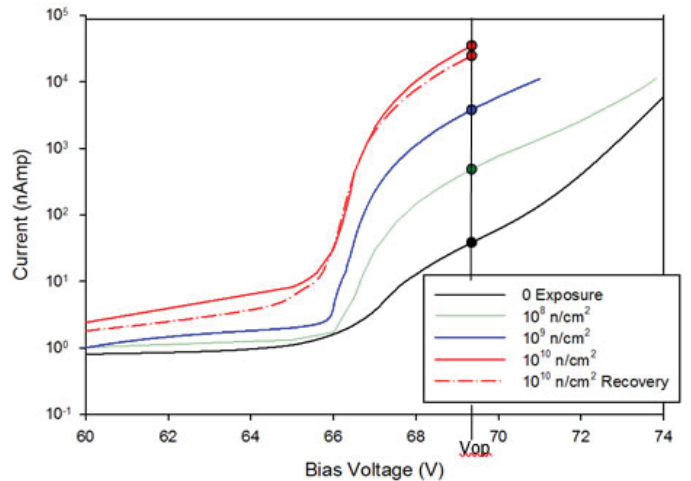


Fig. (24) Dark Current Measurements of the 15um Pixel Sized SiPM with different cumulative Exposures to 14 MeV Neutrons

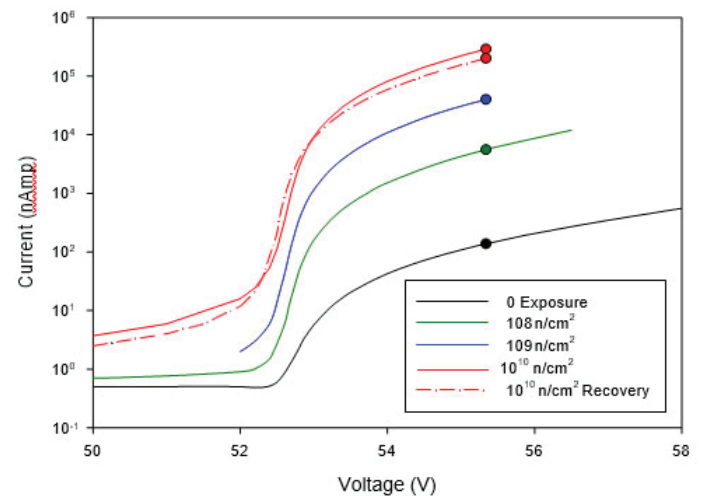


Fig. (26) Dark Current Measurements of the 50um Pixel Sized SiPM with different cumulative Exposures to 14 MeV Neutrons

Factor Increase in Dark Current at Operating Voltage (Vop) With Different Cumulative Gamma Radiation Exposures				
Radiation Exposure Amount	15 μm SiPM	25 μm SiPM	50 μm SiPM	
1 kRad		1.3	0.8528	1.1
3 Days after 1 kRad Exposure		1.3	1.2	1.1
10 kRad		3.3	1.9	1.8
100 kRad		14.2	5.7	8.5
2 Days after 100 kRad Exposure		10	5.8	8.7
1 MRad		42.3	41.3	78.4
1 Day after 1 MRad Exposure		40	40	75.7
8 Days after 1 MRad Exposure		34.1	32.7	62.3

Fig. (27.a) SiPMs Irradiated with Different Cumulative radiation exposures and recovery Factor increase in dark current at operating voltage (Vop)

Factor Increase in Dark Current at Operating Voltage (Vop) With Different Cumulative Neutron Radiation Exposures				
Radiation Exposure Amount	15 μm SiPM	25 μm SiPM	50 μm SiPM	
10 ⁸ n/cm ²		12.7	16.5	40.5
10 ⁹ n/cm ²		98.9	135.2	291.5
10 ¹⁰ n/cm ²		912.5	1144.4	x2108.3
5 Days after 10 ¹⁰ n/cm ² Exposure [Recovery]		646.9	838.8	1468.6

Fig. (27.b) SiPMs Irradiated with Different Cumulative radiation exposures and recovery Factor increase in dark current at operating voltage (Vop)

trends before and after each cumulative gamma irradiation and neutron radiation, one can observe how each exposure increases the dark current at the operating voltage by some factor. These factors have been calculated and placed in a table seen in Figure (27). The table illustrates the factor increase in dark current at operating voltage between different cumulative radiation exposures from before radiation exposures and between different recovery times after each exposure for each SiPM. This chart does illustrate that there is some recovery for both radiation damage, but one can observe that the neutron radiation damage recovers more than the gamma radiation damage.

C. Initial Output Pulses Images

The SiPM's pulse height distribution for an average of 4-5 detected photoelectrons before and after exposure to 1 MRad gamma irradiation are shown in Figures (28) and (29). By comparing the trends before and after the gamma irradiation, one can observe that the single photoelectron peaks in the initial distribution are no longer resolved after irradiation. This is due to the increased dark current noise after irradiation. To show the change in the initial output pulses between different cumulative exposures

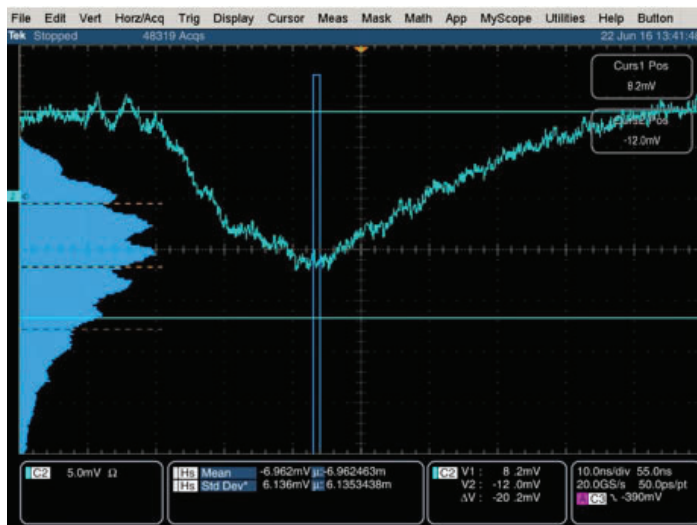


Fig. (28) Image of the 15um SiPM's initial output pulses before exposure to 1 MRad gamma irradiation.



Fig. (29) Image of the 15um SiPM's initial output pulses after exposure to 1 MRad gamma irradiation.

to gamma irradiation, the images of the 15um SiPM are shown in Figure (30).

D. Optical Saturation Curves

The SiPM's optical saturation curve before and after exposure to 1 MRad gamma irradiation and to 1010 n/cm² of 14MeV neutrons are shown in Figure (31) and Figure (32). The lines are plotted to indicate the SiPM's total number of pixels. The measured photons are linearly proportional to the number of incident photons up to the level when the SiPMs count rate begins to saturate for all optical saturation curves as expected. By comparing the trends before and after the gamma irradiation and neutron radiation, one can observe that the saturation curves do not significantly change. Figures (33) - (35) illustrates the difference between the 15um, 25um, and 50 um pixel sized SiPMs before and after different cumulative Gamma irradiation exposures.

Figures (36) - (38) show this difference with different cumulative neutron irradiation exposures. By comparing the trends before and after each cumulative gamma irradiation and neutron radiation, one can observe a slight change in the saturation curves but there are no real significant changes. This change could be due to a slight gain change of the SiPMs.

E. Monitored Current

This SiPM's current was graphed versus time as seen in Figures (39) and (40). Figure (39) shows each different SiPM's current as they were exposed to 14 MeV Neutrons with the cumulative exposures of magnitude: 108 n/cm², 109 n/cm², and 1010 n/cm². Figure (40) shows each different SiPM's current as they were exposed to gamma rays with the cumulative exposures of magnitude: 1 kRad, 10 kRad, 100 kRad, and 1 MRad. These graphs expand on the measured dark current graph's recovery data. Here one can easily see how the SiPMs recovered after each exposure as time went on.

IV. Conclusion

From the data, it can be concluded that the gamma radiation affected the optical transmission of the epoxy/silicone samples. This means that the coating on the SiPMs is darkening, and as such, will not allow as many photons through, thereby making the SiPMs less effective. As can be observed on the graph, at 450nm, which is the wavelength of light being read out in the EM Calorimeter, approximately 5% of the signal will be lost after this

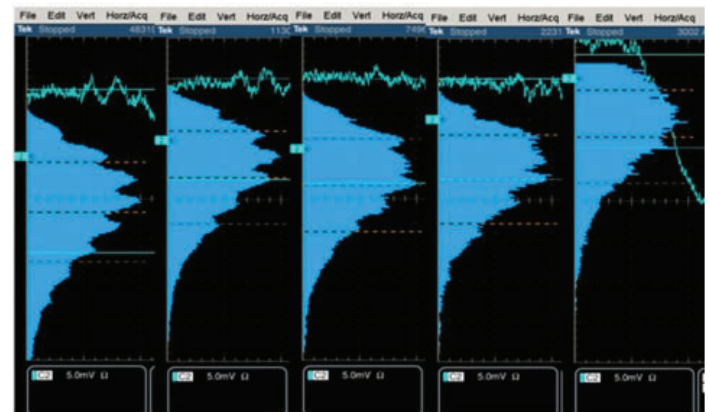


Fig. (30) Image of the 15um SiPM's initial output pulses exposure (left to right) 0 Rad, 1 kRad, 10 kRad, 100 kRad, and 1 MRad gamma irradiation.

much radiation damage to the Molding Epoxy right. However, the gamma ray radiation level in the sPHENIX calorimeters are not expected to reach such a high level, since they only reach on the order of a few kRad per year.

The neutron radiation did not affect the optical transmission

significantly. However, neutrons cause a much larger increase in dark current than gammas. By observing the graphs, it can be concluded that the dark current at the operating voltage has a higher factor increase from neutron radiation than from gamma irradiation. The 15µm SiPM's dark current at operating voltage

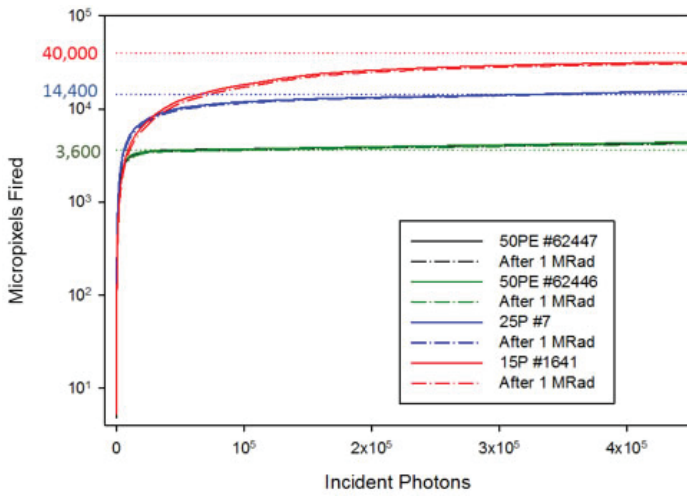


Fig. (31) Optical Saturation Curves of SiPMs Before and After Exposure to 1 MRad Gamma Irradiation

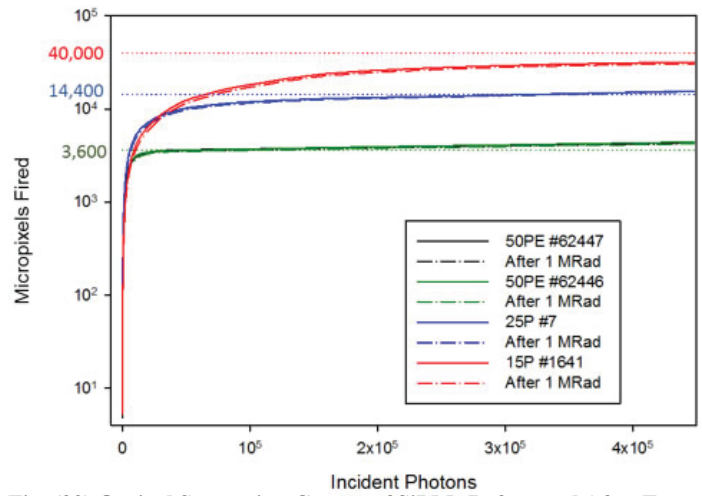


Fig. (32) Optical Saturation Curves of SiPMs Before and After Exposure to 10^{10} n/cm² of 14 MeV Neutrons

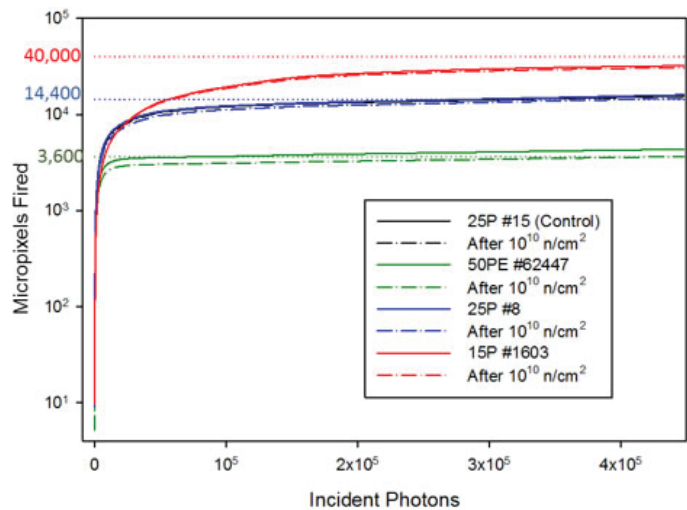


Fig. (33) Optical Saturation Curves of the 15µm Pixel Sized SiPM with different cumulative exposures to Gamma Irradiation

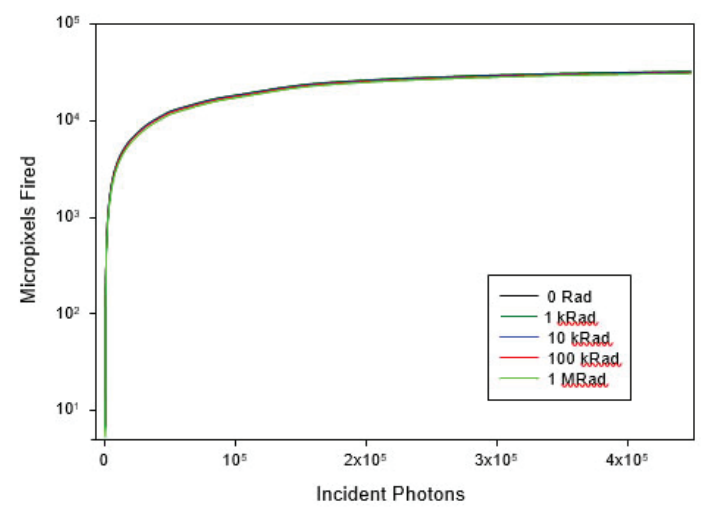


Fig. (34) Optical Saturation Curves of the 25µm Pixel Sized SiPM with different cumulative exposures to Gamma Irradiation

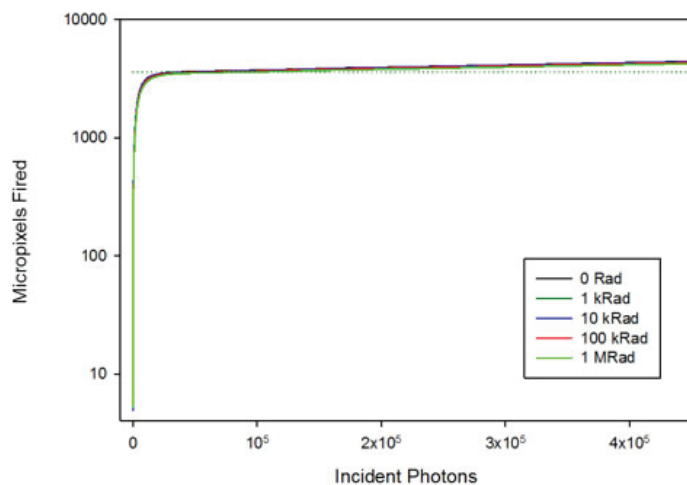


Fig. (35) Optical Saturation Curves of the 50µm Pixel Sized SiPM with different cumulative exposures to Gamma Irradiation

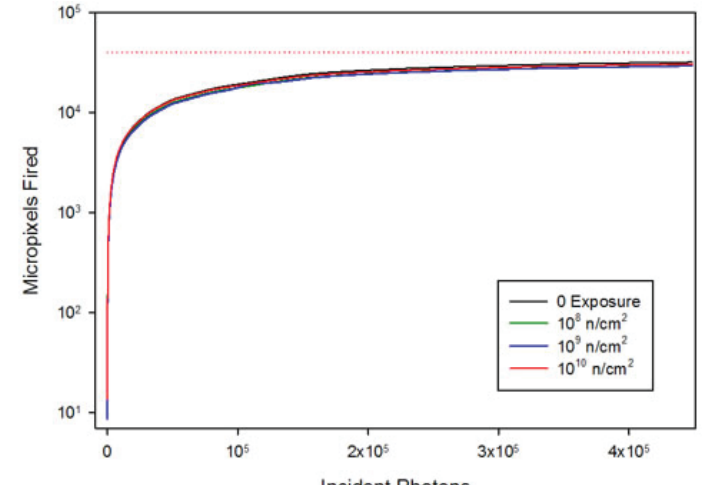


Fig. (36) Optical Saturation Curves of the 15µm Pixel Sized SiPM with different cumulative exposures to 14 MeV Neutrons

increased by a factor of 912.5 after being exposed to 1010 n/cm² of 14 MeV neutrons and only increased by a factor of 42.3 after being exposed to 1 MRad of gamma irradiation. The graphs also reveal a trend that the SiPMs with larger pixels showed more damage than those with smaller pixels. You can see this trend in the tables, but there are some instances where this trend does not follow. These instances seem to only differ from this trend in the gamma radiation and are not significantly different than the trend. These could mean there is no real trend and should be looked into in farther research. It was also observed that the dark current decreased with time after the exposure. The 15 μ m SiPM's increased dark current at the operation voltage decreased by 19% 8 days after 1 MRad of gamma irradiation. The same SiPM's increased dark current at operation voltage decreased by 29% only 5 days after 1010 n/cm² of neutron radiation. The neutron radiation gave more damage to the SiPMs dark current characteristic than the gamma irradiation, but it also has a higher recovery rate. The monitored current nicely illustrates how the SiPMs dark current at operating voltage is affected by each type of radiation at different cumulative exposures. The SiPM with the least dark current was the 15 μ m, regardless of how much or what type of radiation.

The SiPM's initial output pulse images agree with the dark

current graphs and farther show the effects of the radiation damage to the SiPMs dark current. The optical saturation curves do not appear to be affected by either the gamma radiation or neutron radiation. The monitored current graphs farther expand on the measured dark current graph's recovery data.

In conclusion, we determined that gammas and neutrons produce different types of radiation damage in SiPMs. The amount of damage depended on the size of the pixels in the SiPMs, the amount of radiation and what type of radiation the SiPM was exposed to. We further determined that the radiation induced dark current partially decreased over time differently for each types of radiation damage. Over all, one can observe that the window samples made of silicone materials are not significantly affected by either radiation and would be better for a high radiation environment. The SiPM with the least dark current was the 15 μ m, regardless matter how much or what type of radiation. The conclusion is that the smaller pixels show less damage, i.e., increase in current, than larger pixels.

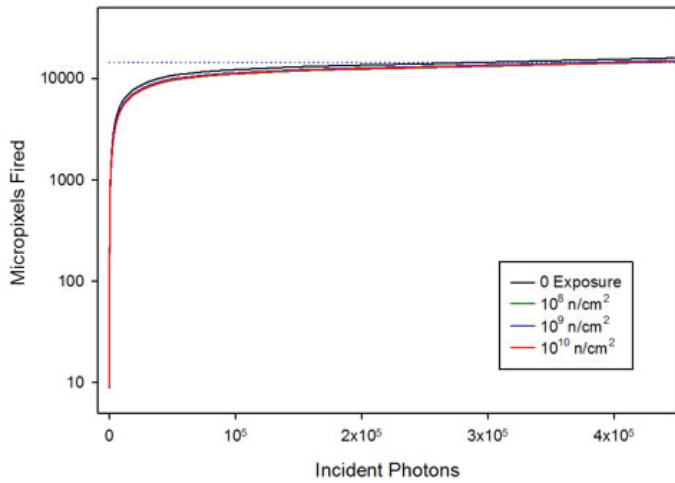


Fig. (37) Optical Saturation Curves of the 25um Pixel Siz SiPM with different cumulative exposures to 14 MeV Neutrons

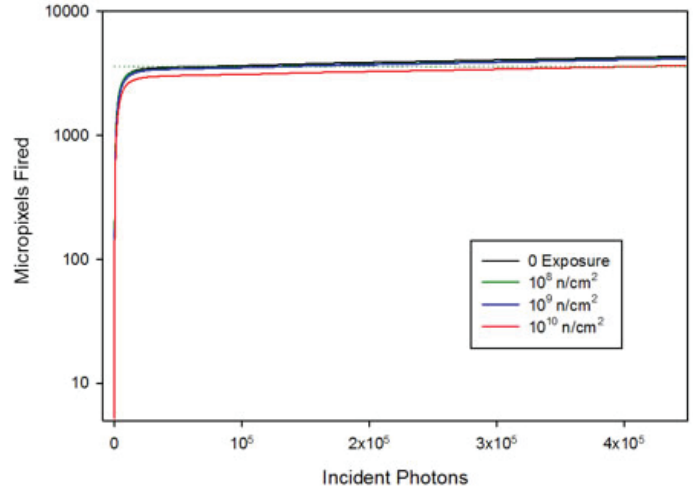


Fig. (38) Optical Saturation Curves of the 50um Pixel Siz SiPM with different cumulative exposures to 14 MeV Neutrons

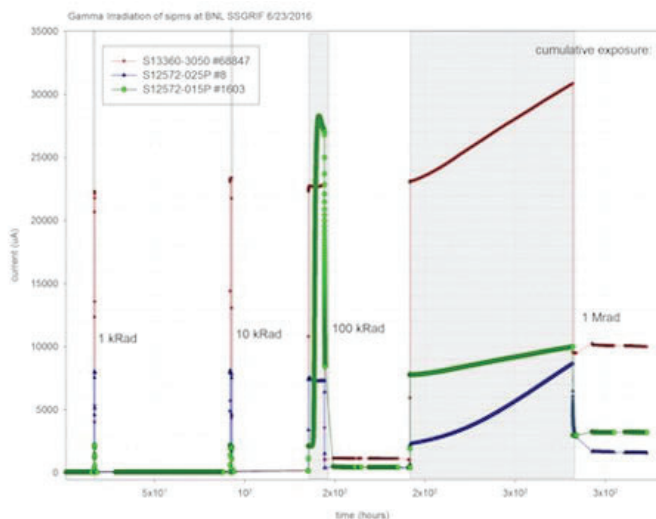


Fig. (39) Monitored Current vs. Time of each Different SiPM with different cumulative exposures to Gamma Irradiation

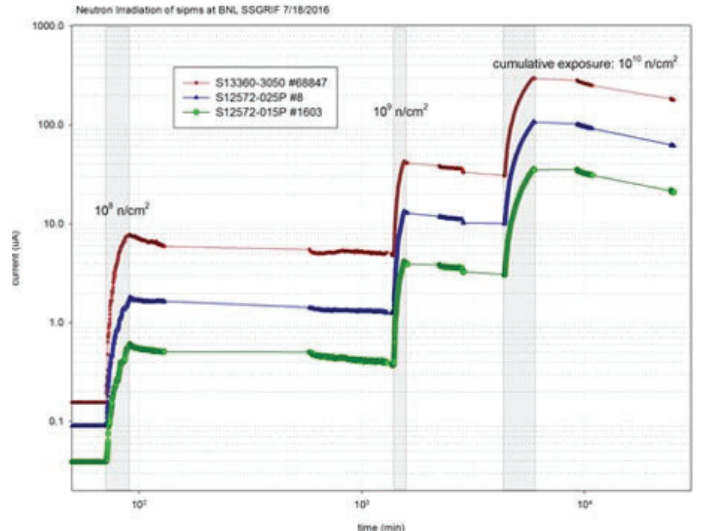


Fig. (40) Monitored Current vs. Time of each Different SiPM with different cumulative exposures to 14 MeV Neutrons

V. References

- ¹A. Heering, Yu Musienko, et al. Nucl. Instrum. Methods 824 (2016) 114.
- ²E. Garutti, R. Klanner, et al. Silicon Photomultiplier characterization and radiation damage investigation for high energy particle physics applications., 2014 JINST 9 C03021 [doi:10.1088].
- ³Hamamatsu Photonics K.K. <http://www.hamamatsu.com/jp/en/S133603050VE.html>.
- ⁴R. Pagano, S. Lombardo, et al. Nucl. Instrum. Methods 767 (2014) 342.
- ⁵Yu Musienko, A. Heering, et al. Nucl. Instrum. Methods 787 (2015) 312.
- ⁶Yu Musienko, D. Renker, et al. Nucl. Instrum. Methods 610 (2009) 87-92.

Oxidation of ethanol under the surface of CeO₂ supported on Platinum using an electrochemical chamber setup

Joesene Soto, Angel Ortiz, and Carlos Cabrera

Chemistry Department, University of Puerto Rico, Río Piedras Campus, San Juan, Puerto Rico

Kenneth Goodman and Pamela Carrillo

Department of Chemistry, Stony Brook University, Stony Brook New York 11974

Michael G. White, United States

Chemistry Department, Brookhaven National Laboratory, Upton, New York 11973

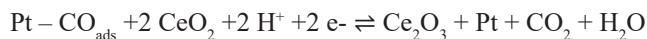
Abstract

Cerium Oxide (CeO₂) nanoparticles supported on polycrystalline Platinum (Pt) have demonstrated properties of an excellent co-catalyst for the electrochemical oxidation of ethanol (EOR). Ceria dissociates water and releases oxygen via the redox reaction Ce⁴⁺/Ce³⁺, and Pt has high catalytic properties making a great metal-oxide interface for EOR. The EOR has been extensively studied because of its potential for fuel cells. The preliminary results presented here involved testing of an electrochemical cell which was part of a new instrument that will eventually allow electrocatalysts for EOR prepared under ultra-high vacuum (UHV) conditions and characterized by surface science techniques such as XPS and also be tested for their electrochemical activity under ambient conditions. We evaluated different surface concentrations of CeO₂ in order to obtain the best EOR performance. The mixed oxide, TiO₂-CeO₂, and an oxide supported metal co-catalyst, Rh/CeO₂, were also studied.

I. Introduction

Global energy consumption has increment drastically through the years and researches are developing new technological methods to obtain energy using renewable resources, fuel cells, among other clean energy procedures¹. Methanol has been the most common alcohol for fuel cells. Platinum is the best performing anode material for methanol oxidation but its high cost makes a challenge for the commercialization of a fuel cell with it. Recently the Ethanol oxidation reaction(EOR) acquire attention because is less toxic and also has more capability of energy storage per volume compared to methanol^{2,3}. Also the production of ethanol in great quantities is possible due to the fermentation of sugars, biomass feed stocks, urban residues and forestry^{4,5}. Electrochemical oxidation of alcohols produces carbon monoxide⁶ a toxic waste for this type of reactions using Platinum, because carbon monoxide binds to the surface of Platinum poisoning the electrode and reducing the capability of oxidizing the alcohols tested⁷.

Leaving to a problem on how we can remove carbon monoxide of the Pt surface to ensure a considerable oxidation of the alcohols. Researchers decided to continue to use Pt as the anode for ethanol oxidation but they implemented other elements to its surface mostly metal oxides in order to complete the reaction producing CO to CO₂ and reduce the poisoning of the Pt electrode. The interest in ceria(CeO₂) as this metal oxide has increment because of its oxygen carrying facility and oxygen releases reversibility without distortion of its lattice⁷. Ceria dissociates water and releases oxygen via the redox reaction Ce⁴⁺/Ce³⁺(Reaction 1)⁸.



Reaction 1.

These work intended to evaluate different samples of ceria in order to see its catalyst capabilities along a Pt electrode for the EOR. Electrochemical techniques such as cyclic voltammetry's are going to be done to achieve the ethanol oxidation. Onset potentials values are going to be measured because the catalytic performance must need a low potential to maximize the results without consuming its reactants at such high potentials and currents.

II. Methodology

All the cyclic voltammograms were run using an electrochemical chamber setup that is part of an ultra high vacuum (UHV) chamber capable of making electrochemical measurements, LEED, TPD, XPS and Clusters. We used a Platinum foil polycrystalline electrode along a Pt counter electrode and Ag/AgCl (0.197 vs NHE) as our reference electrode. Sulfuric acid (0.1M) was used to perform the electrochemical cleaning and a solution of 0.1M EtOH dissolved in 0.1M H₂SO₄ to perform the experiments. The working electrode was modified with different samples of ceria (Table 1) with a drop cast of 50μL on its surface. Using an oven at 100°F for 30 minutes and then proceed to make the cyclic voltammetry experiments. The first cycle of each cyclic voltammetry was used to compare their onset potentials in order to find the best catalyst for the EOR.

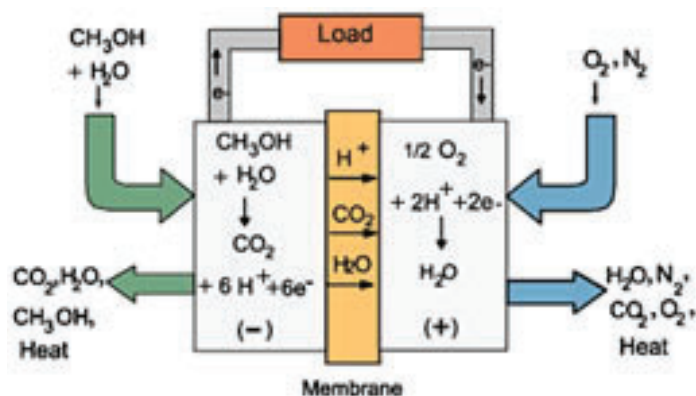


Figure 1. Representative diagram of the Mechanism of the methanol oxidation.

III. Results

See figures 2 through 7.

Table 1. Onset potentials of the Ceria samples studied

Sample	Current(I)	Onset Potential
Pt	0.3130	0.2962
CeO ₂	0.1592	0.2595
Commercial CeO ₂	0.1989	0.2934
CeO ₂ 0.1%	0.1366	0.2363
CeO ₂ 0.2%	0.2496	0.2283
CeO ₂ 0.02%	0.5680	0.2018
TiO ₂ -CeO ₂ -Nafion	0.1532	0.3210
Pt Nafion	0.1893	0.1992
Rh/CeO ₂ -Pt-Nafion	0.1117	0.2611

IV. Discussion and conclusions

Ceria was used because of its capability of enhancing the EOR using a Pt electrode as the oxidation metal. Different samples from laboratory 1% synthesized ceria and 1% commercial

ceria nanoparticles around 10 to 20nm deposited on the surface of a Pt electrode, were tested to compare their catalytic behavior during the EOR using onset potential as the parameter to be evaluated. Bare Platinum was analyzed first and the onset potential was 0.300 V, for the commercial ceria nanoparticles we obtained 0.294 V and for synthesized ceria nanoparticles 0.260 V. Since the laboratory synthesized ceria obtained the lowest onset potential we decided to continue the experiments with it, but we also decided to reduce the coverage of ceria in the Pt electrode surface because high concentrations of ceria can block active sites of Platinum lowering the current of the electrode and decreasing the oxidation of ethanol. After three different dilutions of Ceria to 0.2%, 0.1% and 0.02%, ceria 0.02% obtained the lowest onset potential with 0.202 V. We also analyzed TiO₂-CeO₂ and Rh/CeO₂. Table 1. has the onset potential values for all the samples. The oxidation of ethanol was achieved using the electrochemical chamber setup but the results suggest more studies in order to highlight a catalyst for EOR. It's clear that the amount of ceria in the surface of the Pt electrode provides different results but they do not guaranty a reproducible result for the oxidation of ethanol. Future studies are emphasized on controlling the size of the nanoparticles us-

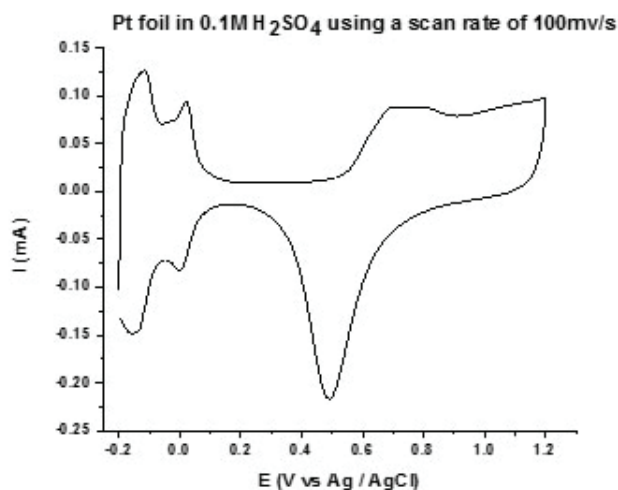


Figure 2. Voltammogram representing the electrochemical clean of Pt foil with the use of 0.1M H₂SO₄.

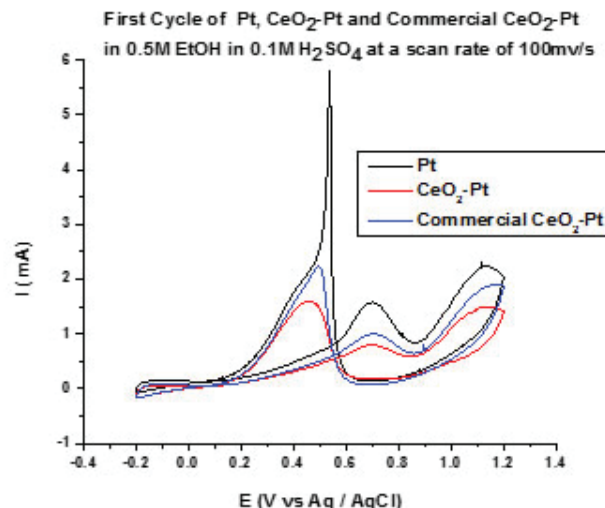


Figure 3. Ethanol oxidation using bare Pt foil, Pt modified with 1% of commercial CeO₂ and laboratory synthesized CeO₂.

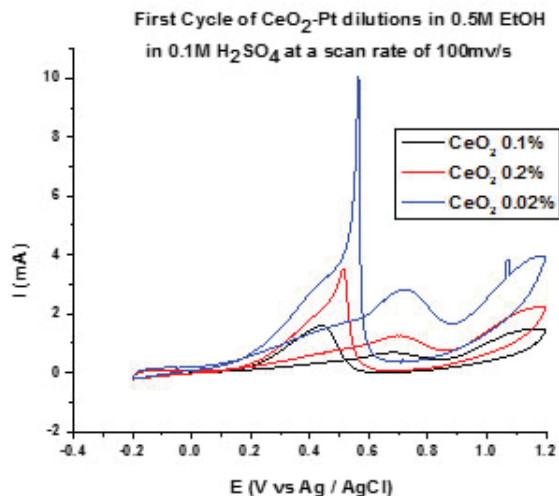


Figure 4. Ethanol oxidation using bare Pt foil, Pt modified with different concentrations of laboratory synthesized CeO₂.

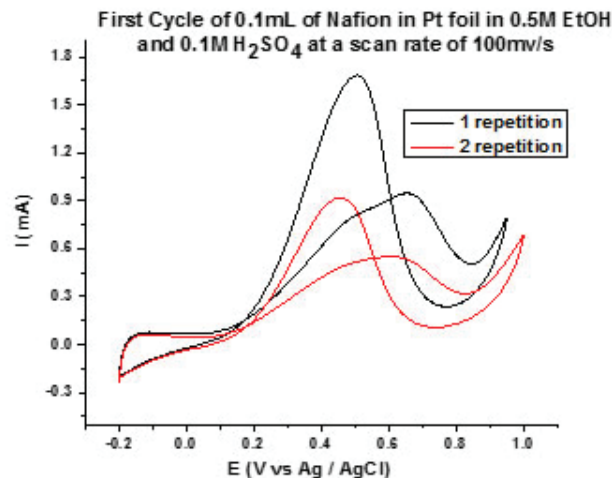


Figure 5. Ethanol oxidation using Pt modified with 2% of Nafion.

ing size selected cluster deposition in the Pt electrode providing a variation of ceria size and density in the surface of Pt. Electrochemical techniques such as chronoamperometries are needed to be done in order to analyze the catalytic behavior through time of the nanoparticles. For characterization X-ray Photoelectron spectroscopy (XPS) should be done to monitor the oxidation changes before and after each EOR with the cyclic voltammetry's.

V. Acknowledgments

This project was supported in part by the National Science Foundation, Louis Stokes Alliance(s) for Minority Participation (LSAMP) at the University of Puerto Rico, Rio Piedras campus, under the LSAMP Internship Program at Brookhaven National Laboratory.

Michael White laboratory for letting us make experiments in his facilities and with the use of his students samples.

VI. References

- ¹Abruña, H. D., Energy in the Age of Sustainability. *Journal of Chemical Education* **2013**, *90* (11), 1411-1413.
- ²Mann, J.; Yao, N.; Bocarsly, A. B., Characterization and Analysis of New Catalysts for a Direct Ethanol Fuel Cell. *Langmuir* **2006**, *22* (25), 10432-10436.
- ³González, M. J.; Hable, C. T.; Wrighton, M. S., Electrocatalytic Oxidation of Small Carbohydrate Fuels at Pt–Sn Modified Electrodes. *The Journal of Physical Chemistry B* **1998**, *102* (49), 9881-9890.
- ⁴Xu, C.; Tian, Z.; Shen, P.; Jiang, S. P., Oxide (CeO₂, NiO, Co₃O₄ and Mn₃O₄)-promoted Pd/C electrocatalysts for alcohol electrooxidation in alkaline media. *Electrochimica Acta* **2008**, *53* (5), 2610-2618.
- ⁵Wang, Y.; Zou, S.; Cai, W.-B., Recent Advances on Electro-Oxidation of Ethanol on Pt- and Pd-Based Catalysts: From Reaction Mechanisms to Catalytic Materials. *Catalysts* **2015**, *5* (3).
- ⁶Spendelow, J. S.; Babu, P. K.; Wieckowski, A., Electrocatalytic oxidation of carbon monoxide and methanol on platinum surfaces decorated with ruthenium. *Current Opinion in Solid State and Materials Science* **2005**, *9* (1–2), 37-48.
- ⁷Díaz, D. J.; Greenleach, N.; Solanki, A.; Karakoti, A.; Seal, S., Novel Nanoscale Ceria–Platinum Composite Electrodes for Direct Alcohol Electro-Oxidation. *Catalysis Letters* **2007**, *119* (3), 319-326.
- ⁸Ostroverkh, A.; Johaneck, V.; Kus, P.; Sediva, R.; Matolin, V., Efficient Ceria-Platinum Inverse Catalyst for Partial Oxidation of Methanol. *Langmuir* **2016**, *32* (25), 6297-309.

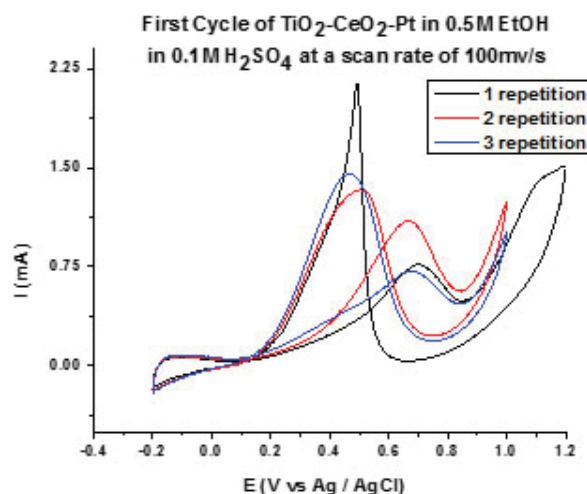


Figure 6. Platinum foil modification with 5mM TiO₂-CeO₂ and a drop of 2% Nafion.

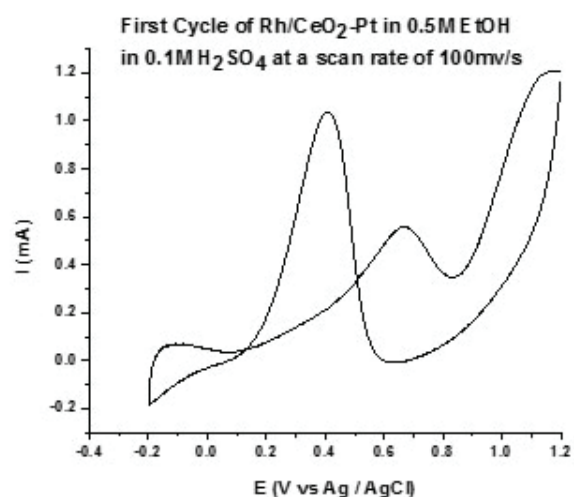


Figure 7. Platinum foil modification with 5mM Rh-CeO₂ and a drop of 2% Nafion.

Integrated Facility Management: Keeping the laboratories alive

Derek Squires

Stony Brook University, Stony Brook NY 11794

John Biemer

Facilities Operations Office, Brookhaven National Laboratory, Upton, NY 11973

Abstract:

During my internship I have had a role in various facility management projects. Building 480 has a number of electrical panels that are outdated and have electrical grounding issues. Working with one of the junior engineers, Meghan Donnelly, I helped locate and document where each panel is and what specific issue needs to be reconciled. Many of the panels either had a faulty grounding or didn't have a ground altogether. This can be common for panels that are very old because electrical practices were different when the laboratory started and many of the electrical safety codes have been modified over time. In the basement of building 535 there is a coil that froze during the most recent winter and will be replaced. To prevent this from happening again a warm air bypass will be considered. This involves flushing the coil of its chilled water and having warm air fed into the coils pipes to ensure no moisture can freeze against the walls of the pipes. My role in this project is to help estimate the cost of the project, develop alternative ideas, and calculate the cost savings of performing the traditional winterization. During this summer I have developed further proficiency in Microsoft Excel and AutoCAD. Additionally, I have gained insights and skills related to assessing mechanical system failures and developed a deeper understanding of the role each system plays in sustaining scientific facilities.

Electrical safety plays a vital role in facility management. Many of the buildings at Brookhaven National Laboratory were built decades ago and some of these buildings have electrical grounding issues. Building 480 is a building with many old electrical panels and very advanced equipment (i.e. an electron microscope). To maintain the safety of this building I helped document the various electrical panels that had servicing requirements. The project involved locating each of the electrical panels in the building, creating a key plan demonstrating the location of the panels and what services needed to be completed. Many of the panels have issues with grounding and knockout seals. These issues are electrical safety hazards and rectifying them will lead to safer working conditions for all building occupants. This project was also important because it will help guide the electricians to the proper panels and allow them to make the necessary changes. To complete this project there was a combination of time spent in the building and on AutoCAD to complete the necessary drawings.

In addition to the grounding project at building 480, I also participated in a few other facilities related projects. Building 535 had a coil freeze during the most recent winter and needs to be replaced. Prior to my internship the replace coil was ordered and received but there has been much discussion regarding the prevention of the new coils from freezing. Working with the Facility Project Manager (FPM) and the Facility Complex Engi-

neer (FCE), different approaches to the problem were researched and discussed. At building 815 there is a rooftop air-handler that has damper control issues. The actuators that open and close the dampers have not worked for some time and the decision was made to replace the entire unit. Again, I collaborated with the FPM and the FCE to coordinate the unit specifications and helped verify this information. The order has not been placed yet due to ongoing negotiations with the supplier, Daikin-McQuay.

Electrical safety is an important concern at any facility but especially a DOE funded laboratory. Major injuries can occur when improper standards are in place and this includes the proper grounding for electrical panels. At building 480, the electricians assigned to the task were responsible for inspecting all of the electrical panels in the western section of the building. This section of the building is much older than the eastern section and many of the panels have been there since the building was constructed. Many of the panels had been missing ground bars, or knockout seals. Other issues included the need for a cleaning, improper ground connections, and improperly sized wire conductors. When constructing an electrical panel, grounding is extremely important to ensure that maintenance operations and for the overall protection of the equipment a panel feeds. The purpose of this grounding is to charge the metal aspects of a panel or device with the same voltage. If there is no different in voltage between two media then there can be no current flow. Ground is also referred to as "earthing" because the metal components being grounded are typically connected to parts of the building that connect to the earth. Other ground set ups can even be directly in contact with the earth. If there is no ground or a ground is improperly set up, when a person touches the electrical panel there could be a current flowing through the panel and that current can flow through the person leading to potentially fatal injuries.

The process that I followed to complete this project was rather straightforward, though time consuming. First, Ariel Nunez, the FCE, guided myself and a junior engineer, Meghan Donnelly, through the building to each of the various panel locations. This walk-through was necessary because there were no key plans that had the various panels located. During the walk-through, Mr. Nunez detailed the information necessary for the project, and a general idea of how to make the drawings in the most convenient way possible for the electricians. The end goal was to have either one or multiple smaller drawings that laid out exactly what needed to be done at each panel, what the panel received its power from, and what the panel provided power to. Additional information included the voltage, amperage, number of phases, and the hazard category (in case certain personal protective equipment (PPE) was needed).

After the walk-through, Ms. Donnelly and I had a meeting to discuss what approach we wanted to take on the project. We assumed different roles and responsibilities. My task was to ac-

cumulate the information regarding the maintenance of the panels. I documented where the panels were on one of the generic key plans we found and I documented exactly what services were required, along with the power requirements of the panels. Ms. Donnelly took the role of confirming the one-line diagrams for where the panels were fed from and what they were feeding. She also confirmed the panel schedule's to make sure we knew exactly what room and equipment would be affected when the maintenance is performed.

Next, we went panel by panel throughout the building and collected all of the information we needed. This process was relatively tedious and time-consuming because there are over 50 panels in the building. After we collected the information, we each went to work on the key plan drawing in AutoCAD. Initially, I took the role of placing all of the panels on the drawing and labeling them. Then, Ms. Donnelly reviewed them and made suggestions on how we could improve the efficacy of the layout and how we could make everything simpler for the electricians. Together we made revisions and ensured that all of the labels were logically formatted. Once the drawing was completed we began to construct the final layout of the building. We experimented with trying to fit all of the panels on one large plot, 22"x34", but realized that it would be impractical to have the electricians navigate the building with that type of map. Instead, we went with Mr. Nunez's suggestion of making smaller 11"x17" plots with different sections of the building on each plot. The final result was six plots for the building. Each plot covers a different section of the building and each of the panels labeled with the required services indicated. To the left of each key plan, we were able to construct a table with additional information. This table is where we indicated the voltage, amperage, feeds, and what equipment was affected by the particular panel.

A major facilities concern is the freezing of cooling coils in the winter. To combat this issue it is very common to implement some sort of coil maintenance procedure in the latter months of the fall or early months of the winter. In the Instrumentation Division, building 535, a coil in one of the air handlers froze last winter. This happened during one of the more particularly cold weeks and the replacement coil has already arrive to the building. In the past, the freeze protection procedure has been to drain the coil of the chilled water used by the Central Chilled Water Facility (CCWF) and then refill the coil with a glycol water mixture. Typically the mixture is 50/50 glycol to water. In the spring, the coils are drained of the glycol water mixture and the chilled water is re-introduced into the system. Before the coil is given the chilled water, however, the system must be tested for the glycol content. There must be less than 1ppm (parts per million) glycol present in the coil in order for the system to be placed back into service. This process involves very costly materials and labor each winter. In 2016 the total cost of the service was estimated to be \$10,441.08. The actual cost was actually \$12,199.26 because there were overtime hours used to perform the procedure. This cost is substantial and there has been a great deal of research into alternative service methods.

One of the possibilities would be to never turn off the chilled water supply to the air handler coil. This method would maintain constant flow of water through the coil and therefore no chance that stagnant water will have time to freeze. The cost involved in this method, however, will be substantial. It will not only cost money to produce and supply the chilled water, but it will also

reduce the efficacy of the heating system. When the chilled water is not supplied, the air handler is producing tempered and warm air into the building to maintain comfortable temperature to the building occupants. If the already cold winter air needs to pass the chilled water coil, it will put more stress onto the heating system.

A more logical solution is to utilize a warm-air bypass system. This strategy involves draining the coils of the chilled water in the beginning of the winter. Then when the air handler begins to produce warm air for the building, a bypass pipe is connected into the supply air discharge section of the air handler and re-routed into the chilled water coil. The warm air will be traveling through the coil constantly and will either warm any remaining moisture to a temperature well above freezing, or it will evaporate the moisture altogether. This method has already been utilized by other buildings at the laboratory and has been successful. The initial costs have been estimated by the Modernization Project Office (MPO) to be dependent on whether the work was done externally or internally. Externally, the project would cost roughly \$29,000 because it would involve outside contractors and mechanics. Internally, the job would cost only \$10,000.

The warm-air bypass system is most likely to be the solution implemented because it will cost just as much money as it would to drain the system and fill it with glycol. Additionally, the yearly maintenance costs will be minimal because the only work needed each year will be to drain the coil of the chilled water and then simply open a few valves and allow the supply air to begin traveling through the coil. Also, there will be no testing needed to ensure glycol cannot invade the CCWF. One of the downsides to this solution, however, is that taking airflow from the supply air will reduce the airflow sent to the building occupants. Also, it is important that the airflow volume is large enough to travel the entire length of the coil. These risks were considered in the decision and are thought to be minimal enough as to allow for this project to move forward. The project is awaiting final approval from management but is very likely to occur before the cold, harsh winter months arrive.

Acknowledgements

I want to thank John Biemer, Ariel Nunez, and Meghan Donnelly for their help and support in completion this project.

Relationship analysis between Order Chiroptera and burned forest areas

Emma Squires

School of Natural Resources and Ecology, Paul Smith's College, Paul Smiths, NY 12970

Timothy Green and Kathy Schwager

Environmental Protection Division, Brookhaven National Laboratory, Upton, NY 11973

Abstract

Fires can be beneficial to forest health, especially in the Central Pine Barrens Region of Long Island which is a fire dependent ecosystem, but fire can be detrimental to some fauna living in the forest. The northern long-eared bat (*Myotis septentrionalis*) is a species which has been federally listed as threatened; some research has pointed to the fact that fires might be beneficial to the *M. septentrionalis* population in the long term by creating snags in which the species can roost. In the immediate short term, fires can burn parts of the bats which are not protected by fur, or smoke inhalation can harm adults and non-volant young. The purpose of this research was to determine if there is any difference between bat species utilizing burned and unburned forests at Brookhaven National Laboratory (BNL), with particular focus placed on the presence or absence of *M. septentrionalis*. Static acoustic surveys were conducted by placing detectors in burned and unburned forest locations to determine what species were using each forest type, and the bat calls were identified using Sonobat® and SCAN'R® (automated snapshot characterization and analysis software). 87% of the total collected calls were in the northeastern portion, or areas which had experienced fire in the past 10 years, although more research is needed to identify any significant correlation. This knowledge can help BNL determine where are possible roost areas are. This is beneficial for the planning of prescribed fires, so that during the pupping season additional preparation of the burn units will be conducted to minimize the impacts on the roosts.

I. Introduction

There have been multiple studies showing the possible benefits of prescribed fires on the presence of bat species (Lacki *et al.*, 2009; Cox *et al.*, 2015). The northern long-eared bat (*Myotis septentrionalis*) was once a common bat species in the region, but its population sizes have been decreasing drastically due to white nose syndrome (*Pseudogymnoascus destructans*) (WNS), a fungal disease which has been decreasing bat populations globally (USFWS, 2013). *M. septentrionalis* has recently been federally listed as threatened. Understanding the habitats in which these species live and their responses to habitat modification are key to the conservation of the populations (Cox *et al.*, 2015). Prescribed fire, or fires in general, have the ability to create roost sites for many different species of bats, assisting their population. Fire can affect the ecosystem by killing trees, creating snags, or weakening trees to allow insects or diseases to take over. It has the ability to alter forest composition, and the habitats of the species living there (Cox *et al.*, 2015; Johnson *et al.*, 2011; Lacki *et al.*, 2009; Perry, 2012). In addition to creating roost trees, fires can also increase the amount of light penetration. This then increases the temperatures in roost trees, and can facilitate in raising pups

(Dodd & Lacki, 2015).

While fire can possibly benefit species of bats, it also has the ability to decrease bat population sizes. During the day some species of bats enter torpor, a strategy which helps the individual save energy by lowering body temperature and slowing bodily functions (Dodd & Lacki, 2015). If the temperature is less than 4 degrees Celsius the night before, the bats may not be able to awake from their torpor in time, and be killed by the fire. Bats which roost closer to the ground may suffer from burns on parts of their bodies which are not covered by fur, such as their ears and wings. Other individuals may be harmed by smoke inhalation, or mothers during pupping season may not be able to get their non-volant pups out of the fire to safety (Perry, 2012). Snags provide important roosts for bats (Kunz & Fenton, 2005), and fire may destroy ones which had been previously used as roosts for the bats (Lacki *et al.*, 2009).

The purpose of this study was to compare the frequency of bat calls in forests which had previously been burned by a fire to those which had not had a fire before. This was to see if fire did in fact affect bat foraging frequency in an area. The methods did not allow for determining the size of the population or how many individuals were in an area, but rather the species located in the area and how often they flew by the detector's location. The information gives an idea of how often the site is used by the different species.

II. Materials and Methods

A. Study Site

This study was conducted at Brookhaven National Laboratory (BNL) in Upton, New York, from June through August, 2016. BNL is located in the Central Pine Barrens Region of Long Island, which is a fire dependent ecosystem. On the project site, two general types of stands were classified, those which had experienced fire within the last 10 years, and those which had not. In 2006 and 2011 low intensity prescribed burns were conducted in the northeastern portion (Northeast Unit) of the study site, and in 2012 a moderate-high intensity wildfire burned through some of the prescribed burn units. The tree species composition in the burned sites (in the Northeast Unit of the Laboratory) consists mostly of scarlet and black oak (*Quercus coccinea* and *Q. velutina*) and pitch pine (*Pinus rigida*), while the species composition in the non-burned sites was mostly mixed oak and scattered *P. rigida*. The sites in the southern portion (South Unit) consisted of closed canopy pitch pine-mixed oak forest with little understory and high basal area. The two forest stands were broken up into smaller study sites of approximately 20 acres (Figure 1).

B. Static Surveys

Bat calls were mainly collected by using static surveys. These surveys were completed using Song Meter SM2BAT+® detectors.

The Song Meters were deployed in approximately the middle of each plot. The detector was tied onto the trunk of a tree and had two Wildlife Acoustics® SMX-US ultrasonic microphones attached, approximately 2 meters away from the detectors. The microphones were attached to PVC poles and stood approximately 3.66 meters off the ground, at bat flying height. Microphones faced opposite directions in order to maximize the range and amount of calls collected. The Song Meters were recording from a half hour after sunset until sunrise, cycling between 10 minutes of recording followed by 10 minutes of not recording (Cox *et al.*, 2015). The detectors each remained in the plot for a minimum of one week. If rain was in the forecast, then plastic bags were put over the microphones in order to protect them from the rain so that they were not damaged.

C. Mobile Surveys

In addition to the static surveys, mobile surveys were conducted. An AR 125 Ultrasonic Receiver® by Binary Acoustic Technology® was placed on the top of a vehicle and connected to a laptop computer. Spectral Tuning and Recording Software (SPECT'R III®) was used to record the calls collected by the receiver, and DeLorme Street Atlas USA 2012 Plus® was used to collect the GPS locations of the vehicle at the time of the calls. Surveys were conducted between 2100 and 2230, after the bats have left their day roost to forage for the night. During the survey, the speed of the vehicle was maintained between 5 and 10 miles per hour. There were a total of three survey routes, each of which was done three times. The species location was then mapped on Google Earth™ to determine the habitat type in which they are foraging.



Figure 1. Map of the different sites

D. Call Analysis

Every few days, call data was downloaded from the detectors. The .wav sound files were then run through Snapshot Characterization and Analysis Routine (SCAN'R®), and files with less than 5 chirps were 'failed,' or set aside to look at later. Calls which passed were identified as to which species made them based upon the minimum frequency of the call, the shape of the call, and the slope of the call in octaves per second (Sc). The call classification was then compared to a program which automatically classifies the calls as to which species made them by using an algorithm which is based on thousands of species calls located in the software's reference library, SonoBat®. Calls which failed the SCAN'R® scan were then run through SonoBat®, because that

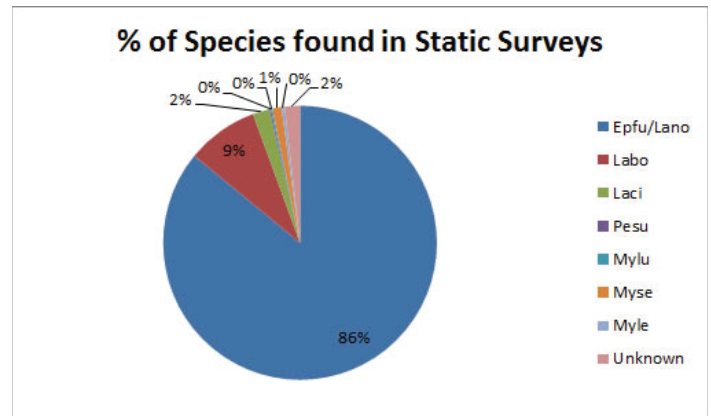


Figure 2. Total percents of bat species located during the study: Epfu= Big brown bat, Lano = Silver haired bat, Labo= Red bat, Laci= Hoary bat, Pesu= Tri-colored bat, Mylu= Little brown bat, Myse= Northern long eared bat, Myle= Small-footed bat

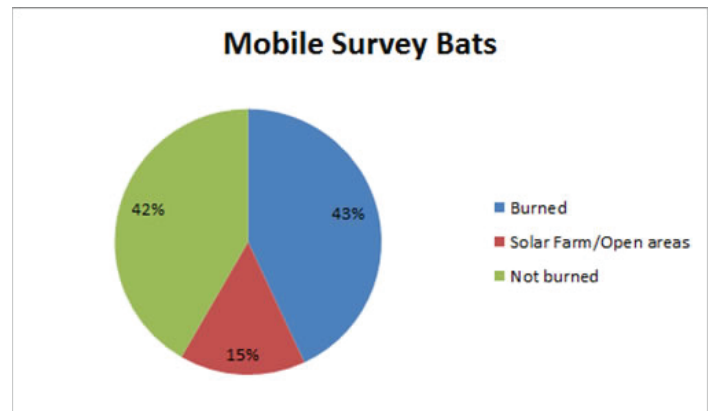


Figure 3. Percent bat species located in each stand during mobile surveys.

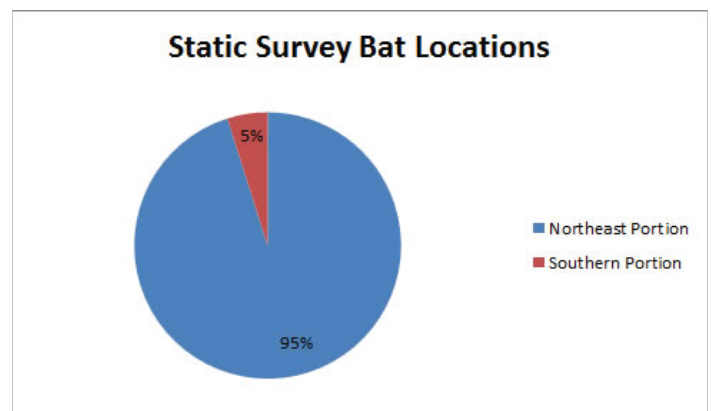


Figure 4. Percent bat species located in each stand during static surveys.

program can sometimes identify bat species based on less than 5 chirps. Species identified as the big brown bat (*Eptesicus fuscus*) or the silver-haired bat (*Lasionycteris noctivagans*) through Sono-Bat® and SCAN'R® were grouped together for the results.

III. Results

A total of 552 calls were positively identified to species. Of those calls, 95% were located in the Northeast Unit of the study site (Figure 4), and the majority of the calls from different species came from the Northeast Unit (Figures 6, 7, 9, 10). *M. septentrionalis* was located in the Northeast Unit 83% of the time, but represented only 1% of the collected calls (Figures 1, 8). The majority of the calls (86%) came from the *E. fuscus*/*L. noctivagans* characterized group (Figure 1). The mobile surveys yielded 144 positively identified calls. Of those calls, 43% were collected in the Northeast Unit (*Q. coccinea*/*Q. velutina*/*P. rigida*), and 42% were collected in the South Unit (*Quercus spp.* and scattered *P. rigida*). The remaining 15% of the calls were located near the solar farm and other areas with mostly open landcover (Figure 3). 79% of the mobile survey calls were made by *E. fuscus*/*L. noctivagans*, and none were made by *M. septentrionalis*. When both mobile and static surveys are taken into consideration (696 calls), 87% of the calls came from the Northeast Unit of the study site (Figure 5).

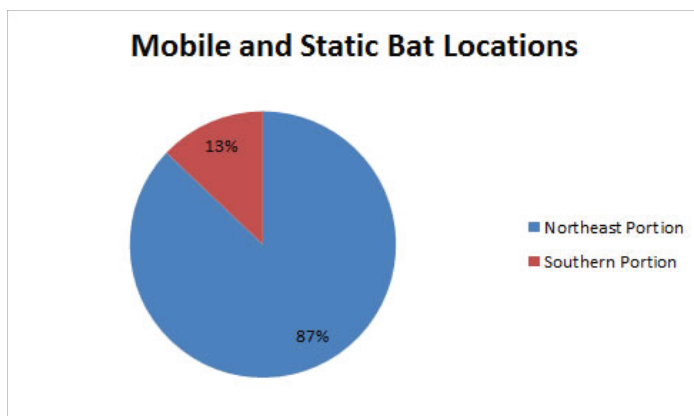


Figure 5. Percent bat species located in each stand during static and mobile surveys.

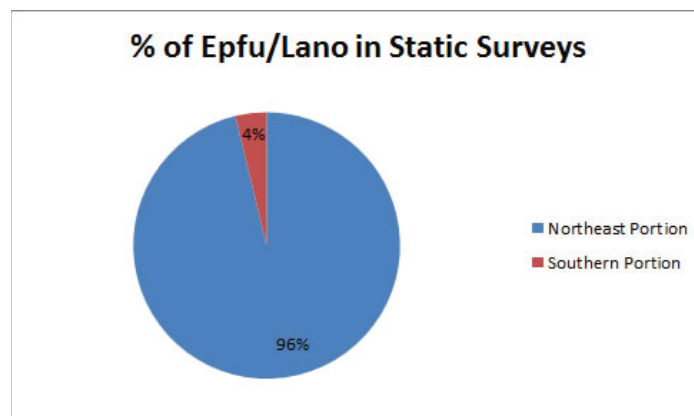


Figure 6. Percent of *E. fuscus* and *L. noctivagans* located in each stand of the study site

IV. Discussion

Fire affects species of bats differently, although the bat's natural history determines the impact of the fire (Perry, 2012). One of the reasons why bats may utilize forests which have recently experienced a burn is because insect activity has been found to increase after prescribed fires (Lacki *et al.* 2009). For this study, *E. fuscus* and *L. noctivagans* were characterized together to minimize classification errors due to their similar call structure and frequency (Cox *et al.*, 2015; Yates & Muzika, 2006). While these species were characterized together, the majority of them identified were *E. fuscus*. Very few, if any, bats located in this area are *L. noctivagans*. In addition to WNS, the lack of calls by *M. septentrionalis* might be due to the fact that they require continuous forest cover (Yates & Muzika, 2006). While Yates and Muzika (2006) stated that there is no apparent negative correlation between *M. septentrionalis* and fragmentation, they also stated that there is an inverse relationship between the presence of the species and the presence of edge habitat. Every detector was 152.4 - 241.4 meters from a road, so that could partially explain the lack of *M. septentrionalis* detected.

As the study continued, fewer calls were detected. This could be due to the second half of the study being done in an area that had not burned in the past 10 years, therefore it may not provide suitable habitat. Alternatively, it could be due to timing. Popping season occurs from June to August (Singleton, 2012), and female bats may forage differently while taking care of their young because of different energy requirements of the pups (Yates & Muzika, 2006). Yates and Muzika (2006) found a decrease in the number of calls in their study during July 7-20 when the juvenile bats started to fly. During this study, there was a decrease in calls during that time as well, however, at the last location surveyed between July 25 and August 3 more calls were collected than during the other two static surveys in the South Unit. This location was also near a pond with standing water, which may make the area more attractive to bats (Cox *et al.*, 2015; Yates & Muzika, 2006). None of the static survey sites in the Northeast Unit had a nearby water source, but more calls were recorded there than it the South Unit which was near water.

In this study, basal area was not a factor that was measured. Forests in the Northeast Unit had less canopy cover and more light reaching the forest floor where the South Unit had a more mature, closed canopy. Cox *et al.* (2015) found that bat activity was generally higher in areas with lower overstory basal area. This could be because species like *Lasiurus borealis* (eastern red bat), *E. fuscus*, *L. noctivagans*, and *L. cinereus* (hoary bat) tend to

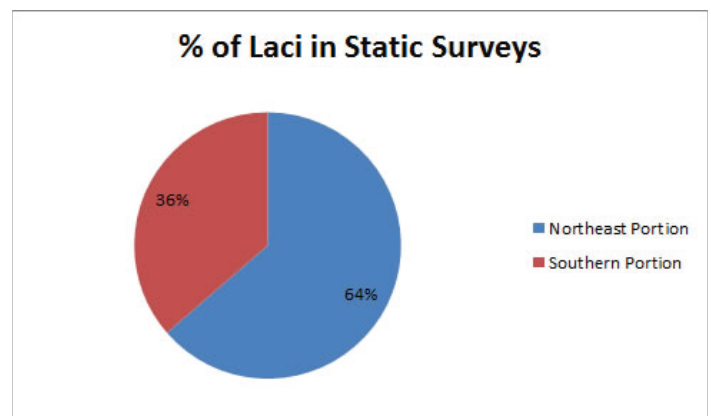


Figure 7. Percent of *L. cinereus* located in each stand of the study site

fly in areas where there is less clutter. The more open area caused by fire thinning can create more favorable roost sites for bats as well (Perry, 2012). Maternity roosts are especially likely to be located in areas with less canopy basal area to increase the solar exposure and warmth to the roost for the pups (Johnson *et al.*, 2011; Perry, 2012). In the study area snags were also created by insects killing some of the trees.

A way to test if it was the location or the time of the year which reduced the number of calls would be by having detectors in the Northeast Unit and the South Unit at the same time in a future study. This study lasted for only three months and locations change over time, so further studies will need to be done to test these results (Cox *et al.*, 2015).

V. Acknowledgements

I would like to thank Kathy Schwager and Timothy Green for all of their help for the duration of this study. I would also like to thank my fellow interns, Amber Evans, Sean Foote, Kaitlyn Irwin, William O’Connell, Claire O’Kane, and Julia Riley for all of their assistance with my research.

This project was supported in part by the U.S. Department of Energy, Office of Science, Office of Workforce Development for Teachers and Scientists (WDTS) under the Science Undergraduate Laboratory Internships Program (SULI)

VI. References

Cox, M. R., Willcox, E. V., Keyser, P. D., & Vander Yacht, A. L. (2015, October 22). Bat response to prescribed fire and overstory thinning in hardwood forest on the Cumberland Plateau, Tennessee. *Forest Ecology and Management*, 359, 221-231. doi:10.1016/j.foreco.2015.09.048

Dodd, L., Lacki, M. (Producer). (2015). *Fire and the Northern Long-Eared Bat: Vulnerability and Management Considerations*. [Video webinar]. Retrieved from <http://www.firesciencenorthatlantic.org/events-webinars-source/2015/8/5/nafse-webinar-fire-and-the-northern-long-eared-bat-vulnerability-and-management-considerations>

Johnson, J. B., Ford, W. M., & Edwards, J. W. (2011, December 15). Roost networks of northern myotis (*Myotis septentrionalis*) in a managed landscape. *Forest Ecology and Management*, 266, 223-231. doi:10.1016/j.foreco.2011.11.032

Kunz, T. H., & Fenton, M. B. (Eds.). (2005). *Bat Ecology*. Chicago, IL: The University of Chicago Press.

Lacki, M. J., Cox, D. R., Dodd, L. E., & Dickinson, M. B. (2009, October 15). Response of northern bats (*Myotis septentrionalis*) to prescribed fires in Eastern Kentucky Forests. *Journal of Mammalogy*, 90(5), 1165-1175. <http://dx.doi.org/10.1644/08-MAMM-A-349.1>

Perry, R. W. 2012. A review of fire effects on bats and bat habitat in the eastern oaks region. In: Dey, Daniel C.; Stambaugh, Michael C.; Clark, Stacy L.; Schweitzer, Callie J., eds. Proceedings of the 4th fire in eastern oak forests conference; 2011 May 17-19; Springfield, MO. Gen. Tech. Rep. NRS-P-102. Newtown Square, PA: U.S. Department of Agriculture, Forest Service, Northern Research Station: 170-191.

Singleton, C. (2012, June 8). Sunset Bat Tours Return to DFG’s Yolo Bypass Wildlife Area. Retrieved August 05, 2016,

from <https://cdfgnews.wordpress.com/tag/bats/>
 United States of America, Department of the Interior, Fish and Wildlife Services. (2013). *Endangered and Threatened Wildlife and Plants; 12-Month Finding on a Petition To List the Eastern Small-Footed Bat and the Northern Long-Eared Bat as Endangered or Threatened Species; Listing the Northern Long-Eared Bat as an Endangered Species* (191st ed., Vol. 78, pp. 61046-61080). Retrieved from https://www.fws.gov/frankfort/pdf/northern_longeared_bat.pdf.

Yates, M. D. and Muzika, R. M. (2006), Effect of Forest Structure and Fragmentation on Site Occupancy of Bat Species in Missouri Ozark Forests. *The Journal of Wildlife Management*, 70: 1238–1248. doi:10.2193/0022-541X(2006)70[1238:EOFSAF]2.0.CO;2

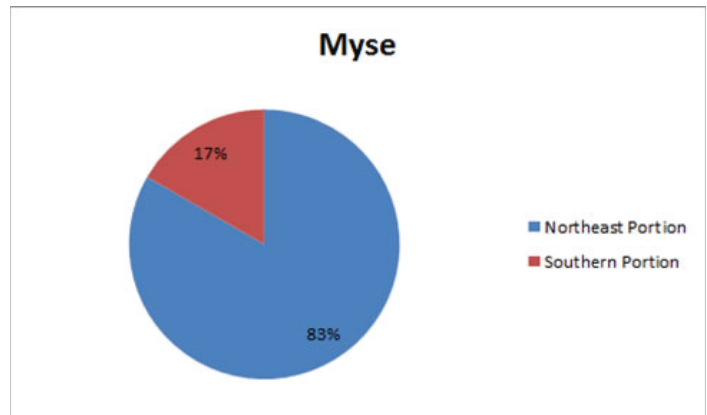


Figure 8. Percent of *M. septentrionalis* located in each stand of the study site

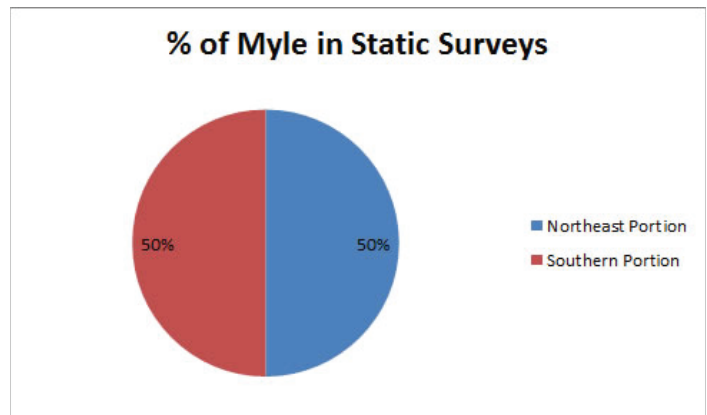


Figure 9. Percent of *Myotis leibii* (small-footed myotis) located in each stand of the study site

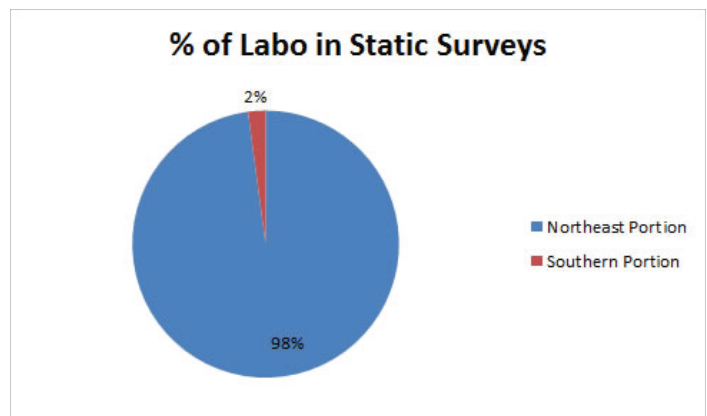


Figure 10. Percent of *L. borealis* located in each stand of the study site

Analysis and design of thermal management concepts for sPHENIX calorimeters

Emily Tacopina

Mechanical Engineering, The University of Rhode Island, Kingston, RI 02881

Donald Lynch and Robert Pisani

Physics Department, Brookhaven National Laboratory, Upton, NY 11973

Abstract

The PHENIX detector is currently undergoing an upgrade to become sPHENIX, the newest experiment on the Relativistic Heavy Ion Collider (RHIC) at Brookhaven National Laboratory. Part of this upgrade is using silicon photomultipliers (SiPM) to sample the energy absorbed in the Electromagnet and two Hadron Calorimeters which will be major subsystems for the sPHENIX experiment. The SiPMs have a low signal-to-noise ratio (SNR) which causes variations in performance based on temperature fluctuations. Since the SNR improves with low and stable temperatures, a thermal analysis must be performed to decide on a cooling method that will keep the SiPMs at a stable temperature. The outer Hadronic calorimeter (outer HCal) has a large surface area of carbon providing a massive heat sink. For the outer HCal natural convection alone removes the necessary amount of heat to keep the SiPM cool. The inner Hadronic calorimeter (inner HCal) has less surface area and stainless steel has a lower thermal conductivity than the outer HCal which requires evaluating heat transfer methods to keep the SiPMs cool. Forcing air to blow through the sector causes the heat generated from the electronics to be removed from the sector allowing the temperature to remain low enough for the SiPMs to operate. The Electromagnetic calorimeter (EMCal) produces a greater amount of heat in a smaller area than the hadron calorimeters. This heat cannot be removed by natural convection or forced air convection, the heat will need to be removed by the movement of a noncorrosive liquid.

I. Background

The PHENIX detector is currently undergoing an upgrade to become sPHENIX, the newest experiment on RHIC at BNL. This detector is being designed in hopes to further understand the nature of the quark-gluon plasma recently detected by PHENIX. sPHENIX will be comprised of an outer and inner hadron calorimeter, an electromagnet calorimeter and a solenoid. One factor of the upgrade will be to use silicon photomultipliers to sample the energy absorbed in the three calorimeters. Due to the SiPMs having a low signal-to-noise ratio (SNR) each of the calorimeters must be kept at a constant low temperature. Warm temperatures cause noise which causes variations in performance; low temperatures minimize noise. Each calorimeter must undergo a thorough thermal analysis to determine the cooling method that must be installed to obtain acceptable data.

There are 32 sectors in each of the calorimeters. A different amount of heat is generated per calorimeter. An individual sector of the outer hadronic calorimeter generates 43.01 Btu/hr. One sector of the inner hadronic calorimeter generates 145.4 Btu/hr. The electromagnetic calorimeter is divided into two components called the north and south split perpendicularly relative to the

beam pipe. These components each have 32 sectors; every individual sector produces 491.3Btu/hr of power. The heat generated causes an increase in temperature within the sector. A cooling method is required if the heat produced causes too great of a temperature increase.

Analyzing the thermal characteristics will yield the amount of necessary cooling for each calorimeter.

II. Theory

The conduction equation is used when finding the heat transfer across a solid.

$$Q = \frac{k * A}{L} * \Delta T \quad 1$$

Q is the heat generated, k is the thermal conductivity of the material, A is the cross sectional area, L is the length and ΔT is the change in temperature across the material.

The heat transfer by the movement of a fluid is referred to as the convective heat transfer. The equation to calculate convection is equal to:

$$Q = h * A * \Delta T \quad 2$$

Q is the amount of heat generated, h is the coefficient of convection, A is the area through which the heat transfer is taking place and ΔT is the change in temperature across that area.

The heat transfer equation below states that the heat transferred from the wall must equal the increase in fluid enthalpy thus:

$$Q = \dot{m} C_p \Delta T \quad 3$$

Where Q is the amount of heat, \dot{m} is the mass flow rate, C_p is the specific heat of the fluid and ΔT is the change in temperature across the surface area where heat is applied.

III. Methods and Results

A. Outer Hadronic Calorimeter

Looking at an individual sector the amount of heat produced by the electronics was known and the temperature rise was unknown. In a conservative manner, it was assumed that heat could only transfer out of the endplates, the surrounding walls were insulated and no heat could transfer through the scintillating tiles. The only temperature known was the ambient. Using an electrical analogy through the sector from the electronics, the heat source, to the ambient air the temperature at the surface of the electronics was able to be found. Beginning with the electronics channel to the surrounding air it was accepted that the power would be spread uniformly over the entire sector because the electronics are equally spaced. The area used was the total area of all of the channels. Presuming a natural heat coefficient of 2 Btu/hr the change in temperature between the surface of the circuit board and surrounding air was found to be 16.133°F. The change in temperature of the surrounding air to the absorber was then calculated using equation 2. The cross sectional area was taken as if you are looking from the top in. To measure the temperature change across the

absorbers equation 1 was used. Taking the cross sectional area of one absorber and multiplying it by 10, which is the number of absorbers, the area was found. Assuming natural convection from the outside wall to the atmosphere the last change in temperature was found.

Upon completion of the change in temperature calculations each temperature was determined. Beginning with an ambient of 70°F and working from the outside in the temperature changes were added until the electronics surface was reached. The temperature at the surface of the circuit boards will be 93.15 °F which is acceptable for the electronics to function. The temperature of the SiPMs will be the same as the sector enclosed air, which was measured to be 76.175°F. The SiPM needs to work at approximately 77°F to acquire no interference. The SiPM temperature found using free convection is acceptable. No cooling method



Figure 1: Outer HCal top and side view



Figure 2: Outer HCal prototype, close up of the circuit board and the SiPMs

Table 3: Cost and qualities analysis

Type	S-800 ultra-quiet inline fan	Inline vent duct exhaust fan blower	Inline vent duct exhaust fan blower 51db	TD-100 S&P series inline fan
Size	8"	8"	4"	4"
CFM (each fan)	711	720	176	101
Total Cost (# of fans)	\$676.00 (4)	\$327.96 (4)	\$1600.00 (16)	\$2176.00 (32)
Dimension	10.38"x16.64"x9.94"	15"x8.5"x15"	11.5"x11.5"x8"	9.2"x6"x6"
RPM	3150	2550	2890	2500
Pro	Quiet, high air flow, Fan curve	Vibration free	51db noise level high efficiency	Quiet, small
Con	No fan curve	Does not say about sound and no fan curve	No fan curve	Cannot work in air-streams greater than 104°F

needs to be produced because natural convection alone does a sufficient job of cooling the SiPMs on the outer HCal.

Table 1: Change in Temperature

Channel to inner air $\Delta T1$	16.1 (°F)
Inner air to absorber $\Delta T2$	0.6 (°F)
Inside absorber to outside edge of absorber $\Delta T3$	2.8 (°F)
Outer surface of absorber to ambient $\Delta T4$	2.8 (°F)

Table 2: Outer HCal Temperature range

T_{ambient}	70 °F
$T_{\text{outside wall}}$	72.8 °F
$T_{\text{inside absorber}}$	75.6 °F
$T_{\text{inner air (SiPM)}}$	76.2 °F
$T_{\text{surface channel}}$	92.3 °F

B. Inner Hadronic Calorimeter

Method 1: Heat transfer assuming the inner air of the top channels is blocked and can only transfer to through the absorbers.

The 48 channels produce heat which is transferred to the inner air then the absorbers. For the rest of the thermal analysis the sector was split up into two halves and the heat transfer was found through one half. The heat is conducted through the absorbers to the mirror plate. There is heat that is produced at either end of the sector, so the extra heat generated needs to be acknowledged. The change in temperature in the end air was calculated due to the heat transfer through the mirror and the end channel. Accounting for the additional heat generated the conduction through the endplate was found and the change in temperature from the outside of the end plate to the ambient. Once all of the changes in temperatures



Figure 3: Fan models correspondent to table 3 below

were found starting from the ambient the temperature at each surface was able to be found. The desired temperature is approximately 77°F. Natural convection was used originally to calculate the temperature. Using this method and natural convection the temperature was too high.

Method 2: Heat transfer assuming the only place heat can escape the sector is through the endplates.

The 48 channels and the two end channels produce heat which transfers to the inner air of the sector. The inner air transfers the heat to the inside of the endplate. The end plate transfers the heat from the inside to the outside using conduction. Through convection the outside of the endplate transfers heat to the ambient air. It is assumed the absorbers, side plates, and top cover are insulated and there are no air gaps therefore making this a conservative approach. Starting from the ambient and adding all of the change in temperatures assuming natural convection only the temperature found at the surface of the electronics was too large for the SiPM to function.

Method 3: Volumetric flow rate

The mass flow rate was determined from the heat generated, specific heat of air and the desired change in temperature. The specific heat of air is $0.2404 \frac{Btu}{lb \cdot ^\circ R}$ and the desired change in temperature is 7°F to have the SiPMs be the same temperature as the outer HCal. The volumetric flow rate was found once the mass flow rate was determined to be $1.4398 \frac{lb}{min}$. The volumetric flow rate is equal to the mass flow rate divided by the density of air. The desired volumetric flow rate is $19.4 \frac{ft^3}{min}$. Upon discovering the required volumetric flow rate of air fan blowers were looked at to see if this flow rate is possible. This volumetric flow rate is an achievable CFM with a fan blowing air across the sector. There needs to be $620.8 \frac{ft^3}{min}$ of air flowing through the entire inner calorimeter. The pressure drop across the sector is $0.0342 \frac{lb_f}{ft^2}$.

C. Electromagnetic Calorimeter

The Electromagnetic calorimeter is divided into two components called the north and south which are split perpendicularly relative to the beam pipe. These components each have 32 sectors; every individual sector produces 144 Watts of power. There are 8 preamp boards and an interface board in a package and there are 6 packages in each sector. Using the electrical analogy method from the circuit board to the inner air through the one endplate to the atmosphere the temperature rise was calculated. If only nat-



Figure 4: Inner HCal prototype

ural convection was used the temperature rise would be unrealistically high. Repeating the same method but using the forced convection coefficient of air the temperature rise was still greater than the desired temperature. The desired temperature at the EMCal is approximately 60°F, lower than both the inner and outer HCal. This is because the EMCal is the closest to the beam pipe and the most susceptible to radiation damage. Radiation damage to the SiPMs can be lessened at the lower temperature. Changing directions liquid cooling was considered.

An idea that arose was to have four tubes carrying a cool liquid parallel to the circuit boards to remove heat and continuously cycle the generated heat out of the sector. Stands will provide a connection from the tube to the surface of the circuit board. Originally water was used as the liquid and the mass flow rate was determined from the rated volumetric flow rate of the 3/8" copper tube. The volumetric flow rate used was 0.2gal/min and the mass flow rate of water was 100.3 lbm/hr. From there the change in temperature was determined over every package, as shown in Table 4. Although, the temperature increase within the tube was minimal using water it is a corrosive liquid thus the mixture ethylene glycol water (EGW) was considered. A volumetric flow of 0.2gal/min and a mass flow of 104.5lbm/hr were used to calculate the temperature rise in the tube between the ambient and the end of the sector as shown in Table 5.

The simple temperature increase in the tube was the first step, following this is an in depth analysis of one stand connection to the preamp board as seen in figure 5. An electrical analysis had to be performed to determine the temperature at the inside surface of the tube, the outside surface of the tube and the enclosed air. The stand originally was not accounted for and the temperature of the enclosure air was too high. The tube is connected to the stand which goes through the preamp board and to a copper layer which touches the SiPMs. To calculate the temperature at the SiPMs and the enclosure air temperature the stand and copper layer was modeled as a fin. The tube was the base and the stand was one fin coming off the pipe, the copper layer is only exposed on one side so folding it in half doubled the thickness and put the two insulated sides together. After the fin model was determined, the fin area efficiency was found using the hyperbolic tangent equation. Knowing the effective area, the final calculation was performed to determine the enclosure air temperature and the temperature at the SiPM.

IV. Discussion

The Outer HCal has a large surface area of carbon steel providing a massive heat sink.

The volume of carbon steel in one sector of the outer HCal

Table 4: Water temperature increase in tube

T ambient	50.0
T6	50.2
T5	50.5
T4	51.0
T3	51.6
T2	52.5
Tend	53.4

Table 5: EGW temperature increase in tube

T ambient	50
T6	50.200
T5	50.500
T4	51.100
T3	51.800
T2	52.700
Tend	53.800

is 60.5 cubic feet. Carbon steel has a thermal conductivity of $30 \frac{Btu}{hr \cdot ft \cdot ^\circ F}$. These values correspond with the result obtained from the thermal analysis. Natural convection removes the necessary amount of heat to keep the temperature at 77°F. The approach taken assumed the sector walls were insulated calculating the temperature of the SiPMs to be 76.175°F. Realistically the sector walls will not be insulated; there will be gaps where heat can escape allowing the temperature to remain lower than calculated. Taking a conservative approach permits the engineer to be confident with the conclusion that no outside cooling method needs to be installed.

The Inner HCal has a stainless steel volume of 3.4 cubic feet and a thermal conductivity of $9.36 \frac{Btu}{hr \cdot ft \cdot ^\circ F}$. The fans shown in table 3 have different capabilities but all are able to provide enough CFM to cool the Inner HCal. The two 8" fans produce over 700 CFM which is more than the 640CFM needed for the entire inner hadronic calorimeter. Ductwork that brings the blown air to each sector will cause a pressure drop which decreases the flow rate that will reach the sector. The amount and size of ductwork necessary will be determined later in the design process; the number of fans accounted for in table 3 reflects the maximum number of fans that would need to be used. The calculation is conservative and assumes that no conduction to the absorbers or through the side walls will take place; realistically there will be more forms of heat transfer occurring decreasing the temperature.

The EMCal will need to be liquid cooled using a tube that runs from the ambient side of the sector to the end and back. The north and south components do not connect so the 64 sectors each need to be cooled individually. The liquid used in the calculations was EGW 40/60. In order to use the electrically analogy method of determining the enclosure air and the temperature of the SiPMs the effective area of the pipe, stand, and copper layer needed to be determined. The SiPM temperature calculated is 65.6°F when

the fluid ambient temperature is 50°F. For the future the individual stand calculation needs to be repeated for each stand because there will be a slight temperature increase in the tube from one stand to the next and the stand length changes. Each stand will be different lengths because the geometry of each of the modules in the sector is different as seen in figure 7. A lower ambient fluid temperature should be considered. The next analysis will need to acknowledge the inner air that also will affect the temperature of the SiPMs along with the conduction through the copper.

V. Acknowledgements

This project was supported in part by the U.S. Department of Energy, Office of Science, and Office of Workforce Development for Teachers and Scientists (WDTS) under the Science Undergraduate laboratory Internships Program (SULI). I would like to thank my mentor Donald Lynch (Chief Engineer), Robert Pisani (Senior scientific associate), Rich Ruggiero (Chief Designer) and the sPHENIX engineering team for their support and advice. I would also like to thank my fellow interns; Spencer lady-Locks, Brenna Buckley, Dan Cacace and Howard Giese. Working with sPHENIX scientists and engineers I have expanded my knowledge of engineering and gained additional understanding of how to approach complicated problems.

VI. References

- ¹Cengel, Yunus A., and Afshin J. Ghajar. Heat and Mass Transfer, Fundamentals & Applications. 5th ed. New York, NY: Mc-Graw Hill Education, 2015.
- ²Engineering and Operating Guide, DOWTHERM, Feb. 2008 PDF <http://msdssearch.dow.com/publishedliterature>
- ³F. P. Incropera, D. P. Dewitt, T. L. Bergman, and A. S. Lavine, Fundamentals of Heat and Mass Transfer, 6th Ed., Wiley, 2007.



Figure 5: Model of one stand

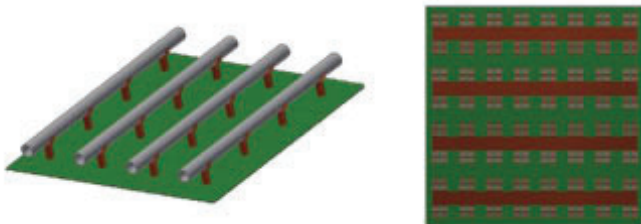


Figure 6: Model of one package



Figure 7: Modeling of an EMCal sector, side view

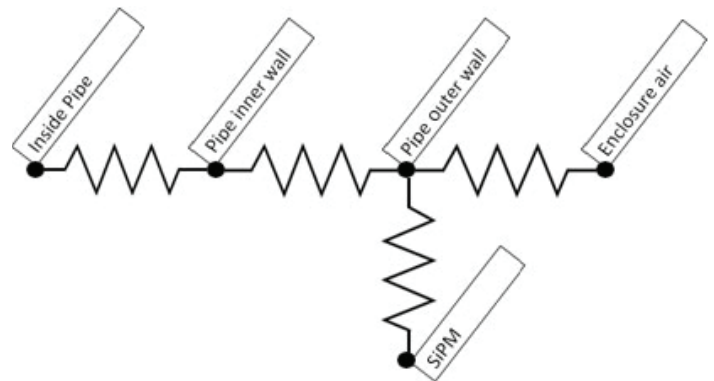


Figure 8: Electrical analogy of one stand

Table 6: Temperature distribution for one individual stand

liquid cooling	°F
T center of tube	50.0
T inside wall of tube	52.2
T outside wall of tube	52.2
T inner air	121.1
T at SiPM	65.6

Development of automated batch workflow and real-time data processing for x-ray fluorescence tomography

Derek Tropsf

Department of Applied Physics and Mathematics, Columbia University, New York, NY 10027

Yong Chu

NSLS-II, Brookhaven National Laboratory, Upton, NY 11973

The unprecedented spatial resolution of the Hard X-ray Nano-probe (HXN) beamline at the National Synchrotron Light Source II (NSLS-II) allows for material characterization on the scale of 10 nanometers (nm)¹. Such resolution enables new frontiers of advanced material characterization. One of the important techniques, currently being developed at the HXN beamline, is 3D x-ray fluorescence microscopy, or fluorescence tomography, which allows scientists to visualize internal structures and quantify elemental composition. When excited by the incidence x-ray beam, the atoms in a sample emit characteristic fluorescence x-rays providing a unique fingerprint of elemental composition. Tomographic reconstruction of a set of 2D projection fluorescence images can reveal the 3D distribution of elemental composition within a sample – however, this technique requires the processing of large amounts of data. Currently, raw data is processed and analyzed in the PyXRF software developed at HXN. Although PyXRF provides an intuitive graphical user interface and advanced plotting capabilities², the software does not support real time data processing or automated batch workflow. This inherent bottleneck makes large data processing a timely and impractical endeavor. During my summer research, I developed a new automated workflow that processes large quantities of data in real time. The software I produced utilizes key functionality from PyXRF to eliminate the need for manual data processing and allows for immediate data analysis upon completion of an experiment. With such improvements, future efforts with HXN will focus on the problem of self-absorption in fluorescence tomography.

I. ANALYZING MATERIALS: X-RAY FLUORESCENCE TOMOGRAPHY

Many of the properties of a material come down to answering two questions – how and what. How are the atoms that constitute a material geometrically arranged? Also, what atoms make up the material? The question of how can be answered through the technique of diffraction. By diffraction, properties such as bond distance between atoms can be determined. Although diffraction can also determine what elements make up a material, another method – x-ray fluorescence tomography – is better suited for the inquiry of what elements are present. X-ray fluorescence tomography has the ability to not only identify elemental composition, such as the presence of arsenic in soil, but create a three dimensional reconstruction of the composition as well.

A. Fluorescence

Fluorescence is the result of an interaction between x-rays – light with wavelength ranging from 0.01 to 10 nm – and electrons

in atoms. An electron is bound to an atom with a certain amount of energy. If an incident x-ray has enough energy, an electron can be ejected from the atom – known as the photoelectric effect – or an electron can be raised to a higher energy level. In either case, a vacancy exists where the electron once was. So long as the vacancy exists, the atom is in an excited state and is unstable. In order to regain stability, an electron from an outer orbital will move down and fill the hole.

This process releases a fluorescent x-ray photon equal in energy to the energy difference between the initial and final states of the transferred electron. Each atom has distinct energy differences between orbital levels which results in the energy of emitted fluorescent x-rays being dependent on atomic number Z through equations (1) and (2). Equation (1) is Moseley's law where K is a constant dependent on spectral series and σ is the shielding constant that is less than one³. Equation (2) relates the energy of a photon E in keV to wavelength in angstroms.

$$\frac{1}{\lambda} = K(Z - \sigma)^2 \quad (1)$$

$$\lambda = \frac{12.4}{E} \quad (2)$$

Ultimately, this means that fluorescent x-rays identify elements analogous to how fingerprints identify people. Through this technique, the question of "what" can be answered.

B. Tomography

Collecting fluorescent x-rays with a detector is how scientists determine elemental composition of a material; however, the result is a two dimensional picture that is only a slice of a three dimensional material. In order to create a three dimensional image of elemental composition, tomography is used on the fluorescent x-ray data. The basic methodology behind tomography can be seen in Figure 1 and mathematically represented in the radon transform seen in equation (3). With the line s that is not intersecting the origin as a detector, let the parallel lines that terminate on the aforementioned line be x-rays that interact with a material which is represented by the dark circle at the center of the coordinate system. The angle α increases over some range, usually 180 degrees, to obtain different projections of the material. The data is then put through the radon transform, equation (3), to produce a three dimensional structure. The radon transform adds up the attenuation on each parallel x-ray path. These values are then mapped to a new coordinate system specified by the angle α and projection axis s ⁴. Of course, a detector for fluorescent x-rays would not be placed to intersect the path of incident x-rays as that

would wipe away the characteristic elemental information. See Figure 5.A for a more accurate depiction of the actual detector setup.

$$p(s, \alpha) = \int_u \mu(x, y) du \quad (3)$$

II. HXN AND X-RAY FLUORESCENCE TOMOGRAPHY

At HXN, x-ray fluorescence tomography experiments are conducted in order to find the elemental composition of a material with as high a resolution as possible. The data collected must be analyzed and processed before a three dimensional reconstruction can be created. PyXRF is powerful software developed at HXN to analyze fluorescence data. Figure 2 shows the analysis done by PyXRF. Figure 2 is a graph of the total summed fluorescent spectrum of an experiment of a sample composed of a $\text{Ce}_{.08}\text{Gd}_{.02}\text{O}_2$ (GDC) oxygen ion conductive phase and a CoFe_2O_4 (CFO) electronic conductive phase⁵. The horizontal axis is energy in keV while the vertical axis is counts. What the graph depicts is how many times the detector was hit by a fluorescent photon of a certain energy. From almost this graph alone, the tale of a material's composition can be told. First, it can be seen that the peaks of the graph are almost sitting on top of a hill. A line can be seen that marks the top of this hill where the peaks turn into troughs and back again. This is information associated to the ion chamber as part of the beamline. The broad energy range of scattered x-rays and photoelectrons from the ion gas inflate the count total for all energies. Just above and below the hill are peaks of various colors. These subpeaks are the result of different interactions such as Compton scattering, elastic scattering, and background noise. Specifics are given by the legend in the top right of Figure 2. Finally, the remaining evident global peaks remain. These peaks are the main energy edges that convey elemental information. If incident x-ray energy is held constant, then fluorescent x-ray energy can be calculated for all elements. With this knowledge, the presence of peaks at certain energies reveals the elements of a material. For example, two such elements that are revealed from

this sample are Iron and Gadolinium (Fe and Gd). Spectrum data in the range of 6.2 to 6.6 keV give rise to Figure 3 where as roughly 6.0 to 6.2 keV yields Figure 4. What is shown is a mapping of the concentration of Fe and Gd respectively. Notice that in both figures the overall shape of the sample is the same. As revealing as this information is, these graphs and figures are but one slice. Data collection at all angles is necessary to get a true depiction of the three dimensional concentration of elements – hence why tomography is desired.

III. PYXRF AND WORKFLOW

A. Finding a Bottleneck

When fluorescent tomography experiments are conducted at HXN, data is usually collected over a range of 180 degrees at increments of three degrees, including the degree of zero. This results in 61 separate collections of data – each of which has its own total spectrum graph as in Figure 2. Although PyXRF is a powerful tool with an intuitive graphical user interface, the process of analyzing data is manual. PyXRF does not support automated batch workflow nor realtime data analysis, therefore getting to the point of three dimensional reconstruction is a time intensive endeavor that is highly impractical. Such an inherent bottleneck is cause for an investigation into the development of an analysis workflow that is automated and supports realtime analysis.

B. Automation and Real Time Analysis

Figure 5 is the workflow before any changes. The red arrow pointing to Figure 5.B shows the location of the bottleneck. As x-ray fluorescence data is collected, the information is stored into a large data base at NSLS-II. When collection of data for all angles is finished, the associated data for each angle is put into an h5 file format that is then analyzed by PyXRF. This last step is entirely manual and must be completed by a user via keyboard and mouse. Figure 6 has been developed to remove the aforementioned bottleneck. Essentially, PyXRF has been turned into a black box that is used to automate the analysis process. Functions from PyXRF were augmented to support a framework that allows

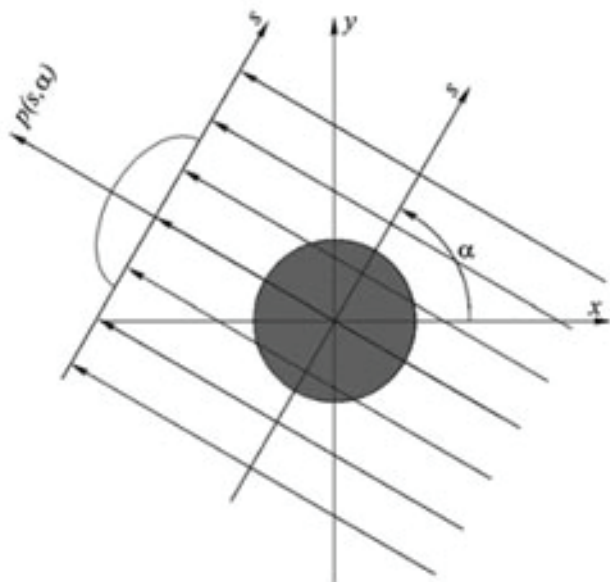


FIG. 1. Visualization of tomography at an angle α^4

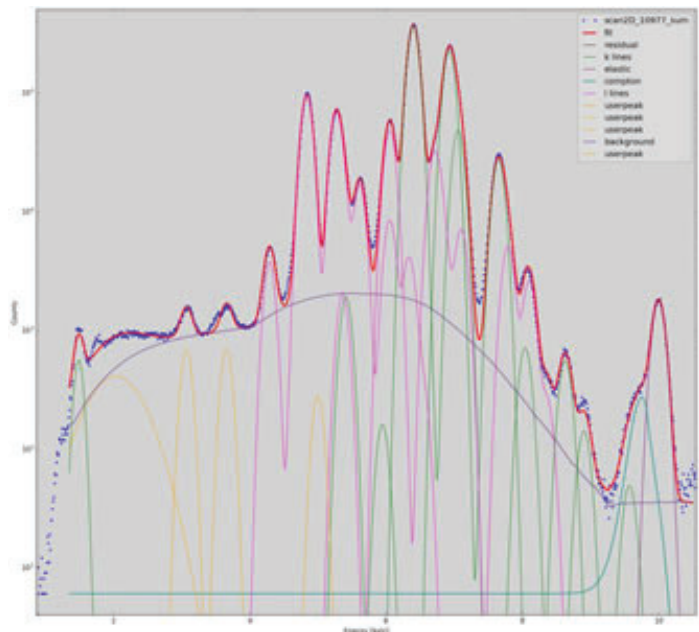


FIG. 2. Graph of Counts vs Energy in keV generated in PyXRF for a material⁴

for the input of simple parameters for general users to quickly analyze data and produce images for visual analysis that will later be used in tomographic reconstruction. More complicated parameters can be used to show detailed information regarding the collected data, such as energy edge ratios. The result is a successful implementation of an automated workflow and realtime data processing. These changes ultimately accelerate the process of significant data analysis and production of three dimensional reconstruction of elemental composition. Although such improvements may seem mundane, they are actually imperative to such things as accurate experimentation. Under the new workflow, experimental data can be quickly checked for potential issues that might have occurred mid-experiment. Further developments of the software underlying the workflow will focus largely on automating the creation of three dimensional images.

IV. THE FUTURE

The new workflow may help remedy a seminal problem inherent in the method of x-ray fluorescence tomography. Incident x-rays interact with the material to produce fluorescent x-rays – however, fluorescent x-rays may also interact with the material as well. On their transit out of the material towards the detector, fluorescent x-rays may become absorbed, scatter, or even produce different fluorescent x-rays. It is as if fingerprints are swapped and the scientist is lied to at times. A fluorescent x-ray emitted from Fe could have a trajectory that intersects directly with another atom. The x-ray could be just the right energy to interact and produce a different fluorescent x-ray. This problem of a material absorbing its own fluorescent x-rays is known as self absorption. Without

solving for this, all collected data incorrectly depicts elemental composition. Future endeavours with the new workflow in place include the task of tackling this problem. Automated analysis of small areas of a two dimensional total spectrum image – take Figures 3 and 4 but for all energies – could allow beamline scientists to compare energy edge ratios as a function of distance from the detector. Such information could then be factored into the data in order to correct for self absorption.

V. CONCLUSION

Self absorption is an interesting problem that will take a combination of intuition, knowledge, and hardwork to overcome. Without a proper foundation set in place to handle large quantities of information, much of the effort towards a solution would be all for naught. The development of a new automated workflow is a foundation necessary not only for significant progress towards a solution for self absorption, but to increase the capacity for scientific work to be done at the HXN beamline. In combination with the exceptional resolution of the HXN beamline, the new workflow will continue to make strides in the realm of x-ray fluorescence tomography.

¹NLSL-II. X-ray nanoprobe (hxn). Face Sheet. BNL. Upton, NY.

²Li Li. <https://github.com/nsls-ii/pyxrf>.

³Ron Jenkins. X-ray techniques: Overview. Encyclopedia of Analytical Chemistry.

⁴Robert Cierniak. X-ray computed tomography in biomedical engineering. pages 68–72, 2011.

⁵W. Harris K. Brinkman et al. Characterization of 3d interconnected microstructural network in mixed ionic and electronic conducting ceramic composites. Nanoscale, 6:4480–4485, 2014.

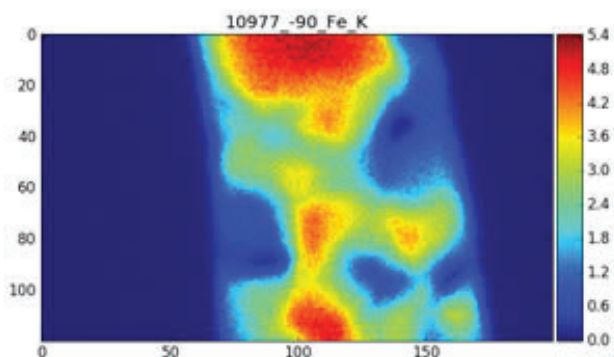


FIG. 3. Fe composition of sample at -90 degrees

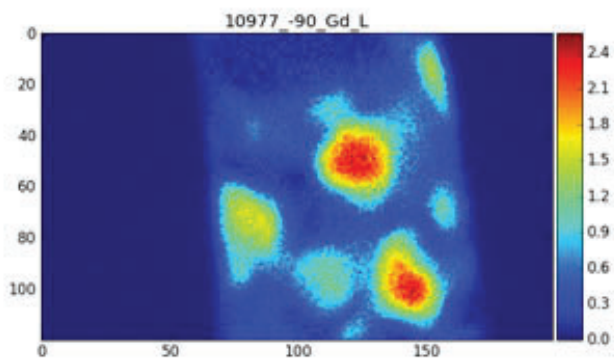


FIG. 4. Gd composition of sample at -90 degrees

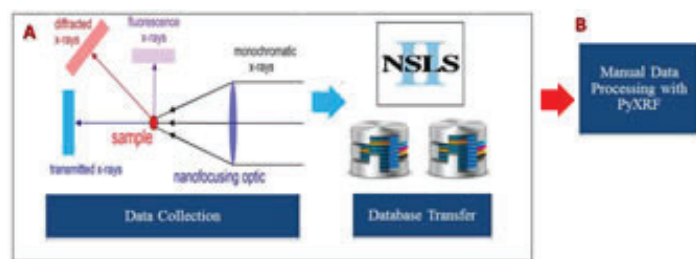


FIG. 5. HXN workflow from data collection to analysis in PyXRF

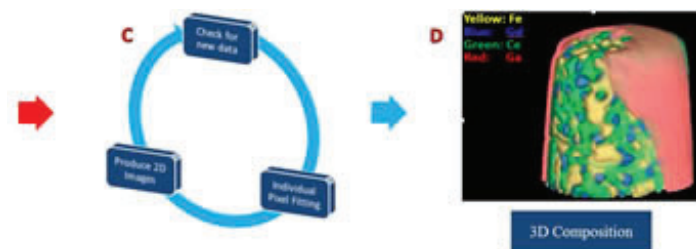


FIG. 6. Changes to original workflow starting at the red arrow in Figure 5

Development of computer vision and image processing libraries at the National Synchrotron Light Source - II

William Watson

Department of Computer Science, Johns Hopkins University, Baltimore, MD 21218

Kazimierz Gofron

Department of Photon Sciences, Brookhaven National Laboratory, Upton, NY 11973

Abstract

The beamline microscopes at the National Synchrotron Light Source – II (NSLS-II) at Brookhaven National Laboratory facilitate characterization of X-ray beam properties to empower the study of material properties and functions with nanoscale resolution. The hutches contain detectors and cameras to monitor the state of the X-ray beam and samples. Since the hutch must be sealed during operation, robots help to automate the process of sample transfers and camera movement without human intervention. However, in order to automate these processes, the development of computer vision and image analysis software is required. By building a general purpose computer vision module with the support of OpenCV, an open-source computer vision library, computers now have the ability to determine if a robot has improperly mounted a sample or pin, and can warn users and scientists of potential errors within the hutches. This wrapper module allows users to simplify computer vision processes and programs with succinct code. Computer vision also allows computers to determine the position, spread, and intensity of the x-ray beams automatically from images provided by cameras on the beamline. By integrating computer vision to the Experimental Physics and Industrial Control System (EPICS), an open source control system for scientific instruments, computers can, in real-time, observe and report of the status of a beamline without human interference or control. This helps to prevent improper mounting of samples and possible collisions that could result in downtime and damage to beamline components. Computer Vision (CV) integrated with EPICS allows for automated robot error checking, beam analysis, and robotic experimentation without input from beamline scientists. The CV library has potential for more applications to other beamlines. I have added computer vision to my repertoire of computer techniques. I am now familiar with EPICS and the OpenCV library implemented in the Python programming language.

I. Introduction

The development of CV and image analysis software at NSLS-II will provide beamline scientists and users the tools needed to interpret data and streamline experimental processes automatically from camera images. The development of an easy to use python CV module will allow controls engineers and scientists to quickly develop smaller applications that process camera images efficiently and make experimental decisions based upon the data collected. This will allow beamline scientists, controls engineers, and users to automate tedious and costly processes. Applications will be able to determine the position, spread, and intensity of

X-Ray beams. Applications will be able to isolate and compute the centroid, or center of mass, of features within the images. Finally, programs will be able to provide assistance to users and scientists in the alignment of goniostats and samples within the hutches of the various beamlines.

An easy, user-friendly python module implements many OpenCV functions, along with the appropriate pre-processing and additional algorithms, to allow for the development of succinct and elegant computer vision code. My python module, currently known as cvlib, allows for small programs to quickly delegate processes for the purposes of image processing. It has significantly reduced the amount of code required of programmers to write in order to implement certain procedures. This library implements a software design technique known as modular programming, emphasizing the separation of tasks and functions, allowing for the construction of large programs with minimal waste. Many functions take optional arguments, allowing for inexperienced users to develop quick flexible applications, while the more advanced will have unfettered access to the minute details of each function.

OpenCV is an open source computer vision library that was designed for computational efficiency. It is written and optimized in C/C++ code, resulting in some of the fastest computation that a high-level programming language can provide.¹ As of OpenCV version 3.1.0, the library implements the Open Computing Language (OpenCL), allowing for algorithms to make the most of hardware acceleration in the underlying computer platform. OpenCV includes licenses to Intel's Integrated Performance

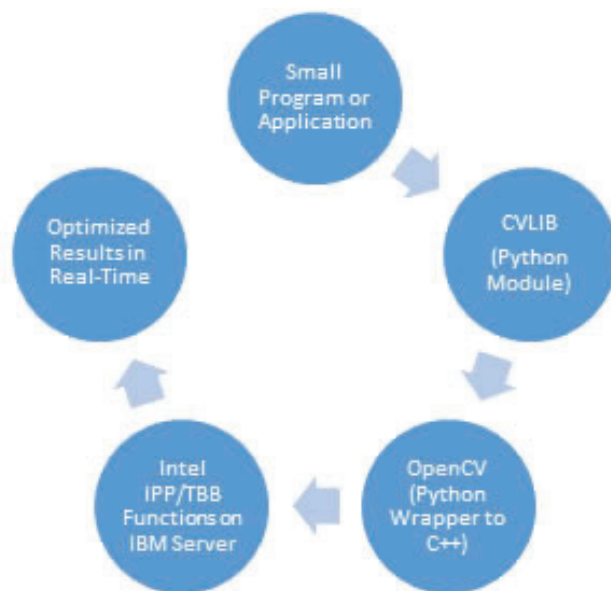


Figure 1: Infrastructure Layout for Computer Vision

Primitives (IPP) library, as well as the Intel Threading Building Blocks (TBB) library.

The Intel IPP library is a crucial package necessary for the computational efficiency of OpenCV. Integrated heavily within the functions of OpenCV, the Intel IPP library, implemented in C/C++, allows for applications to take full advantage of low-level processing power, speeding up computation times for various functions by factors of three to nine.² This results in a low average computational cost for images, allowing for real-time analysis of images on the beamlines. OpenCV makes extensive use of the Intel TBB library, which allows for parallel programming on multi-core processors.³ TBB allows for applications to create synchronized tasks that it delegates to low-level processors, allowing tasks to be completed in parallel instead of sequentially, drastically improving the computation time needed for real-time analysis.

For the IXS beamline, this extensive infrastructure is hosted on a dedicated IBM Image Server that is built and optimized for computational speed and efficiency, providing near instantaneous results to users. Debian ‘Jessie’, the current stable release of a powerful Linux distribution, was installed on the IBM Image Server to replace the old operating system. With the infrastructure running locally on the beamline, computer vision applications can be integrated with the Experimental Physics and Industrial Control System (EPICS). EPICS is an open source control system for scientific instruments, allowing beamlines to store data from all the instruments and devices along the beamline in one convenient database.⁴ By accessing these values from Process Variables, or PV values, computer scripts can adjust motor and instrument con-

trols quickly, while retrieving image data directly from cameras. By allowing scripts to adjust these parameters, computer vision can be used to determine the position of samples or mounts within an image and automatically adjust the motors to correctly calibrate the beamline. The use of the computer vision module to directly send motor adjustment to calibrate beam position or correct goniostat alignments can eliminate manual calibration. By integrating this module and OpenCV with EPICS, engineers will be able to develop robotic vision for the beamlines.

II. Computer Vision Applications and Results

A. BPM-1 Camera (IXS)

At the Inelastic X-Ray Scattering (IXS) Beamline at NSLS-II, cameras are used to record and interpret data received from the hutches regarding the shape and intensity of the beam. One particular example is the Beam Position Monitor (BPM-1) X-Ray camera located in B Hutch, downstream from the double crystal monochromator at IXS. This camera captures images of monochromatic X-Ray beam downstream of the double crystal monochromator.

The X-Ray beam originates in the undulator, is focused vertically by Compact Refractive Lens (CRL), then passes through various slits, and is monochromatized by a double and high resolution monochromator crystals. The beam is focused by Kirkpat-

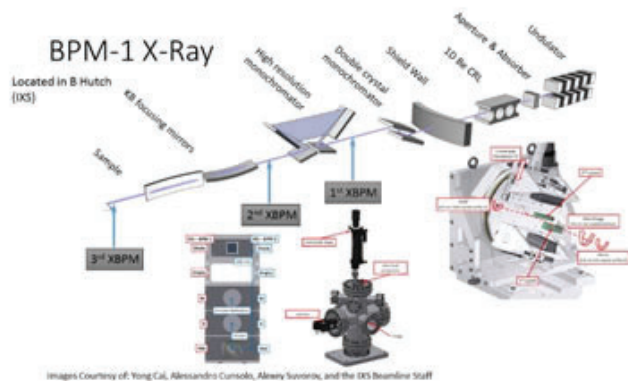


Figure 2: IXS Beamline Schematic⁵

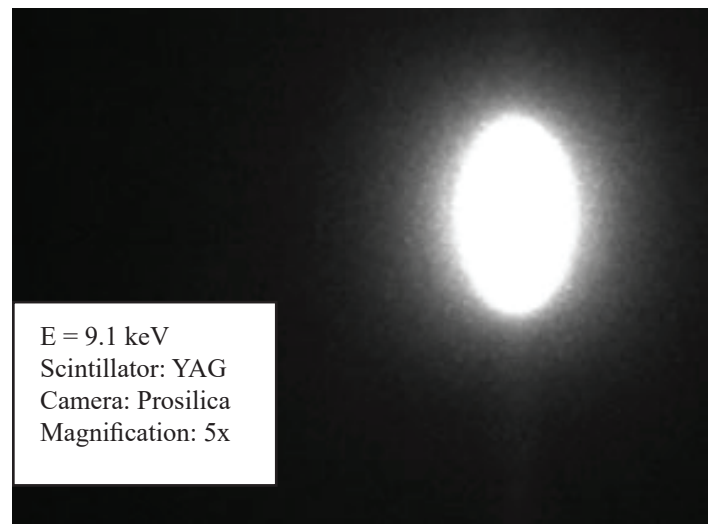
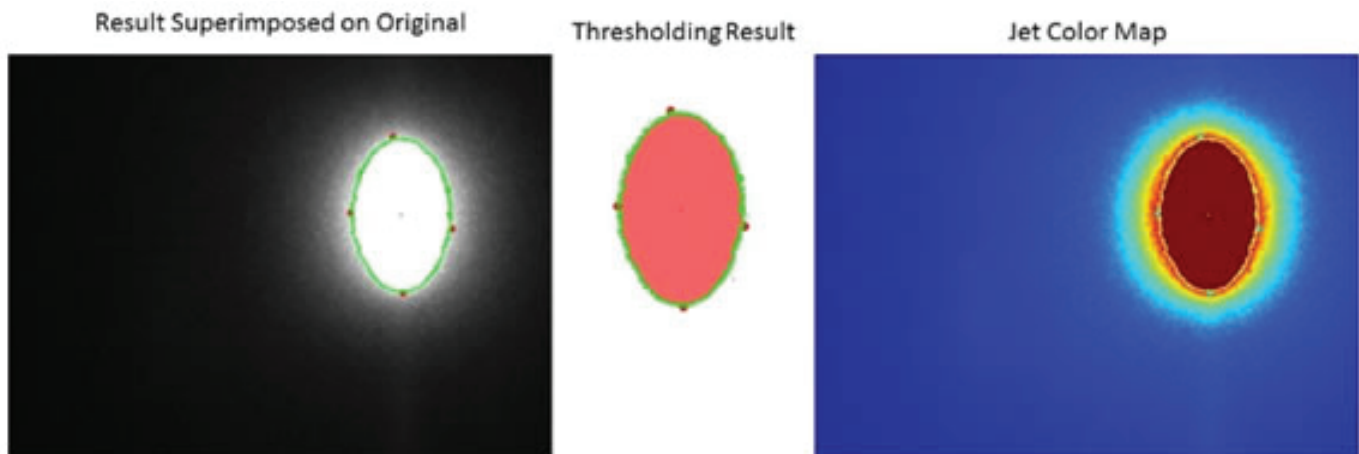


Figure 3: BPM-1 Captured Image



Images Courtesy of: Yong Cai, Alessandro Cunsolo, Alexey Suvorov, and the IXS Beamline Staff
Figure 4: BPM-1 Image Results

rick-Baez (K-B) mirror pair onto the sample. Before the X-ray beam hits the sample and continues to the end station in D Hutch, cameras record the properties of the beams. As the beam passes through the double crystal monochromator, it generates visible light in a YAG scintillator crystal, allowing a replica of the beam to be passed to a camera, in this case BPM-1. The beam is oval because it is viewed at 45° with respect to the surface of the scintillator.

The application developed for the BPM-1 camera allows beamline scientists to quickly discover the position, spread, intensity, and centroid of the beam. As the images are captured from the camera, a simple three step process is used to retrieve the pertinent information. As images are loaded into the application, a simple binary threshold is applied, resulting in a binary image. A binary image is an image where only two values are present, high and low. In this case, high corresponds to white (255) and low corresponds to black (0). For this program, the threshold is set to only retrieve the pure white pixels. Then, the findContours() method is applied, returning the beam's contour. The contour only surrounds the intense, bright white pixels. The resulting image displays the contour, the centroid, and the four extrema of the contour found.

With the contour, centroid, and extrema found, the program outputs relevant information of the beam, such as the perimeter, orientation, maximum point, height, area, minimum point, sum

Figure 5: Console Output

```
Object Details:
perimeter: 2356.99022925
orientation: 179.838363647
max: (925, 198)
height: 372
extrema: {'B': (938, 568), 'R': (1054, 415),
          'L': (813, 377), 'T': (914, 196)}
area: 65058.5
min: (1047, 564)
sum intensity: 20426526
width: 241
centroid: (933, 382)
mean intensity: 227.842390577
```

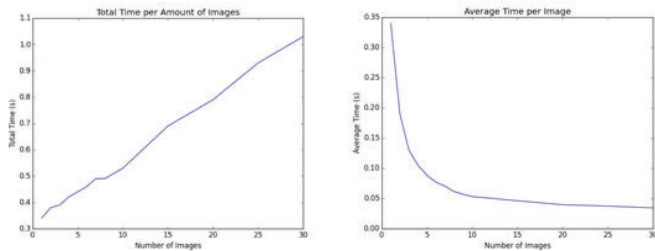


Figure 6: Total Time Chart (Left) and Average Time Chart (Right)

Console Output:

```
Object 1:
perimeter: 125.840619564
orientation: 179.981033325
max: (131, 78)
height: 55
extrema: {'B': (129, 122), 'R': (135, 98),
          'L': (126, 92), 'T': (132, 67)}
area: 270.5
min: (134, 83)
sum intensity: 62689
width: 9
centroid: (130, 95)
mean intensity: 126.644444444
```

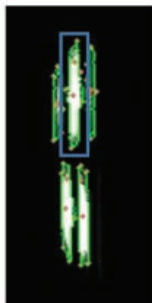


Figure 8: Merlin Image Results

of pixels, width, and mean intensity. From these values, beamline scientists can easily discover the beam's intensity from the sum of the pixel values, while knowing the spread of the beam from the height and width values. By using these values as parameters, beamline scientist can calculate the offset of the beam to the center of the image frame and recalibrate the beam as needed. With EPICS integration, beam alignment can happen instantaneously without the need for human input. As a result, pertinent information and beam alignment can be easily done in real-time.

Due to the overhead that comes with python, a single image takes approximately 0.350 seconds to calculate. The average time per image can be reduced to approximately 0.034 seconds, allowing for the program to process 30 images per second if need be.

B. Merlin Quad X-Ray Detector (IXS)

The Merlin Detector in D Hutch at IXS collects information regarding X-Rays. Using direct detection, the Merlin Detector collects X-Ray intensities after the X-Ray passes through six crystals that divide the beam into six streaks. At the time of testing this program, IXS only configured five streaks to be monitored, as the images were collected during initial calibration.

The purpose of this program was to isolate the individual streaks found within the collected images. When isolated, the program will process each streak to discover the position, center, spread, intensity, and the maximum value. By passing the image to the program, a simple binary threshold was applied, enabling OpenCV to find the contours in order of size. By enumerating through the list of contours, filtered for small noise interference, the program can extract data for each streak and record it efficiently. The Merlin Detector collected information on five streaks in the input image, and correctly discovered the contours in the resulting image on the right. A JET color map is provided to accentuate the pixel values. The program can return the information for all streaks within a Merlin image in approximately 0.321 seconds for one image. When multiple images are sent in sequentially, being processed by one instance of the program, it can process approxi-

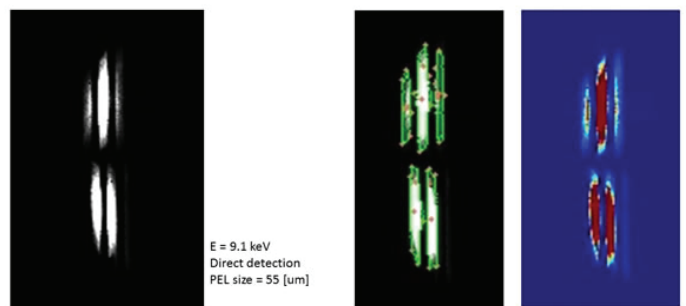


Figure 7: Console Output for the largest X-Ray Streak (Blue Rectangle)

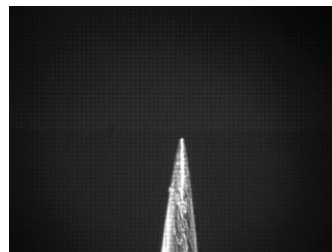


Figure 9: On-Axis Pin Image Captured from IXS

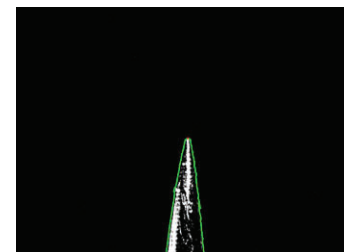


Figure 10: Image Results with contour and Top Pin Extrema (1723, 1306)

mately 30 images per second. The python overhead for compiling and garbage collection becomes negligible upon a large number of images being process by one instance of the program.

C. On Axis Pin Locator and Alignment (IXS)

One of the major problems encountered along the beamlines is the centering and alignment of crystals and pins in the hutches. Currently, beamline scientists have to manually calibrate the motors to align a pin properly using cameras to provide visual confirmation of the sample. This results in a tedious and costly procedure that can be easily automated with the use of computer vision and robotics.

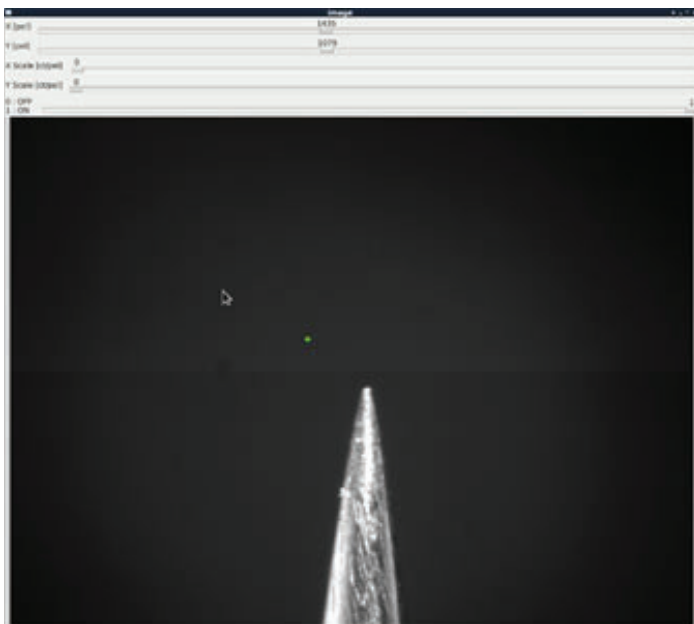


Figure 11: Screenshot of the point and click GUI, with track bars, live image, and green cross marking new position



Figure 12: 'Perfect' template images

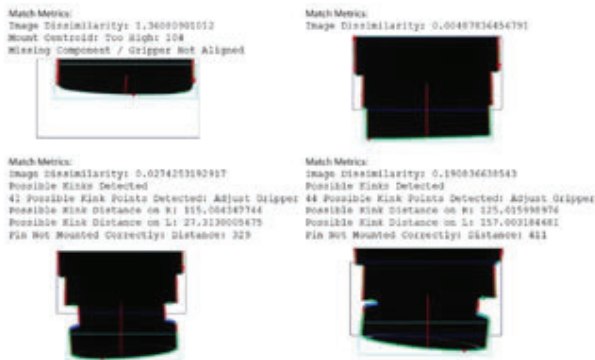


Figure 14: Image Results for the Pin/Gripper Analysis

For this program, images of the pin are captured from the On-Axis Camera located in D Hutch at the IXS Beamline. The camera collects images of the pin, and motors help calibrate the position of the pin. The camera provides visual confirmation of the pin. The purpose of this particular application is to measure the position of both the x and y pixel position of the tip of the pin. By using this, we can measure the rotational difference of the pin. The application should discover and plot the sinusoidal regression that corresponds to the pixel positions of the pin tip. The program should use the results of the sine curve, specifically the amplitude and phase, to compute the correct adjustments for the motors to properly align the pin. A point and click GUI was made in order to facilitate the quick and easy calibration of the motors without manually adjusting it within the hutch or traversing different screens to adjust motor positions.

The program uses a flood fill to black out the entire background of the image. The image is then adjusted by a bitwise not operator, which negates the values of the pixels, i.e. white to black and vice versa. By contouring the pin, the program can discover the tip easily. With this point recorded, the program can let the pin rotate and construct a sine curve based upon the data. From this, the program can adjust motor positions to calibrate the pin so that it does not wobble when the motors are rotating.

For the point and click GUI, Images are fetched directly from EPICS, with the center of the image and the current selected position marked by two distinct cursors. A simple click will adjust the x and y pixel positons of the cursor, and EPICS will update



Figure 13: Case Samples for Pin and Gripper

Number of Images	Total Time	Average Time
1	0.544	0.544
2	0.751	0.3755
3	0.965	0.315
4	1.162	0.2905
5	1.361	0.2722
6	1.565	0.2608333
7	1.802	0.25742857
8	1.999	0.249875
9	2.182	0.24355556
10	2.429	0.2429
11	2.621	0.23827273
12	2.803	0.23355833
13	3.064	0.23569231
14	3.264	0.23314286
15	3.482	0.23213333
16	3.617	0.226125
17	3.824	0.2248118
18	4.1	0.22777778
19	4.302	0.22642105

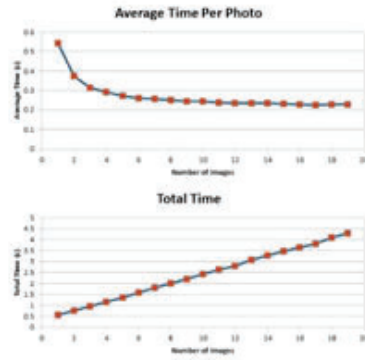


Figure 15: Time Charts for Pin/Gripper

with the new values, using the stored motor counts to compute the necessary distance the pin must travel to reach the new point. This application will allow scientists to easily calibrate the pin within the camera frame without traversing multiple screens.

D. ABBIX Beamlines: Pins in a Robot Gripper (AMX)

Computer vision can help assist users and scientists to the improper mounting of pins as they are picked up by a robotic gripper. This application was made to provide a detailed analysis of a robotic gripper picking up a pin and to report to the user if an anomaly has occurred, in order to prevent possible damage to the equipment or sample. The images for this application were provided by Jean Jakoncic, a beamline scientist for the Highly Automated Macromolecular Crystallography Beamline (AMX).

The purpose of this application is to find the pin and gripper region of interests (ROI), compare the apparatus to a set of 'perfect' templates, and to find kinks in order to check if the pin is properly mounted. The centroid is also discovered, along with the extreme points to provide assistance for alignment.

By thresholding the image and discovering the contours, the program can parse through the list of points and use logic checks to discover kink points along the contour. The points can be used to check for alignment if the pin and gripper are not entirely in the frame. Finally, template matching can quickly locate a bounding rectangle for the gripper and pin. The blue points are kink points, the red points are extrema, and the cyan point is the centroid. The red lines are vertical tangents, and the green line outlines the pin.

The program stabilizes around 0.227 seconds per image.

E. ABBIX Beamlines: Crystal Goniostat Rotational Alignment (AMX)

Crystal alignment in a goniostat is a time consuming process that can be handled by computer vision. At the AMX beamline, a crystal placed inside a loop rotates in a goniostat, with a full range of 360 degrees. The crystal is not centered so the crystal appears to wobble. The program processes images every 15 degrees for improved accuracy. By using an in range threshold, the only part of the image left is the crystal. With the background and extra noise eliminated by the thresholding, a contour can easily be found and a centroid can be plotted.

The contour and centroid for the crystal is discovered. By plotting the y coordinate of the centroid against the angle, a sine curve is generated. By using the least squares optimization procedure, the program finds the best fit sine curve to the given data. From the amplitude and phase of the best fit curve, the program can compute and send to EPICS the pin motor adjustments, allowing the motors to calibrate the crystal. The equation generated finds the best possible solution, with an amplitude and phase shift. Using certain formulas, the program can decompose the equation into the correct motor adjustments. MC stands for motor counts, and PEL stands for picture elements. MC/PEL is the conversion factor to convert pixel positions to actual measurements used for calibration. The total time taken for all 24 images was 0.858 seconds, with an average time per image of approximately 0.035

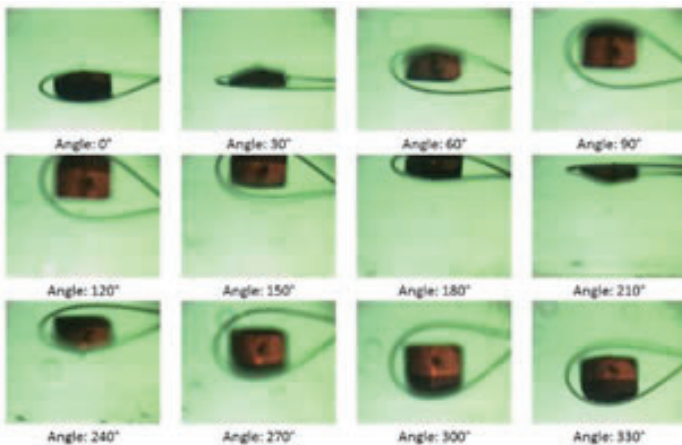


Figure 16: Crystal Images Every 30 Degrees

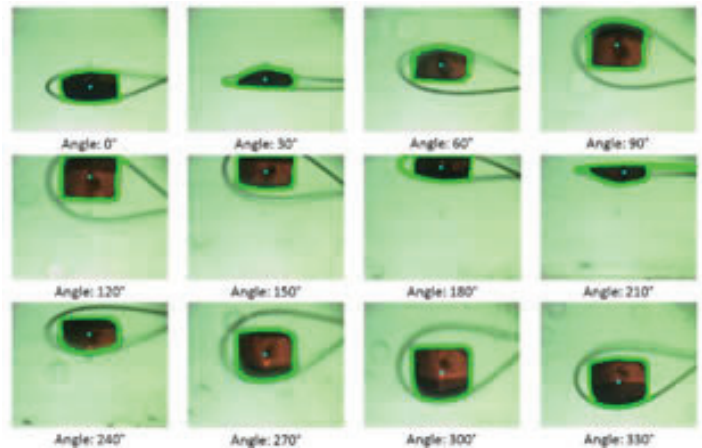


Figure 17: Results of Contouring, with Centroid Drawn

Figure 18:

Right: Graph generated

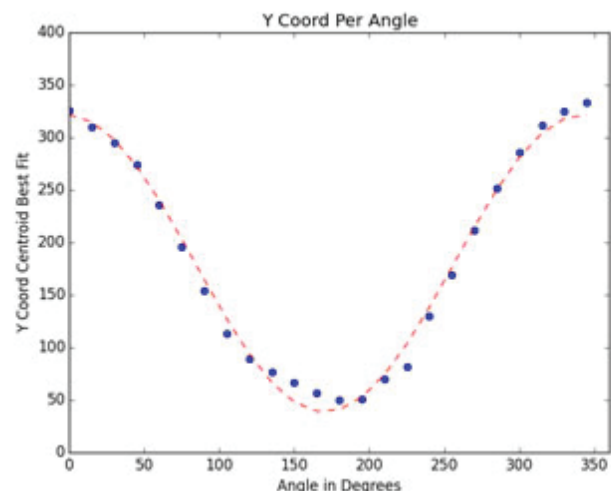
Equation:

$$141.58 \times \sin(\text{angle} + 1.61) + 180.19$$

Adjustment:

$$x = -\frac{MC}{PEL} \times \text{Amplitude} \times \sin(\text{phase})$$

$$x = -\frac{MC}{PEL} \times \text{Amplitude} \times \cos(\text{phase})$$



seconds. The optimized version of the loop centering program was deployed at the AMX beamline, and takes only 6 seconds to center the crystal loop. The time is limited by the motor rotational speed of the goniostat. This will be useful in the quick alignment of crystals and can be applied to all beamlines.

III. Conclusions

By building the infrastructure and general purpose wrapper libraries, beamlines can take full advantage of computationally efficient computer vision to help automate tedious processes along the beamlines. Computer vision can center samples in goniostats quickly. Programs can automate robotic movements and sample detection. Scientists can build applications to help with the assistance of alignment and calibration of samples, crystals, and beams along the beamlines. Users can discover and record data related to objects within an image. Programs can be developed to help prevent potential problems by alerting users of anomalies and mitigating damage to samples. With the integration of EPICS, and the newest version of OpenCV, this project integrates easily to the current systems installed on the beamlines and can efficiently fetch and interpret image data directly from the cameras along the beamline.

IV. Acknowledgements

This project was made possible by the support from my mentor Kazimierz Gofron. Images from the IXS Beamline are courtesy of Yong Cai, Alessandro Cunsolo, and Alexey Suvorov. Images from the ABBIX Beamline AMX are courtesy of Jean Jakoncic. This project was supported in part by the U.S. Department of Energy, Office of Science, Office of Workforce Development for Teachers and Scientists (WDTS) under the Science Undergraduate Laboratory Internships Program (SULI).

V. References

- ¹(Intel), Kay M. “Intel® Integrated Performance Primitives (Intel® IPP).” *Intel® Software*. Intel, 2016. Web. 09 Aug. 2016. <<https://software.intel.com/en-us/intel-ipp>>.
- ²Intel. “Threading Building Blocks.” *Threading Building Blocks*. Intel Corporation, 2016. Web. 09 Aug. 2016. <<https://www.threadingbuildingblocks.org/>>.
- ³Johnson, Andrew N. “EPICS - Experimental Physics and Industrial Control System.” *Argonne National Laboratory*. Argonne National Laboratory, 31 May 2016. Web. 9 Aug. 2016. <www.aps.anl.gov/epics/>.
- ⁴OpenCV Developer Team. “About OpenCV.” *OpenCV*. Itseez, 2016. Web. 9 Aug. 2016. <<http://opencv.org/about.html>>.
- ⁵Yong Cai, Alessandro Cunsolo, Alexey Suvorov. “IXS Schematic Diagram.” *Inelastic X-Ray Scattering Beamline (10-ID)*. National Synchrotron Light Source II, Brookhaven National Laboratory.

A numerical model of the transverse feedback system for the National Synchrotron Light Source II storage ring

Zechun Yang

Department of Physics, Auburn University, Auburn, AL 36849

Gabriele Bassi

Photon Science, Brookhaven National Laboratory, Upton, NY 11973

The basic algorithm to model the effect of the transverse feedback (TFB) system on synchrotron beam stability relies on a standard implementation of the TFB system diagnostics, in which electrostatic or strip-line pickups are used as beam position monitors (BPMs) to detect the position of the beam centroid, and strip-line kickers are used to kick the momentum of the beam in order to suppress any unstable bunch centroid motion (dipole instability). This is accomplished by imposing a specific phase advance relation between the pickup and the kicker. The implementation of the algorithm on the code SPACE (Self-consistent Parallel Algorithm for Collective Effects) is in progress. To mimic the experimental conditions, the kick induced on the bunch centroid at the kicker location requires the knowledge of the amplitude of the dipole motion at the pickup location. This is accomplished by calculating the average momentum of the bunch from the bunch centroid position at previous turns. The additional knowledge of the beta functions at the pick-up and kicker location, together with the desired damping time (200 μ s in the case of the TFB system of the National Synchrotron Light Source II (NSLS-II)), completely define the kick strength. This basic model can be extended to meet more realistic experimental conditions, via including perturbations due to noise in the experimental parameters.

I. INTRODUCTION

In this work, we have performed electron beam dynamics simulations to study effect of the Transverse feedback (TFB) system on the stability of the electron beam, thus on the stability of the radiation power delivered to the beamlines for experimental studies. The simulations have been done with the code for collective effects SPACE (Self-consistent Parallel Algorithm for Collective Effects), with parameters of the National Synchrotron Light Source-II (NSLS2) storage ring, which is located at the Brookhaven National Laboratory. We have focused on single bunch simulations, with collective effects model by short-range, broad-band wake fields, with parameters chosen to reproduce the experimental results. We have first simulated the longitudinal beam motion to study the effect of bunch lengthening and energy spread increase. We then simulated the longitudinal-transverse (synchrotron- betatron) motion of the electron beam, and studied the effectiveness of the TFB system with the new algorithm implemented in SPACE.

II. SYNCHROTRON POWER AND INSTABILITIES

A. Source of the synchrotron radiation and power

Synchrotron radiation is generated by an accelerated charge that is orbiting around the synchrotron ring. While the charged

particle is accelerating, the synchrotron radiation is emitted. By using Larmor's formula from classical electrodynamics, the synchrotron radiation power can be approximated by the equation

$$P = \frac{2}{3} \frac{e^2 c}{\rho^2} \beta^4 \gamma^4 \quad (1)$$

where e is the charge of electron, c is speed of light, ρ is the radius of the synchrotron ring, $\beta = v/c$ where v is the velocity of the electron and $\gamma = \frac{1}{\sqrt{1-\beta^2}}$. Also, from Larmor's formula, we are able to calculate the energy lost per turn due to radiation,

$$\delta E = \frac{2\pi\rho}{c\beta} P = \frac{4\pi}{3} \frac{e^2}{\rho} \beta^3 \gamma^4 \quad (2)$$

where δE is the energy lost per turn.¹ Thus, faster the electrons move, more radiation is emitted by the electrons. However, there are many difficulties to obtain a high intensity constant radiation output.

B. Radio frequency cavity and instabilities

As we have shown above, there is energy loss due to radiation. In order to keep a constant power output, the electrons have to gain the same amount of energy from an outside source. Those energies are compensated by the radio frequency (RF) cavity, which has been selected at a fixed frequency such that the electron will gain exactly the amount of energy that is lost due to synchrotron radiation².

However, when the electrons are moving, they will also generate electromagnetic fields, also called "wake fields", which act as a driving force causing the electron beam to oscillate, leading to potential beam instabilities. One of such occurrence is when the beams are accelerated by the RF cavity, and the high order modes (HOM) of the RF field couple with beam oscillations that the same frequency, which causes the instability to grow³.

Besides the RF cavity, there are some other physical mechanisms which may cause instabilities. Some examples are the wake field interaction with the resistive wall, which may lead to transverse instabilities, the beam interaction with objects in the vacuum chamber (such as vacuum pumps, beam position moni-

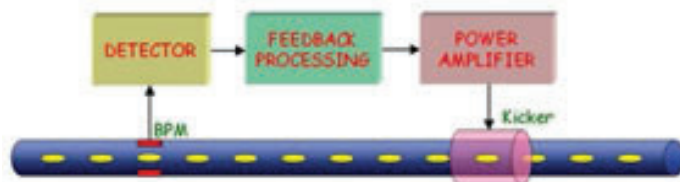


FIG. 1. Schematic view of a feedback system³

tors, etc.), the beam interaction with ions that are left in the vacuum chamber, and all other possible causes of instabilities³. Thus, due to the possible instabilities in the synchrotron radiation system, in order to achieve a constant output of synchrotron light, a feedback system, and its numerical modeling for a proper understanding of its effects, is a fundamental requirement.

III. TRANSVERSE FEEDBACK SYSTEM

As we saw in the previous section, a feedback system is a fundamental requirement in order to achieve a stable output of the synchrotron light. For NSLS-II, the transverse feedback system is required only in the transverse plane.

A. Design of the transverse feedback system

The goal of a feedback system is to suppress the oscillations of the electron beam which may cause instabilities. A schematic view of the feedback system is given in Fig. 1. The beam position monitor (BPM) measures the average position of the electron beam and acts the detector, the feedback processing is responsible to calculate the power that the kicker needs, the power amplifier supplies the power to the kicker, and the kicker produces an electromagnetic field to kick the beam in order to suppress the instability.³ For NSLS-II, the layout of the feedback system is shown in Fig. 2, which is a complex design. The NSLS-II TFB system is designed to provide a damping time as fast as 200 μ s to suppress transverse instabilities at the nominal current of 500mA.⁴ However, even though the design is complex and is hard to analyze from first principles, it is possible to simplify the analysis by assuming that the kick follows the following formula. Let $\langle x_n \rangle_p$ be the position of the beam at the n-th turn at the BMP position, and let k be the kick at the kicker. Then we may approximately say that

$$k = P_0 \langle x_n \rangle_p + P_1 \langle x_{n-1} \rangle_p + P_2 \langle x_{n-2} \rangle_p + P_3 \langle x_{n-3} \rangle_p. \quad (3)$$

In the next section, we will discuss a "kick" model we implemented in our algorithm of the TFB system.

B. A simple analysis of transverse feedback system with a linear model

Suppose we have an electron beam that is performing betatron oscillations with constant beta function, β_x . Let $\langle x_t \rangle$ be the average position and $\langle p_t \rangle$ be the average momentum of the particles at time t. Then we may write the equation of motion as following,

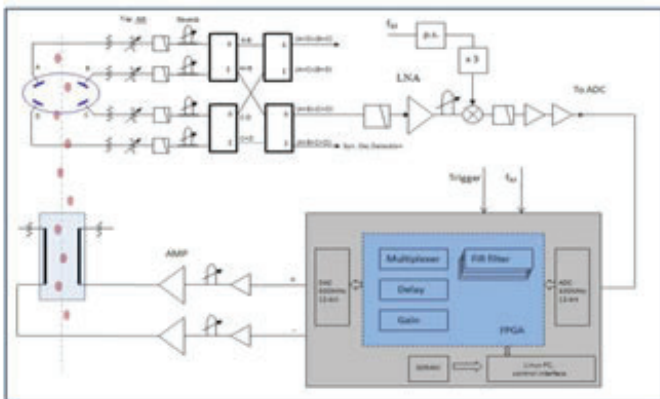


FIG. 2. Layout of the transverse feedback system for NSLS-II⁴

$$\langle x_t \rangle = \langle x_{t_0} \rangle \cos(\omega_\beta(t-t_0)) + \langle p_{t_0} \rangle \sin(\omega_\beta(t-t_0)), \quad (4)$$

and

$$\langle p_t \rangle = \langle p_{t_0} \rangle \cos(\omega_\beta(t-t_0)) - \langle x_{t_0} \rangle \sin(\omega_\beta(t-t_0)), \quad (5)$$

where $\langle p_{t_0} \rangle$ and $\langle x_{t_0} \rangle$ are constants, $\omega_\beta = c / \beta_x$, $\langle p_t \rangle = x' / \omega_\beta$, where ' stands for time derivative.⁵ However, since the synchrotron detectors record the beam position turn-by-turn, we use the number of turns n instead of time as independent variable. So, it will be worth to transform our equations into turn domain, and we will get

$$\langle x_m \rangle = \langle x_n \rangle \cos(2\pi\nu_x \Delta) + \langle p_n \rangle \sin(2\pi\nu_x \Delta), \quad (6)$$

and

$$\langle p_m \rangle = \langle p_n \rangle \cos(2\pi\nu_x \Delta) - \langle x_n \rangle \sin(2\pi\nu_x \Delta), \quad (7)$$

where $\langle x_m \rangle$ and $\langle p_m \rangle$ are the position and momentum at turn m respectively, $\Delta = m-n$ and ν_x is the betatron tune. Now, suppose the electron beam is performing harmonic oscillations around $(\langle x \rangle, \langle p \rangle) = (0, 0)$ in phase space, and let A be amplitude defined as

$$A^2 = \langle x \rangle^2 + \langle p \rangle^2. \quad (8)$$

Then A is constant during the harmonic oscillations, which means $A = A_{t_0}$. Further more, suppose that there is a kicker that kicks the beam at turn n with the kick k, and suppose that the kick is short enough in the time domain. Then the following equations hold,

$$\langle x_n \rangle^- = \langle x_n \rangle^+ \quad (9)$$

and

$$\langle p \rangle^- = \langle p \rangle^+ + k \quad (10)$$

where $\langle \rangle^-$ means before kicker and $\langle \rangle^+$ means after kicker. Thus, suppose that $k \ll 1$. Let A_k be the amplitude after the kick and A_p be the amplitude before the kick. We have

$$A_k = A_p + 2\langle p_n \rangle^- k + k^2 \approx A_p + 2\langle p_n \rangle^- k. \quad (11)$$

Let $\Delta A = A_k - A_p$. Then we have

$$\frac{\Delta A}{A} = \frac{2\langle p_n \rangle^- k}{A^2}. \quad (12)$$

Now, for simplicity, instead of using the kick given in equation (3), we use the following equation for the kick,

$$k = P_0 \langle x_n \rangle_p + P_1 \langle x_{n-1} \rangle_p, \quad (13)$$

where $\langle x_n \rangle_p$ is the average position of the particle at the pickup location during turn n, and P_0 and P_1 are constants. Now, let S be the distance between the pickup and the kicker and C be the circumference of the synchrotron ring. Then we can write

$$\langle p \rangle^- = \langle x_n \rangle_p \cos \Delta\phi + \langle p_n \rangle_p \sin \Delta\phi, \quad (14)$$

where $\Delta\phi = 2\pi\nu_x S / C$ and $\langle p_n \rangle_p$ is the average momentum of the particle at the pickup location during turn n. Now, from equation (6) and (7), we know that

$$\langle x_{n-1} \rangle_p = \langle x_n \rangle_p \cos(2\pi\nu_x) - \langle p_n \rangle_p \sin(2\pi\nu_x), \quad (15)$$

and by using equation (8), we can write $\langle\langle x_n \rangle_p\rangle$ and $\langle\langle p_n \rangle\rangle$ in polar coordinates, such that

$$\langle x_n \rangle_p = A \cos \theta \quad (16)$$

and

$$\langle p_n \rangle_p = A \sin \theta. \quad (17)$$

Then, by taking the average over all possible angles in equation (12), we have

$$\begin{aligned} \left\langle \frac{\Delta A}{A} \right\rangle_\theta &= \left\langle \frac{2 \langle p_n \rangle^- k}{A^2} \right\rangle_\theta \\ &= \left\langle \frac{2(\langle x_n \rangle_p \cos \Delta\varphi + \langle p_n \rangle_p \sin \Delta\varphi)k}{A^2} \right\rangle_\theta \\ &= \left\langle \frac{2(\langle x_n \rangle_p \cos \Delta\varphi + \langle p_n \rangle_p \sin \Delta\varphi)(P_0 \langle x_n \rangle_p + P_1 \langle x_{n-1} \rangle_p)}{A^2} \right\rangle_\theta \end{aligned}$$

Now, by using equation (14), (16), (17), and the definition of average, we have

$$\begin{aligned} \left\langle \frac{\Delta A}{A} \right\rangle_\theta &= \frac{1}{2\pi} \int_0^{2\pi} \frac{2(A \cos \theta \cos \Delta\varphi + A \sin \theta \sin \Delta\varphi)}{A^2} \\ &\quad \times (P_0 A \cos \theta + P_1 (\langle x_n \rangle_p \cos(2\pi\nu_x) + \langle p_n \rangle_p \sin(2\pi\nu_x))) d\theta \\ &= \frac{1}{2\pi} \int_0^{2\pi} \frac{2(\cos \theta \cos \Delta\varphi + \sin \theta \sin \Delta\varphi)}{A} \\ &\quad \times (P_0 A \cos \theta + P_1 (A \cos \theta \cos(2\pi\nu_x) - A \sin \theta \sin(2\pi\nu_x))) d\theta \\ &= \frac{1}{2\pi} \int_0^{2\pi} 2(\cos \theta \cos \Delta\varphi + \sin \theta \sin \Delta\varphi) \\ &\quad \times (P_0 \cos \theta + P_1 (\cos \theta \cos(2\pi\nu_x) - \sin \theta \sin(2\pi\nu_x))) d\theta \\ &= \frac{1}{2} (P_0 \cos \theta + P_1 \cos(\Delta\varphi - 2\pi\nu_x)). \end{aligned}$$

Now, in order to achieve exponential damping, let

$$-\frac{1}{\tau} = \left\langle \frac{\Delta A}{A} \right\rangle_\theta = \frac{1}{2} (P_0 \cos \theta + P_1 \cos(\Delta\varphi - 2\pi\nu_x)),$$

where τ is the damping time constant. Thus we have obtained one of the conditions that P_0 and P_1 must satisfy. Besides the condition given by equation (18), we impose the condition that when $\langle x_n \rangle_p = \langle x_{n-1} \rangle_p$ the kick has to be zero, i.e.

$$\begin{aligned} 0 &= k \\ &= P_0 \langle x_n \rangle_p + P_1 \langle x_{n-1} \rangle_p \\ &= (P_0 + P_1) \langle x_n \rangle_p. \end{aligned}$$

Therefore,

$$P_0 + P_1 = 0. \quad (19)$$

Thus, the two conditions given by equation (18) and (19) allow the analytical computation of P_0 and P_1 , that is

$$P_0 = -\frac{2}{\tau(\cos \Delta\varphi - \cos(\Delta\varphi - 2\pi\nu_x))} \quad (20)$$

and

$$P_1 = -P_0. \quad (21)$$

IV. SPACE CODE AND NUMERICAL SIMULATIONS

SPACE is a code for beam dynamic simulations. It solves a system of Vlasov-Fokker-Planck equations to simulate the

beam dynamics⁶. For this project, we have used the SPACE code to compute the time evolution of a single electron beam in the NSLS-II storage ring with parameters listed in Fig. 3. We did simulations without the TFB system first, then we added our TFB system model second. In the simulations we used broad-band resonators to model the short range wake field effects, with longitudinal shunt impedance $R_{sh,x} = 15 - 18k\Omega$, frequency $f_{rx} = 25\text{GHz}$, and quality factor $Q = 1$, and transverse shunt impedance $R_{sh,y} = 0.9 - 1.0M\Omega$, frequency $f_{ry} = 22\text{GHz}$, and quality factor $Q = 1$.

A. Longitudinal Case

We have first studied the longitudinal case with the above parameters. We computed the bunch length and energy spread of the bare lattice model with SPACE. The turn by turn data of bunch length are shown in Fig. 4, and the maximum, minimum, and average of the bunch length are shown in Fig. 5. According to the microwave instability theory⁷, we expect the energy spread to increase at a certain current threshold, below which only the bunch length increases. Below the microwave instability threshold the Vlasov-Fokker-Planck equation admits a stationary (time independent) solution (called Haissinski solution), thus constant values of the bunch length and energy spread after a certain transient. As we can see, the instability threshold is between 0.3-0.4mA as the bunch length of the beam is starting to oscillate instead of being stabilized. The turn by turn data for the energy spread are shown in Fig. 6, and the maximum, minimum, and average of the energy spread are shown in Fig. 7. As we can see in the results, the energy spread calculation agrees with the bunch, length calculation, showing the same threshold around 0.3-0.4mA.

B. Transverse Case

For the transverse case, we have compared our simulations with SPACE to the measurements performed at NSLS-II. The measurements have been done by A. Blednykh et al.⁸, and are shown in Fig. 8. As we can see in the plot, we have a close agreement between the measurements of the experiment and our simulation. As one may notice in the experimental explanation in the next section.

NSLS-II Storage Ring Parameters (Bare Lattice)

Parameter	Symbol	Value	Unit
Beam energy	E_0	3	GeV
Circumference	C	791.9581	m
Revolution period	T_0	2.64	μs
RF Voltage	V_{RF}	1.86	MV
Energy loss per turn	U_s	288	keV
Momentum compaction	η	3.7×10^{-4}	
Synchrotron tune	ν_s	0.007	
Horiz. average beta-function	β_x	7.7	m
Vert. average beta-function	β_y	3.8	m
Bunch length	σ_τ	11	ps
Long. radiation damping	τ_s	27	ms
Transv. radiation damping	τ_x	54	ms

FIG. 3. NSLS-II storage ring parameters for numerical simulations.

V. SIMULATION OF TRANSVERSE FEEDBACK SYSTEM

For our model of the TFB system, we used the kick from equation (13), where the coefficients are set according to equation (20) and (21). We have set the damping time constant $\tau = 200\mu\text{s}$. We also kicked the beam at the 5000th turn, to induce betatron oscillations in order to enhance the effect to see.

In Fig. 9, we show the spectrum of the transverse motion, which is the discrete-time Fourier transform of the average position, $\langle x \rangle$. As one may see, the spectra without the TFB system is the same as the one in Fig. 8. However, once the feedback system is on, the transverse motion had been dumped extremely quickly. The spectra with the TFB system on have been multiplied 20 times for comparison with the spectra without the TFB system. So, we will not be able to see anything on the right figure if the two plots were on the same scale.

In Fig. 10, we show the bunch size of the transverse motion, which is the standard deviation of the positions of the particles. As we can see in the left frame, which is the one without the TFB system, the bunch size increases as the current increases. This also could be a possible explanation of the anomaly in the measurement data on Fig. 8, which is that at such high current, the bunch size is getting bigger, and the storage ring could not accumulate more electron beam anymore. Also, once we have the TFB on,

the bunch sizes are no longer increasing as the current increases, which means we may be able to exceed the accumulation threshold seen in the measurements with our TFB system. However, as one may notice, at current above 0.7mA, there was no increasing in the bunch size without TFB system, but when the TFB system is on, there is an unexpected increase in the bunch size. Further studies are needed to understand this case.

In Fig. 11, we show the average amplitude of the particles as we defined in equation (8). As we can see, without the TFB system, the amplitude of the electron beam is increasing as the current increases until 0.7mA. With TFB system on, the amplitude did not increase until 0.7mA, too. The reason why this effect happens at 0.7mA requires further studies in order to be understood. Also, at 5000th turn, one can see a pick, which is caused by the kick we applied, that has been almost damped immediately by our TFB system.

VI. CONCLUSION AND FUTURE PLANS

As we have shown in the previews sections, we have developed a model for the TFB system. In the numerical model, we have seen the effects due to the feedback system. We have shown that the TFB system is able to stabilize the electron beam and it is able to help us to achieve a stable output of the synchrotron radiation. However, there are also many parts of the model that

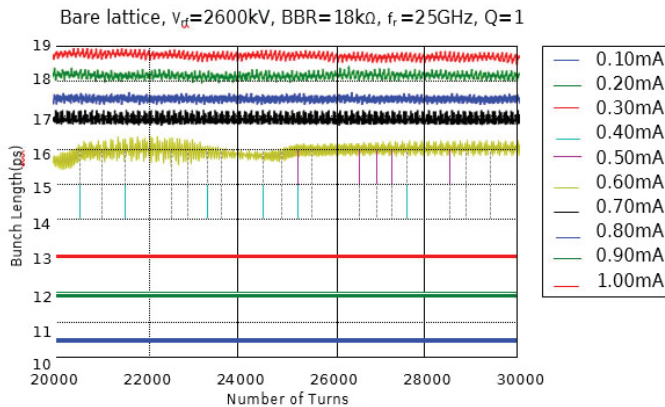


FIG. 4. The turn by turn data of the bunch length for the bare lattice.

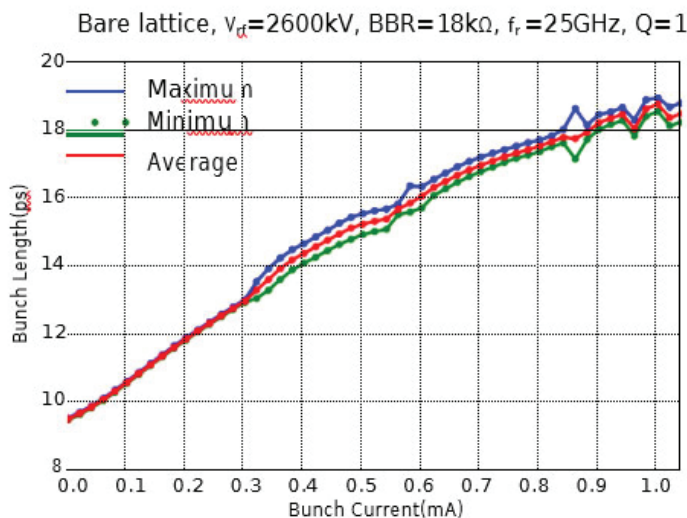


FIG. 5. The maximum, minimum, and average of the electron beam length as a function of current

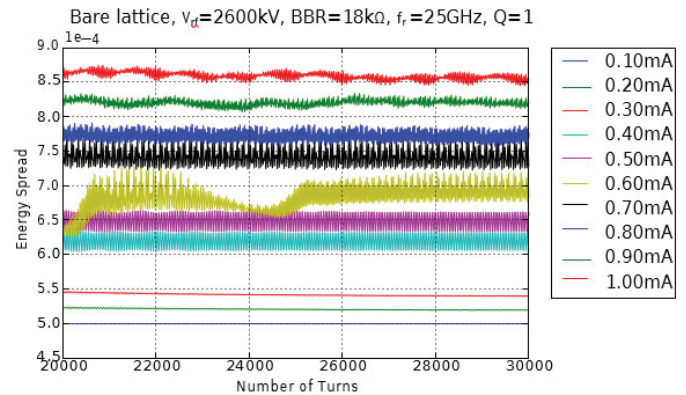


FIG. 6. The turn by turn data of the energy spread for the bare lattice

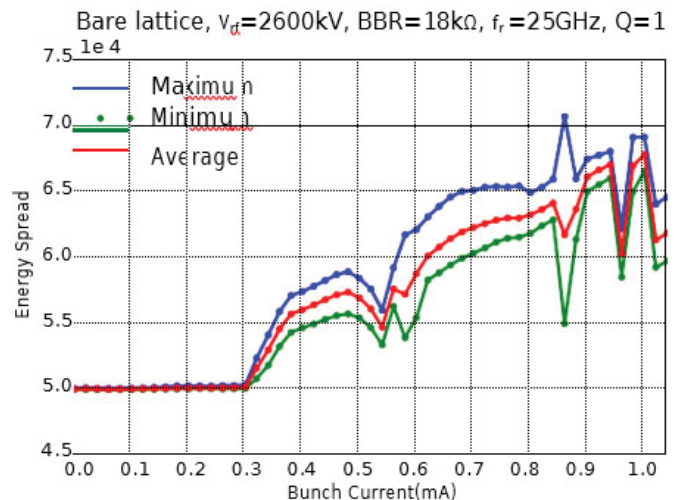


FIG. 7. The maximum, minimum, and average of the electron energy spread as a function of current

need further development to understand unexplained phenomena such as the unusual behavior of the beam at current above 0.7mA, that was shown in Fig. 10 and 11, to study the tune shift due to the transverse feedback system, and to investigate effects due to noise.

VII. ACKNOWLEDGEMENTS

This project was supported in part by the U.S. Department of Energy, Office of Science, Office of Workforce Development for Teachers and Scientists (WDTS) under the Science Undergraduate Laboratory Internships Program (SULI).

VIII. REFERENCES

- ¹J. D. Jackson, Classical Electrodynamics (John Wiley & Sons, Inc., Hoboken, NJ, 1999).
- ²D. Teytelman, Architectures and Algorithms for Control and Diagnostic of Coupled-bunch Instabilities in Circular Accelerators, Ph.D. thesis, Stanford University (2003).
- ³M. Lonza and H. Schmickler, "Multi-bunch Feedback Systems," in CAS - CERN Accelerator School: Advanced Accelerator Physics Course: Trondheim, Norway, August 18-29, 2013 (2014) pp. 503–546, arXiv:1601.05258 [physics.acc-ph].
- ⁴W. Cheng, "NSLS2 transverse feedback system design,".
- ⁵H. Wiedemann, Particle Accelerator Physics (Springer, 1993).
- ⁶G. Bassi, A. Blednykh, and V. Smaluk, "Self-consistent simulations and analysis of the coupled-bunch instability for arbitrary multibunch configurations," Phys. Rev. Accel. Beams 19, 024401 (2016).
- ⁷A. Chao, Physics of Collective Beam Instabilities in High Energy Accelerators (John Wiley & Sons, Inc., New York, NY, 1993).
- ⁸A. Blednykh et al., "NSLS-II Commissioning with 500 MHz 7-CELL PETRA-III Cavity," in Proceedings, 5th International Particle Accelerator Conference (IPAC 2014) (2014) p. TUPRI069.

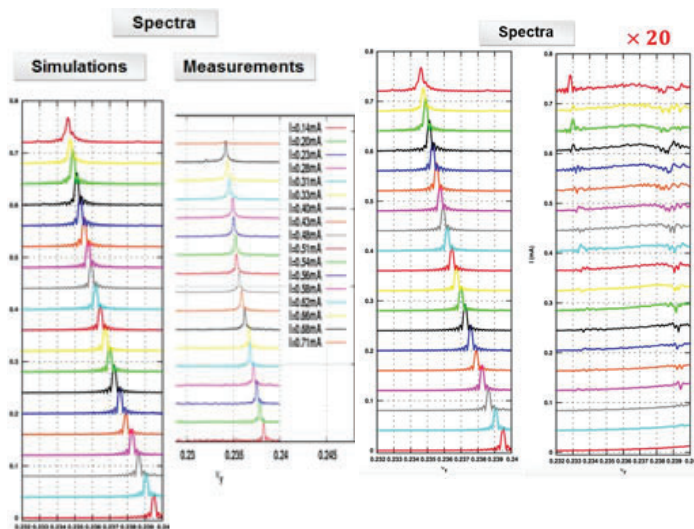


FIG. 8. The tune calculation and measurement. The measurement are from A. Blednykh et al⁸

FIG. 9. The spectra of the transverse motion at different single bunch current: left frame is without transverse feedback system and right frame is with transverse feedback system.

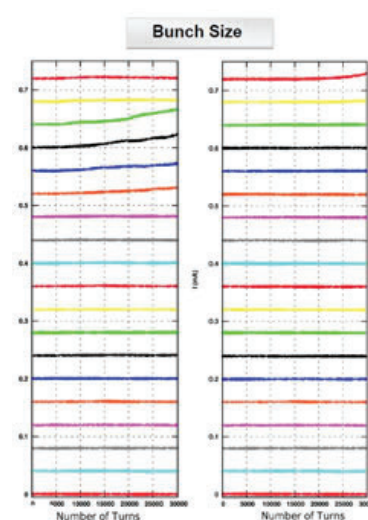


FIG. 10. The bunch size of the transverse motion: left frame is without transverse feedback system and right frame is with transverse feedback system.

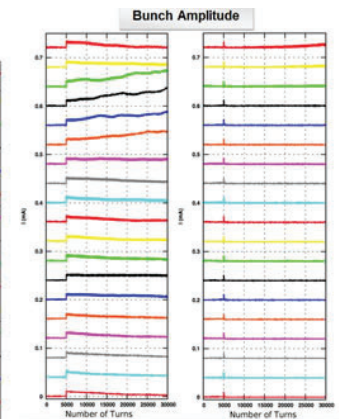


FIG. 11. The amplitude of the transverse motion: left frame is without transverse feedback system and right frame is with transverse feedback system.

Charge transfer efficiency of charge-coupled devices for the Large Synoptic Survey Telescope

Daniel Yates

Physics Department, Pacific University, Forest Grove, OR, 97116 Andrei Nomerotski

Physics Department, Brookhaven National Laboratory, Upton, NY, 11973

ABSTRACT:

The Large Synoptic Survey Telescope (LSST), currently under construction in Chile, is a large survey telescope that, upon completion, will conduct a ten-year survey in the search for dark energy and dark matter. The U. S. Department of Energy and Brookhaven National Laboratory (BNL) are participants in the construction of LSST, with BNL's Physics and Instrumentation Divisions being responsible for the construction of the telescope's digital sensor array. Consisting of 21 rafts of 9 charge-coupled devices (CCDs) each, the camera focal plane will contain 3.2 gigapixels, giving 3 gigabytes of raw data every second. These CCD sensor arrays require a very high ratio of charge transferred between pixels, referred to as the charge transfer efficiency (CTE). Typical CTE values on the order of 0.999999 or better are required to ensure accurate imaging. Our focus is on analysis methods to accurately determine CTE values of the detectors to ensure they meet stringent LSST standards. We are using ROOT within Python to determine how flux and ellipticity change as a function of number of pixel transfers for data taken with ^{55}Fe x-ray hits and comparing them to Monte Carlo simulations. Currently, we are achieving CTE values consistent with CTE values required by LSST. We also see that the difference in flux between the trailing and leading pixels (dFlux) in an x-ray hit increases linearly with the number of transfers and exponentially with varying CTE values.

I. INTRODUCTION

A. Large Synoptic Survey Telescope

The Large Synoptic Survey Telescope (LSST) will be one of the largest optical telescopes ever create. Upon completion, LSST will conduct a ten-year survey of the night sky in order to increase our understanding of dark energy and dark matter, as well as the structure of both our own solar system and the Milky Way Galaxy. LSST will utilize a unique three-mirror design that will give it a 3.5° field of view. In order to map this large of an area, LSST will use the largest camera ever created. The 64cm digital sensor array within the camera will consist of 21 rafts of 9 charge-coupled devices (CCDs) each, giving the focal plane a total of 3.2 gigapixels.^[1]

B. Charge-coupled Devices

CCDs have wide ranging applications; from the camera on a cell phone to the focal planes on large telescopes like the Hubble Space Telescope, CCDs have extreme importance in science and technology. The CCD works on the premise of transferring charge packets of electrons between pixels to eventually be read out by amplifiers. Light incident on the CCD creates electrons within each pixel via the photoelectric effect; these electrons are then captured within a potential well created in the CCD. After an exposure, the charge packets are transferred pixel by pixel down the column until eventually reaching the serial amplifier for readout.

Figure 1 depicts the transfer of a charge packet between pixels in a CCD. The charge transfer efficiency (CTE) is the ratio of charges transferred between pixels, and a high CTE value is required to ensure accurate readout after thousands of pixel transfers. While a CTE value of 0.999 (99.9%) may seem like a very good efficiency, after 500 transfers only 60.6% of the initial charge will have been transferred correctly. Typical CTE values for CCDs are on the order of 10^{-6} or better to ensure survival of the charge packet across thousands of transfers. The charge transfer inefficiency (CTI) is also used to express efficiency of CCDs. It is the ratio of charge that is not transferred to the total charge; thus, the CTE and CTI must sum to one.^[2]

^{55}Fe X-rays Soft x-rays are a common source used to analyze properties of the CCD, especially CTE. ^{55}Fe is a widely used source for characterizing CTE values of CCDs. Upon the quantum mechanical absorption of a K-shell electron into the nucleus, ^{55}Fe decays into a manganese atom; an x-ray is then emitted when an electron drops from an outer shell to fill in the K-shell gap. The 5.9 keV $K\alpha$ x-ray and 6.5 keV $K\beta$ x-ray are known to deposit 1620 and 1778 e^- in the silicon of the CCD, respectively, with other spectral lines occurring due to Auger effects in the CCD. These well-known spectral lines allow calibration of CCDs from an ^{55}Fe source and can be used to determine CTE and hit structure.^[2]

II. METHODS

A. Footprint Finding

Determining CCD characteristics such as the CTE and ellipticity of hits requires first identification of the hits via our footprint finding algorithm. The coding requires input parameters to determine what constitutes a hit. A minimum threshold for flux and number of adjacent pixels above the input threshold are first used to determine whether or not pixels signal an x-ray hit. Once a hit has been signaled, the footprint finder then extends by the growth factor on each side of the pixels to create a stamp encompassing the x-ray hit. Figure 2 shows an example of x-ray hits and a stamp taken around one hit. In addition, the initial footprint finding also calculates general image information like background noise and standard deviation of pixel fluxes.

Once a stamp is created for a given footprint, centroid coordinates of the hit are extracted from the stamp and input as fitting parameters into the ngmix fitting program.^[4] The fitter takes the centroid inputs, as well as guesses for ellipticity of the hit, and fits a 2-dimensional Gaussian onto the hit in order to extract values for flux, spread, ellipticity, and more accurate coordinates of the centroid of the hit. Furthermore, flux values for individual pixels within the footprint are calculated by the fitter, which can be used to analyze the development of the hit as it transfers hundreds of times across the CCD.

As mentioned, the initial footprint finding program requires four different fitting parameters in order to determine what constitutes a hit: threshold, grow, minimum pixel number (npixMin), and isotropy. Our first task was to determine optimal fitting pa-

rameters to ensure the footprint finder locates any and all x-ray hits with minimal virtual hits. The isotropy parameter was set at true, as the x-rays will create symmetric hits within the silicon of the CCD. We decided to let the threshold vary throughout the tests so that we could determine how many footprints were found as a function of the threshold. Knowing that initially the program calculates the standard deviation of the image taking into account the background noise of the detector (stdevclip), we decided to let the threshold sweep across integer multiples of the stdevclip as we tested the other two footprint finding parameters. To determine how the other factors affected the number of located footprints, the grow parameter was varied between 0 and 4, and the npixMin factor was varied from 1 to 4. By varying the threshold from 2 to 100 times the stdevclip, we were able to quantify how the number of found footprints at a given threshold was affected by the grow and npixMin parameters.

B. ⁵⁵Fe Flux Analysis

The next step in the analysis method was to analyze ⁵⁵Fe data taken a CCD in an attempt to determine the CTE values for the different section of the detector. In order to do this, we decided to divide each section of the detector into eleven bins of 182 pixels each and plot the average flux of the footprints within each bin. Because every footprint should deposit one of two amounts of charge within the CCD, each footprint should have the same amount of total flux. By examining how the average flux of a footprint changes across the detector bins we can determine the efficiency of the charge transfers within a section of the detector.

In order to accomplish this, the footprint finding analysis code was modified in order to allow different sections and bins of the detector to be analyzed individually rather than as just one collection of footprints for the entire detector. First, footprints were sorted into one of the eleven bins in each detector depending upon which pixel the centroid of the hit was located in. The flux associated with each footprint was filled into a histogram of the flux for a given bin. We fit the $K\alpha$ peak with a Gaussian curve to determine the average flux associated with each bin (figure 3), and then plotted the average bin flux vs. bin number for each section of the CCD.

Once the slope of the graph of flux vs. bin number is obtained, simple conversion factors of 182 pixels/bin and $3.8 \text{ e}^-/\text{ADU}$ can be used to obtain the change in electrons per pixel from the slope. This change in electrons per pixel is the CTI for that section of the detector, from which the CTE value is easily obtained.

C. Toy Monte Carlo

The final step of this research was creating a Toy Monte Carlo (TMC) simulation that could be used to determine how the footprints change as a function of transfers and CTE. Preexisting TMC code used parameters such as the flux, flux spread, pixel location, and shear inputs to create a virtual x-ray hit within a CCD. The TMC coding was then modified to transfer the flux between the pixels with a known CTE value, thus allowing us to simulate the transfer of charge that will occur within a CCD. By simulating the transfer of charge packets, we were able to track the evolution of the footprints as a function of number of transfers and CTE. Specifically, we looked at the quantity dflux— defined as the flux in the trailing pixel minus the flux in the leading pixel—to see how it changes as the number of transfers increase (figure 4).

III. RESULTS

A. Footprint Finding

The footprint finding analysis confirmed that the previously used grow factor was adequate for the cluster finding needed on the CCDs. Figure 5 shows the number of found footprints as a function of the threshold for grow factors 0-4. As was expected, the number of located footprints falls off as the threshold increases, as more and more pixels get screened out. Furthermore, the number of footprints identified decreases with the grow factor rather than increasing with it. This is due to the fact that larger grow factors will contribute to two footprints getting merged into one and thus being falsely identified as merely one footprint, as shown in figure 6. A grow factor of 2 had been used previously, and our analysis seems to confirm that this is a good medium, as we aren't yet into the region where significant overlap of x-ray footprints occurs like with grow factors of 3 or 4. Although a grow factor of 0 gives the most found footprints, a larger grow factor is needed for analysis to ensure that we capture every pixel containing charge as a result of the x-ray hit. Pixels adjacent to the hit may have acquired some charge as a result of the hit but don't have enough to trigger a flux above the given threshold; by having a grow factor of 2 applied, we ensure that all of the pixels containing charge from the hit are accounted for in further data analysis.

In analyzing the minimum pixel number (npixMin) required to trigger a footprint, we found one interesting result. As expected, the number of found footprints decreased with an increase in npixMin, as more adjacent pixels above the given threshold is less likely and requires a hit near the intersection of four pixels to ensure that they all meet the threshold required by the footprint finding algorithm. However, with npixMin equaling one, an increasing threshold doesn't immediately lead to a drop off in located footprints, as is the case with higher npixMin values (figure 7). In fact, there is a substantial region of threshold values where the number of found footprints is consistent. The average number of footprints found in the range of 20-70 times stdevclip is 31,338 with a standard deviation of 255 footprints. The use of npixMin equaling 1 gives us much more flexibility in the threshold parameter needed for the footprint-finding program.

B. ⁵⁵Fe Flux Analysis

For the ⁵⁵Fe analysis, we specifically looked at data from a single CCD, the e2v- 113-03 sensor. As described, by analyzing the average flux in different sections of the CCD and how it changes across the sections, we can determine the CTE value for each section of the CCD. Our analysis method gave CTE values that are on the order of 10^{-7} or better, which is consistent with expected CTE values for CCDs nowadays. Furthermore, the data was analyzed with a program used by Ivan Kotov (BNL Instrumentation Division) to determine CTE values for the detector. A comparison of CTE values for the two analysis methods is shown in figure 8. There was good agreement between the two methods, with an average percent difference of $2.6 \times 10^{-5} \%$ between calculated CTE values for the two different analysis methods.

C. Toy Monte Carlo

Finally, the TMC simulations let us examine the evolution of the x-ray hit footprints as they transfer between pixels. By running the simulations at varying CTE values, we were able to get a relationship between dFlux (trailing pixel flux minus leading

pixel flux), number of transfers, and CTE. Figure 9 shows a plot of dFlux versus the number of transfers.

The interesting result from figure 9 is the sinusoidal nature of the plot for low CTE values. While we did not expect this result, it can be explained fairly easily: with low CTE values, much of the charge packet in the center pixel will be left behind and acquired by the trailing pixel. Over dozens of transfers, this will result in the trailing pixel gaining flux while the leading pixel doesn't acquire any, leading to larger dFlux values. This will continue to occur until the flux in the trailing pixel exceeds the flux in the center pixel, at which point the trailing pixel will be triggered as the center pixel, and the gap in dFlux will diminish as more transfers occur around the new center pixel.

Seeing as the sinusoidal curves occur at low CTE values, we can ignore them in the analysis, as those CTE values are unrealistic for modern CCDs that will be used for LSST. As seen in figure 10, the higher CTE values indeed show a linear relationship between dFlux and the number of transfers (Ntransfers). By extracting the slope of these plots and then plotting CTE vs. slope, we can determine a relationship between CTE and the slope of the plot of dFlux vs Ntransfers. Figure 11 shows a plot (log-log) of CTI vs. slope, and we see that there is indeed the expected exponential relationship between the two.

IV. CONCLUSIONS

Analysis of the e2v-113-03 CCD sensor shows CTE values consistent with what is expected. After optimizations of the footprint finding coding showed that a value of 1 for npixMin was optimal, we were able to determine CTE values for each section of the detector that are consistent with efficiency values of modern day detectors and other analysis methods for the dataset. Toy Monte Carlo results show an exponential relationship between CTE and the slope of dFlux vs. Ntransfers, indicating that CTE could be determined by the evolution of an x-ray footprint as it is transferred across the CCD. Moving forward, modifications to the Toy Monte Carlo coding are needed in hopes of determining the most accurate measurement that can be used to determine the CTE of a CCD.

V. ACKNOWLEDGEMENTS

This project was supported in part by the U.S. Department of Energy, Office of Science, Office of Workforce Development for Teachers and Scientists (WDTS) under the Science Undergraduate Laboratory Internships Program (SULI).

I wish to thank Ivan Kotov and Paul O'Connor for the ⁵⁵Fe data sets, Erin Sheldon and Merlin Fisher-Levine for their analysis code, Hyeyun Park for assistance with the analysis code, and Andrei Nomerotski for mentoring me this summer.

VI. REFERENCES

- ¹ *The Large Synoptic Survey Telescope*. www.lsst.org.N.p., 2016. Web. 8 Aug. 2016.
- ² James R. Janesick, *Scientific Charge-coupled Devices*, 1st Ed. (SPIE, Bellingham, WA, 2001).
- ³ Agarwal, Tarun. *Working Of Charge Coupled Device*. 2016. Web. 8 Aug. 2016.
- ⁴ Sheldon, Erin. "Esheldon/Ngmix". *GitHub*. N.p., 2016. Web. 7 Aug. 2016.

VII. Appendix

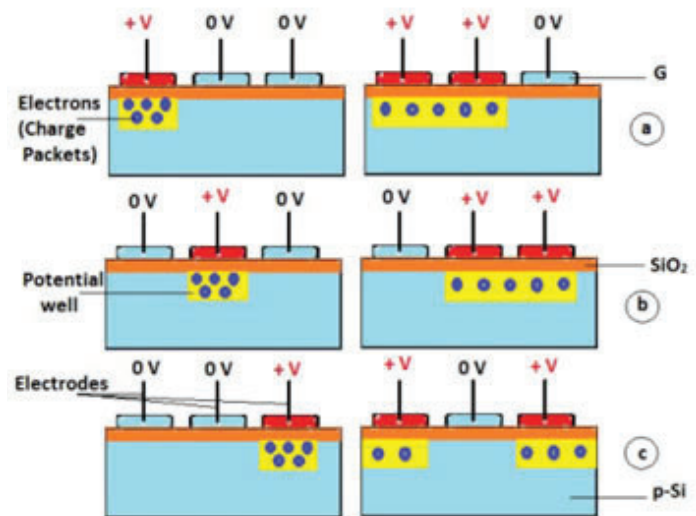


Figure 1. Depiction of charge packet transfer within CCD.^[1]

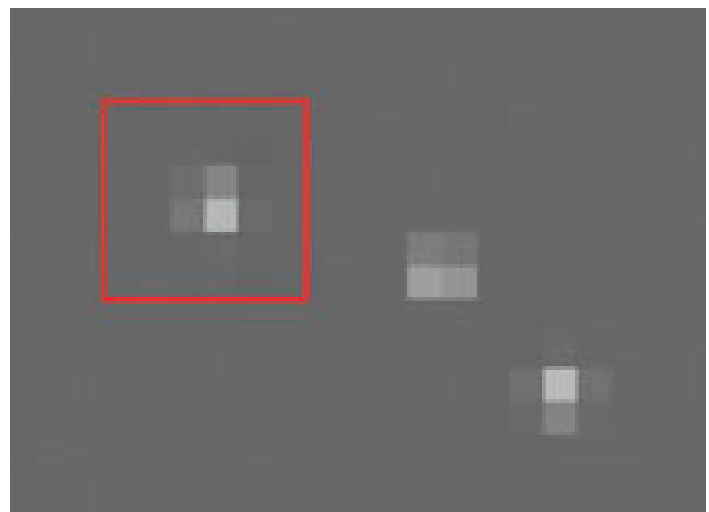


Figure 2. Example of x-ray hits on CCD, with grow factor of 2 around the left hit.

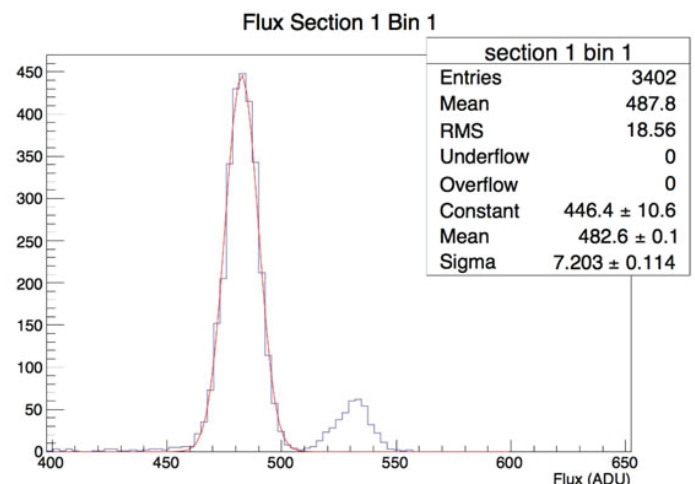


Figure 3. Histogram of flux in one bin of one detector section. Histogram shows both K α and K β peaks, with a Gaussian fit on the K α peak.



Figure 4. Example of trailing and leading pixels in x-ray hit on CCD.

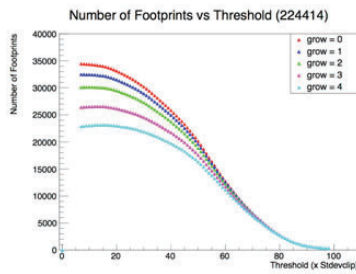


Figure 5. Varying grow factors on footprint finding coding for ⁵⁵Fe data.



Figure 6. Example of two separate footprints with a grow factor of 1 (left), and the footprints merging into one footprint when a grow factor of 3 is applied (see figure 7).

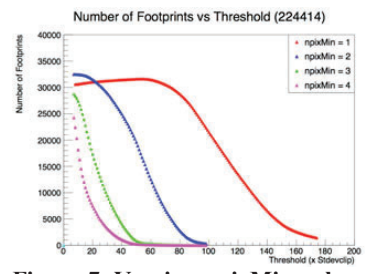


Figure 7. Varying npixMin values for footprint finding coding.

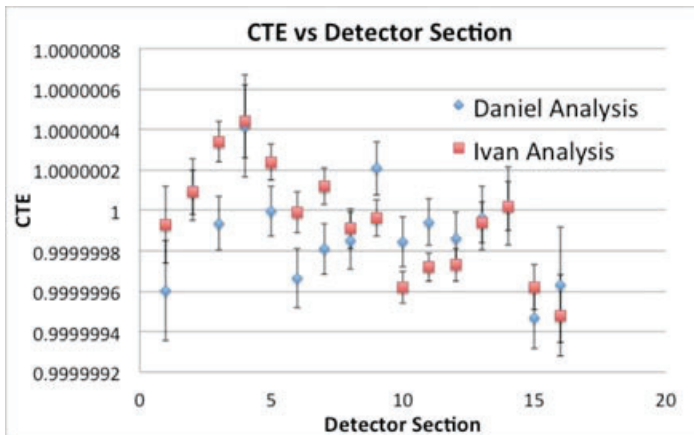


Figure 8. Comparison of calculated CTE values for sections of e2v-113-03 detector data.

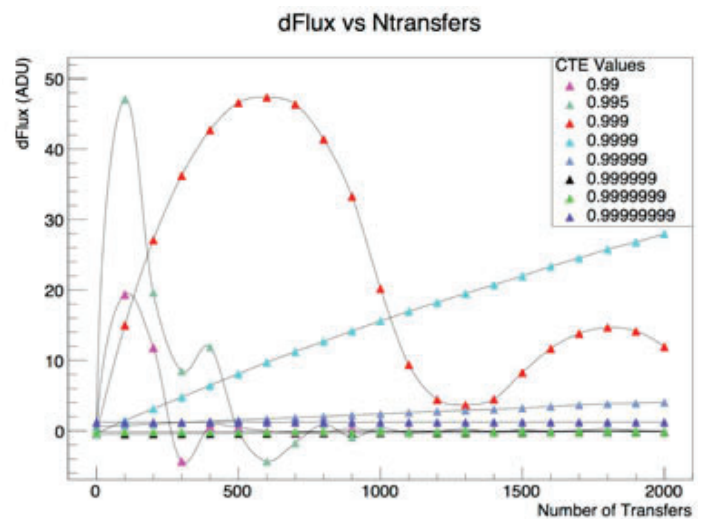


Figure 9. Plot of dFlux vs .Ntransfers for varying CTE values.

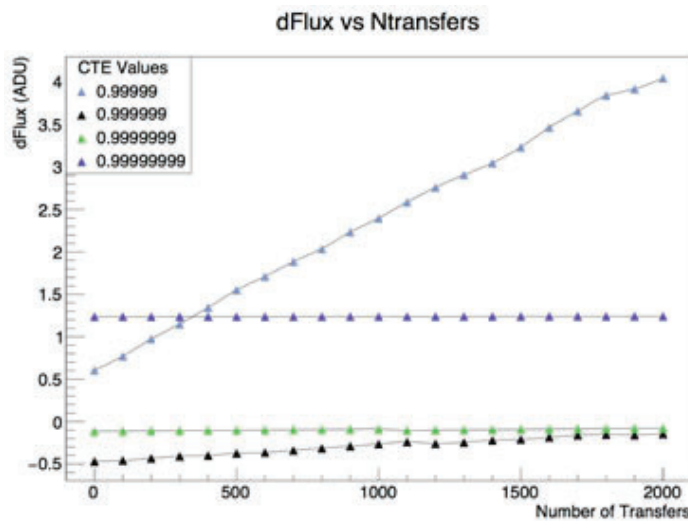


Figure 10. Plot of dFlux vs Ntransfers for high CTE values.

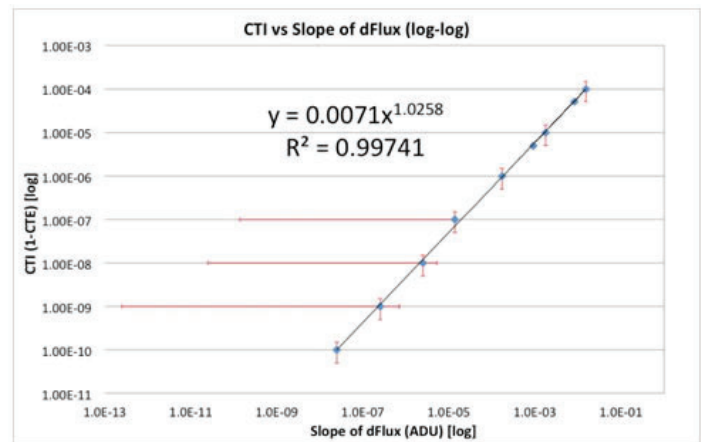


Figure 11. Log-log plot of CTI vs. slope (of dFlux vs Ntransfers) for Toy Monte Carlo simulations with trendline fit.